

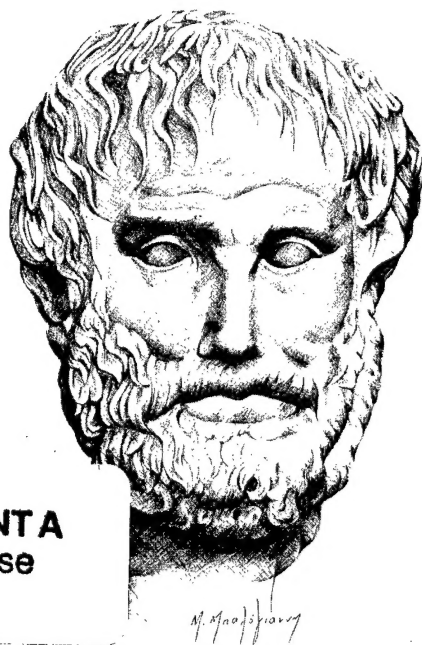
HELLENIC SOCIETY OF THEORETICAL
AND APPLIED MECHANICS (HSTAM)

ARISTOTLE UNIVERSITY
OF THESSALONIKI (AUTH)

6th NATIONAL CONGRESS OF MECHANICS

PROCEEDINGS VOLUME II

EDITORS
E.C.AIFANTIS
A.N.KOUNADIS



DISTRIBUTION STATEMENT A
Approved for Public Release
Distribution Unlimited

20020125 230

*Dedicated to the memory
of P.S.Theocaris*

THESSALONIKI,
JULY 19-21, 2001

6th National Congress of Mechanics

Thessaloniki, 19-21 July 2001

Hellenic Society of Theoretical and Applied Mechanics (HSTAM)

Aristotle University of Thessaloniki (AUT)

PROCEEDINGS

Volume II

Thursday 19 July 2001

Editors: *E. C. Aifantis* and *A. N. Kounadis*

Dedicated to the memory of
P. S. Theocaris

Thessaloniki 13 July 2001

Foreword

It was an honor that HSTAM (Hellenic Society of Theoretical and Applied Mechanics) assigned to the Laboratory of Mechanics of the General Department of AUT the responsibility of organizing the 6th National Congress of Mechanics in cooperation with the Department of Civil Engineering of AUT.

Special thanks to A. Kounadis and D. Beskos, president and secretary of HSTAM respectively, as well as to G. Manolis and D. Talaslidis who served as vice-chairmen of the organizing committee.

The Congress is dedicated to the memory of P. Theocaris whose influence on the Mechanics Community of Greece will remain for many years. My predecessor G. Lianis and A. Armenakas served as honorary chairmen of the Congress. My thanks go to them, as well as to the rest of the members of the organizing committees.

The Congress was organized during a very interesting period of substantial activity in the educational and scientific community in Greece. More than two months before the Congress, the University administration, at first, and the undergraduate student body as a whole, later, opposed certain educational proposals passed by the State, and daily university activities came to a standstill. This had a serious impact on the conference organization including the disruption of usual e-mail correspondence.

It was the determination of my graduate students G. Efremidis and P. Sapalidis, the help of F. Akintayo, K. Kosmidis, K. Kalaitzidou/S. Marras (currently at MTU/USA), the assistance of undergraduate students Th. Atmakidis and D. Dodou, as well as the encouragement of A. Kounadis, which helped me decide not to postpone the meeting. Special thanks go to George Efremidis who took upon himself the responsibility of completing the process of collecting the manuscripts, coordinating the e-mail correspondence, and other organizational details. My colleagues D. Beskos and G. Manolis were always available for consultation and advice. Many faculty of the General Department including its past and newly elected Chairman, as well as the Dean of Engineering were very supportive of this event.

The active participation of the travel agency Aethra, the publisher Giahoudi-Giapouli and the personal involvement of the owner of Philip pion Hotel Helena Thoidou, who took the initiative to help with respective arrangements without requiring pre-payment, is worth mentioning. The financial support of the General Department, the College of Engineering, and the Research Committee of AUT, as well as of Democritus University of Thrace is

acknowledged. Also we acknowledge with thanks the financial support of the Ministry of Education, the Ministry of Culture and the Municipality of Thessaloniki. We also hope to have some financial support from the Ministry of Macedonia-Thrace and the Academy of Athens; but, at the time this foreword was composed, we had not yet received a definite decision from these governmental agencies, mainly due to difficulties in communication or decision-making during this unusual period of academic life.

Finally, sincere thanks go to all participants, especially those from abroad invited by HSTAM and myself or personally encouraged by me to attend. They all honored their commitment to participate despite the minimal information that could be distributed due to the aforementioned unforeseen circumstances. Many of the participants facilitated us greatly by pre-registering, thus enabling us to respond to initial financial obligations related to the Congress organization. It should be noted that as a result of the unusual circumstances mentioned above, it was not possible to activate a panel for a thorough review of the papers, which were accepted on the basis of their abstracts only.

Last, but not least, I would like to personally acknowledge the support and encouragement of the Minister of Yugoslavia, Professor Dragoslav Sumarac, for developing in Thessaloniki a Balkan Center of Mechanics with support from ERO and MTU with the participation of leading researchers of Mechanics and Materials of an international stature. In this respect, the sincere interest of Sam Sampath and the continuous help of my students I. Mastorakos, Avraam and Dimitris Konstantinidis in the organization of related research activities at AUT, as well as the scientific support of my student I. Tsagrakis, the research associate Mike Zaiser, and my physics colleague S. Logothetidis at AUT, are gratefully acknowledged.

*Elias C. Aifantis
Chairman*

6th NATIONAL CONGRESS OF MECHANICS

Thessaloniki. 19 – 21 July, 2001

Hellenic Society of Theoretical and Applied Mechanics (HSTAM)
Aristotle University of Thessaloniki (AUT)

ORGANIZING COMMITTEES

- *Chairmanship*

E. Aifantis,	Chairman, AUT
G. Lianis,	Honorary Chairman, Emeritus Professor, AUT
A. Armenakas,	Honorary Chairman, Emeritus Professor, NTUA
	Past President of HSTAM

- *HSTAM Council*

A. Kounadis,	Academy of Athens / NTUA, President
J. Katsikadelis,	NTUA, Vice-President
D. Beskos,	University of Patras, Secretary General
A. Vakakis,	NTUA, Treasurer
I. Vardoulakis,	NTUA
A. Mavraganis,	NTUA
D. Panayotounakos,	NTUA
H. Georgiadis,	NTUA
V. Koumoussis,	NTUA
G. Papadopoulos,	University of Athens
M. Papadrakakis,	NTUA

- *National Committee*

N. Alikakos,	University of Athens	A. Liolios,	DUTH
N. Aravas,	University of Thessaly	A. Mamalis,	NTUA
A. Bountis,	University of Patras	C. Massalas,	University of Ioannina
I. Dafalias,	NTUA	A. Payatakes,	University of Patras
G. Dassios,	University of Patras	P. Perdikaris,	University of Thessaly
V. Dougalis,	University of Athens	S. Pnevmatikos,	University of Patras
E. Economou,	University of Crete	D. Theodorou,	University of Patras
G. Fytas,	University of Crete	D. Tsahalis,	University of Patras
E. Gdoutos,	DUTH	G. Tsamasphyros,	NTUA
A. Liakopoulos,	University of Thessaly	P. Varotsos,	University of Athens

• ***AUT Committees***

G. Manolis / D. Talaslidis: Vice-Chairmen

A. Anagnostopoulos	G. Kourouklis
J. Antonopoulos	P. Latinopoulos
P. Argyrakis	S. Logothetidis
G. Athanasiadis	G. Manos
Ch. Baniotopoulos	S. Natsiavas
S. Bantis	S. Nychas
K. Bouzakis	M. Pagitsas
N. Charalambakis	C. Panayiotou
A. Charalambopoulos	P. Papadopoulos
J. Ganoulis	G. Penelis
A. Goulas	K. Pitilakis
J. Hadjidemetriou	N. Platakis
S. Ichtiaroglou	G. Theodorou
G. Kanelis	A. Trochidis
A. Karabelas	G. Tsagas
Th. Karakostas	D. Tsipas
A. Kehagias	K. Tsouros
C. Kiparissides	C. Tzimopoulos

• ***Local Arrangements Committee***

Section of Mechanics: S. Ambatjidis, E. Douka, M. Matsikoudi, S. Papargyri

Graduate students: G. Efremidis, P. Sapalidis, F. Akintayo, I. Mastorakos, K. Kosmidis,
K. Kalaitzidou, S. Marras

Undergraduate students: Th. Atmakidis, D. Dodou

TABLE OF CONTENTS

VOLUME I

THERMOMECHANICS OF LOCAL STRUCTURAL REARRANGEMENTS <i>G. Maugin</i>	1
QUANTUM PLASTICITY <i>K. Valanis</i>	9
ON STRAIN GRADIENTS IN PLASTICITY <i>J. Kratochvil</i>	14
ENABLING NONLINEAR COMPUTATIONS THROUGH EFFICIENT TIME-STEPPING <i>E. Koronaki, C. Theodoropoulos, A. Boudouvis I. Kevrekidis</i>	21
RHEOLOGY OF DENSE LIGNITE-WATER SUSPENSIONS; TRANSITION STRESSES ON FLOW CURVES <i>T. Goudoulas, E. Kastrinakis, S. Nychas</i>	27
COMPUTER SIMULATION OF THE NONLINEAR EVOLUTION OF INCLINED FILM FLOWS <i>N. Malamataris, M. Vlachogiannis, V. Bontozoglou</i>	33
AN IMPROVED COASTAL CIRCULATION MODEL BASED ON THE CHARACTERISTIC-GALERKIN TECHNIQUE <i>H. Mpimpas, P. Anagnostopoulos</i>	39
ON THE EFFECT OF THE RELATIVE VISCOSITY OF TWO FLUIDS ON THE DYNAMICS OF AXISYMMETRIC CORE-ANNULAR FLOW IN A TUBE <i>C. Kouris, J. Tsamopoulos</i>	45
A COMPARISON OF THE ACCURACY OF VARIOUS INTERPOLATION TECHNIQUES FOR PROCESSING RANDOMLY SCATTERED BATHYMETRIC DATA <i>N. Volakos, R. Barber</i>	52
INTERRELATION BETWEEN STOKES AND PAPKOVICH - NEUBER EIGENMODES FOR SPHEROIDAL STOKES FLOW <i>M. Hadjinicolaou, P. Vafeas</i>	59
NUMERICAL STUDY OF OSCILLATORY FLOW PAST PAIRS OF CYLINDERS AT LOW REYNOLDS AND KEULEGAN-CARPENTER NUMBERS <i>P. Anagnostopoulos, A. Koutras, S. Seitanis</i>	66
INVERSE DESIGN OF AERODYNAMIC SHAPES USING ANT COLONY OPTIMIZATION <i>T. Zervogiannis, V. Assouti, K. Gagas, A. Kaounis, K. Giannakoglou</i>	72
STRATIFIED TWO -PHASE FLOW OF VAPOUR BOUNDARY LAYER- CONDENSATE FILM OVER A CYLINDER <i>D. Smyrniaios, N. Pelekasis, J. Tsamopoulos</i>	78
FLUID DISPLACEMENT BY AIR IN A CAPILLARY TUBE <i>Y. Dimakopoulos, J. Tsamopoulos</i>	84

FLOW BETWEEN TWO ROTATING HEATED SPHERES <i>V. Loukopoulos</i>	90
AN EXPERIMENTAL METHODOLOGY FOR ENHANCING 2-D FLOW CHARACTERISTICS IN A 3-D TURBULENT FLOW <i>G. Sideridis, E. Kastrinakis, S. Nychas</i>	96
FORCES FROM JET FLOWS ON INCLINED DISCS <i>J. Demetriou, D. Dimitriou</i>	102
FLOW IN OPEN CHANNELS LINED WITH DIFFERENT MATERIALS <i>J. Demetriou, C. Pourliotis, P. Sarantos</i>	108
AIRLIFT PUMP PERFORMANCE OPTIMISATION FOR DEEP-SEA MINING <i>D. Margaris</i>	114
BOUNDARY SHEAR IN COMPOUND NON-SYMMETRICAL CHANNELS <i>K. Nanou-Giannarou, J. Demetriou</i>	121
USE OF HEIGHT DENSITY FUNCTION FOR THE EVALUATION OF MEASUREMENTS WITH A LASER DOPPLER ANEMOMETER <i>Th. Panidis</i>	127
DAMAGE MODELS FOR VISCOELASTIC COMPOSITES <i>R. Schapery</i>	134
DAMAGE LOCALIZATION AND FRACTURE IN LAMINATE COMPOSITES <i>P. Ladeveze</i>	140
CYLINDRICAL SHELLS AND THEIR STABILITY (CHOICE OF THE DEFLECTION FUNCTION AND CRITICAL EXTERNAL RADIAL PRESSURE) <i>D. Ruzic, Lj. Markovic</i>	146
ESSENTIAL STRUCTURE OF DAMAGE MECHANICS MODELS <i>D. Krajcinovic</i>	155
FATIGUE OF MATERIALS AND STRUCTURES <i>J. Lemaitre</i>	163
LARGE DEFLECTION ANALYSIS OF BEAMS WITH VARIABLE STIFFNESS. AN ANALOG EQUATION SOLUTION <i>J. Katsikadelis, G. Tsiatas</i>	172
CRUSHING OF SHIP'S BOW STRUCTURE DURING COLLISION WITH BRIDGE PIERS <i>N. Hajdin, R. Mandic</i>	178
BEM SOLUTION OF VISCOPLASTIC PROBLEMS IN METALLIC STRUCTURES IN THE PRESENCE OF TEMPERATURE GRADIENTS <i>C. Providakis, S. Kourtakis</i>	184
ROCK DISCONTINUITIES IN TUNNEL DESIGN: NUMERICAL SIMULATION OF THE EFFECTS OF FILLED AND OPEN JOINTS <i>C. Stiakakis, Z. Agioutantis, G. Paschalis</i>	191
ON THE NUMERICAL PERFORMANCE OF A SIMPLIFIED METHOD OF ANALYSIS FOR CREEPING STRUCTURES LOADED CYCLICALLY <i>K. Spiliopoulos</i>	198

STATIC AND DYNAMIC ANALYSIS OF SHELL PANELS USING THE ANALOG EQUATION METHOD	
<i>J. Yiotis, J. Katsikadelis</i>	204
NUMERICAL STUDIES OF ANCHORS AND REBARS IN CONCRETE SPECIMENS BY DAMAGE MODELS	
<i>G. Hatzigeorgiou, M. Sfakianakis, D. Theodorakopoulos, D. Beskos</i>	210
ON THE FLEXURAL MODES OF THE BICKFORD BEAM THEORY	
<i>C. Sophocleous, K. Soldatos</i>	216
A REALISTIC ESTIMATION OF THE EFFECTIVE BREADTH OF RIBBED PLATES	
<i>J. Katsikadelis, E. Sapountzakis</i>	222
ON THE STUDY OF TIE PLATES IN PIN CONNECTIONS	
<i>I. Mademlis, S. Marnoutsidis, A. Avdelas</i>	228
THE EFFECT OF DECK ROUGHNESS IN CONJUNCTION WITH OTHER PARAMETERS ON THE DYNAMIC RESPONSE OF STEEL HIGHWAY BRIDGES UNDER VEHICULAR LOADING	
<i>G. Michaltsos, D. Sophianopoulos</i>	234
LQR AND H OPTIMAL STRUCTURAL CONTROL IN ASEISMIC DESIGN	
<i>E. Zacharenakis, K. Arvanitis, A. Soldatos, G. Stavroulakis</i>	240
RELIABILITY BASED OPTIMIZATION USING NEURAL NETWORKS	
<i>M. Papadrakakis, N. Lagaros</i>	246
A NUMERICAL ESTIMATION OF THE INTERRELATION BETWEEN ACCELERATION PARAMETERS AND DAMAGE INDICATORS IN EARTHQUAKE ENGINEERING	
<i>A. Elenas, A. Liolios, L. Vasiliadis, M. Sakellari, P. Koliopoulos</i>	254
ELASTOPLASTIC RESPONSE SPECTRA FOR THE DESIGN OF STRUCTURES SUBJECTED TO EXPONENTIAL BLAST LOADING	
<i>N. Pnevmatikos, C. Gantes</i>	261
ANALYTICAL ESTIMATION OF TOTAL DISPLACEMENT'S COMPONENTS OF R/C SHEAR WALLS WITH ASPECT RATIO 1.0-1.5 SUBJECTED TO SEISMIC LOADS	
<i>T. Salonikios</i>	267
COMPETITION AMONG GENETIC ALGORITHMS TO IMPROVE ROBUSTNESS IN OPTIMIZATION	
<i>C. Dimou, V. Koumousis</i>	275
YUGOSLAV INVESTIGATIONS CONCERNING THE PATCH LOADING ON GIRDERS	
<i>N. Hajdin, B. Coric, N. Markovic, D. Lucic</i>	282
SYNTHESIS OF NEW PHENOLIC POLYMERS VIA ENZYMATIC POLYMERIZATION AND THEIR PROPERTIES	
<i>S. Kobayashi</i>	290
ADAPTIVE FINITE ELEMENT ANALYSIS OF LIMIT-LOAD STATES IN DRY AND SATURATED SOILS	
<i>W. Wunderlich, R. Findei, H. Cramer</i>	298
MEASUREMENT OF THE MECHANICAL PROPERTIES OF MEMS MATERIALS	
<i>W. Sharpe Jr.</i>	306

BEHAVIOR OF PARTICLE REINFORCED COMPOSITES WITH SOFT MATRICES <i>C. Sciammarella, F. Sciammarella</i>	314
INDENTATION FAILURE OF SANDWICH PANELS <i>E. Gdoutos, I. Daniel, K.-A. Wang</i>	320
ESTIMATION OF THE CONCRETE CHARACTERISTICS USING PATTERN RECOGNITION METHODS <i>M. Titsias, D. Fotiadis, A. Likas</i>	327
DESTRUCTIVE AND ULTRASONIC NON-DESTRUCTIVE TESTING OF 28-DAY AND 28-YEAR OLD CONCRETE <i>I. Prassianakis, P. Giokas</i>	333
EXPERIMENTAL QUANTIFICATION OF CRACK TIP PARAMETERS FOR PARTICULATE METAL MATRIX COMPOSITES <i>S. Kourkoulis, V. Kytopoulos</i>	339
ON SELECTING A COMPATIBLE SUBSTITUTE FOR THE KENHCREAE POROS STONE USED IN THE EPIDAUREAN ASKLEPIEION <i>N. Ninis, S. Kourkoulis</i>	348
NON-LINEAR MECHANICS AND BUCKLING ANALYSIS OF COMPOSITE SHELLS WITH EMBEDDED PIEZOELECTRIC ACTUATORS AND SENSORS <i>D. Varelis, D. Saravanos</i>	357
A NEW DESIGN METHODOLOGY FOR HIGH TEMPERATURE STRUCTURAL COMPONENTS MADE OF CONTINUOUS FIBER CERAMIC COMPOSITES EXHIBITING THERMALLY INDUCED ANISOTROPIC DAMAGE <i>D. Vlachos, Y. Pappas, R. De Stefano, V. Kostopoulos</i>	365
EXPERIMENTAL AND THEORETICAL STRESS ANALYSIS OF INCOMPRESSIBLE BONDED ELASTOMERIC DISCS SUBJECTED TO COMPRESSION <i>P. Kakavas</i>	375
OPTICAL DEVICE FOR PROSTATE CANCER DETECTION <i>G. Anastassopoulos, J. Lytras, M. Sunaric, V. Moulitanitis, S. Panteliou, A. Bekos, N. Kalinderis, D. Hatzichristou</i>	381
EXPERIMENTAL VERIFICATION OF SHEAR WALL MODELING USING FINITE ELEMENT ANALYSIS <i>A. Papachristidis, G. Badaloukas, B. Badalouka</i>	388
FAILURE OF A COMPOSITE WITH A BROKEN FIBER <i>D. Zacharopoulos, E. Gdoutos, D. Karalekas</i>	394
MICROMECHANICS OF CARBON FIBRE MODEL COMPOSITES UNDER TENSILE, COMPRESSIVE AND FATIGUE LOADING CONDITIONS <i>C. Koimtzoglou, S. Goutianos, C. Galiotis</i>	401
DYNAMIC BEHAVIOR OF A HANGED CABLE FOR DEEP WATER APPLICATIONS <i>I. Chatjigeorgiou, S. Mavrakos</i>	408
EXPERIMENTS FOR THE ESTIMATION OF UNSATURATED HYDRAULIC CONDUCTIVITY <i>G. Arampatzis, Ch. Tzimopoulos</i>	416

VOLUME II

CONTINUUM THEORY OF SELF-HEALING INTERFACE CRACKS <i>M. Marder, E. Gerde</i>	1
MATERIAL DEGRADATION AND FRACTURE IN HYDRIDE FORMING METALS <i>A. Varias, A. Massih</i>	7
SOME PROBLEMS OF ELECTROMECHANICAL FRACTURE OF DIELECTRIC AND PIEZOELECTRIC BODIES <i>D. Bardzokas, A. Zobnin</i>	13
CONTROL OF DYNAMIC STRESS AND FRACTURE OF PIEZOELECTRIC BODIES WITH CRACKS <i>D. Bardzokas, M. Filshtinsky</i>	22
OPTIMIZATION AND SOFT COMPUTING FOR INVERSE AND CRACK IDENTIFICATION <i>G. Stavroulakis, H. Antes</i>	28
MECHANICAL BEHAVIOR OF MULTILAYERED NANOCOMPOSITE FILMS <i>V. Singh, X. Nie, P. Gupta, E. Meletis</i>	33
A COMPARATIVE STUDY OF MECHANICAL PROPERTIES OF STATE-OF-THE-ART AMORPHOUS CARBON FILMS <i>C. Charitidis, S. Logothetidis</i>	40
THE ROLE OF POINT DEFECTS ON THE GROWTH AND BREAKDOWN OF METAL PASSIVE FILMS IN ELECTROLYTE SOLUTIONS <i>M. Pagitsas, A. Diamantopoulou, D. Sazou</i>	46
FAILURE RESISTANCE TO THERMAL SHOCK OF THERMAL BARRIER COATINGS USING THE FINITE ELEMENT METHOD <i>A. Kekatou, V. Sfakiotakis, D. Katsareas, N. Anifantis</i>	52
FINITE ELEMENT ANALYSIS OF THE ELASTIC MECHANICAL BEHAVIOUR OF LDPE FILM <i>D. Briassoulis, E. Schettini</i>	57
ADAPTIVE COMPOSITES INCORPORATING SHAPE MEMORY ALLOY WIRES; RECORDING THE INTERNAL STRESS BY LASER RAMAN SPECTROSCOPY <i>J. Parthenios, G. Psarras, D. Bollas, C. Galiotis</i>	63
A HEMIVARIATION ALINE QUALITY APPROACH TO THE RESISTANCE OF ALUMINIUM RIVETED CONNECTIONS <i>M. Zygomas, M. J. Kontoleon and C. C. Baniotopoulos</i>	70
ANALYSIS OF "CONVEX ENERGY" STRUCTURAL SYSTEMS UNDER STOCHASTIC LOADING <i>M. Kontoleon, C. Baniotopoulos, M. Betti, C. Borri</i>	78
FRICTION EVOLUTION IN FRACTAL INTERFACES <i>O. Panagouli, E. Mistakidis</i>	84

NUMERICAL STUDY OF THE F.E. MESH DEPENDENCY IN NONCONVEX-NONSMOOTH ENGINEERING PROBLEMS	
<i>E. Mistakidis, N. Politis</i>	90
FUZZY SETS IN ENGINEERING ANALYSIS AND DESIGN	
<i>E. Mistakidis, D. Georgiou</i>	96
BENDING AND WARPING IN FIBER REINFORCED RECTANGULAR BEAMS	
<i>C. Demakos</i>	102
ON THE POTENTIAL REPRESENTATIONS FOR POLYADICS AND ANISOTROPIC MEDIA	
<i>G. Dassios</i>	109
THE APPLICATION OF NOTHER'S THEOREM TO NON-LINEAR ANISOTROPIC ELASTIC-MATERIALS	
<i>J. Jaric, K. Kishimoto, T. Wang, M. Omiya</i>	115
MICROMECHANICAL MODELING OF THE BEHAVIOR OF POROUS SHAPE MEMORY ALLOYS	
<i>D. Lagoudas, P. Entchev</i>	120
VARIATIONAL FORMULATION AND MATERIAL BALANCE LAWS OF DISSIPATIONLESS THERMOELASTICITY	
<i>V. Kalpakides, G. Maugin</i>	126
THE INFINITE ISOTROPIC WEDGE UNDER LINEARLY DISTRIBUTED LOADING	
<i>J. Stabouloulou, E. Theotokoglou</i>	133
SIZE EFFECT ON FAILURE LOAD OF MARBLE BEAMS UNDER THREE POINT BENDING	
<i>I. Vardoulakis, G. Exadaktylos, S. Kourkoulis</i>	140
FINITE ELEMENT TECHNIQUES FOR STRAIN-GRADIENT ELASTICITY PROBLEMS	
<i>E. Amanatidou, N. Aravas</i>	149
THE ELASTIC PUNCH PROBLEM REVISITED	
<i>G. Exadaktylos</i>	155
GRADIENT ELASTIC BERNOULLI-EULER BEAMS IN BENDING AND BUCKLING	
<i>S. Papargyri-Beskou, K. Tsepoura, D. Polyzos, D. Beskos</i>	163
DUAL MODE VIBRATION ISOLATION BASED ON NONLINEAR MODE LOCALIZATION	
<i>X. Jiang, A. Vakakis</i>	170
A FRACTIONAL BROWNIAN MOTION MODEL FOR TIMESERIES PRODUCED BY CONSTANT ENERGY MOLECULAR DYNAMICS SIMULATIONS	
<i>T. Karakasidis, I. Andreadis</i>	177
VIBRATIONAL PROPERTIES OF A $\Sigma 5(310)[001]$ NiO GRAIN BOUNDARY STUDIED BY MOLECULAR DYNAMICS SIMULATION	
<i>T. Karakasidis</i>	183
ANALYTICAL SOLUTION OF THE NONLINEAR DAMPED DUFFING OSCILLATOR	
<i>D. Panayotounakos, G. Exadaktylos, A. Vakakis</i>	189

NONLINEAR EFFECTS ON THE ELASTIC STABILITY OF A COLUMN-FOOTING SYSTEM ON ELASTIC BASE	
<i>Ch. Younis, D. Panayotounakos</i>	196
THE CONTINUOUS TIME HOMOGENEOUS MARKOV SYSTEM WITH FIXED SIZE AS A LINEAR ELASTIC CONTINUUM	
<i>G. Tsaklidis, K. Soldatos</i>	209
STUDY OF THE DYNAMIC CHARACTERISTICS DURING CALLUS FORMATION	
<i>G. Foutsitzi, A. Charalambopoulos, D. Fotiadis, C. Massalas</i>	216
ON THE ELECTROENCEPHALOGRAPHY (EEG) PROBLEM FOR THE ELLIPSOID ALBRAIN MODEL	
<i>G. Kamvyssas, F. Kariotou</i>	222
MATHEMATICAL MODELS FOR BIOMAGNETIC FLUID FLOW AND APPLICATIONS	
<i>E. Tzirtzilakis, N. Kafoussias</i>	227
LAMELLAR INHOMOGENEITIES IN PIEZOELECTRIC SOLIDS	
<i>C. Dascalu, D. Homentcovschi</i>	233
ON A NEW CRACK MODEL FOR PIEZOELECTRIC SOLIDS	
<i>C. Dascalu, D. Homentcovschi, V. Kalpakides, E. Hadjigeorgiou</i>	239
ON THE STOCHASTIC MICROMECHANICAL THEORY OF DISCRETE MATERIAL SYSTEMS	
<i>Y. Haddad</i>	245
A CONSTITUTIVE LAW FOR POWDER COMPACTION	
<i>S. Subramanian, P. Sofronis</i>	251
CONTINUUM MICROPOLAR MODELLING OF DISCONTINUOUS MASONRY-LIKE SYSTEMS	
<i>P. Trovalusci, R. Masiani</i>	257
SOME ASPECTS OF A MICROPOLAR PLASTICITY THEORY	
<i>P. Grammenoudis, Ch. Tsakmakis</i>	263
DESCRIPTION OF PLASTIC ANISOTROPY EFFECTS AT LARGE DEFORMATIONS	
<i>D. Schick, Ch. Tsakmakis</i>	269
"COLD" WORK AND STABILITY IN SOFTENED MATERIALS	
<i>N. Charalambakis</i>	276
SOME BASIC SOLUTIONS TO DYNAMIC PROBLEMS IN RANDOM MEDIA	
<i>C. Karakostas, G. Manolis</i>	280
ANALYSIS OF RAYLEIGH WAVES IN MICRO STRUCTURED SOLIDS BY DIPOLAR GRADIENT ELASTICITY	
<i>H. Georgiadis, I. Vardoulakis, E. Velgaki</i>	289
THE 3D THERMO-ELASTODYNAMIC PROBLEM OF MOVING LOADS IN A HALF - SPACE	
<i>G. Lykotrafitis, H. Georgiadis</i>	295
THE ATTITUDE MOTION OF A CARRIER-ROTOR SYSTEM WITH ALMOST SYMMETRIC INERTIA ELLIPSOID, UNDER BODY-FIXED TORQUES	
<i>K. Dimitrakopoulou, A. Mavraganis</i>	301

GRADIENT ANISOTROPIC DAMAGE IN MMCS FOR BRIDGING LENGTH SCALES BETWEEN MACROSCOPIC RESPONSE AND MICROSTRUCTURE <i>G. Voyiadjis, R. Dorgan</i>	309
TWO SCALE DAMAGE MODEL FOR FATIGUE REPRESENTATION OF GRADIENT EFFECTS <i>R. Desmorat</i>	318
GRADIENT ELASTIC BARS UNDER UNIAXIAL STATIC OR DYNAMIC LOAD <i>K. Tsepoura, S. Papargyri - Beskou, D. Polyzos, D. Beskos</i>	328
EVOLUTION OF PERSISTENT SLIP BANDS IN FATIGUED METALS <i>E. Douka, B. Polyzos, A. Trochidis</i>	335
CRACK IDENTIFICATION IN BEAM STRUCTURES <i>Y. Bannios, E. Douka, A. Trochidis</i>	342
FRACTALS AND FRACTIONAL CALCULUS IN SOLID MECHANICS <i>A. Carpinteri, B. Chiaia, P. Cornetti</i>	349
CHARACTERIZATION OF MATERIALS WITH PORES AND INCLUSIONS AT DIVERSE SCALES <i>G. Frantziskonis</i>	359
SEMI-ANALYTICAL SOLUTION FOR A 1-D SIMPLIFIED THMPC MODELLING OF A NON-SATURATED SOIL <i>M - A. Abellan, J - M. Bergheau, J. M. Huyghe, R. de Borst</i>	365
COMPACT, HIGH-POWER, SYNTHETIC JET ACTUATORS FOR FLOW SEPARATION CONTROL <i>J. Gilarranz, O. Rediniotis</i>	371
LOCALIZED PERIODIC MOTIONS IN SYSTEMS OF COUPLED OSCILLATORS <i>V. Koukouloyannis, S. Ichtiaroglou</i>	379
EFFECT OF THE PARAMETERS ON THE DYNAMIC BEHAVIOR OF A SMALL PARTICLE IN AN ANNULAR DISTRIBUTION OF N BODIES <i>T. Kalvouridis, F. Psarros</i>	385
RESEARCH AND CHALLENGES OF ENGINEERING MECHANICS AND MATERIALS IN THE TWENTY FIRST CENTURY <i>K. Chong, D. Davis</i>	391
DAMAGE MECHANICS APPLICATION ON REPAIR OF DESTROYED STRUCTURES <i>D. Sumarac</i>	397

VOLUME III

COMPUTATIONAL ASPECTS OF MATERIAL INSTABILITIES	
<i>R. de Borst, H. Askes, M. Gutierrez, G. Wells</i>	1
EXPERIMENTAL STUDIES OF PLASTIC INSTABILITIES IN SOLID SOLUTIONS	
<i>H. Neuhaeuser, F. Klose, H. Dierke, A. Ziegenbein, A. Nortmann</i>	9
COMBINED MEASUREMENTS OF ACOUSTIC EMISSION AND LASER EXTENSOMETRY DURING PORTEVIN-LE CHATELIER DEFORMATION IN AN Al-Mg ALLOY	
<i>A. Ziegenbein¹, F. Chmelik, H. Neuhaeuser</i>	16
SERRATED YIELDING AND NONUNIFORM PLASTIC DEFORMATION OF PORTEVIN - LE CHATELIER EFFECT IN COMMERCIAL Al-Mg ALLOYS	
<i>K. Chihab, H. Ait-Amokhtar</i>	22
TIME SERIES ANALYSIS AND THE DETERMINISTIC STRUCTURE OF THE PLC EFFECT	
<i>D. Kugiumtzis, E. Aifantis</i>	29
SOME DYNAMICAL SYSTEM CONSIDERATIONS FOR DISLOCATIONS	
<i>G. Stagika, S. Ichtiaroglou, E. Aifantis, I. Groma</i>	35
THE DISLOCATION MODEL OF LOCAL BEND	
<i>N. Tokiy, T. Konstantinova, V. Varyukhin, A. Tokiy</i>	40
MULTISCALE PLASTICITY: LINKING DISCRETE AND CONTINUUM APPROACHES	
<i>L. Kubin, B. Devincre</i>	47
MACROSCOPIC MATERIAL BEHAVIOR FROM MICROSCOPIC SIMULATIONS	
<i>S. Luding, M. Laetzel</i>	53
MODELLING OF LAMINATED COMPOSITE STRUCTURES	
<i>A. Fernandes, J. Pouget</i>	61
INVARIANT RELATIONS IN A BOUSSINESQ TYPE EQUATION	
<i>E. Meletlidou, J. Pouget, G. Maugin, E. Aifantis</i>	67
KINK DYNAMICS IN A LONG-RANGE INTERACTION MODEL	
<i>T. Ioannidou, J. Pouget and E. Aifantis</i>	73
MAGNETIC SOLITONS	
<i>P. Sutcliffe</i>	79
THE PROPAGATION OF STRAIN WAVES IN MATERIALS WITH MICROSTRUCTURE	
<i>A. Potapov, V. Rodyushkin</i>	85
GOVERNING EQUATIONS AND BALANCE LAWS FOR MICROPOLAR CONTINUUM	
<i>S. Lisina, A. Potapov, G. Utkin</i>	90
SPLITTING UP OF MULTISTABLE SOLITONS IN SOLIDS	
<i>A. Potapov, V. Kazhaev, S. Gromov</i>	96

MODELING THE CRUSHING OF A CELLULAR MATERIAL	
<i>M. Zaiser, E. Aifantis</i>	102
APPENDIX WITH THE LATE PAPERS	111
AUTHOR INDEX	

6th National Congress on Mechanics

Session A

Volume II

CONTINUUM THEORY OF SELF-HEALING INTERFACE CRACKS

M. Marder and Eric Gerde

Computational and Applied Mathematics and Department of Physics
The University of Texas at Austin
Austin Texas, 78712, USA

1. SUMMARY

We have studied microscopic and macroscopic properties of self-healing cracks moving along interfaces. Here we obtain the properties of such cracks in a continuum context employing conformal mapping.

2. INTRODUCTION

The first dynamic fracture calculation was performed by Yoffe[22]. She considered a crack of finite length moving in steady state, opening at one end and closing at the other. This self-healing crack was a mathematical artifact designed to make calculations for the moving crack resemble those for static cracks of finite length.

Cracks that open at one end and close at the other appeared again years later in studies of separation along an interface[20, 7, 8, 12, 21]. The cracks in these solutions were controversial for two reasons. *First*, sufficiently near the crack tips, the crack surfaces intersect each other infinitely often. This difficulty is a generic feature of interface cracks. *Second*, in some of the solutions, energy flowed out of the crack tip that was opening and into the crack tip that was closing. This behavior seemed unphysical. As a result, it was not clear whether cracks of this sort were physically acceptable.

Solutions of this type have also appeared in a geophysical context, where they may explain the anomalously small amounts of heat generated during earthquakes[14, 5, 1, 2, 15, 17, 6, 18]. They have been observed explicitly in model laboratory studies[3, 4]. Recently, we have shown that solutions of this sort arise in atomic models on a lattice, where there is no doubt over whether they are physical.

In order to connect our atomic-scale solutions to macroscopic behavior, it is necessary to have a complete catalog of self-healing cracks from the continuum point of view. Analyses of this sort have recently been performed[11, 9], but they are quite lengthy, and treat more general orthotropic elastic properties than we need. We have therefore derived the properties of self-healing cracks using the familiar techniques of conformal mapping[16] extended to the case of steadily propagating solutions[13], and our goal here is to present this analysis. We also found [19] quite helpful.

3. FIELDS APPROACHING ONE CRACK TIP

We consider a two-dimensional isotropic elastic solid in contact with a rigid substrate along a flat interface. Consider solutions of the equations of elasticity that are stationary in a moving frame traveling to the right along direction x at velocity v . With c_l and c_t longitudinal and transverse wave speeds, define

$$\alpha^2 = 1 - v^2/c_l^2, \quad \beta^2 = 1 - v^2/c_t^2. \quad (1)$$

Also define the complex spatial variables

$$z_\alpha = x + i\alpha y, \quad z_\beta = x + i\beta y. \quad (2)$$

Then solutions to moving elastic problems can be obtained from two complex potential functions $\phi(z_\alpha)$ and $\psi(z_\beta)$. In terms of these functions, displacements are given by [13]

$$u_x = \phi(z_\alpha) + \overline{\phi(z_\alpha)} + i\beta \left[\psi(z_\beta) - \overline{\psi(z_\beta)} \right] \quad (3a)$$

$$u_y = i\alpha \left[\phi(z_\alpha) - \overline{\phi(z_\alpha)} \right] - \left[\psi(z_\beta) + \overline{\psi(z_\beta)} \right]. \quad (3b)$$

Define also $\Phi = \partial\phi(z)/\partial z$ and $\Psi = \partial\psi(z)/\partial z$. Then, with μ a Lamé constant, the stress tensor is given by

$$\sigma_{yy} = -\mu(1 + \beta^2) \left[\Phi(z_\alpha) + \overline{\Phi(z_\alpha)} \right] - 2i\beta\mu \left[\Psi(z_\beta) - \overline{\Psi(z_\beta)} \right] \quad (4a)$$

$$\sigma_{xx} = \mu(1 + 2\alpha^2 - \beta^2) \left[\Phi(z_\alpha) + \overline{\Phi(z_\alpha)} \right] + 2i\beta\mu \left[\Psi(z_\beta) - \overline{\Psi(z_\beta)} \right]. \quad (4b)$$

$$2\sigma_{xy} = 2\mu \left\{ 2i\alpha \left[\Phi(z_\alpha) - \overline{\Phi(z_\alpha)} \right] - (\beta^2 + 1) \left[\Psi(z_\beta) + \overline{\Psi(z_\beta)} \right] \right\}. \quad (4c)$$

Let R denote the region along the x axis where the crack faces are separated. For an interface crack running over a rigid substrate, the boundary conditions are

$$e_{xx}(x, 0) = 0 \quad \text{and} \quad e_{xy}(x, 0) = 0 \quad \text{for } x \text{ outside } R \quad (5a)$$

$$\sigma_{yy}(x, 0) = 0 \quad \text{and} \quad \sigma_{xy}(x, 0) = 0 \quad \text{for } x \text{ inside } R \quad (5b)$$

Now define the analytic continuations of the functions Φ and Ψ . Actually, what we need is the continuation of their complex conjugates along the x axis. Define

$$\bar{\Phi}^+(x) = \lim_{y \rightarrow 0} \overline{\Phi(x + iy)} \quad \text{for } x \text{ outside } R \quad (6a)$$

$$\bar{\Phi}^-(x) = \lim_{y \rightarrow 0} \overline{\Phi(x + iy)} \quad \text{for } x \text{ inside } R, \quad (6b)$$

with a similar definition for $\bar{\Psi}^\pm$. These four new functions have analytic continuations into the upper half plane. The plus and minus functions will turn out to differ only by a phase factor.

Making use of these functions, the boundary conditions (5) become

$$(\Phi + \bar{\Phi}^+) + i\beta(\Psi - \bar{\Psi}^+) = 0 \quad (7)$$

$$i\alpha(\Phi - \bar{\Phi}^+) - (\Psi + \bar{\Psi}^+) = 0 \quad (8)$$

$$-\mu(1 + \beta^2)(\Phi + \bar{\Phi}^-) - 2i\beta\mu(\Psi - \bar{\Psi}^-) = 0 \quad (9)$$

$$\mu 2i\alpha(\Phi - \bar{\Phi}^-) - \mu(1 + \beta^2)(\Psi + \bar{\Psi}^-) = 0 \quad (10)$$

Solving these four equations, one can express Φ in terms of Φ^+ and Φ^- as follows:

$$\Phi = -\frac{(2\alpha\beta - 2)(1 + \beta^2)\bar{\Phi}^+ + ((1 + \beta^2)^2 - 4\alpha\beta)\bar{\Phi}^-}{(\beta^2 - 1)((1 + \beta^2) - 2\alpha\beta)}. \quad (11)$$

In addition, one can similarly find Ψ in terms of Φ^+ and Φ^- .

Equation 11 can be employed to determine all the fields outside the interface crack. As a first example, find the asymptotic form of fields approaching the crack tip.

Suppose

$$\Phi(z) = Cz^\lambda + \bar{D}z^{\bar{\lambda}}. \quad (12a)$$

Then

$$\bar{\Phi}^+(z) = \bar{C}z^{\bar{\lambda}} + Dz^\lambda \quad (12b)$$

$$\bar{\Phi}^-(z) = \bar{C}z^{\bar{\lambda}}e^{-2\pi i\bar{\lambda}} + Dz^\lambda e^{-2\pi i\lambda} \quad (12c)$$

The reason for the factors of $\exp[-2\pi i\lambda]$ in Eq. (12) is that approaching the negative x axis from above $\log z$ has imaginary part $-i\pi$, while $\log z$ has $i\pi$.

Inserting Eq. (12) into Eq. (11) and isolating coefficients of z^λ produces a homogeneous system of two equations for the two unknowns C and D . The condition that the determinant of the system vanish is

$$q^2 + 2pq + 1 = 0, \text{ where } q = e^{2\pi i\lambda}, \text{ and} \quad (13)$$

$$p = 1 + \frac{2((1 + \beta^2) - 2\alpha\beta)^2}{(\alpha\beta - 1)((1 + \beta^2)^2 - 4\alpha\beta)}. \quad (14)$$

Also

$$q = -p \pm \sqrt{p^2 - 1}. \quad (15)$$

There is a fixed ratio between D and C which is

$$r \equiv \frac{D}{C} = -\frac{e^{2i\pi\lambda}(\beta^2 - 1)((1 + \beta^2) - 2\alpha\beta)}{(1 + \beta^2)^2 + (2\alpha\beta - 2)e^{2i\pi\lambda}(1 + \beta^2) - 4\alpha\beta} \quad (16)$$

One has $p > 1$ which implies that $\lambda = -1/2 + i\epsilon$ with ϵ real, which implies that q is real and r is real. This result has previously been derived by Deng[10].

4. FIELDS AROUND SELF-HEALING CRACK

One can proceed similarly to find the fields produced by a self-healing crack. Now take Φ to have the form

$$\begin{aligned} \Phi(z) = & A_1(z-t)^\lambda(z+t)^{\bar{\lambda}} + \bar{A}_1 r(z-t)^{\bar{\lambda}}(z+t)^\lambda \\ & + A_2(z-t)^\lambda(z+t)^{\bar{\lambda}+1} + \bar{A}_2 r(z-t)^{\bar{\lambda}}(z+t)^{\lambda+1} \\ & + A_3(z-t)^{\lambda+1}(z+t)^{\bar{\lambda}} + \bar{A}_3 r(z-t)^{\lambda+1}(z+t)^{\bar{\lambda}} \end{aligned} \quad (17)$$

These are the only functions that exhibit the necessary singularity at the crack tips, increase no faster than a constant far away from the crack, and have no branch cuts or other singularities in the region outside the crack. It appears at first that A_2 and A_3 can be treated independently. However, they cannot, since

$$(z-t)^{\lambda+1}(z+t)^{\bar{\lambda}} = (z-t)^\lambda(z+t)^{\bar{\lambda}}(z-t) \quad (18)$$

$$= z(z-t)^\lambda(z+t)^{\bar{\lambda}} - t(z-t)^\lambda(z+t)^{\bar{\lambda}}, \quad (19)$$

$$\text{while } (z-t)^\lambda(z+t)^{\bar{\lambda}+1} = z(z-t)^\lambda(z+t)^{\bar{\lambda}} + t(z-t)^\lambda(z+t)^{\bar{\lambda}} \quad (20)$$

One could just take $A_3 = 0$, but it is more symmetrical to take $A_3 = A_2$.

Thus, the solutions are governed by four real constants, which are the real and imaginary parts of A_1 and A_2 . What do they correspond to? Two of them correspond to the two components of the complex stress intensity factor near one of the crack tips, or equivalently to the far-field stresses. The other two correspond to the slip produced by the moving crack. To see that one has to consider the slip, note that if the crack is stationary, it is clearly possible to glue an upper and lower surface together in such a way as to have a puckered region of separation, like a bump in a rug, but with no stresses at infinity. The boundary condition outside the crack was given in terms of strains, not displacements, which also leaves the freedom for one side of the crack to be higher than the other. However, there is no physical reason to employ that freedom, and the slip in the y direction will always be zero. However, the slip in the x direction is generally nonzero, and has to be specified independently of the external stresses.

The other fields that enter into Eq. (11) are

$$\begin{aligned} \bar{\Phi}^+(z) = & \bar{A}_1(z-t)^{\bar{\lambda}}(z+t)^{\lambda} + A_1 r(z-t)^{\lambda}(z+t)^{\bar{\lambda}} \\ & + \bar{A}_2(z-t)^{\bar{\lambda}}(z+t)^{\lambda+1} + A_2 r(z-t)^{\lambda}(z+t)^{\bar{\lambda}+1} \\ & + \bar{A}_2(z-t)^{\bar{\lambda}+1}(z+t)^{\lambda} + A_2 r(z-t)^{\lambda+1}(z+t)^{\bar{\lambda}} \end{aligned} \quad (21)$$

and

$$\begin{aligned} \bar{\Phi}^-(z) = & q\bar{A}_1(z-t)^{\bar{\lambda}}(z+t)^{\lambda} + q^{-1}A_1 r(z-t)^{\lambda}(z+t)^{\bar{\lambda}} \\ & + q\bar{A}_2(z-t)^{\bar{\lambda}}(z+t)^{\lambda+1} + q^{-1}A_2 r(z-t)^{\lambda}(z+t)^{\bar{\lambda}+1} \\ & + q\bar{A}_2(z-t)^{\bar{\lambda}+1}(z+t)^{\lambda} + q^{-1}A_2 r(z-t)^{\lambda+1}(z+t)^{\bar{\lambda}} \end{aligned} \quad (22)$$

To find the stress intensity factor, simply insert Eqs. (17)–(21) into Eqs. (3) and (4), to obtain stresses and strains in terms of A_1 and A_2 . One has to employ the expression for $\bar{\Psi}$ in terms of $\bar{\Phi}^+$ and $\bar{\Phi}^-$, which is not written out here. Then one just picks out the dominant coefficient of σ_{yy} approaching the right hand crack tip. Define the stress intensity factor to be the complex coefficient of r^{λ} approaching the right-hand crack tip.

To calculate the slip, one has to perform two integrals. These are

$$I_1 = \int_{-1}^1 dx (1-x)^{\lambda}(1+x)^{\bar{\lambda}} = -\frac{\pi}{\sin \pi \lambda} \quad (23)$$

and

$$I_2 = \int_{-1}^1 dl (1-l)^{\lambda+1}(1+l)^{\bar{\lambda}} \quad (24)$$

$$= I_1 - \int_{-1}^1 dl l (1-l)^{\lambda}(1+l)^{\bar{\lambda}} = 2I_1(1+\lambda) \quad (25)$$

All the integrals needed to calculate the slips S_x, S_y

$$S_x = \int_{-t}^t dx e_{xx} \quad S_y = \int_{-t}^t dx e_{xy} \quad (26)$$

can be obtained from these two. For example, understanding x to be approaching the y axis from above,

$$\int_{-t}^t dx (x-t)^{\lambda}(z+t)^{\bar{\lambda}} = t^{\lambda+\bar{\lambda}} \int_{-1}^1 dx (x/t-1)^{\lambda}(x/t+1)^{\bar{\lambda}} \quad (27)$$

$$= t^{-1} \int_{-1}^1 t dl (l-1)^{\lambda}(l+1)^{\bar{\lambda}} = t^{-1} e^{i\pi\lambda} \int_{-1}^1 t dl (1-l)^{\lambda}(l+1)^{\bar{\lambda}} = e^{i\pi\lambda} I_1 \quad (28)$$

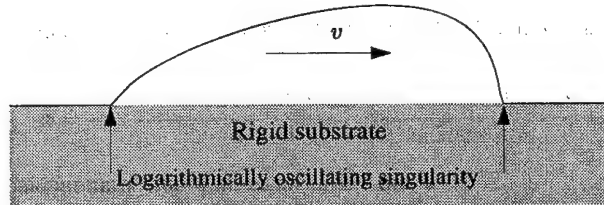


Figure 1: Picture of self-healing crack obtained from the methods outlined in this paper. For this solution, $v/c_t = .866$, $c_t^2/c_t^2 = 3$, the horizontal slip S_x divided by the crack length is -0.05 , and the stresses far from the crack are $\sigma_{xy}/\mu = 0.0056$ and $\sigma_{yy}/\mu = -0.00188$, with μ a Lamé constant. The stress in the y direction is indeed compressive. The scale in the vertical direction is arbitrary.

All the other integrals involved in computing the slip can be worked out similarly. Upon setting $S_y = 0$, the constants A_1 and A_2 are finally determined by specifying the two components of the stress intensity factor, and the slip S_x .

5. SOLUTIONS

Figure 1 shows a solution determined with these techniques. Upon inspection, it seems physically reasonable, as the upper crack surface does not appear to cross the rigid substrate. In fact, like all crack solutions at the interface between dissimilar materials, the crack surface crosses the substrate infinitely often. However, the crossings occur so close to the tips of the crack that they are invisible at this scale.

Based upon such arguments, it would be hard to determine whether this solution is physically allowed or not. We have carried out additional analyses that involve the solution of atomic-scale models for semi-infinite interface fractures. These atomic solutions are based upon solving Newton's laws for atoms, and cannot involve crack-interface crossings or other unphysical effects. The solution depicted in Figure 1 happens to be one such that the asymptotic crack tip fields, approaching the tip, match smoothly with known solutions of the atomic model, going away from the tip. Therefore, we believe that this solution is physically realizable.

We do not believe that this conclusion could be reached through arguments couched purely at the continuum level. At the same time, the atomic calculations are not powerful enough to treat structures with two crack tips. They can only handle one semi-infinite crack and its tip at a time. The atomic and continuum descriptions of self-healing cracks are complementary. Both must be combined in order to reach physical conclusions.

This research was supported by the National Science Foundation (DMR-9531187), the U. S.-Israel Binational Foundation (920-00148), and a fellowship from the Computational and Applied Mathematics Program.

6. REFERENCES

- [1] Andrews, D. J. and Ben-Zion, Y. Wrinkle-like slip pulse on a fault between different materials. *J. Geo. Res.* 102, 553–571 (1997).
- [2] Ben-Zion, Y. and Andrews, D. J. Properties and implications of dynamic rupture along a material interface. *Bulletin of the Seismological Society of America* 88, 1085–1094 (1998).
- [3] Brown, S. R. Frictional heating on faults: Stable sliding versus stick slip. *J. Geophys. Res.* 103, 7413–7420 (1998).

-
- [4] Brune, J. N., Brown, S., and Johnson, P. A. Rupture mechanism and interface separation in foam rubber models of earthquakes: a possible solution to the heat flow paradox and the paradox of large overthrusts. *Tectonophysics* 218, 59–67 (1993).
 - [5] Cherepanov, G. P. Super-deep penetration. *Engineering Fracture Mechanics* 47, 691–713 (1994).
 - [6] Cochard, A. and Rice, J. R. Fault rupture between dissimilar materials: Ill-posedness, regularization, and slip-pulse response. *J. Geophys. Res.* (2000). (submitted).
 - [7] Comninou, M. and Dundurs, J. Can solids slide without slipping? *Int. J. Solids Struct.* 14, 251–260 (1978).
 - [8] Comninou, M. and Dundurs, J. Elastic interface waves and sliding between two solids. *J. Appl. Mech.* 45, 325–330 (1978).
 - [9] Das, S. and Patra, B. Moving griffith crack at the interface of two dissimilar orthotropic half planes. *Engineering Fracture Mechanics* 54, 523–531 (1996).
 - [10] Deng, X. Complete complex series expansions of near-tip fields for steadily growing interface cracks in dissimilar isotropic materials 42, 237–242 (1992).
 - [11] Dhaliwal, R. J. and Saxena, H. S. Moving griffith crack at the interface of two orthotropic elastic layers. *J. Math. Phys. Sci.* 26, 237–254 (1992).
 - [12] Freund, L. B. Discussion: Elastic interface waves involving separation. *J. Appl. Mech.* 45, 226–227 (1978).
 - [13] Freund, L. B. *Dynamic Fracture Mechanics*. Cambridge University Press, Cambridge (1990).
 - [14] Heaton, T. H. Evidence for and implications of self-healing pulses of slip in earthquake rupture. *Phys. Earth Planet. Interiors* 64, 1–20 (1990).
 - [15] Mora, P. The weakness of earthquake faults. *Geo. Phys. Res. Let.* 26, 123–126 (1999).
 - [16] Muskhelishvili, N. I. *Some Basic Problems in the Mathematical Theory of Elasticity*. Noordhoff, Groningen (1952).
 - [17] Place, D. and Mora, P. The lattice solid model to simulate the physics of rocks and earthquakes: incorporation of friction. *J. Comp. Phys.* 150, 332–372 (1999).
 - [18] Ranjith, K. and Rice, J. R. Slip dynamics at an interface between dissimilar materials. *Journal of the Mechanics and Physics of Solids* (2000). (in press).
 - [19] Rice, J. R. Elastic fracture mechanics concepts for interfacial cracks. *Journal of Applied Mechanics* 55 (1988).
 - [20] Weertman, J. Theory of velocity of earthquake dislocations. *Geo. Soc. Am. Mem.* 142, 175–183 (1975).
 - [21] Weertman, J. Unstable slippage across a fault that separates elastic media of different elastic constants. *J. Geo. Res.* 85B3, 1455–1461 (1980).
 - [22] Yoffe, E. H. The moving griffith crack. *Philosophical Magazine* 42, 739–750 (1951).

MATERIAL DEGRADATION AND FRACTURE IN HYDRIDE FORMING METALS

A.G. Varias

Solid Mechanics and Material Technology, Malmö University, SE 205 06, Malmö, Sweden
Solid Mechanics Research Office, Makedonias 17, N. Iraklio 141 21, Athens, Greece

A.R. Massih

Quantum Technologies AB, Uppsala Science Park, SE-751 83, Uppsala, Sweden
Luleå University of Technology, SE-971 87, Luleå, Sweden

1. SUMMARY

The degradation of metals, caused by the formation of brittle hydrides, is simulated. The coupling of hydrogen diffusion, hydride precipitation, non-mechanical energy flow and hydride/solid-solution deformation is considered. Crack growth is simulated by using de-cohesion model with time-dependent de-cohesion energy, due to gradual hydride precipitation. The hydrogen embrittlement model has been tested successfully against experimental data and analytical solutions on hydrogen thermal transport. The simulation of Zircaloy-2 hydrogen embrittlement and delayed hydride cracking initiation has also been performed, under K-field dominance as well as under conditions leading to loss of K-field dominance. The effects of near-tip stress intensification and temperature gradient on hydride precipitation have been studied. The numerical simulation predicts hydride precipitation at a small distance from the crack tip. When the remote loading is sufficient, the near tip hydrides fracture. Thus a micro-crack is generated, which is separated from the main crack by a ductile ligament, in agreement with experimental observations.

2. INTRODUCTION

Hydride-induced embrittlement, in metals such as zirconium, results from the simultaneous operation of several coupled processes (i.e. hydrogen diffusion, hydride precipitation, non-mechanical energy flow and hydride/solid-solution deformation). The heat transfer process, which is associated with temperature gradient, is important, due to hydrogen thermal transport, e.g. within zirconium-base nuclear fuel cladding. Varias and Massih [1],[2] developed a model, where the coupling of all processes, including heat transfer and hydride fracture, is considered. The model is based on the thermodynamic theory of irreversible processes and takes into account hydrogen thermal transport. The time-dependent fracture toughness of the material ahead of a crack tip, due to gradual hydride precipitation, is also taken into account in a new version of the de-cohesion model for crack growth. A brief discussion of the embrittlement/fracture model follows. Details of the model and relevant references are given in [1].

3. MATHEMATICAL MODEL FOR HYDRIDE INDUCED EMBRITTLEMENT

The governing equations of all processes are presented. Hydrogen diffusion is simulated by enforcing the conservation of hydrogen mass:

$$\frac{dC^{HT}}{dt} = -\frac{\partial J_k^H}{\partial x_k} \quad (1)$$

C^{HT} is the total hydrogen concentration and J_k^H are the components of hydrogen flux. C^{HT} is related to the concentration of hydrogen in the solid solution, C^H , and the hydride, $C^{H,hr}$:

$$C^{HT} = fC^{H,hr} + (1-f)C^H \quad (2)$$

f is the hydride volume fraction. C^H is equal to the hydrogen terminal solid solubility, C^{TS} , when $f \neq 0$, and $C^{H,hr}$ can be considered constant, independent of temperature. Hydrogen diffusion in the hydride is also significantly slower than in the metal and therefore it can be neglected. Then, the total hydrogen flux in a hydride/solid-solution composite is given by the following relation:

$$J_k^H = -(1-f) \frac{D^H C^H}{RT} \left(\frac{\partial \mu^H}{\partial x_k} + \frac{Q^H}{T} \frac{\partial T}{\partial x_k} \right) \quad (3)$$

R is the gas constant and T is the absolute temperature. Also D^H and Q^H are the diffusion coefficient and the heat of transport of hydrogen in the solid solution, respectively. Hydrogen thermal transport is taken into account by the temperature gradient term. The effects of stress and hydrogen concentration on diffusion are both included in the gradient of the chemical potential of hydrogen in the solid solution, μ^H :

$$\mu^H = \mu^{H,0} + \bar{V}^H \left(\frac{1}{2} M_{ijkl} \sigma_{ij} \sigma_{kl} - \frac{1}{3} \sigma_{mm} \right) \quad (4)$$

$\mu^{H,0}$ is the stress free hydrogen chemical potential, which depends on hydrogen concentration. In the present study the law for ideal solutions is adopted. \bar{V}^H is hydrogen molal volume. Also M_{ijkl} and σ_{ij} are metal's elastic compliance and stress tensor, respectively.

The precipitation of the hydride (MH_x) occurs under chemical equilibrium conditions, when the terminal solid solubility of hydrogen in the metal, C^{TS} , is reached:

$$C^{TS} = C^{TS,0} \exp\left(\frac{\bar{w}_{acc} + \bar{w}_{int}}{xRT}\right) \exp\left[\frac{\bar{V}^H}{RT} \left(\frac{\sigma_{mm}}{3} - \frac{1}{2} M_{ijkl} \sigma_{ij} \sigma_{kl} \right)\right] \quad (5)$$

$C^{TS,0}$ is the terminal solid solubility of hydrogen, under stress-free conditions. Hydrides expand during precipitation. Consequently, hydrogen solubility is affected by the strain

energy of hydride accommodation, \bar{w}_{acc} , as well as by the interaction energy of the applied stress field with the expanding hydride, \bar{w}_{int} , both defined per mole of hydride.

The non-mechanical energy flow is governed by the following differential equation, which is derived by enforcing conservation of energy:

$$\rho c_p \frac{dT}{dt} + \frac{\Delta \bar{H}^{hr}}{\bar{V}^{hr}} \frac{df}{dt} = \frac{\partial}{\partial x_i} \left(k \frac{\partial T}{\partial x_i} \right) - J_n^H \frac{\partial \mu^H}{\partial x_n}. \quad (6)$$

ρ , c_p and k are the density, the specific heat at constant pressure and the thermal conductivity of the metal, respectively. Also $\Delta \bar{H}^{hr}$ and \bar{V}^{hr} are the enthalpy associated with the formation of a mole of hydride and the hydride molal volume, respectively. Therefore the variation of the heat content in the metal-hydride composite depends on conducted heat, heat generated during hydrogen diffusion and heat released during hydride formation.

The deformation of the hydride/solid-solution composite is coupled with hydrogen diffusion and energy flow due to the strains, which are caused by hydrogen dissolution, hydride formation and thermal expansion:

$$\frac{d\sigma_{ij}}{dt} = M_{ijkl}^{-1} \left(\frac{d\epsilon_{kl}}{dt} - \frac{d\epsilon_{kl}^H}{dt} - \frac{d\epsilon_{kl}^E}{dt} \right), \quad (7)$$

$$\frac{d\epsilon_{ij}^H}{dt} = \frac{1}{3} \delta_{ij} \frac{d}{dt} [f\theta^{hr} + (1-f)C^H \bar{V}^M \theta^H], \quad (8)$$

$$\frac{d\epsilon_{ij}^E}{dt} = \alpha \delta_{ij} \frac{dT}{dt}. \quad (9)$$

θ^{hr} is the trace of hydride expansion strain and $\theta^H = \bar{V}^H / \bar{V}^M$ is the expansion of the metal lattice due to hydrogen dissolution. \bar{V}^M and α are the molal volume and the thermal expansion coefficient of the metal. It is assumed that the elastic and thermal properties of the hydride and the solid solution are identical.

Hydride fracture and therefore crack growth is simulated by considering cohesive tractions along the crack path. At a material particle along the crack path, cohesive traction is related to the respective normal displacement through a simple trapezoid variation. The energy of decohesion, i.e. the energy required per unit crack advance, and the maximum cohesive traction are given by the following relations:

$$\phi_0 = f\phi_0^{hr} + (1-f)\phi_0^M, \quad (10)$$

$$\sigma_{max} = \sqrt{f\sigma_{hr}^2 + (1-f)\sigma_M^2}. \quad (11)$$

ϕ_0^M and ϕ_0^{hr} are the de-cohesion energies, when there is no hydride and when there is only hydride, along the crack plane, respectively. ϕ_0^{hr} is derived from the threshold stress intensity factor for delayed hydride cracking [1]. Also σ_{hr} is hydride fracture strength and σ_M is equal to three times the yield stress of the metal [1]. In the following the hydrogen embrittlement and fracture model is applied to Zircaloy-2 and δ -hydride ($\text{ZrH}_{1.66}$).

4. SIMULATION OF SAWATZKY EXPERIMENT

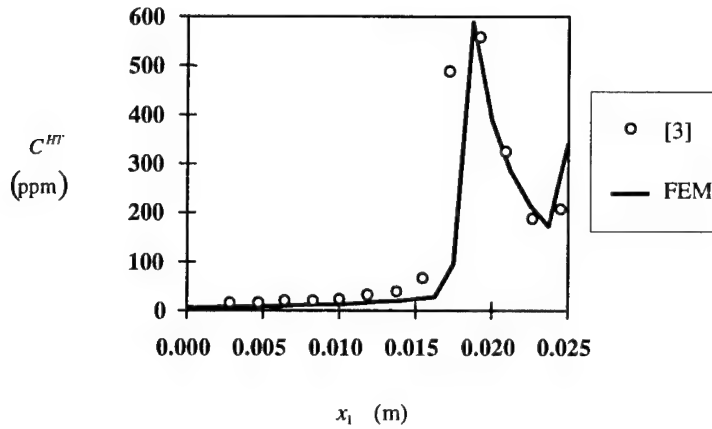


Figure 1: Hydrogen distribution in a Zircaloy-2 cylinder, after a 34-day anneal under a temperature difference 130°C - 477°C; experimental [3] and finite element results [1].

A Zircaloy-2 cylinder of 1.2 cm in diameter and 2.5 cm in length, with initial uniform hydrogen concentration 130 ppm by weight ($\approx 837 \text{ mole/m}^3$) was subjected to a temperature difference of 347°C for 34-days [3]. Hot and cold end temperatures of 477°C and 130°C, respectively, were imposed, by placing the specimen between a heated stainless steel cylinder and a water-cooled brass plate. Glass wool was wrapped around the specimen to reduce heat losses through the cylindrical surface of the specimen. Also any hydrogen losses were minimized, by developing, before the experiment, an oxide surface layer, which is impermeable to hydrogen. The measured hydrogen concentration is compared with the respective FEM prediction in Figure 1.

5. HYDRIDE PRECIPITATION AND FRACTURE UNDER K-FIELD DOMINANCE

A semi-infinite crack is considered in a homogeneous material under mode-I loading and plane strain conditions [2]. K-field traction is applied on a semi-circular boundary of radius equal to 0.1 m; only half of the space is analyzed, due to symmetry with respect to the crack line. The stress intensity factor initially increases at a rate equal to $0.2 \text{ MPa}\sqrt{\text{m}}\cdot\text{s}^{-1}$ for 100 s and subsequently remains constant at the maximum value of $20 \text{ MPa}\sqrt{\text{m}}$. The temperature of the material is equal to 300° C. Initial total hydrogen concentration is equal to 1000 ppm. Zero hydrogen flux is prescribed along the crack face and the remote semi-circular boundary. Due to symmetry conditions, hydrogen flux is also taken equal to zero along the crack line. A Cartesian coordinate system is considered with origin at the crack tip and x_1 -axis parallel to the crack plane. The progress of hydride precipitation and the development of a microcrack along the crack plane, ahead of the main crack, is shown in Figure 2.

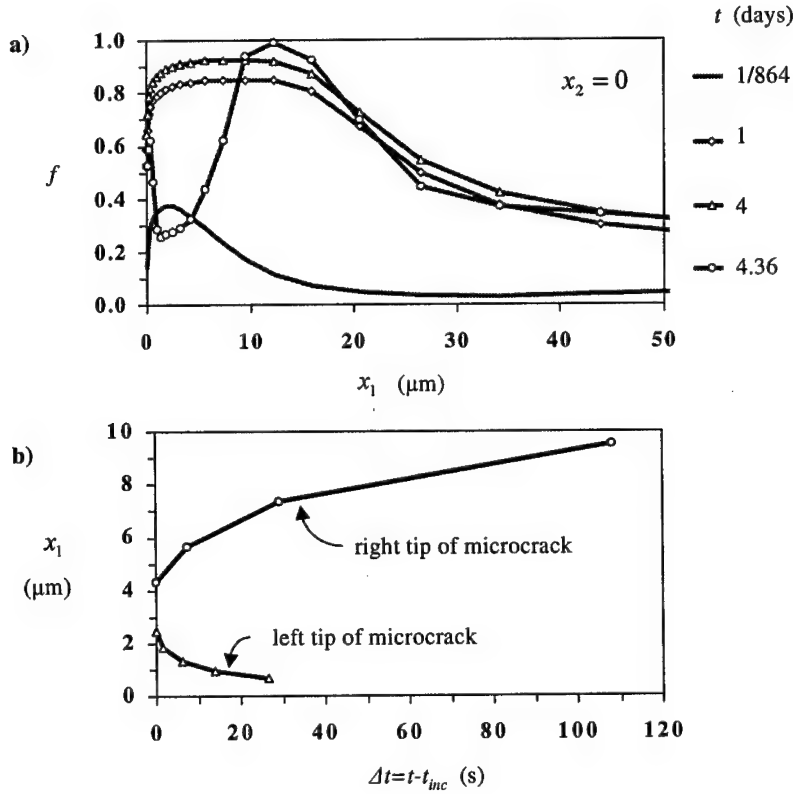


Figure 2: (a) Hydride volume fraction distribution along the crack line and (b) microcrack propagation, under K-field dominance [2]; $t_{inc} = 4.36$ days.

6. HYDROGEN EMBRITTLEMENT IN A CRACKED PLATE UNDER TENSION

Hydrogen embrittlement in the cladding of light water reactor fuel rods has been investigated [1], [2]. The most critical case corresponds to a crack along the rod axis, due to fuel pellet-cladding mechanical interaction and associated tensile hoop stresses. The geometry has been approximated by a cracked plate. The plate thickness, w , is equal to the cladding wall thickness ($w = 0.8$ mm). A long planar surface crack of depth a ($= 0.1w$) has been considered on one side. A remote tensile stress, σ_{ap} , is applied normal to the crack faces and builds up gradually, at a rate of 10 MPa/s, up to the maximum value of 500 MPa. Zirconium oxidation is assumed to produce a constant inflow of hydrogen on the crack-side surface of the plate and the crack faces, which is equal to 0.122×10^{-7} mole/(m²·s). A zero hydrogen flux is considered on the other side of the plate. The surface temperature is constant, being equal to 567 K, on the crack side, and 607 K, on the other side. The initial temperature distribution is assumed to be linear across the thickness of the plate. The initial hydrogen concentration is equal to 2500 mole/m³ (≈ 388 ppm). Symmetry conditions require that the heat and hydrogen fluxes on the crack plane as well as on the remote plane, where σ_{ap} is applied, are zero. Plane strain conditions prevail. A Cartesian coordinate system is considered with origin at the crack tip and x_1 -axis parallel to the crack plane. Figures 3a and 3b show the distribution of hydride

volume fraction and normalized stress trace along the crack plane, respectively. After 5 days, steady-state conditions are approached. According to Fig. 3b, there is no region of K-field dominance, due to hydrogen thermal transport. Also according to Fig. 3a, severe material embrittlement is limited only to a very small area near the crack tip.

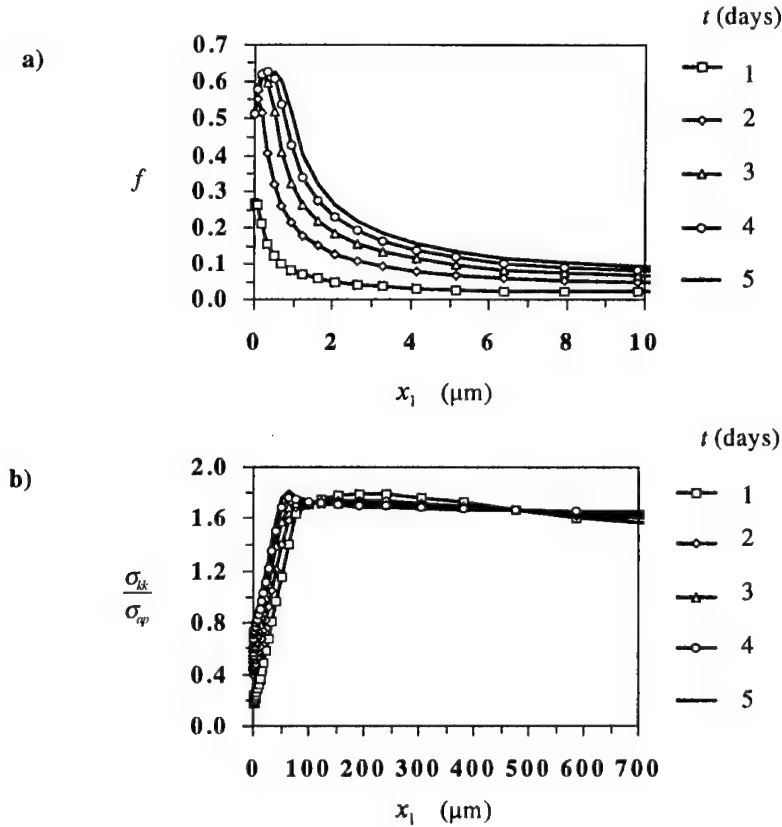


Figure 3: (a) Hydride volume fraction and (b) stress trace distributions along the crack plane in a plate under tensile loading and temperature gradient [2].

Acknowledgements: Financial support for the study on hydride induced embrittlement in metals is currently provided by the Foundation for Knowledge and Competence Development (Project Grant Hög 2000, KK-Stiftelsen, Sweden).

7. REFERENCES

- [1] Varias, A.G. and Massih, A.R., Simulation of hydrogen embrittlement in zirconium alloys under stress and temperature gradients, *Journal of Nuclear Materials* 279, 273-285 (2000).
- [2] Varias, A.G. and Massih, A.R., Numerical modeling of delayed hydride cracking in zirconium alloys, in *Advances in Mechanical Behaviour, Plasticity and Damage Vol. 2*, D. Miannay, P. Costa, D. Francois and A. Pineau (Eds), *Elsevier Science, Oxford* (2000) 1219-1224.
- [3] Sawatzky, A., Hydrogen in Zircaloy-2: Its distribution and heat of transport, *Journal of Nuclear Materials* 2, 321-328 (1960).

SOME PROBLEMS OF ELECTROMECHANICAL FRACTURE OF DIELECTRIC AND PIEZOELECTRIC BODIES

D.I. Bardzokas

National Technical University of Athens
Faculty of Applied Sciences, Department of Mechanics
Lab. of Strength and Materials, Zographou Campus, Theocaris Bld.
GR-157 73, Athens, Greece, email: bardim@central.ntua.gr

A.I. Zobnin

Moscow State University
of Engineering Ecology
214, Staraya Baaasmannaya
str. 107884, Moscow,
Russia

1. SUMMARY

Methods of fracture mechanics are applied in analysis of electrical breakdown of dielectrics and electromechanical fracture of piezoelectrics. Griffith's energy balance method as well as the intensity factor approach and invariant integral theory are used when formulating criteria of electrical breakdown and electromechanical fracture. The controlling factors for these phenomena proved to be the stress intensity factors and the charge density intensity factor at the crack tip or at the edge of electrode. Several problems of electrical breakdown of dielectrics are considered and the results are correlated with experimental data. The piezoelectric theory of Mindlin is used in analysis of the effect of non-uniform electric field on the crack instability. The obtained solution of antiplane crack problem shows that the stress state of dielectrics and its strength appreciably affected by the non uniform electric field.

2. INTRODUCTION

The analysis of solid state devices of piezoelectronics shows that mechanical or electrical loading causes stress and electrical field intensification at crack tips as well as at sharp edges of surface or embedded electrodes. Therefore discontinuity surfaces present always in real materials may become unstable under certain conditions and rapidly propagate causing eventual fracture of a body as a whole. Griffith's energy balance method has provided a powerful tool both for the theoretical study of fracture processes and for practical calculations for structural members. It is of interest that as early as 1927, as the dawn of fracture mechanics, Griffith's approach was used first by Gorowits in analysis of fracture of dielectrics subjected to strong electric field (see Skanavi, [21]). A generalization to piezoelectric media of the energy balance conditions was made only half a century later in papers of Parton [14] and Kudryavtsev *et al.* [8,9]. Griffith's energy accounting was applied

by Suo *et al* [23] to study crack growth for ferroelectric ceramics under small-scale hysteresis.

The general theory of the motion of singularities developed by Cherepanov [5] for an electromagnetic continuum is based on the invariance of certain Γ -integrals with respect to their integration path around a singular point.

There is a characteristic feature which is common to linear problems of electroelasticity dealing with unbounded crack-containing piezoelectric media. It is that the mechanical stresses, strains, and electric field components go to infinity at the tip of a crack, the order of singularity, $1/2$, being independent of the length of the crack (Parton and Kudryavtsev, [15]). For a crack lying in the interface between two unlike materials, the near-tip electroelastic fields are of a more complex oscillating nature (Kudryavtsev *et al.*, [8,9]; Suo *et al.*, [23]). The oscillating singularity is rather limited in space, however, Kudryavtsev *et al.* [8] estimate its size at about 2.5×10^{-4} of the crack length. In bounded piezoelectric bodies all the microscopic processes in the vicinity of the crack tip must be controlled by the coefficients of singularities (intensity factors) when an annulus exists around the crack in which the field is described by the above-mentioned singular solutions. When the charge density intensity factor K_q is introduced, it proves possible (Senik, [19]; Parton *et al.*, [15]) to define a certain critical value of this quantity, K_q^c , and to write

$$K_q = K_q^c \quad (1)$$

as the condition for the electrical breakdown of a dielectric medium. An alternative but totally equivalent expression may be written in terms of Γ -integrals. The well-known crack extension criteria are adaptable to the electromechanical fracture of dielectrics and piezoelectrics as was discussed by Parton *et al.* [16,17] and by Bardzokas *et al.* [3].

If there are cracks or inclusions in the piezoelectric medium under study, special attention should be given to the electroelastic conditions associated with these imperfections. Parton [14] and Polovinkina and Ulitko [18] took the conditions of ideal contact between two sides of a crack

$$D_n^+ = D_n^-, \quad \varphi^+ = \varphi^- \quad (2)$$

D_n being the normal component of the induction and φ the electric potential. Deeg [6], Pak [13], Sosa [21] and Suo *et al.* [23] adopted another set of boundary conditions on a perfectly insulating crack

$$D_n^+ = D_n^- = 0 \quad (3)$$

In air-filled cracks, however, this condition should not be fulfilled due to possible ionization and breakdown of air gap as stated by Balygin [2] and Koikov and Izykin [7]. McMeeking [10] modeled cracks containing a conducting fluid with the use of following boundary conditions

$$\varphi^+ = \varphi^- \quad (4)$$

Senik [19] investigated general electrical boundary conditions to be satisfied in the case of a long dielectric inclusion. The special cases considered in the study are the ideal contact conditions, a perfectly insulating inclusion, and inclusions with a high or low permittivity (2-4).

3. ELECTRICAL FRACTURE OF DIELECTRICS

a) Energy Balance Approach

As it was proposed by Senik and Parton, the phenomenon of electrical fracture (or breakdown) of linear dielectrics can be considered as the extending of some perfectly conducting surfaces between electrodes exposed to a sufficiently high difference in electrical potential. Such perfectly conducting surfaces may be initiated by a crack tip as well as by a sharp edge of electrode or inclusion due to considerable concentration of electroelastic fields. Without discussing the possible mechanism of its formation and propagation it can be said with confidence that a fixed part of power delivered to dielectrics must be consumed to create unit area of new conducting surface. The extending of conducting surfaces and hence the breakdown of dielectrics depends on the relative values of energy release rate in the vicinity of crack tip or electrode edge and the energy required to create unit area of the mentioned surface.

One way of formulating a local breakdown condition is by calculating the flow of energy to the new formed conducting surface. Consider two states a of linear dielectric body which contains a perfectly conducting embedded electrode Σ of arbitrary shape and has the electroded outer surface being at zero potential. Let $V^{(0)}$ be the potential of Σ in a certain initial state «0» of the body and $V^{(1)}$ is the same value in a state «1», in which the electrode surface Σ has received an increment in the form of a conducting surface $\Delta\Sigma$. According to Parton *et al.* [16,17] the macroscopic energy flow $\Delta A_{\Delta\Sigma}$ due to the formation of $\Delta\Sigma$ is given by

$$\Delta A_{\Delta\Sigma} = -\frac{1}{2}(Q_{\Delta}^{(1)}V^{(1)} + Q_*) \quad (5)$$

where

$$Q_{\Delta}^{(1)} = \int_{\Delta\Sigma} D_n^{(1)} ds, \quad Q_* = \int_{\Delta\Sigma} D_n^{(1)} \varphi^{(0)} ds$$

The breakdown condition can be written as $\gamma \Delta\Sigma = -\Delta A_{\Delta\Sigma}$ and hence with regard to (5) as

$$2\gamma = \lim_{\Delta\Sigma \rightarrow 0} \frac{1}{\Delta\Sigma} (Q_{\Delta}^{(1)}V^{(1)} + Q_*) \quad (6)$$

According to (6) the dielectric strength is determined by breakdown parameter γ which is to be estimated from experiment. The quantity γ is expected to be the macroscopic parameter depending on the material properties of both dielectrics and electrode.

The electric fields in the vicinity of the edge of electrode in linear dielectrics display the singularity as follows

$$D_i = \frac{K_q}{\sqrt{2\pi r}} f_i(\theta) + O(1) \quad (7)$$

where r, θ are the polar coordinate tied with the edge of the electrode and K_q is the charge density intensity factor depending on the properties of dielectrics and on the applied electric loads. The use of asymptotic formulae like (7) in (6) makes it possible to relate this criterion to the breakdown condition (1).

b) Electrical Breakdown between Two Axial Circular Electrodes

By way of illustration let us study some simple problems of breakdown of dielectrics by applying the foregoing principles. Consider an unbounded homogeneous dielectric layer

$-h \leq z \leq h$ having dielectric permittivity ε and placed between two homogeneous half spaces $z > h$ and $z < -h$ with equal dielectric permittivities, ε^+ . Two axial circular electrodes of radius a disposed on the interfaces ($z = \pm h$) are supposed to be at equal in magnitude but opposite in sign potentials, $\pm V_0$. This problem of electrostatics is reduced to that of solving of a system of dual integral equations involving the Bessel function (Parton *et al.*, [11]). Upon expanding the unknown function in a Legendre series, the system of dual integral equations yields an infinite system of linear algebraic equations in unknown coefficients d_m ($m=0,1,2,\dots$). It should be emphasized that d_m depend only on two dimensionless parameters $\varepsilon_0 = \varepsilon/\varepsilon^+$ and $\delta = 2h/a$. Having obtained the coefficient d_m one can define the density distribution function for electrical charges on the electrode

$$q(r) = \frac{2V_0(1+\varepsilon_0)\varepsilon}{\pi\sqrt{a^2-r^2}} \sum_{n=0}^{\infty} (4n+1)d_n \frac{n!2^n P_{2n}\left(\sqrt{1-(r/a)^2}\right)}{(2n-1)!!} \quad (8)$$

displaying singularities $O(1/\sqrt{a \mp r})$ in the vicinity of the edge of electrode when $r \rightarrow \pm a$. The charge density intensity factors can be obtained then from (8) in the form

$$K_q = \lim_{r \rightarrow a} (q(r)\sqrt{2\pi(a-r)}) = \frac{2V_0(1+\varepsilon_0)\varepsilon}{\sqrt{\pi a}} \sum_{n=0}^{\infty} (-1)^n (4n+1)d_n \quad (9)$$

From Eq. (9) and (1) there follows the formula for breakdown voltage

$$V_c = \frac{\sqrt{\pi a} K_q^c}{2\varepsilon(1+\varepsilon_0) \sum_{n=0}^{\infty} (-1)^n (4n+1)d_n} \quad (10)$$

The validity of criterion (1) has been demonstrated by comparing the breakdown voltage from (10) with known vacuum breakdown data obtained by Slivkov [20] using two unlikely charged axial circular electrodes.

4. CRITERIA FOR ELECTROMECHANICAL FRACTURE OF PIEZOELECTRICS CONTAINING ELECTRODES AND CRACKS

a) Fracture of Piezoelectrics Initiated by Edges of Electrodes

Because of the coupling of electric and elastic fields in piezoelectrics the considerable concentration of such fields in the vicinity of electrode edge may result sometimes in the fracture of a piezoelement, both electrically and mechanically. The electrical breakdown of piezoelectrics can be considered in the same way as the breakdown of dielectrics or as the extending of some perfectly conducting surface between two charged electrodes. From the viewpoint of continuum mechanics this surface is considered to be a mathematical surface which has no mechanical loads on its faces. The real electrode is assumed to be perfectly conducting and flexible, all the components of mechanical fields are continuous on its surface.

Consider a piezoelectric body with an embedded electrode Σ which receives an increment $\Delta\Sigma$. The outer boundary is entirely electroded and supposed to be at zero potential and free of mechanical loads. Assume that the body has no body forces or free charges present. According to Bardzokas *et al.* [3] the expression for the energy flow due to the formation of the additional perfectly conducting surface $\Delta\Sigma$ is found to be

$$\Delta A_{\Delta\Sigma} = \frac{1}{2} \int_{\Delta\Sigma} (\sigma_{ij}^{(0)} u_i^{(1)} - (\varphi^{(1)} + \varphi^{(0)}) D_j^{(1)}) n_j ds \quad (11)$$

The electrode «extension» condition may then be written as

$$2\gamma \Delta\Sigma = -\Delta A_{\Delta\Sigma} \quad (12)$$

where γ is the energy density consumed to create the new conducting surface. Upon integration in (11) over the two-side surface $\Delta\Sigma$ the breakdown condition (12) takes the form

$$\gamma = \gamma^{(e)} + \gamma^{(E)} \quad (13)$$

where

$$\gamma^{(e)} = -\frac{1}{4} \lim_{\Delta\Sigma_+ \rightarrow 0} \frac{1}{\Delta\Sigma_+} \int_{\Delta\Sigma_+} \sigma_{ij}^{(0)} (u_i^{(1)+} - u_i^{(1)-}) n_j ds \quad (14)$$

$$\gamma^{(E)} = \frac{1}{4} \lim_{\Delta\Sigma_+ \rightarrow 0} \frac{1}{\Delta\Sigma_+} \int_{\Delta\Sigma_+} (\varphi^{(0)} + V^{(1)}) (D_j^{(1)+} - D_j^{(1)-}) n_j ds \quad (15)$$

It should be emphasized that (14) is equivalent to the local fracture condition for an elastic body while (15) can be transformed into (6). It follows thus from (13) that the total fracture energy density γ can be broken in the case of the electromechanical fracture of piezoelectrics into two parts: the mechanical component $\gamma^{(e)}$ is consumed to create the additional free mechanical surface $\Delta\Sigma$ and the electrical component $\gamma^{(E)}$ is associated with the advent of the new perfectly conducting surface $\Delta\Sigma$.

For a piezoelectric medium the crack contour or the edge of an electrode may be considered as a distributed sink for the released energy. The most important way in the study of electromechanical fracture of piezoelectrics is examination of the flow of energy to the fracture domain in the vicinity of above-mentioned singular line. The path independent integral developed by Cherepanov [5] and by Parton and Kudryavtsev [15] provides the effective tool for such an analysis which results in derivation of local fracture and breakdown criteria of piezoelectrics. Parton and Kudryavtsev [15] introduced for a piezoelectric medium under plane strain conditions the energy-sink vector $\Gamma_k = \Gamma_k^{(E)} + \Gamma_k^{(e)}$ ($k=1,2$) where the electrical part, $\Gamma_k^{(E)}$, and the mechanical part, $\Gamma_k^{(e)}$, are given by

$$\Gamma_k^{(E)} = \oint_L \left(-\frac{1}{2} D_i E_i + D_i E_k n_i \right) d\ell, \quad \Gamma_k^{(e)} = \oint_L \left(\frac{1}{2} \sigma_{ij} e_{ij} - \sigma_{ij} n_i u_{j,k} \right) d\ell$$

L is an arbitrary closed contour enclosing the edge of electrode and n_i are the components of the unit vector normal to L . It was shown that Γ_k is path-independent if the deformation of L does not involve the appearance of new singularities of electric field inside of L . In the plane problem for curvilinear electrode it can be found that only the normal components of the sink vector, say $\Gamma_n^{(E)}$ and $\Gamma_n^{(e)}$ are different from zero. Hence in accordance with the general theory of the motion of singularities the simplest condition for the electromechanical fracture of piezoelectrics can be presented as $\Gamma_n = \Gamma_n^{(E)} + \Gamma_n^{(e)} \leq \Gamma_c$ where Γ_c is a certain macroscopic quantity defining a given piezoelectrics-electrode system

b) Fracture of Piezoelectrics Initiated by Crack Tip

Both electrode edge and crack tip act as seats of electromechanical fracture of piezoelectrics. Fracture conditions can be derived on the basis of classical fracture mechanics. Consider a piezoelectric body which contains a crack of arbitrary shape and has no body forces or free charges present. Let the two-side surface of the crack receive an increment $\Delta\Sigma$. Parton and

Kudryavtsev [15] showed that the energy flow due to formation of the discontinuity $\Delta\Sigma$ is given by

$$\Delta A_{\Delta\Sigma} = \frac{1}{2} \int_{\Delta\Sigma} (\sigma_{ij}^{(0)} u_i^{(1)} + D_j^{(0)} \varphi^{(1)}) n_j ds - \frac{1}{2} \int_{\Delta\Sigma} D_j^{(1)} (\varphi^{(1)} + \varphi^{(0)}) n_j ds \quad (16)$$

Note that the integration in (16) is performed over the two surfaces $\Delta\Sigma_1$ and $\Delta\Sigma_2$ of the additional discontinuity, the normals to these surfaces being directed inward the crack. The crack propagation condition may then be written as

$$\gamma(\Delta\Sigma_1 + \Delta\Sigma_2) = -\Delta A_{\Delta\Sigma} \quad (17)$$

where γ is the surface energy density.

In piezoelectric medium, the crack propagation criterion depends, of course, on the electric boundary conditions assumed at the surfaces of the crack. If the crack is considered to be a mathematical surface the conditions which are natural to be assumed are (2). In such a situation the energy flow due to the formation of the discontinuity and the local fracture condition for piezoelectrics are equivalent to that for elastic body. In reality, however, a mechanical loading causes a finite opening of the crack, so the electric potential may suffer discontinuity on the crack surface (Suo *et al.*, [23]). The normal component of the electrical displacement must be continued at the surface of an opened crack in a piezoelectric medium (Senik, [19]) and with regard to that the fracture condition (17) takes the form

$$\gamma = -\frac{1}{4} \lim_{\Delta\Sigma_1 \rightarrow 0} \frac{1}{\Delta\Sigma_1} \int_{\Delta\Sigma_1} \left(\sigma_{ij}^{(0)} (u_i^{(1)+} - u_i^{(1)-}) n_j + \frac{1}{\epsilon_n^*} (D_n^{(1)} - D_n^{(0)}) D_n^{(1)} \right) ds \quad (18)$$

where ϵ_n^* specifies the reduced dielectric permittivity of the crack.

5. ANALYSIS OF EFFECT OF NON-UNIFORM FIELD ON THE CRACK INSTABILITY - ANTIPLANE SHEAR OF THE CRACKED BODY IN NON-UNIFORM ELECTRIC FIELD

Consider the effect of non-uniform electric field, $E_3^0 = E_{30}x_2$ ($E_{30} = \text{const}$), on an unbounded continuum having the plane tunnel crack ($|x_1| < \ell$, $x_2 = 0$, $|x_3| < \infty$) with the faces exerted by uniformly distributed stresses, $\sigma_{23} = p_3 = \text{const}$. Taking into account the following relationship

$$\begin{aligned} \sigma_{ij} &= c_{12} u_{k,k} \delta_{ij} + c_{44} (u_{i,j} + u_{j,i}) + d_{12} P_{k,k} \delta_{ij} + d_{44} (P_{i,j} + P_{j,i}) \\ E_{ij} &= d_{12} u_{k,k} \delta_{ij} + d_{44} (u_{i,j} + u_{j,i}) + b_{12} P_{k,k} \delta_{ij} + b_{44} (P_{i,j} + P_{j,i}) + b_{77} (P_{j,i} - P_{i,j}) + b^0 \delta_{ij} \\ E_i^L &= -a P_i \end{aligned}$$

and substituting them in Eq. (19)

$$\begin{aligned} \sigma_{ij,j} &= 0 \\ E_{ji,j} + E_i^L - \varphi_j + E_i^0 &= 0 \\ -\epsilon_0 \varphi_{ji} + P_{i,j} &= 0 \end{aligned} \quad (19)$$

E_{ij} , E_i^L , E_i^0 and P_i are the non-symmetrical electrical tensor, local electrical force, external electric field and polarization vector, respectively, we obtain:

$$\begin{aligned}
a\ell_2^2 \nabla^2 P_3 - (aP_3 - E_3^0) &= 0 \\
a\ell_2^2 \nabla^2 u_3 + \frac{d_{44}}{c_{44}} (aP_3 - E_3^0) &= 0
\end{aligned} \tag{20}$$

where ∇^2 is two-dimensional Laplace operator and $a\ell_2^2 = b_{44} + b_{77} - d_{44}^2/c_{44}$. Because of symmetry of the problem (20); must be solved in the half-plane $x_2 > 0$ with regard to the following boundary conditions on $x_2 = 0$

$$\begin{aligned}
\sigma_{23} &= P_3, \quad E_{23} = 0 \quad (|x_1| < \ell) \\
u_3 &= P_3 = 0 \quad (|x_1| > \ell).
\end{aligned}$$

The solution of the stated problem can be expressed in an integral form

$$\begin{aligned}
u_3 &= \int_0^\infty \left(B(\xi) \exp(-\xi x_2) - \frac{d_{44}}{c_{44}} A(\xi) \exp(-x_2 \sqrt{\xi^2 + \ell_2^{-2}}) \right) \cos(\xi x_1) d\xi \\
P_3 &= \frac{E_{30} x_2}{a} + \int_0^\infty A(\xi) \exp(-x_2 \sqrt{\xi^2 + \ell_2^{-2}}) \cos(\xi x_1) d\xi \\
\sigma_{23} &= \frac{d_{44}}{a} E_{30} - c_{44} \int_0^\infty B(\xi) \exp(-\xi x_2) \cos(\xi x_1) d\xi
\end{aligned} \tag{21}$$

with the unknown functions $A(\xi)$ and $B(\xi)$ satisfying the following dual integral equations

$$\begin{aligned}
\int_0^\infty A(\xi) \exp(-x_2 \sqrt{\xi^2 + \ell_2^{-2}}) \cos(\xi x_1) d\xi &= \frac{1}{a} \left(\frac{d_{44}}{c_{44} \ell_2^2} + E_{30} \right), \quad (0 \leq x_1 < \ell) \\
\int_0^\infty A(\xi) \cos(\xi x_1) d\xi &= 0, \quad (\ell < x_1 < \infty)
\end{aligned} \tag{22}$$

$$\begin{aligned}
\int_0^\infty \xi B(\xi) \cos(\xi x_1) d\xi &= \frac{1}{c_{44}} \left(-P_3 + \frac{d_{44}}{a} E_{30} \right), \quad (0 \leq x_1 < \ell) \\
\int_0^\infty B(\xi) \cos(\xi x_1) d\xi &= 0, \quad (\ell < x_1 < \infty)
\end{aligned} \tag{23}$$

The approximate solution of (22) can be obtained in the form of Bessel series expansion while according to Bateman and Erdelyi [4] the exact solution of (23); has the form

$$B(\xi) = \frac{1}{c_{44}} \left(-P_3 + \frac{d_{44}}{a} E_{30} \right) \frac{J_1(\xi \ell)}{\xi} \tag{24}$$

The main result of the performed calculations is the following expression for the shear stresses on the crack line

$$\sigma_{23} = P_3 - \left(P_3 - \frac{d_{44}}{a} E_{30} \right) \frac{|x_1|}{\sqrt{x_1^2 - \ell^2}}, \quad (|x_1| > \ell) \tag{25}$$

It is seen from (25); that σ_{23} displays singularities $1/\sqrt{x_1 \pm \ell}$ at the crack tips. The same results was obtained by Askar *et al.* [1] but the singular part of the stress field is not of prime importance because the problem involves parameter ℓ_2 having the dimension of length, values are very small for many known materials. It is more essential that (25); gives the exact expression for the stress distribution along the crack line.

6. REFERENCES

- [1] Ascar, A., P.C.Y. Lee and A.S. Cuckmak (1971). The effect of surface curvature and discontinuity on the surface energy density and other induced fields in elastic dielectrics with polarization gradient. *Intern. J. Solids and Struct.*, 7, 523-538.
- [2] Balygin, I.E. (1974). *Electrical Properties of Dielectric Solids*. Energiya, Leningrad.
- [3] Bardzokas, D., B.A. Kudryavtsev and N.A. Senik (1994) On criteria for electromechanical fracture of piezoelectrics initiated by edges of electrodes. *Intern. J. Strength of Mater.*, 42-46.
- [4] Bateman, H. and A. Erdelyi (1954). *Tables of Integral of Transformations*. McGraw-Hill, New York *et al.*
- [5] Cherepanov, G.P. (1977). Invariant Γ -integrals and their application in mechanics. *Prikl. Mat. I Mekh.*, 41, 99-412.
- [6] Deeg, W.F. (1980). The analysis of dislocation, crack and inclusion problems in piezoelectric solids. Ph.D. Thesis, Stanford University, CA.
- [7] Koikov, S.N. and A.N. Izykin (1968). *Electrical Aging of Dielectric Solids*. Energiya, Leningrad.
- [8] Kudryavtsev, B.A., V.Z. Parton and V.I. Rakitin (1975). Fracture mechanics of piezoelectric materials. Rectilinear tunnel crack in the conductor-piezoelectric interface. *Prikl. Mat. I Mech.*, 39, 149-159.
- [9] Kudryavtsev, B.A., V.Z. Parton and V.I. Rakitin (1975). Fracture mechanics of piezoelectric materials. An axisymmetric crack in the interface with a conductor. *Prikl. Mat. I Mech.*, 39, 352-362.
- [10] McMeeking, R.M. (1987). On mechanical stresses at cracks in dielectrics with application to dielectric breakdown. *J. Appl. Phys.*, 62, 3116-3122.
- [11] Nowacki, W. (1983). *Electromagnetic Effects in Solids*. PWN, Warsaw.
- [12] Pak, Y.E. (1990). Crack extension force in a piezoelectric material. *J. Appl. Mech.*, 57, 641-653.
- [13] Parton, V.Z. (1976). Fracture mechanics of piezoelectric materials. *Acta Astro.*, 3, 671-683.
- [14] Parton, V.Z. and B.A. Kudryavtsev (1988). *Electromagnetoelasticity*. Gordon and Breach, New York.
- [15] Parton, V.Z., B.A. Kudryavtsev and N.A. Senik (1988). On one possible criterion for the electric breakdown of dielectrics in highly non-homogeneous fields. *Dokl. Akad. Nauk SSSR*, 298, 611-615.
- [16] Parton, V.Z., J.J.N. Mustafae and N.A. Senik (1991). *Methods of Fracture Mechanics and Breakdown of Dielectrics*. Inst. Fiz. Akad. Nauk Azerbaijan SSR, Baku.
- [17] Polovinkina, I.B. and A.F. Ulitko (1978). On the equilibrium of piezoceramic bodies containing cracks. In: *Thermal Stresses in Structural Members*, pp. 10-17, Naukova Dumka, Kiev.
- [18] Senik, N.A. (1987). Application of fracture mechanics to dielectric breakdown problems. In: Proc. 1st USSR Nat. Conf. Fracture Mechanics, Lvov. Oct. 20-21, 1986, p. 298.
- [19] Slivkov, I.N. (1972). *Electric Insulation and Breakdown in Vacuum*. Atomizdat, Moscow.
- [20] Skanavi, G.I. (1958). *Physics of Dielectrics (Strong Fields)*. Fizmatizdat, Moscow.
- [21] Sosa, H. (1992). On the fracture mechanics of piezoelectric solids. *Intern. J. Solids and Struct.*, 29, 2613-2622.

- [22] *Suo, Z., C.-M. Kuo, D.M. Barnett and J.R. Willis (1992). Fracture mechanics for piezoelectric ceramics. J. Mech. and Phys. Solids, 40, 739-765.*

CONTROL OF DYNAMIC STRESS AND FRACTURE OF PIEZOELECTRIC BODIES WITH CRACKS

D.I. Bardzokas

National Technical University of Athens
Faculty of Applied Sciences, Department of Mechanics
Lab. of Strength and Materials, Zographou Campus, Theocaris Bld.
GR-157 73, Athens, Greece, email: bardim@central.ntua.gr

M.L. Filshtinsky

Department of Mathematical Physics, State University of Sumy.
Rimsky-Korsakov st. 2, 244007 Sumy, Ukraine

1. SUMMARY

Several inverse problems of somewhat optimal control of failure parameters and also of stresses in typical points of a body are stated and solved in the monographs [1,2]. The approach to the solution of the problem of optimal control of parameters, regulating the fracture of a piezoelectric body with cracks and a piezoelectric bimorph with an interphase crack is proposed here as well.

2. INTRODUCTION

Rapid development of production technologies and also significant progress of the investigation of the fracture mechanics stimulates consideration of new problems of fracture control of piezoceramic bodies. Fracture control is necessary in different fields of industry, e.g. during cutting of metals, cracking of marble plates, drilling of boreholes, mining of deposits, etc.

In a piezoelectric body the interaction of elastic waves with failures like cracks in their vicinities there appear singular conjugate mechanical and electrical fields which may bring to mechanical and electrical fracture of the body. The analysis of probability of the fracture is based on the results of solving of the dynamic boundary problem of electroelasticity. The speed of energy release in the process of the crack propagation is expressed by the stress intensity factor (SIF), which are the functionals determined from solutions of integral equations of the electroelasticity boundary problem.

The methods of the optimal control theory for systems with concentrated and distributed parameters have been studied for instance by Lee and Markus [3], Krasovski [4] and Butkovski [5]. Certain questions related to the control of fracture in the body with cracks as well as the dynamic elastic plates are discussed by M.L. Filshtinsky [6,7].

3. CONTROL OF THE DYNAMIC STRENGTH OF A BODY ON THE BASES OF SPATIAL DISTRIBUTION OF THE OUTER LOAD

Direct problems of electroelasticity determining such a failure parameter as a stress intensity factor were studied in the monographs [1,2]. Solutions of the extremal (reverse) problems of electroelasticity may be simplified due to the fact that the failure parameters are represented in the form of functionals determined by solutions of integral equations of the corresponding boundary problem,

Problem 1. Let in a piezoelectric space occur a crack and in some portion Λ of the semi-space boundary act the distributed shear load $\tau(x_1, t) = \text{Re}\{p(x_1)e^{-i\omega t}\}$. Using the results of the [2] we can present the stress intensity factor in the form

$$K_{III}^{\pm} = c_{44}^E \sqrt{\frac{\pi}{s'(\pm 1)}} |\Omega_0(\pm 1)| \cos(\omega t - \delta^{\pm}), \quad (1)$$

$$\Omega_0(\pm 1) = \int_{\Lambda} p(x_1) \Omega_1(\pm 1, x_1) dx_1, \quad \delta^{\pm} = \arg[-\Omega_0(\pm 1)].$$

Here $\Omega_1(\delta, x_1)$ is the solution of the integral equation [2]

$$\int_L p'(\zeta) g_1(\zeta, \zeta_0) ds + \int_L p(\zeta) g_2(\zeta, \zeta_0) ds = N(\zeta_0),$$

$$g_1(\zeta, \zeta_0) = \text{Im} \frac{e^{i\psi_0}}{\zeta - \zeta_0} + A k_{15}^2 \text{Im} \frac{e^{-i\psi_0}}{\zeta - \bar{\zeta}_0},$$

$$g_2(\zeta, \zeta_0) = \frac{\pi i \gamma^2}{4} (1 + k_{15}^2) [A H_0^{(1)}(\gamma r_{10}) \cos(\psi + \psi_0) -$$

$$- H_0^{(1)}(\gamma r_0) \cos(\psi - \psi_0) + H_2^{(1)}(\gamma r_0) \cos(\psi + \psi_0 - 2\alpha_0) -$$

$$- A H_2^{(1)}(\gamma r_{10}) \cos(\psi - \psi_0 + 2\alpha_{10})],$$

$$N(\zeta_0) = \frac{\pi}{c_{44}^E} X_3(\zeta_0) + \pi i \tau \gamma (1 + k_{15}^2) e^{i(\alpha_1 \xi_{10} + \alpha_2 \xi_{20})} \cos(\psi_0 - \beta) -$$

$$- A e^{i(\alpha_1 \xi_{10} - \alpha_2 \xi_{20})} \cos(\psi_0 + \beta), \quad p(\zeta) = \frac{[U_3]}{2}, \quad p'(\zeta) = \frac{dp(\zeta)}{ds},$$

$$H_2(\gamma r) = \frac{4i}{\pi \gamma^2 r^2} + H_2^{(1)}(\gamma r), \quad r_0 = |\zeta - \zeta_0|, \quad r_{10} = |\bar{\zeta} - \zeta_0|,$$

$$\alpha_0 = \arg(\zeta_0 - \zeta), \quad \alpha_{10} = \arg(\zeta_0 - \bar{\zeta}), \quad \zeta_0 = \xi_{10} + i \xi_{20},$$

$$\psi = \psi(\zeta), \quad \psi_0 = \psi(\zeta_0); \quad \zeta, \zeta_0 \in L = \cup L_j.$$

with the side

$$N(\zeta_0) = \left[\frac{\pi i \gamma P_0}{2 c_{44}^E} H_1^{(1)}(\gamma r_0^*) + \frac{\pi k_{15}^2 Q_0}{2 e_{15}} \left(i \gamma H_1^{(1)}(\gamma r_0^*) - \frac{2}{\pi r_0^*} \right) \right] \cos(\psi_0 - \alpha_0^*),$$

$$r_0^* = |\zeta_0 - x_{10}|, \quad \alpha_0^* = \arg(\zeta_0 - x_{10}).$$

at $P_0 = 1$ (i.e. a "standard" solution corresponding to the concentrated force of a single amplitude).

We must formulate the following problem: let us find such "control" $p(x_1)$ limited by Chebyshev metrics $|p(x_1)| \leq B(x_1)$ where the quantity $|\Omega_0|$ would assume maximum value in some of the cut tips (e.g. in the tip b). Formalized statement has the form

$$|\Omega_0(1)| \rightarrow \max, \quad |p(x_1)| \leq B(x_1), \quad B(x_1) > 0. \quad (2)$$

Solution of this simple problem at the mentioned symmetric limitations of the control norm is as follows

$$p(x_1) = B(x_1) e^{-i \arg \Omega_0(1, x_1)}, \quad (3)$$

Here

$$\max |\Omega_0(1)| = \int_{\Lambda} B(x_1) |\Omega_0(1, x_1)| dx_1. \quad (4)$$

Above we assumed as a control the function characterizing a spatial distribution of the load on the boundary $x_2 = 0$. It is necessary now to consider the dynamic loading, and in this case as a control we must assume the function characterizing the load change with time (evolutionary control).

Problem 2. Let on the boundary of a free from semi-space pizeoelectric force with an inner crack act the concentrated load of $p(x_1, t) = P(t) \delta(x_1 - x_{10})$ type. Let us assume the time moment $t = T$ and the function $c(t) > 0$. It is necessary to maximize $|K_{III}|$ in one of the crack tips at $t = T$ on the bases of the function $P(t)$ at limiting $|P(t)| \leq c(t)$.

According to the [2] a formalized statement of the problem has the following form.

$$|K_{III}(T)| = \frac{1}{\sqrt{2s'(1)}} \left| \int_{-\infty}^{\infty} \hat{P}(\omega) \Omega_0^*(1, \omega) e^{-i\omega T} d\omega \right| \rightarrow \max, \quad (5)$$

$$|P(t)| \leq c(t), \quad c(t) > 0.$$

To solve the problem let us use the representation $\hat{P}(\omega)$ as an illustration of the control $P(t)$ by Fourie and substitute it into the formula (5). We will obtain

$$|K_{III}(T)| = \frac{1}{2\sqrt{\pi s'(1)}} \left| \int_{-\infty}^{\infty} P(t) R(T-t) dt \right|, \quad (6)$$

$$R(T-t) = \int_{-\infty}^{\infty} e^{-i\omega(T-t)} \Omega_0^*(1, \omega) d\omega.$$

On the basis of considerations in the [2] we conclude that $\text{Im} R(T-t) = 0$. Therefore the expression (6) has the maximum value on the element

$$P(t) = c(t) \text{sgn } R(T-t). \quad (7)$$

In this case

$$\max |K_{III}(T)| = \frac{1}{2\sqrt{\pi s'(1)}} \int_{-\infty}^{\infty} c(t) |R(T-t)| dt. \quad (8)$$

The mentioned problem of optimization of the intensity stress factor was considered at symmetric limitations of control load. The given statement may be somewhat generalized removing the requirement of the limitation symmetry.

Problem 3.

$$|K_{III}(T)| \rightarrow \max, \quad A(t) \leq P(t) \leq B(t), \quad (9)$$

Here $A(t), B(t)$ are assumed piecewise-infinite, limited functions, the meaning of $K_{III}(T)$ and $P(t)$ follows from the previous problem.

Introducing the substitution $P^*(t) = P(t) - [A(t) + B(t)]/2$ we arrive at the problem with symmetric limitations

$$|P^*(t)| \leq \frac{B(t) - A(t)}{2}.$$

Therefore the final solution has the form

$$\begin{aligned} P(t) &= \frac{1}{2} \{ A(t) + B(t) - [A(t) - B(t)] \operatorname{sign} \gamma(T) \operatorname{sign} R(T-t) \}; \\ \gamma(T) &= \frac{1}{2} \int_{-\infty}^{\infty} [A(t) + B(t)] R(T-t) dt, \end{aligned} \quad (10)$$

Hence

$$\max |K_{III}(T)| = \frac{1}{2\sqrt{\pi s'(1)}} \left\{ |\gamma| + \frac{1}{2} \int_{-\infty}^{\infty} [B(t) - A(t)] R(T-t) dt \right\}, \quad (11)$$

For checking the initial conditions under the functions $A(t), B(t)$ in reality it is necessary to assume $A(t)\eta(t)$ and $B(t)\eta(t)$ where $\eta(t)$ is a single function of Heavyside.

Up to now there was stated a problem of maximization of the stress intensity factor in any tip of the crack. And here the quantity K_{III} in the other tips was not controlled. In this connection let us state the following problem of optimal control.

Problem 4. In a piezoelectric semi-space let there be k crack, it is bounded with vacuum and is free of forces everywhere except some portions on the boundary Λ . On the portion Λ there acts a distributed load $\tau(x_1, t) = \operatorname{Re} \{ p(x_1) \exp(-i\omega t) \}$.

Let us demand that the intensity factor K_{III} in the tips of all the cracks and stress amplitudes at some specific points of the body acquire the given values at minimal "energetic" expenses for control $\|p(x_1)\|_{L^2(\Lambda)} \rightarrow \min$ (L^2 is a complex Hilbert space on the set Λ).

The expression K_{III} for j crack due to (6.1) has the form

$$\begin{aligned} K_{III}^{(j)} &= c_{44}^E \sqrt{\frac{\pi}{s'(\pm 1)}} |\Omega_0^{(j)}(\pm 1)| \cos(\omega t - \delta_j^\pm), \\ \Omega_0^{(j)}(\pm 1) &= \int_{\Lambda} p(x_1) \Omega_1^{(j)}(\pm 1, x_1) dx_1, \quad \delta_j^\pm = \arg[-\Omega_0^{(j)}(\pm 1)] \quad (j = \overline{1, k}). \end{aligned} \quad (12)$$

The stress amplitudes at specific points z_j ($j = \overline{2k+1, n}$) are calculated with using the

$$\sigma_{13} = c_{44}^E (1 + k_{15}^2) \partial_1 u_3 - e_{15} \partial_2 \Phi, \quad D_1 = \varepsilon_{11}^E \partial_2 \Phi, \quad \sigma_{23} = c_{44}^E (1 + k_{15}^2) \partial_2 u_3 + e_{15} \partial_1 \Phi, \\ D_2 = -\varepsilon_{11}^E \partial_1 \Phi, \quad D_3 = 0, \quad u_3 = u_3^{(0)} + u_3^*$$

$$U_3(x_1, x_2) = -\frac{1}{4} \int_L [U_3] \left\{ \frac{\partial G(\zeta, z)}{\partial \zeta} d\zeta - \frac{\partial G(\zeta, z)}{\partial \bar{\zeta}} d\bar{\zeta} \right\} + U_3^{(0)} - A U_3^{(1)},$$

$$F(x_1, x_2) = \frac{1}{2\pi i} \int_L \left\{ f(\zeta) H(\zeta, z) d\zeta - \overline{f(\zeta) H(\zeta, z)} d\bar{\zeta} \right\}, \quad U_3^{(1)} = \tau e^{i(\alpha_1 x_1 - \alpha_2 x_2)}, \quad \zeta = \xi_1 + i\xi_2,$$

$\bar{\zeta} = \xi_1 - i\xi_2$ and may be represented as follows

$$T_{i3}(z_j) = \int_{\Lambda} p(x_1) G(x_1, z_j) dx_1 \quad (i=1, 2), \quad (13)$$

where $G(x_1, z_j)$ are known functions determined from the solution of the direct problem.

The formalized statement of the problem is the following

$$\|p(x_1)\|_{L^2(\Lambda)} = \left\{ \int_{\Lambda} |p(x_1)|^2 dx_1 \right\}^{1/2} \rightarrow \min, \quad (14)$$

at limitations of the equalities types

$$\int_{\Lambda} p(x_1) H_j(x_1) dx_1 = \alpha_j \quad (j = \overline{1, n}). \quad (15)$$

Here

$$H_j(x_1) = \begin{cases} \Omega_1^{(j)}(-1, x_1), & j = \overline{1, k} \\ \Omega_1^{(j)}(1, x_1), & j = \overline{k+1, 2k} \\ G(x_1, z_j), & j = \overline{2k+1, n} \end{cases}$$

The quantities α_j are defined.

To solve the stated problem let us introduce the sub-space M with the basis $\{\overline{H}_j(x_1)\}_{j=1}^n$ into L^2 . Any element $p \in L^2$ let us represent in the form [8]

$$p = \sum_{m=1}^n c_m \overline{H}_m + h^\perp,$$

where h^\perp belongs to an orthogonal compliment M up to L^2 . The constants c_m uniquely determined from the constraint equation (15). We have

$$\sum_{m=1}^n (H_j, \overline{H}_m) c_m = \alpha_j \quad (j = \overline{1, n}). \quad (16)$$

The determinant of the system (16) (Gramm's determinant) is different from zero therefore the system is uniquely solvable.

In virtue of the equality

$$\|p\|^2 = \left\| \sum_{j=1}^n c_j \overline{H}_j \right\|^2 + \|h^\perp\|^2$$

and the arbitrariness of the element h^\perp we obtain $h^\perp = 0$ from the condition (14).

So the extreme element $p = \sum_{j=1}^n c_j H_j$, where c_j is determined from the (16).

4. REFERENCES

- [1] Filshinsky, M.L. and Bardzokas, D.I., *Boundary integral equations method in diffraction problems of electroelastic waves*, Sumy, (1999) (In Russian).
- [2] Bardzokas, D.I. and Filshinsky, M.L., *Electroelasticity of piecewise-uniform bodies*, Sumy. (2000) (in Russian).
- [3] Lee, E.B. and Markus, L., *Foundations of optimal control theory*, N.Y. 1967.
- [4] Krasovski, N.N., *Theory of control motion*, Nauka 1968 (In Russian).
- [5] Butkovski, A.G., *Methods of the control systems with distribution of parameters*, Nauka (1975) (in Russian).
- [6] Filshinsky, M.L., *Control of fracture of a piezoceramic body with crack*, Dynamics and Strength of Mech., V15, p.p.93-96, (1987).
- [7] Filshinsky, V.A. and Filshinsky, M.L., *On the selection of minimum functional for the optimal elastic plate from initial state with given conditions*, Prikl. Mech. V22 (2), p.p. 90-94 (1986).
- [8] Kolmogorov, A.N. and Fomin, S.F., *Elements of function theory and functional analysis*, Nauka, (1968) (In Russian).

OPTIMIZATION AND SOFT COMPUTING FOR INVERSE AND CRACK IDENTIFICATION

G.E. Stavroulakis

Department of Mathematics
University of Ioannina, GR-45110 Ioannina, Greece
and Department of Civil Engineering
Carolo Wilhelmina Technical University, D-38106 Braunschweig, Germany

H. Antes

Department of Civil Engineering
Carolo Wilhelmina Technical University, D-38106 Braunschweig, Germany

1. SUMMARY

A quite general approach for the formulation of inverse problems in engineering goes through some error minimization. In fact, the predictions of some suitably parametrized mathematical model is adjusted, in the least square sense, to some available measurements. For the effective use of this approach in engineering several problems must be solved. Crack identification problems in statics and dynamics are used as model problems for the presentation of our numerical experience in this presentation. The mechanical problems are automatically solved by boundary element methods. The arising optimization problems are solved by using numerical optimization or soft computing tools (namely, neural networks, filter algorithms and genetic optimization).

2. PROBLEM FORMULATION

General thoughts

Inverse problems arise during structural health monitoring in engineering mechanics. The attempt to determine cracks and other flaws from vibrational dynamical data (eigenmodes, eigenvalues) is mainly restricted to slender structures [1]. Even in this case unilateral effects (e.g., the partial or total closing of a crack and possible frictional stick-slip effects) pose challenging questions, which have not been solved till now in a satisfactory way. For structures of more complicated form and/or loading, like the ones used in civil engineering, the sensitivity of the eigenmodal information with respect to small local changes is low. Consequently, other methods have to be examined for the study of health monitoring problems. Our recent experience with a general approach to study inverse problems and applications on crack identification are outlined in the sequel.

Least square error minimization

A general formulation of an inverse problem is a least square error minimization, where some deviation between measurements and the predictions of an appropriate model is minimized. Usually the output of the mechanical system (for instance, displacements, stresses etc.) is minimized, although other measures (like the satisfaction of the system's governing

equations) have also been proposed [2]. In crack identification appropriate variables for the abovementioned problem are the position, length, orientation etc. of the crack.

In general the above described error optimization problem is ill-posed. In the language of numerical optimization this is, roughly speaking, explained by a bad numerical scaling of the error function. Moreover, if an insufficient number of measurements are taken into account, the previous optimization problem may have multiple solutions.

As it has been pointed out by the present authors in previous contributions (see, e.g., [4], [7], [8]) the error measure is a nonlinear, nonquadratic and in general nonconvex function of the unknown variables. As a consequence local minima may arise which are of completely useless as solutions of the inverse problem. This problem, which practically makes the solution of an inverse problem in engineering mechanics not possible if no suitable initial estimate of the solution is available, has not been discussed in details in the literature.

Finally, taking into account unilateral effects introduces nondifferentiability of the error measure and poses the question if closed cracks can be identified.

Numerical algorithms and difficulties

Classical, local numerical optimization algorithms usually does not work. Either the bad scaling of the problem causes premature stopping of the algorithm, or, due to nonconvexity, lack of a suitable starting point leads to a useless local minimum. In static inverse problems logarithmic scaling of the error least square may help in some cases. In general, regularization procedures (like the Tikhonov regularization) must be used to help the numerical optimization. Nevertheless, they do not resolve the problems with local minima. Moreover, they are not usually available in general purpose numerical optimization libraries, so that their use by engineers requires a considerable investment for the preparation of the computer programs.

Filter-driven optimization algorithms (e.g., the Kalman-Bucy filter) and neural networks (for example, of the backpropagation type) have some potential to avoid local minima and lead, generally, to efficient solution methods. The filter algorithms lead to more effective solution methods than classical numerical optimization. In backpropagation neural networks most of the work is given for the training of the network. The use of the trained network has, practically, zero cost and makes even online applications feasible. Both filter and neural network approaches have their limits to tackle nonconvex problems. In fact, they may avoid some local minima, but no guarantee is given, in general, that a global minimum can be computed. This can be easily explained from the fact that both algorithms are nothing more than variants of iterative (also distributed, in the case of neural networks) algorithms for the solution of the initial error minimization problems. The addition of some momentum helps them avoid some 'mild' local minima, but may be insufficient if more wild nonconvexity appears.

Robust methods of global optimization (like genetic algorithms or simulated annealing) are most suitable for the guaranteed solution of the inverse problem. Unfortunately their computer implementation is quite expensive and they are less suitable for online applications. Especially their use in the area of time-domain dynamical problems seems, for the time being, to be prohibitive.

Another classification of the above mentioned algorithms is of some importance. Algorithms of the direct optimization type require that an automatic, parametrized model (i.e. a computer

program) of the mechanical problem is available. This model is coupled with the optimization routine for the solution of the inverse problem. The boundary element methods used in our investigations have the advantage that they require a minimum of effort for the computer implementation of this parametrized model. On the other hand, methods of the neural network type, work in a batch-type way and require that a certain number of 'training examples' are available. These examples, for instance the solution of several mechanical problems where the position of the crack changes etc., may be completed in a semi-automatic way, by using available software. This point may be of interest within some mixed numerical-experimental study.

3. NUMERICAL EXPERIENCE

For static crack identification problems, with or without unilateral contact effects along the crack sides, filter-driven numerical optimization algorithms are quite efficient and robust, at least for the studied academic small-scale problems. Our investigations in this area have been documented in [7]. Neural networks and genetic algorithms have been used by the authors for the solution of static and harmonic dynamic crack and of flaw identification problems. Harmonic dynamic problems are, of course, less suitable for the correct description of unilateral contact effects. The results of [4] show that the nonconvexity of the output error function is enhanced for harmonic dynamic loadings, therefore the use of genetic optimization is required. General dynamic analysis loadings are used in several nondestructive testing methods and seems to be more suitable for the detection of, even partially closed, cracks. One application of this type is outlined here.

Let us consider an elastic layer with a hidden crack or delamination. Impact-echo is a well-known NDE method for the detection of the crack [3]. A detailed numerical modeling of this method, extended such as to cover unilateral contact, frictional and adhesive effects, is presented in [5], [9]. Figure 1 shows the impact-echo waveforms for different plate depths and the corresponding for the case with a classical crack and a crack with frictionless unilateral contact effects. For the inverse problem the case with frictional contact (with a friction coefficient equal to 0.30) has been considered. The results are not depicted in Figure 1. On the assumption that the measured waveform corresponds to a unilateral crack without friction behind a layer of depth equal to $d=1.75$, the output error minimization problem is used for the solution of the inverse analysis. For clarity of the presentation, but also for better numerical performance the logarithm of this function is used in the minimization procedure. For this case the error function is plotted in Figure 2. Here the following code is used: crack type 1 corresponds to the classical crack case, crack type 2 is the unilateral crack case and crack type 3 is the frictional crack case. The seven different layer depths are used in the other direction of this plot. Although the problem is of a mixed continuous-discrete type, and genetic algorithms are able to solve it directly, we solved it using only continuous variables.

In a preliminary investigation the problem has been solved by a genetic optimization algorithm. In order to reduce the time used in the computer implementation the results of the parametric investigation (cf., Fig. 1) are first produced and stored off-line. All other results for the intermediate crack thicknesses are produced by interpolation between the tabulated, stored waveforms (a strategy which is analogous to the response function approximation which is widely used in complicated structural optimization tasks). The genetic optimization method is the same with the one used in [4] with respect to flaw identification problems using frequency domain data. It should be mentioned here that a back-propagation neural network approach has been able to solve this problem partially. In fact, for a given crack type the

question of determining the depth of the layer is a trivial task for the neural network. The problem is due to overtraining of the neural network (see [6], [8]).

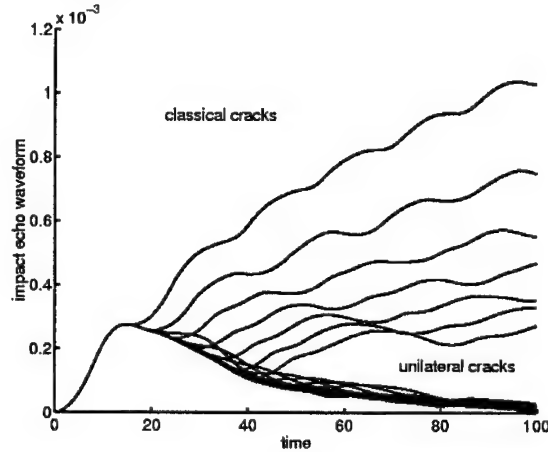


Figure 1: Impact-echo waveforms for classical and unilateral cracks and for several layer thicknesses.

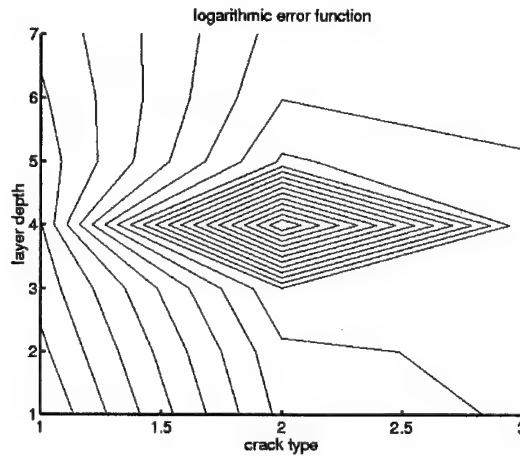


Figure 2: Plot of the logarithm of the error function.

4. DISCUSSION

A general approach for the formulation and for the solution of inverse problems in mechanics has been outlined, with some references on crack identification problems. For the effective solution of the arising numerical optimization problems several tools from optimization and soft computing can be used. The most effective one depends on the concrete application.

It should be emphasized that in industrial health monitoring, the comparison between measurements and some parametrized model is usually done by some experienced users.

Their experience may, in some cases, be summarized within some rules. The here proposed approach makes this procedure automatic. If the human experience, which is accumulated for one specific application can be quantified, one may integrate this experience in the solution procedure of the error minimization problem. The link is provided by the fuzzy inference theory. Details of this on-going research will appear soon.

Acknowledgements: Partial support from the German Research Foundation (DFG) is gratefully acknowledged.

5. REFERENCES

- [1] Dimarogonas, A.D., Vibration of cracked structures: A state of the art review. *Engineering Fracture Mechanics*, 55(5), 831-857, 1996.
- [2] Natke, H.G., Einführung in Theorie und Praxis der Zeitreihen- und Modalanalyse. Vieweg Verlag, Braunschweig, Wiesbaden, 3rd Ed., 1991.
- [3] Pratt, D., Sansalone, M., Impact-echo signal interpretation using artificial intelligence. *ACI Materials Journal*, 89(2), 179-187, 1992.
- [4] Stavroulakis, G.E., Antes, H.: Flaw identification in elastomechanics: BEM simulation with local and genetic optimization. *Structural Optimization*, 16(2/3), 162-175, 1998.
- [5] Stavroulakis, G.E., Antes, H., Panagiotopoulos, P.D.: Transient elastodynamics around cracks including contact and friction. *Computer Methods in Applied Mechanics and Engineering*, Special Issue: Computational Modeling of Contact and Friction, Eds.: J.A.C. Martins and A. Klarbring, 177(3/4), 427-440, 1999.
- [6] Stavroulakis, G.E., Impact-echo from a unilateral interlayer crack. LCP-BEM modelling and neural identification. *Engineering Fracture Mechanics* 62(2-3), 165-184, 1999.
- [7] Stavroulakis, G.E., Antes, H.: Unilateral crack identification. A filter-driven, iterative, boundary element approach. *Journal of Global Optimization*, 17(1-4), 339-352, 2000.
- [8] Stavroulakis, G.E., *Inverse and crack identification problems in engineering mechanics*. Habilitation Thesis, T.U. Braunschweig and Kluwer Academic Publishers, Dordrecht, Boston, London, 2000.
- [9] Stavroulakis, G.E., Antes, H.: Transient dynamic analysis of layered structures with unilateral interfaces. *Philosophical Transactions of the Royal Society. Special Issue on Nonsmooth Mechanics*, Guest Editor F. Pfeiffer (in press).

MECHANICAL BEHAVIOR OF MULTILAYERED NANOCOMPOSITE FILMS

V. Singh, X. Nie, P. Gupta and E.I. Meletis

Materials Science & Engineering Program

Mechanical Engineering Department

Louisiana State University, Baton Rouge, Louisiana, 70803 USA

1. SUMMARY

Nanoscale composites consisting of alternating layers of metallic and ceramic phases may offer novel mechanical properties and considerable potential as high strength, high toughness and high wear resistance surface coating materials. In the present work, the mechanical and tribological properties of a nanolayered Cr/DLC (diamondlike carbon) composite model system was investigated. Nanolaminate Cr/DLC composites were synthesized using a hybrid chemical vapor deposition/physical vapor deposition system that combines intensified plasma and sputter deposition. High-resolution transmission electron microscopy was used to analyze the structure, metal/ceramic interface and characteristics of the multilayers. Microhardness and nanoindentation experiments were conducted to determine elastic moduli and hardness as a function of interlamellar spacing. Friction and wear behavior of nanolaminates was studied by conducting pin-on-disc experiments. It was observed that the layer thickness of the multiplayer composites has a systematic effect in the mechanical properties.

2. INTRODUCTION

Diamond-like carbon (DLC) films are known for their unique combination of properties, but they suffer from low thermal stability (above 400°C) and low toughness. Due to the inherent residual stresses present, DLC films have a tendency to peel off thereby limiting their applications (involving high contact stresses) and deposition thickness. Chromium coatings are well known for their high hardness, good corrosion and wear resistance.

Multilayer metal or ceramic (oxide, nitride)/DLC nanocomposites are presently attracting significant interest for improving surface-sensitive properties [1-8]. Similarly, studies have also been conducted on multilayer DLC coatings involving different types of DLC (e.g. amorphous diamond and hydrogenated DLC) in an effort to improve wear resistance, adhesion and toughness [8,9]. Very little attention has been paid to multilayer Cr/DLC or Cr/C nanocomposites. The present study is concerned with the synthesis and mechanical properties of the former type of coatings.

3. EXPERIMENTAL

3.1 Processing

Silicon (100) wafers were used as the substrate material. The samples were cleaned ultrasonically in acetone, dried in air prior to processing utilizing an IPAP (Intensified Plasma-assisted Processing) system [10]. The chamber was first evacuated down to 10^{-6} Torr and purged with Ar several times. Then, samples were sputter-cleaned for 20 min. using Ar^+ at a pressure of 25 mTorr and -1500 V bias voltage. Chromium layers were deposited by sputtering of a Cr target (99.5%), 10 cm from substrate, using 100 W magnetron power, 10 mTorr pressure, 20 sccm Ar flow rate and -400 V substrate bias. Two N doped Cr layers, Cr(N)-1 and Cr(N)-2, were also synthesized under the same conditions and by adding N_2 at 2 and 6 sccm flow rate, respectively. DLC deposition was performed in a CH_4/Ar discharge of 1/3.57 ratio (total flow rate 38.4 sccm) at 100 mTorr pressure, -1000 V substrate bias and $<80^\circ\text{C}$ temperature. After processing, the specimen was cooled inside the chamber in argon. A small area on each sample surface was covered, preventing deposition and allowing to measure coating thickness by profilometry. Multilayers synthesized were Cr/DLC (nm/nm): 200/20, 200/200, 100/200, 60/200 and Cr(N)/DLC 60/200. All multilayers were $>1\text{ }\mu\text{m}$ in thickness.

3.2 Structural Characterization

X-ray diffraction (XRD) experiments were performed using a Rigaku Miniflex 20 diffractometer with a $\text{Cu-K}\alpha$ source over the 30° to 85° range at $0.5^\circ/\text{min}$ scanning rate. XRD patterns were obtained for bulk Cr, PVD Cr and Cr(N) (nitrogen-doped Cr).

High-resolution transmission electron microscopy (TEM) of Cr/DLC multilayer samples was performed on a JEOL JEM 2010 electron microscope operated at 200 keV with a point-to-point resolution of 2.3 Å. Cross sectional slices were obtained by cutting the samples along a direction normal to the coating surface. Cross-sectional specimens for TEM observation were prepared by mechanical grinding, polishing, and dimpling followed by Ar-ion milling using a Gatan Precision Ion Polishing System (PIPSTM, Model 691) at 4.5 keV at an angle of 5° .

3.3 Indentation Experiments

Surface hardness of multilayers was measured by Knoop microhardness (0.1 N). The reported values are the average of at least three measurements. Nanoindentation measurements were taken using a Hysitron Triboscope[®] instrumented nanoindentation/nanoscratch device incorporated on a Digital Instrument Dimension 3100 atomic force microscope. The Triboscope[®] allows AFM imaging of surfaces prior and after indentation. A three-sided, Berkovich-type pyramidal indenter was employed to carry out nanoindentation measurements. The indenter shape function was calibrated using fused silica. The hardness, H , and indentation modulus, $E/(1-\nu^2)$, (ν is the Poisson's ratio) stabilized at a contact depth between 70 and 100 nm. These values were below 10% of the coating thickness and were taken as representative of the coating.

3.4 Tribological Experiments

Pin-on-disc experiments (ISC-200 tribometer) were conducted on Cr/DLC and Cr(N)/DLC multilayers along with DLC, Cr and Cr(N) films to characterize their tribological behavior. The pin material was Al_2O_3 ball of 9.5 mm diameter. The wear experiments were performed in laboratory air having a relative humidity of $48 \pm 7\%$, at a sliding velocity of $0.1\text{ m}\cdot\text{s}^{-1}$ for a distance of 1 km under a load of 2.5 N. The coefficient of friction (f) was monitored continuously during the experiments with the aid of a linear variable-displacement transducer

and recorded on a dedicated, data acquisition computer attached to the tribometer. The wear rate of DLC and Cr/DLC multilayer films was calculated from the trace of surface profile (average of four traces) taken across the wear track by using profilometry.

4. RESULTS AND DISCUSSION

4.1 Microstructural Characterization

The structure of Cr and Cr(N) films was studied by XRD. Figure 1 shows XRD patterns obtained from bulk Cr, PVD Cr, and two Cr(N) films. The PVD Cr showed evidence of $\langle 211 \rangle$ texture. Doping of Cr film with N was found to reduce intensity, broaden and shift the Cr peaks to lower 2θ values. These observations suggest that N remains in the Cr lattice producing an ultrafine (amorphous), expanded structure. Such effects have been previously reported [11]. The microstructure of the films was characterized by TEM. Figures 2(a) and (b) are cross sectional TEM of the 200/20 Cr/DLC multilayer. The DLC layers were found to be amorphous and Cr possessed a columnar structure, especially in thick layer (200 nm). It is evident that the DLC penetrates into the valleys of Cr columns resulting in an interface with no defects, thereby providing good adhesion. The columnar structure of Cr however produces a variation in the DLC thickness, Fig. 2(b). The XRD patterns suggest that the columnar structure is suppressed in the Cr(N) layers and more than likely a nanosize grain structure develops.

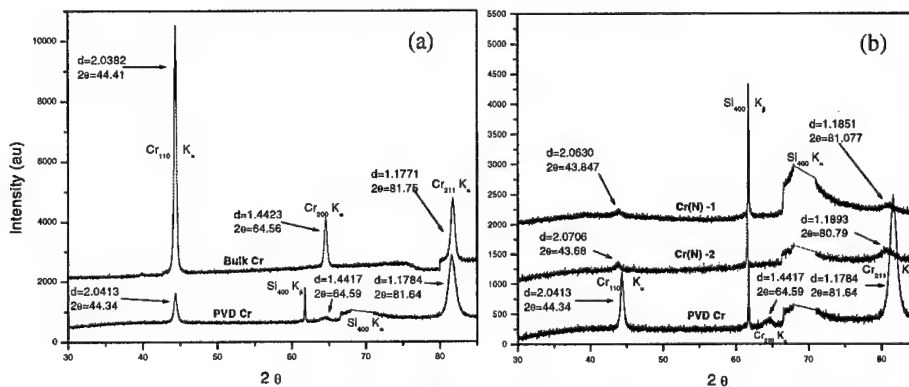


Figure 1: XRD pattern of (a) bulk and PVD Cr, and (b) PVD Cr and Cr(N)

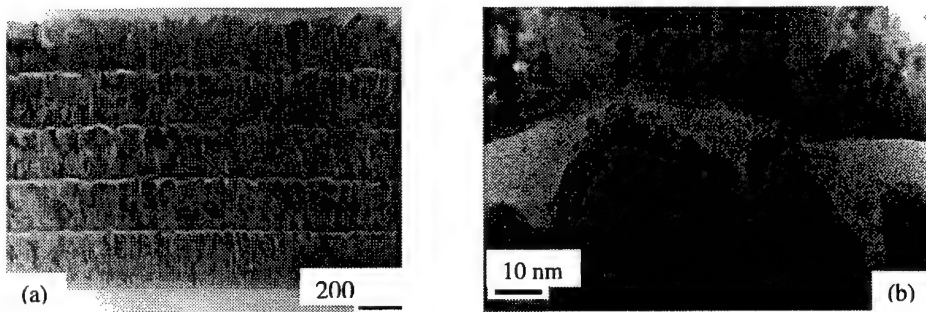


Figure 2: XTEM micrograph of Cr/DLC (200/20) (a) overview and (b) high-resolution image of the Cr/DLC interface

4.2 Mechanical Properties

Figures 3(a) and (b) present the nanoindentation results of multilayers with Cr/DLC thickness ratio 1, 0.5 and 0.3. With respect to microstructural effects, it is known from deformation theory that the relationship between strength and grain size of polycrystalline materials can be described by the Hall-Petch equation. By using H instead of σ this relation gives:

$$H = H_0 + k_1 \cdot d^{1/2} \quad (1)$$

where, d is the given grain size, H_0 is an intrinsic materials parameter (internal friction) and k_1 is a constant, which is related to hardening contribution of grain boundaries. If d represents thickness of Cr single layer in the multilayers, then the above relationship gives:

$$H = 10.9 + 33.3d^{1/2} \text{ GPa} \quad (2)$$

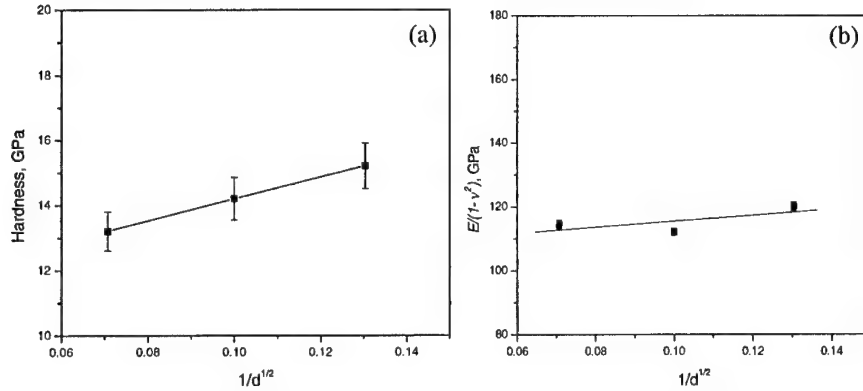


Figure 3: Nanoindentation results of Cr/DLC multilayers (a) hardness and (b) reduced elastic modulus, $E/(1-v^2)$

The results show that as the layer thickness of Cr, d , reduces the Cr layer hardness increases, which leads to an increase in multilayer hardness inversely proportional to square root of metallic layer thickness. Similar observations were made previously by Ding et. al. [4]. The reduced elastic modulus, $E/(1-v^2)$, is also plotted in Figure 3(b). $E/(1-v^2)$ shows a slight upward trend with increasing $1/d^{1/2}$ but the change is not clear and may lie within the experimental scatter. Previous studies on Al/ Al_2O_3 and Ti/TiN multilayers have also reported minor changes in elastic modulus of the multilayers with changing the volume fraction of the components [4]. Such effects need to be further investigated by systematically varying layer thickness.

Figure 4(a) presents Knoop microhardness (0.1 N) values for all layers tested in the present study. A similar trend to that shown in Fig. 3(a) of increasing hardness with decreasing Cr layer thickness is also observed here. The DLC hardness is significantly higher than those of the Cr layers. Multilayers possess an intermediate hardness of their two components. In Fig. 4(b) the microhardness values of the multilayers are plotted as a function of $1/d^{1/2}$, where d is either the single layer thickness of Cr in multilayers or the average grain size in pure Cr [12]. A clear upward trend in hardness with decreasing Cr thickness (either as layer in multilayers or grain size in pure Cr) is shown in the graph. Two sources seem to contribute toward the hardness of the multilayers, i.e. the decreasing thickness of the Cr layer and the increasing volume fraction of the harder DLC layer. Indirect support for the former contribution is provided by the fact that the Cr(N)/DLC layer exhibited higher hardness than that of the Cr/DLC with the same layer thickness (60/200), Fig. 4(a). Similarly, comparing the pure Cr curve with that shown by the multilayers is clear that a contribution of at least 20 GPa is provided by the DLC layer. It is interesting to note that the results may also suggest a higher

slope in the multilayer curve which may be attributed to higher volume fraction of DLC with decreasing Cr layer thickness.

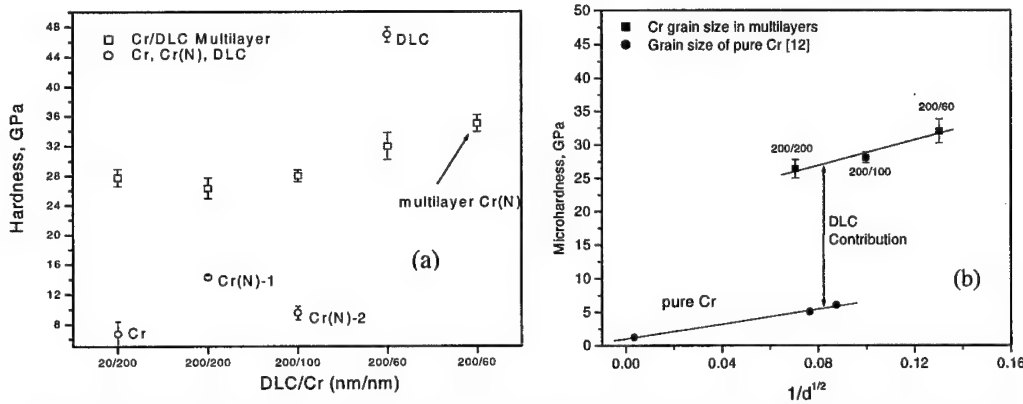


Figure 4: (a) Microhardness of various coatings and multilayers and (b) hardness vs grain size

4.3 Tribological Behavior

Figure 5 presents the steady-state coefficient of friction (f_{ss}) and wear rate of multilayers, DLC and Cr films. The results show that films with low volume fraction of DLC (Cr/DLC=200/20), which is the lubricating phase, show higher f_{ss} and wear rate. Similarly high wear rate and friction is shown by the Cr films. In all multilayers with higher volume

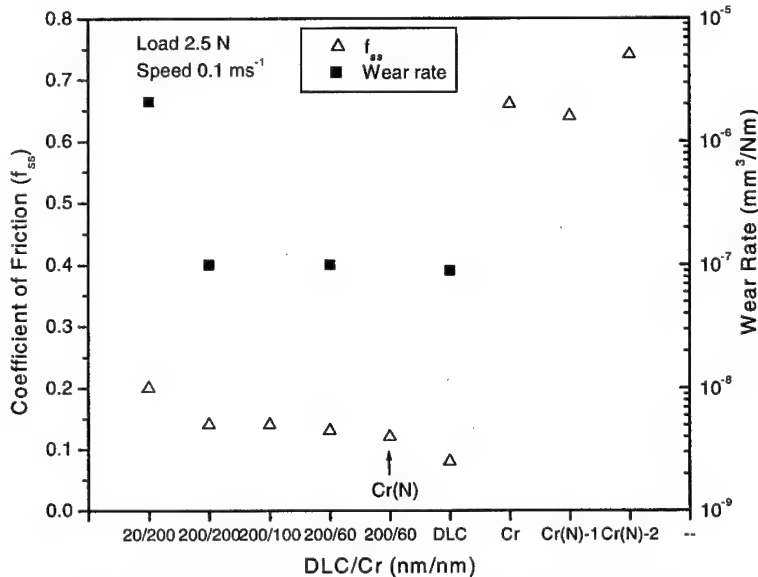


Figure 5: Wear behavior of multilayers, DLC, Cr and Cr(N)

fraction of DLC (200 nm layers) the results showed that wear rate remains low. Also, decreasing Cr layer thickness (increasing hardness) decreases f_{ss} . Further more, the behavior of the Cr(N)/DLC multilayer that exhibited higher hardness than its Cr/DLC counterpart,

seems to be consistent with this trend. Stockemer et. al. has also reported enhanced tribological behavior due to presence of N in Cr layers [13]. Thus, the present results indicate a correlation between hardness and friction and suggest that reducing the Cr layer thickness below 60 nm may produce further improvements. Such experiments are currently in progress in our laboratory.

5. CONCLUSIONS

- (a) DLC layers were found to be amorphous whereas Cr layers exhibit a nanocrystalline structure at low thickness and develop a columnar structure in higher thickness.
- (b) Cr/DLC interfaces were found to be defect-free, dense and continuous.
- (c) A decrease in Cr layer thickness was found to increase hardness and have relatively small effect on elastic modulus in Cr/DLC multilayers.
- (d) Cr/DLC multilayers with a significant volume fraction of DLC were found to possess low coefficient of friction and low wear rate.
- (e) Wear resistance and coefficient of friction were found to correlate with the hardness of the multilayers that is controlled by the thickness of Cr layers and the DLC volume fraction.

Acknowledgements: This work was supported by the U.S. Army Research Office grant DAAG55-98-1-0279 and Louisiana Board of Regents.

6. REFERENCES

- [1] Lyubimov, V.V., Voevodin, A.A., Yerokhin, A.L., Timofeev, Y.S., Archipov, I.K., Development and testing of multilayer physically vapour deposited coatings for piston rings, *Surface and Coatings Technology* 52, 145–151 (1992).
- [2] Subramanian, C. and Strafford, K.N., Review of multicomponent and multilayer coatings for tribological applications, *Wear* 165, 85-95 (1993).
- [3] Chu, X., Barnett, S.A., Wong, M.S., Sproul, W.D., Reactive unbalanced magnetron sputter deposition of polycrystalline TiN/NbN superlattice coatings, *Surface and Coatings Technology* 57, 13-18 (1993).
- [4] Ding, Y., Farhat, Z., Northwood, D.O., Alpas, A.T., Mechanical properties and tribological behaviour of nanolayered Al/Al₂O₃ and Ti/TiN composites, *Surface and Coatings Technology* 68/69, 459-467 (1994).
- [5] Kupfer, H., Richter, F., Friedrich, S., Spies, H.J., Deposition and properties of TiN/carbon multilayers for corrosion protection of steel, *Surface and Coatings Technology* 74-75, 333-338 (1995).
- [6] Labdi, S., Saint, C., Henne, L., Houdy, Ph., Nanostructure study of Ti/TiN multilayers: Effect of the deposition temperature, *Materials Research Society Symposium Proceedings* 441, 711-716 (1997).
- [7] Oral, B., Ernst, K-H., Schmutz, C.J., Adhesion and structural changes of multi-layered and multi-doped a-C:H films during annealing, *Diamond and Related Materials* 5932–937, (1996).
- [8] Voevodin, A.A., Walck, S.D., Zabinski, J.S., Architecture of multilayer nanocomposite coatings with super-hard diamond-like carbon layers for wear protection at high contact loads, *Wear* 203-204, 516-527 (1997).
- [9] Fedoseev, D.V., Dub, S.N., Lupich, I.N., Maslyuk, B.A., Multilayer diamond-like carbon coatings, *Diamond and Related Materials* 1, 543-545 (1992).

- [10] Adjaottor, A.A., Ma, E., Meletis, E.I., On the mechanism of intensified plasma-assisted processing, *Surface and Coatings Technology* 89, 197-203 (1997).
- [11] Rebholz, C., Ziegele, H., Leyland, A., Matthews, A., Structure, mechanical and tribological properties of nitrogen-containing chromium coatings prepared by reactive magnetron sputtering, *Surface and Coatings Technology* 115, 222-229 (1999).
- [12] Provenzano, V., Valiev, R., Rickerby, D.G., Valdre, G., Mechanical properties of Nanostructured chromium, *Nanostructured Materials* 12, 1103-1108 (1999).
- [13] Stockemer, J., Winand, R., Vanden B.P., Comparison of wear and corrosion behaviors of Cr and CrN sputtered coatings, *Surface and Coatings Technology* 115, 230-233 (1999).

A COMPARATIVE STUDY OF MECHANICAL PROPERTIES OF STATE-OF-THE-ART AMORPHOUS CARBON FILMS

C. Charitidis, S. Logothetidis

Department of Physics, Aristotle University of Thessaloniki,
GR-54006 Thessaloniki, Greece

1. SUMMARY

In this study the mechanical properties of various state-of-the-art amorphous carbon (a-C) films, namely very thin (sp^2 , sp^3 -rich), and thin, hard and sp^3 -rich layered-structure sputtered a-C films, electron beam evaporated (EBE) a-C films and tetrahedral a-C films (ta-C) grown with the vacuum arc technique are compared. Aspects that are important in assessing the potential use of a-C films are not only the elastic properties (hardness (H) and elastic modulus (E)) of the film, but also the adhesion of films onto the substrate, and the ratio of H and E (H/E) which defines the wear resistance of the films.

2. INTRODUCTION

a-C films is a group of very similar but still very different materials. Depending on the deposition technique, their properties range from graphite-like to diamond-like. Due to their outstanding and tunable properties (hardness, wear resistance, coefficient of friction, transparency, chemical inertness, relatively low electron affinity and biocompatibility), a-C films exhibit an increasing number of applications in nanoscale components such as those used in magnetic hard discs, wear-resistant coatings, outer layer for medical implants and they are promising in semiconductor devices, optical film applications and in large area electron field emitting devices.

Studying the mechanical response of materials at the nanoscale has received much attention in recent years due to the development of new nanostructured materials and continued miniaturization of engineering and electronic components, thin film technology and surface coatings. The technique of nanoindentation with the high load (displacement) resolution in the mN- and nm- range and the continuous depth-sensing indentation tests provide the capabilities to assess the detailed mechanical responses of the film-substrate system, especially at contact scales of the order of, or less than, the film thickness.

3. EXPERIMENTAL

The sputtered a-C films studied here were deposited in an Alcatel SCM 600 magnetron sputtering apparatus which has been described elsewhere [1,2]. Briefly, the a-C thin films were deposited on c-Si (001) substrates using a graphite (99.999% purity) target. During

deposition, the sputtering Ar gas was at a partial pressure of 1.5×10^{-2} Torr, the target to substrate distance was fixed at 65 mm, and the discharge power equal to 100 W. The only parameter varying was the substrate bias voltage V_b . A phase modulated ellipsometer, mounted on the deposition system, allows in-situ and real-time spectroscopic ellipsometry (SE) measurements in the energy region 1.5-5.5 eV, and was used to estimate the thickness and the composition (sp^2 and sp^3 content) of the deposited film [3].

To investigate the mechanical behavior of a-C thin films two series of a-C films with thickness 30 and 90 nm, respectively, were prepared. The a-C films with thickness 30 nm were deposited either with negative or positive V_b . a-C films 30 nm thick, deposited with negative V_b were found to be sp^3 -rich (45%), dense ($\sim 2.65 \text{ g/cm}^3$) and with compressive stress above 6 GPa. On the other hand, films deposited with positive V_b are sp^2 -rich, exhibit low density (1.9 g/cm^3) and compressive stress ($\sim 1 \text{ GPa}$). The films with thickness 90 nm were deposited in sequential thin layers with alternating (positive/negative) V_b . In detail, firstly a layer of $\sim 10 \text{ nm}$ with $V_b = +10 \text{ V}$ and subsequently a layer of $\sim 20 \text{ nm}$ with $V_b = -20 \text{ V}$ was deposited. This procedure was repeated three times in sequence for the development of films with total thickness $\sim 90 \text{ nm}$. The development of a-C films in the form of layered structure, consisting of sequential layers of the above mentioned two different types of a-C films, provides stable, thick and sp^3 -rich a-C films potentially for many practical applications [4].

The ta-C films, 90 nm thick, were prepared at room temperature on silicon substrates in a filtered cathodic vacuum arc (FCVA) system that incorporates an off-plane, double bend (S-bend) magnetic filter [5]. The sp^3 content for ta-C films was approximately 88% [6], as it was found by EELS and synchrotron radiation SE.

Sp^2 -rich a-C films were deposited by the EBE technique in a water-cooled UHV chamber (base pressure $< 1 \times 10^{-9}$ Torr). The 400 mA electron beam was accelerated by a 7 kV voltage and it was scanning the surface of the carbon chunks (99.999% pure graphite) screened by a double electromagnet assembly. The distance between the source C material and the Si substrate was $\sim 30 \text{ cm}$ and the working pressure was $\sim 2 \times 10^{-5}$ Torr. X-ray Reflectivity (XRR) showed a density $\sim 1.75 \text{ gr/cm}^3$, in good agreement with the sp^2 character of the film identified by XPS [7].

A-C films, 1000 nm thick, were also deposited using an unbalanced DC magnetron sputtering deposition system (UBMS) on c-Si with a chromium adhesive layer with a thickness of 200 nm. UBMS technique provides the optimum level of ion energy (i.e. bias voltage) and high ion current to produce dense, and hence hard, films. XRR showed an average density $\sim 2.66 \text{ gr/cm}^3$ for the whole film.

In nanoindentation a load is continuously applied to the indenter and the depth of penetration of the indenter (displacement into the specimen) is measured as a function of load. From the unloading slope of the load-displacement data the contact stiffness, contact area, and mechanical properties such as hardness and modulus of the materials are calculated using well-established models [8]. The continuous stiffness measurements (CSM) option offers a significant improvement in the nanoindentation technique. In CSM a small sinusoidal force (AC force) is superimposed on the quasi-static force (DC force) applied to the indenter. The resulting modulation in the displacement (AC displacement amplitude) and the phase shift between the AC force and displacement is measured using a lock-in amplifier. The contact stiffness is calculated from the amplitude and phase shift using a dynamic model [9]. The advantage of CSM is that the contact stiffness can be directly obtained continuously during indentation without the need for discrete unloading cycles, and with a time constant that is at least three orders of magnitude smaller than the time constant of the more conventional method of determining stiffness from the slope of an unloading curve. The measurements can

be made at exceedingly small penetration depths. Recently, CSM has been attempted for applications to thin films [10].

The elastic properties (hardness, H and elastic modulus, E) of the films were conducted using a Nano Indenter XP system with the CSM option. The H and E of each of the films were measured with a Berkovich, three-sided pyramid diamond indenter with nominal angle of 65.3° between the tip axis and the faces of the triangular pyramid, which was forced into the specimen surface by using a coil and magnet assembly. The system has load (displacement) resolution of 50 nN (<0.01 nm). A detailed description of the system has been presented elsewhere [10]. Prior to each indentation test, two indents in 100 nm depth were conducted in fused silica to evaluate the tip condition. In all CSM depth-sensing tests a total of ten indents were averaged to determine the mean H and E values for statistical purposes, with a spacing of 50 μm .

4. RESULTS AND DISCUSSION

Figure 1(a) shows the plots of H & E as a function of contact depth obtained from two monolithic sputtered a-C films, deposited with $V_b=+10$ and -10 V, with the same thickness 30 nm. Indentation was conducted by applying the CSM technique in different contact depths. For the film deposited with $V_b=-10$ V the maximum H (E) value was ~ 18 (185) GPa, whereas that deposited with $V_b=+10$ V was ~ 8 (130) GPa. Since the a-C films were deposited on Si, their hardness (elastic modulus) approaches at large contact depths, the value of Si, 12.5 (168) GPa. The above values of H and E for each V_b were estimated from the regime of the shallow data points (Fig.1) as more representative of the film properties. The high internal stresses (6-7 GPa), calculated by measuring the radius of the curvature of the substrate before and after film deposition by the modified Stoney expression [3] in sputtered a-C films are closely related to adhesion problems and crack creation in the films, and thus limit their maximum thickness for good adherence on the substrate at ~ 40 nm.

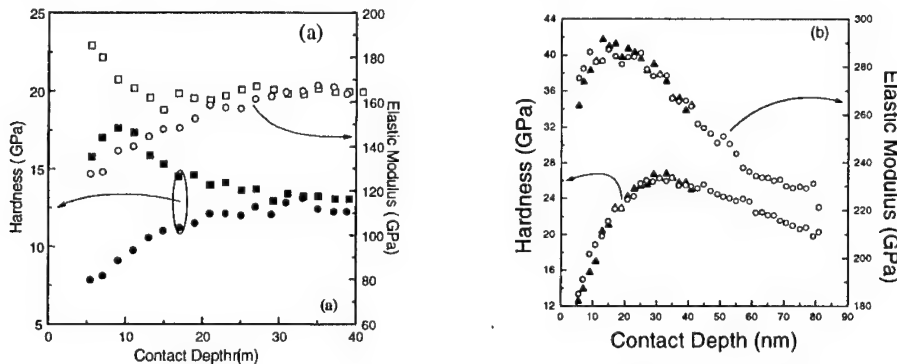


Figure1: Nanoindentation data of H and E vs. indentation contact depth obtained from: (a) monolithic a-C films 30 nm thick, deposited with $V_b=+10$ V (circles) and $V_b=-10$ V (squares) and (b) layered structure sputtered a-C film.

Figure 1(b) shows the nanoindentation results for an a-C film 90 nm thick, where H and E are plotted as a function of contact depth. At shallow depths, about 15-30 nm, elastic properties more representative of the films were obtained but still influenced by the substrate. The maximum H (E) value ~ 27 (290) GPa must be closer to the film one, although theoretically a contact depth of ~ 15 nm would be more representative of the film mechanical properties independent of the substrate effect [11]. This is because the indenter penetrating into the film

deforms not only the film but usually also the substrate and thus the composite (i.e., film and substrate) property is obtained. Therefore, significant roles in the arrangement of the test play the film thickness and the minimum possible contact depth as well as the imperfections of indenter tip shape.

From Fig. 1(b) and load/unload nanoindentation curves, not shown here, (i.e. the maximum penetration depth and the residual depth), we have found that a-C films deposited in sequential layers by altering V_b exhibit much higher hardness and elastic deformation (~80%) than the films deposited with $V_b > 0$ (~50%) and higher to those deposited with $V_b < 0$, (~70%). The film deposited in sequential layers with alternating V_b led to the development of stable and rich in sp^3 bonded material, resulting in harder a-C films than the ones developed solely with negative V_b (Fig. 1(a)). The deposited layers with $V_b > 0$ seem to be essential for the stress relaxation of the whole film making practicable the growth of thicker and stable a-C films [1].

The $H(E)$ of UBMS a-C film was found 32 (280) GPa, as shown in Figure 2(a). Figure 2 (b) shows $H(E)$ measurements vs. contact depth for ta-C films of 70 nm. The $H(E)$ values were found 42 (410) GPa. These values compare well with those found in the literature [6].

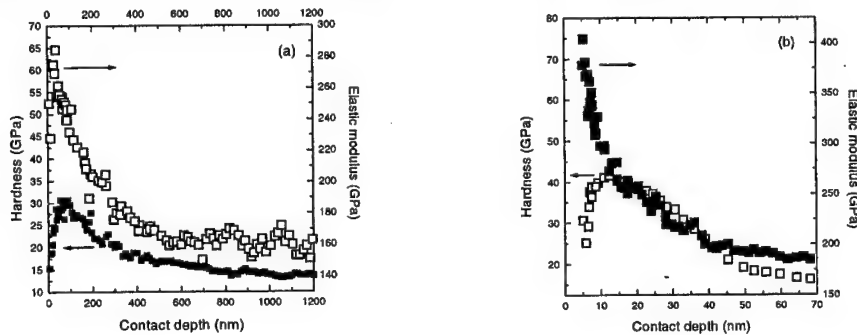


Figure 2: CSM measurements of $H(E)$ of the a-C film deposited by UBMS technique (a), and of ta-C film (b).

In Figure 3, CSM measurements of $H(E)$ vs. contact depth for EBE a-C film, 300 nm thick are shown. Since $H(E)$ values, 3 (80) GPa, of the film are lower than that of the Si substrate, the $H(E)$ values increase with contact depth until the $H(E)$ values reach a maximum value, that of the Si substrate ($H=12.5$ GPa).

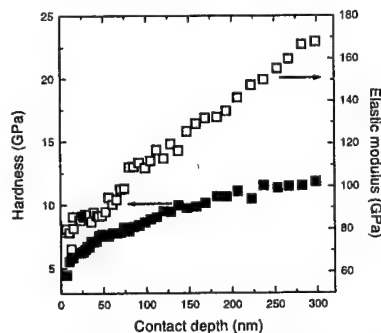


Figure 3: CSM measurements of $H(E)$ of the a-C film deposited by EBE technique.

Values of the hardness, elastic modulus, plastic resistance parameter (H/E) and coefficient of friction for the films examined in this work are included in Table 1.

Table 1. Summary of nanoindentation results of a-C films

	Thickness (nm)	H (GPa)	E (GPa)	H/E
MS a-C (sp ² -rich)	30	8	130	0.06
MS a-C (sp ³ -rich)	30	18	185	0.097
MS a-C layered structured (sp ² / sp ³)	90	27	290	0.093
EBE a-C	300	3	80	0.016
UBMS a-C	1000	32	280	0.11
ta-C	90	42	400	0.1

With regards to density, a clear correlation between the measured density values [7] and the H & E of the carbon based films seems to exist (Figure 4). The denser films, which also correspond to those of higher sp³ content present the highest H (and E) values.

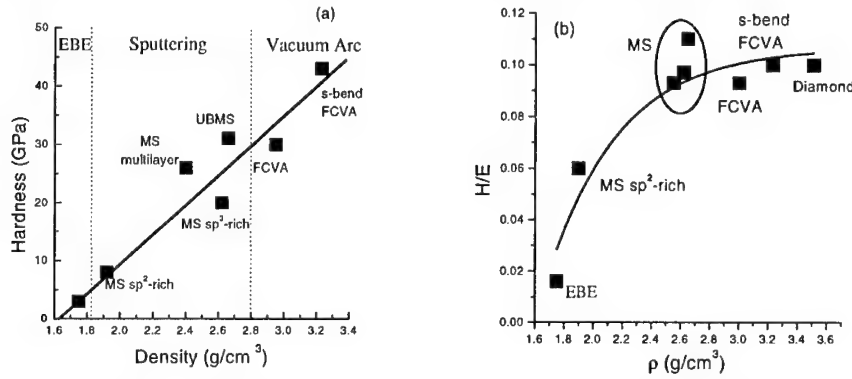


Figure 4. H (a) and H/E (b) as a function of density for a-C films deposited by different deposition techniques (where MS: Magnetron Sputtering, FCVA: Filtered Cathodic Vacuum Arc, EBE: Electron Beam Evaporation, UBMS: Unbalanced Magnetron Sputtering).

The material's hardness is directly correlated with the bond strength, the bulk modulus and the total free energy. Recent studies have shown that the hardness H is linearly correlated with microstructural characteristics such as the covalency a_c , the bond length d and the bond strength and the constants of elastic (C_{11}) and plastic (C_{22}), according to the following Equation (under the condition that there is no new surface or crack formation):

$$H \approx \frac{E_o a_c}{d^2} \left(C_{11} \frac{1}{\sqrt{d}} + C_{22} \frac{1}{d} \right) \Leftrightarrow H \approx \left[\frac{E_o a_c (\sqrt{d} C_{11} + C_{22})}{m} \right] \rho$$

where m is the atomic mass. Thus, the covalency and the bond strength dominantly affect the film hardness. When the variations in the bond length are small compared to the constants C_{11} and C_{22} the hardness follows a linear relation with the density ρ , as shown in Figure 4.

An important material property is the wear resistance which is predicted not only by the hardness alone but from the elastic strain to failure, which is related to the ratio of H and E (H/E). The ratio H/E , so-called 'plasticity index', is widely quoted as an important measure in determining the limit of elastic behavior in a surface contact, which is clearly important for the avoidance of wear [11,12]. For a-C films studied in this work, the effective H/E ratios as a function of density are shown in Figure 4(b). The ratio H/E obtained from various MS a-C films is almost the same with that of harder ta-C films and significant larger than that of other stiff and hard material [13]. Taking into account that the MS technique is easily implemented in industrial scale, the process simplicity and control, and film homogeneity the MS a-C films are good candidates for applications where both wear resistance and elasticity are required.

5. CONCLUSIONS

The study presented here concerns the mechanical behavior of a-C films deposited by different deposition techniques on Si, as it was investigated by nanoindentation technique. The results confirm that the mechanical properties of a-C films vary strongly. Ta-C films are considerable harder than sputtered a-C films. In terms of wear resistance and elastic behavior both sputtered a-C and ta-C films showed good performance. Each film type has specific advantages and the entire range of properties should be studied carefully to select the appropriate coating for a particular application.

Acknowledgements: This work was partially supported by the General Secretariat for Research and Technology of Greece, under the project PENED-99ED645.

6. REFERENCES

- [1] Gioti M., Logothetidis S. and Charitidis C., Appl. Phys. Lett. 73, 184 (1998).
- [2] Logothetidis, S., Appl. Phys. Lett. 69, 158 (1996).
- [3] Logothetidis S. and Gioti M., Mater. Sci. Eng. B 46, 119 (1997).
- [4] Charitidis C., Logothetidis S. and Douka P., Diam. Relat. Mater. 8, 558 (1999).
- [5] Martinez E., Andujar J.L., Polo M.C., Esteve J., Robertson J. Milne W.I., Diam. Relat. Mater. 10, 145-152 (2001).
- [6] Robertson J., Thin Solid Films, 383 81-88 (2001).
- [7] Patsalas P., PhD Thesis, Thessaloniki (2001).
- [8] Oliver W.C. and Pharr G.M., J. Mater. Res. 7, 1564 (1992).
- [9] Pethica J.B. and Oliver W.C., Phys. Scr. T 19, 61 (1987).
- [10] Logothetidis S. and Charitidis C., Thin Solid Films 353, 208 (1999).
- [11] Menck J., Munz D., Quandt E., Weppelmann E.R., and Swain M.V., J. Mater. Res. 12, 2475 (1997).
- [12] Charitidis C., Logothetidis S., Douka P., Diam. Relat. Mater. 8, 558 (1999).
- [13] Leyland A., Matthews A., Wear 246, 1-11 (2000).
- [14] Martin-Gil Jesus, Martin-Gil F. J., Sarikaya M., Qian M., Jose-Yacaman M., Rubio A., Appl. Phys. 81(6), 2555 (1997).

THE ROLE OF POINT DEFECTS ON THE GROWTH AND BREAKDOWN OF METAL PASSIVE FILMS IN ELECTROLYTE SOLUTIONS

M. Pagitsas, A. Diamantopoulou, D. Sazou

Laboratory of Physical Chemistry, Department of Chemistry
Aristotle University of Thessaloniki, 54 006 Thessaloniki, Greece

1. SUMMARY

A point defect model is extended in this study in order to explain the growth and breakdown (local and uniform) of the oxide film formed on iron in acid solutions. According to this model there is a continual generation and annihilation of point defects, oxygen and iron cation vacancies, at the Fe/film and film/solution interfaces, respectively. Certain chemical species in the solution induce general corrosion (uniform dissolution of the oxide) while others induce pitting corrosion (localized dissolution). Monoperiodic current oscillations are related to general corrosion while complex oscillations are related to pitting corrosion. The proposed model explains the different types of corrosion. It is suggested that monoperiodic oscillations are associated with the formation of surface complexes leading to the general corrosion while complex oscillations are associated with the occupation of an anion vacancy by halides leading to the pitting corrosion. Both the general and pitting corrosion are followed by the removal of the oxide film from the entire Fe surface due probably to an increase of the electrostatic compressive stress produced by the electric field and a decrease of the surface tension at the film/solution interface.

2. INTRODUCTION

A passive oxide film, which is typically only a few nanometers thick, is formed on Fe during its anodic polarization in aqueous sulfuric acid solutions. The passive films formed on metals and alloys are of a great technological importance because they control the protective properties of the metallic materials against corrosion. It is only during the last decade that the use of advanced *in-situ* analytical techniques has made possible a clarification of most of the features of the passive film that grows on Fe ($\text{FeO}_{x/2}$) [1]. It was shown that the $\text{FeO}_{x/2}$ has a crystalline structure with numerous defects and the film composition is consisted with the $\text{Fe}_3\text{O}_4/\gamma\text{-Fe}_2\text{O}_3$ structure. Moreover, it has been shown that the oxide film has semiconductive properties [2]. The $\text{FeO}_{x/2}$ formed at less positive potentials is less stable because is thinner and contains more Fe^{2+} , and hence less Fe^{3+} , than that formed at more positive potentials.

The $\text{FeO}_{x/2}$ is formed on Fe at a critical potential, called as Flade potential (E_F). The E_F is considered as the potential at which an outer layer of the unstable Fe_3O_4 turns to $\gamma\text{-Fe}_2\text{O}_3$ through oxidation of a part of the Fe^{2+} . It was observed that close to E_F current oscillations occur under potentiostatic conditions. These oscillations are monoperiodic of a relaxation type and are attributed to the spontaneous formation and dissolution of the passive iron oxide

film [3, 4]. Since the E_F depends on the pH ($E_F=0.58-0.058\text{pH}$, vs. NHE at 293 K) the initial anodic dissolution of Fe (active state) and generation of Fe^{2+} result in an increase of the local pH. Thus the E_F shifts towards less positive values and the oxide formation is favored (passive state). In the subsequent stage, H^+ ions come towards the passive Fe, where the concentration of Fe^{2+} is almost zero, the pH decreases, the E_F shifts towards positive values and reactivation of the passive Fe occurs. Although, oscillations maintain monoperiodicity by varying a number of control parameters, halides, X^- ($\text{X}^-: \text{Cl}^-, \text{Br}^-, \text{I}^-$) induce complex current oscillations [5]. On contrary, in the presence of HF monoperiodic oscillations occur, similar to those of the halide-free system. Microscopic observations of the Fe during oscillations reveal pitting corrosion in the presence of X^- and general corrosion in the presence of HF.

The aim of the present work is to explain the difference between pitting and general corrosion in terms of the physicochemical processes responsible for these types of corrosion. Emphasis is placed on the role of point defects in the oxide (oxygen and iron-cation vacancies), which might be sources of internal stresses affecting the mechanical properties of the film as well.

3. EXPERIMENTAL

The electrochemical measurements were performed at a constant temperature (293 K) by means of a Wenking POS 73 potentiostat from Bank Electronic interfaced to a computer equipped with an analog-to-digital, and vice versa, converter PCL-812PG of a maximum sampling rate equal to 30 kHz. The pretreatment of the Fe and the experimental procedure are described in Ref. 5.

The sulfuric acid solution was prepared with H_2SO_4 (Merck, proanalysis 96% w/w) using twice-distilled water. In halide-containing solutions, NaCl or NaF, both from Fluka (puriss p.a.), were added to the H_2SO_4 solution. The Fe purchased from Johnson Matthey Chemicals was 99.99% in purity. The solution was deaerated with purified N_2 .

4. NON-LINEAR DYNAMICAL RESPONSE OF THE $\text{Fe}/\text{H}_2\text{SO}_4$ SYSTEM TO THE CHEMICAL PERTURBATION INDUCED BY HALIDE SPECIES

The current-potential (I - E) polarization behavior of the $\text{Fe}/0.75 \text{ M } \text{H}_2\text{SO}_4$ system is shown in Fig. 1a. Region (I) corresponds to the active state where the Fe dissolution occurs from the bare Fe surface. In the limiting current region (II), Fe is dissolved in the presence of a ferrous salt layer. Region (III) refers to the passive-active transition state, where current oscillations appear within a narrow region ($\approx 30 \text{ mV}$) at $E < E_F$. Region IV refers to the passive state, where an oxide ($\text{FeO}_{x/2}$) is formed on the Fe surface. This region is extended from the E_F to the transpassivation potential, E_t , where dissolution of Fe starts along with the oxygen evolution. The oscillations are monoperiodic of a relaxation type (Fig. 1b). All these features are related to the general corrosion. By adding NaCl (Fig. 1c, d) there are distinct differences in both I - E and I - t curves attributed to the pitting corrosion. By adding NaF (Fig. 1e) there is only accelerated general dissolution (i.e. shorter oscillation period, Fig. 1f). On the basis of the experimental results, the following criteria can be used for characterizing pitting corrosion:

- Substantial increase of the current in the passive state.
- No access to the transpassivation potential.
- Complex periodic and aperiodic current oscillations.
- Occurrence of an induction period of time before the onset of oscillations.

- Deviation of the maximum oscillatory current from the kinetics of the active state.

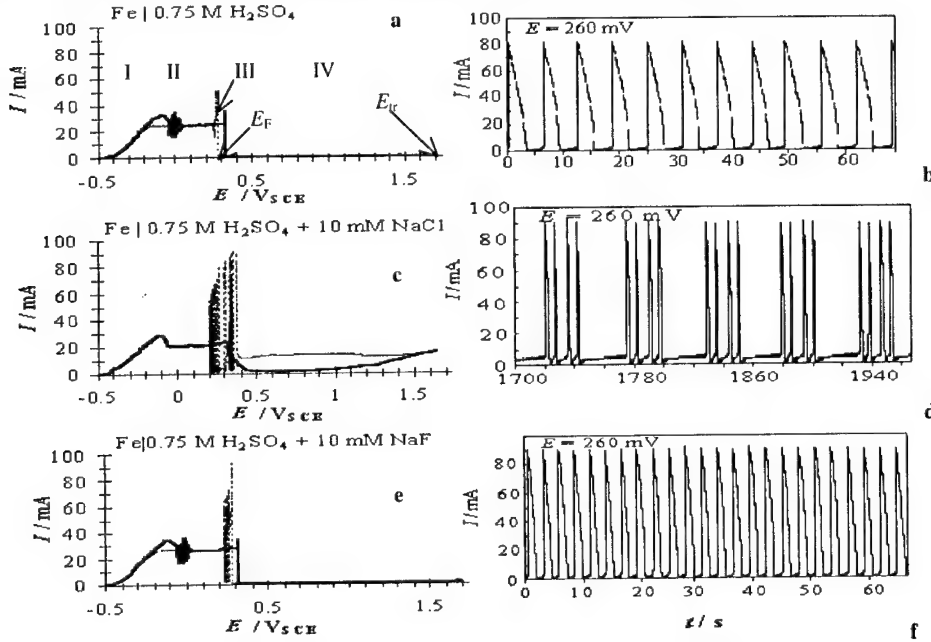


Figure 1: Left column: Anodic I - E curves of the non-perturbed and perturbed systems. Thick line: potential scan towards positive potentials, thin-dashed line: inverse backward scan, $dE/dt = 2$ mV s^{-1} . Right column: Examples of potentiostatic current oscillations.

Aside the chemical properties of the species, the non-linear dynamical response of the system should be also related to the ionic and electronic properties of the oxide. A point defect model (PDM) is used for the description of the oxide growth [6] and is extended to account for the processes underlying the different types of corrosion and breakdown mechanisms.

5. THE ROLE OF POINT DEFECTS ON THE OXIDE GROWTH

According to the PDM, the $FeO_{x/2}$ is considered to contain a high concentration of point defects, namely cation, V_{Fe}^{2+} and anion (oxygen), V_O^{2-} vacancies. Other charge carriers (i.e. interstitials, excess of electrons or holes) are not taken into account. The oxide growth occurs at the $Fe/FeO_{x/2}$ interface as it is illustrated in Fig. 2, according to the following processes:

- (a) Formation of oxygen vacancy V_O^{2-} at the $Fe/FeO_{x/2}$ interface via the reaction



where the Fe^0 is an iron atom and V_m is a hole in the iron lattice while the Fe_{Fe} is an iron cation in the oxide lattice.

- (b) Transfer of oxygen vacancies by a flux $J_{V_O^{2-}}$ to the $FeO_{x/2}/H_2SO_{4(aq)}$ interface. The flux $J_{V_O^{2-}}$ consists of an electromigration and a diffusion term and depends on the concentration of oxygen vacancies, $c_{V_O^{2-}}$ ($J_{V_O^{2-}} \propto c_{V_O^{2-}}$).

- (c) Occupation of the oxygen vacancy by an oxygen from the H_2O and formation of the oxide oxygen, O_O according to the reaction



Under steady-state conditions the net result of these processes is the oxide growth as can be expressed by the overall reaction

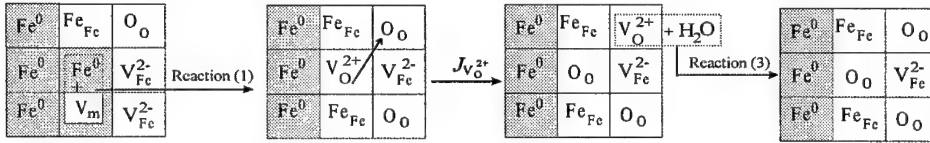
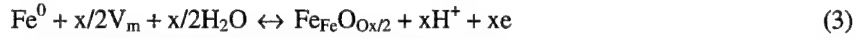


Figure 2: Oxide growth processes catalyzed by the oxygen vacancies according to a PDM.

6. THE ROLE OF POINT DEFECTS ON THE OXIDE BREAKDOWN

On the basis of the non-linear dynamical response of the system (Fig. 1), two different types of physicochemical processes may lead to the breakdown of the oxide film formed on Fe. One refers to systems where general corrosion occurs ($Fe|0.75M H_2SO_4$ and $Fe|0.75M H_2SO_4 + NaF$) and the other to systems where pitting corrosion occurs ($Fe|0.75M H_2SO_4 + NaCl$).

Oxide breakdown processes at the $Fe|0.75 M H_2SO_4$ system (general corrosion)

- (a) Formation of iron cation vacancies, V_{Fe}^{x-} via the reaction



- (b) Transfer of V_{Fe}^{x-} by a flux $J_{V_{Fe}^{x-}}$ to the $Fe|FeO_{x/2}$ interface. The flux $J_{V_{Fe}^{x-}}$ depends on the concentration of cation vacancies, $c_{V_{Fe}^{x-}}$ ($J_{V_{Fe}^{x-}} \propto c_{V_{Fe}^{x-}}$).

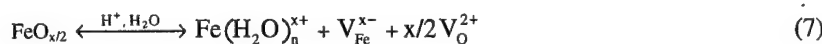
- (c) Transformation of V_{Fe}^{x-} to iron holes V_m in the iron lattice according to the reaction



Under steady-state conditions the net result of processes (4) and (5) is the electrodisolution of iron expressed by the overall reaction



An additional reaction takes place at the $FeO_{x/2}|H_2SO_{4(aq)}$ interface, which represents the acid-catalyzed chemical dissolution of the oxide



The overall reactions (3) and (6), which are catalyzed by the oxygen V_O^{2+} and cation V_{Fe}^{x-} vacancies, respectively, are in equilibrium expressed through a Schottky-pair reaction:



where “null” is a neutral anion vacancy/cation vacancy pair. The Schottky-pair reaction refers to the electroneutrality of the oxide.

Oxide breakdown processes at the Fe|0.75 M H_2SO_4 + NaCl system (pitting corrosion)

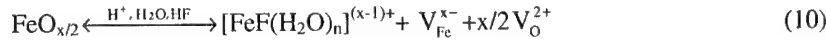
Chlorides occupy an oxygen vacancy at the $FeO_{x/2}|H_2SO_4$, Cl^- interface according to the reaction



where the Cl_O^+ is an oxygen vacancy occupied by Cl^- . Reaction (9) perturbs the Schottky-pair reaction and new anion vacancy/cation vacancy pairs are formed. The new V_O^{2+} are occupied by additional Cl^- while the concentration of cation vacancies, $c_{V_{Fe}^{x-}}$ increases along with the flux $J_{V_{Fe}^{x-}}$. Thus reaction (9) inhibits the oxide growth (overall reaction (3)) and accelerates the Fe electrodisolution (overall reaction (6)). The V_{Fe}^{x-} are accumulated at the $Fe|FeO_{x/2}$ interface and lead to the formation of a void. Oxide breakdown and pit initiation occurs when the void exceeds a critical size.

Oxide breakdown processes at the Fe|0.75 M H_2SO_4 + NaF system (general corrosion)

Due to the low pH of the solution, the fluoride species are present as HF and the occupation of an oxygen vacancy is unlikely for this neutral species. Thus HF does not lead to pitting corrosion. On the other hand, the HF is characterized by a high tendency to form complexes with Fe^{3+} (equilibrium constant $K_F=1.5 \times 10^5 \text{ M}^{-1}$ as compared with $K_{Cl}=4.27 \text{ M}^{-1}$) [7] and, therefore catalyzes the chemical dissolution of the oxide according to the reaction



The surface complexes are transferred to the solution faster since they have a lower charge than the uncomplexed iron cations bound the O^{2-} of the oxide matrix. Moreover, reaction (10) shows that in the presence of HF, an anion vacancy/cation vacancy pair is generated and thus the Schottky-pair reaction is not perturbed and the $Fe|FeO_{x/2}$ interface remains intact.

In summary, it is shown that both reactions (7) and (10) are complexation reactions that occur at the $FeO_{x/2}$ |solution interface and lead to a general corrosion. A uniform dissolution of the oxide occurs through a gradual removal of the oxide monolayers as it is shown in Fig. 3a. The removal of the last oxide-monolayer leads to the transition from the passive to active state. On the other hand, occupation of an anion vacancy via reaction (9) is the process that leads to pitting corrosion. This reaction leads to a perturbation that propagates to the $Fe|FeO_{x/2}$ interface as it is shown in Fig. 3b.

Both the general and pitting corrosion are followed eventually by the complete removal of the oxide film from the entire Fe surface due probably to an increase of the electrostatic compressive stress produced by the electric field and a decrease of the surface tension at the

$\text{FeO}_{x/2}/\text{H}_2\text{SO}_{4(\text{aq})}$ interface [8]. These effects are closely related with the composition of the oxide film formed on Fe in the passive-to-active transition region.

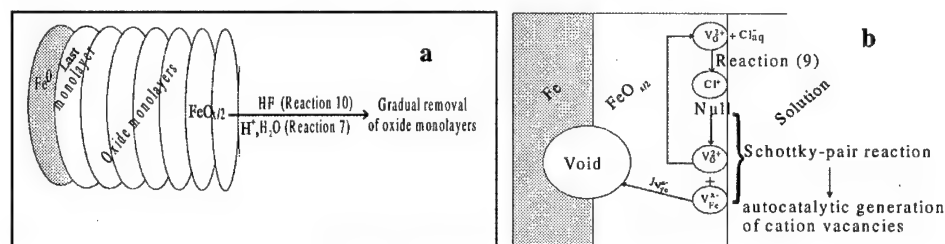


Figure 3: Schematic plots of the oxide breakdown for (a) general and (b) pitting corrosion.

7. CONCLUSIONS

The main conclusions of this study are:

- Complex periodic and aperiodic current oscillations occurring at the passive-active transition state of the halide-containing $\text{Fe}/\text{FeO}_{x/2}/\text{H}_2\text{SO}_{4(\text{aq})}$ system reflect pitting corrosion processes whereas monoperiodic current oscillations reflect general corrosion processes.
- The oxide growth depends on the transformation of iron holes into oxygen vacancies.
- The breakdown of the oxide film occurs through different mechanisms, namely through pitting and general corrosion. Processes related to pitting corrosion result in an increase of the iron-cation vacancies at the $\text{Fe}/\text{FeO}_{x/2}$ interface leading to the formation of a void. Processes related to general corrosion result in the generation of oxygen vacancy/iron-cation vacancy pair at the $\text{FeO}_{x/2}/\text{H}_2\text{SO}_{4(\text{aq})}$ interface leading to a gradual removal of oxide monolayers.

8. REFERENCES

- Toney, M.F., Davenport, A.J., Oblonsky, L.J., Ryan, M.P., Vitus, C.M., Atomic Structure of the Passive Film Formed on Iron, *Physical Review Letters* 79, 4248-4285 (1997).
- Bojinov, M., Fabricius, G., Laitinen, T., Makela, K., Saario, T. and Sundholm, G., Conduction Mechanism of the Anodic Film on Fe-Cr Alloys in Sulfate Solutions, *Journal of Electrochemical Society* 146, 3238-3247 (1999).
- Sazou, D., Karantonis, A. and Pagitsas, M., Generalized Hopf, Saddle-Node Infinite Period Bifurcations and Excitability during Electrodissolution and Passivation of Fe in a Sulfuric Acid Solution, *International Journal of Bifurcation & Chaos* 3, 981-997 (1993).
- Alligood, K.T., Sauer, T.D. and Yorke, J.A. *Chaos. An Introduction to Dynamical Systems*, Springer-Verlag, N. Y. (1996) p. 496.
- Pagitsas, M. and Sazou, D., Current Oscillations Induced by Chlorides during the Passive-Active Transition of Iron in a Sulfuric Acid Solution, *Journal of Electroanalytical Chemistry* 471, 132-145 (1999).
- Macdonald, D. D., The Point Defect Model for the Passive State, *Journal of Electrochemical Society*, 139, 3434-3449 (1992).
- Kortly, S., Sucha, L., *Handbook of Chemical Equilibria in Analytical Chemistry*, Ellis Horwood Ltd, John Wiley & Sons, N. Y. (1978).
- Sato, N., A Theory for Breakdown of Anodic Oxide Films on Metals, *Electrochimica Acta* 16, 1683-1692 (1971).

FAILURE RESISTANCE TO THERMAL SHOCK OF THERMAL BARRIER COATINGS USING THE FINITE ELEMENT METHOD

A. C. Kekatou, V. G. Sfakiotakis, D. E. Katsareas and N. K. Anifantis

Mechanical and Aeronautics Engineering Department,
University of Patras, GR-26500 Rion, Greece

1. SUMMARY

The failure resistance to thermal shock of a thermal barrier coating containing an interfacial crack is investigated via the Finite Element method. Linear elastic fracture mechanics analysis is used to determine the effects of various material property combinations. The Strain Energy Release Rate G , is obtained using the Crack Flank Displacement method. Resulting transient G illustrates that increasing the insulating characteristics of the coating leads to lower failure resistance of the TBC, which is also the case during extreme thermal expansion coefficient mismatch. On the other hand mechanical property mismatch has no effect on the failure resistance of the TBC.

2. INTRODUCTION

Thermal barrier coatings (TBCs) provide thermal insulation and oxidation resistance at high temperatures. Application of TBCs can be found in both aerospace and automotive applications, among these ceramic TBCs are used in high heat flux environments in order to protect the underlying metal substrates from potentially damaging high temperatures reached in such an environment.

TBCs have durability problems due to the material and thermal mismatch between the coating and the metallic substrate. Thermal cycling, residual stresses and environmental effects may initiate debonding and cracking that can have a profound effect on the response of the TBC, interfacial damage accumulation and spalling [1]. Considering the performance life of corresponding components, fracture is the most important type of damage. Interfacial cracks in multimaterial media present special analytical problems not encountered in fractured homogeneous media since they produce stress intensification from both geometric and material discontinuities. Williams [2], assumes traction free crack faces and results in crack surface interference and oscillatory interpretation of near field singularities. Comninou [3] reformulated this problem assuming non-zero traction conditions and eventual crack contact the crack tip. However, the prediction of strain energy release rate by both approaches yields the same values, and thus both approaches can be correlated on this basis.

Because of the complexity of these problems, numerical procedures are a necessity when stress intensities are desired for general configurations and heating conditions. Among them, the finite element and boundary element methods have been developed which utilize special crack tip elements to obtain stress intensity factors (SIFs) [4-5]. Smelser's technique of

computing the Strain Energy Release Rate, called Crack Flank Displacement method, utilizes the displacement field information provided by finite element solution.

The aim of the present work is to investigate in which way delamination and spalling fracture could possibly be suppressed by means of material compatibility without reducing the barrier effect of the TCB. As a first step, the energy release rate of an interface crack under thermal shock is obtained. Subsequently, the effect of various model and material parameters is discussed. The problem of domain dimensions in relation to crack length and the bending constraints imposed in reference [6] are re-examined and discussed also.

3. FAILURE MODELING

Figure 1(a) depicts the domain of the problem that consists of two subdomains, the thin layer of the coating with thickness h_C , and the thick layer of the substrate with thickness h_S . In the following, subscripts C, S assign coating and substrate characteristics. Along the interface exists a perfect bonding condition that is broken by an interfacial crack of length $2a$. The outer boundary surface is traction free and the lateral and bottom surfaces subject to conditions of symmetry. The entire system shown is initially at a uniform temperature T_0 , and the coating surface is then subjected to a convective cooling. Considering adiabatic and traction free crack surfaces, time variations of temperature and displacement fields were obtained by solving the uncoupled quasi steady-state plane strain thermoelasticity problem utilizing the Finite Element method. For this purpose, both materials were assumed homogeneous, isotropic and linear elastic. It was also assumed that no residual stresses present or crack surface interference occurs.

Around the crack tip (Figure 1(b)) the singularity of the stress field is described by the complex stress intensity factor

$$K = K_0 e^{i\theta} \quad (1)$$

where K_0 , θ are the modulus and the argument of the complex SIF.

Utilizing the finite element solution and the displacement method, the SIF modulus may be found from

$$K_0 = \frac{2\pi}{(1/2 + i \ln \gamma / 2\pi) \sqrt{(\delta u)^2 + (\delta v)^2}} \quad (2)$$

where γ depends on the material parameters

$$\gamma = \frac{\mu_S + \mu_C \kappa_S}{\mu_C + \mu_S \kappa_C} \quad (3)$$

and for plane strain conditions considered here, $\kappa_\alpha = 3 - 4\nu_\alpha$, $\alpha = S, C$.

In equation (3) δu , δv are the opening and shearing modes of crack surface deformation, as illustrated in Figure 1(b). This model yields the modulus of the SIF with high accuracy, provided that the size of the elements surrounding the crack tip is small enough.

4. PREDICTION OF TBC EFFICIENCY

The fracture modeling of delamination involves the calculation of the SIFs K_I , K_{II} and the corresponding strain energy release rates the sum of which is the total energy release rate G . This energy rate indicates the conditions of stable fracture, and thus is a measure of TBC efficiency. In other words, optimum TBC action is achieved when this energy is maximized. For the complex stress intensification occurring near the tip of interfacial cracks, if any contact conditions are negligible, the modulus of the total strain energy release rate is

$$G = \frac{\pi K_0^2}{4} \left(\frac{1-\nu_c}{\mu_c} + \frac{1-\nu_s}{\mu_s} \right) \quad (6)$$

where ν_α , μ_α , are the Poisson ratio and the shear modulus, respectively and K_0 is obtained using equation (2).

5. NUMERICAL RESULTS AND DISCUSSION

The effect of changing the material property combination, during sudden convective cooling of a center interfacial crack, is studied for a crack length of $a=1.5625$ mm. However it should be noticed that G decreases, as the crack gets shorter. The coating thickness is retained throughout the analysis and is $h_c=12.5$ mm. Figure 1(a) illustrates a simplified model of a Thermal Barrier Coating (TBC) which in general is a “thin coating” case, which in turn means that the domain of the problem at hand is semi-infinite. Under these considerations the depth of the substrate is infinite (compared to the coating) and so is the length of the specimen. The initial temperature of the TBC is $T_0=1000$ °C and the ambient temperature $T_A=20$ °C, while the free surface of the coating is cooled at a rate of $h=50$ W/m²/°C. It is understood that as h increases, maximum transient G increases.

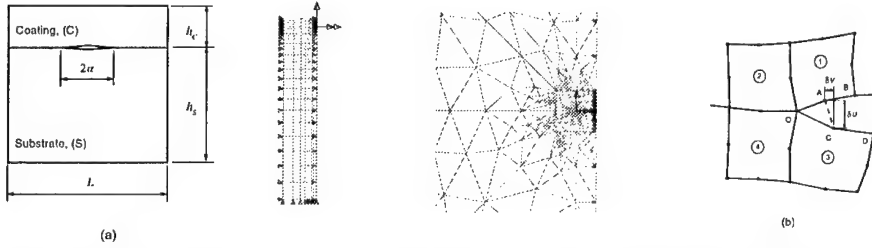


Figure 1: (a) Thermal Barrier Coating under sudden convective cooling. (b) Finite Element model of the TBC.

Figure 1(b) depicts the Finite Element Model of the TBC. The problem has one vertical axis of symmetry therefore only half needs to be discretized, whereas the length L and depth h_s of the substrate are taken to be finite but sufficiently larger than the h_c . No special crack elements have been used nor contact between crack faces has been modeled, since the later is a case that produces insignificant values of G and therefore poses no threat to the fracture toughness of the TBC.

The graph of Figure 2(a) shows that a coating-substrate thickness ratio of $h^*=h_c/h_s=1/20$ and length ratio of $h_c/L=1/15$, are more than sufficient for the solution to converge to the infinite problem (constraints perpendicular to the edges won't have any effect on the solution) maximum transient value of G . On the same Figure one can see that a spatial discretization of 983 quadratic triangular and rectangular elements and time step of $\Delta t=1$ sec, can produce a converged solution compared to a finer mesh (3456 elements) with one tenth of that time step. There is also a time curve produced with $r/a=0.0001$ compared to $r/a=0.05$ used throughout the analysis showing that this distance from the crack tip is sufficient for obtaining converged crack opening and sliding displacements.

The materials used for these convergence tests are Zirconia (ZrO_2) as a coating ($E_c=200$ GPa, $\nu_c=0.23$, $\rho_c=5900$ kg/m³, $\alpha_c=10.2 \times 10^{-6}$ 1/°C, $k_c=2.2$ W/m/°C, $C_c=460.6$ J/kg/°C) and nodular

cast Iron (Fe) as a substrate ($E_S=168$ GPa, $\nu_S=0.31$, $\rho_S=7289$ kg/m³, $\alpha_S=13.7 \times 10^{-6}$ 1/°C, $k_S=48.9$ W/m/°C, $C_S=418.4$ J/kg/°C).

Effect of mechanical properties

Figure 2(b) illustrates the effect of Young modulus ratio $E^*=E_C/E_S$ when all other properties of the two materials are the same as those of the substrate (in this case taken to be as nodular cast Iron). It is clear that the Young modulus mismatch in a Thermal Barrier Coating has no significant effect on the maximum transient Strain Energy Release Rate (G) and therefore poses no threat to the TBC's fracture toughness.

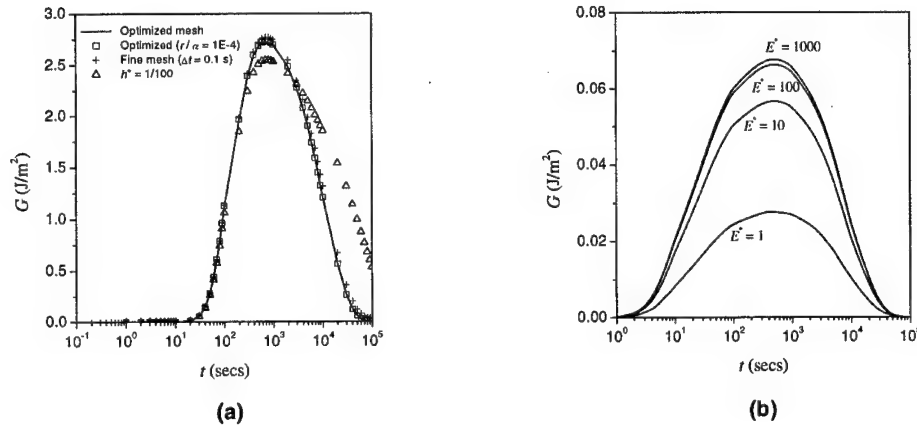


Figure 2: (a) Convergence graph showing transient Strain Energy Release Rate (G) for different coating-substrate thickness ratios, mesh densities, time steps, r/α ratios. (b) Transient Strain Energy Release Rate for various Young modulus combinations.

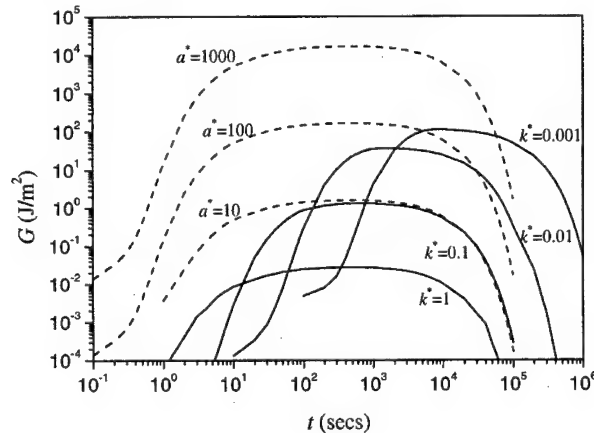


Figure 3: Transient Strain Energy Release Rate for various thermal expansion coefficient and thermal conductivity combinations.

In Figure 3 one can notice that, the effect of thermal expansion coefficient ratio $\alpha^* = \alpha_c / \alpha_s$ is most significant since increasing it one order of magnitude results in an increase of the maximum transient G of two orders of magnitude. It is also noticed that when this ratio is lower than unit the crack closes, therefore producing very small values of G .

Effect of thermal properties

The transient value of Strain Energy Release Rate for various ratios of the thermal conductivity $k^* = k_c / k_s$, is depicted in Figure 3. The effect of the mismatch is less pronounced than in the thermal expansion case, but it also produces a delayed (in time) peaking of G . It is also noticed that decreasing the coatings conductivity and thus increasing its insulating characteristics leads to higher G transients and therefore to lower failure resistance of the TBC.

6. CONCLUSIONS

- a) Although Thermal Barrier Coatings aim on protecting the substrate from thermal shock using their insulating characteristics, it seems that the higher the insulation the lower the failure resistance. Therefore extra care must be taken in the thermal conductivity mismatch during TBC design.
- b) High thermal expansion coefficients of coating in comparison with substrate lead to very low resistance to fracture. In the opposite case interface cracks tend to close thus posing no threat to the failure resistance of the TBC. Thermal expansion coefficients should be as close as possible during the design of a TBC.
- c) Lowering the thermal conductivity of the coating, in respect of the substrate, causes a noticeable delay in the occurrence of the maximum Strain Energy Release Rate, thus making it an extremely unpredictable cause of possible failure.
- d) The Modulus of Elasticity mismatch has insignificant effect on the failure resistance of the TBC.
- e) Care should be taken during FEM modeling of a TBC, one should move the artificial boundary at least 20 times the thickness of the coating away from the interface.

A future parametric analysis should also include convection coefficient, initial and ambient temperature, Poisson coefficient, crack length, residual stress, contact analysis and interchanging cooling with heating effects on the failure resistance of a TBC.

7. REFERENCES

- [1] Kokini, K., Material compatibility in interfacial transient thermal fracture of ceramic-to-metal bonds, *Journal of Applied Mechanics* 55, 767-772 (1988).
- [2] Williams, M.L., The stresses around a fault or crack in dissimilar media, *Bulletin of the Seismological Society of America*, 49, 199-204, 1957.
- [3] Comninou, M., The interface crack, *ASME Journal of Applied Mechanics*, 44, 631-636, 1977.
- [4] Katsareas, D. and N. Anifantis, Boundary element analysis of thermally stressed interface cracks, *Engineering Fracture Mechanics*, 50, 51-60, 1995.
- [5] Smelser, R.E., Evaluation of stress intensity factors for bimaterial bodies using numerical crack flank displacement data, *International Journal of Fracture*, 15, 135-143, 1979.
- [6] Reynolds, R.R., K. Kokini and G. Chen, The mechanics of the interface crack using the finite element method, *ASME Journal of Engineering Materials and Technology*, 112, 38-43, 1990.

FINITE ELEMENT ANALYSIS OF THE ELASTIC MECHANICAL BEHAVIOUR OF LDPE FILM

Demetres Briassoulis and Evelia Schettini¹

Agricultural University of Athens, Department of Agricultural Engineering,
Iera Odos 75, 11855 Athens, Greece

1. SUMMARY

In the Mediterranean Europe, Low-Density Polyethylene (LDPE) films are the most widely used plastic covering materials of greenhouse. The investigation of the mechanical behaviour of the LDPE greenhouse films is a significant issue because all service conditions for the LDPE films involve mechanical stress under various loading conditions and the durability of these materials mainly depends on their mechanical behaviour. In this paper the elastic mechanical behaviour of LDPE films under various combinations of pre-tensioning and uniform pressure schemes is investigated experimentally and numerically using the finite element method of analysis.

2. INTRODUCTION

The economic and technical developments of the last years have increased the application of plastic films in the agricultural sector due to their good mechanical and optical properties, ease of forming and low market cost [1, 2].

In the regions of the Mediterranean Europe, Low-Density Polyethylene (LDPE) films are the most widely plastic covering materials of greenhouse used. Good quality products with a predictable life-time have contributed to increasing the quality and quantity of the crop production and to reducing some technical problems related to the greenhouse design and environmental implications connected with their final disposal.

All service conditions for the LDPE greenhouse films involve mechanical stress under various loading conditions while the durability of these materials mainly depends on their mechanical behaviour. Therefore, the investigation of the mechanical behaviour of the LDPE films is a significant issue.

In this paper the elastic mechanical behaviour of LDPE films under various combinations of pre-tensioning and uniform pressure schemes is investigated both experimentally and numerically (no viscous behaviour is considered in the present work). The results of the experimental set-up, involving monitoring the mechanical behaviour of a pre-tensioned and uniformly loaded square piece of film, are compared against the results obtained from analytical expressions reported in the literature [3, 4] and the results obtained using the finite element method of analysis.

¹ *Post doctoral fellow supported by the European Commission (SMT4- CT98-9034, DG 12-RSMT)*

3. EXPERIMENTAL PROCEDURE

The experimental set-up employed in the present study, shown in Fig. 1, consists of an open wooden box which rests on a steel bearing construction. A system of two frames supports the film by pressure and friction against the top edges of the walls of the box. The loaded area of the LDPE film is square with a clear side dimension of $L=1$ m; the film is pre-tensioned by applying appropriate weights along the four sides before fixing the system of the two frames. To avoid the slippage of the film the faces of the lower frame and the top edge of the box in contact with the film are covered by rubber and sand paper while the lower frame applies pressure to the film against the box by means of a system of screws installed in the upper frame. The pressure inside the box, applied by means of pressurised air, is monitored by means of a pressure transducer. The deflection along the central line of the film is evaluated by employing an image capturing and processing technique (by using a digital camera). The strains are to be monitored during the second phase of this research work.

The material properties of the LDPE film used, such as the modulus of elasticity E and tensile stress at yield σ_y in the parallel and transverse directions, were obtained at the laboratory by applying standard testing methods (Table 1) [5]. The Poisson's ratio is rarely reported in literature [6]. Fig. 2 shows the stress-strain curve in the parallel direction for the LDPE film used.

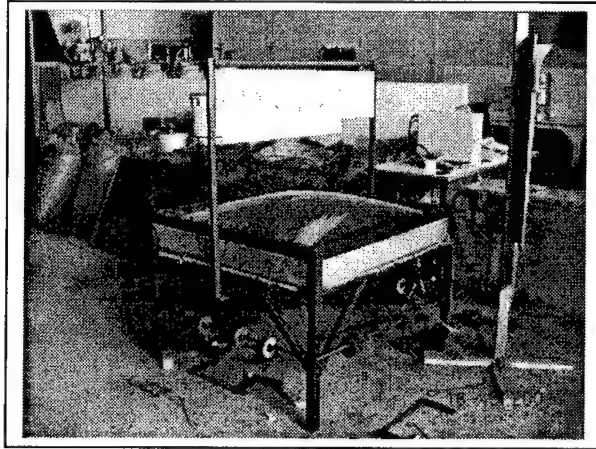


Figure 1: The experimental set-up used.

Table 1: Material properties obtained at the laboratory applying standard testing methods.

i- direction	E_i [MPa]	σ_i at yield [MPa]
x	102,97	7,984
y	110,35	6,997

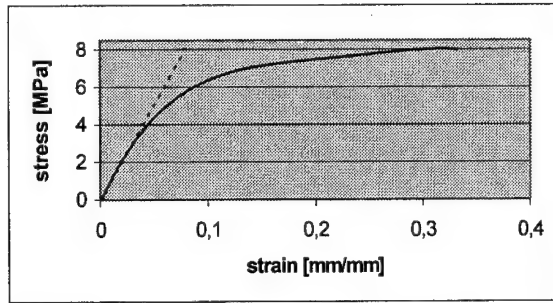


Figure 2: Stress-strain curve in the parallel direction for the LDPE greenhouse film.

4. ANALYTICAL SOLUTION

Timoshenko and Woinowsky-Krieger [4] give an approximate solution for a uniformly loaded square plate with sides of length $2a$ and clamped edges. This solution doesn't take into account the pretensioning effects on the behaviour of the plate. This method consists of a combination of the known solutions given by the theory of small deflections (this is insignificant in the present application) and the membrane theory.

The load q can be calculated by:

$$q = \frac{w_o E t^3}{a^4} \left(1.37 + 1.94 \frac{w_o^2}{t^2} \right) \quad (1)$$

where E is the modulus of elasticity, t is the thickness of the plate, w_o is the deflection at the center of the plate; the numerical constants depend on the geometry of the plate and on Poisson's ratio ν (assumed $\nu=0.25$ in the analytical derivations).

5. NUMERICAL SIMULATION

The simulation of the mechanical behaviour of the LDPE film is performed by using the finite element method of analysis. ANSYS [7], a commercial finite element program, as well as a research program employing the finite shell element RFNS [8, 9] are employed.

The performance of two specific finite elements of ANSYS, a membrane and a finite strain shell element, is investigated with respect to the best possible simulation of the film's elastic behaviour. A finite element model of the plastic film investigated experimentally, with the same geometry and isotropic material properties, is studied numerically under appropriate boundary conditions and by applying different analysis options. Models with 416 elements are used with the ANSYS programme. The material properties used were (assuming average isotropic properties): modulus of elasticity $E=106,66$ MPa, thickness of the film $t=0,000195$ m, stress at yield $\sigma_y=7.98$ MPa. Analyses are performed for different Poisson's ratio values for comparison purposes. Nonlinear analysis, including membrane action and geometric nonlinearities such as large strain, large displacements and stress stiffening have been considered. The membrane element available doesn't allow material nonlinearities to be considered. The shell element allows modeling of plastic behaviour but there is a need to introduce indirectly an artificial membrane action. The RFNS elements allows for membrane action, large

displacements and large rotations. Time dependent behaviour is not considered in the present research work. Material nonlinearities are not considered during the first preliminary numerical analysis stage of the present work.

In the case of large deflection and non linear analysis, the shell element stress output quantities (ANSYS and RFNS) are Cauchy stresses in the rotated element coordinate system while for the membrane element stress output engineering stresses are calculated referred to the rotated element coordinate system.

6. RESULTS AND DISCUSSION

In the case where no pretension is applied on the film, the results obtained using the analytical solution (an approximate solution) and the numerical simulations are shown in the Table 2. The agreement between the three solutions is good. The deflection at the center is obtained for different values of the applied uniform pressure and for Poisson's ratio $\nu=0,25$ (this value is chosen in connection with the numerical constants of Eq. (1)). The modulus of elasticity and the film geometry are those described in the numerical simulation section.

Table 2: Deflection at the center applying Eq. (1) and numerical analyses.

Pressure [Pa]	Deflection at the center [m]		
	Analytic solution Eq. (1)	Numerical solution ANSYS membranc element	Numerical solution RFNS element
250	0,0729	0,0661	0,0675
800	0,1074	0,0960	0,1002
1500	0,1324	0,1234	0,1243
2400	0,1549	0,1470	0,1465

The results obtained from the numerical modelling of the elastic mechanical behaviour of LDPE film (i.e. without considering material nonlinearities) by using the finite element method of analysis are shown in Table 3 and Figs. 3 and 4. The numerical and the experimental maximum deflection at the center of the film are shown in Table 3 for different levels of pressure. The pretension is 60 N/m and the Poisson's ratio is assumed to be $\nu=0,4$. The Poisson's ratio of the LDPE film is not known and Courtney [10] considers $\nu=0,4$ as a reasonable value for Polyethylene.

Table 3: Numerical and experimental deflection at the center of the film.

Pressure [Pa]	Deflection at the center [m]		
	Experimental results	Numerical solution ANSYS membrane element	Numerical solution RFNS element
130	0,047	0,042	0,051
250	0,050	0,055	0,064
600	0,079	0,080	0,085
1500	0,120	0,113	0,117116
2500	0,159	0,139	0,140138

For low values of pressure (i.e. in the linear elastic region) the agreement between the experimental results and the numerical analysis results is good. For higher values of the pressure numerical analysis is only approximate (linear elastic). This is because for values of stress (e.g. von Mises stress) above 3 MPa, the behaviour of the material becomes rather nonlinear as it is shown in Fig. 2. Thus, it should be expected that the experimental values for the maximum deflection become increasingly higher than those calculated numerically based on the assumption of a linear elastic behaviour. This behaviour is already under numerical and experimental investigation.

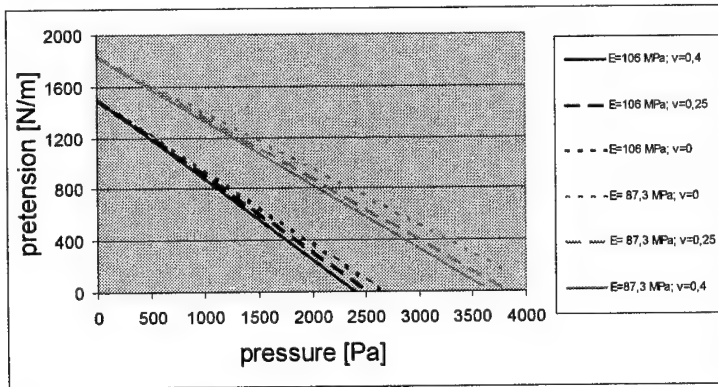


Figure 3: Pressure and pretension force interaction curves (using ANSYS membrane element)

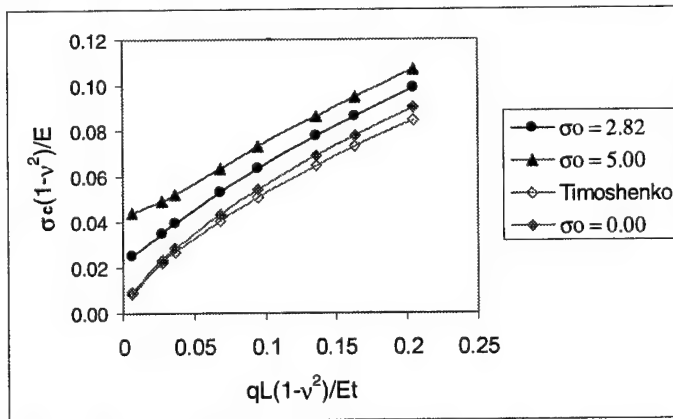


Figure 4: Interaction pressure-pre-tensioning maximum stress at center σ_c curves ($\nu=0.25$; finite element 10x10 model with the RFNS element; σ_0 = pretensioning stress in MPa)

Fig. 3 shows the relationship, for three values of Poisson's ratio, between the value of pressure and the uniform pretension force all around the film corresponding to the limit cases when the maximum membrane stress reaches the stress at yield. This diagram is obtained by employing the ANSYS membrane element for modeling a film of square 1x1 m shape. The material properties used for this figure are relating to the same LDPE film but in two different periods of its lifetime. The modulus of elasticity $E=87,3$ MPa and stress at yield $\sigma_y=9,45$ MPa are related to the material following the production while $E=106$ MPa and $\sigma_y=7,98$ MPa are related to the material following the production.

MPa correspond to the same film after a two-years storage period. The increase of the modulus of elasticity results in a decrease of the pretension force needed to reach the stress at yield for the same value of pressure. However, it should be mentioned that these lines are based on assuming linear elastic behaviour up to the yield stress. In reality, the material behaviour is nonlinear at much lower stress levels as will be analysed following the completion of the second phase of this work.

Another plot of interaction pressure-pre-tensioning stress curves is shown in Fig. 4 for the case of Poisson's ratio $\nu=0.25$ and $E=106.0$ MPa for comparison purposes against the corresponding values obtained by Timoshenko and Woinowsky-Krieger [4]. Here the effective stress σ_{eff} based on Von-Mises criterion is employed ($\sigma_{\text{eff}} = \sigma_c$ at center). The RFNS element is used by employing a 10×10 model.

7. CONCLUSIONS AND PROSPECTIVES

This study is the first step in the analysis of the state of stress of greenhouse LDPE films under various loading conditions. The results obtained in this paper validated the selected ANSYS membrane and the RFNS elements performance in the linear elastic region on the basis of the agreement achieved with the experimental results for low level pressures. In the second phase of this work, the experimental investigation will continue with strain measurements on the film while the numerical procedure will also include material nonlinearities to be able to simulate the film behaviour at higher values of pressure. Both, the ANSYS and the RFNS finite element models will be used subsequently for studying the load carrying and load redistribution mechanisms developing by greenhouse covering LDPE films in transferring external loads such as wind and snow loads to the main structure. The final aim is to formulate technical suggestions for the reliable design of LDPE film covered greenhouses, making more efficient use of LDPE greenhouse plastic films.

8. REFERENCES

- [1] Briassoulis, D.; Waaijenberg, D.; Gratraud, J. and von Elsner B., Mechanical properties of covering materials for greenhouses. Part 1: General Overview., *J. Agric. Engng. Res.*, 67, 81-96 (1997).
- [2] Osswald, T. A. and Menges, G., *Material Science of Polymers for Engineers*. Hanser/ Gardner Publications, Inc. Cincinnati (1996).
- [3] Leonard, J. W., *Tension Structures. Behavior and analysis.*, McGraw- Hill (1988).
- [4] Timoshenko, S. and Woinowsky-Krieger, S., *Theory of plates and shells.*, McGraw- Hill (1959).
- [5] Briassoulis D. and Aristopoulou A., Adaptation and Harmonisation of Standard Testing Methods for Mechanical Properties of Low Density Polyethylene (LDPE) Films, *Polymer Testing*, to be published
- [6] Briassoulis, D.; Waaijenberg, D.; Gratraud, J. and von Elsner B., Mechanical properties of covering materials for greenhouses. Part 1: General Overview., *J. Agric. Engng. Res.*, 67, 81-96 (1997).
- [7] ANSYS, v. 5.6, ANSYS Inc., Canonsburg, USA, (2000).
- [8] Briassoulis D., The Four-node C⁰ Shell Element Reformulated, *Int. J. Numer. Meth. Eng.*, 39, 2417-2455 (1996).
- [9] Briassoulis D., Nonlinear Formulation of the RFNS Element, *in preparation*.
- [10] Courtney T.H., *Mechanical behaviour of materials*. McGraw Hill (1990).

ADAPTIVE COMPOSITES INCORPORATING SHAPE MEMORY ALLOY WIRES; RECORDING THE INTERNAL STRESS BY LASER RAMAN SPECTROSCOPY

J. Parthenios, G. C. Psarras, D. Bolas and C. Galiotis
Institute of Chemical Engineering and High Temperature Chemical Processes
Foundation of Research and Technology-Hellas
P.O. BOX 1414, Patras 265 00, Greece
e-mail: c.galiotis@iceht.forth.gr

1.SUMMARY

Pre-strained Shape Memory Alloy (SMA) wires have been integrated in composite laminates consisting of an epoxy resin reinforced by aramid fibres. The SMA wires, in tandem with their reinforced role, can act as sensors and/or actuators changing the structural behavior of the composite materials due to their ability to generate recovery stresses. Past work has shown that aramid fibres can act as stress and/or temperature sensors, as the Raman vibrational wavenumbers of their skeletal backbone shift, according to the applied stress and/or temperature. By exploiting the sensing ability of aramid fibres, the mechanical response of SMA wires/aramid fibres/epoxy composites was examined by means of laser Raman spectroscopy.

We report on the transmitted stresses from wires to fibres as a function of activation temperature in these composite systems. Transmitted compressive stresses were measured at temperatures of 60, 80 and 100 °C for SMA composite specimens by employing different SMA wire volume fractions. Composite specimens were of dimensions that prevent their geometric failure due to generated stresses during SMA wire activation. The results show that the stress values of 100 °C are not significantly different than those at 80 °C in all cases, while the transmitted stresses are dependent on the inter-wire distance.

2.INTRODUCTION

The integration of pre-strained SMA wires in fibre reinforced polymer composites leads to adaptive or smart composite materials since the wires can operate as actuating and/or sensing elements. The actuating/sensing capabilities of SMA wires are based on their functional properties which are directly associated with the Shape Memory Effect [1]. This effect is related to the reversible (thermoelastic) martensitic transformation [1,2] shown in Fig. 1, where the SMA material original shape is regained. Martensitic transformation is generally defined by the M_s , M_f , which are the start and finish temperatures of the forward

transformation, respectively, and the A_s , A_f the corresponding start and finish temperatures of the reverse process, respectively. These values are mainly determined by the SMA composition since they are metal alloys such as Ni-Ti or Ni-Ti-X (where X stands for Cu, Co, Fe or Nb).

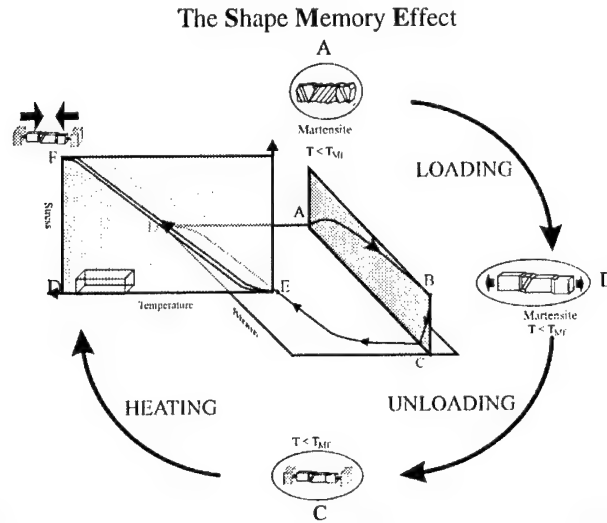


Figure 1: The SMA material is deformed (AB) and unloaded (BC) at a temperature below M_f . The deformation is restored during heating to a temperature above A_f (CD). The original dimensions are re-gained (DA). Under constraint conditions, at point C, the SMA material is prevented from returning to its original shape during heating. Thus, high recovery stresses are gradually generated starting at point E.

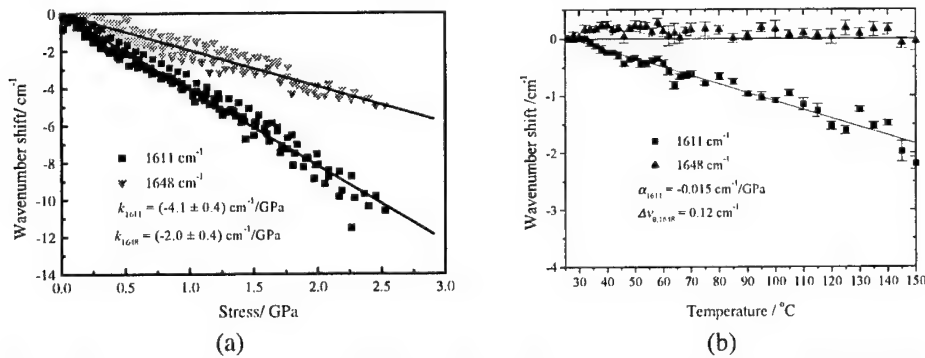


Figure 2: Raman wavenumber shift as a function of the applied stress for the (a) 1611 cm⁻¹ and (b) 1648 cm⁻¹ Raman bands of the PPTA repeat unit in Kevlar 29 fibres

Among other functional properties of SMA wires, the generation of recovery stresses is exploited in the SMA composites for altering their shape or stress state. The strain recovery of the pre-strained wires is biased by the elastic stiffness of the host matrix and thus compressive stresses are generated gradually starting at point E (Fig. 1). Stresses are generated at a constant rate ($d\sigma/dt$) beyond a critical temperature, A_f [1]. After overcoming a temperature hysteresis the reverse process occurs during cooling (Fig. 1, EFE).

Laser Raman spectroscopy is considered as a powerful method for stress (or strain) and/or temperature measurements in fibrous composite materials. Previous work has shown that

Raman vibrational wavenumbers of certain chemical bonds on the skeletal backbone of PPTA repeat unit of the aramid fibres shift to lower values under tension and/or temperature and to higher values under compression. These vibrations recorded at 1611 and 1648 cm^{-1} correspond mainly to ring/C-C stretching and to amide/C=O stretching, respectively. [3,4]. Well-defined relationships between Raman wavenumber and applied stress, strain or temperature can be obtained by these fibres, which are the corresponding calibration curves shown in Fig.2. Thus, aramid fibres can be used as sensors, in tandem with their reinforcing role, to determine the stress state and the temperature of the composite material.

3. EXPERIMENTAL

In this study Kevlar 29 of $15\text{ }\mu\text{m}$ diameter supplied by Du Pont were used as reinforced fibres. The epoxy resin-Kevlar 29 fibres unidirectional prepreg was made by Advanced Composites Group U.K., with 53.5% volume fraction of fibres. The SMA wires were NiTi(12%)Cu of $150\text{ }\mu\text{m}$ diameter, supplied by Memry Co. The Young's modulus of the fibres is comparable to that of SMA wires, while the glass transition temperature (T_g) of the resin is high enough, in order not to be reached during the SMA wires activation.

The specimens consisted of two prepreg plies into which three and five martensitic SMA wires were placed in parallel and pre-strained by 3%, before being incorporated into the autoclave bag. This was made obtainable by using a specially designed mould [4]. The lay up of the composite specimen is abbreviated to $O_i/W_j/O_i$, where $i = 1$ is the number of the plies and $j = 3, 5$ is the number of the wires. The cure involved initial curing at $70\text{ }^\circ\text{C}$ for 12 h followed by post-curing at $140\text{ }^\circ\text{C}$ for 1 h. The dimensions of the manufactured specimens were the same, regardless the number of the SMA wires. Based on past work, the determination of these dimensions was carefully made in order to avoid geometrical failure [4]. The type of activation was the active one using a stabilized DC source. The activation levels corresponded to the temperatures of $60, 80$ and $100\text{ }^\circ\text{C}$, as these were measured by suitable tiny thermocouples, situated on the surface of the specimens. The experimental setup allows, during SMA activation the simultaneous control of the wire temperature and the recording of the Raman spectra(Fig.3).

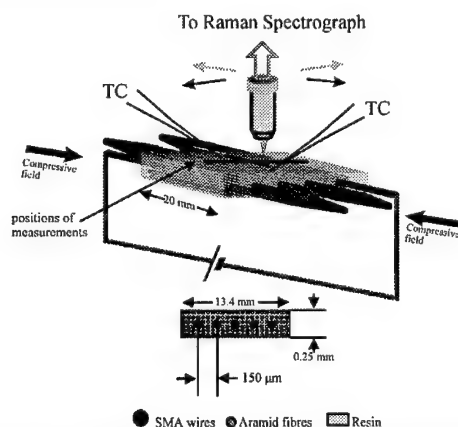


Figure 3: Experimental set-up employed for the fibre stress and temperature mapping during SMA wire activation

It should be noted that the specimens were free of mechanical load during SMA wire activation. The measurements took place normal to the direction of the wires, with a step more or less equal to the diameter of the aramid fibers. The part of experimental set-up for Raman spectra acquisition has been described in detail elsewhere [4,5].

4. RESULTS AND DISCUSSION

The wavenumber shift for each vibrational mechanism, namely 1611 cm^{-1} and 1648 cm^{-1} , depends on three terms. The mechanical field that is created by the stresses which are the result of the activation of the SMA wires, the temperature that is interfused from the wires to the aramid fibers through the epoxy resin and the residual thermal stresses. These residual stresses were formed due to the mismatch of thermal expansion coefficients of aramid fibres and the epoxy resin matrix and influenced by the passive martensitic-to-austenitic transformation that undergo the SMA wires during composite curing. Thus, for each of the Raman bands, the total wavenumber shift is given by:

$$\Delta\nu = \Delta\nu_M + \Delta\nu_0 + \Delta\nu_R \quad (1)$$

where $\Delta\nu_M$, $\Delta\nu_0$ and $\Delta\nu_R$ are the contributions of generated stress, temperature and residual stress in the Raman wavenumber shift, respectively. It is worth noting here that all the band shifts are referred to the change of band positions as compared to the corresponding values of the free-standing fibers in the air. Both bands have been proved stress sensitive, with the first to be more sensitive than the second one (Fig.2a). Furthermore it is clear that the position of the 1611 cm^{-1} depends on the fibre temperature while the 1648 cm^{-1} equivalent can be considered as temperature insensitive. So, the determination of the axial stress, σ , transmitted to the Kevlar 29 fibres by wire activation, is determined using the universal equation[3]:

$$\Delta\nu = k\sigma \quad (2)$$

where k is the sensitivity in stress for a given Raman band. Since the position of the 1648 cm^{-1} band is sensitive only to stress, the axial stress, σ , transmitted to the Kevlar fibres is determined via the equation[4]:

$$\sigma = \frac{\Delta\nu_{1648} - \Delta\nu_{R,1648} - C}{k_{1648}} \quad (3)$$

where $\Delta\nu_{1648}$ is the total wavenumber shift for the 1648 cm^{-1} band, k_{1648} is its stress sensitivity, $\Delta\nu_{R,1648}$ is the wavenumber component due to the residual stress of the as-fabricated specimens and $C \approx 0.117\text{ cm}^{-1}$. Similarly the fibre temperature, θ , in the embedded Kevlar 29 fibres is estimated in $^{\circ}\text{C}$ using the equation:

$$\theta = \frac{\Delta\nu_{1611} - \Delta\nu_{R,1611} - k_{1611} \cdot \sigma}{\alpha_{1611}} \quad (4)$$

where $\Delta\nu_{1611}$ is the total wavenumber shift for the 1611 cm^{-1} band, k_{1611} is its stress sensitivity, $\Delta\nu_{R,1611}$ is the wavenumber component due to the residual stress of the as-fabricated specimens, σ the axial stress in the fibres calculated from equation (3) and α_{1611} is the temperature sensitivity of the 1611 cm^{-1} band. The determination of the component $\Delta\nu_R$, either for 1648 cm^{-1} or 1611 cm^{-1} , which correspond to the residual thermal stresses has been made with a methodology described in detail elsewhere[4].

In Fig. 4a, the axial stress in the fibre derived from Eq. (3), as a function of the position across the wire direction for the $O_1/W_3/O_1$ specimen is given for activation temperatures of 100°C and in Fig. 4b and c for the $O_1/W_3/O_1$ for two activation temperatures of 80 and 100°C respectively.

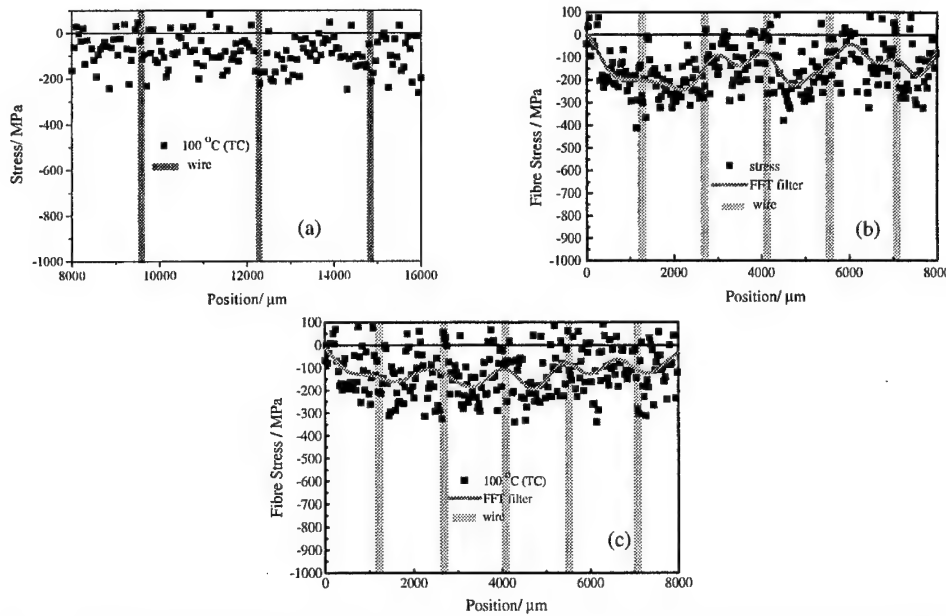


Figure 4: The transmitted fibre stress data, as derived from Eq. (3), (a) for the $O_1/W_3/O_1$ specimen at 100 °C, for the $O_1/W_3/O_1$ specimen at (b) 80 °C and (c) 100 °C levels of activation

At temperatures below 80 °C for the $O_1/W_3/O_1$ specimen and 60 °C for the $O_1/W_5/O_1$ specimen the transmitted stresses to the fibres were too low to be quantified by the stress sensitive 1648 cm^{-1} Raman band and therefore these results are not presented here. As can be seen in Fig. 4a, the transmitted compressive stresses in most fibres are of average 90 MPa and around 100 MPa near the wire position. These values correspond to an SMA wire volume fraction of 1.0% (three wires) and the higher level of SMA wire activation. By increasing the SMA wire volume fraction to 2.6% (five wires) the average compressive stresses increase to 150 MPa and around 200 MPa near the wire position, as is shown in Fig. 4c.

The comparison of Figs. 4a and c reveals the differences between the transmitted stress distribution across the wire direction as the SMA volume fraction increases from 1% to 2.6%. In the case of $O_1/W_3/O_1$ specimen, the peaks of the stresses appear in the vicinity of the wires, while in the case of the higher volume fraction specimen the high stress peaks are located in the middle of the inter-wire distance. This result can be attributed to the wire-wire interaction as the inter-wire distance is reduced, by increasing the SMA wire volume fraction; in the mid-wire distance, the overall compressive field is produced by the overlapping of the two compressive fields generated by the two subsequent wires.

In Figs b and c is shown that the increase of temperature from 80 °C to 100 °C for the $O_1/W_3/O_1$ specimen does lead to an increase of stresses transmitted to the fibres due perhaps to a possible softening of the host matrix at that temperature. It should be noted that the scatter of the stress data that can be observed in these figures could be attributed to the fibre location, orientation, diameter variability and to the accuracy of measurements. A method based on FFT has been proposed and applied successfully for filtering the experimental noise [5].

Finally, in Figs. 5a and b the temperature as a function of the position across the wire direction for both specimens is given for activation temperature of 100 °C. The corresponding

fibre temperature distributions have their maximum values near the wires, which is not unexpected bearing in mind the low thermal conductivity of the epoxy matrix. The values of temperature increase from the edge of the specimen, where the material is contact with the environment and reach their maximum value at the mid-width position. The observed scatter is attributed to the reasons mentioned earlier. Point temperature measurements obtained via thermocouples are also shown in Fig. 5 for comparison with those obtained via laser Raman spectroscopy at the corresponding points.

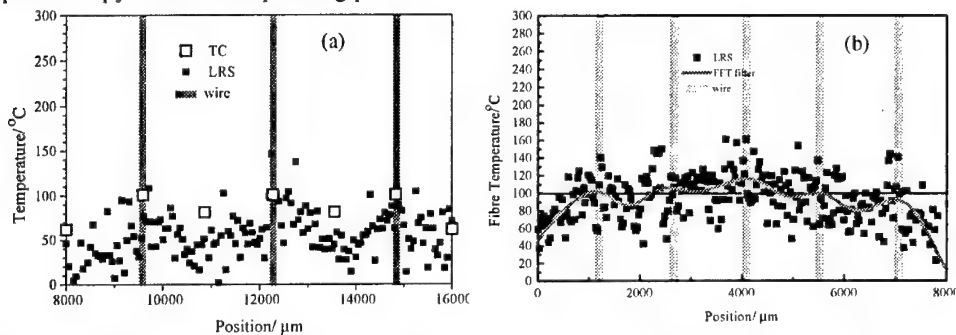


Figure 5: The fibre temperature data, as derived from Eq. (4), (a) for the $O_1/W_3/O_1$ specimen at 100 °C and (b) for the $O_1/W_3/O_1$ specimen at 100 °C levels of activation. In (a) the open squares and the thin horizontal line in (b) correspond to thermocouple temperature.

5. CONCLUSIONS

SMA composite specimens consisting of pre-strained martensitic NiTiCu wires and Kevlar 29/LTM217 epoxy prepregs were fabricated by autoclave curing. The geometry of the specimens was carefully selected to prevent the buckling failure during the activation of the SMA wires. The stress state of SMA composite specimens of different SMA wire volume fraction and at different levels of activation was examined via the technique of laser Raman spectroscopy. By increasing the SMA wire volume fraction, the stresses transferred to kevlar fibres also increase as expected, but after a critical inter-wire distance the wire-wire interaction alters the stress profile of the specimen. Finally, recovery stresses in the fibres seem to saturate by increasing the level of wire activation for constant SMA wire volume fraction.

Acknowledgements: The reported studies are part of an EU BRITE/EURAM project (No: BRPR-CT97-468).

6. REFERENCES

- [1] Duering TW, Melton KN, Stoeckel D. Engineering aspects of shape memory alloys. London: Butterworth-Heinemann, 1990.
- [2] Van Humbeeck J, Stalmans R. Characteristics of shape memory alloys. In: Otsuka K, Wayman CM, editors. Shape memory materials. Cambridge: Cambridge University Press, 1998. p. 149-183.
- [3] Galiotis C, Micromechanics of reinforcement using laser Raman spectroscopy. In: Summerscales J, editor. Microstructural characterisation of fibre-reinforced composites. Woodhead, 1998.

- [4] Psarras GC, Parthenios J, Galiotis C. Adaptive composites incorporating shape memory alloy wires; Part I probing the internal stress and temperature distributions with a laser Raman sensor. *J. Mater. Sci.* **36** 2001, p. 535-546.
- [5] Parthenios J, Psarras GC, Galiotis C. Adaptive composites incorporating shape memory alloy wires; Part II development of internal recovery stresses as a function of activation temperature. *Comp. Part A*, accepted Jan. 2001, in press.

A HEMIVARIATIONAL INEQUALITY APPROACH TO THE RESISTANCE OF ALUMINIUM RIVETED CONNECTIONS

M. Zygomalas, M. J. Kontoleon and C. C. Baniotopoulos

Department of Civil Engineering
Aristotle University of Thessaloniki, GR-54006 Thessaloniki, Greece

1. SUMMARY

A hemivariational inequality approach is herein proposed for the calculation of the bearing resistance of aluminum riveted joints. Taking into account nonlinear effects and describing the resistance in bearing strength by means of a nonmonotone multivalued reaction-displacement law obtained by experimental testing, the problem is formulated as a hemivariational inequality one. The latter is equivalent to a substationarity problem of the potential energy of the aluminium joint at hand. This problem can be effectively treated numerically by applying an appropriately chosen nonsmooth nonconvex optimization algorithm. In the last part of the paper, the results of a numerical application are compared to those of an experimental testing program that has been performed at the laboratory to investigate the resistance of aluminium riveted joints.

2. INTRODUCTION

The various structural components in aluminium structures are assembled and connected each other by means of a variety of fasteners. The respective connections are characterized as bolted, welded, riveted and adhesive ones. Among them, riveted connections exhibit a lot of advantages, as are e.g. the easy assemblage, the repairing and the replacing of damaged components. Classic methods for the analysis of these joints assume that the contact between the adjacent elements of the connection is complete. The consequence of this assumption is that the compression forces are undertaken by the connected plates, whereas the tension ones by the rivets [1,2]. In the case that the loading leads to the development of moments, shear and tension forces, one of the main reasons for the failure of the joint is the loss of the resistance in bearing strength. Specifically, the phenomenon of concentration of stresses around the holes of the rivets appears, introducing nonlinear effects that in turn lead to bearing strength failure. Thus, the part of the joint around the hole usually becomes the weakest part of the structure. To overcome this weak point, many experimental, theoretical and numerical methods for the investigation of the behaviour of these joints have been applied. An effective methodology to take into consideration these nonlinear effects is to

simulate the aluminium connections by means of the Finite Element Method in combination to the principles of Nonsmooth Mechanics [3].

Nonlinear effects result from the nonlinear material properties of aluminum and the fact that in the area of the rivets, unilateral contact conditions develop active contact and separation areas between the contact fronts of the connection plates. The contact and separation effects can be described by means of the unilateral contact law of Signorini-Fichera [3]. From a mathematical point of view, these phenomena introduce a Boundary Value Problem that leads to Variational Inequality Problems or equivalently to Quadratic Optimization Problems [3]. The resistance in bearing strength of the rivet can be described by a nonmonotone multivalued reaction-displacement law as the result of the concentration of the stresses around the hole. The vertical branch in the diagram corresponds to the abrupt loss of the bearing strength. Within this framework, the formulation of the problem is obtained by means of a variational-hemivariational inequality. The theory of hemivariational inequalities or "Panagiotopoulos inequalities" leads to a substationarity problem of the potential or complementary energy of the structure that expresses the principle of minimum potential energy of the connection at the state of equilibrium. The solutions of this problem are the so-called substationarity points that represent equilibrium positions of the joint and can be derived from the inclusion of $\partial \Pi$, where Π is the potential or complementary energy and ∂ denotes the generalized gradient [3]. Substationarity points include local minima, local maxima and saddle points. In the present paper, we investigate the behaviour of riveted joints by taking into account the effect of bearing strength failure and nonlinear effects such as plasticity and interface interaction by means of a three-dimensional model pre-defining active, nonactive and sliding regions. It is obvious that the proposed model describes the behaviour of the joint in the most detailed way and the respective numerical applications give reliable results leading to new improved principles in the design of safe aluminium structures. The above mentioned substationarity problem can be solved with an appropriately chosen nonsmooth nonconvex optimization procedure capable to handle superpotentials and it converges to a substationarity solution. For the solution of the problem, the so-called NSOLIB program based on the Proximal Bundle Method has been used. The proximal bundle method proceeds to a polyhedral approximation of the objective function with the cutting-plane method and additionally, it uses a weighting parameter to consider a quadratic stabilization term in the polyhedral approximation of the objective function, succeeding to collect second order information in order to obtain the curvature of the function. The bundle contains information about the subgradients of past iterations and is used for the calculation of a search direction. Line search is performed upon the search direction in order, either to converge to a new optimal point or to update the bundle of subgradients.

3. FORMULATION OF THE DISCRETE PROBLEM

The aluminium connection under investigation consists of two flanges interconnected by one bolt in a global orthogonal Cartesian coordinate system $Ox_1x_2x_3$ of \mathbb{R}^3 . Having as scope to extend this modelling into n bolts we assume that the behaviour of the flanges is elastoplastic, this of the rivet linear elastic, whereas the resistance in bearing strength of the rivets exhibits a nonmonotone reaction-displacement law. We denote by $\bar{\mathbf{P}}_i, \bar{\mathbf{P}}_n$ the load vectors applied on the nodes of the free boundary Γ_U of each flange and $\Gamma_{su}, \Gamma_{sbu}, \Gamma_{sl}, \Gamma_{sbl}$ the opposite fronts of the interfaces between the upper flange and the rivet and between the lower flange and the rivet respectively (Fig. 1). The unknown forces developed on Γ_{su} and Γ_{sbu} or on $\Gamma_{sl}, \Gamma_{sbl}$ form the vectors $\bar{\mathbf{P}}$ and $-\bar{\mathbf{P}}$ respectively.

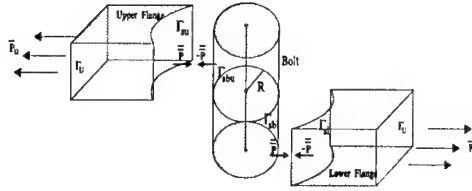


Figure 1. The discretized riveted connection.

Thus for the upper, lower flange and the rivet of the joint, we have respectively the following total load vectors:

$$\mathbf{P}_l = \begin{pmatrix} \bar{\mathbf{P}}_l \\ -\bar{\mathbf{P}} \end{pmatrix} \quad \mathbf{P}_u = \begin{pmatrix} \bar{\mathbf{P}}_u \\ -\bar{\mathbf{P}} \end{pmatrix} \quad \mathbf{P}_b = \begin{pmatrix} -\bar{\mathbf{P}}_l \\ \bar{\mathbf{P}} \end{pmatrix} \quad (1)$$

Let us now assume that the parts of the joint that are in sticking or in slipping contact are respectively *a priori* known. The resistance in bearing strength is described by means of a relation between the forces that are developed on the interfaces of the rivet with the flanges and the relative displacement of the opposite interfaces of the lower and upper flange with the rivet, written in the form:

$$-\bar{\mathbf{P}}_j \in \partial \phi_j([u_j]) \quad (2)$$

where $\phi_j: \mathbf{R}^3 \rightarrow \mathbf{R}$ is a locally Lipschitz function. Within an elastoplastic analysis framework, the equilibrium equations, the compatibility relations and the constitutive equations hold. Following the methodology proposed in [3], the following discrete problem is formulated:

Find $\mathbf{u}_l, \mathbf{u}_u, \mathbf{u}_b \in \mathbf{X}$ such as to satisfy the following hemivariational or "Panagiotopoulos" inequality:

$$\begin{aligned} & \mathbf{s}_l^T \mathbf{e}_l(\mathbf{u}^* - \mathbf{u}) + \mathbf{s}_u^T \mathbf{e}_u(\mathbf{u}^* - \mathbf{u}) + \mathbf{s}_b^T \mathbf{e}_b(\mathbf{u}^* - \mathbf{u}) + \sum_{j=1}^k \phi_j^0([u_j], [\mathbf{u}_j^*] - [\mathbf{u}_j]) - \mathbf{F}_l^T (\lambda_l^* - \lambda_l) \\ & - \mathbf{F}_u^T (\lambda_u^* - \lambda_u) \geq \bar{\mathbf{P}}_l^T (\bar{\mathbf{u}}_l^* - \bar{\mathbf{u}}_l) + \bar{\mathbf{P}}_u^T (\bar{\mathbf{u}}_u^* - \bar{\mathbf{u}}_u) \quad \forall \mathbf{u}^* \in \mathbf{X}, \quad \mathbf{u}^* = \{\mathbf{u}_l^*, \mathbf{u}_u^*, \mathbf{u}_b^*\} \end{aligned} \quad (3)$$

where $m=u, l$ denotes the upper and lower flange of the connection and \mathbf{X} the set of kinematically admissible variations. In the above relations for each flange we denote by \mathbf{F}_{0m} the natural flexibility matrix, \mathbf{e}_m the total strain vector, \mathbf{s}_m the stress vector, \mathbf{e}_{Em} the elastic strain, \mathbf{e}_{pm} the plastic strain, λ_m the plastic multipliers vector, \mathbf{F}_m the yield functions, \mathbf{H}_m the workhardening matrix, \mathbf{N}_m the matrix of gradients of yield functions with respect to the stresses and \mathbf{R}_m the vector of positive constants, whereas for the rivet \mathbf{F}_{0b} is the natural flexibility matrix, \mathbf{e}_b the strain vector and \mathbf{s}_b the stress vector.

Taking into account that $\mathbf{K} = \mathbf{G}\mathbf{F}_0^{-1}\mathbf{G}^T$ is the stiffness matrix of each component of the connection, the previous hemivariational inequality (3) expresses the principle of virtual work

in inequality form. The potential energy of the riveted aluminium structure has the form:

$$\begin{aligned}
 \Pi(\mathbf{u}, \boldsymbol{\lambda}) = & \frac{1}{2} \mathbf{u}_l^T \mathbf{K}_l \mathbf{u}_l + \frac{1}{2} \mathbf{u}_u^T \mathbf{K}_u \mathbf{u}_u + \frac{1}{2} \mathbf{u}_b^T \mathbf{K}_b \mathbf{u}_b - \mathbf{u}_l^T \mathbf{G}_l \mathbf{K}_{0l} \mathbf{N}_l \boldsymbol{\lambda}_l - \mathbf{u}_u^T \mathbf{G}_u \mathbf{K}_{0u} \mathbf{N}_u \boldsymbol{\lambda}_u + \\
 & \frac{1}{2} \boldsymbol{\lambda}_l^T \mathbf{H}_l \boldsymbol{\lambda}_l + \frac{1}{2} \boldsymbol{\lambda}_u^T \mathbf{H}_u \boldsymbol{\lambda}_u + \frac{1}{2} \boldsymbol{\lambda}_l^T \mathbf{N}_l^T \mathbf{F}_{0l}^{-1} \mathbf{N}_l \boldsymbol{\lambda}_l + \frac{1}{2} \boldsymbol{\lambda}_u^T \mathbf{N}_u^T \mathbf{F}_{0u}^{-1} \mathbf{N}_u \boldsymbol{\lambda}_u + \mathbf{e}_{0l}^T \mathbf{F}_{0l}^{-1} \mathbf{N}_l \boldsymbol{\lambda}_l + \mathbf{e}_{0u}^T \mathbf{F}_{0u}^{-1} \mathbf{N}_u \boldsymbol{\lambda}_u - \\
 & \mathbf{e}_{0l}^T \mathbf{F}_{0l}^{-1} \mathbf{G}_l^T \mathbf{u}_l - \mathbf{e}_{0u}^T \mathbf{F}_{0u}^{-1} \mathbf{G}_u^T \mathbf{u}_u - \mathbf{e}_{0b}^T \mathbf{F}_{0b}^{-1} \mathbf{G}_b^T \mathbf{u}_b + \mathbf{R}_l^T \boldsymbol{\lambda}_l + \mathbf{R}_u^T \boldsymbol{\lambda}_u + \sum_{j=1}^k \phi_j^o([\mathbf{u}_j]) - \bar{\mathbf{P}}_l^T \bar{\mathbf{u}}_l - \bar{\mathbf{P}}_u^T \bar{\mathbf{u}}_u \\
 & \forall \boldsymbol{\lambda}_l, \boldsymbol{\lambda}_u \geq 0
 \end{aligned} \quad (4)$$

and the equivalent substationarity problem reads:

Find $\mathbf{u} \in X$ such that the potential energy of the structure $\Pi(\mathbf{u}, \boldsymbol{\lambda})$ is substationarity in $\mathbf{v} = \mathbf{u}$ where $\mathbf{v} \in X$.

A finite element analysis is next used for the modeling of the aluminium connection at hand. Due to the uniform external loading applied at the edges of the flanges causing bearing strength failure and the symmetry in the geometry of the connection, we start studying the single-bolted area of Fig.1. The area consists of an upper and lower flange and a bolt. We construct a finite element model for the single-riveted area and in order to describe the nonlinear behaviour of the components, an elastoplastic analysis is applied under the assumption of small strains [1]. A compulsion is applied at the edges Γ_U of the flanges through a sequence of displacements simulating the action of shear forces that lead to bearing strength failure. The contact area between the rivet and the flanges introduces an inequality constraint problem along the boundary which is divided into three nonoverlapping parts. For the first part of the boundary an area of complete contact between the adjacent nodes of the rivet and the flanges is simulated. For the second part we simulate slip conditions and finally, for the third part we assume that free boundary conditions hold. Friction only slightly affects the model and therefore, is not taken into consideration. In order to apply the mathematical formulation for the discretized problem, the overall behaviour of the aluminium connection can be described by means of a reaction-displacement law.

The reactions along the degrees of freedom of the elements may be written as: $\Delta R^i = \mathbf{K}_T^i du^i$

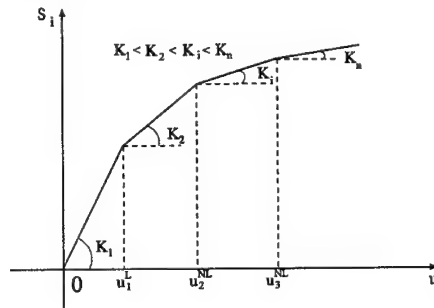


Figure 2. Nonlinear reaction-displacement diagram for the single bolt connection.

where \mathbf{K}_T^i is the tangential stiffness matrix in the form $\mathbf{K}_T^i = \mathbf{K}_L^i + \mathbf{K}_{NL}^i$ consisting of the

linear and nonlinear matrices \mathbf{K}_L^i and \mathbf{K}_{NL}^i where $\mathbf{K}_L^i = \int_{\Omega} \mathbf{B}_L^T \mathbf{C} \mathbf{B}_L d\Omega$ and

$\mathbf{K}_{NL}^i = \int_{\Omega} \mathbf{B}_{NL}^T \mathbf{C} \mathbf{B}_{NL} d\Omega$ where \mathbf{B}_L^T , \mathbf{B}_{NL}^T are the strain-displacement matrices and \mathbf{C} , \mathbf{C}_{ep} are

the elastic and elastoplastic matrix.

Therefore, the total reaction at the end of increment i for the nodes of the body Ω will be given from the following relation $R_i = \int_{\Omega} du^i \Delta R^i d\Omega$.

Applying this method for a work-hardening material law, we obtain an overall reaction-displacement diagram as shown in Fig. 2. The slope of the curve for the first elastic increments remains constant E_1 . Once the model enters in the subsequent steps, the tangential matrix is updated producing the different slopes E_2, E_3, \dots, E_n .

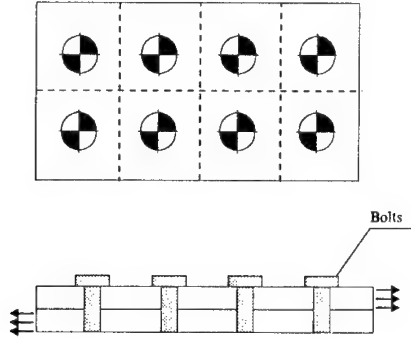


Figure 3. Ground plan of a riveted aluminium connection.

This way, for the multi-riveted aluminium connection (Fig.3), the initial matrix \mathbf{K}_b^0 of the multi-bolted structure is assembled into the form:

$$\mathbf{K}_b^0 = \begin{bmatrix} K_{b,11}^0 & K_{b,12}^0 & \dots & K_{b,1n}^0 \\ K_{b,21}^0 & K_{b,22}^0 & \dots & K_{b,2n}^0 \\ \vdots & \vdots & \vdots & \vdots \\ K_{b,n1}^0 & K_{b,n2}^0 & \dots & K_{b,nn}^0 \end{bmatrix} \quad (5)$$

where n is the number of rivets. The diagonal terms which express the equivalent stiffness of each single rivet model are already known from the previously calculated reaction-displacement law. Indeed, for the elastic slope denoted by E_1 we obtain the following relation:

$$K_{b,ii}^0 = E_1 \quad i = 1, 2, \dots, n \quad (6)$$

The non-diagonal terms can be calculated from the interaction of each bolt with the others. Therefore, we assume a matrix of correlation factors $\lambda_{i,j}$ where $i, j = 1, 2, \dots, n$, having the following form:

$$\begin{bmatrix} \lambda_{b,11} & \lambda_{b,12} & \dots & \lambda_{b,1n} \\ \lambda_{b,21} & \lambda_{b,22} & \dots & \lambda_{b,2n} \\ \vdots & \vdots & \ddots & \vdots \\ \lambda_{b,n1} & \lambda_{b,n2} & \dots & \lambda_{b,nn} \end{bmatrix} \quad (7)$$

The relation between the stiffness terms $K_{b,ij}$ and the correlation factors is given by the relation $K_{b,ij} = \lambda_{b,ij} K_{b,ii}$ where $\lambda_{b,ii}=1.0$ for $i=1,2,\dots,n$. The non-diagonal correlation factors $\lambda_{b,ij}$, $i \neq j$ are calculated applying unit relative displacements along the X_1 direction at the top and bottom surface of one rivet and restraining the remaining relative displacements of the considered and the other rivets. The reactions $R_{b,i}$ that develop in each rivet $i=1,\dots,n$, determine the correlation factors from the relation $\lambda_{b,ij} = R_{b,ij} / R_{b,i}$. Applying on the boundary nodes of Γ_U external forces along the X direction, the reactions that are developed at the nodes of the rivets constitute the load vector \mathbf{P} :

$$\mathbf{P}^T = [R_{b,1} \quad R_{b,2} \quad \dots \quad R_{b,n}] \quad (8)$$

Thus, the previously formulated substationarity problem is transformed into the equivalent substationarity problem of finding $\mathbf{u} \in \mathbf{X}$ such that the potential energy of the structure $\Pi(\mathbf{u}, \lambda)$ is substationarity in $\mathbf{v}=\mathbf{u}$, where $\mathbf{v} \in \mathbf{X}$ where:

$$\Pi(\mathbf{u}, \lambda) = \frac{1}{2} \mathbf{u}^T \mathbf{K}_b \mathbf{u} - \mathbf{P}^T \mathbf{u} + \sum_{j=1}^k \phi_j^0([u_j]) \quad (9)$$

Π is the potential energy that the aluminium joint absorbs. An iterative optimization procedure assuming that a nonmonotone law holds for the resistance in bearing strength of the rivets is in the sequel proposed. The method converges to a solution of a displacement field that expresses a position of equilibrium of the riveted aluminium connection.

4. NUMERICAL APPLICATION

The method proposed in the previous section is used to analyze a riveted aluminium connection. In particular, the connection between two aluminum plates shown in Fig.4 is considered. A nonmonotone behaviour of the resistance in bearing strength of the rivets is assumed to hold. The bearing resistance is calculated based on the geometry of the connection according to Eurocode 9.

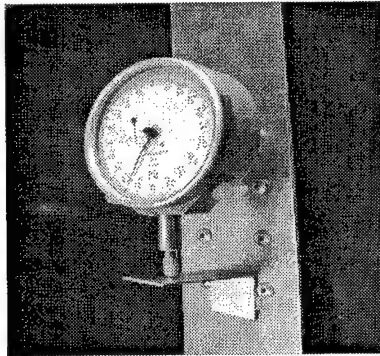


Figure 4. The riveted aluminum connection under numerical and experimental investigation.

The connection consists of 6 rivets with diameter 4 mm. The thickness of each plate is 1 mm. The aluminium is considered to have yield stress 110 N/mm^2 and ultimate stress 138 N/mm^2 . The connection is simulated by means of a three-dimensional finite element model using 6-node solid prismatic elements with 3 degrees of freedom at each node.

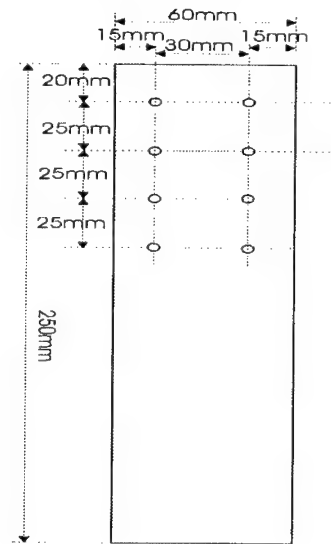


Figure 5. Geometrical data of the aluminium riveted connection.

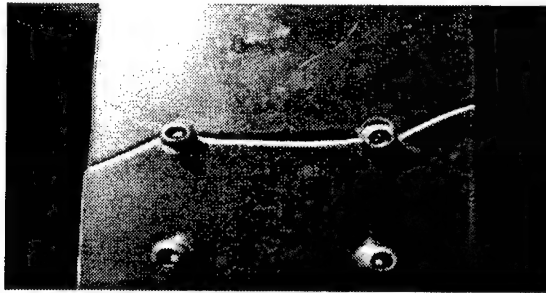


Figure 6. Experimental results – Yield lines

The external loading is applied along the direction of the X_1 axis at the free edge of the plates on the plain X_2, X_3 . The overall reaction-displacement diagrams for the aluminium connection is obtained by the single bolted model through an elastoplastic analysis of 12 increments at each fixed edge of the flanges. Applying the optimization program NSOLIB, the resistance in bearing strength for each rivet is next calculated in a reliable way and seem to be in good accordance to the experimental ones. In Fig.6 the picture the typical development of yield lines appeared on the aluminum plates during the final stages of the test are depicted. The class of rivets, the flanges thickness and the number of rivets do have significant influence on

the resistance in bearing strength of this type of aluminium connections. Having this in mind and in order to obtain safe results a large relevant numerical and experimental research activity is under performance at the Laboratory of the Institute of Steel Structures at the Department of Civil Engineering, A.U.Th.

Acknowledgements: The third author acknowledges the support of the Greek General Secretariat for Research and Technology within the Greek-Czech Research and Technology Collaboration Framework (Research project: "Prediction of the critical parameters affecting the structural response of welded elements in aluminium structures").

5. REFERENCES

- [1] Ivanyi, M. & Baniotopoulos, C.C. (eds.), *Semirigid Connections in Structural Steelwork*, CISM Lecture Notes 219, Springer, Wien, New York Berlin, (2000).
- [2] Baniotopoulos, C.C. & Wald, F. (eds.), *The Paramount Role of Joints into the Reliable Response of Structures*, Kluwer, Dordrecht (2000).
- [3] Panagiotopoulos, P.D., *Inequality Problems in Mechanics and Applications. Convex and Nonconvex Energy Functions*, Birkhäuser Boston Inc. (1985).

ANALYSIS OF “CONVEX ENERGY” STRUCTURAL SYSTEMS UNDER STOCHASTIC LOADING

M.J. Kontoleon, C.C. Baniotopoulos*

Department of Civil Engineering.

Aristotle University of Thessaloniki, GR-54006 Thessaloniki, Greece

*corresponding author. E-mail: ccb@civil.auth.gr

M. Betti, C. Borri

Department of Civil Engineering

University of Florence, I-50139 Florence, Italy

1. SUMMARY

The behaviour of “convex energy” structural systems under stochastic loading is herein investigated. The loading is assumed to be a second-order stochastic process applied on a structure with unilateral contact boundary conditions. The problem is formulated as a stochastic variational problem where the stochastic parameter of the loading has been taken into account by using a second-order perturbation method.

2. INTRODUCTION

The stochastic behaviour of structural elements with unilateral response is a field that has recently attracted the interest of a plethora of researchers. Until now, such problems have been studied by means of the Monte Carlo methods [1], whereas analytical solutions have not been obtained mainly due to the high complexity of both the stochastic nature of the actions and the highly non-linear unilateral behaviour of the respective structural systems (e.g. steel bolted connections). Within a Nonsmooth Mechanics framework the unilateral contact problems of monotone nature can be formulated as constrained minimization problems of the potential or complementary energy of the structures [2] and are numerically treated by means of efficient convex optimisation algorithms [3]. As a matter of fact, for this class of problems the response has to be treated with utmost care because explicit and conditionally stable integration algorithms cannot be employed. This highly non-linear behaviour coupled with the stochastic nature of the actions has to be taken into account in the analysis procedures in order to successfully achieve the respective process of the stochastic structural response.

In recent years, several methods of stochastic analysis have been developed for structural systems with uncertain parameters, including the direct Monte Carlo method, the Monte Carlo simulation with Neumann expansion, the Taylor series and the perturbation techniques [4]. The latter, due to the fact that they are probably the most well known effective methods for general non-linear problems [5] have been widely used in the field of stochastic mechanics to estimate the response statistics, primarily due to their analytical tractability and the computational time-saving advantages. In the present paper with respect to a linear elastic body the continuous problem is first formulated as a variational equality problem expressing

the principle of the virtual work at the state of equilibrium. Combining the second-order perturbation method with the potential energy equilibrium principle, the problem is expressed by a deterministic system of zeroth, first and second order equations from which we obtain the first two statistic moments for the displacements. The zeroth order variational equality of the problem leads to a variational inequality that is due to the unilateral contact conditions.

A recent development is the application of the perturbation method incorporated with both the FEM and the stochastic field theory [6]. In the present paper the discrete problem is accomplished by coupling the stochastic perturbation method with the finite element method. The second order version of the perturbation technique is used, since it is computationally feasible, even for large structural systems. Specifically, discretizing the previously mentioned system of variational equalities and solving a quadratic optimization problem for the zeroth order equation and linear systems for the first and second order equations, the two first statistical moments for the displacements can be evaluated. It is important to point out that conventional methods applied to the investigation of such problems may lead to erroneous results. For this reason in the present paper an appropriately modified F.E. model is employed for a more realistic description of the effect of the stochastic actions joined with the unilateral contact elements. To conclude with, it could be mentioned that the aim of the present paper aims to integrate in a unified effective framework the two main aspects introduced above.

3. FORMULATION OF THE STOCHASTIC VARIATIONAL PROBLEM

In the orthogonal Cartesian system (O, x_1, x_2, x_3) , a deformable elastic body Ω with boundary Γ is first considered (Fig. 1). The total boundary is made up of three non-overlapping parts denoted by Γ_U , Γ_F , Γ_S . On Γ_U the displacements have the given values U_i . On Γ_F the surface forces have the given values F_i . On Γ_S , unilateral contact boundary conditions hold [2,3].

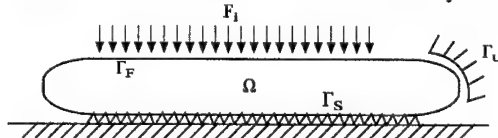


Figure 1: Boundary conditions on an elastic body Ω .

Assuming that the unilateral contact is frictionless and defining the positive normal direction inwards the boundary, the unilateral contact boundary conditions can be expressed in the following form: $-S_N \in \partial j_N(u_N)$ where j_N is a proper, convex, lower semi-continuous function, ∂j_N is the sub-differential of j_N , and u_N and S_N are respectively the normal (with respect to the boundary) displacements and the reaction forces on Γ_S . Under the assumption of small strains and displacements, the boundary stochastic value problem under consideration consists of the equation of equilibrium, the compatibility relations, the constitutive relations and the boundary conditions holding on Γ_S . We define a field U^* of strains and displacements ϵ^*_{ij} , u^*_i to be kinematically admissible if it satisfies the compatibility relations, the kinematical boundary conditions on Γ_U , and the kinematical conditions imposed by the boundary conditions on Γ_S . Volume forces are denoted by p_i , whereas actual strains and displacements at the position of equilibrium are denoted by ϵ_{ij} and u_i respectively. The differences $\delta\epsilon_{ij} = \epsilon^*_{ij} - \epsilon_{ij}$ and $\delta u_i = u^*_i - u_i$ represent the kinematically admissible variations. Moreover, σ^*_{ij} denotes the stress field obtained from ϵ^*_{ij} by means of the elasticity law. The stochastic potential energy principle can be expressed as a generalization of the principle of minimum potential energy for the inclusion of the stochastic effects. As it is well-known, the expression of the principle of minimum potential energy can be written in the following form:

$$\int_{\Omega} \sigma_{ij}^* (\varepsilon_{ij}^* - \varepsilon_{ij}) d\Omega = \int_{\Omega} p_i (u_i^* - u_i) d\Omega + \int_{\Gamma_s} S_N (u_N^* - u_N) d\Gamma + \int_{\Gamma_r} F_i (u_i^* - u_i) d\Gamma \quad \forall u_i^* \in U^* \quad (1)$$

The basic idea of the second order moment analysis involves the expansion of all the random functions about the averages of the random field $\{b^r(x)\}$, $r = 1, \dots, R$, via Taylor series and retaining up to the second order terms. In this formulation the random field $\{b^r(x)\}$ represents the probabilistic nature of the random loads. The following notation is introduced:

$$b_0^r = E[b^r] = \int_{-\infty}^{+\infty} b^r p_B(b^r) db^r \quad (2)$$

$$f^0(x) = f(x, b_0^r), \quad f'^r = \frac{\partial f}{\partial b^r}, \quad f''^{rs} = \frac{\partial^2 f}{\partial b^r \partial b^s} \quad (3)$$

$$db^r = \theta \Delta b^r = \theta (b^r - b_0^r) \quad (4)$$

$$\kappa_2(b^r, b^s) = Cov(b^r, b^s) = \int_{-\infty}^{+\infty} \int_{-\infty}^{+\infty} (b^r - b_0^r)(b^s - b_0^s) p_B(b^r, b^s) db^r db^s \quad (5)$$

where $f(x)$ is a given function, $p_B(b^r, b^s)$ a joint probability density function, and θ is a small enough parameter. For the random functions the expansion is done by means of a second order perturbation about the mean b_0^r for the given small value θ . With respect to the displacement field, the second order expansion may be written in the following form:

$$u_i[b(x), x] = u_i[b_0, x] + \theta \sum_{r=1}^R \frac{\partial u_i}{\partial b^r} \Delta b^r + \frac{\theta^2}{2} \sum_{r=1}^R \sum_{s=1}^R \frac{\partial^2 u_i}{\partial b^r \partial b^s} \Delta b^r \Delta b^s \quad (6)$$

Similarly we can expand all the random functions about the mean value of the random field. Substituting the expanded function (6) into the variational equilibrium equation (1) and separating terms of equal order terms to θ , we obtain the zeroth, first and second order equations.

Zeroth order (θ^0 terms)

In the zeroth order, all the functions with superscript "⁰" are deterministic functions, i.e. evaluated at the average b_0^r . The equation may be written as follows:

$$\int_{\Omega} \sigma_{ij}^0 (\varepsilon_{ij}^* - \varepsilon_{ij}^0) d\Omega = \int_{\Omega} p_i (u_i^* - u_i^0) d\Omega + \int_{\Gamma_s} S_N^0 (u_N^* - u_N^0) d\Gamma + \int_{\Gamma_r} F_i^0 (u_i^* - u_i^0) d\Gamma \quad \forall u_i^* \in U^* \quad (7)$$

This equation is the standard deterministic variational statement, and the usual convex variational approach can be employed directly. Variational equality (7), taking into account the inequality that describes the virtual work of the unilateral contact reactions:

$$\int_{\Gamma_s} [S_N^0 (u_N^* - u_N^0) + k (u_{+N}^* - u_{+N}^0)] d\Gamma \geq 0 \quad \forall u_N^* \in U^* \quad (8)$$

yields the following variational inequality:

$$\int_{\Omega} \sigma_{ij}^0 (\varepsilon_{ij}^* - \varepsilon_{ij}^0) d\Omega - \int_{\Omega} p_i (u_i^* - u_i^0) d\Omega - \int_{\Gamma_r} F_i^0 (u_i^* - u_i^0) d\Gamma + \int_{\Gamma_s} k (u_{+N}^* - u_{+N}^0) d\Gamma \geq 0 \quad \forall u_i^* \in U^* \quad (9)$$

It has been proven in [2] that variational inequality (9) yields the equations of equilibrium and the boundary conditions on Γ_s and Γ_r . Thus, it completely characterizes the position of equilibrium. It has been proven that any solution of the above variational inequality problem minimizes over the set U^* , at the position of equilibrium, the following potential energy of Ω :

$$\Pi = \int_{\Omega} \sigma_{ij}^0 \varepsilon_{ij}^0 d\Omega - \int_{\Omega} p_i u_i^0 d\Omega - \int_{\Gamma_r} F_i^0 u_i^0 d\Gamma + \int_{\Gamma_s} K (u_{+N}^0) d\Gamma \quad \forall u_i^* \in U^* \quad (10)$$

A dual approach with respect to stresses and forces can be also equivalently applied. The variational inequality problem expressing the principle of complementary work in its inequality form can be then formulated giving equivalently rise to a minimization problem of the complementary energy of the body Ω [2].

First order (θ^1 terms)

The first order equation can be similarly obtained by grouping the first order terms with respect to θ :

$$\int_{\Omega} \delta u_{i,j} C_{ijkl} u'_{k,l} d\Omega = \int_{\Gamma_s} S'_N \delta u_N d\Gamma + \int_{\Gamma_F} F'_i \delta u_i d\Gamma \quad (11)$$

Using the chain rule we can express the first derivative of the reaction force in the unilateral boundary Γ_s by the first variation of the displacement:

$$S'_N = \frac{\partial S_N}{\partial b^r} = \frac{\partial S_N}{\partial u_N} \frac{\partial u_N}{\partial b^r} = \frac{\partial S_N}{\partial u_N} u'_N \quad (12)$$

Substituting equation (12) into (11), the first order equation can be written with respect to the first order derivative as follows:

$$\int_{\Omega} \delta u_{i,j} C_{ijkl} u'_{k,l} d\Omega = \int_{\Gamma_s} \frac{\partial S_N}{\partial u_N} u'_N \delta u_N d\Gamma + \int_{\Gamma_F} F'_i \delta u_i d\Gamma \quad (13)$$

Equation (13) yields a variational equation where the only unknown is the first derivative of the displacement field.

Second order (θ^2 terms)

Multiplying the joint probability density function by the second order terms and integrating over the domain of the random field $\{b^r(x)\}$, one can obtain the second order equation:

$$\int_{\Omega} \delta u_{i,j} C_{ijkl} u'_{k,l} \kappa_2(b^r, b^s) d\Omega = \int_{\Gamma_s} S''_{Nrs} \delta u_N \kappa_2(b^r, b^s) d\Gamma + \int_{\Gamma_F} F''_{irs} \delta u_i \kappa_2(b^r, b^s) d\Gamma \quad (14)$$

Using again the chain rule we can express the second derivative of the reaction force in the unilateral boundary Γ_s , by the first variation, that has been evaluated in the first order equation, and the second derivative of the displacement. Using the chain rule into (14), the second order equation can be written with respect to the second order derivative as follows:

$$\begin{aligned} \int_{\Omega} \delta u_{i,j} C_{ijkl} u'_{k,l} \kappa_2(b^r, b^s) d\Omega = & \int_{\Gamma_s} \left(\frac{\partial^2 S_N}{\partial u_N^2} \cdot \left(\frac{\partial u_N}{\partial b^r} \right)^2 + \frac{\partial S_N}{\partial u_N} u''_{Nrs} \right) \delta u_N \kappa_2(b^r, b^s) d\Gamma + \\ & + \int_{\Gamma_F} F''_{irs} \delta u_i \kappa_2(b^r, b^s) d\Gamma \end{aligned} \quad (15)$$

Similarly to the first order, (15) yields a variational equation where the only unknown is the second derivative of the displacement field.

Solving the zeroth, first and second order variational equations, the probability distributions of the displacements, respectively the expected value and the covariance, can be calculated by the following expressions:

$$E[u_i] = u_i^0 + \frac{1}{2} u''_{irs} \kappa_2(b^r, b^s) \quad (16)$$

$$\kappa_2(u_i, u_j) = E[(u_i - u_i^0)(u_j - u_j^0)] = Cov(u_i, u_j) = u''_{irs} u''_{jrs} \kappa_2(b^r, b^s) \quad (17)$$

With the proposed theoretical approach, one retains up to the second order terms of the Taylor series. Since the complete knowledge of the probabilistic structure of the random response is in practice not possible to be obtained, the herein applied perturbation method provides us the most important statistical moments of the response. Assuming that the variance of the random loads is not very large, when compared with their mean value, the developed method may produce very satisfactory results.

4. FORMULATION OF THE STOCHASTIC DISCRETE PROBLEM

In this section the computational implementation of the stochastic finite element method is presented. This is based on the spatial discretization of the sequence of variational expressions (10), (13), (15) presented in the previous section. The zeroth, first and second

order variational equations of the stochastic unilateral problem can be now written in the following discrete forms:

Zeroth order (θ terms)

The problem is discretized by means of an appropriately chosen finite element scheme (cf. e.g. Fig. 2). The detachment conditions holding on the unilateral contact boundary (simulating the possibility of partial separation of the adjacent nodes) can be mathematically described by the following law obtained by assembling in matrix terms the unilateral conditions for all the n points of the boundary Γ_S :

$$\mathbf{u}_N^0 \geq \mathbf{0} \quad \mathbf{S}_N^0 \geq \mathbf{0} \quad \mathbf{u}_N^{0T} \mathbf{S}_N^0 = 0 \quad (18)$$

Relations (19) give rise to a Linear Complementarity Problem (LCP) that completely describes mathematically the development of the detachment phenomena along the unilateral contact boundary. The minimum of the potential energy function (10) can be written in the following discrete form:

$$\Pi(\mathbf{u}^0) = \min \left\{ \frac{1}{2} \mathbf{u}^{0T} \mathbf{K} \mathbf{u}^0 - \mathbf{F}^{0T} \mathbf{u}^0 \mid \mathbf{A} \mathbf{u}^0 \leq \mathbf{d} \right\} \quad (19)$$

where \mathbf{A} is an appropriately chosen matrix, \mathbf{d} a vector which defines the unilateral contact conditions holding on the discretized boundary Γ_S , and \mathbf{u}^0 is the displacement vector for the whole discretized structure including the normal, with respect to the boundary, vector \mathbf{u}_N^0 .

First order (θ^1 terms, R systems of equations)

The continuous equation (13) can be written in a discrete form as follows:

$$\mathbf{K} \mathbf{u}'' = \mathbf{F}'' \quad (20)$$

where \mathbf{K} is the stiffness matrix. The vector \mathbf{F}'' contains both the first order derivatives of the displacement and the first order derivative of the applied random load:

$$\mathbf{F}'' = \int_{\Gamma_S} \frac{\partial \mathbf{S}_N}{\partial \mathbf{u}_N} \mathbf{u}_N'' d\Gamma + \int_{\Gamma_F} \mathbf{F}_i'' d\Gamma \quad (21)$$

In relation (22) the only unknown is the first derivative of the random displacement field. Indeed, the derivative of the unilateral reaction \mathbf{S}_N is obtained from the boundary condition law and \mathbf{F}_i'' is given for the problem at hand.

Second order (θ^2 terms, one system of equation)

Similarly to the first order case, equation (15) can be written in a discrete form as follows:

$$\mathbf{K} \mathbf{u}^{(2)} = \mathbf{F}'' \kappa_2(b^r, b^s) \quad (22)$$

where $\kappa_2(b^r, b^s)$ is the covariance matrix and

$$\mathbf{u}^{(2)} = \frac{1}{2} \sum_{s=1}^R \sum_{r=1}^R \mathbf{u}'' \kappa_2(b^r, b^s) \quad (23)$$

Once the solutions of the above equilibrium equations (19), (20), (22) are obtained for \mathbf{u}^0 , \mathbf{u}'' and $\mathbf{u}^{(2)}$ the first two statistical moments for the displacements can be evaluated. Similarly to the continuous approach, the random discrete displacement field can be calculated. The second order accurate displacements expectations and the first order estimate of the covariance are obtained by substituting the previous expression into the expected value and the covariance relation:

$$E[\mathbf{u}] = \mathbf{u}^0 + \frac{1}{2} \sum_{s=1}^R \sum_{r=1}^R \mathbf{u}'' \kappa_2(b^r, b^s) = \mathbf{u}^0 + \mathbf{u}^{(2)} \quad (24)$$

$$\kappa_2(u_i, u_j) = \sum_{s=1}^R \sum_{r=1}^R u_i'' u_j'' \kappa_2(b^r, b^s) \quad (25)$$

5. ON THE NUMERICAL TREATMENT

The previously presented method can be applied to a numerical application that concerns the stochastic analysis of a typical "convex energy" structural system, i.e. a steel column-base plate connection (under stochastic loading). A two-dimensional finite element plane stress model can be constructed for the analysis of the stochastic structural behaviour of this column-base plate connection (Fig. 2) (for details, see [3]).

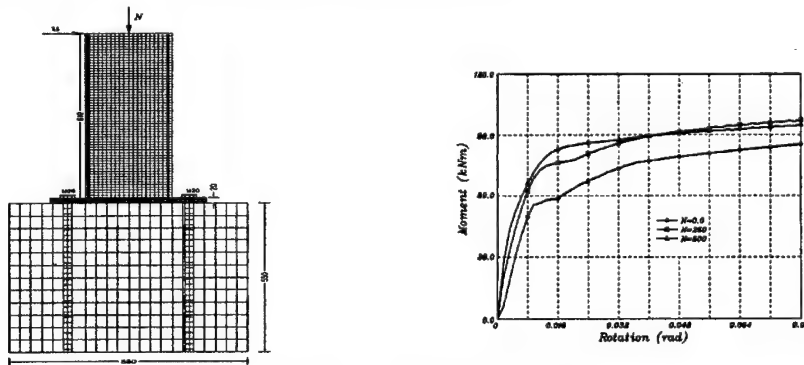


Figure 2: On the numerical application.

The connection consists of an RHS 120/200/10 steel column, which is connected to a concrete block by means of a steel base plate. The thickness of the base plate is assumed 20 mm. The model contains all the essential features that characterize the separation problem: monotone unilateral contact conditions hold along the interfaces between the base and the plate. The third dimension of the connection can be also considered by assigning different thickness values to the various regions of the FEM mesh. The proposed method appears to be effective even for the numerical treatment of problems with very large number of unknowns. We underline here that this kind of MDOF problems cannot be numerically treated by applying the existing standard method used for the solution of the stochastic structural problems.

6. REFERENCES

- [1] Panagiotopoulos, P.D., Analysis of the stochastic unilateral contact problem, *Comp. & Struct.* 7, 581-586 (1977).
- [2] Panagiotopoulos, P.D., *Inequality Problems in Mechanics and Applications. Convex and Nonconvex Energy Functions*, Birkhäuser Boston (1985).
- [3] Baniotopoulos, C.C., Numerical Simulation: Principles, Methods and Models in: *Semi-rigid Connections in Structural Steelwork*, M. Ivanyi, C.C. Baniotopoulos (Eds.), Springer Wien NewYork, Berlin (2000).
- [4] Lei, Z., Qiu, C., Neumann dynamic stochastic finite element method of vibration for structures with stochastic parameters to random excitation, *Comp. & Struct.* 77, 651-657 (2000).
- [5] Liu, W.K., Probabilistic finite element methods in nonlinear dynamics, *Comput. Methods Appl. Mech. Engng.* 56, 61-81 (1986).
- [6] Elishakoff, I., Ren, Y.J., Shinozuka, M., Variational Principles developed for and applied to analysis of stochastic beams, *J. Engrg. Mech.* 122, 559-565 (1996).

FRICITION EVOLUTION IN FRACTAL INTERFACES

O.K. Panagouli

Dept. of Architectural Engineering, University of Thessaly
38334 Volos, Greece

E.S. Mistakidis

Dept. of Civil Engineering, University of Thessaly
38334 Volos, Greece

1. SUMMARY

This paper provides informations about the influence of the fractality of interfaces in cracked structures to the friction mechanism. For that, a fractal approach based on self-affine fractal curves is used for the modeling of the multiscale topography of these interfaces. In the sequence, the evolution of the friction mechanism is studied in structures with different fractal interfaces (structures with different fractal dimensions). This study is based on the assumption that the friction between rough surfaces results from the gradual plastification of the asperities. Finally, interesting results with respect to the relation between the fractal dimension and the response of the structures near the interfaces are obtained.

2. INTRODUCTION

Surface topography plays an important role in contact problems. It is well known that the topography of engineered surfaces and interfaces is too complex to be described by few parameters. It has been shown that the roughness of these surfaces has multiscale nature and needs new advanced mathematical techniques for its description.

Fractal geometry provides both a general description and a mathematical model for complex forms found in nature. This fact makes fractal geometry central to various fields of science such as physics, biology, geology and material science. In applied mechanics the property of fractality appears very often. For instance the cracks and interfaces in rocks, in composite materials, in concrete and masonry structures are of fractal type. Experimental data [1], [2], [3], [4] verify the fractality of rough surfaces and interfaces.

Mandelbrot first introduced the term “fractal” in [5]. According to his definition a set $\mathcal{F} \subset \mathbb{R}^n$ is a fractal if \mathcal{F} has fractional “Hausdorff” dimension, or if the dimension of \mathcal{F} is an integer strictly larger than its topological dimension. The mathematical concept of the Hausdorff dimension, which presupposes a scaling down procedure for any physical object up to infinitely small scales, is applicable to mathematical models rather than to physical objects. Moreover, the Hausdorff dimension cannot be obtained by experimental procedures. On the other hand, it must be mentioned here that there is no canonical definition of physical fractals. For that, many methods based on experimental or numerical calculations have been developed

for the estimation of fractal dimension of an object, parameter which is of a great importance because of its scale independent character.

The mathematical approach to the theory of fractals followed here [6] is based on an iterative procedure which seems to be appropriate for the problems in mechanics. More specifically, this approach uses classical geometrical manipulations (for example affine transformations, scaling and rotations) to express relations between parts of fractal sets.

The main purpose of this paper is to investigate the influence of the fractality of an interface on the development of the friction mechanism. For that, it is assumed that different interfaces, with multiscale topography, are developed in a certain structure in which the material is assumed to have an elastic-plastic behaviour. For every structure, resulting from each fractal interface, the same boundary conditions and loading are assumed. In the method proposed here the fractal interfaces, in all cases, are taken to have elementary parts of almost the same size δ . This is due to the fact that they are developed in the same structure with the same material. In the sequence, the results corresponding to different interfaces are studied with respect to the way that the friction mechanism is developed. Finally, it is examined how the friction mechanism is affected by the fractal dimension of the interfaces and usefull conclusions are derived.

3. SELF-AFFINE FRACTAL CURVES

Here, self-affine fractal curves are defined by means of the notion of fractal interpolation functions [6]. Fractal interpolation functions realize a passage from a discrete set of data in \mathbb{R}^2 $\{(x_i, y_i), i = 0, 1, \dots, N\}$ to a continuous model where $\mathcal{F}(x_i) = y_i, i = 0, 1, \dots, N$. If C^0 is the set of continuous functions $\mathcal{F} : [x_0, x_N] \rightarrow \mathbb{R}$, then there is a sequence of functions $\mathcal{F}_{m+1}(x) = (T\mathcal{F}_m)(x)$, where $T : C^0 \rightarrow C^0$ is an operator defined by:

$$(T\mathcal{F})(x) = c_i l_i^{-1}(x) + d_i \mathcal{F}(l_i^{-1}(x)) + f_i, \text{ for } x \in [x_{i-1}, x_i], i = 1, 2, \dots, N. \quad (1)$$

The operator T converges to a fractal curve \mathcal{F} , as $m \rightarrow \infty$. The transformation l_i transforms $[x_0, x_N]$ to $[x_{i-1}, x_i]$ and it is defined by the relation

$$l_i(x) = a_i x + b_i. \quad (2)$$

The affine fractal curve \mathcal{F} is also the unique (see [6]) attractor of the hyperbolic iterated function system $\{\mathbb{R}^2 | w_i, i = 1, 2, \dots, N\}$ defined by the transformation

$$(x, y) \rightarrow w_i(x, y) = \begin{pmatrix} a_i & 0 \\ c_i & d_i \end{pmatrix} \begin{pmatrix} x \\ y \end{pmatrix} + \begin{pmatrix} b_i \\ f_i \end{pmatrix} \quad i = 1, \dots, N, \quad (3)$$

where the factors d_i are the hidden variables of the transformation and they have to satisfy $0 \leq d_i < 1$. Moreover, the remaining coefficients are given by

$$a_i = \frac{(x_i - x_{i-1})}{(x_N - x_0)}, \quad b_i = \frac{(x_N x_{i-1} - x_0 x_i)}{(x_N - x_0)} \quad (4)$$

$$c_i = \frac{(y_i - y_{i-1})}{(x_N - x_0)} - d_i \frac{(y_N - y_0)}{(x_N - x_0)} \quad (5)$$

$$f_i = \frac{(x_N y_{i-1} - x_0 y_i)}{(x_N - x_0)} - d_i \frac{(x_N y_0 - y_N x_0)}{(x_N - x_0)}. \quad (6)$$

This type of functions gives profiles where if higher approximations of an interpolation function

are taken, the resulting profile appears more rough and it is never smooth. This is equivalent to the fact that the more the profile is magnified, the more roughness keeps appearing. Moreover, the roughness of the profile is strongly affected by the free parameters d_i , $i = 1, 2, \dots, N$ of the interpolation function. As these parameters take larger values the resulting profiles appears more rough as it is shown in Fig. 1.

It must be mentioned here that an important advantage of the fractal interpolation functions presented here is that their fractal dimension can be obtained numerically. Indeed, let us suppose that the affine curve \mathcal{F} resulting from the above procedure is consisting of elementary parts of the size δ where $\delta_* < \delta < \Delta_*$. By using dividers which are set to this prescribed opening δ and moving with these dividers along the curve so that each new step starts where the previous step leaves off, the number of steps $N(\delta)$ is obtained. It is well known [7] that a curve is said to be of fractal nature if by repeating this procedure for different values of δ the relation

$$N(\delta) \sim (\delta)^{-D} \quad (7)$$

is obtained in the interval $\delta_* < \delta < \Delta_*$, where this interval is very small compared to $[x_N, x_0]$. Let $N_i(\delta)$ denote the number of dividers (boxes) of side length δ which intersect \mathcal{F} in the interval $[x_{i-1}, x_i]$ for $i = 1, 2, \dots, N$. Then, because of the structure of the aforementioned fractal interpolation functions the following relation holds

$$N(\delta) = N_1(\delta) + N_2(\delta) + \dots + N_N(\delta). \quad (8)$$

It has been proved [6] that under the assumption that $|d_i| > a_i$ for $i = 1, 2, \dots, N$

$$N_i(a_i\delta) = \frac{|d_i|}{a_i} N(\delta). \quad (9)$$

From this equation it results (when δ is very small compared to $[x_N, x_0]$) that

$$N_i(\delta) = \frac{|d_i|}{a_i} N\left(\frac{\delta}{a_i}\right) \quad i = 1, 2, \dots, N. \quad (10)$$

By substituting (10) to (8) it is obtained that

$$N(\delta) = \sum_{i=1}^N \frac{|d_i|}{a_i} N\left(\frac{\delta}{a_i}\right). \quad (11)$$

By taking into account the basic assumption (in order for an object to be fractal) $N(\delta) \sim (\delta)^{-D}$ and therefore $N\left(\frac{\delta}{a_i}\right) \sim (\frac{\delta}{a_i})^{-D} a_i^D$, relation (11) takes the form:

$$\delta^{-D} \sim \sum_{i=1}^N |d_i| a_i^{D-1} \delta^{-D} \iff \sum_{i=1}^N |d_i| a_i^{D-1} = 1. \quad (12)$$

It easily results that if the interpolation points are collinear then \mathcal{F} is the segment which connects (x_0, y_0) , (x_N, y_N) and has dimension 1.

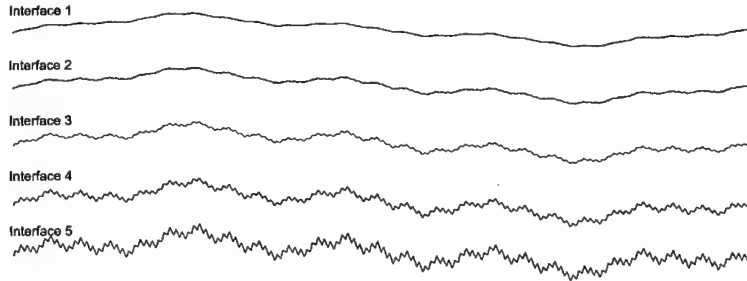
4. NUMERICAL STUDY OF THE FRICTION EVOLUTION

Here five structures are considered corresponding to interfaces with different Hausdorff dimensions, i.e. different asperities. First, five interpolation functions $\mathcal{F}^{(i)} \in C^0$, $i = 1, 2, \dots, 5$ interpolating the set of data $\{(0,0), (0.625,0.075), (1.25,0.025), (1.875,-0.025), (2.50,-0.075), (3.125,0.0)\}$ are considered. Their free parameters are taken to have the values given in Table 1.

	d_1	d_2	d_3	d_4	d_5
$\mathcal{F}^{(1)}$	0.20	0.20	0.25	0.20	0.20
$\mathcal{F}^{(2)}$	0.25	0.25	0.30	0.25	0.25
$\mathcal{F}^{(3)}$	0.35	0.35	0.40	0.35	0.35
$\mathcal{F}^{(4)}$	0.45	0.45	0.50	0.45	0.45
$\mathcal{F}^{(5)}$	0.55	0.55	0.60	0.55	0.55

Table 1. Free parameters of the fractal profiles

The remaining coefficients of the interpolating function are calculated by using equations (4)-(6). In the sequence, the approximations $m = 1, 2, \dots$ are obtained using the iterative scheme $\mathcal{F}_{m+1}^{(i)}(x) = (T\mathcal{F}_m^{(i)})(x)$, $i = 1, 2, \dots, 5$, where the operator T is given by relation (1). The fourth approximation of each interpolation function $\mathcal{F}^{(i)}$, $i = 1, 2, \dots, 5$ is given in Fig. 1. In Table 2, where the characteristics of these interfaces are given, δ represents the length of the linear parts each interface consists of, and h represents the maximum height of the asperities in reference to the piecewise linear interpolation function interpolating the same set of data. It must be mentioned here that the fourth approximation of each interface consists of 5^4 linear parts. Generally, the m -th approximation of a fractal interpolation function interpolating a set of data $\{(x_i, y_i), i = 0, 1, \dots, N\}$ consists of N^m linear segments.

Figure 1: Fourth approximation of fractal interpolation functions $\mathcal{F}^{(i)}$, $i = 1, 2, \dots, 5$

Name	Fractal Dimension	Iteration	δ	h
Interface 1	1.030	4	$0.005 \div 0.0055$	0.0158
Interface 2	1.163	4	$0.005 \div 0.0062$	0.0210
Interface 3	1.365	4	$0.005 \div 0.0084$	0.0332
Interface 4	1.518	4	$0.005 \div 0.0128$	0.0482
Interface 5	1.640	4	$0.005 \div 0.0199$	0.0668

Table 2. Characteristics of the considered fractal profiles

As it was expected all the interpolation functions present a multiscale character. In the sequence the five structures with interfaces corresponding to the $\frac{1}{5}$ of the five interfaces of Table 2 are considered (Fig. 2a-e). The material is assumed elastic-plastic with modulus of elasticity $E = 2.1 \times 10^8$ kN/m², Poisson ratio $\nu = 0.3$. The plasticity law is presented in Fig. 2f. The thickness of the structures is constant and equal to 0.02m. Plane strain conditions are assumed to hold. The structures have the vertical displacements fixed in both horizontal edges. The horizontal displacement is fixed at the lower edge while at the upper edge a total displacement of 0.1 m is applied in 300 loading steps (increments). The aim is to study the evolution of the friction as a result of the gradual plastification of the asperities.

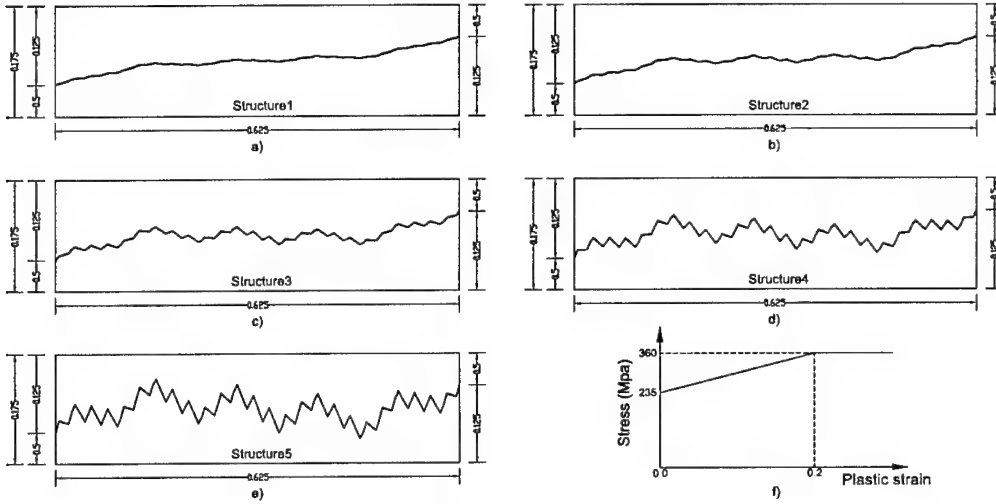


Figure 2: The five structures considered and the assumed elastoplastic material law

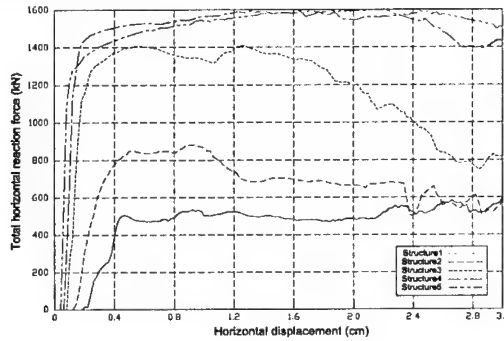


Figure 3: Total horizontal reaction force

The mathematical formulation of the problem is based on a generalization of the procedure presented in [8] pp. 568 in which the Total Lagrange formulation is used. The unilateral contact problem is solved by minimizing at each step of the iterative procedure the potential energy of the structure. The structures were solved using a Finite element code developed according the previous formulation.

In Fig. 3 the total horizontal force at the upper horizontal edge of the structures is plotted against the developed horizontal displacement. The diagram of structure 1 results to a maximum value of the total horizontal force equal to 550 kN. After reaching this value, the horizontal force remains rather constant as the material near the interface is plastified and the upper part of the structure slips on the lower part without the occurrence of further plastification. The diagram of Structure 2 is similar to the previous with the only difference that the maximum horizontal force reaches the value of about 900 kN. On the other hand, the diagrams of the rest structures differ significantly from the previous. The diagram of Structure 3 gives a maximum value of the horizontal force of 1400 kN (significantly larger than that of Structure 2). After that value, the total horizontal force is reduced. This happens because as relative tangential displacement is developed, the new contact areas present lower resistance and the total force required for the movement is reduced. Finally, it must be noticed here that the diagrams

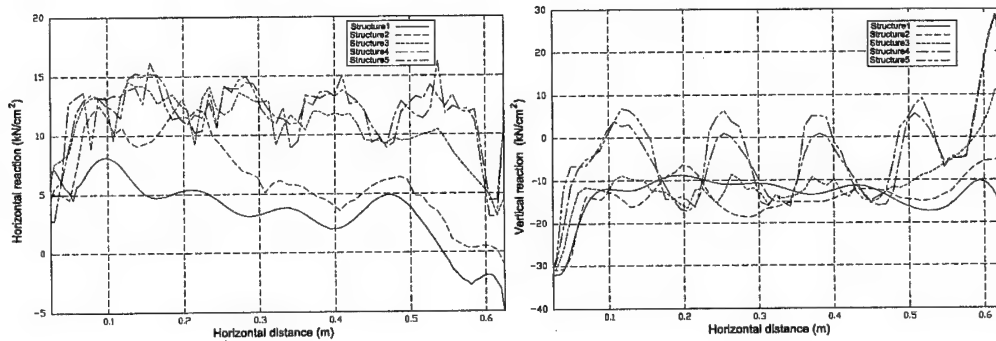


Figure 4: Distribution of the horizontal reaction forces (horizontal displacement 0.01m)

corresponding to structures 4 and 5 appear minor differences. The maximum value of the total horizontal force is similar (about 15% larger than the force corresponding to Structure 3) and its value remains rather constant (at least for the displacement under consideration). This happens, in contrast to the case of Structure 3, because the relative interface slip is reduced and the contact area does not change significantly.

Figure 4a presents the distribution of the horizontal stress on the upper edge of the structure. It is noticed that the distribution strongly depends on the fractal dimension of the interface. This influence is greater for small values while it is reduced for large values (notice that the distributions corresponding to Structure 4 and Structure 5 are very similar).

The same remarks hold also for the distribution of the vertical stresses of the upper edge of the structure which are presented in 4b. The distribution that corresponds to Structure 1 gives rather small variations. These variations increase together with the value of the fractal dimension. The shape of the vertical stress distribution follows the shape of the fractal interface, with the greater values corresponding to the peaks of the fractal curve. But, after a critical value of the fractal dimension, the differences in the results and the overall response are minor despite the differences to the characteristics of the fractal curves.

REFERENCES

- [1] Saouma, V.E., Barton, C.C. and Gamaleding, N.A., Fractal characterization of fracture surfaces in concrete, *Engineering Fracture Mechanics* 35(1/2/3), 47-53 (1990).
- [2] Mandelbrot, B., Passoja, D.E. and Paullay, A.J., Fractal character of fracture surfaces of metals, *Nature* 308, 721-722 (1984).
- [3] Xie, H., The fractal effect of irregularity of crack branching on the fracture toughness of brittle materials, *Int. Journal of Fracture* 41, 267-274 (1989).
- [4] Xie, H., Fractal nature on damage evolution of rock materials, in *2nd Int. Symposium of Mining Tech. and Science*, CUMT Press, (1991).
- [5] Mandelbrot, B., *The Fractal Geometry of Nature*, W. H. Freeman and Co., N. York (1982).
- [6] Barnsley, M., *Fractals Everywhere*, Academic Press, Boston, N. York (1988).
- [7] Falconer, K.J., *Fractal Geometry: Mathematical Foundations and Applications*, J. Wiley, Chichester (1990).
- [8] Mistakidis, E.S., Panagiotopoulos, P.D. and Panagouli, O.K., Fractal surfaces and interfaces in structures. Methods and algorithms. *Chaos Solitons & Fractals*, 2(5) 551-574 (1992).

NUMERICAL STUDY OF THE F.E. MESH DEPENDENCY IN NONCONVEX-NONSMOOTH ENGINEERING PROBLEMS

E.S. Mistakidis

Dept. of Civil Engineering, University of Thessaly
38334 Volos, Greece

N.P. Politis

Dept. of Civil Engineering, Rice University
Houston, TX-77005-1892, U.S.A.

1. SUMMARY

In this paper, the effect of the F.E. discretization density on the results of both convex and nonconvex - nonsmooth frictional contact interface problems is investigated. Various cases of monotone and nonmonotone interface laws are considered and interesting results are obtained.

2. INTRODUCTION

There are many problems in Mechanics where constitutive or boundary laws are represented by relations involving decreasing branches (for example reaction-displacement laws in interface problems, general nonmonotone friction laws, adhesive contact laws in laminated composite problems). Inclusions with nonmonotone relations were introduced in Mechanics by P.D. Panagiotopoulos [1], [2] who termed them hemivariational inequalities. They represent an appropriate tool enabling the study of nonmonotonicity into the mathematical model reflecting the mechanical response. The mathematical analysis of hemivariational inequalities uses methods of nonsmooth and nonconvex analysis [3]. Concerning the numerical treatment, an appropriate discretization is necessary. Then, the continuum problem is replaced by its finite dimensional one. With a model having a finite number of degrees of freedom, there exist a number of methods for the numerical treatment of the problem.

In this paper the heuristic nonconvex optimization approach of [4] is followed according to which the hemivariational inequality is replaced with a sequence of variational inequality problems. The numerical solution of the discretized version of the variational inequalities is then obtained by quadratic programming algorithms.

This approach is applied in order to investigate the dependency of the initial problem on the F.E. discretization used. For this reason several model problems are examined with various F.E. discretization densities. The examples treated here include frictional contact problems with a strongly nonlinear nature. The dominant role of the possible vertical branches of the reaction-displacement diagrams is studied. Interesting results are obtained with respect to the accuracy expected in such kind of problems.

3. FORMULATION

In this Section, the formulation of the unilateral contact problem with nonmonotone friction is briefly presented. The static analysis problem is described by the following relations:

- *Stress equilibrium equations:*

$$\bar{\mathbf{G}}\bar{\mathbf{s}} = \begin{bmatrix} \mathbf{G} & \mathbf{G}_N & \mathbf{G}_T \end{bmatrix} \begin{bmatrix} \mathbf{s} \\ -\mathbf{S}_N \\ -\mathbf{S}_T \end{bmatrix} = \mathbf{p} \quad (1)$$

where \mathbf{G} is the equilibrium matrix of the discretized structure, \mathbf{p} , \mathbf{s} are the loading and stress vectors respectively and $\bar{\mathbf{G}}$ is the enlarged equilibrium matrix such as to take into account the normal to the interface (\mathbf{S}_N) and tangential (\mathbf{S}_T) interface tractions.

- *Strain-displacements compatibility equations:*

$$\bar{\mathbf{e}} = \bar{\mathbf{G}}^T \mathbf{u} \text{ or explicitly } \begin{bmatrix} \mathbf{e} \\ [\mathbf{u}]_N \\ [\mathbf{u}]_T \end{bmatrix} = \begin{bmatrix} \mathbf{G}^T \\ \mathbf{G}_N^T \\ \mathbf{G}_T^T \end{bmatrix} \mathbf{u} \quad (2)$$

where \mathbf{u} , \mathbf{e} are the displacement and strain vectors respectively and $[\mathbf{u}]_N$, $[\mathbf{u}]_T$ are the relative normal and tangential displacements of the interface respectively.

- *Linear material constitutive law for the structure:*

$$\mathbf{e} = \mathbf{e}_0 + \mathbf{F}_0 \mathbf{s} \text{ or } \mathbf{s} = \mathbf{K}_0 (\mathbf{e} - \mathbf{e}_0). \quad (3)$$

Here \mathbf{F}_0 and $\mathbf{K}_0 = \mathbf{F}_0^{-1}$ are the natural and stiffness flexibility matrices of the unassembled structure and \mathbf{e}_0 is the initial deformation vector.

- *Classical equality boundary conditions written in the general form:*

$$\mathbf{E}\mathbf{u} = \mathbf{u}_0 \text{ and } \mathbf{Z}\mathbf{s} = \mathbf{F} \quad (4)$$

where \mathbf{E} and \mathbf{Z} are appropriately defined transformation matrices and \mathbf{u}_0 , \mathbf{F} denote the known nodal boundary displacements (support) and boundary loading (traction). Note that in any point of the boundary, only one of the equations in (4) can be active.

- *Unilateral contact conditions:*

$$[\mathbf{u}]_N \leq 0, \mathbf{S}_N \leq 0, [\mathbf{u}]_N \mathbf{S}_N = 0 \quad (5)$$

- *Nonmonotone friction conditions, i.e. the condition*

$$-\mathbf{S}_T \in \bar{\partial} \tilde{\Phi}_T([\mathbf{u}]_T)$$

is assumed to hold in the tangential to the interface direction, where $\tilde{\Phi}_T$ is an appropriately defined nonconvex superpotential producing the nonmonotone frictional law and $\bar{\partial}$ denotes the generalized gradient of Clarke-Rockafellar [3].

According to [1],[2],[4] the potential energy of the structure has the form

$$\Pi(\mathbf{u}) = \frac{1}{2} \mathbf{u}^T \mathbf{K} \mathbf{u} - \bar{\mathbf{p}}^T \mathbf{u} + \tilde{\Phi}_T(\mathbf{u}, \mathbf{S}_N), \mathbf{u} \in V_{ad} \quad (6)$$

where V_{ad} is the kinematically admissible set given by

$$V_{ad} = \{\mathbf{u} \in \mathbb{R}^n \mid \mathbf{E}\mathbf{u} = \mathbf{u}_0, [\mathbf{u}]_N \leq 0\}. \quad (7)$$

Following the approach of the [1], problem (6) is split in the subproblems

$$\Pi_1(\mathbf{u}) = \frac{1}{2} \mathbf{u}^T \mathbf{K} \mathbf{u} - \bar{\mathbf{p}}_1^T \mathbf{u}, \mathbf{u} \in V_{ad} \quad (8)$$

and

$$\Pi_2(\mathbf{u}) = \frac{1}{2} \mathbf{u}^T \mathbf{K} \mathbf{u} - \bar{\mathbf{p}}_2^T \mathbf{u} + \tilde{\Phi}_T(\mathbf{u}), \mathbf{u} \in V_{ad}^2 \quad (9)$$

by fixing in the first (resp. the second) the values of \mathbf{S}_T (resp. \mathbf{S}_N). In the previous relations, $\bar{\mathbf{p}}_1$ is a new force vector containing the effect of the assumed known tangential forces \mathbf{S}_T on the structure

$$\bar{\mathbf{p}}_1 = \bar{\mathbf{p}} + \mathbf{G}_T \mathbf{S}_T \quad (10)$$

and $\bar{\mathbf{p}}_2$ is a force vector containing the effect of the assumed known normal forces \mathbf{S}_N

$$\bar{\mathbf{p}}_2 = \bar{\mathbf{p}} + \mathbf{G}_N \mathbf{S}_N. \quad (11)$$

Finally, V_{ad}^2 is V_{ad} without the unilateral contact conditions, i.e.

$$V_{ad}^2 = \{\mathbf{u} \in \mathbb{R}^n \mid \mathbf{E} \mathbf{u} = \mathbf{u}_0\} \quad (12)$$

The solution algorithm is based on a multilevel decomposition of the normal and tangential actions. The problem arising in the normal to the interface direction is solved by minimizing the potential energy problem (8). In the second step the substationarity problem (9) is solved. The two subproblems are solved repeatedly until convergence. For the numerical treatment of the substationarity problems corresponding the second subproblem the heuristic nonconvex optimization approach presented in [4] is applied.

3. NUMERICAL INVESTIGATION OF THE CONVERGENCE PROPERTIES

The method is applied to the analysis of the two-dimensional simple structure of Fig. 1a. The structure consists of two shear walls which are in contact through the vertical interface OA . The material of the structure is assumed to be linear elastic with modulus of Elasticity $E = 2.0 \times 10^7 \text{ kN/m}^2$ and Poisson ration $\nu = 0.16$. The thickness of the shear walls is $t = 0.2 \text{ m}$. For the behaviour of the interface in the tangential to the interface direction, the three different laws of Fig. 1b,c,d were considered. The diagram of Fig. 1b (Law-1) is a classical Coulomb friction diagram which is considered here as a reference to which the nonmonotone diagrams will be compared. The diagram of Fig. 2c (Law-2) has a decreasing branch of constant slope while the diagram of Fig. 2d (Law-3) is a sawtooth diagram representing a much more complicated interface behaviour.

The five different discretizations of Fig. 2 are considered with the characteristics of Table 1. A two-dimensional constant stress triangular element has been employed for the discretization.

Discretization	Elements	Nodes	Interface nodes
1	164	120	20
2	280	190	32
3	708	442	64
4	974	595	80
5	1248	752	100

Table 1. Characteristics of the considered discretized models

The structure is loaded with horizontal forces as shown in Fig. 1a. In order to study the behaviour of the structure, twelve load cases (LC) are considered. In these load cases the loads p are increasing linearly from 22.0 kN/m to 264.0 kN/m.

The five structures were analyzed for the three different interface laws. The results are presented in the Figures that follow.

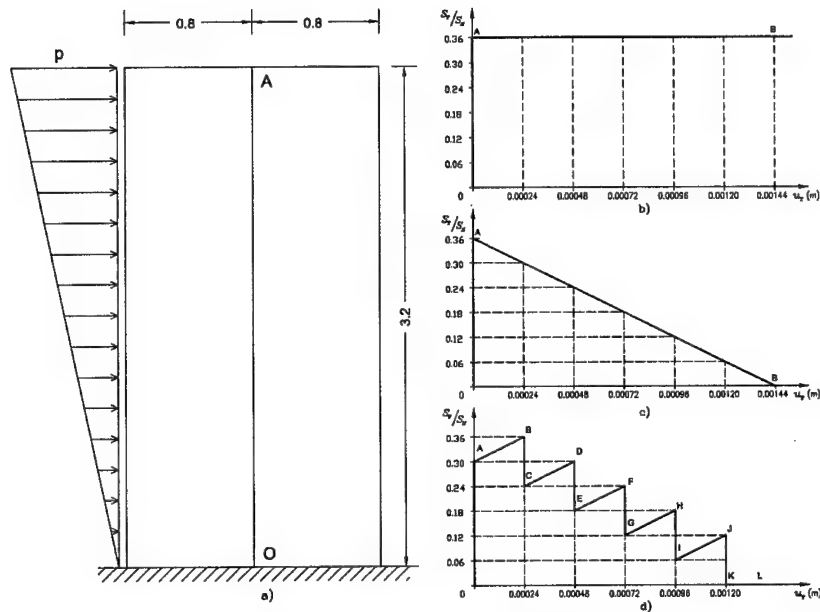


Figure 1. The considered structure and the tangential interface laws

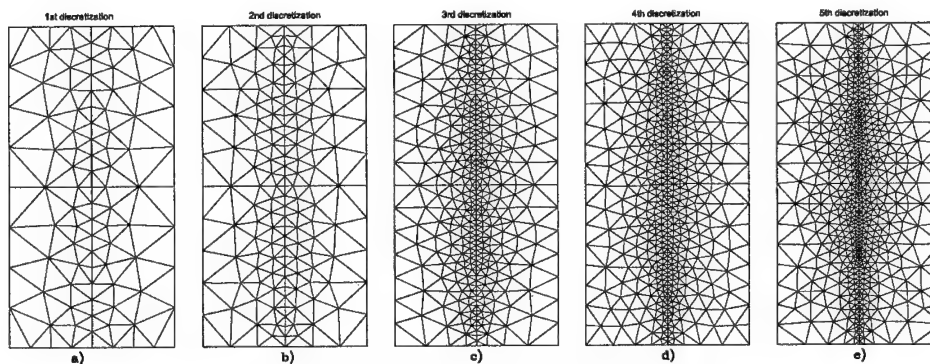


Figure 2. The five discretizations considered

Fig. 3a presents the contact stresses for the 5th load case for the various F.E. discretizations. It is noticed that the results are identical, i.e. the contact stress distribution does not rely on the F.E. discretization for the considered problem. Fig.3b presents the distribution of the contact stresses for the 3rd discretization and for the various load cases. Note that the results increase almost linearly with the external loading. Moreover, the contact stresses differ very slightly for the various interface laws.

Let us first consider the case of the Coulomb friction law shown in Fig. 1b. In this case the results for the tangential stresses are independent of the F.E. discretizations. Fig. 4 gives the distribution of the relative tangential displacements for loadcases 2 and 4. Notice that the differences between the 4th and 5th discretizations are very small.

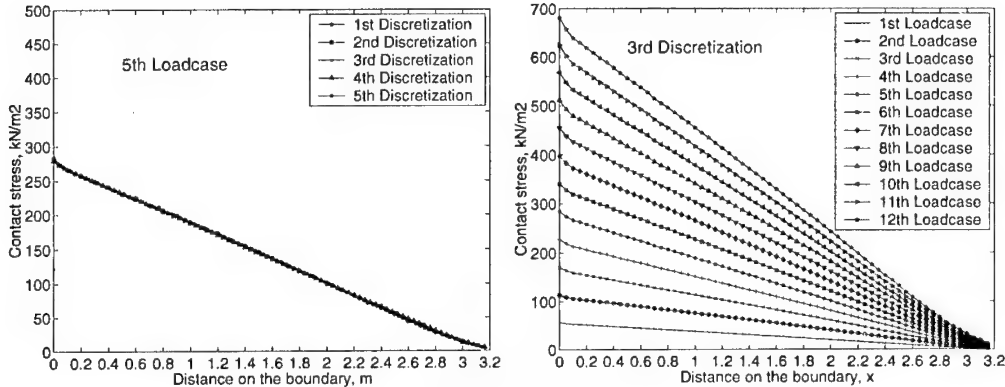


Figure 3. Contact stresses diagrams

Then the case of the linearly decreasing tangential interface law shown in Fig. 1c, is considered. The results of the tangential stresses for the load cases 11 and 12 are presented in Fig. 5. It is clear that the tangential stresses depend on the F.E. discretizations. It is observed that the results for the last two F.E. meshes considered in this example are very close and it is concluded that the final F.E. mesh discretization is sufficient.

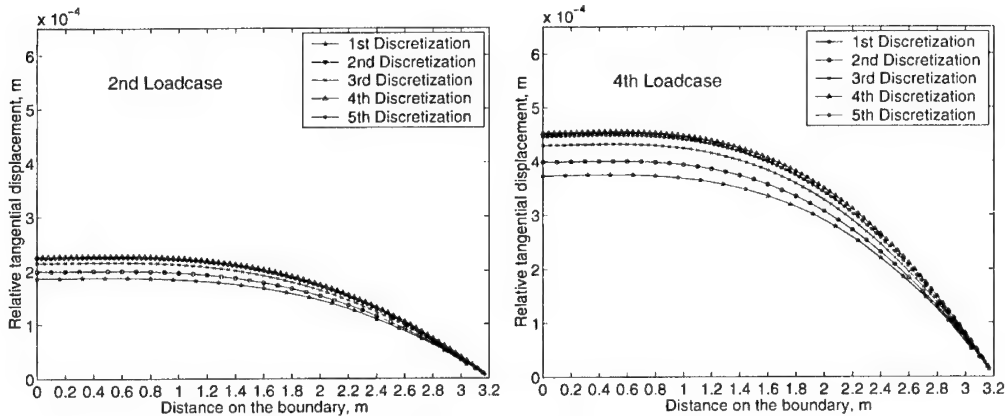


Figure 4. Results for Law-1 (Coulomb law)

Similar results are obtained for the sawtooth tangential interface law depicted in Fig. 3d. As it can be seen in Fig. 6 the frictional stresses depend on the F.E. discretization. Here the results for the load cases 8 and 9 are presented. Note that the distributions of the tangential stresses exhibit a shape like the one of the interface law. Again the results obtained for the 4th and 5th F.E. meshes are close enough to consider the last one satisfactory. The most important difference between this case and the previous one is that, due to the sawtooth shape of the friction law, the diagrams present abrupt jumps. The exact location of this jump changes, depending on the discretization. Therefore, a specific point on the interface, might present, for successive discretizations, great differences of the tangential stresses. This fact does not hold in this extend for the two previous cases of interface laws.

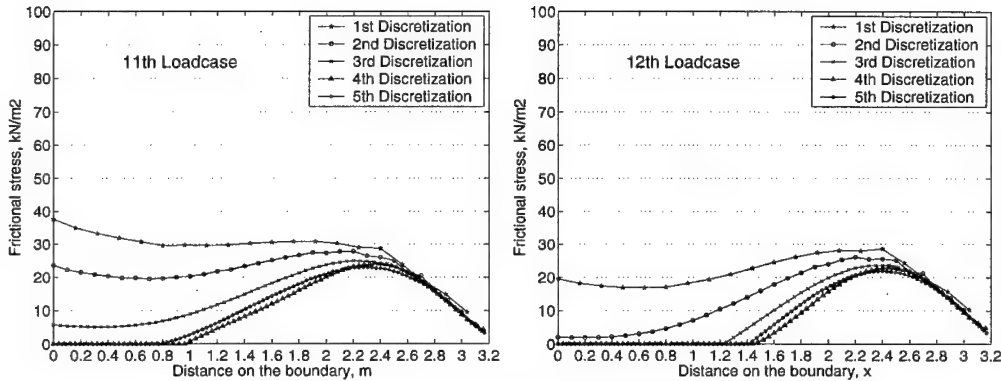


Figure 5. Results for Law-2 (decreasing branch law)

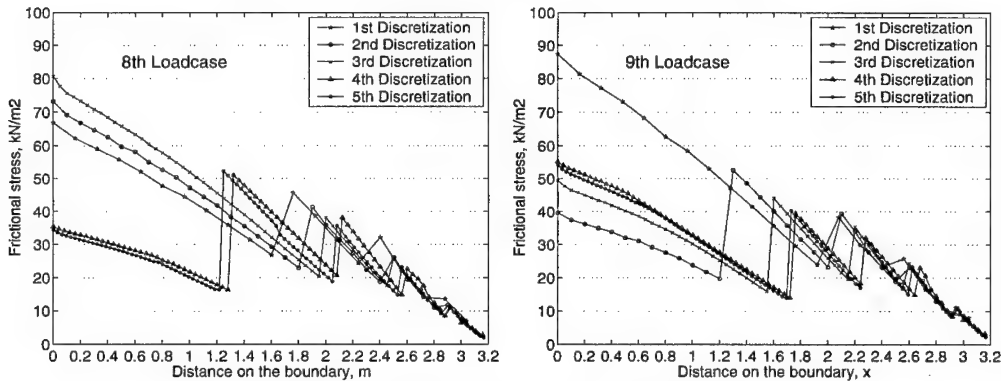


Figure 6. Results for Law-3 (sawtooth law)

From the above analysis it is concluded that the normal stresses for all the tangential interface laws are independent of the F.E. mesh discretization. Hence, in the case that only the normal stresses are of interest, very good results can be achieved even by considering a quite sparse F.E. discretization that does not demand great computational power and time. The same conclusions hold as well, in the case of calculation of the frictional stresses when the Coulomb law is considered. On the other hand for the laws depicted in Fig. 1c and 1d the tangential stresses strongly depend on the F.E. mesh density. Moreover, one must be very careful in the case that sawtooth laws are considered, or in general, if the tangential laws exhibit vertical branches, because the exact location of the jumps of the tangential stresses diagrams depend very strongly on the F.E. discretization considered.

REFERENCES

- [1] Panagiotopoulos, P.D. *Inequality problems in mechanics and applications. Convex and nonconvex energy functions*, Birkhäuser, Basel - Boston - Stuttgart (1985). Russian translation, MIR Publ., Moscow (1988).
- [2] Panagiotopoulos, P.D., *Hemivariational inequalities. Applications in mechanics and engineering*, Springer, Berlin - Heidelberg - New York (1993).
- [3] Clarke, F. H., *Optimization and nonsmooth analysis*, New York, J. Wiley, (1983).
- [4] Mistakidis, E.S and Stavroulakis, G.E., *Nonconvex optimization in Mechanics. Algorithms, heuristics and engineering applications by the F.E.M.*, Kluwer, Boston (1997).

FUZZY SETS IN ENGINEERING ANALYSIS AND DESIGN

E.S. Mistakidis

Dept. of Civil Engineering, University of Thessaly
38334 Volos, Greece

D.N. Georgiou

Dept. of Mathematics, University of Patras
26500 Patras, Greece

1. SUMMARY

In this paper a new approach to the problem of estimating the structural response of systems with uncertain characteristics is presented. The approach is based on the theory of fuzzy sets which allow the engineers to describe the uncertain variables. The uncertain parameters are expressed as fuzzy numbers with certain characteristics. The concurrent effect of the various uncertainties on the structural response is obtained by applying certain methodologies of the theory of fuzzy sets. The output parameters of the design process are obtained as new fuzzy numbers expressing the uncertainties of the output parameters. A numerical application gives an idea of the applicability of the proposed methodology in various aspects of the engineering processes.

2. INTRODUCTION

Design in engineering practice is a procedure where the structural engineer attempts to create a structure that will withstand all the loads it is expected to encounter during its intended life. It has been realized though that the actual strength of the structure cannot be precisely known due to various uncertainties. For example, the actual system is far more complex than the idealized model considered by the design engineer. Also, the actual material properties are not exactly known. Usually, minimum values are specified by the design engineer that it is more likely to be surpassed in several members. Moreover, the majority of the structures are statically indeterminate a fact that has as a result the dependence of the stresses on the relative stiffnesses of the various interconnected members. As a consequence, variances in the material properties results in differences in the values of the developed stresses.

Another uncertainty factor is connected to loads. For example, environmental loads, such as snow or wind, have unpredicted future magnitudes. Moreover, seismic loading, the main action in earthquake zones, has an inherent uncertain character. Only maximum values over a range of years are specified by the seismic codes, which are reviewed frequently, giving usually larger values than the previous ones.

It is therefore clear that the structural resistance and structural loading can only be assessed with a degree of uncertainty. But, classical mathematics is not equipped to deal with uncertain

or imprecise descriptions. Traditionally, the design engineers take into account these uncertainties in the design by using the so called "safety factors", i.e. reducing the design strength and increasing the applied loading.

Active research effort took place during the previous years in order to rationalise the design process by introducing design criteria which directly or indirectly employ statistical and probabilistic tools into structural design codes [1], [2], [3]. These methods had the inherent difficulty that required a lot of statistical data for their application that were usually not available. In the sequel probabilistic methods evolved [4] which employed first-order probabilistic theory which used only the mean values and the standard deviation of the random variables.

Another field where imprecise description can help in order to solve engineering problems is that of preliminary design of structures. It is well known that the decisions taken in the preliminary design of a structure plays an important role as it restricts the set of available design alternatives in the later stages of the design process. Experienced designers recognize this difficulty and attempt to begin the design process with a complete but approximate, imprecise description of the structure. As the design process advances from the preliminary design to the final design, the imprecision is gradually eliminated. The basic idea is that fuzzy sets allow the designer to describe the designed structure as approximately as desired at the early stages of the design process. This approximate description in terms of imprecise input parameters is employed to calculate the approximate corresponding output parameters. The later are compared with given performance criteria and the information obtained by this comparison is then utilized in order to determine appropriate values of the input parameters.

In this paper a new approach to the problem of estimating the structural response of systems with uncertain or imprecise characteristics is presented. The approach is based on the theory of fuzzy sets [5], [6], [7], [8] which allows the designers to describe the uncertain or imprecise variables. The method is presented briefly in the following. First the uncertain or imprecise parameters are expressed as fuzzy numbers with certain characteristics. The concurrent effect of the various uncertainties on the structural response is obtained by applying certain methodologies of the theory of fuzzy sets. Then the output parameters of the design process as e.g. the displacements or the stresses of the structure are obtained as new fuzzy numbers expressing the uncertainties of the output parameters.

3. PRELIMINARIES

A fuzzy set is a set of objects without clear boundaries or without well-defined characteristics. In contrast with ordinary sets where for each object it can be decided whether it belongs to the set or not, a partial membership in a fuzzy set is possible. Formally a fuzzy set is defined as follows:

Let X be a set. A is called a *fuzzy set* of X if A is the set of ordered pairs:

$$A = \{(x, \mu_A(x)) : x \in X \text{ and } \mu_A(x) \in [0, 1]\},$$

where $\mu_A(x)$ is the grade of membership of x in A . The function $\mu_A(x)$ is called the *membership function* of A .

One of the most important concepts of fuzzy sets is the concept of an α -cut. Given a fuzzy set A of X and any number $\alpha \in [0, 1]$, the α -cut, which is denoted ${}^\alpha A$ is the crisp set:

$${}^\alpha A = \{x \in X : \mu_A(x) \geq \alpha\}.$$

That is, the α -cut of a fuzzy set A of X is the crisp set ${}^\alpha A$ that contains all the elements of X whose membership grades in A are greater than or equal to the specified value of α .

A fuzzy set A of the set of real numbers \mathbb{R} is called *fuzzy number* if there is at least on $x \in \mathbb{R}$ such that $\mu_A(x) = 1$ (*normality assumption*) and for every real numbers x, y, w with $x < w < y$

$$\mu_A(w) \geq \min\{\mu_A(x), \mu_A(y)\}.$$

This second property is the so-called convexity property.

A *triangular fuzzy number* $A = (a_1, a_2, a_3)_T$, with $a_1 \leq a_2 \leq a_3$ has a membership function which in general has the following form:

$$\mu_A(x) = \begin{cases} 0, & x \leq a_1 \\ \frac{x-a_1}{a_2-a_1}, & a_1 < x \leq a_2 \\ \frac{a_3-x}{a_3-a_2}, & a_2 < x \leq a_3 \\ 0, & x \geq a_3. \end{cases}$$

By $\langle r, c, d \rangle$ we denote the triangular fuzzy number $(c-r, c, c+d)_T$. Also, by (r, c) we denote the symmetric triangular fuzzy number $(r-c, r, r+c)_T$. The numbers r and c express the *center* and the *spread* respectively.

A fuzzy set $A = (a_1, a_2, a_3)$ on the set of real numbers is called an *L-R fuzzy number* if the membership of x can be calculated by:

$$\mu_A(x) = \begin{cases} L\left(\frac{a_2-x}{a_2-a_1}\right), & a_1 < x \leq a_2 \\ R\left(\frac{x-a_2}{a_3-a_2}\right), & a_2 < x \leq a_3 \\ 0, & \text{otherwise.} \end{cases}$$

Here L and R are continuous strictly decreasing functions defined on $[0, 1]$ with values in $[0, 1]$ and satisfying the conditions:

- (i) $L(x) = R(x) = 1$ if $x \leq 0$ and
- (ii) $L(x) = R(x) = 0$ if $x \geq 1$.

Clearly, the triangular fuzzy numbers are special cases of $L-R$ fuzzy numbers with $L(x) = R(x) = 1 - x$.

Let $X_i, i = 1, 2, \dots, n$ be subsets of the set of the real numbers \mathbb{R} , Y be a subset of \mathbb{R} and $A_i, i = 1, 2, \dots, n$ fuzzy sets of $X_i, i = 1, 2, \dots, n$. Therefore it is assumed that these fuzzy sets are normalized and convex (i.e., they are fuzzy numbers). Also, let f be a function of the set $X_1 \times X_2 \times \dots \times X_n$ into the subset Y of \mathbb{R} , that is

$$f : X_1 \times X_2 \times \dots \times X_n \rightarrow Y.$$

For each $x_i \in X_i, i = 1, 2, \dots, n$,

$$y = f(x_1, x_2, \dots, x_n)$$

is the value of the performance parameter y that corresponds to the values x_1, x_2, \dots, x_n .

The algorithm to determine a fuzzy set A on Y by the fuzzy sets $A_i, i = 1, 2, \dots, n$ through the function f , is described by the following steps (see [5-7]):

1. Select appropriate values a_1, a_2, \dots, a_m in the interval $(0, 1]$. Let $k = 1$.
2. For each a_i , determine closed intervals ${}^{a_i}A_i = [b_{i1}, b_{i2}]$ of X_i that represent the a_i -cuts of fuzzy sets $A_i, i = 1, 2, \dots, n$.

3. Generate all combinations of the endpoints of the closed intervals ${}^{a_i}A_i = [b_{i1}, b_{i2}]$, $i = 1, 2, \dots, n$. Clearly, each combination is an n -tuple, (b_1, b_2, \dots, b_n) , where $b_i \in \{b_{i1}, b_{i2}\}$ and $i = 1, 2, \dots, n$.
4. For every n -tuple (b_1, b_2, \dots, b_n) generated in Step 3, we find the values:

$$y_l = f(b_1, b_2, \dots, b_n), \quad l = 1, 2, 3, \dots, 2^n.$$

5. We determine as the a_i -cut of the fuzzy set A of Y the following closed interval

$${}^{a_i}A = [\min\{y_l : l = 1, 2, 3, \dots, 2^n\}, \max\{y_l : l = 1, 2, 3, \dots, n\}].$$

6. If $k < m$, increase k by one and return to Step 2; otherwise, stop.

4. APPLICATIONS IN ENGINEERING DESIGN PROBLEMS

The values involved in an engineering design are termed parameters. Three kinds of parameters are distinguished: the input ones, the output ones and the performance ones. Input parameters are independent parameters whose values are determined during the design process. An output parameter involved in the design process is any parameter that is dependent on the input parameters and, possibly on the same performance parameters, but is not subject to any functional requirement. On the other hand, a performance parameter is subject to some functional requirement. Also, the term functional requirement refers to a value, range of values or fuzzy number that is specified for a performance parameter.

The first step in the application of fuzzy sets in the design process is to distinguish the various kinds of parameters involved in the problem. In the sequel, the preferences regarding the values of the input parameters are expressed by appropriate fuzzy sets. Given an input parameter d_i that takes values in set D_i , let preferences for different values of d_i be expressed by a fuzzy set F_i on V_i . For each $x \in V_i$, the value $F_i(x)$ gives the degree of acceptability of using the specific value x . Therefore, the set V_i may be referred as the set of acceptable or desirable values of the parameter d_i , and the set $F_i(x)$ may be viewed as the grade of membership of the value x in this set. The index i in the above is used to distinguish different input parameters in the same design problem.

Membership grades $F_i(x)$ express the designer's desire to use the various values $d_i \in V_i$ for the input parameter d_i . These membership grades are obtained either by the personal experience of the designer or by quantifying serviceability requirements. For example the height of a beam member or the width of a wall element may have an upper limiting value depending on architectural requirements. On the other hand, membership functions or fuzzy sets representing objective preferences are determined by quantifying the recommendations of the building codes. For example, the limiting horizontal displacement of a building under seismic action is determined by the various building codes but it results to damages in non-structural elements. It is therefore rather easy to construct a membership function to express the preference of the engineer for smaller values of this displacement. For the above purposes, the use of triangular fuzzy numbers seems to be more convenient.

Once the fuzzy sets expressing the preferences of the designer are determined for all the input parameters, the procedure presented in Section 2 is applied in order to determine the associated fuzzy sets for the performance parameters. The procedure is demonstrated in the following example.

EXAMPLE: SEISMIC DESIGN OF A CONCRETE FRAME

Let us assume that we want to design the concrete frame of Fig. 1. The frame is part of a typical structure and is examined alone for the sake of simplicity and comprehension of the results. The design engineer uses rectangular columns which have predefined one of the dimensions while the other one will be determined from the solution process. For this dimension the preferred size is 50 cm. The acceptability decreases linearly with a minimum value of 40 cm and a maximum value of 80 cm. Similarly, the beams are assumed to have a rectangular shape with their width fixed to a dimension of 25cm while their height has a desired dimension of 50cm. The acceptability of this dimension decreases linearly with a minimum value of 40cm and a maximum value of 60cm. These limiting values come for example from architectural, serviceability or other reasons. For example, dimensions larger than the maximum values would result to a redesign of the basic dimensions of the frame considering e.g. a different number of columns, different arrangement of the plan view or even a completely different structural system. On the other hand, dimensions smaller than the minimum values would not be acceptable from the national or international building codes. The above "functional requirements" result to the fuzzy numbers of Fig. 2.

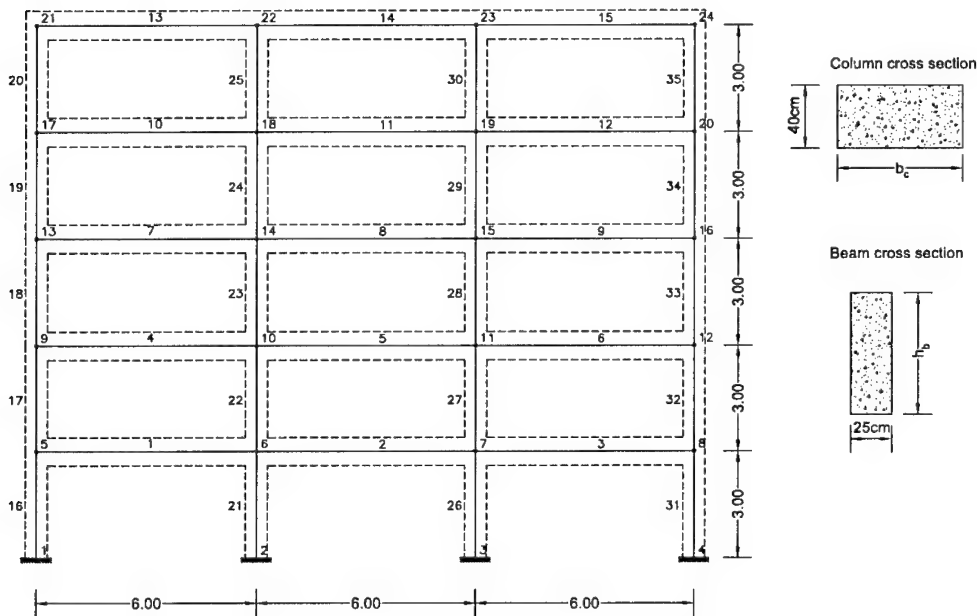


Figure 1. Seismic design of a concrete frame

The beams of this system are loaded with a dead load of 15.0 kN/m and a live load of 15.0 kN/m. The structure is located in a seismic zone with the following characteristics: Spectral acceleration: 0.24g, Soil type: A, Effective damping: 5%, Importance factor: 1.00, Foundation factor: 1.00.

The objective is the optimal design of the frame in such a manner that the maximum horizontal displacement under seismic loading is smaller than 10 cm. The complete diagram for the acceptability of the top floor horizontal displacement is presented in Fig. 3a. This diagram means that structures with top horizontal displacement less than 5cm are completely acceptable while structures with a maximum displacement of 10 cm are acceptable but less desired,

because under the design earthquake damages will appear in non-structural elements (e.g. the wall fillings).

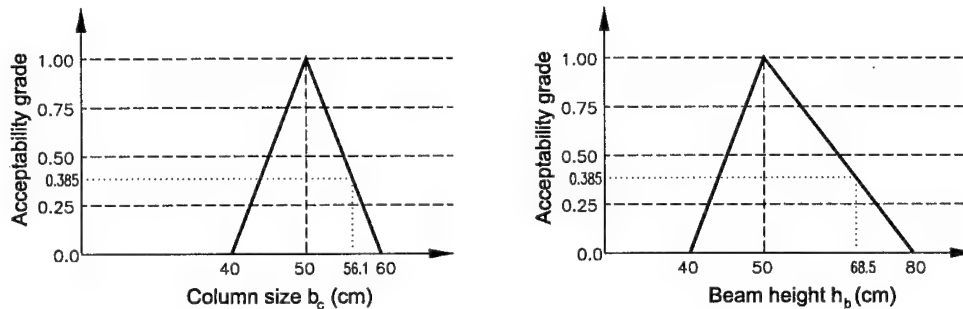


Figure 2. The acceptability diagrams for the beam and column sections

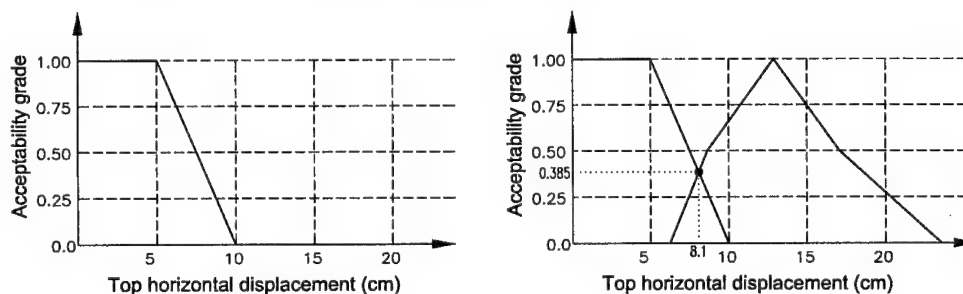


Figure 3. Acceptability diagram for the top horizontal displacement

The application of the algorithm of Section 2 gave as a result the diagram of Fig. 3b. Notice that although the input fuzzy numbers were triangular ones, the displacement fuzzy number is not triangular. The intersection of this diagram with the acceptability diagram of the displacement results to the "optimal" point A which corresponds to a horizontal displacement of 8.1 cm. The related membership grade is 0.385. This membership grade defines also the optimal values of the design variables (see dotted lines at the diagrams of Fig. 2).

REFERENCES

- [1] Mayer, M., *Safety of Structures*, Springer, Berlin, (1926).
- [2] Freudenthal, A.M., The safety of structures, *Transactions of ASCE*, 112,125-180(1947).
- [3] Pugsley, A.G., *Concepts of Safety in Structural Engineering*, 1951.
- [4] Benjamin, J.R., *Statistics of Civil Engineers*, McGraw-Hill, New York, (1964).
- [5] Wood K. L. and Antonsson, E.K. Computations with imprecise parameters in engineering design: Background and theory, *ASME J. of Mechanisms, Transmissions and Automation in Design* 111(4), 616-625 (1989).
- [6] Otto K. N. and Antonsson, E.K., Extensions to the Taguchi method of product design, *ASME J. of Mechanical Design* 115(1), 5-13 (1993).
- [7] Otto K. N. and Antonsson, E.K., Tuning parameters in engineering design, *ASME J. of Mechanical Design* 115(1), 14-19 (1993).
- [8] Zimmermann H. J., *Fuzzy Set Theory and Its Applications*, Kluwer, Boston, (1985).

BENDING AND WARPING IN FIBER REINFORCED RECTANGULAR BEAMS

C. B. Demakos

Department of Civil Engineering, Technological Educational Institution of Piraeus
GR-72244 Piraeus, Greece
email: cdem@teipir.gr

1. SUMMARY

A closed-form solution is proposed for the study of the stresses developed inside fiber reinforced composite beams of rectangular shape, which are subjected to simultaneously existing torsion and bending. The model studied consists of similar, parallel dispersed fibers inside a matrix, which form an angle with the longitudinal axis of the beam. The elastic properties of the composite material and the torsional rigidity as well as the stresses of the beam are determined by using Sokolnikoff's approach in conjunction with the theory of anisotropic elasticity.

2. INTRODUCTION

Various theories [1-3] have been presented for composite thin-walled cylindrical tubes neglecting the warping effect. Librescu *et al* [4-5] developed a refined theory for laminated beams of arbitrary thin-walled closed cross-section taking into account torsional-related warping effects. These theories were modified later for taking into account the transverse flexibility and warping restraint [6] in open cross-section beams.

In this paper, the stresses are evaluated analytically in fiber reinforced beams with solid cross-section of orthogonal shape, due to simultaneously applied torsion and bending moments. The beam is clamped-free, whereas it consists of identical, parallel fibers oriented at the same angle with respect to the beam axis.

3. STRESS-STRAIN LAW IN THE FIBER REINFORCED BEAM

Without loss of generality, the analysis assumes a clamped-free straight composite beam(Fig. 1) subjected to a torsional moment, M_x and a

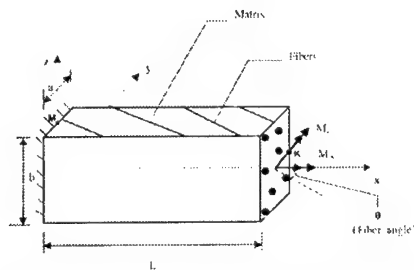


Figure 1: Geometry and loadings in the fiber reinforced beam.

bending moment, M_y , at its free-tip. The beam consists of identical Boron fibers at a volume percentage $v_f = 0.4$ oriented at the same θ - angle with respect to x- central axis of beam inside a matrix of a soft Epoxy with elastic properties illustrated in Table 1.

The deformation field is described by the cross-sectional displacements $u(x)$, $v(x)$, $w(x)$ in x- y- and z-directions, respectively, and the twist angle about the x- axis denoted by $t(x)$. Assuming that linear elasticity conditions prevail in the beam, the strain components are expressed as follows [7]:

$$\begin{aligned}\epsilon_{xx} &= u_{,x} - y v_{,xx} - z w_{,xx} + W_{,x} \\ \gamma_{xz} &= y t_{,x} + W_{,z} \\ \gamma_{xy} &= -z t_{,x} + W_{,y}\end{aligned}\quad (1)$$

where $W(x, y, z)$ is the warping function and comma (,) stands for the partial derivative of a function with respect to the variable followed. The elastic properties of the composite at its principal 1-, 2- and 3-directions are provided in various investigations [8-11]. In these relations 1-axis is the strong direction of material along Boron fibers, whereas p_i and G_i denote the Poisson's ratio and shear modulus of i-phase, respectively. In this way, the strain-stress law in principal, 1-, 2- and 3-directions of composite material (Fig. 1), is expressed by:

$$\begin{pmatrix} \epsilon_{11} \\ \epsilon_{22} \\ \epsilon_{33} \\ \epsilon_{23} \\ \epsilon_{13} \\ \epsilon_{12} \end{pmatrix} = \begin{pmatrix} S_{11} & S_{12} & S_{13} & 0 & 0 & 0 \\ S_{12} & S_{22} & S_{23} & 0 & 0 & 0 \\ S_{31} & S_{32} & S_{33} & 0 & 0 & 0 \\ 0 & 0 & 0 & S_{44} & 0 & 0 \\ 0 & 0 & 0 & 0 & S_{55} & 0 \\ 0 & 0 & 0 & 0 & 0 & S_{66} \end{pmatrix} \begin{pmatrix} \sigma_{11} \\ \sigma_{22} \\ \sigma_{33} \\ \tau_{23} \\ \tau_{13} \\ \tau_{12} \end{pmatrix} \quad (2)$$

where the elements of the compliance tensor $[S]$ are determined by the elastic properties of the composite in principal directions. For evaluating the stress distribution on the local system O- x,y,z of the beam section, we rotate the tensor $[e_{ij}]$, involved in relation (2), about 3-axis through an angle θ , and we obtain [8, 12-13]:

$$\begin{pmatrix} \sigma_{xx} \\ \sigma_{yy} \\ \sigma_{zz} \\ \tau_{yz} \\ \tau_{xz} \\ \tau_{xy} \end{pmatrix} = \begin{pmatrix} C_{11} & C_{12} & C_{13} & 0 & 0 & C_{16} \\ C_{21} & C_{22} & C_{23} & 0 & 0 & C_{26} \\ C_{31} & C_{32} & C_{33} & 0 & 0 & C_{36} \\ 0 & 0 & 0 & C_{44} & C_{45} & 0 \\ 0 & 0 & 0 & C_{54} & C_{55} & 0 \\ C_{61} & C_{62} & C_{63} & 0 & 0 & C_{66} \end{pmatrix} \begin{pmatrix} \epsilon_{xx} \\ \epsilon_{yy} \\ \epsilon_{zz} \\ \gamma_{yz} \\ \gamma_{xz} \\ \gamma_{xy} \end{pmatrix} \quad (3)$$

Assuming further conditions of beam slenderness [14] in our problem, we have:

$$\sigma_{yy} = \sigma_{zz} = \tau_{yz} = 0 \quad (4)$$

and deleting deformations ϵ_{yy} , ϵ_{zz} and γ_{yz} from stress-strain law (3), we obtain a system of 3 eqs. as follows:

$$\begin{pmatrix} \sigma_{xx} \\ \tau_{xz} \\ \tau_{xy} \end{pmatrix} = \begin{pmatrix} R_{11} & 0 & R_{13} \\ 0 & R_{22} & 0 \\ R_{13} & 0 & R_{33} \end{pmatrix} \begin{pmatrix} \epsilon_{xx} \\ \gamma_{xz} \\ \gamma_{xy} \end{pmatrix} \quad (5)$$

In latter relation the R_{ij} - elements of the stiffness tensor can be determined as functions of the elastic properties and the θ -fiber angle.

4. STRESS FIELDS IN THE COMPOSITE BEAM

For the analysis followed, adopting Sokolnikoff's solution [16] in conjunction with the theory of anisotropic elasticity, we obtain for the twist and warping function, respectively:

$$t_{,x} = \frac{M_x}{D} - \frac{R_{13}}{2R_{33}} w_{,xx} \quad (6)$$

$$W(x,y,z) = \frac{M_x}{D} \varphi(y,z) + \frac{R_{13}}{2R_{33}} [w_{,xx} y z - 2u_{,x} y + v_{,xx} (y^2 - \frac{a^2}{12})] \quad (7)$$

where D and $\varphi(y,z)$ represent the torsional rigidity and two-dimensional torsion function, respectively. The torsional rigidity for an anisotropic rectangular beam is expressed by [7]:

$$D = R_{33} a b^3 \frac{32f^2}{\pi^4} \sum_{j=1,3,5,\dots}^{\infty} \frac{1}{j^4} [1 - \frac{2f}{j\pi} \tanh(\frac{j\pi}{2f})] \quad (8)$$

where

$$f = \frac{a}{b} \sqrt{\frac{R_{22}}{R_{33}}} \quad (9)$$

By inserting rels (8)-(9) into rels (1) and thus the transformed expressions for strains into stress-strain law (5), we obtain for the stresses developed inside the beam:

$$\begin{aligned} \sigma_{xx} &= (R_{11} - \frac{R_{13}^2}{R_{33}}) (u_{,x} - y v_{,xx} - z w_{,xx}) + R_{13} \frac{M_x}{D} (\varphi_{,y} - z) \\ \tau_{xz} &= R_{22} \frac{M_x}{D} (\varphi_{,z} + y) \\ \tau_{xy} &= R_{33} \frac{M_x}{D} (\varphi_{,y} - z) \end{aligned} \quad (10)$$

Furthermore considering the equilibrium conditions at the free-point of the beam and taking into account the symmetry of section with respect to y - and z -axes, we obtain for the warping function:

$$\begin{aligned} W(x,y,z) &= \frac{M_x}{D} [\varphi(y,z) - \frac{R_{13}^2}{2(R_{11}R_{33} - R_{13}^2)} \frac{(I_{zz} - I_{\varphi z})}{I_z} yz] - M_y' \frac{R_{13}}{2(R_{11}R_{33} - R_{13}^2) I_z} \\ &\quad [yz - \frac{I_z}{I_{yy}} (y^2 - \frac{a^2}{12})] \end{aligned} \quad (11)$$

where

$$I_{zz} = \int_S z^2 dS, \quad I_{\varphi z} = \int_S z \frac{\partial \varphi}{\partial y} dS \quad (12)$$

The torsion function $\phi(y,z)$ depends on the elastic properties and the geometry of section and may be expressed in relation to the f -parameter and variable \bar{z} equal to $2z/b$, as follows:

$$\phi(y,z) = z y -$$

$$\frac{8b}{\pi^2} y \sum_{n=1,3,5} \frac{1}{n^2} (-1)^{\frac{n-1}{2}} + \frac{8ba}{\pi^3 f} \sum_{n=1,3,5} (-1)^{\frac{n-1}{2}} \frac{\sin(n\pi \bar{z}/2)}{n^3 \cosh(n\pi f/2)} \sinh(n\pi f y/a) \quad (13)$$

In this way, the stress fields derived by rels (10) are completely determined.

5. RESULTS AND DISCUSSION

The elastic properties of the constituent phases and the composite material including fibers at volume fraction $v_f = 0.4$, which form an angle of 30° are illustrated in Table 1.

E_f (GPa)	400
ν_f	0.2
E_m (GPa)	2.5
ν_m	0.36
E_{11} (GPa)	161.5
E_{22} (GPa)	4.15
$G_{12}=G_{13}$ (GPa)	2.12
G_{23} (GPa)	1.21
$\nu_{13}=\nu_{12}$	0.296
ν_{23}	

Table 1: Elastic properties of the constituent phases and composite.

The elastic properties of the beam material in local, O-xyz ,cartesian system are illustrated normalized vs. θ -angle in Figure 2. These variations obtained are in full agreement with experimental results reported in the literature [12, 15-17].

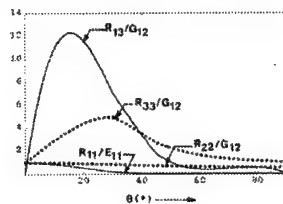


Figure 2: The elastic moduli of composite in local system vs. θ -fiber angle.

Prior studying the stress field, we plot the variation of normalized torsional rigidity, D/D_0 , in relation to the fiber angle, θ , for various aspect ratios, a/b , of the section (Fig. 3). In this figure, D_0 , is the torsional rigidity of a similar beam with Boron fibers parallel to the central axis of the beam. The optimum value of torsional rigidity increases with specified aspect ratio, a/b , and this is due to shear modulus R_{33} of the fiber composite augmented in a similar way (Fig. 2). Fig. 4 illustrates the σ_{xx} -stresses normalized to the respective stress $(\sigma_{xx})_0 = (M_y / I_{yy}) z$, which is developed in an isotropic beam similarly loaded by a bending moment M_y .

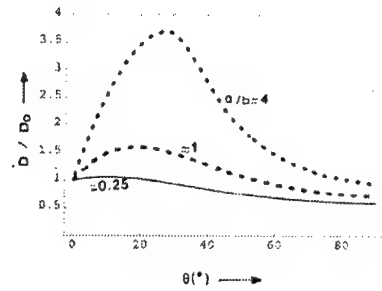


Figure 3: The torsional rigidity, D/D_0 , vs. the fiber angle, θ .

These stresses remain similar at any section of the beam and are plotted for square ($a/b=1$) and rectangular ($a/b=4$) sections. The size of normal stresses

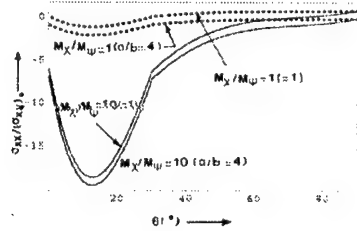


Figure 4: Normal stresses, $\sigma_{xx}/(\sigma_{xx})_0$, vs. fiber-angle, θ , for various torsion-to-bending moments ratio, M_x/M_y .

is strongly affected by the torsion-to-bending moments ratio, M_x/M_y . Fig. 5 illustrates the variation of normalized shear stresses, τ_{xz} and τ_{xy} at the midpoints K and M of the smaller and longer sides of section, respectively. These stresses are plotted normalized to the maximum shear stress, $\max \tau_0$, developed in an isotropic beam of the same configuration,

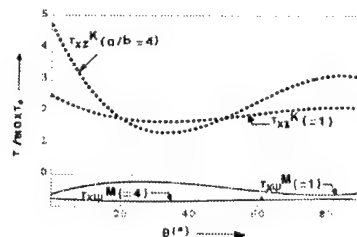


Figure 5: Shear stresses, τ_{xz} and τ_{xy} , at the midpoints K and M of section sides vs. fiber-angle, θ .

which is subjected to similar warping conditions. In view of this figure, it seems that the shear stresses at the midpoint, K, of the smaller section side are significantly higher than the respective stresses appeared in an isotropic beam. This variation of stresses is due to the strong influence of the torsional rigidity, D , rather on stresses τ_{xz} than on stresses τ_{xy} . It

should be referred that the maximum shear stress is not developed at the same point of section in other composite beams including the same fibers, which are differently inclined to the beam axis.

6. CONCLUSIONS

The main conclusions of our analysis are:

- a) The moduli expressing the elastic coupling are significantly influenced by the fiber orientation inside the composite beam.
- b) The torsional rigidity of fiber reinforced beams varies strongly with the aspect ratio of sections.
- c) The normal stresses attain higher absolutely values in beams subjected to pronounced torsion relatively to the bending moment applied.
- d) The maximum shear stress in beams appears at various points of the section depending on its aspect ratio and the anisotropy of the material.

7. REFERENCES

- [1] Mansfield, E. H. and Sobey, A. J., The Fiber Composite Helicopter Blade, Part 1: Stiffness Properties, Part 2: Prospects of Aeroelastic Tailoring, *Aeronautical Q.*, 30, 413- 449, (1979).
- [2] Chang, S. I. and Libove, C, Shear Flows, Strain and Rate of Twist in Single- Cell Thin-Walled Beams with Anisotropic Composite Walls: Simple Theory Compared with Nastran and Experiment", in *ASME Winter Annual Meeting Proc.*, Chicago, Il.,27 November-2 December, 49-70, (1988).
- [3] Libove, C., Stresses and Rate of Twist in Single-Cell Thin-Walled Beams with Anisotropic Walls, *AIAA Jnl.*, Vol. 26, pp. 107-118, (1988).
- [4] Librescu, L. and Song, O., Behaviour of Thin-Walled Beams Made of Advanced Composite Materials and Incorporating non-Classical Effects, *Appl. Mech. Rev.*, 44(11), 30-53, (1991).
- [5] Schmidt, R. and Librescu, L., Further Results Concerning the Refined Theory of Anisotropic Laminated Composite Plates, *Jnl of Engineering Mathematics*, 13, 407-425, (1994).
- [6] Song, O. and Librescu, L., Dynamic Refined Theory of Thin-Walled Beams of Open-Cross Sections,in *ASME Winter Annual Meeting Proc.*, New Orleans, LA, 28 November-3 December, 233-240, (1993).
- [7] Lekhnitskii, S.G., *Theory of Elasticity of an Anisotropic Elastic Body*, Holden-Day Inc.,San Francisco, (1963).
- [8] Hull, D. and Clyne, T. W., *An Introduction to Composite Materials*, 2nd edition, Cambridge University Press, (1996).
- [9] Spencer, A., The Transverse Moduli of Fibre Composite Material, *Comp. Sci. and Technology*, 27, 93-109, (1986).
- [10] Halpin, J. C. and Tsai, S. W., Environmental Factors in Composite Design, *Technical Report: Air Force Materials Laboratory AFML-TR-67- 423* , (1967).
- [11] Nye, J. F., in *Physical Properties of Crystals-Their Representation by Tensors and Matrices*", Clarendon: Oxford, (1985).
- [12] Jones, R. M., *Mechanics of Composite Materials*, McGraw-Hill Kogakusha co., (1975).
- [13] Reuter, R. C.,Coincise Property Transformation Relations for an Anisotropic Lamina, *Jnl of Comp. Mats* ,4, 270-272, (1971).
- [14] Sokolnikoff, I. S., *Mathematical Theory of Elasticity*, 2nd edition, McGraw-Hill Co., (1956).

- [15] Hashin, Z., Analysis of Composite Materials- A Survey, Trans. ASME, Jnl of Appl. Mech, 50, 481-505, (1983).
- [16] Pipes, R. B. and Cole, B. W., On the off-Axis Strength Test for Anisotropic Materials, Journal of Composite Materials,2, 246-256, (1973).
- [17] Jones, R. M., Stiffness of Orthotropic Materials and Laminated Fiber-Reinforced Composites, AIAA Jnl ,2, 112-114, 1974).

6th National Congress on Mechanics

Session B

Volume II

ON THE POTENTIAL REPRESENTATIONS FOR POLYADICS AND ANISOTROPIC MEDIA

George Dassios

Division of Applied Mathematics, Department of Chemical Engineering
University of Patras and ICEHT/FORTH, GR-265 00 Patras, Greece

1. SUMMARY

Helmholtz, in his celebrated paper on vortex motion published in 1858, introduced his famous representation that allows decomposing any smooth vector field in terms of an irrotational and a solenoidal field. In fact, the irrotational part is expressed in terms of a scalar potential and the solenoidal part is expressed in terms of a vector potential. The implications of this decomposition to Theoretical Physics and in particular to Mechanics are immense. In order to appreciate just one component of the contribution of Helmholtz's decomposition theorem to Mechanics it is enough to consider studying elastic wave propagation without reference to the decomposition of the displacement field into longitudinal and transverse waves [3].

In the present work, two principal generalizations of the Helmholtz theorem are reported. The first one concerns potential decomposition of polyadics (tensor products) of any rank and the second one refers to potential decomposition of vector fields that describe anisotropic media. In the first place it is shown that a polyadic of the n -th rank can be expanded into $n + 1$ terms, each one of which involves a potential that is a polyadic of some rank between the zeroth and the n -th. As we move from terms involving potentials of higher rank to terms involving potentials of lower rank the tensorial character of the terms is taken up by iterative applications of the gradient operator. The special case of a first rank tensor recovers the Helmholtz decomposition theorem. The importance of this generalization, as it is applied mainly to dyadic fields, is obvious. As far as anisotropic media are concerned it is shown that the anisotropic response of the medium can be incorporated into a dilation and a rotation of the gradient operator via contraction with a positive definite symmetric dyadic. Then, a sequence of identities relating the above type of deformed gradients leads to potential representation of any vector field that lives within an anisotropic environment. The implication of this type of generalization to Continuum Mechanics is under current investigation, where an elegant way to deal with anisotropy is furnished.

2. DECOMPOSITION OF POLYADICS

A polyadic $\mathbf{F}^{(n)}$ of the n th rank is a tensor product of n vector spaces [1,6]. In fact, if

$$\mathbf{B} = \{\hat{\mathbf{x}}_1, \hat{\mathbf{x}}_2, \dots, \hat{\mathbf{x}}_d\} \quad (1)$$

denotes a Cartesian orthonormal basis of a vector space with dimension $d \in \mathbb{N}$ then a representation of $\mathbf{F}^{(n)}$ with respect to the basis \mathbf{B} is furnished by the expression

$$\mathbf{F}^{(n)} = \sum_{i_1=1}^d \sum_{i_2=1}^d \cdots \sum_{i_n=1}^d f_{i_1 i_2 \cdots i_n} \hat{\mathbf{x}}_{i_1} \otimes \hat{\mathbf{x}}_{i_2} \otimes \cdots \otimes \hat{\mathbf{x}}_{i_n} \quad (2)$$

For $n=0$ we have a scalar function, for $n=1$ we obtain a vector function, for $n=2$ we deal with a matrix function and so on.

In particular, the vector function

$$\mathbf{F}^{(1)} = \mathbf{f} \quad (3)$$

enjoys the celebrated Helmholtz decomposition theorem [2,7,8]

$$\mathbf{f} = \nabla \Phi + \nabla \times \mathbf{A} \quad (4)$$

where Φ is a scalar potential which generates the irrotational part $\nabla \Phi$ of \mathbf{f} and \mathbf{A} is the vector potential which gives rise to the solenoidal part $\nabla \times \mathbf{A}$ of \mathbf{f} . Furthermore, the gauge condition

$$\nabla \cdot \mathbf{A} = 0 \quad (5)$$

ensures that only two of the three components of \mathbf{A} are independent and therefore the three components of $\mathbf{f} = (f_1, f_2, f_3)$ are representable by the potential function Φ and two out of the three components of \mathbf{A} .

Using techniques from vector and dyadic analysis it is possible to show that for the case of a dyadic the decomposition (4) is generalized to

$$\mathbf{F}^{(2)} = \nabla \otimes \nabla \Phi + \nabla \otimes \nabla \times \mathbf{A} + \nabla \times \nabla \times \mathbf{B}^{(2)} \quad (6)$$

where Φ is a scalar, \mathbf{A} is a vector and $\mathbf{B}^{(2)}$ is a dyadic potential [4]. Hence, a dyadic field can be represented as the (gradient) \otimes (gradient) of a scalar, plus the (gradient) \otimes (rotation) of a vector, plus the (rotation) \times (rotation) of a dyadic. It is observed that in the first (the scalar) term the double vectorial character is provided by the two gradient operators, in the second (the vector) term one vectorial character is furnished by the gradient operator and the other by the vector potential itself, and in the last (the dyadic) term the dyadic potential carries all the double vectorial character of the term.

The number of components of the dyadic field $\mathbf{F}^{(2)}$ is d^2 , while the number of components for the three potentials are $1 + d + d^2$. The gauge conditions that will reduce the number of independent potentials to d^2 are given by the d equations

$$\nabla \cdot \mathbf{B}^{(2)} = 0 \quad (7)$$

and the single equation

$$\nabla \otimes \nabla : \mathbf{B}^{(2)} = 0 \quad (8)$$

A little extra work leads to the general decomposition

$$\begin{aligned} \mathbf{F}^{(n)} = & \nabla \otimes \nabla \otimes \dots \otimes \nabla \mathbf{P}_0 \\ & + \nabla \otimes \nabla \otimes \dots \otimes \nabla \times \mathbf{P}_1^{(1)} \\ & + \nabla \otimes \nabla \otimes \dots \otimes \nabla \times \nabla \times \mathbf{P}_2^{(2)} \\ & \\ & + \nabla \otimes \nabla \times \dots \times \nabla \times \mathbf{P}_{n-1}^{(n-1)} \\ & + \nabla \times \nabla \times \dots \times \nabla \times \mathbf{P}_n^{(n)} \end{aligned} \quad (9)$$

with the Gauge conditions

$$\nabla \cdot \mathbf{P}_n^{(n)} = \mathbf{0}^{(n-1)} \quad (10)$$

$$\nabla \otimes \nabla : \mathbf{P}_n^{(n)} = \mathbf{0}^{(n-2)} \quad (11)$$

$$\nabla \otimes \dots \otimes \nabla \otimes \mathbf{P}_n^{(n)} = 0 \quad (12)$$

where the symbol \textcircled{n} stands for n successive contractions.

Once the conditions (10)-(12) are considered, the total number of independent components of the polyadic potentials $P_0, P_1^{(1)}, \dots, P_n^{(n)}$ are d^n , exactly as the number of components of the polyadic field $F^{(n)}$.

3. ANISOTROPIC HELMHOLTZ DECOMPOSITION

Next we restrict our attention to the case of a vector field (polyadic of rank one) in \mathbb{R}^3 and define the S-gradient operator by

$$\nabla_s = \tilde{S} \cdot \nabla \quad (13)$$

where \tilde{S} is a symmetric positive definite real matrix (dyadic). It can be shown that

$$\nabla_s = \begin{pmatrix} s_1 \frac{\partial}{\partial s_1} \\ s_2 \frac{\partial}{\partial s_2} \\ s_3 \frac{\partial}{\partial s_3} \end{pmatrix} \quad (14)$$

where s_1, s_2, s_3 are three positive real number and the three differentiations $\frac{\partial}{\partial s_1}, \frac{\partial}{\partial s_2}$ and $\frac{\partial}{\partial s_3}$ represent three directional derivatives along the three orthogonal directions $\hat{s}_1, \hat{s}_2, \hat{s}_3$. All these are consequences of the fact that \tilde{S} is symmetric and positive definite which secures that it has three real and positive eigenvalues occurring along three orthogonal directions. In contrast to ∇ which represents three orthogonal differentiations of the same weight, the S-gradient ∇_s incorporates three orthogonal differentiations of different weight. Hence, anisotropy enters the scheme in a natural way. The basis of our representation is buried within the identity

$$(\nabla_s \cdot \nabla_T) \mathbf{h} = \nabla_T \nabla_s \cdot \mathbf{h} - \nabla_s \times (\nabla_T \times \mathbf{h}) \quad (15)$$

where

$$\nabla_s = \tilde{S} \cdot \nabla \quad (16)$$

$$\nabla_T = \tilde{T} \cdot \nabla \quad (17)$$

and \tilde{S}, \tilde{T} are any symmetric positive definite matrices [5]. In view of (14) and the relative representations

$$\nabla_T = \begin{pmatrix} \tau_1 \frac{\partial}{\partial \tau_1} \\ \tau_2 \frac{\partial}{\partial \tau_2} \\ \tau_3 \frac{\partial}{\partial \tau_3} \end{pmatrix} \quad (18)$$

we define the ST-Laplacian as

$$\nabla_s \cdot \nabla_T = \sum_{i=1}^3 s_i \tau_i \frac{\partial^2}{\partial \tau_i \partial s_i} \quad (19)$$

which for $\tilde{S} = \tilde{T}$ reads as

$$\nabla_s \cdot \nabla_s = \sum_{i=1}^3 s_i^2 \frac{\partial^2}{\partial s_i^2} \quad (20)$$

and for $\tilde{S} = \tilde{T} = \tilde{I}$ degenerates to

$$\nabla_1 \cdot \nabla_1 = \sum_{i=1}^3 \frac{\partial^2}{\partial s_i^2} = \Delta \quad (21)$$

and recovers the isotropic Laplacian.

Obviously the $\hat{\mathbf{t}}_1, \hat{\mathbf{t}}_2, \hat{\mathbf{t}}_3$ basis does not, in general, coincide with the $\hat{\mathbf{s}}_1, \hat{\mathbf{s}}_2, \hat{\mathbf{s}}_3$ basis.

Denoting by

$$\Phi(\mathbf{r}) = \nabla_s \cdot \mathbf{h}(\mathbf{r}) \quad (22)$$

the scalar S-potential and by

$$\mathbf{A}(\mathbf{r}) = -\nabla_T \times \mathbf{h}(\mathbf{r}) \quad (23)$$

the vector T-potential, formula (15) is written as

$$(\nabla_s \cdot \nabla_T) \mathbf{h}(\mathbf{r}) = \nabla_T \Phi(\mathbf{r}) + \nabla_s \times \mathbf{A}(\mathbf{r}). \quad (24)$$

Consequently, if \mathbf{h} is a solution of the ST-poisson equation

$$(\nabla_s \cdot \nabla_T) \mathbf{h} = \mathbf{f} \quad (25)$$

then we arrive at the representations

$$\mathbf{f}(\mathbf{r}) = \nabla_T \Phi(\mathbf{r}) + \nabla_s \times \mathbf{A}(\mathbf{r}) \quad (26)$$

where Φ and \mathbf{A} are given by (22) and (23) respectively.

It can also be shown that the gauge condition is written as

$$\nabla_T \cdot \mathbf{A}(\mathbf{r}) = 0. \quad (27)$$

Taking into consideration the fact that the importance of the classical Helmholtz decomposition relies with the fact that it expresses a base-dependent field in an isotropic medium in terms of invariant irrotational and solenoidal quantities, it is obvious that the generalized decomposition theorem (26) resumes the corresponding importance for general anisotropic media.

4. REFERENCES

- [1] Brand, L., *Vector and Tensor Analysis*, New York: London, Wiley (1947).
- [2] Ciarlet, P., A decomposition of $L^2(\Omega)^3$ and an application to magnetostatic equations, *Math. Mod. Meth. Appl. Sci.*, 3, (1993) 289-301.
- [3] Dassios, G. and Kleinman, R., *Low frequency scattering*, Oxford University Press (2000).
- [4] Dassios, G. and Lindell, V. I., On the Helmholtz decomposition for polyadics, *Quarterly of Applied Mathematics* (to appear).

- [5] Dassios, G. and Lindell, V. I., Generalized Helmholtz decomposition and static electromagnetics, *Journal of Electromagnetic Waves and Applications*, Vol.14, (2000) 1415-1428.
- [6] Lindell, I. V., *Methods for Electromagnetic Field Analysis*, 2nd ed., Oxford University Press (1995).
- [7] Tai, C. T., Generalized Vector and Dyadic Analysis 72, *IEEE Press*, New York (1992).
- [8] Wills, A. P., Vector Analysis with an Introduction to Tensor Analysis, *Dover, New York*, (1958).

THE APPLICATION OF NOTHER'S THEOREM TO NON-LINEAR ANISOTROPIC ELASTIC MATERIALS

Jovo Jaric

University of Belgrade, Faculty of mathematics, Department of mechanics,
11000 Belgrade, Studentski trg 16, Yugoslavia

Kikuo Kishimoto

Tokyo Institute of Technology,
Department of Mechanical and Intelligent Systems Engineering, Japan

Tiejun Wang

Xi'an Jiaotong University, Department of Engineering Mechanics, China

Masaki Omiya

Tokyo Institute of Technology
Department of Mechanical and Intelligent Systems Engineering, Japan

1. SUMMARY

The known isotropic tensor function representations can be used to immediately yield representations for anisotropic tensor functions. Making use of this concept we are able to derive conservation laws for all classes of nonlinear anisotropic materials in the same way as we do for isotropic materials. More precisely, we approach the problem of conservation laws for anisotropic materials using Noether's theorem as we do for isotropic nonlinear materials.

2. INTRODUCTION

Since the paper of Knowles and Sternberg (1972), a huge number of papers were published in connection with application of Noether's theorem to the problem of conservation laws, and particularly to the path-independent integrals. Almost all of them were dealing with anisotropic materials. Very recently, new method has been applied to this problem. This method is known under the name Stroh formalism, and has been used very successfully for different problems for linear anisotropic materials. Therefore, this method is limited to the linear anisotropic materials. But non-linear constitutive relations of materials play an increasing important and key role in contemporary theoretical and applied mechanics.

The problem how to represent anisotropic tensor functions, i.e. how to deal with constitutive equations of anisotropic materials, was pushed a head by the papers of Boehler (1978, 1979). In these works the elegant concept of anisotropic tensors (Smith and Rivlin, 1957a) or structural tensors (Lokhin and Sedov, 1963; Sedov and Lokhin 1963, Boehler, 1978, 1979) which characterize the anisotropy was extended to join the so called principle of isotropy of space that an anisotropic tensor function is expressible as an isotropic one with the structural

tensors as the additional tensor agencies (see also Liu, 1982). Thus, the known isotropic tensor function representations can be used to immediately yield representations for anisotropic tensor functions (see, for example, Boehler and Raclin, 1977; Boehler 1977; Liu 1982; Spencer 1982; Boehler, 1987b). Along this line, constitutive laws of transversely isotropic, orthotropic and clinotropic materials for complex irreversible mechanical phenomena such as yielding, failure, creep and damage are well formulated, as described for instance in the articles by Boehler (1982; 1985a; 1987a; 1990; 1993) and Betten (1990; 1991).

Making use of this concept we are able to derive conservation laws for some classes (for all, Xsiao, 1995) of nonlinear anisotropic materials in the same way as we do for isotropic materials. More precisely, we may approach the problem of conservation laws for anisotropic materials using Noether's theorem as we do for isotropic nonlinear materials. It is the aim of this paper.

2. ANISOTROPIC FUNCTIONS RELATIVE TO $O(3)$

Here we give some facts concerning constitutive equations of anisotropic functions. For details we refer to [1], [2].

In most cases, mainly for solid materials, material symmetry groups are provided by the 3-dimensional orthogonal subgroups, including the full and proper orthogonal groups [3]. The usually known isotropic functions are the tensor functions possessing invariance under the full orthogonal group $O(3)$. The tensor functions possessing invariance under the proper subgroups of $O(3)$ are called anisotropic functions. General aspects of representation of anisotropic functions for most anisotropic functions remain open. The existing results for representation of anisotropic functions, except those for polynomial functions, were derived mainly from the method of isotropic extension. The essential idea of this method is to introduce some unit vectors $\mathbf{m}_1, \dots, \mathbf{m}_n$, and some second order

tensors $\mathbf{M}_1, \dots, \mathbf{M}_b$, called *structural tensors*, to characterize the material symmetry group and then to extend anisotropic functions to isotropic functions with extended arguments. As a result, representation problems for the former can be reduced to those for the latter and hence the well-known results for isotropic functions can be used to derive the desired results for anisotropic functions.

Formally, let R be the reals, V be a 3-dimensional Euclidean space and $L(V)$ be the space of second order tensors. We use the following abbreviations: $\mathbf{v} = (\mathbf{v}_1, \dots, \mathbf{v}_p)$, $\mathbf{A} = (\mathbf{A}_1, \dots, \mathbf{A}_q)$, where $\mathbf{v}_i \in V$ and $\mathbf{A}_i \in L(V)$. Let g be the group which preserves the symmetric characteristics of material, i.e.

$$g = \{Q \in G, Q\mathbf{m} = \mathbf{m}, Q\mathbf{M}Q^T = \mathbf{M}\}, \quad (1)$$

where $G \subset O(3)$. Thus, g is characterized by the set $\{\mathbf{m}, \mathbf{M}\}$ and the group $G \subset O(3)$ and therefore we write simply $g = (G; \mathbf{m}, \mathbf{M})$. The abbreviations introduced above stand also for \mathbf{m} and \mathbf{M} .

Theorem [1]: A function f is invariant relative to g if and only if it can be represented by

$$f(\mathbf{v}, \mathbf{A}) = \hat{f}(\mathbf{v}, \mathbf{A}, \mathbf{m}, \mathbf{M}), \quad (2)$$

where \hat{f} is invariant relative to G .

The function f is either scalar-valued, vector-valued or tensor-valued function.

Then making use of this theorem Liu [1] find g for some crystal classes. Here we list some of them having $O(3)$ as the group of symmetry:

Transverse isotropy

$$g_1 = (O(3); \mathbf{n}_1, N_1), \quad g_2 = (O(3); \mathbf{n}_1), \quad g_3 = (O(3); N_1), \quad g_5 = (O(3); \mathbf{n}_1 \otimes \mathbf{n}_1),$$

Orthotropy

$$g_6 = (O(3); \mathbf{n}_1 \otimes \mathbf{n}_1, \mathbf{n}_2 \otimes \mathbf{n}_2),$$

Triclinic system

$$g_7 = (O(3); \mathbf{n}_1, \mathbf{n}_2, \mathbf{n}_3),$$

Monoclinic system

$$g_9 = (O(3); \mathbf{n}_1, \mathbf{n}_2),$$

Rhombic system

$$g_{12} = (O(3); \mathbf{n}_1, \mathbf{n}_2 \otimes \mathbf{n}_2)$$

and so on, where $(\mathbf{n}_1, \mathbf{n}_2, \mathbf{n}_3)$ are orthonormal set and N_i is skew-symmetric tensor associated with \mathbf{n}_i , i.e. $\langle N_i \rangle = \mathbf{n}_i$.

3. ANISOTROPIC ELASTIC MATERIALS

From the last section we see that some classes of anisotropic materials can be characterized by isotropic function

$$\varepsilon(F, \mathbf{m}, M),$$

where $F = \nabla \mathbf{x}$ is deformation gradient. Here we identify \hat{f} with the internal energy density ε . Then the material symmetry requires that

$$\varepsilon(FQ, Q\mathbf{m}, QMQ^T) = \varepsilon(F, \mathbf{m}, M) \quad (4)$$

for any $Q \in O(3)$, and, hence the following relation holds

$$e_{ABC} \left(x_{k,A} \frac{\partial \varepsilon}{\partial x_{k,B}} + \frac{\partial \varepsilon}{\partial m_A} \cdot m_B + \frac{\partial \varepsilon}{\partial M_{AD}} \cdot M_{BD} \right) = 0. \quad (5)$$

In addition to (4) material frame-indifference requires

$$e_{klm} \frac{\partial \varepsilon}{\partial x_{k,B}} x_{l,B} = 0. \quad (6)$$

In (5) and (6), for the sake of generality, we used the special x_k and material coordinates X_K , respectively. We write also the material form of balance law of momentum, in the absence of body force, i.e.

$$\nabla \cdot \mathbf{T} = \rho_o \ddot{\mathbf{x}}, \quad (7)$$

where

ρ_o - mass density in the reference configuration,

$\mathbf{T} = (T_{kk})$ - Piola - Kirchhoff stress tensor, $\mathbf{T} = \rho_o \partial_F \varepsilon$.

Now, let

$$L(\mathbf{F}, \dot{\mathbf{x}}, \mathbf{m}, \mathbf{M}) = \rho_v \left(\varepsilon - \frac{1}{2} \dot{\mathbf{x}} \cdot \dot{\mathbf{x}} \right), \quad (8)$$

$\mathbf{m}, \mathbf{M} = \text{const.}$

Then the balance law (7) may be written as

$$\nabla \cdot \partial_F L = 0, \quad (9)$$

since $\partial_x L = 0$.

Further we set $\xi = (\mathbf{X}, t)$. We distinguish the partial derivative $\partial_\xi = (\partial_{\xi^\alpha})$ from the

$$\text{total derivative } \nabla = \left(\frac{d}{d\xi^\alpha} \right) = (\cdot, \alpha).$$

4. THE APPLICATION OF MODIFIED NOETHER'S THEOREM

We refer to [4] for the derivation of modified Noether's theorem. Here we follow the same procedure and the same notation. Thus

$$\Psi = \mathbf{x}, \quad \nabla \Psi = \nabla x(x_{k,\alpha}),$$

but

$$\omega = (\mathbf{m}, \mathbf{M}), \quad \nabla \omega = 0$$

because of (8)₂. This requirement is justified on physical background. We also write $\zeta = (\mathbf{n}, \mathbf{N})$. Then (3.14) in [4] becomes

$$L_{\alpha,\alpha} + \partial_{\Psi_\alpha} L \cdot (\Phi_{k,\alpha} - \Psi_{\beta,\alpha} \varphi_{\beta,\alpha}) + \partial_\omega L \cdot \zeta = 0$$

since $\partial_\Psi L = \partial_{\omega,\alpha} L = 0$. Having in mind the conditions (5) and (6) which must be satisfied by ε , and utilizing the method of Lagrange multipliers we write the above equation in the following form

$$\begin{aligned} & L_{\alpha,\alpha} + \frac{\partial \varepsilon}{\partial x_{k,\alpha}} (\Phi_{k,\alpha} - x_{k,\beta} \varphi_{\beta,\alpha}) + \frac{\partial \varepsilon}{\partial \mathbf{m}_K} \cdot \mathbf{n}_K + \frac{\partial \varepsilon}{\partial \mathbf{M}_{KL}} \cdot \mathbf{N}_{KL} - e_{klm} \frac{\partial \varepsilon}{\partial x_{k,B}} x_{l,B} \lambda_m - \\ & - e_{ABC} \left(x_{k,A} \frac{\partial \varepsilon}{\partial x_{k,B}} + \frac{\partial \varepsilon}{\partial \mathbf{m}_A} \cdot \mathbf{m}_B + \frac{\partial \varepsilon}{\partial \mathbf{M}_{AB}} \cdot \mathbf{M}_{BD} - \frac{\partial \varepsilon}{\partial \mathbf{M}_{DB}} \cdot \mathbf{M}_{DA} \right) \Lambda_C = 0. \end{aligned} \quad (10)$$

The Lagrange multipliers λ and Λ are, generally, functions of $(\mathbf{F}, \dot{\mathbf{x}}, \mathbf{m}, \mathbf{M})$. Now we

postulate that (10) must be satisfied for any ε , $\partial_F \varepsilon$, $\partial_m \varepsilon$, $\partial_M \varepsilon$, i.e. it must hold for any "isotropic" material. Then by standard but very long procedure, from (10) we obtain

$$\varphi_K = e_{KLM} X_L A_M + C_K,$$

$$\varphi_4 = A$$

$$\Phi_k = e_{klm} x_l a_m + c_k \quad (11)$$

$$\mathbf{n}_A = e_{ABC} \mathbf{m}_B A_C$$

$$\mathbf{N}_{KL} = (e_{KAB} \mathbf{M}_{AL} + e_{LAB} \mathbf{M}_{KA}) A_B,$$

where (A, A, C, a, c) are arbitrary constants.

5. CONSERVATION LAWS

By taking all of arbitrary constants c , a , A , C , A zero except one, in turn, we obtain the corresponding conservation law. Thus, as in classical case, there are five conservation laws. The first three belong to the case of spatial invariance. They are balance of momentum, balance of moment of momentum and balance of energy. The case of material invariance is more important, particularly for fracture mechanics. They are

Conservation of linear material momentum

$$\frac{d}{dt} \int_V \rho_0 \dot{\mathbf{x}} \mathbf{F} dV + \int_S \left[\rho_0 \left(\boldsymbol{\varepsilon} - \frac{1}{2} \dot{\mathbf{x}} \cdot \dot{\mathbf{x}} \right) \mathbf{I} - \mathbf{F}^T \mathbf{T} \right] \mathbf{N} dS = 0, \quad (12)$$

Conservation of angular material momentum

$$\begin{aligned} \frac{d}{dt} \int_V \rho_0 \mathbf{X} \times \dot{\mathbf{x}} \mathbf{F} dV + \int_S \mathbf{X} \times \left[\rho_0 \left(\boldsymbol{\varepsilon} - \frac{1}{2} \dot{\mathbf{x}} \cdot \dot{\mathbf{x}} \right) \mathbf{I} - \mathbf{F}^T \mathbf{T} \right] \mathbf{N} dS - \\ - \int_V \left(\frac{\partial \boldsymbol{\varepsilon}}{\partial \mathbf{m}} \cdot \mathbf{x} \mathbf{m} + \frac{\partial \boldsymbol{\varepsilon}}{\partial \mathbf{M}} \cdot \mathbf{x} \mathbf{M}^T - \mathbf{M}^T \times \frac{\partial \boldsymbol{\varepsilon}}{\partial \mathbf{M}_{DB}} \right) dV = 0. \end{aligned} \quad (13)$$

Note. If we consider static problem then (12) becomes

$$\int_S \left(\rho_0 \boldsymbol{\varepsilon} \mathbf{I} - \mathbf{F}^T \mathbf{T} \right) \mathbf{N} dS = 0. \quad (14)$$

This was the starting point of Gurtin and his collaborators. Moreover, since they did not assume anything in connection with functional dependence of $\boldsymbol{\varepsilon}$ then they conclude that Eshelby's energy momentum tensor, the left side of (14), holds for all materials and in all ranges of their behavior, i.e. for elastic, plastic viscous as well as intermediate range.

6. REFERENCES

- [1] Liu, I. S.: On representations of anisotropic invariants, *Int. J. Eng. Sci.*, 20 (1982), 267-277
- [2] Xiao, H. : Isotropic extension of anisotropic tensor functions, *ZAMM*. 76, (1996) 4, 204-214
- [3] Spencer, A. J. M.: *Theory of Invariants*, In: Eringen, A. C. (ed.) *Continuum Physics*. Vol. I. Academic Press, New York, 1971, pp. 239-353
- [4] Jaric, J., J-integral and Inverse Noether's Theorem in Fracture Mechanics, *Solid Mechanics*, Scientific Meeting of the Serbian Academy of Sciences and Arts, Second Serbian-Greek Symposium on Solid Mechanics (1997).

MICROMECHANICAL MODELING OF THE BEHAVIOR OF POROUS SHAPE MEMORY ALLOYS

D. C. Lagoudas

Department of Aerospace Engineering, Texas A&M University
College Station, TX 77843-3141 USA

P. B. Entchev

Department of Aerospace Engineering, Texas A&M University
College Station, TX 77843-3141 USA

1. SUMMARY

A micromechanics-based model for the behavior of porous shape memory alloys (SMAs) is presented in this work. The porous SMA is modeled as a two-phase composite with SMA matrix and elastic inhomogeneities, which in the limit represent pores. The Mori-Tanaka averaging technique is used to derive the strain concentration factors. Different cases of random orientation of pores are investigated to be able to accurately model actual pore geometries.

2. INTRODUCTION

Over the last decade shape memory alloys (SMAs) [1] have attracted large interest in various fields of applications. The use of SMAs has promoted extensive research on developing SMA constitutive models. Different researchers have used two different modeling approaches: micromechanics-based and phenomenological. A micromechanics-based model based on the analysis of phase transformation in single crystals of copper-based SMAs has been presented by Patoor et al. [2]. Another micromechanical model for SMAs capturing different effects of SMA behavior such as superelasticity, shape memory effect and rubber-like effect has been presented by Sun and Hwang [3, 4]. Tanaka [5], Liang and Rogers [6], Brinson [7] and Boyd and Lagoudas [8] have presented phenomenological constitutive models. Another model describing solids with trilinear stress-strain response has been proposed by Abeyaratne and Knowles [9]. Recently Birman [10] reviewed the existing constitutive models.

A relatively new area of applications utilizing the properties of SMAs is the area of *active* composites [11]. The design of these composites involves embedding SMA elements in the form of wires, short fibers, strips or particles into a matrix material. Then, controlling the phase transformation of the SMA inclusions through heating or cooling allows to control the overall behavior of the composite and change its macroscopic properties. Both fabrication and modeling of SMA-based active composite materials have been the subject of a number of research papers.

A form of an active composite is an SMA matrix with pores of different shape, size and orientation. Driven by biomedical applications recently emphasis has been given to *porous* SMAs. Russian and Chinese scientists have reported initial progress in manufacturing and

testing of these new materials. Fabrication techniques for producing porous NiTi have also been established in the US [12, 13]. It is envisioned that this new material will find applications in the field of medicine as well as in various energy absorption devices and mechanisms.

In a previous work two methods for modeling of porous NiTi SMAs - one based on the unit cell Finite Element Method and the second using the incremental Mori-Tanaka averaging scheme - have been presented [14]. The effective stress-strain response has been obtained for various loading paths and different values of porosity (pore volume fractions) as well as for two different pore shapes - cylindrical and spherical. The results of both methods were found to be in good agreement.

The current work continues with further investigation of the incremental averaging method. One of the objectives of this work is to investigate the effect of different pore geometries on the effective behavior. Motivated by micrographs of porous NiTi specimens (see Figure 1) random distribution of pores is considered in this work. Thus the current establishes a macroscopic constitutive model for the porous SMA material using the properties of the dense SMA and information about pore shape, volume fraction as well as given pore orientation. Analytical expressions for the overall elastic and tangent stiffness of the porous SMA material are derived and an evolution equation for the overall transformation strain is also derived. The properties of the porous SMA material are obtained by using the constitutive model for dense SMA to model the matrix and treating the inhomogeneities as elastic phases with stiffness equal to zero. The modeling results are compared with recently obtained experimental data on binary NiTi porous SMAs.

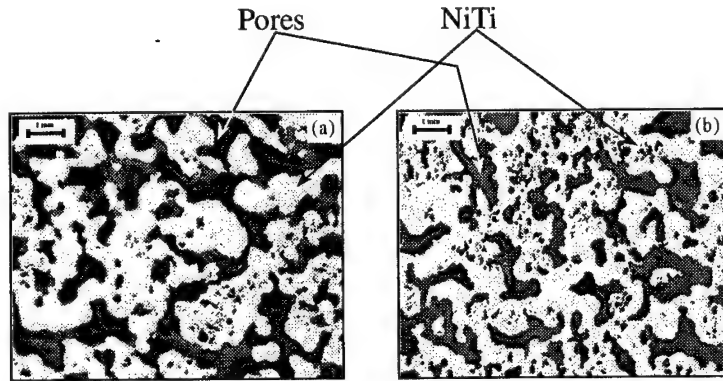


Figure 1: Micrographs of a porous NiTi SMA specimen: (a) transverse cut; (b) axial cut

3. DERIVATION OF A CONSTITUTIVE MODEL FOR A COMPOSITE WITH SMA MATRIX AND ELASTIC INHOMOGENEITIES

The development of the model starts by considering a composite material with an SMA matrix and elastic inhomogeneities. Let the Cauchy stress in the matrix be denoted by σ^m , the linearized strain be ϵ^m and the transformation strain be ϵ^m . The matrix is characterized by its elastic stiffness \mathbf{L}^m (compliance $\mathbf{M}^m = (\mathbf{L}^m)^{-1}$) and tangent stiffness \mathbf{T}^m . Similarly, let the stress in the inhomogeneities be σ^i and the strain be ϵ^i . The inhomogeneities are characterized by the elastic stiffness \mathbf{L}^i (compliance $\mathbf{M}^i = (\mathbf{L}^i)^{-1}$). Let the volume fraction of the matrix phase be c^m and the volume fraction of the inhomogeneities be $c^i = 1 - c^m$. The

composite is characterized by its effective elastic stiffness \mathbf{L} , tangent stiffness \mathbf{T} and effective stress, strain and transformation strain Σ , \mathbf{E} and \mathbf{E}^t .

In this work the matrix will be the SMA, which will be modeled by a rate-independent constitutive model. One of the characteristics of SMAs is the change in the elastic stiffness with phase transformation, in addition to the inelastic strain induced by the martensitic phase transformation. The rate form of the constitutive equation for the matrix is therefore given by

$$\dot{\sigma}^m = \mathbf{L}^m : (\dot{\epsilon}^m - \dot{\epsilon}^{*m}), \quad (1)$$

where $\dot{\epsilon}^{*m}$ reflects the change of the elastic stiffness during transformation and is given by

$$\dot{\epsilon}^{*m} \equiv \dot{\epsilon}^m + \dot{\mathbf{M}}^m : \sigma^m. \quad (2)$$

The rate form of the constitutive equations for the inhomogeneities is given by

$$\dot{\sigma}^i = \mathbf{L}^i : \dot{\epsilon}^i. \quad (3)$$

The macroscopic constitutive law for the SMA composite is written as

$$\Sigma = \mathbf{L} : (\mathbf{E} - \mathbf{E}^t), \quad (4)$$

where Σ and \mathbf{E} are the overall stress and strain tensors and \mathbf{E}^t is the macroscopic transformation strain. An alternative formulation using stress and strain rates and the overall tangent stiffness is given by

$$\dot{\Sigma} = \mathbf{T} : \dot{\mathbf{E}}. \quad (5)$$

To connect the macroscopic stress and strain rates to the respective microscopic ones the following *instantaneous* strain and stress concentration factors $\mathbf{A}(\mathbf{x})$ and $\mathbf{B}(\mathbf{x})$ are defined as (assuming that the local strain is driven by the macroscopic strain):

$$\dot{\epsilon} = \mathbf{A}(\mathbf{x}) : \dot{\mathbf{E}}, \quad \dot{\sigma} = \mathbf{B}(\mathbf{x}) : \dot{\Sigma}. \quad (6)$$

Using the constitutive equations for the phases and the concentration factors given by equation (6) the following expressions for the overall elastic stiffness \mathbf{L} , tangent stiffness \mathbf{T} and the evolution of the overall transformation strain \mathbf{E}^t are derived:

$$\mathbf{L} = c^m \mathbf{L}^m \mathbf{A}^{el,m} + \{\mathbf{L}^i \mathbf{A}^{el,i}\}, \quad (7)$$

$$\mathbf{T} = c^m \mathbf{T}^m \mathbf{A}^m + \{\mathbf{T}^i \mathbf{A}^i\}, \quad (8)$$

$$\dot{\mathbf{E}}^t = \dot{\mathbf{E}} - c^m \mathbf{M} \mathbf{L}^m : (\mathbf{A}^m : \dot{\mathbf{E}} - \langle \dot{\epsilon}^{*m} \rangle_m) - \mathbf{M} \{\mathbf{L}^i \mathbf{A}^i\} : \dot{\mathbf{E}} - \dot{\mathbf{M}} : \Sigma, \quad (9)$$

where $\mathbf{A}^{el,m}$ and $\mathbf{A}^{el,i}$ are the average *elastic* strain concentration factors, \mathbf{A}^m and \mathbf{A}^i are the average *instantaneous* strain concentration factors and $\langle \dot{\epsilon}^{*m} \rangle_m$ is the volume average of $\dot{\epsilon}^{*m}$ over the matrix phase. Note that the elastic strain concentration factors must be calculated assuming elastic behavior of the phases. The curly braces in the above equations (7)-(9) indicate either summation over the number of inhomogeneity phases or averaging over the phase's distribution. For example, the last term in the expression for the elastic stiffness is evaluated as:

$$\{\mathbf{L}^i \mathbf{A}^{el,i}\} = \begin{cases} \sum_{j=1}^N c_j^i \mathbf{L}_j^i \mathbf{A}_j^{el,i} & \text{for } N \text{ inhomogeneity phases} \\ c^i \frac{\int_0^{2\pi} \int_0^{2\pi} \rho(\varphi, \theta) \mathbf{L}^i \mathbf{A}^{el,i} \sin \theta d\varphi d\theta}{\int_0^{2\pi} \int_0^{2\pi} \rho(\varphi, \theta) \sin \theta d\varphi d\theta} & \text{for distribution of phases} \end{cases} \quad (10)$$

In the first case (N inhomogeneity phases) in the equation above c_j^i is the volume fraction of j^{th} inhomogeneity phase and \mathbf{L}_j^i and $\mathbf{A}_j^{el,i}$ are the corresponding elastic stiffness and strain concentration factor. $\rho(\varphi, \theta)$ is the orientation distribution function and the integration

is performed over a unit sphere. In the most general case the function ρ may indicate not only the distribution of phase orientations but also of shapes and, possibly, of material properties.

The concentration factor \mathbf{A}^i is evaluated using the Mori-Tanaka method. The average strain concentration factor for the matrix \mathbf{A}^m is evaluated using the identity $c^m \mathbf{A}^m + c^i \mathbf{A}^i = \mathbf{I}$.

4. RESULTS AND DISCUSSION

Assuming that the elastic stiffness of the inhomogeneities in the limit approaches zero, the above-presented theory is applied to obtain results for porous SMAs. The constitutive behavior of the SMA matrix is modeled using the rate-independent model developed by Lagoudas et al. [15] and numerically implemented by Qidwai and Lagoudas [16].

To evaluate the Eshelby tensor \mathbf{S}^E the shape of the inhomogeneities must be chosen. It can be seen from Figure 1 that the voids in the porous SMA have very random distribution and irregular shapes. It could be asserted that the pores can be approximated as randomly distributed ellipsoids, which would lead to isotropic effective properties of the porous SMA. However, spherical pore shape would also result in isotropic effective properties. In the following the effective properties for a composite with elastic phases obtained using random orientation of ellipsoids will be compared to the effective properties obtained using spheres.

For a composite with elastic isotropic matrix with stiffness \mathbf{L}^m and random distribution of elastic isotropic ellipsoidal inhomogeneities with stiffness \mathbf{L}^i the overall elastic stiffness is given by equation (7). The elastic strain concentration factor $\mathbf{A}^{el,i}$ is given by the following equation:

$$\mathbf{A}^{el,i} = \tilde{\mathbf{A}} \left[c^m \mathbf{I} + c^i \left\{ \tilde{\mathbf{A}} \right\} \right]^{-1}, \quad (11)$$

where $\tilde{\mathbf{A}}$ is defined as:

$$\tilde{\mathbf{A}} = \left[\mathbf{I} + \mathbf{S}^E (\mathbf{L}^m)^{-1} (\mathbf{L}^i - \mathbf{L}^m) \right]^{-1} \quad (12)$$

and the Eshelby tensor is evaluated using the matrix stiffness \mathbf{L}^m and the shape of the inhomogeneities. The averaging indicated by the curly braces is performed over all possible orientations of the ellipsoid (i.e, the distribution function is $\rho=1$). Initially, tensor $\tilde{\mathbf{A}}$ is found in the local coordinate system of the inhomogeneity and then is transferred to the global coordinate. The two coordinate systems are related to each other by the rotation \mathbf{Q} . Taking into account all possible orientations of the inhomogeneities results in

$$\left\{ \tilde{\mathbf{A}} \right\} = \frac{1}{4\pi} \int_0^{\pi} \int_0^{2\pi} \tilde{\mathbf{A}}(\varphi, \theta) \sin \theta d\varphi d\theta \quad (13)$$

and the components of $\tilde{\mathbf{A}}(\varphi, \theta)$ are given by

$$\tilde{A}_{ijkl}(\varphi, \theta) = Q_{mi} Q_{nj} \tilde{A}_{mnpq} Q_{pk} Q_{ql}. \quad (14)$$

Thus the following final expression for the overall elastic stiffness is obtained:

$$\mathbf{L} = \mathbf{L}^m + c^i (\mathbf{L}^i - \mathbf{L}^m) \left\{ \tilde{\mathbf{A}} \right\} \left[c^m \mathbf{I} + c^i \left\{ \tilde{\mathbf{A}} \right\} \right]^{-1}. \quad (15)$$

Results obtained for two different inhomogeneity shapes - prolate spheroids and cylinders - are compared with the results for spherical inhomogeneities. For the case of prolate spheroids

two of the principal axes of the ellipsoid are selected to be equal ($a_2 = a_3$) while the third axis is selected to be $a_1 = 2a_2$. For the case of cylindrical inhomogeneities the ratio a_1/a_2 is set to a very large number. The above-described averaging procedure has been implemented for the case of porous material ($\mathbf{L}^i = \mathbf{0}$). The elastic properties of the matrix were taken to be the same as the elastic properties of NiTi in the austenitic phase, i.e., Young's modulus $E = 70\text{GPa}$ and Poisson's ratio $\nu = 0.33$. The averaging procedure results in isotropic effective material properties due to the randomness of the orientation of the inhomogeneities. Two of the effective material parameters of the composite are obtained - effective Young's modulus and effective bulk modulus. The values of these material parameters are normalized by the corresponding matrix properties. The values of the normalized effective Young's modulus for different pore volume fractions is plotted in Figure 2a and the normalized effective bulk modulus is plotted in Figure 2b. It is observed from these figures that there is very slight discrepancy between the results for different pore shapes and there is very good agreement between the results for the case of spherical pores and prolate spheroids.

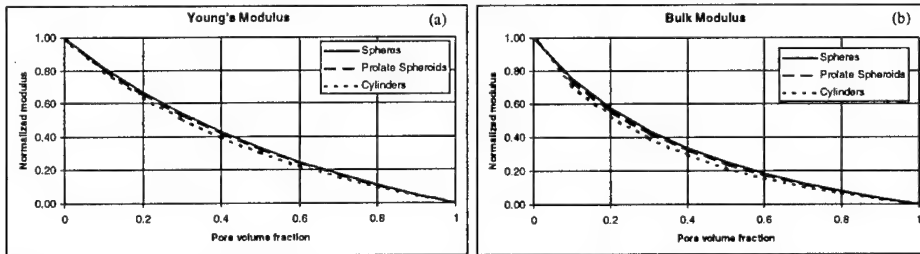


Figure 2: (a) Normalized effective Young's modulus; (b) Normalized effective bulk modulus

The results presented here are normalized and, therefore, are valid for all possible values of the matrix stiffness. Therefore, it could be asserted that the selection of a spherical pore shape would give adequate representation of porosity for the case of porous SMA. The use of random pore distribution in the case of porous SMAs would be computationally very expensive, since the averaging (see equations (13)-(14)) must be performed at every increment. Thus, the results for porous SMAs are obtained using spherical pore shape.

The material parameters for the SMA matrix are taken from [16]. The numerical calculations were performed in the pseudoelastic regime of the SMA at 42°C (at the austenitic finish temperature). The developed micromechanical procedure was implemented using User-Material (UMAT) subroutine, which is compiled and used by the commercial FEM package ABAQUS. The numerical calculations were performed using a two-element mesh under uniaxial loading. The effective stress-strain response for different pore volume fractions as well as the comparison between the local and macroscopic behavior for 50% porosity is shown in Figure 3.

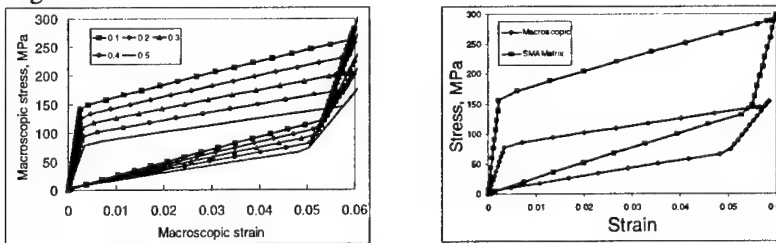


Figure 3: Effective stress-strain response of porous NiTi

Acknowledgements: The authors acknowledge the financial support of the Office of Naval Research Grant No. M00014-99-1-1069 monitored by Dr. Roshdy Barsoum.

5. REFERENCES

- [1] Wayman, C. M., Phase transformations, nondiffusive, in *Physical Metallurgy*, Cahn, R. W. and Haasen, P. (Eds.), North-Holland Physics Publishing, New York (1983) 1031-1075.
- [2] Patoor, E., Eberhardt, A. and Berveiller, M., Micromechanical modelling of the shape memory behavior, in *Proc. ASME WAM'94: Mechanics of Phase Transformation and Shape Memory Alloys. Vol. AMD 189/PVD 292*, Brinson, L. C. and Moran, B. (Eds.) (1994).
- [3] Sun, Q. P. and Hwang, K. C., Micromechanics modeling for the constitutive behavior of polycrystalline shape memory alloys - I. Derivation of general relations, *J. Mech. Phys. Solids* 41 (1), 1-17 (1993).
- [4] Sun, Q. P. and Hwang, K. C., Micromechanics modeling for the constitutive behavior of polycrystalline shape memory alloys - II. Study of the individual phenomena, *J. Mech. Phys. Solids* 41 (1), 19-33 (1993).
- [5] Tanaka, K., A thermomechanical sketch of shape memory effect: One-dimensional tensile behavior, *Res Mechanica* 18, 251-263 (1986).
- [6] Liang, C. and Rogers, C. A., A multi-dimensional constitutive model for shape memory alloys, *Journal of Engineering Mathematics* 26, 429-443 (1992).
- [7] Brinson, L. C., One-dimensional constitutive behavior of shape memory alloys: Thermomechanical derivation with non-constant material functions and redefined martensite internal variable, *J. of Intell. Mater. Syst. And Struct.* 4, 229-242 (1993).
- [8] Boyd, J. G. and Lagoudas, D. C., A thermodynamic constitutive model for the shape memory materials. Part I. The monolithic shape memory alloys, *Int. J. Plasticity* 12 (6), 805-842 (1996).
- [9] Abeyaratne, R. and Knowles, J. K., Continuum model of a thermoelastic solid capable of undergoing phase transformation, *J. Mech. Phys. Solids* 41, 541-571 (1993).
- [10] Birman, V., Review of mechanics of shape memory alloy structures, *Appl Mech Rev* 50 (11), 629-645 (1997).
- [11] Lagoudas, D. C., Boyd, J. G. and Bo, Z., Micromechanics of active composites with SMA fibers, *ASME Journal of Material Science and Technology* 5, 337-347 (1994).
- [12] Vandygriff, E. C., Lagoudas, D. C., Thangaraj, K. and Chen, Y.-C., Porous shape memory alloys, Part I: Fabrication and characterization, in *Proceedings of ASC 15th Annual Technical Conference* (2000).
- [13] Thangaraj, K., Chen, Y.-C. and Salama, K., Fabrication of porous NiTi shape memory alloy by elemental powder sintering, in *Proceedings of 2000 ASME International Mechanical Engineering Congress & Exposition*, Redmont, J. and Main, J. (Eds.) (2000).
- [14] Qidwai, M. A., Entchev, P. B., Lagoudas, D. C. and DeGiorgi, V. G., Modeling of the thermomechanical behavior of porous shape memory alloys, *International Journal of Solids and Structures* (accepted).
- [15] Lagoudas, D. C., Bo, Z. and Qidwai, M. A., A unified thermodynamic constitutive model for SMA and finite element analysis of active metal matrix composites, *Mechanics of Composite Materials and Structures* 3, 153-179 (1996).
- [16] Qidwai, M. A. and Lagoudas, D. C., Numerical implementation of a shape memory alloy thermomechanical constitutive model using return mapping algorithms, *Int. J. for Numerical Methods in Engng* 47, 1123-1168 (2000).

VARIATIONAL FORMULATION AND MATERIAL BALANCE LAWS OF DISSIPATIONLESS THERMOELASTICITY

V. K. Kalpakides

Department of Mathematics
University of Ioannina, GR-45110, Ioannina, Greece

G. A. Maugin

Laboratoire de Modélisation en Mécanique
Université Pierre et Marie Curie, 75252 Paris Cedex 05, France

1. SUMMARY

The concern of this work is the derivation of material balance laws for the Green–Naghdi (G–N) theory of dissipationless thermoelasticity. The lack of dissipation allows for a variational formulation which is used for the application of Noether’s theorem. The balance laws in material manifold are derived and the exact conditions under which they hold are rigorously studied.

2. INTRODUCTION

This work is devoted to the canonical formulation of thermoelasticity theory without dissipation [1]. For this purpose, we use the celebrated theorem of Noether according to which it is possible to obtain a conservation law for every given variational symmetry. We use also what is called [2] “invariance identity” to obtain the non-homogeneous terms of the material balance laws, i.e., the material forces or some kind of moment of such forces. In this manner we obtain all equations of interest, that is, the balance of linear momentum, the equation of entropy, the balance of canonical momentum, the balance of scalar moment of canonical momentum and the energy equation all in the apparently “dissipationless form”.

Dascalu and Maugin [3] used the G–N theory to formulate the corresponding *canonical balance laws of momentum and energy* – of interest in the design of fracture criteria – which, contrary to the expressions of the classical theory, indeed present *no* source of dissipation and canonical momentum [4]. In recent works [5, 6] it has been shown the consistency between the expressions of intrinsic dissipation and source of canonical momentum in dissipative continua. This is developed within the framework of so-called *material* or *configurational forces*, that world of forces which, for instance, drive structural rearrangements and material defects of different types on the material manifold [7, 8, 9].

We use throughout the paper alternatively the vectorial as well as the index notation to represent Cartesian vectors and tensors, thus rectangular coordinate systems are adopted in all cases. The motion of a thermoelastic body is described by the smooth mapping $x_\beta = x_\beta(X_B)$, where $B, \beta = 1, 2, 3, 4$, $X_4 = t$, $x_4 = \alpha$, $\alpha = \alpha(\mathbf{X}, t)$ is the thermal displacement scalar field, a primitive concept according to G-N theory. The temperature field is defined to be the time derivative of α , thus $\Theta(\mathbf{X}, t) := \dot{\alpha}(\mathbf{X}, t)$. Also, we use the notation \mathbf{X} to denote the material space variable, and \mathbf{x} for the spatial position of the particle \mathbf{X} at time t . In a coordinate system these variables will be written as $X_L, L = 1, 2, 3$ and $x_i, i = 1, 2, 3$, respectively. Generally, Greek indices will range from 1 to 4, while the lower-case Latin ones will range from 1 to 3. Also, the capital letters K, L, M, ... will range from 1 to 3 and A, B, ... from 1 to 4. We use two distinct differential operators $\frac{\partial}{\partial X_A}$ and $\frac{D}{DX_A}$. The former is the usual partial derivative operator while the latter denotes the partial derivative which accounts for the underlying function composition. Also, the usual notations $Grad F = \nabla_R F = DF/DX_L$, $Div F = DF_L/DX_L$ and $\dot{F} = DF/Dt$ for gradient, divergence and material time derivative, respectively are used. All the results presented in this paper are given without any proof due to lack of space. The interested reader can find the omitted proofs as well as additional results in a coming paper of the authors.

3. PRELIMINARIES

According to G-N theory the field equations of thermoelasticity of type II [1] i.e., the momentum and energy equations are given respectively as follows

$$\frac{\partial \mathbf{p}}{\partial t} - Div \mathbf{T} = \mathbf{0}, \quad -\left(\frac{D\Psi}{Dt} + \frac{D\Theta}{Dt}\eta\right) + tr(\mathbf{T}\dot{\mathbf{F}}) - \mathbf{S} \cdot \nabla_R \Theta = 0 \quad (1)$$

where $\mathbf{p} = \rho_R \mathbf{v}$ is the physical momentum, $\mathbf{v} = \frac{\partial \mathbf{x}}{\partial t}$ is the velocity field, Ψ is the free energy function per unit volume, \mathbf{T} is the first Piola-Kirchhoff stress tensor, \mathbf{F} is the deformation gradient tensor, \mathbf{S} is the entropy flux vector and η is the entropy density per unit volume. Also, the constitutive equations are given in the form

$$\mathbf{T} = \frac{\partial \Psi}{\partial \mathbf{F}}, \quad \mathbf{S} = -\frac{\partial \Psi}{\partial \beta}, \quad \eta = -\frac{\partial \Psi}{\partial \dot{\alpha}}, \quad (2)$$

where $\beta = \nabla_R \alpha$, $\alpha = \alpha(\mathbf{X}, t)$.

In the sequence, we give some fundamental elements related to variational symmetries and Noether's theorem. Let a C^2 function

$$L = L(X_A, x_\alpha, x_{\alpha,A}), \quad A = 1, 2, \dots, n, \alpha = 1, 2, \dots, m,$$

where $X_A \in G$, G is a smooth domain of R^n and $x_\alpha(X_A)$ is a sufficiently smooth function. Consider the functional $I : C^2(G) \rightarrow R$ given as follows

$$I(x_\alpha) = \int_G L(X_A, x_\alpha, x_{\alpha,A}) dV. \quad (3)$$

The necessary condition for the functional I to attain an extremum is given by the well known Euler-Lagrange equations

$$\frac{\partial L}{\partial x_\gamma} - \frac{D}{DX_A} \left(\frac{\partial L}{\partial x_{\gamma,A}} \right) = 0, \quad \forall X_A \in G \quad (4)$$

where the summation convention is used when repeated indices are appeared.

Consider now the $n+m$ -dimensional Euclidean space E^{n+n} made up by the dependent and independent variables, a group of infinitesimal transformations will be of the form

$$\tilde{X}_A = X_A + \epsilon_w Z_A^w, \quad \tilde{x}_\alpha = x_\alpha + \epsilon_w \zeta_\alpha^w, \quad w = 1, 2, \dots, \mu \quad (5)$$

where Z_A^w and ζ_α^w are C^∞ with respect to X_B, x_β and ϵ_w are reals.

The following *invariance identity* is a necessary and sufficient condition for a group of infinitesimal transformations to be a variational symmetry [2, 10]:

$$\frac{\partial L}{\partial X_A} Z_A^w + \frac{\partial L}{\partial x_\alpha} \zeta_\alpha^w + \frac{\partial L}{\partial x_{\alpha,A}} \left(\frac{D\zeta_\alpha^w}{DX_A} - x_{\alpha,B} \frac{DZ_B^w}{DX_A} \right) + L \frac{DZ_A^w}{DX_A} = 0. \quad (6)$$

Now, we give a version of Noether's theorem [2] convenient to our objective

Theorem of Noether *If the functional (3) is invariant under the μ -parameter group of transformations given by eqs. (5), there exist μ conservation laws of Euler-Lagrange equations (4) given by*

$$-\frac{D\theta_A^w}{DX_A} = \left[\frac{\partial L}{\partial x_\gamma} - \frac{D}{DX_A} \left(\frac{\partial L}{\partial x_{\gamma,A}} \right) \right] (\zeta_\gamma^w - x_{\gamma,B} Z_B^w) = 0, \quad (7)$$

where

$$\theta_A^w = -(LZ_A^w - \frac{\partial L}{\partial x_{\alpha,A}} x_{\alpha,B} Z_B^w + \frac{\partial L}{\partial x_{\alpha,A}} \zeta_\alpha^w). \quad (8)$$

4. VARIATIONAL SYMMETRIES AND CONSERVATION LAWS

Definition *The Lagrangian function of a thermoelastic body without dissipation is defined to be of the form*

$$L(X_L, \dot{x}_i, \dot{\alpha}, \frac{\partial x_i}{\partial X_L}, \frac{\partial \alpha}{\partial X_L}) = \frac{1}{2} \rho_R(X_L) \dot{x}_i \dot{x}_i - \Psi(X_L, \frac{\partial x_i}{\partial X_L}, \dot{\alpha}, \frac{\partial \alpha}{\partial X_L}). \quad (9)$$

Thus, the functional I for the case under discussion will take the form

$$I(x_i, \alpha) = \int_{t_1}^{t_2} \int_{\Omega} L(X_L, \dot{x}_i, \dot{\alpha}, x_{i,L}, \alpha_{,L}) dV dt, \quad (10)$$

where Ω is a smooth domain of R^3 and $[t_1, t_2]$ an interval of R . Notice that L is not an explicit function of x_i by virtue of Galilean invariance (translations in physical space of placements). Neither is it an explicit function of α itself, this implying a sort of *gauge invariance* very similar to that of electrostatic for the electric potential. The variational statement can be written as follows:

Proposition 1 *Let the constitutive relations (2) hold. Among all admissible functions of motion and thermal displacement for a thermoelastic body without dissipation those ones affording an extreme value to the action integral defined by (9–10), will satisfy the equations.*

$$\frac{DT_{Li}}{DX_L} - \frac{D}{Dt}(\rho_R \dot{x}_i) = 0, \quad \frac{DS_L}{DX_L} + \frac{D\eta}{Dt} = 0. \quad (11)$$

Thus the variational statement provides two equations. The first of them is the equation of motion and coincides with the corresponding one of G-N theory, i.e. eq. (1a). The second one is an equation for the balance of entropy. Thus, as far as the variational principle is considered, the field equations for thermoelasticity without dissipation are eqs. (11) instead of (1) of G-N theory. The other required equation, i.e. eq. (1b), is an energy equation and can not directly rise from a variational principle. What can be expected is to appear as a consequence of Noether's theorem considering invariance in time translations.

Invariance under Translations

First, consider invariance in material space and time translations.

Lemma 1 *If the action integral of a thermoelastic body without dissipation is invariant under the group of space and time translations, then it is a homogeneous body.*

Next, we give the main result concerning the group of translations.

Proposition 2 *Let the motion and the temperature functions x_i and Θ satisfy the field equations (11) for a homogeneous thermoelastic body without dissipation through constitutive relations (2), on the domain $\Omega \times [t_1, t_2]$. Then the following conservation laws also hold on $\Omega \times [t_1, t_2]$.*

$$\frac{D}{DX_L}(L\delta_{KL} + T_{Li}x_{i,K} - S_L\beta_K) - \frac{D}{Dt}(\rho_R\dot{x}_i x_{i,K} + \eta\beta_K) = 0, \quad (12)$$

$$\frac{D}{DX_L}(T_{Li}\dot{x}_i - S_L\Theta) + \frac{D}{Dt}(L - \rho_R\dot{x}_i\dot{x}_i - \eta\Theta) = 0. \quad (13)$$

The second of the above conservation laws, eq. (13), corresponds to time translations, thus it is related to the conservation of energy. After some calculation and taking into account equation of motion (11a), it can be written as

$$-(\dot{\Psi} + \dot{\Theta}\eta) + T_{Li}v_{i,L} - S_L\Theta_{,L} = 0, \quad (14)$$

which coincides with eq. (1b).

Invariance under the scaling Group.

In this case we will use the following one-parameter group of scalings in material and physical space

$$\tilde{X}_A = X_A + \epsilon X_A \quad \tilde{x}_\alpha = x_\alpha - \epsilon x_\alpha, \quad (15)$$

In this case the invariance identity becomes

$$\frac{\partial L}{\partial X_A}X_A - 2\left(\frac{\partial L}{\partial x_{\alpha,A}}\right)x_{\alpha,A} + 4L = 0. \quad (16)$$

The most interesting result for the scaling group concerns the linear case for which the following identity holds

Lemma 2 *Let us assume that a thermoelastic body without dissipation admits linear constitutive relations risen from (2), then its Lagrangian satisfies the following identity*

$$\frac{\partial L}{\partial x_{\alpha,A}}x_{\alpha,A} = 2L. \quad (17)$$

Proposition 3 *Let the motion and the temperature functions x_i and Θ satisfy the field*

equations (11) for a homogeneous thermoelastic body without dissipation through linear constitutive relations, on the domain $\Omega \times [t_1, t_2]$. Then the following conservation law also holds on $\Omega \times [t_1, t_2]$.

$$\begin{aligned} & \frac{D}{DX_L} [(L\delta_{KL} + T_{Li}x_{i,K} - S_L\beta_K)X_K + (T_{Li}\dot{x}_i - S_L\Theta)t + T_{Li}x_i - S_L\alpha] + \\ & \frac{D}{Dt} [-(\frac{1}{2}\rho_R\dot{x}_i\dot{x}_i + e)t - (\rho_R\dot{x}_i x_{i,K} + \eta\beta_K)X_K - \rho_R\dot{x}_i x_i - \eta\alpha] = 0, \end{aligned} \quad (18)$$

where $e = e(\mathbf{X}, t)$ is the internal density function per unit volume.

5. MATERIAL BALANCE LAWS

So far, we have presented conservation laws of the G–N equations of thermoelasticity. From the point of view of material mechanics, it is interesting to focus on what can be called *material balance laws*. To obtain such equations we must allow for the presence of sources in the already derived equations. This by turn, can be done by relaxing the assumptions we have posed in order to obtain them. By this manner, for every conservation law, we can obtain a balance (non-conservation) law. Applying this procedure to conservation laws (12) and (18) we obtain.

$$\frac{D}{DX_L} (L\delta_{KL} + T_{Li}x_{i,K} - S_L\beta_K) - \frac{D}{Dt} (\rho_R\dot{x}_i x_{i,K} + \eta\beta_K) = \frac{\partial L}{\partial X_K}, \quad (19)$$

$$\begin{aligned} & \frac{D}{DX_L} [(L\delta_{KL} + T_{Li}x_{i,K} - S_L\beta_K)X_K + (T_{Li}\dot{x}_i - S_L\Theta)t + T_{Li}x_i - S_L\alpha] + \\ & \frac{D}{Dt} [-(\frac{1}{2}\rho_R\dot{x}_i\dot{x}_i + e)t - (\rho_R\dot{x}_i x_{i,K} + \eta\beta_K)X_K - \rho_R\dot{x}_i x_i - \eta\alpha] = \frac{\partial L}{\partial X_L} X_L. \end{aligned} \quad (20)$$

The first one is the well-known *pseudomomentum equation* and the second is the *scalar moment of pseudomomentum equation*. Eq. (20) holds for linear, non-homogeneous thermoelasticity and represents a balance law for scalar moment of pseudomomentum or canonical momentum. The corresponding balance equation in physical space is not often used because it does not play any role in the description of the equilibrium or the motion of a body as does, for instance, the momentum or angular momentum equation. In the case of physical space, the factors that balance the rate of scalar moment of momentum are referred as *scalar moments* or *virials*. So the right hand side term of eq. (20) is a sort of *material scalar moment* or *material virial*.

The above-obtained results can be compared to previously appeared work of other researchers. We must especially refer to the work of Dascalu and Maugin [3] for G–N thermoelasticity and Maugin [11] and Fletcher [12] for elasticity. Let us return to eq. (12) which represents the canonical momentum conservation law. It can be written in the form

$$\text{Div}((\rho_R \frac{\mathbf{v}^2}{2} - \Psi)\mathbf{I} + \mathbf{T}\mathbf{F} - \beta \otimes \mathbf{S}) - \frac{D}{Dt} (\rho_R \mathbf{F}^T \mathbf{v} + \eta\beta) = 0. \quad (21)$$

Eq. (21) coincides with the corresponding one deriving through a vectorial approach in [3]. Conservation laws (12), (13) and (18) restricted to the case of elasticity are in full agreement with the corresponding ones given by [11] and [12]. Introducing the definitions

[13]

$$\mathcal{P}_L^{th} := -(\rho_R \dot{\mathbf{x}} \mathbf{F} + \eta \beta_L) = -\mathbf{p} \cdot \mathbf{F} - \eta \beta = \mathbf{P}^{mech} - \eta \beta, \quad (22)$$

$$\mathbf{b}^{th} := b_{LK} = -(L \delta_{LK} + T_{Li} x_{i,K} - S_L \beta_K), \quad (23)$$

$$\mathbf{f}^{inh} := \frac{\partial L}{\partial \mathbf{X}} = \frac{1}{2} \dot{\mathbf{x}} \cdot \dot{\mathbf{x}} \nabla_R \rho_R - \frac{\partial \Psi}{\partial \mathbf{X}}, \quad (24)$$

$$\mathcal{H} := \frac{1}{2} \rho_R \dot{\mathbf{x}} \cdot \dot{\mathbf{x}} + e, \quad \mathbf{Q} := \mathbf{T} \dot{\mathbf{x}} - \mathbf{S} \Theta, \quad (25)$$

for *canonical momentum* of the present approach, the *canonical material stress* tensor (Eshelby stress tensor), the *material force* of true inhomogeneities, the *Hamiltonian density* (total energy density) and the *material energy flux*, respectively the equations (12), (13) and (20) can be written in vectorial form as follows

$$-Div \mathbf{b}^{th} + \frac{D \mathcal{P}^{th}}{Dt} = \mathbf{f}^{inh}, \quad \frac{DH}{Dt} - \nabla_R \cdot \mathbf{Q} = 0, \quad (26)$$

$$Div(-\mathbf{b}^{th} \cdot \mathbf{X} + \mathbf{Q} t + \mathbf{T} \cdot \mathbf{x} - \mathbf{S} \alpha) + \frac{D}{Dt}(-\mathcal{H} t + \mathcal{P}^{th} \cdot \mathbf{X} - \mathbf{p} \cdot \mathbf{x} - \eta \alpha) = \mathbf{f}^{inh} \cdot \mathbf{X}, \quad (27)$$

respectively. We recall that the eq. (27) holds for non-homogeneous but *linear* thermoelasticity. Under this restriction and in the framework of elasticity it can be compared with eq. (4.89) of [11]. Assuming, as in standard continuum thermodynamics, that entropy and heat flux are related by the usual relation $\mathbf{S} = \mathbf{q}/\Theta$, eq. (26b) will take the classical form of the energy conservation equation [14]

$$\frac{DH}{Dt} - \nabla_R \cdot (\mathbf{T} \cdot \mathbf{v} - \mathbf{q}) = 0. \quad (28)$$

6. CONCLUSIONS

Summing up, we have deduced from the Lagrangian density (9) all field equations and balance laws for the theory of material inhomogeneous, finite deformable, thermoelastic conductors of heat. As a matter of fact, eqs. (11a) and (28) are the local balance equations of linear momentum and energy, respectively. These are all formally identical to those of the classical thermoelasticity of conductors (e.g., as recalled in [14]). Only the equation of canonical momentum (26a) differs from the originally obtained by Epstein and Maugin [4] in material thermoelasticity. But, abstractions being made of material inhomogeneities, it is the same as the one obtained by direct algebraic manipulations by Dascalu and Maugin [3] in the "dissipationless" formulation of thermoelasticity. Indeed, canonical momentum (22) is made of two parts, a strictly mechanical part – which is none other than pull back, changed of sign, of the physical momentum – and a purely thermal part. In addition, the canonical stress tensor (23) contains a contribution of β because from its very definition, it captures material gradients of all fields. One should note that the source term in eq. (26a) has no energetic contents. Furthermore, contrary to common use, even the entropy equation (11b) is source free. This means that in absence of material inhomogeneities, all equations obtained are strict *conservations laws*, hence the qualification of "*dissipationless theory*". In this rather strange – we admit it – approach, the entropy flux and heat flux are derived from the free energy, on the same footing as entropy density, and stress.

References

- [1] A. E. Green and P.M. Naghdi, *J. Elasticity* **31**, 189, (1993)
- [2] D. Lovelock and H. Rund, *Tensors, Differential Forms and Variational Principles* John Wiley and sons, London (1975)
- [3] C. Dascalu and G. A. Maugin , *J. Elasticity* **39**, 201 (1995)
- [4] M. Epstein and G. A. Maugin , *C. R. Acad. Sci. Paris* **II-320**, 63 (1995)
- [5] G. A. Maugin , *Thermomechanics of Inhomogeneous-heterogeneous Systems: Applications to the irreversible Progress of Two- and Three-dimensional Defects*, **ARI**, Springer, **50** 43-56 (1997)
- [6] G. A. Maugin , *Arch. Appl. Mech.* **70**, 31 (2000)
- [7] G. A. Maugin , *Appl. Mech. Rev.* **48**, 213 (1995)
- [8] M. E. Gurtin, *Configurational Forces as Basic Concepts of Continuum Physics*, In Applied Mathematical Sciences, 137, Sprimger, New York (2000)
- [9] R. Kienzler and G. Herrmann, *Mechanics in Material Space*, Springer, Berlin (2000)
- [10] P. J. Olver, *Applications of Lie Groups to Differential Equations*. In Graduate Texts in Mathematics, 107, Springer, New York (1993)
- [11] G. A. Maugin, *Material Inhomogeneities in Elasticity*, In Applied Mathematics and Mathematical Computation, 3, Chapman and Hall, London (1993)
- [12] D. C. Fletcher , *Arch. Rat. Mech. Anal.* **60**, 329 (1976)
- [13] G. A. MAUGIN, *Nonlinear Waves in Elastic Crystals*, Oxford University Press, U.K. (1999)
- [14] G. A. Maugin and A. Berezovski , *J. Thermal Stresses* **22**, 421 (2000)

THE INFINITE ISOTROPIC WEDGE UNDER LINEARLY DISTRIBUTED LOADING

J.H. Stabouloglou and E.E. Theotokoglou

Faculty of Applied Sciences, Dept. of Mechanics-Lab. of Strength of Materials
The National Technical University of Athens, Zographou Campus,
Theocaris, Bld, GR-157 73, Athens, Greece

1. SUMMARY

The problem of the infinite isotropic wedge under linearly distributed loading on the faces is reduced to a self similar problem. The stress field is determined using the equilibrium conditions for forces and moments. The proposed solution is applied to the elastostatic problem of a composite isotropic two materials infinite wedge.

2. INTRODUCTION

The stress analysis in a wedge with infinite radius within the classical linear theory of elasticity has been considered by various investigators. Tranter [1] solved the plane elasticity problem of an infinite isotropic wedge by employing the Airy stress function and by using the Mellin transform. Many applications of this technique were made for the solution of particular problems. Benthem [2] and Baker [3] solved an anisotropic wedge, Matczynski [4] studied the discontinuous boundary conditions and Absi and Morando [5] calculated the stresses in some particular cases of loading. Finally Theocaris, Tsamasphyros and Andrianopoulos [6] confronted the problem of the infinite wedge, systematizing the known results.

In the present paper the special case of an infinite isotropic wedge under linearly distributed loading is considered with a variable-separable solution. Starting from the well known problem of the wedge shaped dam [7], we reduce the elastostatic problem of the infinite isotropic wedge under linearly distributed loading on its faces in a self similar problem. It is observed that the linear distributed loading along the faces fulfills the self-similarity condition as

$$F(ar) = aF(r) \quad (1)$$

In addition a characteristic dimension is not introduced and therefore the stress field of the elastostatic problem is of the form

$$\sigma_{ij}(r, \theta) = h_{ij}(r)g_{ij}(\theta), \quad i, j = r, \theta \quad (2)$$

In the case of linear distributed shear loading along the faces of the wedge, we have

$$\begin{aligned} \sigma_{r\theta}(r, \theta = \alpha) &= h_{r\theta}(r)g_{r\theta}(\alpha) = T_\alpha r = T_\alpha(r) \\ \sigma_{r\theta}(r, \theta = \beta) &= h_{r\theta}(r)g_{r\theta}(\beta) = T_\beta r = T_\beta(r) \end{aligned}$$

Thus

$$h_{r\theta}(r) = r, \quad g_{r\theta}(\alpha) = T_\alpha, \quad g_{r\theta}(\beta) = T_\beta \quad (3)$$

Correspondingly, in the case of normal loading

$$h_{\theta\theta}(r) = r, \quad g_{\theta\theta}(\alpha) = N_\alpha, \quad g_{\theta\theta}(\beta) = N_\beta \quad (4)$$

Using the equilibrium conditions for forces and moments, the unknown functions $h_{ij}(r)$ in the stress field expressions are determined. Selecting appropriate terms from the Michell tables [8], the stress function, the $g_{ij}(\theta)$ functions and the stress field are easily obtained. Finally applying the boundary conditions, the unknown coefficients of the stress field are determined.

The advantages of the proposed solution are:

- (i) the use of self-similarity property in the wedge elastostatic problem not only for concentrated loads at the apex but also for distributed loads along the faces.
- (ii) the determination of the stress function from the Michell tables according to the self-similarity property.

The proposed solution is applied to the elastostatic problem of a composite isotropic two materials infinite wedge under a linearly distributed loading along the external faces of the wedge

3. BASIC THEORY-PROBLEM SOLUTION

It is considered an infinite isotropic wedge under linearly distributed shear loading along its faces (Fig.1). From the equilibrium of the forces in the x, y -directions at the sector $(A'A BB'A)$, it is resulted

$$\begin{aligned}
r h_{rr}(r) \int_{\alpha}^{\beta} g_{rr}(\theta) \cos \theta d\theta - r^2 \left[\frac{T_{\alpha} \cos \alpha - T_{\beta} \cos \beta}{2} + \int_{\alpha}^{\beta} g_{r\theta}(\theta) \sin \theta d\theta \right] = \\
\int_{\alpha}^{\beta} g_{rr}(\theta) \cos \theta d\theta - \left[\frac{T_{\alpha} \cos \alpha - T_{\beta} \cos \beta}{2} + \int_{\alpha}^{\beta} g_{r\theta}(\theta) \sin \theta d\theta \right] \\
r h_{rr}(r) \int_{\alpha}^{\beta} g_{rr}(\theta) \sin \theta d\theta - r^2 \left[\frac{T_{\alpha} \sin \alpha - T_{\beta} \sin \beta}{2} - \int_{\alpha}^{\beta} g_{r\theta}(\theta) \cos \theta d\theta \right] = \\
\int_{\alpha}^{\beta} g_{rr}(\theta) \sin \theta d\theta - \left[\frac{T_{\alpha} \sin \alpha - T_{\beta} \sin \beta}{2} - \int_{\alpha}^{\beta} g_{r\theta}(\theta) \cos \theta d\theta \right]
\end{aligned} \tag{5}$$

The system (5) is valid only in the case that

$$r h_{rr}(r) = r^2 \Leftrightarrow h_{rr}(r) = h_{r\theta}(r) = r \tag{6}$$

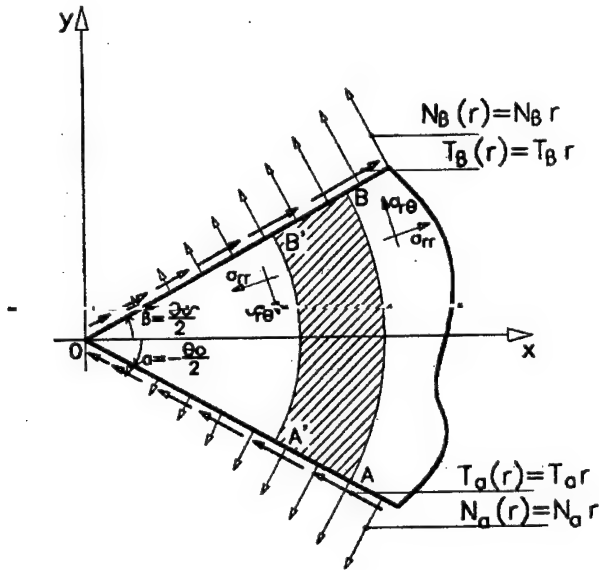


Figure 1: Infinite isotropic wedge under linearly distributed loading

and

$$\begin{aligned}
\int_{\alpha}^{\beta} g_{rr}(\theta) \cos \theta d\theta &= \frac{T_{\alpha} \cos \alpha - T_{\beta} \cos \beta}{2} + \int_{\alpha}^{\beta} g_{r\theta}(\theta) \sin \theta d\theta \\
\int_{\alpha}^{\beta} g_{rr}(\theta) \sin \theta d\theta &= \frac{T_{\alpha} \sin \alpha - T_{\beta} \sin \beta}{2} - \int_{\alpha}^{\beta} g_{r\theta}(\theta) \cos \theta d\theta
\end{aligned} \tag{7}$$

From the equilibrium of the moments at the sector ($A'ABB'B$) occurs

$$\int_{\alpha}^{\beta} g_{r\theta}(\theta) d\theta = 0 \quad (8)$$

The Michell stress-function [8] ensuring the required order of r is

$$M(r, \theta) = \Gamma_{11} r^3 \cos \theta + \Gamma'_{11} r^3 \sin \theta + \Gamma_{32} r^3 \cos(3\theta) + \Gamma'_{32} r^3 \sin(3\theta) \quad (9)$$

Thus, the stress field is

$$\begin{aligned} \sigma_{rr}(r, \theta) &= 2\Gamma_{11} r \cos \theta + 2\Gamma'_{11} r \sin \theta - 6\Gamma_{32} r \cos(3\theta) - 6\Gamma'_{32} r \sin(3\theta) \\ \sigma_{r\theta}(r, \theta) &= 2\Gamma_{11} r \sin \theta - 2\Gamma'_{11} r \cos \theta + 6\Gamma_{32} r \sin(3\theta) - 6\Gamma'_{32} r \cos(3\theta) \\ \sigma_{\theta\theta}(r, \theta) &= 6\Gamma_{11} r \cos \theta + 6\Gamma'_{11} r \sin \theta + 6\Gamma_{32} r \cos(3\theta) + 6\Gamma'_{32} r \sin(3\theta) \end{aligned} \quad (10)$$

and the displacement field is

$$\begin{aligned} 2\mu u_r(r, \theta) &= r^2 \left[(\kappa - 2)(\Gamma_{11} \cos \theta + \Gamma'_{11} \sin \theta) - 3(\Gamma_{32} \cos 3\theta + \Gamma'_{32} \sin 3\theta) \right] \\ 2\mu u_\theta(r, \theta) &= r^2 \left[(\kappa + 2)(\Gamma_{11} \sin \theta - \Gamma'_{11} \cos \theta) + 3(\Gamma_{32} \sin 3\theta - \Gamma'_{32} \cos 3\theta) \right] \end{aligned} \quad (11)$$

where μ is the shear modulus, $\kappa = (3 - 4\nu)$ for plane strain, $\kappa = (3 - \nu)/(1 + \nu)$ for generalized plane stress, ν being the Poisson's ratio and $\Gamma_{11}, \Gamma'_{11}, \Gamma_{32}$ and Γ'_{32} are unknown coefficients to be determined

The boundary conditions along the faces of the wedge (Fig.1) are

$$\begin{aligned} \theta = \alpha = -\frac{\theta_0}{2}; \quad \sigma_{r\theta} = T_\alpha(r) = T_\alpha r, \quad \sigma_{\theta\theta} = 0 \\ \theta = \beta = \frac{\theta_0}{2}; \quad \sigma_{r\theta} = T_\beta(r) = T_\beta r, \quad \sigma_{\theta\theta} = 0 \end{aligned} \quad (12)$$

Taking into consideration relations (10) and (12), we finally obtain

$$\begin{aligned} \Gamma_{11} &= \frac{(T_\alpha - T_\beta) \cos\left(3\frac{\theta_0}{2}\right)}{32 \sin \frac{\theta_0}{2} \cos^3 \frac{\theta_0}{2}}, & \Gamma'_{11} &= -\frac{(T_\alpha + T_\beta) \sin\left(3\frac{\theta_0}{2}\right)}{32 \sin^3 \frac{\theta_0}{2} \cos \frac{\theta_0}{2}} \\ \Gamma_{32} &= -\frac{T_\alpha - T_\beta}{32 \sin \frac{\theta_0}{2} \cos^2 \frac{\theta_0}{2}}, & \Gamma'_{32} &= \frac{T_\alpha + T_\beta}{32 \sin^2 \frac{\theta_0}{2} \cos \frac{\theta_0}{2}} \end{aligned} \quad (13)$$

In a similar way, in the case of a linearly distributed normal loading along the faces of the wedge, it is obtained

$$\begin{aligned}\Gamma_{11} &= \frac{(N_\alpha + N_\beta) \left(3\cos^2 \frac{\theta_0}{2} - \sin^2 \frac{\theta_0}{2} \right)}{32\cos^3 \frac{\theta_0}{2}}, \quad \Gamma'_{11} = \frac{(N_\alpha - N_\beta) \left(\cos^2 \frac{\theta_0}{2} - 3\sin^2 \frac{\theta_0}{2} \right)}{32\sin^3 \frac{\theta_0}{2}} \\ \Gamma_{32} &= -\frac{N_\alpha + N_\beta}{96\cos^3 \frac{\theta_0}{2}}, \quad \Gamma'_{32} = \frac{N_\beta - N_\alpha}{96\sin^3 \frac{\theta_0}{2}}\end{aligned}\quad (14)$$

4. APPLICATION IN THE CASE OF A BIMATERIAL WEDGE

It is considered the case of a bimaterial isotropic wedge (Fig.2). The wedge (1) with mechanical properties (κ_1, μ_1) occupies the sector with angle $\theta_1 (= -\alpha)$ while the wedge 2, with mechanical properties (κ_2, μ_2) , occupies the sector with angle $\theta_2 (= \beta)$.

In the bimaterial wedge the self-similarity property is valid as the equilibriums of forces and moments are only used. Taking into consideration the compatibility of displacements along the interface (Fig. 2)

$$u_i^{(1)}(r, 0) = u_i^{(2)}(r, 0), \quad i = r, \theta \quad (15)$$

the unknown distributions of normal and shear stresses along the interface (OΓ) are given by

$$\begin{aligned}N_r(r) &= N_\gamma r; \quad N_\gamma = \frac{F_R \Theta_T + F_\Theta R_T}{R_N \Theta_T + \Theta_N R_T} \\ T_r(r) &= T_\gamma r; \quad T_\gamma = \frac{F_\Theta R_N - F_R \Theta_N}{R_N \Theta_T + \Theta_N R_T}\end{aligned}\quad (16)$$

in case that

$$R_N \Theta_T + \Theta_N R_T \neq 0 \quad (17)$$

where

$$\begin{aligned}F_R &= \frac{\mu_2(\kappa_1 + 1)}{2\sin \theta_1} \left(-\frac{N_\alpha}{tg \theta_1} + T_\alpha \right) + \frac{\mu_1(\kappa_2 + 1)}{2\sin \theta_2} \left(\frac{N_\beta}{tg \theta_2} + T_\beta \right) \\ F_\Theta &= \frac{\mu_2(\kappa_1 + 1)}{2\sin \theta_1 tg \theta_1} \left(N_\alpha \frac{2 - tg^2 \theta_1}{tg \theta_1} - 3T_\alpha \right) + \frac{\mu_1(\kappa_2 + 1)}{2\sin \theta_2 tg \theta_2} \left(N_\beta \frac{2 - tg^2 \theta_2}{tg \theta_2} + 3T_\beta \right)\end{aligned}\quad (18)$$

$$\begin{aligned}
R_N &= \frac{1}{2} \left\{ \mu_2 \left[(\kappa_1 - 3) - \frac{\kappa_1 + 1}{tg^2 \theta_1} \right] - \mu_1 \left[(\kappa_2 - 3) - \frac{\kappa_2 + 1}{tg^2 \theta_2} \right] \right\} \\
R_T &= \frac{\mu_2 (\kappa_1 + 1)}{tg \theta_1} + \frac{\mu_1 (\kappa_2 + 1)}{tg \theta_2} \\
\Theta_N &= \frac{\mu_2 (\kappa_1 + 1)}{tg^3 \theta_1} + \frac{\mu_1 (\kappa_2 + 1)}{tg^3 \theta_2} \\
\Theta_T &= \frac{1}{2} \left\{ \mu_2 \left[\frac{3(\kappa_1 + 1)}{tg^2 \theta_1} + (\kappa_1 + 5) \right] - \mu_1 \left[\frac{3(\kappa_2 + 1)}{tg^2 \theta_2} + (\kappa_2 + 5) \right] \right\}
\end{aligned} \tag{19}$$

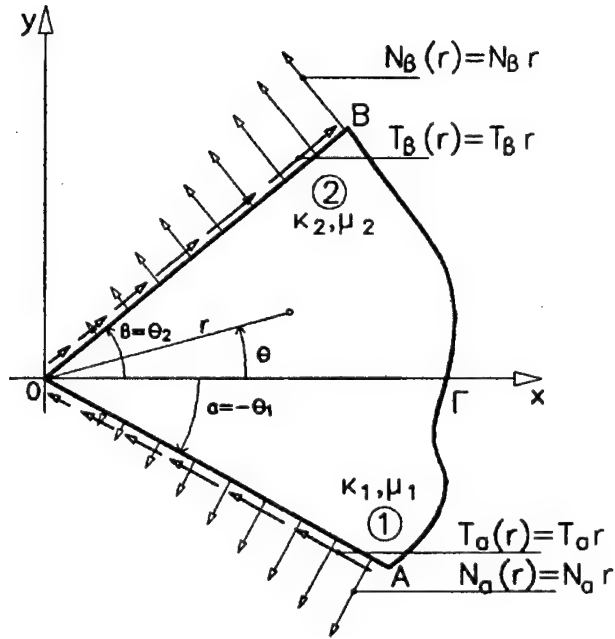


Figure 2: Composite two materials wedge under linearly distributed loads on its faces

5. REFERENCES

- [1] Tranter, C.J., The use of the Mellin transform in finding the stress distribution in an infinite wedge, Quart. Jour. Mech. Appl. Math. 1, 125 (1948).

- [2] Sneddon, I.N., *Fourier transforms*, New York: McGraw-Hill. (1951).
- [3] Sternberg, E. and Koiter, W.T., The wedge under a concentrated couple: a paradox in the two-dimensional theory of elasticity, *Journal Appl. Mech.* 25, 575-581 (1958).
- [4] Benthem, J.P., On the stress distribution in an isotropic infinite wedge. *Quart. Appl. Math.* 21, 189 (1965).
- [5] Baker, B.R., Closed forms for the stress in a class of orthotropic wedges. *Journal Appl. Mech.* 26, 26 (1965).
- [6] Theocaris, P.S., Tsamasphyros G. and Andrianopoulos N., The problem of the infinite wedge, *Acta Mechanica* 34, 63-87 (1979).
- [7] Timoshenko, S.P., Goodier, J.N., *Theory of elasticity*, Tokyo McGraw-Hill Koya Kusha, Ltd (1970).
- [8] Barber, J.R., *Elasticity*, Kluwer Academic Publishers, The Netherlands (1992).

SIZE EFFECT ON FAILURE LOAD OF MARBLE BEAMS UNDER THREE POINT BENDING

I. Vardoulakis

Department of Mechanics, Faculty of Applied Sciences,
National Technical University of Athens, GR-15773 Athens, Hellas

G. Exadaktylos

Department of Mineral Resource Engineering
Technical University of Crete, GR-73100 Chania, Crete, Hellas

S. K. Kourkoulis

Department of Mechanics, Faculty of Applied Sciences,
National Technical University of Athens, GR-15773 Athens, Hellas

1. SUMMARY

An one-dimensional gradient-dependent linear beam theory with intrinsic length scales is introduced for the description of the behaviour of rock materials, like marble. The theory is calibrated with the aid of a series of three point bending tests and is proved to predict accurately the failure as well as the size effect exhibited by the fracture load.

2. INTRODUCTION

A fundamental concern in most problems involving stressed materials is the prediction of their failure. For ideally elastic or perfectly plastic materials, a stress analysis indicates no dependence of the failure load and the failure strain on scale: structures of different sizes are assumed to fail at the same maximum stress.

One of the first attempts to explain size effects is credited to Weibull, who investigated the statistics of failure based on fracture extension. By applying the concept of the "weakest link", he showed that the strength of materials is a function of the volume of the specimen. However, this theory may be inadequate because it ignores the stress redistribution due to localized damage at the scale of rock grains or crystals prior to maximum stress or strain.

Towards this direction an one-dimensional special gradient-dependent linear beam theory with intrinsic length scales is proposed in the present work for the description of the bending behaviour of rock type materials, like marble. After being calibrated, with the aid of experimental results, available from various sources [1-4], the theory is applied for the prediction of the failure load of Dionysos-Pentelikon marble under three-point bending (3PB)

and it is proved that it predicts the size dependency exhibited by both the critical extension strain and the failure load.

3. THE GRADIENT DEPENDENT BENDING THEORY

Theoretical considerations

In the present case the bending problem is studied in two dimensions. The beam is assumed to have rectangular cross section and the deformation quantities are assumed to be of infinitesimal magnitude. The longitudinal section of the beam is referred to a Cartesian coordinate system Oxz positioned on the neutral axis of the beam with z denoting the distance from the neutral surface. The corresponding displacements are denoted as u and w , respectively (Fig.1). The kinematic quantities of the axial strains ϵ_{xx} , ϵ_{yy} and the engineering shear strain γ_{xz} , are defined as usual:

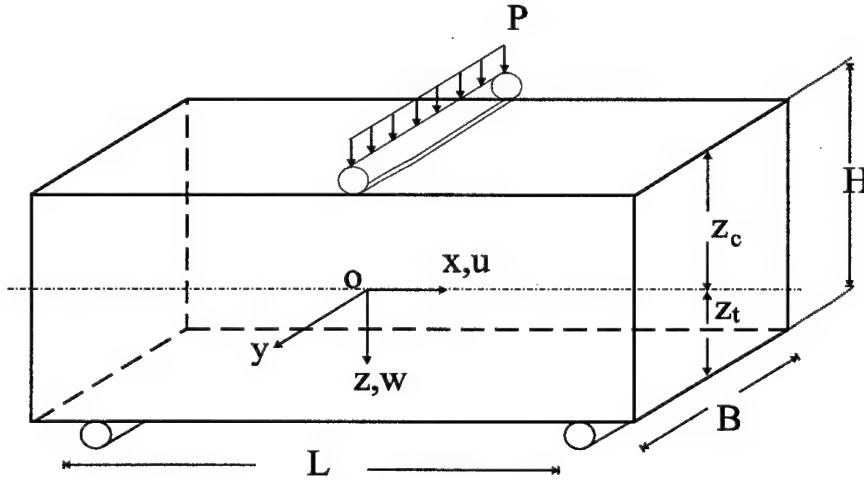


Figure 1: The configuration of the problem.

$$\epsilon_{xx} = u_{,x}, \quad \gamma_{xz} = u_{,z} + w_{,x}, \quad \epsilon_{zz} = w_{,z} \quad (1)$$

where partial differentiation with respect to x or z is indicated as usual by a subscript x or z preceded by a comma. Next, the following kinematic assumption is introduced:

$$u = \psi(x)z \Leftrightarrow \epsilon_{xx} = \psi_{,x} z \quad (2)$$

where $\psi(x)$ denotes the rotation of the normal cross-section of the beam. Then Eq.(1) yields:

$$\gamma_{xz} = \psi + w_{,x} \quad (3)$$

In the present work a special one-dimensional gradient-dependent linear beam theory with intrinsic length scales is introduced with an elastic strain energy density of the form:

$$w_b = \frac{1}{2} EI \kappa^2 + \frac{1}{\ell_v^2} \gamma^2 + \frac{2}{\ell_s} \kappa \gamma \quad (4)$$

where E is the modulus of elasticity of the material, I is the second moment of area of the cross-section of the beam ($I=BH^3/12$) and κ is the bending curvature defined as:

$$\kappa = \epsilon_{,z} = \psi_{,x}, \quad \epsilon \equiv \epsilon_{xx} \quad (5)$$

Concerning the strain energy density function, introduced in Eq.(4), it is noted that it consists of:

- (i) The familiar energy term due to the bending moment, i.e. $\kappa^2 EI/2$, and two additional terms:
- (ii) One accounting for the correction of shear by employing a meso-structural length scale, ℓ_v , introduced by Timoshenko and
- (iii) One accounting for surface energy [1-3] by employing a micro-material length scale, ℓ_s .

Eq.(4) yields the following constitutive relations for the shear force Q and bending moment M :

$$Q = \frac{\partial w_b}{\partial \gamma} = EI \left(\frac{1}{\ell_v^2} \gamma + \frac{1}{\ell_s} \kappa \right), \quad M = \frac{\partial w_b}{\partial \kappa} = EI \left(\kappa + \frac{1}{\ell_s} \gamma \right) \quad (6)$$

By substituting into the equilibrium equation $-Q+(dM/dx)=0$ the values of Q and M as given by Eq.(6) it is obtained:

$$-\left(\frac{1}{\ell_v^2} \gamma + \frac{1}{\ell_s} \kappa \right) + \left(\kappa' + \frac{1}{\ell_s} \gamma' \right) = 0 \quad (7)$$

By recourse to Eq.(3) and taking into account the familiar relation $\kappa = -w_{,xx}$, Eq.(7) becomes:

$$-w'''' + \frac{2}{\ell_s} w'' - \frac{1}{\ell_v^2} w' + \frac{1}{\ell_s} \psi' - \frac{1}{\ell_v^2} \psi = 0 \quad (8)$$

wherein $(.)' \equiv d/dx$. The solution of the above differential equation with respect to ψ is written as:

$$\psi = -w' + \ell_r w'' - (\ell_v^2 - 2\ell_r^2) w''' - \ell_r \ell_v^2 w^{IV} \quad (9)$$

with $\ell_r \equiv \ell_v^2 / \ell_s$. Thus, the engineering shear strain may be determined from Eqs.(3) and (9) as follows:

$$\gamma \equiv \gamma_{xz} = w' + \psi = (1 - 2\alpha^2) \ell_v^2 \kappa' - \alpha \ell_v (\kappa - \ell_v^2 \kappa'') \quad (10)$$

where it was set that:

$$\alpha \equiv \ell_r / \ell_v = \ell_v / \ell_s \quad (11)$$

Substituting Eq.(10) into the second of Eqs.(6) the constitutive relation for M is derived as:

$$M = (EI)[(1 - \alpha^2)\kappa + (1 - 2\alpha^2)\ell_r \kappa' + \ell_r^2 \kappa''] \quad (12)$$

In the limiting case of vanishingly small microstructural length ℓ_v (i.e. $\alpha=0$) the above relationship degenerates to the classical formula $M=(EI)\kappa$ provided by the conventional Bernoulli-Euler beam bending theory. In view of Eq.(12) and, also, of the familiar relation for

the moment distribution $M=PL[1-(2x/L)]$ (valid for $x \geq 0$) it is obtained for the case of a 3PB test:

$$\eta^4 k'' + (1-2\alpha^2)\eta^2 k' + (1-\alpha^2)k = 1-2\xi, \quad \xi \geq 0 \quad (13)$$

with $\xi=x/L$, $\eta^2 = \ell_v/L$, $\lambda=PL/4EI$ and $k=\kappa/\lambda$. The approximate solution of Eq.(13) reads as follows:

$$k \cong \frac{1}{1-\alpha^2} \left[(1-2\xi) + \frac{2\eta^2(1-2\alpha^2)}{1-\alpha^2} \right], \quad 0 \leq \xi \leq 1/2 \quad (14)$$

Subsequently, the expression for the deflection of the beam can be obtained from the relation $w_{,xx}=-\lambda k$ by two successive integrations of Eq.(14) with respect to x . The result is finally read as:

$$w = -\frac{\lambda}{2L^2(1-\alpha^2)} \left\{ \left[1 + \frac{2\eta^2(1-2\alpha^2)}{1-\alpha^2} \right] \left[\xi^2 - \frac{\xi^3}{3} \right] + C_1 \xi + C_2 \right\} \quad (15)$$

The constants C_1 and C_2 are determined from the boundary conditions $w(\xi/2)=0$, $w'(0)=0$. The maximum extension strain ϵ_m at the bottom fiber at midsection (i.e. $\xi=0$, $z=H/2$) is then obtained as:

$$\epsilon_m = PLH(1+4\eta^2)/8EI \quad (16)$$

Parameter identification

The meso-structural length scale ℓ_v can be determined directly by the following formula for the shear force correction, introduced in Timoshenko's technical beam bending theory [5]:

$$\beta^2 \equiv \ell_v^2 / L^2 = (1+\nu)(H/L)^2 / 5$$

where ν is the Poisson's ratio. Combining relation $\eta^2 = \ell_v/L$ with Eq.(17) the relative length ratio, α , is obtained:

$$\alpha = \eta^2 / \beta \quad (18)$$

The length ratio α is determined by suitable back analysis of either bending curvature or deflection experimental data. Fig.2 illustrates the variation of the normalized central deflection of the beam, $\omega(0)$, with respect to the material length ratio η for constant aspect ratio of the beam, $L/H=4$ and Poisson's ratio $\nu=0.3$. For comparison reasons the prediction of Timoshenko's theory for the maximum deflection, $\omega_T(0)$, of the beam is also displayed in the same figure [5]:

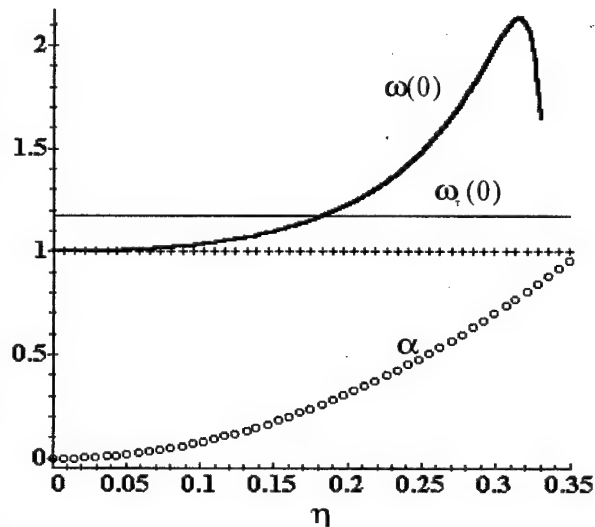


Figure 2: Normalized central deflection by the gradient and Timoshenko's theories, vs. the length ratio η . Variation of the material length ratio, α , is, also,

$$\omega_T = 1 + 2.85(H/L)^2 \quad (19)$$

The dimensionless deflections ω , ω_T , mentioned in previous paragraph were defined as:

$$\omega = w / (12\lambda / L^2) \quad (20)$$

By studying Fig.2 the following conclusions can be drawn: (a) as η increases the length ratio α increases being, however, always lower than unity for $\eta \leq 0.35$ in order for the strain energy of the beam to be a positive definite quantity. (b) The special gradient theory introduced in the present study predicts an increasing maximum deflection as the length ratio η increases, whereas Timoshenko's theory predicts constant central deflection, and (c) Both shear-bending theories (i.e. gradient dependent and Timoshenko's) result always in higher central beam deflections than the classical Bernoulli-Euler's one that gives $\omega=1$. This is attributed obviously to the fact that the strain energy density expression in the two shear-bending theories is enhanced with additional terms.

Deflection measurements

The calibration procedure for the estimation of the numerical value of the length ratio, η , and subsequently of the surface energy ratio, α , by using Eq.(18) and the experimental deflection measurements close to the midspan of the beam [6], is displayed in next Fig.3. The numerical values of the parameters that were used in the present calibration procedure were: $E=85$ GPa, $\nu=0.3$, $\beta=7.45$, $P=31.7$ kN, and $\lambda=0.000614$. The optimum fit of the experimental results was obtained for the following numerical values of the unknown parameters:

$$\eta=0.22, \alpha=0.37 \text{ for } L=0.4 \text{ m} \quad (21)$$

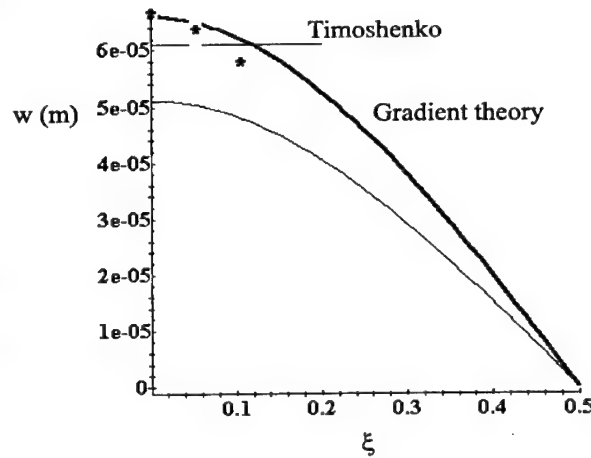


Figure 3: The deflection along the beam semi-axis at level $P=31.7$ kN for a marble beam of length $L=0.4$ m.

3. SIZE EFFECT

In the case of 3PB the beam always fails at midspan according to the well known Saint Venant's hypothesis, stated as: 'fracture of a brittle material initiates when the total extension strain in the material exceeds a critical value, characteristic of the material' [7], or equivalently:

$$\epsilon_m = \epsilon_f \text{ at } \xi = 0, z = H/2 \quad (22)$$

where ϵ_f is the critical extension strain, considered as material property by rock mechanicians. However, very careful measurements, performed in the present work, at three length scales, namely $L=0.16$ m, 0.4 m, and 1 m, preserving the similarity of the beams (constant aspect

ratio of the beam, $L/H=4$), gave the diagram of Fig.4 where ϵ_f is expressed by the following equation:

$$\epsilon_f = 179E-6 + \frac{23E-6}{L} \quad \text{or} \quad \frac{\epsilon_f}{\epsilon_{as}} = 1 + \frac{0.13}{L} \quad (23)$$

where ϵ_{as} is the failure strain for beams of infinite length. It is seen clearly the size effect exhibited by the critical extension strain of marble beams, which cannot be considered as a material property. It is seen from Eq.(23) that the size effect is pronounced in rather small length scales and then it attenuates quickly inversely proportional to the length, L , of the beam, to the asymptotic value $\epsilon_{as} = 179 \mu\epsilon$. Then according to the elementary beam theory and, also, Saint Venant's hypothesis, the failure load is given by the formula:

$$P_f = (8EI / LH) \epsilon_f \quad (24)$$

By virtue of size-dependency of failure strain given by Eq.(23) and using Eq.(24) it is concluded that the failure load increases as the beam length decreases. This is indeed the case as it is illustrated in Fig.5, where the experimental failure load is plotted versus the beam length. In the same figure the asymptotic value of the failure load for large L 's corresponding to the value $\epsilon_{as} = 179 \mu\epsilon$ is also displayed. It is seen that the two loads are the same for large beam lengths. It can be proved that the size dependency of the failure load of marble in 3PB, reduced over the respective one predicted by the classical theory, is described by the equation (Fig. 6):

$$P_f / P^0 = 0.91 + (0.08 / L) \quad (25)$$

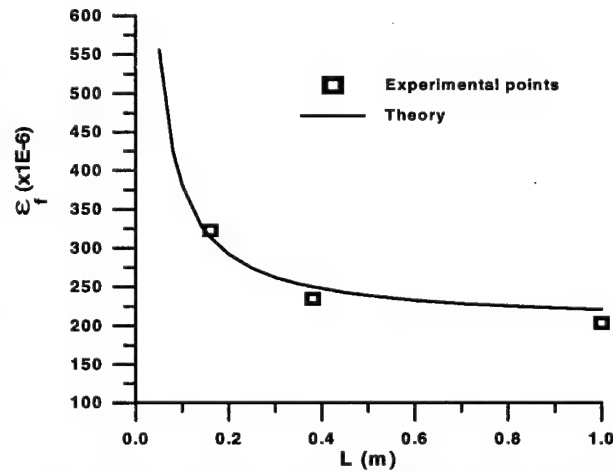


Figure 4: The size effect of the failure extension strain.

where the asymptotic value of 0.91 is due to the slight bimodularity of the specific marble (Dionysos-Pentelikon) [1,2,8-10].

It is interesting to note at this point that both the relative failure extension strain and the relative failure load depend in an inversely proportional manner on the beam length, in direct contrast to the predictions of the elementary beam theory. This $(1/L)$ dependency is probably due to the fact that the surface energy necessary to create the fracture at the midspan of the beam is proportional to L^2 whereas the elastic strain energy stored in the beam until failure is proportional to L^3 .

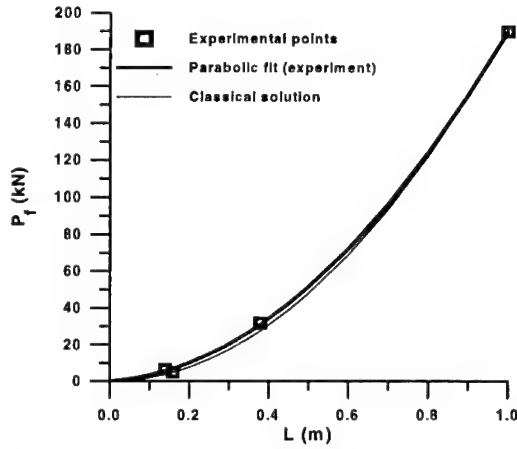


Figure 5: Failure load of Dionysos marble beams characterized by the same aspect ratio $L/H=4$ and different lengths L .

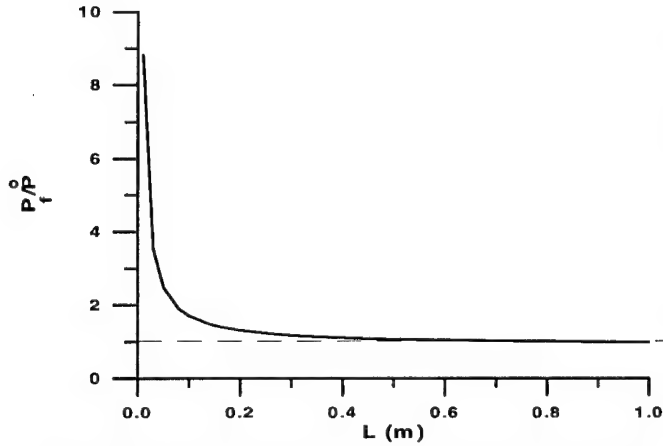


Figure 6: Size dependency of the reduced failure load ratio.

gradient-dependent beam theory is capable to capture the size effect of failure load ratio, with the preservation of similarity of beams, since it is enhanced with the extra length scale referring to surface energy ℓ_s (note that $\alpha = \ell / \ell_s$). Namely, from the following approximate formula that is obtained in the framework of the present theory:

$$\frac{P_f}{P_0} \approx \frac{1}{1 + 4\alpha\sqrt{(1+\nu)/5}(H/L)} \frac{\epsilon_f}{\epsilon_{as}} \quad (26)$$

and in combination with Eqs.(23) and (25) it is derived for an aspect ratio $L/H=4$:

$$\alpha = 0.2(9L + 5) / (9L + 1) \quad (27)$$

The above relationship means that in order to capture the size effect on both failure load and failure extension strain the relative length ratio, α , should depend on the beam length. From Eq.(27) the following asymptotic values of α can be obtained:

4. CONCLUSIONS

A gradient-dependent linear beam theory with intrinsic length scales was introduced in the present study to describe the mechanical behaviour of rock type materials under bending. As it is shown below, in Fig.7, and in contrast to Timoshenko's theory which contains only one intrinsic length scale that is proportional to the aspect ratio of the beam, H/L , the present special linear

$$\alpha|_{L \rightarrow 0} \approx 1, \quad \alpha|_{L \rightarrow \infty} \approx 0.2 \quad (28)$$

In order to check the validity of the above Eq.(27) the value of α for $L=0.4$ m is estimated:

$$\alpha \approx 0.38 \quad (29)$$

The above estimated value for the parameter α is in full agreement with the respective value of the same parameter estimated from the deflection measurements for the beam with $L=0.4$ m, that was $\alpha=0.37$ (Eq.(20)).

Finally, the size effect exhibited by the ratio of failure load to the load at the same maximum extension strain, as it is predicted by the conventional Bernoulli-Euler bending theory, based on Eq.(26) for the surface energy ratio, is displayed in Fig.7. For comparison, Timoshenko's prediction is, also, presented in the same figure by the thin line. This size effect is in accordance with experimental results for Dionysos-Pentelikon marble [3,11,12].

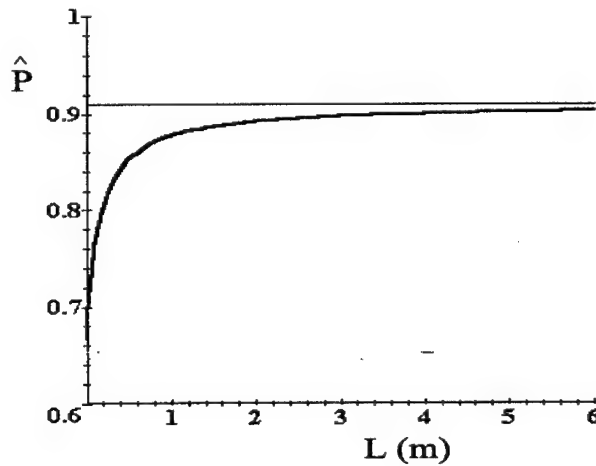


Figure 7: The size effect exhibited by the dimensionless failure load

It is, also, noted that the predictions of the theory introduced in the present work are in very good agreement with the experimental results not only for the failure load but, also, for the critical extension strain. This can be concluded from Fig.4 in which the continuous line depicting the predictions of the present theory almost coincides with the experimental results. The line was drawn using Eqs.(25) and (26) and considering the asymptotic value for the failure strain constant equal to $\varepsilon_{as}=179 \mu s$ [11,12]

Acknowledgements: The financial support of the European Union under the contract SMT4-CT96-2130 is gratefully acknowledged. The authors would like to acknowledge the assistance of Mr. G. Karydas and Mr. T. Gerakis in the execution of the experiments of the present work.

5. REFERENCES

- [1] Exadaktylos, G. E., Vardoulakis, I. and Kourkoulis, S. K., Influence of nonlinearity and double elasticity on flexure of rock beams - I. Technical theory, *International Journal of Solids and Structures*, in press (2001).
- [2] Exadaktylos, G. E., Vardoulakis, I. and Kourkoulis, S. K., Influence of nonlinearity and double elasticity on flexure of rock beams - II. Characterization of Dionysos marble, *International Journal of Solids and Structures*, in press (2001).
- [3] Vardoulakis, I., Exadaktylos, G. E., and Kourkoulis, S. K., Bending of marble with intrinsic length scales: A gradient theory with surface energy and size effects, *Journal de Physique*, 8, 399-406 (1998).
- [4] Zambas, C., Principles for the Structural Restoration of the Acropolis Monuments, in *The Engineering Geology of Ancient Works, Monuments and Historical Sites*, P. Marinos and G. C. Koukis (Eds), A.A. Balkema, Rotterdam, (1988) 1813-1818.
- [5] Timoshenko, S. P. and Goodier, J. N., *Theory of Elasticity*, Mc Graw-Hill, New York (1970).
- [6] Kourkoulis, S. K., Exadaktylos G. E. and Vardoulakis I, U-notched Dionysos Pentelikon marble in three point bending: The effect of nonlinearity, anisotropy and micro-structure, *International Journal of Fracture*, 98, 369-392 (1999).
- [7] Saint-Venant, B., *Notes to the third edition of Navier's: 'Resume des lecons de la resistance des corps solides'*, Paris, (1864).
- [8] Korres, M., *From Pendeli to Parthenon*, Melissa, Athens, Greece (1993).
- [9] Zambas, C., *Mechanical Properties of Pentelik Marbles*, Committee for the restoration of Parthenon publications, Athens, Greece (1994).
- [10] Vardoulakis, I., Exadaktylos, G. E. and Kourkoulis, S. K., Bending on Marble with Intrinsic Length Scales: Experiment and Modeling, in *Proceedings of the 2nd European Mechanics of Materials Conference*, A. Bertram, S. Forest and F. Sidoroff (Eds), Magdeburg, Germany (1997) 401-408.
- [11] Prassianakis I., Kourkoulis S. K., Vardoulakis I., and Exadaktylos G. E., Non-Destructive damage characterization of marble subjected to bending, in *Proceedings of the 2nd International Conference in Non Destructive Testing*, D. Van Hemelrijck, A. Anastasso-poulos and T. Philippidis (Eds.), A. A. Balkema, Rotterdam, (2000) 117-124.
- [12] Kourkoulis S. K., Stavropoulou M. C., Vardoulakis I. and Exadaktylos G. E. Local strains due to punch effect in three point bending of marble beams, in *Proceedings of the 9th International Congress on Rock Mechanics*, Paris, France, G. Vouille and P. Berest (Eds), A. A. Balkema, Rotterdam, (1999) 623-626.

FINITE ELEMENT TECHNIQUES FOR GRADIENT ELASTICITY PROBLEMS

E. Amanatidou and N. Aravas

Department of Mechanical and Industrial Engineering
University of Thessaly, GR-38334 Volos, Greece

1. SUMMARY

Theories with intrinsic or material length scales find applications in the modeling of size-dependent phenomena, such as the localization of plastic flow into shear bands. In gradient-type plasticity theories, length scales are introduced through the coefficients of spatial gradients of one or more internal variables. In elasticity, length scales enter the constitutive equations through the elastic strain energy function, which, in this case, depends not only on the strain tensor but also on gradients of the rotation and strain tensors. In the present paper we focus our attention on the strain-gradient elasticity theories developed by Mindlin and co-workers in the 1960's. In such theories, when the problem is formulated in term of displacements, the governing partial differential equation is of forth order. If traditional finite elements are used for the numerical solution of such problems, then C^1 displacement continuity is required. An alternative "mixed" finite element formulation is developed, in which the displacement and displacement-gradients are used as independent unknowns and their relationship is enforced in an "integral-sense". The resulting finite elements require only C^0 continuity and are simple to formulate. The proposed technique is applied to a number of model problems and comparisons with available exact solutions are made.

2. INTRODUCTION

Classical (local) continuum constitutive models possess no material/intrinsic length scale. The typical dimensions of length that appear are associated with the overall geometry of the domain under consideration. In spite of the fact that classical theories are quite sufficient for most applications, there is ample experimental evidence which indicates that, in certain applications, there is significant dependence on additional length/scale parameters. A first attempt to incorporate length scale effects in elasticity was made by Mindlin [4] and Koiter [3]. More recently, a variety of 'gradient-type' theories have been used in order to introduce material length scales into constitutive models (Aifantis and co-workers [1,7]). In the following we summarize briefly a family of strain-gradient elasticity theories introduced by Mindlin and co-workers [5, 6] and present a variational formulation which is used together with the finite element method for the numerical solution of boundary value problems.

3. A REVIEW OF STRAIN-GRADIENT ELASTICITY THEORIES

Let \mathbf{u} be the displacement field. The following quantities are defined:

$$\varepsilon_{ij} = u_{(i,j)} = \frac{1}{2}(u_{i,j} + u_{j,i}) = \text{strain}, \quad (1)$$

$$\Omega_{ij} = u_{[i,j]} = \frac{1}{2}(u_{i,j} - u_{j,i}) = -e_{ijk}\omega_k = \text{rotation tensor}, \quad (2)$$

$$\omega_i = \frac{1}{2}(\nabla \times \mathbf{u})_i = \frac{1}{2}e_{ijk}u_{k,j} = -\frac{1}{2}e_{ijk}\Omega_{jk} = \text{rotation vector (axial vector of } \Omega), \quad (3)$$

$$\bar{\kappa}_{ij} = \omega_{j,i} = \text{rotation gradient}, \quad \bar{\kappa}_{ii} = 0, \quad (4)$$

$$\bar{\kappa}_{ijk} = u_{k,ij} = \varepsilon_{jk,i} + \varepsilon_{ki,j} - \varepsilon_{ij,k} = \bar{\kappa}_{jik} = \text{second gradient of displacement}, \quad (5)$$

$$\hat{\kappa}_{ijk} = \frac{1}{2}(u_{j,ki} + u_{k,ji}) = \varepsilon_{jk,i} = \hat{\kappa}_{ikj} = \text{strain gradient}, \quad (6)$$

$$\bar{\bar{\kappa}}_{ijk} = \frac{1}{3}(u_{i,jk} + u_{j,ki} + u_{k,ij}) = \frac{1}{3}(\varepsilon_{ij,k} + \varepsilon_{jk,i} + \varepsilon_{ki,j}) = \bar{\bar{\kappa}}_{jik} = \bar{\bar{\kappa}}_{ikj} = \bar{\bar{\kappa}}_{kji} = \\ = \text{symmetric part of } \bar{\kappa}_{ijk} \text{ or } \hat{\kappa}_{ijk} \quad (7)$$

where e_{ijk} is the alternating symbol.

The above quantities are related by the following expressions (Mindlin and Eshel [5]):

$$\bar{\kappa}_{ijk} = \hat{\kappa}_{ijk} + \hat{\kappa}_{jki} - \hat{\kappa}_{kij} = \bar{\bar{\kappa}}_{ijk} + \frac{2}{3}\bar{\kappa}_{ip}e_{pj k} + \frac{2}{3}\bar{\kappa}_{jp}e_{pi k}, \quad (8)$$

$$\hat{\kappa}_{ijk} = \frac{1}{2}(\bar{\kappa}_{ijk} + \bar{\kappa}_{ikj}) = \bar{\bar{\kappa}}_{ijk} - \frac{1}{3}\bar{\kappa}_{jp}e_{kpi} - \frac{1}{3}\bar{\kappa}_{kp}e_{jpi}, \quad (9)$$

$$\bar{\kappa}_{ij} = \frac{1}{2}\bar{\kappa}_{ipk}e_{jpk} = \hat{\kappa}_{pi k}e_{jpk}, \quad \bar{\bar{\kappa}}_{ijk} = \frac{1}{3}(\bar{\kappa}_{ijk} + \bar{\kappa}_{jki} + \bar{\kappa}_{kij}) = \frac{1}{3}(\hat{\kappa}_{ijk} + \hat{\kappa}_{jki} + \hat{\kappa}_{kij}). \quad (10)$$

The alternative forms of the strain-gradient elasticity theory given by Mindlin [4] are summarized in the following. The strain energy density W is written in three equivalent forms:

$$W = \bar{W}(\boldsymbol{\varepsilon}, \bar{\boldsymbol{\kappa}}) = \hat{W}(\boldsymbol{\varepsilon}, \hat{\boldsymbol{\kappa}}) = \bar{\bar{W}}(\boldsymbol{\varepsilon}, \bar{\bar{\boldsymbol{\kappa}}}). \quad (11)$$

Mindlin refers to the description $W = \bar{W}(\boldsymbol{\varepsilon}, \bar{\boldsymbol{\kappa}})$ as "Type I", to $W = \hat{W}(\boldsymbol{\varepsilon}, \hat{\boldsymbol{\kappa}})$ as "Type II", and to $W = \bar{\bar{W}}(\boldsymbol{\varepsilon}, \bar{\bar{\boldsymbol{\kappa}}})$ as "Type III". Mindlin and Eshel [5] present the most general form of \bar{W} , \hat{W} and $\bar{\bar{W}}$ for an isotropic linear elastic material and derive the relationships among the material constants that appear in these three equivalent descriptions.

Using the above forms of the elastic strain energy density, one defines the following quantities:

$$\bar{\sigma}_{ij} = \frac{\partial \bar{W}}{\partial \varepsilon_{ij}} = \frac{\partial \hat{W}}{\partial \varepsilon_{ij}} = \frac{\partial \bar{\bar{W}}}{\partial \varepsilon_{ij}} = \bar{\sigma}_{ji}, \quad \bar{\mu}_{ijk} = \frac{\partial \bar{W}}{\partial \bar{\kappa}_{ijk}} = \bar{\mu}_{jik}, \quad \hat{\mu}_{ijk} = \frac{\partial \hat{W}}{\partial \hat{\kappa}_{ijk}} = \hat{\mu}_{ikj}, \quad (12)$$

$$\bar{\bar{\mu}}_{ij} = \frac{\partial \bar{\bar{W}}}{\partial \bar{\bar{\kappa}}_{ij}}, \quad \bar{\bar{\mu}}_{ijk} = \frac{\partial \bar{\bar{W}}}{\partial \bar{\bar{\kappa}}_{ijk}} = \bar{\bar{\mu}}_{jik} = \bar{\bar{\mu}}_{ikj} = \bar{\bar{\mu}}_{kji}. \quad (13)$$

It is worthy of note that $\bar{\sigma}_{ij}$, $\bar{\mu}_{ijk}$, $\hat{\mu}_{ijk}$, $\bar{\bar{\mu}}_{ij}$ and $\bar{\bar{\mu}}_{ijk}$ are introduced as "conjugate" quantities to ε_{ij} , $\bar{\kappa}_{ijk}$, $\hat{\kappa}_{ijk}$, $\bar{\bar{\kappa}}_{ij}$ and $\bar{\bar{\kappa}}_{ijk}$, and their relationship to "true" couple stress is not obvious.

Let σ_{ij} be the usual stress tensor and μ_{ij} the couple-stress tensor. On an infinitesimal area with unit normal vector \mathbf{n} , the traction vector \mathbf{t} and the couple vector \mathbf{m} are related to $\boldsymbol{\sigma}$ and $\boldsymbol{\mu}$ by $t_i = n_j \sigma_{ji}$ and $m_i = n_j \mu_{ji}$.

If the body force per unit volume is f_i and the body moment per unit volume is $M_i = e_{ijk}\Phi_{[jk]}$, then the principles of linear and angular momentum lead to the well known equations

$$\sigma_{ji,j} + f_i = 0 \quad \text{and} \quad \sigma_{[ij]} + \frac{1}{2}\mu_{pk,p}e_{ijk} + \Phi_{[ij]} = 0, \quad (14)$$

where Φ is the "body double force" per unit volume.

Mindlin and Eshel [5] have shown that the true stress σ is related to $\bar{\sigma}$, $\bar{\mu}$, $\hat{\mu}$, $\bar{\mu}$ and $\bar{\bar{\mu}}$ by the expressions

$$\begin{aligned}\sigma_{(ij)} &= \bar{\sigma}_{ij} - \frac{1}{3}(\bar{\mu}_{ijk,k} + \bar{\mu}_{jki,k} + \bar{\mu}_{kij,k}) - \Phi_{(ij)} = \\ &= \bar{\sigma}_{ij} - \frac{1}{3}(\hat{\mu}_{ijk,k} + \hat{\mu}_{jki,k} + \hat{\mu}_{kij,k}) - \Phi_{(ij)} = \bar{\sigma}_{ij} - \bar{\bar{\mu}}_{ijk,k} - \Phi_{(ij)},\end{aligned}\quad (15)$$

$$\sigma_{[ij]} = -\frac{4}{3}\bar{\mu}_{k[ij],k} - \Phi_{[ij]} = -\frac{2}{3}\hat{\mu}_{[ij]k,k} - \Phi_{[ij]} = -\frac{1}{2}e_{ijk}\bar{\mu}_{pk,p} - \Phi_{[ij]},\quad (16)$$

and the true couple stress μ is
$$\mu_{ij} = \frac{4}{3}\bar{\mu}_{ikp}e_{jkp} = \frac{2}{3}\hat{\mu}_{kpi}e_{jkp} = \bar{\mu}_{ij}.\quad (17)$$

4. VARIATIONAL FORMULATION

A given boundary value problem in strain-gradient elasticity can be formulated in any of the three equivalent ways discussed in the previous section. Here we discuss the Type III formulation and emphasize the calculation of true stresses and true couple stresses.

The governing equations in V are:

$$\sigma_{ji,j} + f_i = 0\quad (18)$$

$$\sigma_{ij} = \bar{\sigma}_{ij} + \bar{\sigma}_{ij}^{(2)}, \quad \bar{\sigma}_{ij}^{(2)} = -\bar{\mu}_{kij,k} - \frac{1}{2}e_{ijk}\bar{\mu}_{pk,p},\quad (19)$$

$$\varepsilon_{ij} = u_{(i,j)}, \quad \omega_i = -\frac{1}{2}e_{ijk}u_{j,k} \quad \text{or} \quad u_{[i,j]} = -e_{ijk}\omega_k,\quad (20)$$

$$\bar{\kappa}_{ij} = \omega_{j,i}, \quad \bar{\bar{\kappa}}_{ijk} = \frac{1}{3}(\varepsilon_{ij,k} + \varepsilon_{jk,i} + \varepsilon_{ki,j}),\quad (21)$$

$$\bar{\sigma}_{ij} = \frac{\partial \bar{W}}{\partial \varepsilon_{ij}}, \quad \bar{\mu}_{ij} = \frac{\partial \bar{W}}{\partial \bar{\kappa}_{ij}}, \quad \bar{\bar{\mu}}_{ijk} = \frac{\partial \bar{W}}{\partial \bar{\bar{\kappa}}_{ijk}}.\quad (22)$$

The corresponding boundary conditions are

$$u_i = \bar{u}_i \quad \text{on} \quad S_u,\quad (23)$$

$$n_j \sigma_{ji} - \frac{1}{2}n_j \bar{\mu}_{k,i}^n e_{ijk} + [(D_p n_p)n_j - D_j](n_k \bar{\mu}_{kji} + n_i n_p n_k \bar{\mu}_{kpi}) = \bar{P}_i \quad \text{on} \quad S_P,\quad (24)$$

$$\omega_i' = \bar{\omega}_i' \quad \text{on} \quad S_\omega,\quad (25)$$

$$n_j \bar{\mu}_{ji}^t + 2n_q n_j n_k \bar{\mu}_{kjp} e_{qpi} = \bar{Q}_i' \quad \text{on} \quad S_Q,\quad (26)$$

$$n_i n_j \varepsilon_{ij} = \bar{\varepsilon} \quad \text{on} \quad S_\varepsilon,\quad (27)$$

$$n_i n_j n_k \bar{\mu}_{ijk} = \bar{R} \quad \text{on} \quad S_R,\quad (28)$$

$$u_i = \bar{u}_i^\alpha \quad \text{on} \quad C_u^\alpha,\quad (29)$$

$$[[\frac{1}{2}s_j \bar{\mu}^n + \ell_j n_k (\bar{\mu}_{kji} + n_i n_p \bar{\mu}_{kpi})]] = \bar{E}_i^\alpha \quad \text{on} \quad C_E^\alpha,\quad (30)$$

where $\bar{\mu}^n = n_i n_j \bar{\mu}_{ij}$, $(\bar{u}, \bar{P}, \bar{\omega}', \bar{Q}', \bar{\varepsilon}, \bar{R}, \bar{u}^\alpha, \bar{E}^\alpha)$ are known functions, $S_u \cup S_P = S_\omega \cup S_Q = S_\varepsilon \cup S_R = S$, $S_u \cap S_P = S_\omega \cap S_Q = S_\varepsilon \cap S_R = 0$, $C_u^\alpha \cup C_E^\alpha = C^\alpha$, $C_u^\alpha \cap C_E^\alpha = 0$, $DA = n_i A_i$, and $D_j A = A_j - n_j DA = A_j - n_j n_j A_j = (\delta_{ij} - n_i n_j) A_j$.

We recall that, if we omit the terms involving $\bar{\kappa}$ in \bar{W} , set $\bar{\mu} = 0$ and $S_\varepsilon = S_R = 0$, then we recover the standard boundary value problem of "micropolar elasticity" (Koiter [3], Mindlin and Tiersten [6]).

In the following we present the variational formulation of the problem, in which \mathbf{u} , $\boldsymbol{\omega}$, $\boldsymbol{\varepsilon}$ and $\bar{\boldsymbol{\sigma}}^{(2)}$ are viewed as primary unknowns. In particular, the quantities \mathbf{u} , $\boldsymbol{\omega}$ and $\boldsymbol{\varepsilon}$ are considered as independent variables subject to suitable side conditions. These side conditions are:

- i) the kinematical equations $u_{i,j} = \varepsilon_{ij} - e_{ijk}\omega_k$ in the entire body, and
- ii) the expression of the tangential part of the $\varepsilon_{ij} - e_{ijk}\omega_k$ on the entire surface S in terms of the tangential derivatives $D_j u_i$ of the displacement, i.e.,

$$D_j u_i = (\varepsilon_{ij} - e_{ijk}\omega_k)^t = \varepsilon_{ij} - e_{ijk}\omega_k - \varepsilon_{ik}n_k n_j - e_{ipk}\omega_k n_p n_j \quad \text{on } S. \quad (31)$$

The integral form of the aforementioned equations is

$$\begin{aligned} \int_V \left[(\bar{\sigma}_{ji} + \bar{\sigma}_{ji}^{(2)})_{,j} + f_i \right] u_i^* dV + \int_{S_p} \left\{ \bar{P}_i - n_j (\bar{\sigma}_{ji} + \bar{\sigma}_{ji}^{(2)}) + \frac{1}{2} n_j \bar{\mu}_{,k}^n e_{ijk} - \right. \\ \left. - [(D_p n_p) n_j - D_j] (n_k \bar{\mu}_{kji} + n_i n_p n_k \bar{\mu}_{kpj}) \right\} u_i^* dS + \\ + \sum_{\alpha} \oint_{C_{\varepsilon}^{\alpha}} \left\{ \bar{E}_i^{\alpha} - \left[\frac{1}{2} s_i \bar{\mu}^n + \ell_j n_k (\bar{\mu}_{jki} + n_i n_p n_k \bar{\mu}_{pj k}) \right] \right\} u_i^* ds = 0, \end{aligned} \quad (32)$$

$$\int_V (e_{ijk} \bar{\sigma}_{[jk]}^{(2)} + \bar{\mu}_{ji,j}) \omega_i^* dV + \int_{S_o} (\bar{Q}_i^t - n_j \bar{\mu}_{ji}^t - 2 n_j n_p n_k \bar{\mu}_{jpk} e_{qpi}) \omega_i^* dS = 0, \quad (33)$$

$$\int_V (\bar{\sigma}_{(ij)}^{(2)} + \bar{\mu}_{ijk,k}) \varepsilon_{ij}^* dV + \int_{S_R} (\bar{R} - n_j n_p n_k \bar{\mu}_{ijk}) n_p n_q \varepsilon_{pq}^* dS = 0, \quad (34)$$

$$\int_V [u_{i,j} - (\varepsilon_{ij} + \Omega_{ij})] \bar{\sigma}_{ji}^{(2)*} dV = 0, \quad (35)$$

$$\int_S [D_j u_i - (\varepsilon_{ij} - e_{ijk}\omega_k - \varepsilon_{ik}n_k n_j + e_{ipk}\omega_k n_p n_j)] X_{ij}^* dS = 0, \quad (36)$$

where $X_{ij}^* = T_{(ij)}^* + n_j n_k T_{(kj)}^* + \frac{1}{2} e_{ijk} n_k \bar{\mu}^{n*}$, $T_{(ij)} = n_k \bar{\mu}_{kij}$, $\bar{\mu}^n = \mathbf{n} \cdot \bar{\boldsymbol{\mu}} \cdot \mathbf{n}$ and $\Omega_{ij}(\boldsymbol{\omega}) = -e_{ijk}\omega_k$.

Equations (32)-(36) are required to hold for all $\mathbf{u}^* \in L^2$ such that $\mathbf{u}^* = 0$ on S_u and C_u^{α} , for all $\boldsymbol{\omega}^* \in L^2$ such that $\boldsymbol{\omega}^* = 0$ on S_{ω} , for all $\boldsymbol{\varepsilon}^* \in L^2$ such that $\mathbf{n} \cdot \boldsymbol{\varepsilon}^* \cdot \mathbf{n} = 0$ on S_{ε} , and for all $\mathbf{X}^* \in L^2$, where L^2 is the space of square integrable functions.

After integration by parts we arrive at the weak statement of the problem, which is as follows.

Find **a)** $\mathbf{u}(\mathbf{x}) \in H^1$ satisfying $\mathbf{u}|_{S_u} = \bar{\mathbf{u}}$ and $\mathbf{u}|_{C_u^{\alpha}} = \bar{\mathbf{u}}^{\alpha}$ (where H^k is the space of functions with square-integrable derivatives through order k), **b)** $\boldsymbol{\omega}(\mathbf{x}) \in H^1$ satisfying $\boldsymbol{\omega}|_{S_{\omega}} = \bar{\boldsymbol{\omega}}^t$, **c)** $\boldsymbol{\varepsilon}(\mathbf{x}) = \boldsymbol{\varepsilon}^T(\mathbf{x}) \in H^1$ satisfying $\mathbf{n} \cdot \boldsymbol{\varepsilon}|_{S_{\varepsilon}} \cdot \mathbf{n} = \bar{\boldsymbol{\varepsilon}}$, and **d)** $\bar{\boldsymbol{\sigma}}^{(2)}(\mathbf{x}) \in L^2$, such that for all $\mathbf{u}^* \in H^1$ satisfying $\mathbf{u}^*|_{S_u} = \mathbf{u}^*|_{C_u^{\alpha}} = 0$, for all $\boldsymbol{\omega}^* \in H^1$ satisfying $\boldsymbol{\omega}^*|_{S_{\omega}} = 0$, for all $\boldsymbol{\varepsilon}^* \in H^1$ $\mathbf{n} \cdot \boldsymbol{\varepsilon}^*|_{S_{\varepsilon}} \cdot \mathbf{n} = 0$ on S_{ε} , for all $\mathbf{T}_{(ij)}^* \in L^2$ and for all $\bar{\mu}^{n*} \in L^2$:

$$\begin{aligned} \int_V (\bar{\sigma}_{ji} + \bar{\sigma}_{ji}^{(2)}) u_{i,j}^* dV + \int_S T_{(ij)} (u_{i,j}^* - 2 n_j n_k u_{[i,k]}^* - n_i n_p n_q u_{(p,q)}^*) dS + \\ + \int_S \frac{1}{2} \bar{\mu}^n e_{ijk} u_{k,j}^* n_i dS = \int_V f_i u_i^* dV + \int_{S_p} \bar{P}_i u_i^* dV + \sum_{\alpha} \oint_{C_{\varepsilon}^{\alpha}} \bar{E}_i^{\alpha} u_i^* ds, \end{aligned} \quad (37)$$

$$\int_V (-e_{ijk} \bar{\sigma}_{[jk]}^{(2)} \omega_i^* + \bar{\mu}_{ij} \bar{\kappa}_{ij}^*) dV - \int_S (2T_{(ij)} n_j n_k e_{ikp} \omega_p^* - \bar{\mu}^n n_i \omega_i^*) dS = \int_{S_Q} \bar{Q}_i' \omega_i^* dS, \quad (38)$$

$$\int_V (-\bar{\sigma}_{(ij)}^{(2)} \varepsilon_{ij}^* + \bar{\mu}_{ijk} \bar{\kappa}_{ijk}^*) dV + \int_S T_{(ij)} (-\varepsilon_{ij}^* + n_i n_j n_p n_q \varepsilon_{pq}^*) dS = \int_{S_R} \bar{R} n_i n_j \varepsilon_{ij}^* dS, \quad (39)$$

$$\int_V [u_{i,j} - (\varepsilon_{ij} - e_{ijk} \omega_k)] \bar{\sigma}_{ji}^{(2)*} dV = 0, \quad (40)$$

$$\int_S [u_{(i,j)} - 2n_j n_k u_{[i,k]} - n_i n_j n_p n_q u_{(p,q)} - (\varepsilon_{ij} + 2n_j n_k e_{ikp} \omega_p - n_i n_j n_p n_q \varepsilon_{pq})] T_{(ij)}^* dS = 0, \quad (41)$$

$$\int_S \left(\frac{1}{2} e_{ijk} u_{k,j} n_i - \omega_i n_i \right) \bar{\mu}^{nn*} dS = 0. \quad (42)$$

5. APPLICATIONS

As an example, we consider the special case where

$$\begin{aligned} \bar{W}(\varepsilon, \bar{\kappa}, \bar{\kappa}) = & \frac{1}{2} \lambda \varepsilon_{ii} \varepsilon_{kk} + \mu \varepsilon_{ij} \varepsilon_{ij} + \ell^2 \left[\frac{2}{9} (\lambda + 3\mu) \bar{\kappa}_{ij} \bar{\kappa}_{ij} - \frac{2}{9} \lambda \bar{\kappa}_{ij} \bar{\kappa}_{ji} + \right. \\ & \left. + \frac{1}{2} \lambda \bar{\kappa}_{ij} \bar{\kappa}_{kkj} + \mu \bar{\kappa}_{ijk} \bar{\kappa}_{ijk} + \frac{2}{3} \lambda e_{ijk} \bar{\kappa}_{ij} \bar{\kappa}_{kpp} \right], \end{aligned} \quad (43)$$

so that

$$\bar{\sigma}_{ij} = \frac{\partial \bar{W}}{\partial \varepsilon_{ij}} = \frac{\partial \bar{W}}{\partial \varepsilon_{ij}} = \frac{\partial \bar{W}}{\partial \varepsilon_{ij}} = 2\mu \varepsilon_{ij} + \lambda \varepsilon_{kk} \delta_{ij}, \quad (44)$$

$$\bar{\mu}_{ij} = \frac{\partial \bar{W}}{\partial \bar{\kappa}_{ij}} = \frac{2\ell^2}{9} [2(\lambda + 3\mu) \bar{\kappa}_{ij} - 2\lambda \bar{\kappa}_{ji} + 3\lambda e_{ijk} \bar{\kappa}_{kpp}], \quad (45)$$

$$\bar{\mu}_{ijk} = \frac{\partial \bar{W}}{\partial \bar{\kappa}_{ijk}} = \frac{\ell^2}{9} [3\lambda (\bar{\kappa}_{ppk} \delta_{ij} + \bar{\kappa}_{ppj} \delta_{ik} + \bar{\kappa}_{ppi} \delta_{kj}) + 18\mu \bar{\kappa}_{ijk} + 2\lambda \bar{\kappa}_{pq} (\delta_{ij} e_{pqk} + \delta_{jk} e_{pqi} + \delta_{ki} e_{pqj})]. \quad (46)$$

For the gradient model presented here, a number of boundary value problems have been solved analytically, so that comparisons with exact solutions can be made (Exadaktylos [2]).

An infinite plate with a hole

We consider the problem of an infinite plate with a hole of radius a subjected to biaxial tension p . With couple-stresses taken into account, the stress-concentration factor, instead of having the usual value 2, depends both on Poisson's ratio and the ratio of the radius of the hole, α , to the material constant ℓ .

The exact solution of this problem has been developed by Exadaktylos [2] and is of the form,

$$u(r) = \frac{p}{2G} \left\{ (1-2\nu)r + \frac{a^2}{r} + \frac{\ell}{c} \left[\frac{a}{r} K_1\left(\frac{a}{\ell}\right) - (1-2\nu) K_1\left(\frac{r}{\ell}\right) \right] \right\} \quad (47)$$

$$\text{where} \quad c = \frac{1-2\nu}{2} K_0\left(\frac{a}{\ell}\right) + \frac{1-\nu}{2} \left(\frac{4\ell}{a} + \frac{a}{\ell} \right) K_1\left(\frac{a}{\ell}\right) \quad (48)$$

and $K_n(x)$ are the well known "modified Bessel functions of the second kind".

The problem is solved by using a nine-node isoparametric element. The quantities $(u_1, u_2, \omega_3, \varepsilon_{11}, \varepsilon_{22}, 2\varepsilon_{12})$ are used as degrees of freedom at all nodes and the quantities

$(\sigma_{11}^{(2)}, \sigma_{22}^{(2)}, \sigma_{(12)}^{(2)}, \sigma_{[12]}^{(2)})$ are additional degrees of freedom at the corner nodes. A bi-quadratic Lagrangian interpolation for $(u_1, u_2, \omega_3, \varepsilon_{11}, \varepsilon_{22}, 2\varepsilon_{12})$ and a bi-linear for $(\sigma_{11}^{(2)}, \sigma_{22}^{(2)}, \sigma_{(12)}^{(2)}, \sigma_{[12]}^{(2)})$ are used in the isoparametric plane.

Figure 1 shows the results of the finite element calculations with the exact solution for the variation of σ_{rr} and $\sigma_{\theta\theta}$ along the radial line $\theta = 2.25^\circ$ (i.e., along the radial line passing through the centers of the row of elements close to the x_1 -axis). The numerical solution agrees well with the analytical solution for the infinite plate.

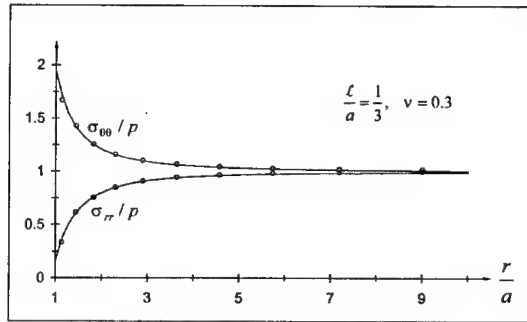


Figure 1: Variation of σ_{rr} and $\sigma_{\theta\theta}$ for the plate with a hole.

Acknowledgements: This work was carried out while the authors were supported by the GSRT of Greece under Grant No. PENED 99 ED 642.

6. REFERENCES

- [1] Aifantis, E. C., On the microstructural origin of certain inelastic models, *J. Eng. Matl. Tech.* 106, pp. 326-330, (1984).
- [2] Exadaktylos, G., On the problem of the circular hole in an elastic material with microstructure, to appear, (2000).
- [3] Koiter, W. T., Couple stresses in the theory of elasticity I and II, *Proc. K. Ned. Akad. Wet. (B)* 67, pp. 17-44 (1964).
- [4] Mindlin, R. D., Microstructure in linear elasticity, *Archs Ration. Mech. Anal.* 10, pp. 51-78 (1964).
- [5] Mindlin, R. D. and Eshel, N. N., On first strain-gradient theories in linear elasticity, *Int. J. Solids Struct.* 4, pp. 109-124 (1968).
- [6] Mindlin, R. D. and Tiersten, H. F., Couple-stresses in linear elasticity, *Archs Ration. Mech. Anal.* 11, pp. 415-448 (1962).
- [7] Ru, C. Q. and Aifantis, E. C., A simple approach to solve boundary-value problems in gradient elasticity, *Acta Mechanica* 101, pp. 59-58 (1993).

THE ELASTIC PUNCH PROBLEM REVISITED

G. Exadaktylos

Department of Mineral Resources Engineering - Laboratory of Mine Design and Mechanics,
Technical University of Crete, GR-73100, Chania, Greece

1. SUMMARY

A contact boundary value problem that has significant practical applications in soil and rock foundations engineering and penetration mechanics is the elastic punch problem. This problem is revisited here in the frame of the proposed *Hooke-Cauchy-Casal-Mindlin* higher order elasticity theory. The closed-form solution is achieved by virtue of the theories of complex potentials and Fourier transforms, as well as the theory of Fredholm integral equations.

2. INTRODUCTION

The proposed grade-2 (or strain-gradient) elasticity theory may be viewed as a generalization of Hooke-Cauchy grade-1 elasticity theory by including apart from the classical Lamé constants λ, μ two additional material length scales ℓ, ℓ' as it was proposed previously by Casal [1]. The length scale ℓ is associated with molecular forces of cohesion whereas ℓ' is associated with the surface energy of the material. The generalization of the present grade-2 theory is based on Mindlin's general theory of elasticity with microstructure [2]. It is worth noticing that the consideration of the surface energy in the present theory leads to a constitutive character of the boundary conditions. This strengthens Aifantis' [3] conjecture of the constitutive character of boundary constraints in materials with microstructure. I. Vardoulakis, noting this fact, states [4]: '*...The problem of constitutive boundary conditions is open and deserves further attention from the theoretical as well as the experimental point of view...*'. Furthermore, A. Pearson in his opening lecture at the IUTAM Symposium on 'Non-Linear Singularities in Deformation and Flow', in Technion, Haifa in 1997 [5], states: '*...The full constitutive nature of boundary conditions is often neglected in many continuum models and so oversimplified forms are imposed in physical models...*'.

This study is a sequel to a previous investigation [6] concerning the half-plane problem under concentrated edge forces and under a uniform distribution of shearing tractions. Both problems involve load-induced concentrations of displacement and strain, respectively, and it is illustrated elegantly how the proposed higher order elasticity theory can remove these physically undesirable singularities. It is mentioned here that this elimination of the logarithmic singularities on normal and tangential displacements, respectively, has been first performed in [7] by employing a Hooke-Mindlin special grade-2 theory.

In the frame of the proposed higher elasticity theory we revisit here the elastic punch problem. It is shown that this mixed-mixed plane strain boundary value problem is reduced to

a regular Fredholm integral equation of the second kind that can be solved analytically or numerically by standard methods.

3. BASIC EQUATIONS OF GRADE-2 ELASTICITY THEORY

In several previous papers [8,9] we have shown that the solution of the static problems in linear, isotropic, gradient-dependent solids requires the solution of the following set of equations (A), (B) and (C), namely:

(A) The stress equilibrium equation in the volume V

$$\partial_j \sigma_{ij} + f_i = 0 \quad (1)$$

where f_i is the body force per unit volume and σ_{ij} may be called Cauchy stress.

(B) In the case of a plane boundary the traction and double traction boundary conditions on the surface ∂V of the considered volume V simplifies as follows

$$n_j \sigma_{jk} = \tilde{P}_k, \quad n_i n_j \mu_{ijk} = \tilde{R}_k \quad (2)$$

wherein n_k is the outward unit normal on the boundary ∂V and $\mathbf{t} = \mathbf{n} \cdot \boldsymbol{\sigma}$ is the Cauchy stress vector associated with the Cauchy stress tensor $\boldsymbol{\sigma}$. In relation (2) the third order stress tensor μ_{ijk} , which is dual in energy to the strain-gradient is called the "double stress" [2].

(C) The constitutive relations for the Cauchy stress and double stress tensors, respectively

$$\begin{aligned} \sigma_{ij} &= \lambda \delta_{ij} \varepsilon_{kk} + 2\mu \varepsilon_{ij} - \ell^2 \nabla^2 (\lambda \delta_{ij} \varepsilon_{kk} + 2\mu \varepsilon_{ij}) \\ \mu_{kij} &= \ell_k (\lambda \delta_{ij} \varepsilon_{\ell\ell} + 2\mu \varepsilon_{ij}) + \ell^2 \partial_k (\lambda \delta_{ij} \varepsilon_{\ell\ell} + 2\mu \varepsilon_{ij}) \end{aligned} \quad (3)$$

where δ_{ij} is the Kronecker delta, ∇^2 denotes the Laplacian operator, ε_{ij} is the symmetric part of the displacement field defined as follows

$$\varepsilon_{ij} = \frac{1}{2} (\partial_j u_i + \partial_i u_j) \quad (4)$$

and

$$\ell_k = \ell' v_k, \quad v_k v_k = 1 \quad (5)$$

is a director. In relationship (4) u_i is the Cartesian component of the displacement vector and $\partial_k \equiv \partial / \partial x_k$, with x_k to denote space coordinates.

4. DISPLACEMENT AND COMPLEX POTENTIALS OF GRADE-2 THEORY

By substituting in stress equilibrium equation (1) the constitutive relations for the stresses given in the first of (3) and expressing the strains in terms of displacements through (4) it can be proved that any solution \mathbf{u} of the displacement-equation of equilibrium in a region V bounded by a surface ∂V , can be expressed by the following Generalized Neuber-Papkovitch representation

$$\mathbf{u} = \mathbf{B}^c - \frac{1}{2} \nabla \left(1 - \frac{1}{k} \right) \left[\mathbf{r} \cdot \mathbf{B}^c + B_0^c \right] - \left(1 - \frac{1}{k} \right) \ell^2 \nabla \nabla \cdot \mathbf{B}^c + \mathbf{u}^+; \quad (6)$$

$$\nabla^2 \mathbf{B}^c = 0, \nabla^2 B_0^c = 0, \bar{D}^2 \mathbf{u}^+ = 0,$$

where $k = (\lambda + 2\mu) / \mu = 2(1 - \nu) / (1 - 2\nu)$, ν is Poisson's ratio, \mathbf{B}^c, B_0^c denote the Neuber's-Papkovitch's functions of classical elasticity when $\ell = 0$, the bold-typed letters denote vectors, ∇ is the gradient operator, $\nabla \cdot$ is the divergence operator, and the operator \bar{D}^2 is defined as follows

$$\bar{D}^2 \equiv 1 - \ell^2 \nabla^2 \quad (7)$$

Thus, the extra unknown displacement vector \mathbf{u}^+ have to be estimated from the double-traction boundary conditions prescribed by the second of relations (3). It is possible to take one of B_1^c, B_2^c equal to zero, but a more elegant theory may be derived by virtue of the complex function theory which has been developed in a rigorous manner by Muskhelishvili [10]. It has shown in [9] that the following complex representation for the displacements holds true

$$2G(u_1 + iu_2) = \kappa \phi(z) - \bar{\psi}(\bar{z}) - z \bar{\phi}'(\bar{z}) - 4\ell^2 \bar{\phi}''(\bar{z}) + (u_1^+ + iu_2^+) \quad (8a)$$

with the identities $\partial / \partial z \equiv (1/2)(\partial / \partial x_1 - i\partial / \partial x_2)$ and $\partial / \partial \bar{z} \equiv (1/2)(\partial / \partial x_1 + i\partial / \partial x_2)$, $\bar{z} = x_1 - ix_2$ is the complex conjugate of $z = x_1 + ix_2$, the prime denotes differentiation with respect to z , and $i \equiv \sqrt{-1}$ is the usual imaginary unit. Also, in relation (8a) $\phi(z), \psi(z)$ denote the Kolosov-Muskhelishvili analytical complex functions that correspond to the relevant classical traction-boundary-value problem, and $\kappa = 3 - 4\nu$ is *Muskhelishvili's* constant for plane strain conditions.

Then, the strains and stresses referred to the Cartesian coordinates x_1, x_2 can be found as follows [9]

$$\left. \begin{aligned} 2\mu(\varepsilon_{11} + \varepsilon_{22}) &= (\kappa - 1)\{\phi'(z) + \bar{\phi}'(\bar{z})\} + (u_{1,1}^+ + u_{2,2}^+), \\ 2\mu(\varepsilon_{22} - \varepsilon_{11} + 2i\varepsilon_{12}) &= 2\left\{\psi'(z) + \bar{z}\phi''(z) + 4\ell^2 \bar{\phi}'''(\bar{z}) - \frac{\partial}{\partial z}(u_1^+ - iu_2^+)\right\}, \\ \sigma_{11} + \sigma_{22} &= 2[\phi'(z) + \bar{\phi}'(\bar{z})], \\ \sigma_{22} - \sigma_{11} + 2i\sigma_{12} &= 2[\bar{z}\phi''(z) + \psi'(z)]. \end{aligned} \right\} \quad (8b)$$

The following complex representation can be also found for the double stresses μ_{yy}, μ_{yyx} which enter into the boundary conditions [9]

$$\begin{aligned} \mu_{222} + i\mu_{221} = & (\ell' + \ell^2 \partial_2) \left\{ \frac{\kappa - 1}{2(1 - 2\nu)} [\phi'(z) + \bar{\phi}'(\bar{z})] + \right. \\ & \left. [\psi'(z) + \bar{z}\phi''(z) + 4\ell^2 \phi'''(z)] + \frac{1}{2(1 - 2\nu)} (u_{1,1}^+ + u_{2,2}^+) - \frac{\partial}{\partial z} (u_1^+ - iu_2^+) \right\} \end{aligned} \quad (8c)$$

5. THE SMOOTH FLAT-ENDED PUNCH PROBLEM

Let us consider the mixed-mixed plane strain problem of a weightless geomaterial that is pressed in frictionless contact and at right angles to its bounding edge by a rigid flat-ended footing or punch of width 2α (Fig. 1). This problem is governed by the following boundary conditions

$$\begin{aligned} \sigma_{12} &= 0, & -\infty < x_1 < \infty, \quad x_2 &= 0, \\ \frac{\partial u_2}{\partial x_1} \Big|_{(x_1, 0)} &= 0, & 0 \leq |x_1| < \alpha, \\ \sigma_{22}(x_1, 0) &= 0, & \alpha < |x_1| < \infty, \\ \mu_{221} = \mu_{222} &= 0, & -\infty < x_1 < \infty, \quad x_2 &= 0, \end{aligned} \quad (9)$$

which are accompanied with the following load and regularity conditions at infinity

$$\begin{aligned} \int_{-\alpha}^{\alpha} \sigma_{22}(x_1, 0) dx_1 &= P, \\ \sigma_{ij}, \mu_{ijk} &\rightarrow 0 \text{ as } \sqrt{x_1^2 + x_2^2} \rightarrow \infty \end{aligned} \quad (10)$$

where P is the total punch pressure.

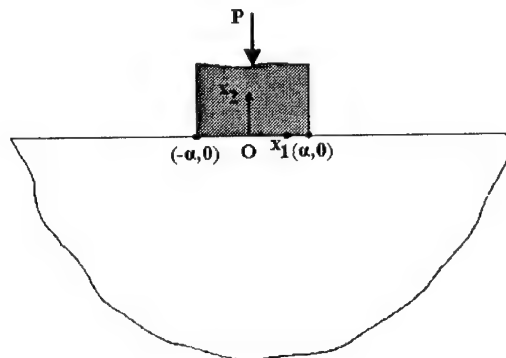


Figure 1: Smooth flat-ended punch.

The classical representations of the complex functions for problems possessing x_1 -axis symmetry are given by

$$2\phi'(z) = Z_I, \quad \psi'(z) = -z\phi''(z) \quad (11)$$

where Z_I denotes the Westergaard stress function. The function for the classical boundary value problem at hand that is prescribed by the first three conditions (9) is the following [11]

$$Z_I = \frac{P}{\pi} \int_0^\infty J_0(\alpha\xi) e^{-i\xi z} d\xi = -\frac{P}{\pi} \frac{1}{\sqrt{\alpha^2 - z^2}}, \quad 0 \leq |x| < \alpha \quad (12)$$

wherein J_0 is the zero-order Bessel function of the first kind. Finally, from equations (8a) and (11) we find

$$\begin{aligned} 2\mu u_1 &= (1-2\nu) \operatorname{Re}(\bar{Z}_I) - x_2 \operatorname{Im}(Z_I) - 2\ell^2 \operatorname{Re}(Z_I') + u_1^+, \\ 2\mu u_2 &= 2(1-\nu) \operatorname{Im}(\bar{Z}_I) - x_2 \operatorname{Re}(Z_I) + 2\ell^2 \operatorname{Im}(Z_I') + u_2^+ \end{aligned} \quad (13)$$

where $\operatorname{Re}(\cdot)$ and $\operatorname{Im}(\cdot)$ denote the real and imaginary parts, respectively, of what they enclose. The unknown gradient displacement functions $u_1^+(x_1, x_2)$, $u_2^+(x_1, x_2)$ may be found from the solution of Helmholtz's equations [e.g. (6)] subjected to the double traction boundary conditions given by the last of equations (9). The general solution of the functions u_1^+, u_2^+ for the half-plane $x_2 \leq 0$, considering the regularity conditions at infinity and symmetry relations furnishes

$$\{u_1^+(x_1, x_2), u_2^+(x_1, x_2)\} = \left\{ F_S[\{\bar{v}(\xi)e^{x_2 a(\xi)}; \xi \rightarrow x_1\}], F_C[\{\bar{v}(\xi)e^{x_2 a(\xi)}; \xi \rightarrow x_1\}] \right\} \quad (14)$$

$x_2 \leq 0,$

In the above expressions ξ is a real-valued transform parameter, the function a is defined as follows

$$a(\xi) \equiv \sqrt{\xi^2 + \ell^{-2}}, \quad 0 \leq \xi < \infty \quad (15)$$

and we have adopted the following Fourier transform notations

$$F_C[f(x); x \rightarrow \xi] \equiv \sqrt{\frac{2}{\pi}} \int_0^\infty f(x) \cos(x\xi) dx, \quad F_S[f(x); x \rightarrow \xi] \equiv \sqrt{\frac{2}{\pi}} \int_0^\infty f(x) \sin(x\xi) dx. \quad (16)$$

Proceeding formally if we substitute the values of the Westergaard terms and expressions (14) appearing in the right-hand-side of equation (8c) the following system of equations is obtained in the transform domain

$$\begin{aligned}
(\ell' + \ell^2 a)(1-v)a\bar{u} + v\xi\bar{u} &= -\sqrt{\frac{\pi}{2}}(1-2v)\frac{P}{\pi} \left[\ell' - 2\ell'\ell^2\xi^2 - 2\ell^4\xi^3 \right] J_0(\alpha\xi), \\
(\ell' + \ell^2 a)a\bar{u} - \xi\bar{v} &= 2\sqrt{\frac{\pi}{2}}\frac{P}{\pi} \left[-\ell^2\xi - 2\ell'\ell^2\xi^2 - 2\ell^4\xi^3 \right] J_0(\alpha\xi), 0 \leq \xi < \infty.
\end{aligned} \tag{17}$$

The solution of the above system of simultaneous linear equations and its subsequent inversion by virtue of Fourier transform formulae gives

$$\begin{aligned}
u_1^+(x_1, x_2) &= \frac{2}{\pi} \int_0^\alpha g(\eta) d\eta \int_0^\infty \left\{ -\frac{[(1-2v)(2\ell^4\xi^2 - \ell'\xi^{-1})a + 4v\ell'\ell^2\xi^2]}{[v\xi^2 + (1-v)a^2](\ell' + \ell^2 a)} \xi a^{-1} + \frac{4\ell'\ell^2\xi a^{-1}}{(\ell' + \ell^2 a)} \right\} \\
&\quad \times \xi \sin(x_1 - \eta) \xi e^{ax^2} d\xi, \\
u_2^+(x_1, x_2) &= -\frac{2}{\pi} \int_0^\alpha g(\eta) d\eta \int_0^\infty \frac{[(1-2v)(2\ell^4\xi^2 - \ell'\xi^{-1})a + 4v\ell'\ell^2\xi^2]}{[v\xi^2 + (1-v)a^2](\ell' + \ell^2 a)} \\
&\quad \times \xi \cos(x_1 - \eta) \xi e^{ax^2} d\xi, \quad x_2 \leq 0.
\end{aligned} \tag{18}$$

where we have set

$$\begin{aligned}
2 \int_0^\alpha g(x_1) dx_1 &= P, \\
g(x_1) &= 0 \quad \alpha < |x_1| < \infty, \quad g(-x_1) = g(x_1) \quad 0 \leq |x_1| < \alpha
\end{aligned} \tag{19}$$

Next the second of the boundary conditions (9) is satisfied if and only if

$$\begin{aligned}
2\mu \frac{\partial u_2}{\partial x_1}(x_1, 0) &= \frac{2(1-v)}{\pi} \int_{-\alpha}^\alpha \frac{g(\eta) d\eta}{(x_1 - \eta)} + \frac{4\ell^2}{\pi} \int_{-\alpha}^\alpha \frac{g(\eta) d\eta}{(x_1 - \eta)^3} + \\
&\quad \frac{1}{\pi} \int_{-\alpha}^\alpha g(\eta) d\eta \int_0^\infty \beta(\xi) \sin(x_1 - \xi) d\xi, \quad 0 \leq |x| < \alpha
\end{aligned} \tag{20}$$

where

$$\beta(\xi) = \frac{[(1-2v)(2\ell^4\xi^2 + \ell'\xi^{-1})a + 4v\ell'\ell^2\xi^2] \xi^2}{[v\xi^2 + (1-v)a^2](\ell' + \ell^2 a)}, \quad 0 \leq \xi < \infty \tag{21}$$

Next we assume the following Riemann-Liouville fractional integral representation for the function $g(x)$

$$g(x_1) = \frac{A}{\pi} \left[\frac{1}{\sqrt{\alpha^2 - x^2}} + \int_x^\alpha \frac{\omega(t)}{\sqrt{t^2 - x^2}} dt \right] \quad 0 \leq x_1 < \alpha \tag{22}$$

where A and ω are an as yet undetermined constant and an undetermined function, respectively. Substituting (22) into (20) and considering the x_1 -axis symmetry of function g we obtain the following nonhomogeneous singular¹ integral equation for the unknown function ω

$$\int_0^{\alpha} \omega(t) dt \int_0^{\infty} [2(1-\nu) + \gamma(\xi)] J_0(\xi \alpha) \sin \xi x d\xi = - \int_0^{\infty} [2(1-\nu) + \gamma(\xi)] J_0(\xi \alpha) \sin \xi x d\xi, \quad 0 \leq x < \alpha \quad (23)$$

in which

$$\gamma(\xi) = \beta(\xi) - 2\ell^2 \xi^2, \quad 0 \leq \xi < \infty \quad (24)$$

The above integral equation Fredholm integral equation of the first kind may be transformed into an Abel equation for the unknown function ω as follows

$$\int_0^x \frac{\omega(t) dt}{\sqrt{x^2 - t^2}} = f(x), \quad 0 \leq x < \alpha, \quad (25)$$

$$f(x) = -\frac{1}{2(1-\nu)} \left\{ \int_0^{\alpha} \omega(t) dt \int_0^{\infty} \gamma(\xi) J_0(\xi t) \sin \xi x d\xi + \int_0^{\infty} [2(1-\nu) + \gamma(\xi)] J_0(\xi \alpha) \sin \xi x d\xi \right\}$$

Finally, the above singular integral equation takes the following form of a Fredholm integral equation of the second kind with a symmetric kernel

$$\omega(t) = -\frac{t}{2(1-\nu)} \int_0^{\alpha} \omega(\tau) d\tau \int_0^{\infty} \xi \gamma(\xi) J_0(\xi \tau) J_0(\xi t) d\xi - \frac{t}{2(1-\nu)} \int_0^{\infty} \xi [2(1-\nu) + \gamma(\xi)] J_0(\xi \alpha) J_0(\xi t) d\xi, \quad 0 \leq t < \alpha, \quad (26)$$

The integral equation (26) may be solved analytically or numerically. The solution permits the evaluation of the function g by virtue of (22). Subsequently the gradient displacements may be found from relations (18) and the total displacements via equations (13). Finally the strains and double stresses can be estimated through relations (8b,c).

Acknowledgements: This article is a partial result of research supported by funds of GSRT of Hellas through the programme PENED 99 ED 642.

¹ Since the kernel $\int_0^{\infty} \gamma(\xi) J_0(\xi t) \sin \xi x d\xi$ is divergent at the upper limit for $t=x$

6. REFERENCES

- [1] Casal, P., La capillarite interne, *Cahier du Groupe Francais d'Etudes de Rheologie C.N.R.S.* VI(3): 31-37, 1961.
- [2] Mindlin, R.D., Micro-structure in linear elasticity, *Arch. Rational Mech. Anal.* 16: 51-78, 1964.
- [3] Aifantis, E.C., A proposal for continuum with microstructure, *Mechanical Research Communication*, 5, 139-145, 1978.
- [4] Vardoulakis, I., Shah, K. R. and Papanastasiou, P., Modelling of tool-rock interfaces using gradient-dependent flow theory of plasticity, *Int. J. Rock Mech. and Mining Sci. & Geomech. Abstr.*, 29(6), 573-582, 1992.
- [5] Pearson, J.R.A., Length scales, asymptotics and non-linear singularities, In: *Non-linear singularities in deformation and flow*, Durban D. and Pearson J.R.A. editors, IUTAM Symposium, Haifa, Israel, 1997.
- [6] Exadaktylos, G., Some basic half-plane problems of the cohesive elasticity theory with surface energy, *Acta Mechanica* 133: 175-198, 1999.
- [7] Ru, C.Q. and Aifantis, E.C., 1993. A simple approach to solve boundary-value problems in gradient elasticity. *Acta Mech.*, 101: 59.
- [8] Exadaktylos, G., Gradient elasticity with surface energy: Mode-I crack problem, *Int. J. Solids Structures*, 35 (5-6), 421-456, 1998.
- [9] Exadaktylos, G. and Vardoulakis, I., Microstructure in Linear Elasticity and Scale Effects: A Reconsideration of Basic Rock Mechanics and Rock Fracture Mechanics, *Tectonophysics*, 2001 (in press).
- [10] Muskhelishvili, N.I., *Some basic problems of the mathematical theory of elasticity*. Groningen: P. Noordhoff, 1965.
- [11] Gladwell, G.M.L., *Contact problems in the classical theory of elasticity*, Sijthoff & Noordhoff, The Netherlands, 1980.

GRADIENT ELASTIC BERNOULLI-EULER BEAMS IN BENDING AND BUCKLING

S. Papargyri-Beskou

General Department, School of Technology
Aristotle University of Thessaloniki, Gr-54006 Thessaloniki, Greece

K. G. Tsepoura

Department of Mechanical and Aeronautical Engineering
University of Patras, GR-26500 Patras, Greece

D. Polyzos

Department of Mechanical and Aeronautical Engineering
University of Patras, GR-26500 Patras, Greece

D. E. Beskos

Department of Civil Engineering
University of Patras, GR-26500 Patras, Greece

1. SUMMARY

The problems of bending and buckling of Bernoulli-Euler beams are solved analytically on the basis of the simple linear theory of gradient elasticity due to Aifantis. The governing equations of equilibrium for bending and buckling are obtained by combining the basic equations of the problem. All the possible boundary conditions (classical and non-classical) are obtained with the aid of the method of weighted residuals for both bending and buckling. Two boundary value problems (one for bending and one for buckling) are solved and the gradient elasticity effect on the response of the flexural beam and its critical (buckling) load is assessed.

2. INTRODUCTION

The importance of linear gradient elastic theories for the description of the mechanical behavior of materials with microstructure has been briefly stated in another work of the authors in these Proceedings [1].

In this paper the problems of bending and buckling of Bernoulli-Euler beams are solved analytically on the basis of the simple linear theory of gradient elasticity due to Aifantis [2,3]. All the possible boundary conditions (classical and non-classical) are obtained with the aid of

the method of weighted residuals. Thus, general boundary value problems of bending and buckling of beams can be easily solved, as demonstrated by the solution of two representative examples for which the gradient effect is also identified and assessed.

The special case of pure bending of Bernoulli-Euler circular cylindrical beams has been briefly considered by Tsagrakis [4] on the basis of the simple gradient elasticity theory of Aifantis and a gradient elasticity theory with surface energy. Vardoulakis et al [5] have considered bending of Timoshenko beams on the basis of gradient elasticity theory with surface energy in an effort to explain experimental results for marble, which could not be explained by classical elasticity theory. Thus, the present paper presents a more systematic and general treatment of bending of beams than in references [4, 5] and in addition considers buckling of beams.

3. GOVERNING EQUATION AND BOUNDARY CONDITIONS FOR BENDING

Consider a straight prismatic beam, which is subjected to a static load $q(x)$ distributed along the longitudinal axis x of the beam, as shown in Fig. 1. The cross-section is characterized by its two axes y and z with the latter one being its axis of symmetry. The loading plane coincides with the plane xz . It is assumed that the bending is not influenced by the presence of shear forces. It is further assumed that in accordance with the Bernoulli-Euler theory, plane cross-sections before deformation remain plane after deformation. Finally, it is assumed that the material obeys the linear gradient theory of elasticity due to Aifantis [2, 3].

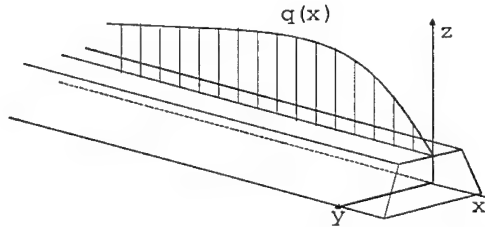


Figure 1: Geometry and loading of a prismatic beam in bending

On the basis of the above assumptions, one can write down the basic equations of a gradient elastic beam in bending. The non-trivial equations of equilibrium, read

$$\int_A \sigma_x dA = 0, \quad \int_A z \sigma_x dA = -M \quad (1)$$

$$\frac{dM}{dx} = V, \quad \frac{dV}{dx} = -q \quad (2)$$

where A is the cross-sectional area, and M and V the bending moment and shear force, respectively. The strain-displacement relation involving the normal strain ϵ_x , reads

$$\epsilon_x = -z \frac{d^2 u}{dx^2} = -zu'' \quad (3)$$

while the normal stress-strain equation has the form

$$\sigma_x = E \left(\epsilon_x - g^2 \frac{d^2 \epsilon_x}{dx^2} \right) = E \left(\epsilon_x - g^2 \epsilon_x'' \right) \quad (4)$$

where u is the lateral beam deflection, E the modulus of elasticity, g^2 the gradient coefficient (for $g=0$ Eq. (4) becomes the classical Hooke's law) and primes indicate differentiation with respect to x . Substituting σ_x of Eq. (4), with ε_x taken from Eq. (3), into Eqs (1)₁ and (1)₂ one obtains first that the axis x passes through the centroid of the cross-section and second that

$$M = EI(u'' - g^2 u^{IV}) \quad (5)$$

where I is the moment of inertia about the y axis. Use of Eq. (5) into Eq. (2)₁ yields

$$V = EI(u''' - g^2 u^{IV}) \quad (6)$$

and subsequently use of Eq. (6) into Eq. (2)₂ yields the governing equation of beam bending

$$EI(u^{IV} - g^2 u^{VI}) = -q \quad (7)$$

The solution of Eq. (7) is the sum of the solution of the homogeneous part of Eq. (7), i. e., the one with $q=0$, and a particular solution of Eq. (7). The former part of the solution is

$$u_h = c_1 x^3 + c_2 x^2 + c_3 x + c_4 + c_5 g^4 \sinh(x/g) + c_6 g^4 \cosh(x/g) \quad (8)$$

where $c_1 - c_6$ are constants to be determined by the boundary conditions (classical plus non-classical) of the particular boundary value problem. All possible boundary conditions can be determined with the aid of the method of weighted residuals, which here reads

$$\int_0^L (EIu^{IV} - g^2 EIu^{VI} + q)w \, dx = 0 \quad (9)$$

where $w = w(x)$ is a weighting function and L is the length of the beam. Integration by parts of the first term of the integrand of Eq. (9) twice and the second one three times brings Eq. (9) to the form

$$\begin{aligned} \int_0^L (EIu^{IV} - g^2 EIu^{VI} + q)w \, dx &= EI \int_0^L u'' w'' \, dx + g^2 EI \int_0^L u'''' w'''' \, dx \\ &+ \int_0^L q w \, dx + EI[u'' w - u'' w']_0^L - g^2 EI[u^{IV} w - u^{IV} w' + u'' w'']_0^L = 0 \end{aligned} \quad (10)$$

Assuming $w = \delta u$, where δ denotes variation, one can finally rewrite Eq. (10) in the form of the variational statement

$$\begin{aligned} \delta \left[\int_0^L \left[\frac{EI}{2} (u'')^2 + g^2 \frac{EI}{2} (u''')^2 + qu \right] dx \right] &= \int_0^L (EIu^{IV} - g^2 EIu^{VI} + q) \delta u \, dx \\ &+ EI[(u'' - g^2 u^{IV}) \delta u]_0^L - EI[(u'''' - g^2 u^{VI}) \delta u]_0^L + g^2 EI[u'' \delta u']_0^L = 0 \end{aligned} \quad (11)$$

Thus, the boundary conditions satisfy the equations

$$\begin{aligned} [u''(L) - g^2 u^{IV}(L)] \delta u'(L) - [u''(0) - g^2 u^{IV}(0)] \delta u'(0) &= 0 \\ [u''''(L) - g^2 u^{VI}(L)] \delta u(L) - [u''''(0) - g^2 u^{VI}(0)] \delta u(0) &= 0 \end{aligned} \quad (12)$$

$$u'''(L)\delta u''(L) - u'''(0)\delta u''(0) = 0$$

For example, consider a simply supported beam for which one has that deflections and bending moments at the two ends are zero (classical boundary conditions). These imply that $\delta u(L) = \delta u(0) = 0$ and $u''(L) - g^2 u^{IV}(L) = u''(0) - g^2 u^{IV}(0) = 0$ and Eqs (12)_{1,2} are satisfied. Assuming as extra (non-classical) boundary conditions $u''(L) = u''(0) = 0$, Eq. (12)₃ is also satisfied.

4. GOVERNING EQUATION AND BOUNDARY CONDITIONS FOR BUCKLING

Consider the beam of the previous section without lateral load subjected to an axial compressive force P , which can cause flexural buckling for a certain value of P called elastic buckling load or critical load P_{cr} to be determined. The presence of P creates the additional term Pu in Eq. (5) for the moment and Pu' in Eq. (6) for the shear force. The governing equation of the problem can be obtained from that of a beam in bending (Eq. (7) with $q = 0$) by simply adding the additional term Pu'' due to the axial load P . Thus one has

$$EI(u^{IV} - g^2 u^{VI}) + Pu'' = 0 \quad (13)$$

The solution of Eq. (13) is of the form

$$u = c_1 x + c_2 + c_3 \sin \xi x + c_4 \cos \xi x + c_5 \sinh \theta x + c_6 \cosh \theta x \quad (14)$$

where

$$\begin{aligned} \xi &= \left(\frac{1}{\sqrt{2g^2}} \right) \sqrt{1 + 4g^2 k^2 - 1} \\ \theta &= \left(\frac{1}{\sqrt{2g^2}} \right) \sqrt{1 + \sqrt{1 + 4g^2 k^2}} \\ k^2 &= P/EI \end{aligned} \quad (15)$$

and $c_1 - c_6$ are constants of integration to be determined from the boundary conditions of the problem at hand.

All possible boundary conditions can be determined, as in the previous section, with the aid of the method of weighted residuals, which here reads

$$\int_0^L (EIu^{IV} - g^2 EIu^{VI} + Pu'') w dx = 0 \quad (16)$$

The first two terms of the integrand of Eq. (16) are treated in exactly the same way as in the previous section. The third term is integrated by parts once and on the assumption that $w = \delta u$ one can finally obtain from Eqs (11) and (16) the variational statement for buckling in the form

$$\begin{aligned} \delta \left[\int_0^L \left[\frac{EI}{2} (u'')^2 + g^2 \frac{EI}{2} (u^{IV})^2 - \frac{P}{2} (u')^2 \right] dx \right] &= \int_0^L (EIu^{IV} - g^2 EIu^{VI} + Pu'') \delta u dx \\ + EI[(u'' - g^2 u^{IV}) \delta u']_0^L - EI[(u''' - g^2 u^{V} + Pu') \delta u]_0^L + g^2 EI[u'' \delta u'']_0^L &= 0 \end{aligned} \quad (17)$$

Thus, the boundary conditions satisfy the same equations as in bending (Eqs (12)) apart from the fact that inside the two brackets of Eq. (12)₂ one should add the terms $Pu'(L)$ and $Pu'(0)$, respectively.

5. SOLUTION OF BOUNDARY VALUE PROBLEMS

This section deals with the solution of two boundary value problems, the first for bending and the second for buckling. Consider a cantilever beam of length L with its built in end at $x=0$, subjected to a static uniformly distributed load q . The classical boundary conditions are $u(0)=u'(0)$ and $M(L)=V(L)=0$ implying, the first two that $\delta u(0)=\delta u'(0)=0$, and the second two, on account of Eqs (5) and (6), that $u''(L)-g^2u^{IV}(L)=u'''(L)-g^2u^V(L)=0$. Thus, Eqs (12)_{1,2} are satisfied. The non-classical boundary conditions are assumed to be $u'''(0)=u''(L)=0$, which satisfy Eq. (12)₃. Use of the above boundary conditions in conjunction with a particular solution $u_p=(q/24EI)x^4$, enable one to determine the constants c_1-c_6 of the homogeneous part of the solution u_h given by Eq. (8). They are

$$\begin{aligned} c_1 &= -qL/6EI, \quad c_2 = (q/4EI)(L^2 + 2g^2), \quad c_3 = -g^2qL/EI \\ c_4 &= (qg^4/EI) \frac{2 + \frac{L}{g}(e^{L/g} - e^{-L/g})}{(e^{L/g} + e^{-L/g})}, \quad c_5 = (qL/EI) \frac{\frac{L}{g}e^{-L/g} - 1}{(e^{L/g} + e^{-L/g})} \\ c_6 &= (-qL/EI) \frac{\frac{L}{g}e^{L/g} + 1}{(e^{L/g} + e^{-L/g})} \end{aligned} \quad (18)$$

Figure 2 shows the variation of the beam deflection $u(\xi)$ along the dimensionless distance $\xi = x/L$ for various values of the gradient coefficient g including the value $g = 0$, which corresponds to the classical elasticity case. It is observed that the deflection increases for increasing values of g .

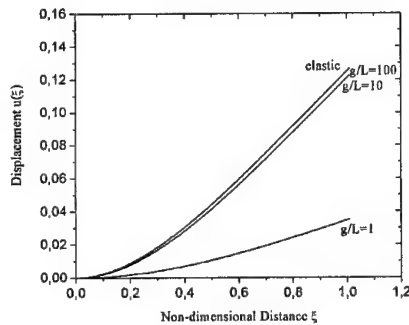


Figure 2: Variation of the deflection of the cantilever beam along its length for various values of the gradient coefficient

Consider a simply supported beam under the action of an axial compressive force P . The classical boundary conditions are $u(0)=u(L)=0$ and $M(0)=M(L)=0$ implying, the first

two that $\delta u(0) = \delta u(L) = 0$ and the second two, an account of Eq. (5), that $u''(0) - g^2 u^{IV}(0) = u''(L) - g^2 u^{IV}(L) = 0$. Thus, Eq (12)_{1,2} are satisfied. The non-classical boundary conditions are assumed to be $u''(0) = u''(L) = 0$, which satisfy Eq. (12)₃ and further imply that $u^{IV}(0) = u^{IV}(L) = 0$.

Thus, the boundary conditions of the problem are $u(0) = u(L) = 0$, $u''(0) = u''(L) = 0$ and $u^{IV}(0) = u^{IV}(L) = 0$ and serve to determine the constants $c_1 - c_6$ of Eq. (14). Indeed one easily finds that $c_1 = c_2 = c_4 = c_5 = c_6 = 0$, the buckling shape has the form

$$u(x) = c_3 \sin \xi x \quad (19)$$

i. e., the same as in the classical case and the buckling condition reads

$$\sin \xi L = 0 \quad (20)$$

Equation (20) is satisfied for $\xi L = n\pi$ ($n = 1, 2, \dots$) and in view of Eq.(15)₁ one can obtain the first critical load for $n = 1$ in the form

$$P_{cr} = (EI/4g^2) \left[\left(1 + \frac{2g^2\pi^2}{L^2} \right)^2 - 1 \right] \quad (21)$$

This expression for $g = 0$ reduces through a limiting process to

$$P_{cr}^0 = \pi^2 EI / L^2 \quad (22)$$

which is the critical (buckling) load of the classical case. Figure 3 depicts the variation of the ratio $P_{cr}/P_{cr}^0 = 1 + (g^2\pi^2/L^2)$ as a function of the gradient term $g^2\pi^2/L^2$. It is apparent that the buckling load increases for increasing values of the gradient coefficient in a linear manner.

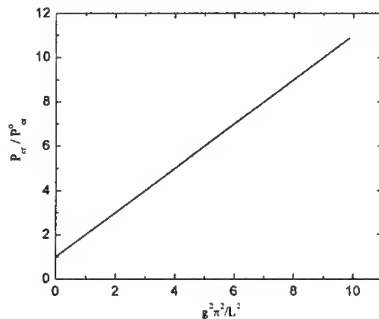


Figure 3: Buckling load of a simply supported beam versus the gradient coefficient

6. CONCLUSIONS

On the basis of the preceding discussion, the following conclusions can be stated :

- 1) Using the simple theory of gradient elasticity due to Aifantis, the governing equations of beam bending and buckling and the corresponding boundary conditions (classical and non-classical) have been derived.
- 2) The boundary conditions have been derived from a variational statement constructed with the aid of the method of weighted residuals without knowledge of the strain energy, which is obtained here as a byproduct of the present approach.
- 3) A characteristic boundary value problem of beam bending has been solved and its gradient elastic solution for the beam deflection has been found to increase for increasing values of the gradient coefficient with the classical elastic solution being an upper bound.
- 4) A characteristic boundary value problem of beam buckling has been solved and its gradient elastic solution for the critical (buckling) load has been found to increase for increasing values of the gradient coefficient with the classical elastic critical load being a lower bound.

Acknowledgements: The authors are grateful to Professor E. C. Aifantis for introducing them into the subject of gradient elasticity theory.

7. REFERENCES

- [1] Tsepoura, K. G., Papargyri-Beskou, S., Polyzos, D. and Beskos, D. E., Gradient elastic bars under uniaxial static or dynamic loads, in Proceedings of 6th National Congress on Mechanics, Aristotle University of Thessaloniki, July 19-21, 2001.
- [2] Altan, B. S. and Aifantis, E. C., On the structure of mode-III crack tip in gradient elasticity, *Scripta Metall. Mater.* 26, 319-324 (1992).
- [3] Ru, C. Q. and Aifantis, E. C., A simple approach to solve boundary-value problems in gradient elasticity, *Acta Mechanica* 101, 56-68 (1993).
- [4] Tsagrakis, I. A., The Role of Gradients in Elasticity and Plasticity : Analytical and Numerical Applications, Doctoral Dissertation, Aristotle University of Thessaloniki, Thessaloniki, Greece (2001) (in Greek).
- [5] Vardoulakis, I., Exadaktylos G. and Kourkoulis, S. K., Bending of marble with intrinsic length scales : a gradient theory with surface energy and size effects, *J. de Physique IV* 8, 399-406 (1998).

DUAL MODE VIBRATION ISOLATION BASED ON NONLINEAR MODE LOCALIZATION

X. Jiang

Dept. of Theoretical and Applied Mechanics
University of Illinois, 1206 W. Green Str., Urbana, IL 61801, USA

A. F. Vakakis

Dept. of Mechanical & Industrial Engineering
University of Illinois, 1206 W. Green Street, Urbana, IL 61801, USA
avakakis@uiuc.edu (*currently of leave of absence*)

and

Division of Mechanics, National Technical University of Athens
P.O.Box 64042, GR-157 10 Zografos, Athens, Greece
vakakis@central.ntua.gr

1. SUMMARY

We study a nonlinear vibration isolation system capable of, (a) isolating its upper part (the 'machine') from periodic disturbances generated at its base; and (b) simultaneously isolating its base from periodic disturbances generated at the level of the machine. By making use of essentially nonlinear (e.g. nonlinearizable) stiffness elements we completely eliminate resonances close to linearized modes, thus achieving vibration isolation over an extended frequency range. Instead, we prove the existence of branches of localized steady state motions in the frequency domain. The vibration isolation performance achieved by the nonlinear system considered has no counterpart in linear theory.

2. INTRODUCTION

We induce localized nonlinear normal modes (NNMs) to a vibration isolation system. NNMs were introduced in previous works [1]. These are free oscillations of discrete or continuous undamped nonlinear systems where all coordinates vibrate in unison, reaching their maximum and minimum values simultaneously. Hence, NNMs are similar to the normal modes of classical linear vibration theory. In contrast to the linear case, however, the number of NNMs can exceed in number the degrees-of-freedom (DOF) of a nonlinear system, due to NNM bifurcations that increase in complexity as the DOF increase. Moreover, a subset of the bifurcated NNMs are localized since they correspond to spatial confinement of vibrational energy [2]. A subset of the localized modes are stable, and, thus, physically realizable. This last result permits the use of nonlinear mode localization for vibration and shock isolation of structures.

3. THEORETICAL ESTIMATION OF THE STEADY STATE RESPONSE

Consider the three DOF system depicted in Figure 1. There are two strongly (essentially) nonlinear, and one weak [of $O(\epsilon)$, $|\epsilon| \ll 1$] stiffness connecting the various components of the system with each other and with the base. The upper mass m_1 represents a 'machine', whereas the other masses of the system are purely auxiliary. Two distinct types of excitations are considered for this system, namely, periodic forces $F_c(t)$ generated at the level of the machine, and base (support) excitations $y_g(t)$ generated at the base and transmitted to the system from below. The problem that we wish to address in this work focuses on *dual mode vibration isolation*, and can be formulated as follows:

Design this system so to isolate, (a) its base from force disturbances generated at the level of the machine, and simultaneously, (b) the machine from excitations generated at the base, with each of these disturbances applied separately from the other.

Assuming weak viscous damping, the equations for the system of Figure 1 are given by,

$$\left. \begin{aligned} m_1 \ddot{x}_1 + \epsilon c_1 (\dot{x}_1 - \dot{x}_2) + f(x_1 - x_2) &= F_c(t) \\ m_2 \ddot{x}_2 + \epsilon c_1 (\dot{x}_2 - \dot{x}_1) + f(x_2 - x_1) + \epsilon k(x_2 - x_3) &= 0 \\ m_3 \ddot{x}_3 + \epsilon c_2 [\dot{x}_3 - \dot{y}_g(t)] + g(x_3 - y_g(t)) + \epsilon k(x_3 - x_2) &= 0 \end{aligned} \right\} \quad (1)$$

where $f(\bullet)$ and $g(\bullet)$ are strongly nonlinear stiffnesses (not linearizable), dot denotes time derivative, and $|\epsilon| \ll 1$. We introduce the new variables, $u \equiv x_1 - x_2$, $v \equiv m_1 x_1 + m_2 x_2$, and $w \equiv x_3$, and assume that the force and ground disturbances are harmonic of frequency ω , $F_c(t) = P_c \sin \omega t$ and $y_g(t) = Y_g \sin \omega t$. Then set (1) is expressed as:

$$\left. \begin{aligned} \ddot{u} + \epsilon \delta_1 \dot{u} + F(u) &= F \sin \omega t + \epsilon (\alpha_1 v - \alpha_2 u - \alpha_3 w) \\ \ddot{v} &= m_1 F \sin \omega t + \epsilon (-\beta_1 v + \beta_2 u + \beta_3 w) \\ \ddot{w} + \epsilon \delta_2 (\dot{w} - \omega Y_g \cos \omega t) + G(w - Y_g \sin \omega t) &= \epsilon (\gamma_1 v - \gamma_2 u - \gamma_3 w) \end{aligned} \right\} \quad (2)$$

where,

$$\begin{aligned} \alpha_1 &= \frac{k}{m_2(m_1 + m_2)}, \quad \alpha_2 = \frac{km_1}{m_2(m_1 + m_2)}, \quad \alpha_3 = \frac{k}{m_2}, \\ \beta_1 &= \frac{k}{(m_1 + m_2)}, \quad \beta_2 = \frac{km_1}{(m_1 + m_2)}, \quad \beta_3 = k, \\ \gamma_1 &= \frac{k}{m_3(m_1 + m_2)}, \quad \gamma_2 = \frac{km_1}{m_3(m_1 + m_2)}, \quad \gamma_3 = \frac{k}{m_3}, \quad \delta_1 = c_1 \left(\frac{1}{m_1} + \frac{1}{m_2} \right), \quad \delta_2 = \frac{c_2}{m_3}, \quad F = P_c / m_1 \end{aligned}$$

The normalized stiffness forces in (2) are defined as,

$$F(u) = \left(\frac{1}{m_1} + \frac{1}{m_2} \right) f(u), \quad G(w) = \frac{1}{m_3} g(w)$$

At this point we assume a specific form for the nonlinear stiffnesses by setting,

$$F(u) = C_1 u^3, \quad G(w) = C_3 w^3 \quad (3)$$

Since the stiffnesses are nonlinearizable of cubic form, they are strongly nonlinear. *It is clear that for this type of problems the standard analytical techniques from nonlinear dynamics [such as, the method of multiple-scales or the standard method of averaging [3] are not directly applicable and a new approach must be followed.*

Forcing Mode I: Forcing at the Machine Level

Setting $Y_g = 0$, we wish to study periodic steady state vibrations of the above set with frequency ω , e.g., equal to that of the forcing term. We resort to the complexification technique introduced in [4] and define the new complex variables,

$$U(t) \equiv \dot{u}(t) + j\omega u(t), \quad V(t) \equiv \dot{v}(t) + j\omega v(t), \quad W(t) \equiv \dot{w}(t) + j\omega w(t) \quad (4)$$

in terms of which, the equations of motion complexify. Since we seek steady state vibrations of approximate frequency ω , we express the new complex variables as follows,

$$\left. \begin{aligned} U(t) &= \varphi(t) e^{j\omega t} \Rightarrow U^* = \varphi^* e^{-j\omega t}, \quad \dot{U} = \dot{\varphi} e^{j\omega t} + j\omega \varphi e^{j\omega t} \\ V(t) &= \sigma(t) e^{j\omega t} \Rightarrow V^* = \sigma^* e^{-j\omega t}, \quad \dot{V} = \dot{\sigma} e^{j\omega t} + j\omega \sigma e^{j\omega t} \\ W(t) &= \lambda(t) e^{j\omega t} \Rightarrow W^* = \lambda^* e^{-j\omega t}, \quad \dot{W} = \dot{\lambda} e^{j\omega t} + j\omega \lambda e^{j\omega t} \end{aligned} \right\} \quad (5)$$

where $\varphi(t)$, $\sigma(t)$ and $\lambda(t)$ represent slowly-varying complex envelopes (or modulations) of the steady state motion. Hence, *the response of the system is decomposed into a 'fast' oscillation with frequency ω and a 'slow' amplitude modulation, that, in essence, represents the envelope of the 'fast' oscillation.* Retaining only terms of frequency ω in the equations of motion we obtain a set of complex modulation equations that govern the slow dynamics (e.g., the envelope) of the response. To seek steady state periodic solutions, we set $\dot{\varphi} = 0$, $\dot{\sigma} = 0$, and $\dot{\lambda} = 0$ and obtain a set of non-homogeneous algebraic that govern the amplitudes and phases of the envelope modulations at steady state:

$$\left. \begin{aligned} \left(\frac{j\omega}{2} + \frac{\varepsilon\alpha_2}{2j\omega} + \frac{\varepsilon\delta_1}{2} \right) \varphi - \frac{3C_1 j}{8\omega^3} \varphi^2 \varphi^* + \left(-\frac{\varepsilon\alpha_1}{2j\omega} \right) \sigma + \left(\frac{\varepsilon\alpha_3}{2j\omega} \right) \lambda &= \frac{F}{2j} \\ \left(\frac{j\omega}{2} + \frac{\varepsilon\beta_1}{2j\omega} \right) \sigma + \left(-\frac{\varepsilon\beta_2}{2j\omega} \right) \varphi + \left(-\frac{\varepsilon\beta_3}{2j\omega} \right) \lambda &= \frac{m_1 F}{2j} \\ \left(\frac{j\omega}{2} + \frac{\varepsilon\gamma_3}{2j\omega} + \frac{\varepsilon\delta_2}{2} \right) \lambda - \frac{3C_3 j}{8\omega^3} \lambda^2 \lambda^* + \left(-\frac{\varepsilon\gamma_1}{2j\omega} \right) \sigma + \left(\frac{\varepsilon\gamma_2}{2j\omega} \right) \varphi &= 0 \end{aligned} \right\} \quad (6)$$

Finally, we represent the complex unknowns in terms of real and imaginary parts, $\varphi = x_1 + jx_2$, $\sigma = y_1 + jy_2$ and $\lambda = z_1 + jz_2$. Setting separately the real and imaginary parts equal to zero we obtain a set of six real nonhomogeneous nonlinear algebraic equations governing x_1 , x_2 , y_1 , y_2 , z_1 and z_2 . This last set we solve numerically for fixed system parameters and varying frequency of excitation ω in order to obtain the *frequency-amplitude* and *frequency-phase plots* of the steady state motion corresponding to the first mode of forcing. Once a solution φ_0 , σ_0 and λ_0 for the complex amplitudes is determined, the steady state responses in terms of the original coordinates are given by,

$$u(t) = \frac{|\varphi_0|}{\omega} \sin(\omega t + \theta_\varphi), \quad v(t) = \frac{|\sigma_0|}{\omega} \sin(\omega t + \theta_\sigma), \quad w(t) = \frac{|\lambda_0|}{\omega} \sin(\omega t + \theta_\lambda) \quad (7)$$

where bars denote amplitudes, e.g., $|\varphi_0| = (x_1^2 + x_2^2)^{1/2}$, and θ phases, e.g., $\theta_\varphi = \arctan(x_2/x_1)$. We note that as a result of the previous approximations we have omitted from the steady state response components with frequency different than ω . The error resulting from this approximation is not expected to be large for the *fundamental* frequency amplitude plots that we discuss here. The stability of the derived steady state solutions (7) is determined by direct numerical integrations of the original equations of motion (2), with initial conditions identical to the ones predicted by the theoretical analysis.

Forcing Mode II: Base-Induced Motion

A similar analysis is performed for the case when there is base excitation of the system. Setting $P_c = 0$ and $Y_g \neq 0$ and performing a similar analysis we obtain the following algebraic set of nonlinear equations that govern the steady state amplitudes and phases:

$$\left. \begin{aligned} \left(\frac{j\omega}{2} + \frac{\varepsilon\alpha_2}{2j\omega} + \frac{\varepsilon\delta_1}{2} \right) \varphi - \frac{3C_1j}{8\omega^3} \varphi^2 \varphi^* + \left(-\frac{\varepsilon\alpha_1}{2j\omega} \right) \sigma + \left(\frac{\varepsilon\alpha_3}{2j\omega} \right) \lambda &= 0 \\ \left(\frac{j\omega}{2} + \frac{\varepsilon\beta_1}{2j\omega} \right) \sigma + \left(-\frac{\varepsilon\beta_2}{2j\omega} \right) \varphi + \left(-\frac{\varepsilon\beta_3}{2j\omega} \right) \lambda &= 0 \\ \left(\frac{j\omega}{2} + \frac{\varepsilon\gamma_3}{2j\omega} + \frac{\varepsilon\delta_2}{2} \right) \lambda + C_3 \left\{ -j \frac{3\lambda^2 \lambda^*}{8\omega^3} + j \frac{3Y_g^3}{8} + j \frac{3Y_g}{8\omega^2} (\lambda^2 + 2\lambda\lambda^*) - j \frac{3Y_g^2}{8\omega} (2\lambda + \lambda^*) \right\} \\ - \left(\frac{\varepsilon\gamma_1}{2j\omega} \right) \sigma + \left(\frac{\varepsilon\gamma_2}{2j\omega} \right) \varphi - \frac{1}{2} \varepsilon \delta_2 \omega Y_g &= 0 \end{aligned} \right\} \quad (8)$$

4. NUMERICAL RESULTS

The numerical solutions were derived for the following values of the system parameters: $\alpha_1=13.333$, $\alpha_2=13.333$, $\alpha_3=20.000$, $\beta_1=6.666$, $\beta_2=6.666$, $\beta_3=10.000$, $\gamma_1=13.333$, $\gamma_2=13.333$, $\gamma_3=20.000$, $\varepsilon=0.1$, $P_c=5.000$, $Y_g=5.000$, $C_1=5.000$, $C_3=5.000$, $m_1=1.000$. Unless indicated otherwise these numerical values hold throughout the rest of this work. Considering first Forcing Mode I, the approximate frequency-amplitude and frequency-phase plots for the system with $\varepsilon\delta_1=0.6$ and $\varepsilon\delta_2=0.4$ are depicted in Figure 2. Branch 1 is *unstable* for low frequencies but becomes *stable* as frequency increases. Branches 2, 3, 4, and 6 are *unstable*, whereas, branches 5 and 7 are *stable*. In the low frequency regions where no stable steady branch exists the system settles into either subharmonic or irregular (chaotic or quasi-periodic of high period) motions. There are three localized branches satisfying, u and v are $O(1)$ quantities, and w is a quantity of $O(\varepsilon)$. Of these, branches 5 and 7 are stable (and, hence, physically realizable), whereas branch 6 is unstable. The actual steady state solution were the motion eventually settles depends on the domains of attraction of the stable steady states and on the initial conditions of the system. However, numerical simulations (shown below) indicate that *when the system starts from rest the eventual steady state reached corresponds to the localized branch 7*.

Considering now Forcing Mode II operation, in Figure 3 we depict the approximate frequency-amplitude plots of the system with the same numerical values for the parameters and forcing parameters $P_c=0$ and $Y_g=5.000$. Branches 1,2 and 4 are *unstable*, whereas branches 3 and 5 are *stable*. There exist three localized branches corresponding to u and v of $O(1)$, and w of $O(\varepsilon)$, namely branches 3, 4 and 5. Note that in this case we seek localization of the steady state motion close to the base of the motion and away from the machine m_1 . Of the localized branches, 3 and 5 are stable, whereas 4 is unstable.

5. CONCLUSIONS

By using essentially nonlinear stiffness elements (with no linear parts) we avoid completely the occurrence of three nonlinear resonances close to linearized normal modes of this three degree-of-freedom system. Such nonlinear resonances (that are counterproductive as far as localization and vibration isolation is concerned) were detected in a previous work [5] where a similar system was considered with weakly nonlinear, linearizable stiffnesses. These resonances cannot be eliminated by parameter selection, and their placement in the frequency domain is determined by the linearized structure of the system. The use of the nonlinearizable stiffnesses introduces new localized steady state branches that are beneficial to the vibration isolation objectives. Indeed, the localized steady branches are primarily responsible for fulfilling the dual mode vibration isolation objective. Clearly, such localization is solely due to the nonlinearities used and cannot be realized in a purely linear setting.

Acknowledgements: This work was supported in part by Grant N00014-00-1-0187 from the Office of Naval Research. Dr. Louise Couchman is the Grant monitor.

6. REFERENCES

- [1] Vakakis A.F., Manevitch L.I., Mikhlin Yu.V., Pilipchuk V.N., Zevin A.A., 1996, *Normal Modes and Localization in Nonlinear Systems*, Wiley Interscience, New York.
- [2] Nayfeh T.A., Emaci E., Vakakis A.F., 1997, 'Application of Nonlinear Localization to the Optimization of a Vibration Isolation System,' *AIAA Journal*, Vol. 35, No. 8, pp. 1378-1386.
- [3] Nayfeh A.H., Mook D.T., 1986, *Nonlinear Oscillations*, Wiley Interscience, New York.
- [4] L.I. Manevitch, 2000, 'Description of localized normal modes in the chain of nonlinear coupled oscillators using complex variables,' *Nonlinear Dynamics* (in press).

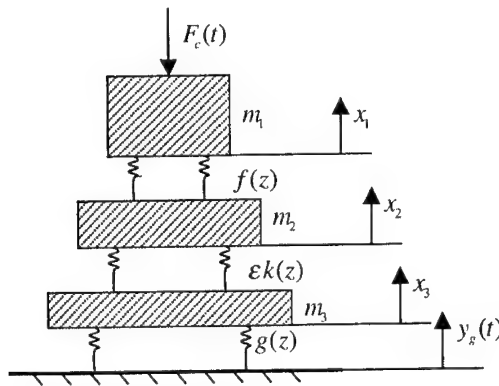


Figure 1. The dual mode nonlinear vibration isolation system.

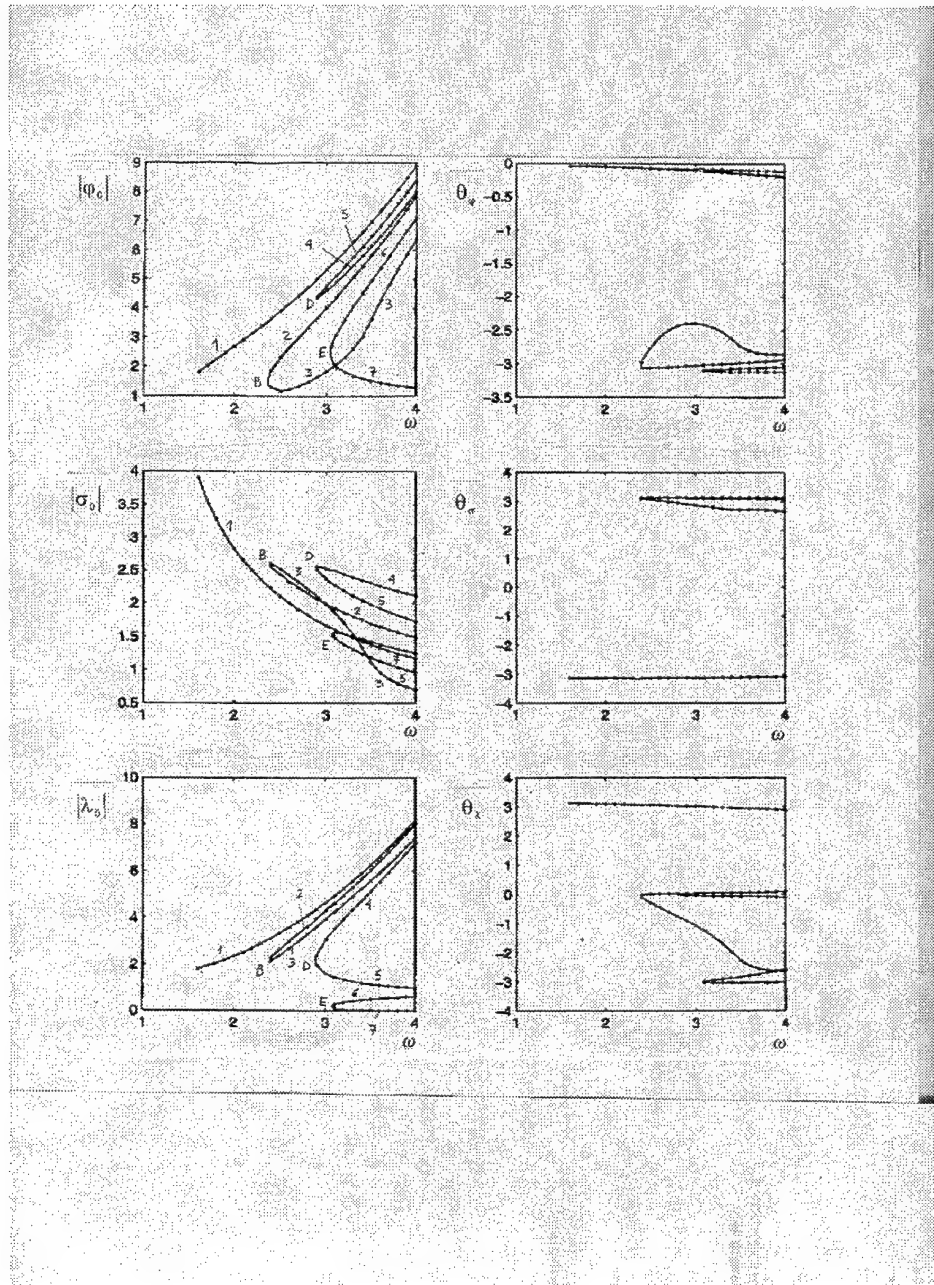


Figure 2. Approximate frequency-amplitude and frequency-phase plots of the system with $\varepsilon\delta_1 = 0.6$ and $\varepsilon\delta_2 = 0.4$ (Forcing Mode I).

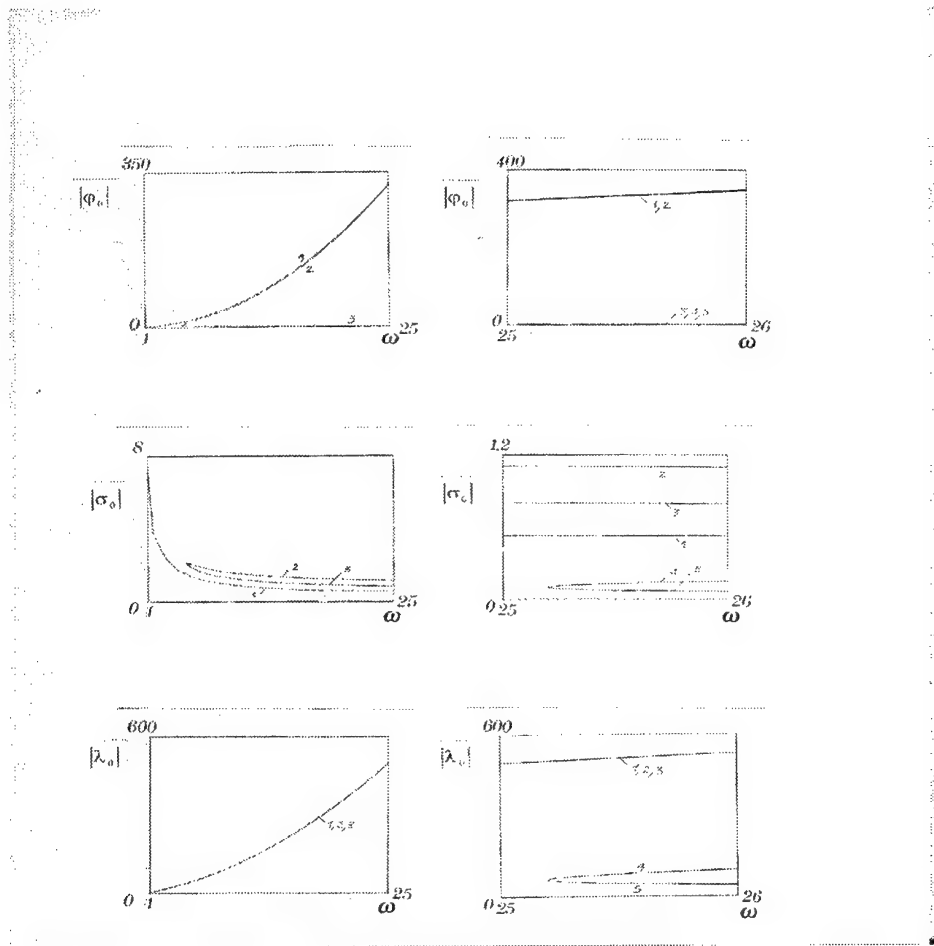


Figure 3. Approximate frequency-amplitude plots of the system with $\epsilon\delta_1 = 0.6$ and $\epsilon\delta_2 = 0.4$ (Forcing Mode II). Due to scaling differences between certain steady state branches, two separate plots for each variable are depicted, namely for $1 < \omega < 25$ and $25 < \omega < 26$.

A FRACTIONAL BROWNIAN MOTION MODEL FOR TIMESERIES PRODUCED BY CONSTANT ENERGY MOLECULAR DYNAMICS SIMULATIONS

T. E. Karakasidis

Department of Civil Engineering
University of Thessaly, GR-38334 Volos, Greece

I. Andreadis

European University of The Hague, Center of Management Studies
Nassauplein 25, 2585EC the Hague, The Netherlands

1. SUMMARY

Molecular dynamics (MD) is a well-established method for simulating materials at the atomic scale. During MD simulations several quantities are calculated giving place to quite a number of time series. Time series analysis of several physical properties of systems can provide insight to the behavior of the system. In the present work we present an analysis of time series of instantaneous temperature and pressure produced during micro canonical (constant energy) MD simulations. Simulations were applied to a nickel oxide grain boundary for a temperature range $0.15-0.80T_m$, T_m being the melting point of the system. We performed a series of analysis for these time series including test for randomness, power spectrum and the structure function test. The obtained results show evidence of fractional Brownian motion. Pressure and temperature time series presents $1/f^\alpha$ noise over the whole range of frequencies of the system. The origins of this observed behavior are discussed. A comparison also is made with results already obtained from constant temperature MD simulations.

2. INTRODUCTION

Molecular Dynamics (MD) is a well-established simulation method used especially in materials science and is based on an atomic description of matter. Matter is described as atoms which interact through a potential function. It is appropriate for the description of transport properties, structure properties as it can provide insight into microscopic mechanisms not easily accessible by experiment and it is widely used in Solid State Physics, Material Physics, Chemical Physics, Fluid physics, Biological systems [1]. MD simulations provide us with a set of trajectories of the atoms we simulate, as they are determined by the interactions between the ions and Newton's law of motion. Useful information is obtained about the system's properties through statistical mechanics as it is possible to relate nearly any experimentally observed property to the motion of atoms [1].

Let consider a system of N interacting particles in a volume V . In the absence of external forces acting on the system the total energy of the system is conserved :

$$H = \sum_{i=1}^N \frac{\vec{p}_i^2}{2m_i} + U(\vec{r}_1, \dots, \vec{r}_N) \quad (1)$$

where r_i are the positions of the atoms and p_i the corresponding conjugate momentum and U the potential energy of the system. We explore then the system properties in the microcanonical ensemble (NVE). At every instant the motion of an atom is determined by:

$$F_i = m_i \frac{d^2 \vec{r}_i}{dt^2} = - \frac{\partial U(\vec{r}_1, \dots, \vec{r}_N)}{\partial \vec{r}_i} \quad (2)$$

As one can see for a system of N particles with three degrees of freedom for each particle, we must solve simultaneously $3N$ coupled differential equations. There are several methods used in MD to integrate the equations of motion [2]. In the present study we used the Verlet algorithm [3] which is accurate and quite stable:

$$\vec{r}_i(t + dt) = 2\vec{r}_i(t) - \vec{r}_i(t - dt) + \frac{2\vec{F}_i(t)}{m_i} dt^2 + O(dt^4) \quad (3)$$

The choice of the timestep dt is a compromise between accuracy, stability and efficiency. In general we choose $dt \ll 1/f_{\max}$ where f_{\max} is the highest phonon frequency of the system. In general dt is of the order of some femtoseconds. An indication of the good choice of dt is the conservation of the total energy. The time accessible by this type of simulations are of the order of nanosecond. So one has to limit to phenomena with characteristic time less than this limit.

The physical model of the system is characterized by the choice of the potential function describing the interaction between the component particles. These interactions arise for a number of reasons: in ionic systems the ions carry charges; all atoms repel each other on close approach due to overlap of their electron orbitals. A model to describe interactions is the rigid-ion model:

$$\phi(r_{ij}) = \frac{q_i q_j}{r_{ij}} + A \exp\left(-\frac{r_{ij}}{\rho}\right) - \frac{C}{r_{ij}^6} \quad (4)$$

A , ρ , C are parameters derived by fitting calculated quantities to experimental data. The details for the parameters are the same as in [4].

During MD simulations several quantities are calculated and times series produced. We examined two of them:

- Pressure
$$P = \left\langle \frac{N}{V} k_B T \right\rangle - \left\langle \frac{1}{3V} \sum_{i=1}^N \sum_{j>i}^N r_{ij} \frac{\partial \phi(r_{ij})}{\partial r_{ij}} \right\rangle \quad (5)$$

- Temperature
$$T = \frac{1}{3Nk_B} \left\langle \sum_{i=1}^N m_i v_i^2 \right\rangle \quad (6)$$

The $\langle \rangle$ mean temporal average.

3. COMPUTATIONAL DETAILS

The MD simulations were performed on an NiO (310)[001] grain boundary in the microcanonical ensemble. A grain boundary is a region of the material where two crystallites meet, and plays an important role in determining several physical properties such as creep, sintering, and corrosion. For a review on grain boundaries and their properties see the excellent book of Sutton and Baluffi [5].

The simulation box containing the grain boundary is a parallelepiped with edges parallel to the directions x : $[310]$, y : $[1-30]$ and z : $[001]$. The simulated system contains 12 (001) planes along the z direction thus resulting a total of 2160 ions (1080 cations and 1080 anions). Periodic boundary conditions are applied in the three directions x , y , z . The dimensions L_x , L_y , L_z of the simulation cell at $T=0K$ are equal to 41.89, 19.77 and 25.01 Å respectively. They vary with temperature as a function of the lattice parameter. Further technical details for performing the simulation runs are the same as in [5].

We perform MD simulations at five temperatures in the range $0.15-0.80T_m$ to examine the behavior of these time series as the behavior of the material become more anharmonic with rising temperature. The runs were 10^{-11} s long and all relevant quantities were saved every 10^{-15} s. The grain boundary is stable all along the temperatures studies as has been observed over very long runs already performed in [4, 6].

4. RESULTS AND DISCUSSION

Characteristic times series of instantaneous temperature and pressure are presented in fig.1a and 1b respectively. The following subsections are presented the results of the various tests performed using the obtained time series.

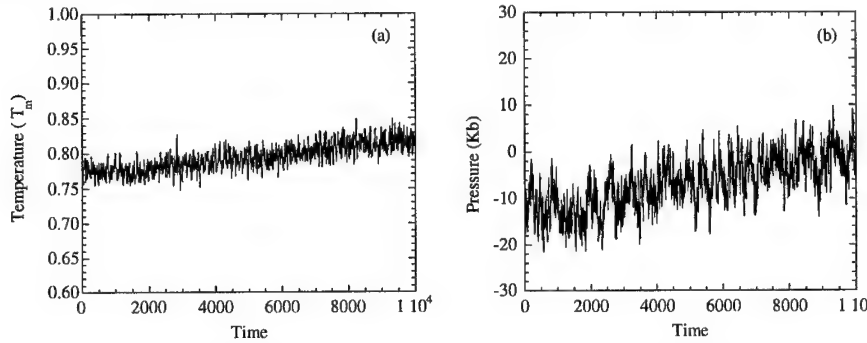


Figure 1 Instantaneous temperature (a) and pressure (b) time series produced during NVE MD simulations at about $0.80T_m$.

4.1 The above and below test for randomness

Let us now recall the above and below median test used to examine whether a time series is coming from a random process [7]. Let us denote by $T(i)$, $i=1, \dots, N$, the time series and M the corresponding median. We construct a sequence of three symbols, denoted by $-1, 0, +1$ according to whether a member of the time series is less, equal or bigger than M . Let N_1 (resp. N_2) be the cardinality of the set of the symbols $\{+1\}$ (resp. $\{-1\}$) and V the total sign change from $\{-1\}$ to $\{+1\}$. Then, we test with a confidence interval 5%, whether the sequence of symbols N_1 (resp. N_2) obeys a Gaussian distribution. Hence we calculate the mean value and the standard deviation of a binomial distribution for the N_1 , N_2 , through the formulas:

$$m_v = \frac{2N_1N_2}{N_1 + N_2} + 1 \quad \text{and} \quad s_v^2 = \frac{2N_1N_2(2N_1N_2 - N_1 - N_2)}{(N_1 + N_2)(N_1 + N_2 - 1)} \quad (7)$$

Finally, we calculate the formula for a variable z expected to obey a gaussian distribution (with mean value m_v and variance s_v):

$$z = \frac{V - m_v}{s_v} \quad (8)$$

If z is found $-1.96 \leq z \leq 1.96$ we may conclude that the time series is characterized by a randomness behavior with a confidence interval of 95%.

In Table 1 we present the results of this test for the temperature (T) and the pressure (P) time series, which suggest that these series exhibit strong evidence of a random behavior. In order to get more insight, we now proceed to calculate the power spectrum of these time series.

Table 1. Results of the above and below median test for the Temperature (T) and Pressure (P) series as a function of system temperature (expressed as percentage of the melting point).

T	T series		P series	
	V	z	V	z
0.14T _m	121	-0.98	855	-0.83
0.29T _m	73	-0.99	1092	-0.78
0.43T _m	73	-0.99	555	-0.89
0.57T _m	97	-0.98	383	-0.92
0.80T _m	113	-0.98	501	-0.90

4.2 Power spectrum

In this section we calculate power spectra $P(f)$ by applying the discrete Fourier transform [8]:

$$P(f) = N \|A(f)\|^2 \quad (9)$$

where $\|A(f)\|$ is the modulus of the complex number

$$A(f) = \frac{1}{N} \sum_{j=1}^N x_j e^{-\frac{i 2\pi f j}{N}} \quad (10)$$

In Fig.2a and b we present the power spectrum of the temperature time series and pressure respectively for a given system temperature. We observe a somewhat different behavior of the two time series: while pressure seems to follow a $1/f^\alpha$ law over the whole frequency region studied, the temperature series seems to present a two regime behavior. At low frequencies it behaves like a nearly Brownian motion while for higher frequencies ($f > 2 \times 10^{12}$ Hz) it follows a power law with exponent ranging from 0.41 up to 1.20. In table 2 we present the obtained exponents.

Table 2 Power spectrum exponents of temperature time series and pressure time series.

T	T series (low frequencies)	T series (high frequencies)	P series
0.14T _m	2.07	0.41	0.86
0.29T _m	2.01	1.20	1.19
0.43T _m	1.98	0.69	1.24
0.57T _m	1.97	0.81	1.28
0.80T _m	1.90	0.63	0.86

This $1/f^\alpha$ behavior has been related e.g. to self-critical phenomena by Bak et al [9,10] and constitutes strong evidence for complex temporal behavior if α is not large. Actually $1/f$ noise can be related to the intimate disordered structure and is expected to be substantially independent of the details of the system under analysis. It has also been suggested that $1/f$ noise is a common characteristic of dynamical systems with extended spatial degrees of freedom revealing conversely self similarity in space [9, 10].

The physical origin of this difference in the behavior of the temperature and pressure time series could be explained perhaps if we take into account the following: The presence of $1/f$ noise indicates a memory effect for high frequencies i.e. small time scales. Pressure, therefore, seems to behave similarly at all time scales. In the case of temperature, we have a

Brownian motion for low frequencies (high time intervals) and $1/f^\alpha$ with α ranging from 0.41 up to 1.20 for higher frequencies which means that for small timescales memory effects are present but at higher timescales we have resemblance to a Brownian motion.

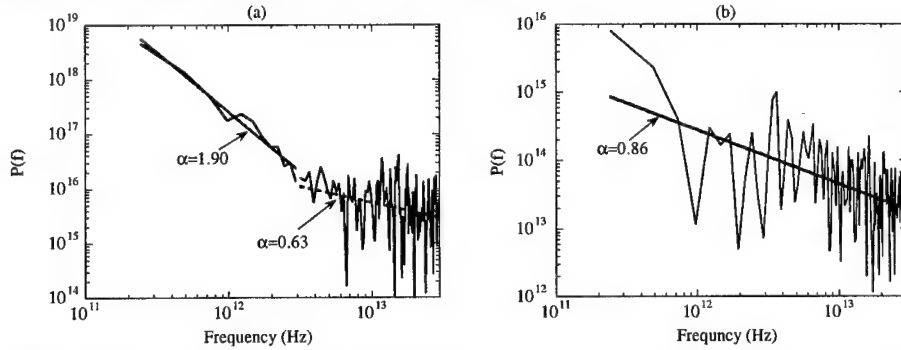


Figure 2(a) power spectrum of the temperature time series for $0.80T_m$ (b) power spectrum of the pressure time series at about $0.80T_m$

We remind here that temperature depends on the squares of the velocities of the independent particles v_i (Eq(6)) which are the derivatives of the displacements of the ions. On the other hand, pressure, as on can see from Eq (5), depends on the average temperature of the system but also on the relative displacement of atomic pairs and their corresponding forces according to the potential (eq.5). This second term apparently influences the behavior of the pressure in an important way, giving rise to a nearly $1/f$ noise behavior over the whole frequency range. This means that in the pressure time series memory effects are present over the whole temperature region. The $1/f^\alpha$ behavior of the power spectra of the temperature and pressure are often indicative of what has been termed fractal noise or fractional Brownian Motion if $\alpha \neq 2$ [11].

It is of interest to compare with the results obtained for the same time series produced during constant temperature molecular dynamics [12]. In that case the temperature presented also a two regime behavior but for low frequencies it presented a white noise behavior while for higher temperature it presented a $1/f^\alpha$ noise behavior with α increasing with temperature, α being greater than 1.

4.3 The structure function test

Next we apply the structure function test, developed by Provenzale et al [11], in order to support and extend the results obtained in the previous subsection indicating the presence of fractional Brownian motion in our time series. This test was originally developed as a tool for distinguishing between a deterministic and a stochastic origin of time series whose power spectrum displays scaling behavior. Let us consider a time series T with a finite length equal to N . For every n , $1 \leq n \leq N$, the structure function associated with T is defined as follows:

$$\Sigma(n) = \sum_{i=1}^{N-n} [T((i+n)\Delta t) - T(i\Delta t)]^2 \quad (11)$$

where Δt denotes the sampling rate of T . According to Mandelbrot [13], for a time series T with a power-law spectrum $P(f) \propto 1/f^\alpha$, where α is positive real, one expects a scaling behavior of the form $\Sigma(n) \propto n^{2H}$ for small values of n , where H is called the scaling exponent. In the case of a fractal noise we have that $\alpha = 2H + 1$ [11].

In figs 3a and 3b we show that the graph of $\log(\Sigma(n))$ versus $\log(n)$ for the time series studied here exhibit indeed a behavior like fractal noise. Results are presented only for the highest temperature as in this case the behavior is quite similar for the other temperatures.

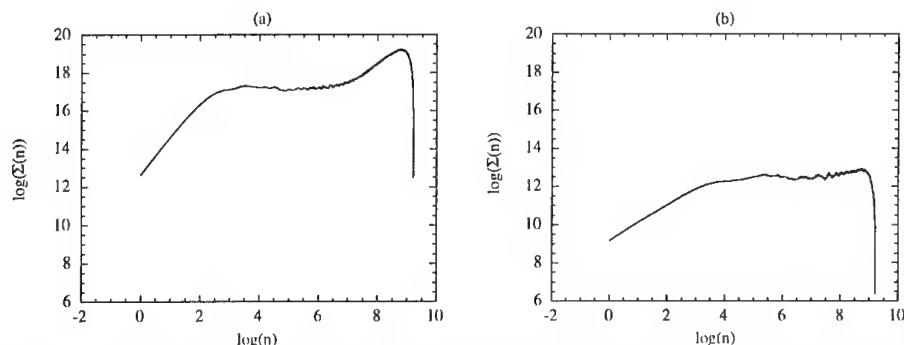


Figure 3 Results of the structure function test for the timeseries of temperature (a) and pressure (b) obtained at about $0.80 T_m$

5. CONCLUSIONS

In this work we have performed an analysis of time series of instantaneous temperature and pressure produced during constant energy molecular dynamics simulations on a model of a grain boundary of NiO. These time series were obtained for different temperatures of the system ranging from $0.15T_m$ - $0.80T_m$, T_m being the melting point of the system. Direct measurements present strong evidence that both time series exhibit strong evidence of a random behavior. The $1/f^\alpha$ behavior of the power spectra of the temperature and pressure are indicative of fractal noise or fractional Brownian Motion if $\alpha \neq 2$.

6. REFERENCES

- [1] Allen M.P. T.J. Tildesley "Computer Simulation of liquids", Clarendon Press, Oxford (1987).
- [2] Berendsen H.J.C. and van Gunsteren W.F., Practical algorithms for dynamic simulations in *Molecular dynamics simulation of statistical mechanical systems*, G. Ciccotti, W.G. Hoover (Ed) North Holland, Amsterdam (1986) 43-65.
- [3] Verlet L., Computer experiments on classical fluids. I. Thermodynamical properties of Lennard-Jones molecules, *Physical Review* 159, 98-103 (1967).
- [4] Sutton A.P. and Balluffi R.W. *Interfaces in Crystalline Materials*, (Oxford University Press) (1996).
- [5] Karakasidis T. and Meyer M., Grain-boundary diffusion of cation vacancies in nickel oxide: A molecular-dynamics study, *Physical Review B* 55, 13853-13864 (1997).
- [6] Meyer M. and Waldburger C., Grain boundary structure of NiO, *Temperature Evolution : a molecular dynamics study*, *Materials Science Forum* 126-128, 229 (1993).
- [7] Spiegel M.R., *Statistics*, McGraw-Hill, New York, (1988).
- [8] Li W., Absence of $1/f$ spectra in Dow Jones average, *Inter. J. of Bifurcation and Chaos*, 1, 583-597 (1991).
- [9] Bak P. Tang C. Wiesenfeld K. Self-organized criticality : an explanation of $1/f$ noise, *Phys. Rev. Lett.* 59, pp.381-387 (1987).
- [10] Bak P. Tang C. Wiesenfeld K., Self-organized criticality, *Phys. Rev. A* 38, 364-374 (1988).
- [11] Provenzale A., Smith L.A., Vio R. and Murane G., Distinguishing Between Low-Dimensional Dynamical and Randomness in Measure Time Series" *Physica D* 58, 31-49 (1992).
- [12] Karakasidis T.E, Andreadis I.A., A fractional Brownian Motion model for time series produced by constant temperature molecular dynamics simulations, to appear in *Int. J. of Bifurcation and Chaos* (2001).
- [13] Mandelbrot B.B. "The Fractal Geometry of Nature", Freeman, San Francisco, (1982).

VIBRATIONAL PROPERTIES OF A $\Sigma 5(310)[001]$ NiO GRAIN BOUNDARY STUDIED BY MOLECULAR DYNAMICS SIMULATION

T. E. Karakasidis

Department of Civil Engineering
University of Thessaly, GR-38334 Volos, Greece

1. SUMMARY

In this communication we present results concerning the study of the vibrational properties of a $\Sigma 5(310)[001]$ NiO grain boundary by Molecular Dynamics simulations. The phonon density of states of the cation and anion sublattice in the boundary region is calculated at $T=300\text{K}$ in the directions parallel and perpendicular to the boundary plane. The obtained results are compared with those obtained for the bulk and the differences are discussed. We have also calculated the mean square displacements of the cations and the anions in the grain boundary region as a function of temperature in the direction perpendicular and parallel to the boundary plane and the results are compared with that of the bulk. The combination of the above results lead to some conclusions about the binding of the atoms in the boundary region.

2. INTRODUCTION

Grain boundaries (GBs) have attracted a great interest in ceramics since these materials are often used in polycrystalline form as many technologically interesting ceramic materials are prepared by powder sintering. GBs may seriously affect several properties such as conductivity, brittle fracture, creep etc. The knowledge of the atomic structure in the boundary region as well as the dynamic properties of the atoms in this region helps understanding such effects. For a review on grain boundaries and their properties one can consult the excellent book of Sutton and Balluffi [1].

Atomistic simulations are well suited for such studies since they can provide macroscopic properties but also a detailed microscopic description of the phenomena. Such methods include lattice statics, lattice dynamics and Molecular Dynamics (MD). In all cases matter is treated at the atomic scale and the atoms interact through an appropriate potential function. Lattice statics and lattice dynamics do not take into account temperature effects explicitly. Molecular Dynamics takes into account explicitly temperature effects and can provide information on time dependent properties so it is better suited for the study of vibrational properties. The equations of motion are solved at each timestep and we obtain successive points of the system in the phase space. From the set of positions and velocities obtained we can calculate several properties through the formalism of Statistical Mechanics [2].

The choice of the material (NiO) and the boundary ($\Sigma 5(310)[001]$) lies on the fact that NiO has a relative simple structure (fcc) and there is earlier work showing the stability of the

given boundary [3-6]. From a computational point of view the relatively small periodicity of the given GB let us simulate a relatively large system.

3. COMPUTATIONAL DETAILS

The simulations were carried out in the NVT ensemble using Nosé's method for constant temperature MD [7]. In order to describe the atomic interactions a rigid ion potential fitted on experimental properties of NiO [8] was used which has already been employed for the study of structural and diffusional properties of NiO GBs [6, 9] and surfaces [10, 11]. The form of the potential is:

$$\varphi(r_{ij}) = \frac{q_i q_j}{r_{ij}} + A \exp\left(-\frac{r_{ij}}{\rho}\right) - \frac{C}{r_{ij}^6} \quad (1)$$

where A , ρ , C are parameters derived by fitting calculated quantities to experimental data, q_i , q_j are the charges of the ions i , j and r_{ij} their corresponding distance. The atomic interactions are truncated with a cut-off radius $r_c = 1.6667 a$ (a being the lattice parameter). The details of the computation have already been described in a previous study [6], some relevant characteristics are briefly reviewed here. The Ewald method [12] was used to calculate Coulomb forces and the parameters are as follows: the convergence parameter α is equal to $5.0/2r_c$, the range of variation of the integers defining the reciprocal space vectors

is given by the following relations $-5 \leq n_x, n_y, n_z \leq 5$, $0 < n_x^2 + n_y^2 + n_z^2 \leq 27$.

The simulation box containing the GB is a parallelepiped with edges parallel to the directions $x=[310]$, $y=[\bar{1}\bar{3}0]$ and $z=[001]$. The system contains 2160 ions (1080 cations and 1080 anions) and the dimensions of the simulation cell are equal to $a(3\sqrt{10} + 2d)$, $3a\sqrt{10}/2$ and $6a$ respectively. The lattice parameter a is set equal to 4.168 Å at $T=0K$ and ad is the distance between the two grains of the GB. Periodic boundary conditions are applied in the directions parallel (y , z) and perpendicular (x) to the GB and they generate a second grain boundary in the system as shown in figure 1. The length of the simulation box in the $[310]$ direction has been chosen large enough to avoid interactions between the two boundaries. We have verified that between the two GB, there is a region where the properties are very close to that of the bulk. For this purpose we have calculated the local values of the nearest neighbor distances [13]. The region where we obtain bulk values extends over 10 $[310]$ interplanar distances.

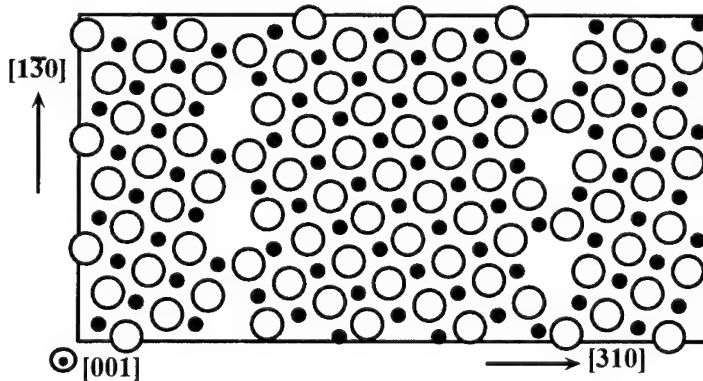


Figure 1- Schematic representation of a (001) plane normal to the boundary axis. Full and empty circles correspond respectively to cations and anions. Anions and cations exchange positions in successive planes.

The starting configuration is obtained by putting together two crystallites with perfect (310) surfaces facing each other. The GB generation then requires the calculation of the distance d between the two surfaces and the determination of possible rigid displacements in the boundary plane (parallel or perpendicular to the tilt axis). To do that, the potential energy of the system is minimized, not only with reference to the atomic positions but also with respect to rigid displacements. The relaxation is performed using Bennett's method [14]. Once the relaxed configuration is obtained is then heated step by step in order to reach the desired temperature. Once the temperature required for the computations is attained we perform an MD run of 3 ps in order to reach an equilibrium configuration. The equations of motion were solved using Verlet's algorithm [15] and a timestep of 10^{-15} s.

The phonon DOS were obtained from the Fourier transform of the velocity autocorrelation function following the methodology of [16] over a duration of 10 ps at $T=300\text{K}$ where velocities were saved every 5 timesteps.

Mean square displacements were calculated at various temperatures using equation:

$$\langle u_p^2 \rangle = \frac{\langle r_p^i(t+\tau) - r_p^i(\tau) \rangle^2}{2} \quad (2)$$

where $\langle \rangle$ indicate an average on time performed over particles i located in the corresponding region (in our case bulk or grain boundary region), and p indicates the corresponding direction in space, τ is the time increment. We covered a temperature range from 300 K to 2800 K. At each temperature we used the lattice parameter that corresponded to zero pressure for the bulk system.

In order to calculate grain boundary properties we take into account ions located on sites like the ones presented in figure 2. This choice lies on the fact that from a previous study [6] it was found that GB diffusion was limited mainly to these sites and the size of this zone (about 10 Å) is compatible to the GB width of 7 Å deduced from diffusion experiments in NiO [17].

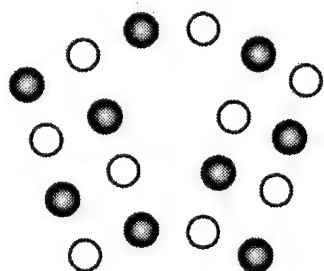


Figure 2 Sites considered as boundary region (projection in the (001) plane, open circles correspond to anions and full circles to cations). Anions and cations exchange positions in successive planes along the [001] axis.

4. RESULTS AND DISCUSSION

Phonon Density of States

In figures 3a-b we present the phonon density of states (DOS) at $T=300\text{K}$ obtained for the cationic and anionic sublattice in the bulk. It is interesting to notice that similar results are obtained for the region located between the two GBs indicating that we have indeed bulk

properties in the region between the two GBs. We can see that cations contribute mainly to low frequencies while anions contribute to high frequencies.

In figure 3c we present results concerning the phonon DOS for the cation sublattice of the GB region calculated for the directions normal to the boundary plane and parallel to it. By comparison with figure 3a we can see that in the direction normal to the boundary plane we have a shift of the pic of 7 THz toward lower frequencies. This is an indication that the cations located in the boundary region are more loosely coupled than the bulk cations. Another remark is that there is an enhancement of frequencies located in the region 10-11 THz for both directions, although it seems to be less important than the observed shift towards lower frequencies.

As far as the anionic sublattice is concerned by comparison of figure 3b with 3d we can see that there is a enhancement of lower frequencies in the region 0-7THz. The enhancement of lower frequencies indicates that the anions are more loosely coupled in the GB region than in the bulk, especially in the direction normal to the boundary plane. We can see also that there seems to exist a slight enhancement of frequencies in the high frequency region in the direction parallel to the boundary plane.

As we can see both for the anion and cation sublattices in the GB region there are some differences in the DOS in the directions normal and parallel to the boundary plane. A common characteristic is that the DOS normal to the boundary planes is shifted towards lower frequency more than the DOS parallel to the boundary plane. As a result we expect an anisotropic behavior in the vibrational behavior. These findings are reinforced by the results obtained from the mean square displacement of the atoms.

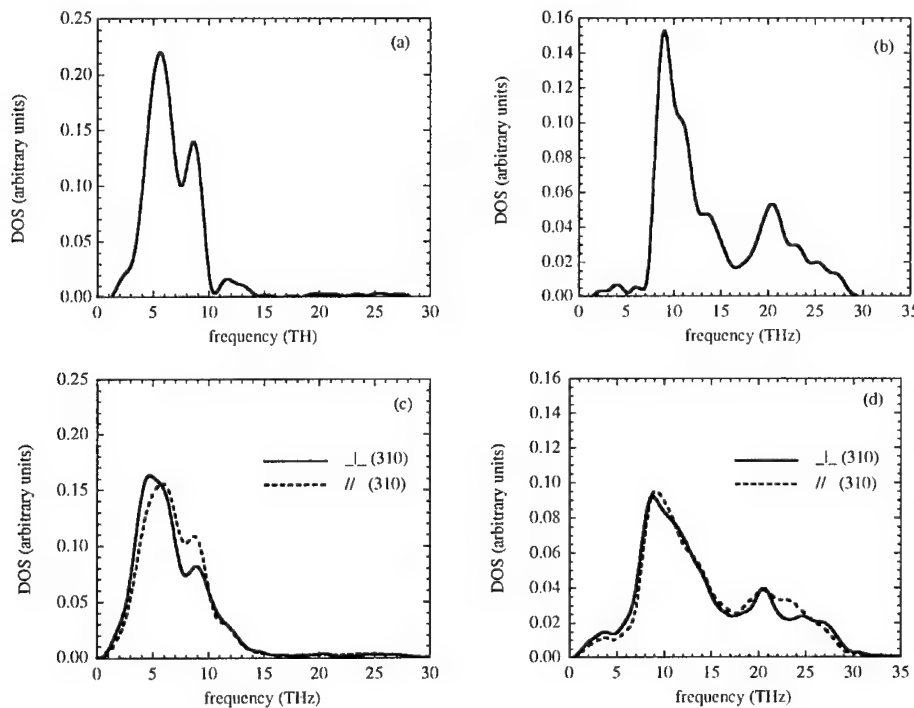


Figure 3 Phonon DOS obtained at T=300K (a) bulk cation sublattice (b) bulk anion sublattice (c) grain boundary region cation Sublattice (d) grain boundary region anion sublattice (\perp (310) corresponds to the boundary plane).

Mean square displacements

The vibrational behavior of the surface is also characterized by the mean square displacements of the atoms. We have calculated the mean square displacements for the cation and anion sublattice in the case of the bulk and in the GB region as a function of temperature. The temperature region explored extends from 300 K up to 2800 K.

As we can see in figure 4a at low temperature the mean square displacements on the cation sublattice are just slightly higher than that of the bulk and nearly the same in the direction parallel and normal to the boundary plane. However as temperature rises we observe that while the mean square displacement parallel to the boundary plane is quite close to that of the bulk, the mean square displacement in the direction normal to the boundary plane becomes significantly higher giving rise to an increasing anisotropy. A similar behavior is observed in the case of the anion sublattice as we can see in figure 4b.

The observed anisotropy is indicative of the fact that the ions are more loosely coupled in the direction normal to the boundary plane than parallel to it. This is in accordance with the indications obtained from the phonon DOS results. In addition we see that as it was expected the anisotropy is small at low temperatures.

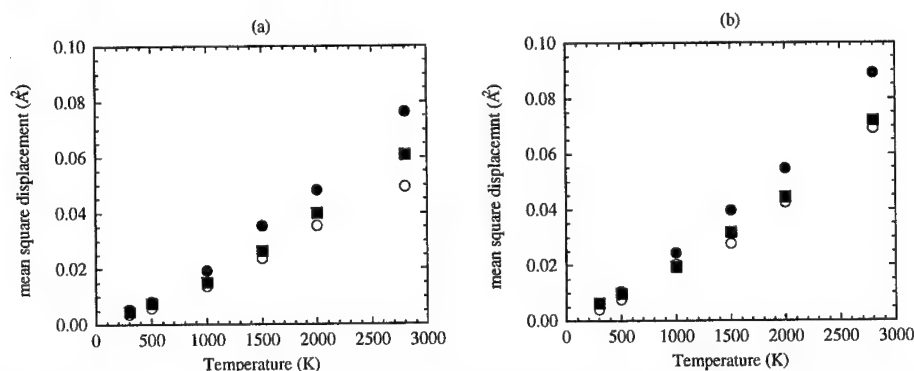


Figure 4 Mean square displacements calculated for the cation sublattice (a) and the anion sublattice (b). Empty circles correspond for atoms in the bulk region while full circles correspond to the direction normal to the boundary plane and full squares to the direction parallel to the boundary plane.

5. CONCLUSIONS

Using molecular dynamics simulations we have studied the vibrational properties of the GB region in a $\Sigma 5(310)[001]$ grain boundary of nickel oxide. We calculated the phonon density of states at $T=300\text{K}$ for the cation and anion sublattice both in the grain boundary region and in the bulk. The grain boundary DOS present a shift toward lower frequencies especially in the direction normal to the boundary. They also present some differences in the two directions studied indicating an anisotropy in the vibrational properties. This is confirmed by the mean square displacements calculated as a function of temperature for both sublattices in the grain boundary region and in the bulk. In fact the amplitude of vibration is higher in the direction normal to the boundary plane than in the direction parallel to it and both are higher than that of the bulk. This anisotropy is small at low temperatures but it becomes more pronounced as temperature rises. The above results indicate that the ions are more loosely coupled in the direction normal to the boundary plane than in the direction parallel to it.

6. REFERENCES

- [1] Sutton A. P. and Balluffi R. W., *Interfaces in crystalline Materials* (Oxford : Clarendon Press) (1995).
- [2] Allen M.P. T.J. Tildesley, *Computer Simulation of liquids* (Clarendon Press, Oxford) (1987).
- [3] Duffy D. M. and Tasker P. W. *Phil. Mag.* A 47, 817 (1983).
- [4] Harding J. H., Parker S. C. and Tasker P. W., in *Non-Stoichiometric Compounds Surfaces, Grain Boundaries and Structural Defects*, J. Nowotny and W. Weppner (Ed), (NATO ASI Series C276) (1989) 337.
- [5] Meyer M. and Waldburger C., Grain boundary structure of NiO, Temperature Evolution : a molecular dynamics study, *Materials Science Forum* 126-128, 229 (1993).
- [6] Karakasidis T. and Meyer M., Grain-boundary diffusion of cation vacancies in nickel oxide: A molecular-dynamics study, *Physical Review B* 55, 13853-13864 (1997).
- [7] Nose S., A unified formulation of the constant temperature molecular dynamic method, *J. Chem Phys.* 81, 511-519 (1984).
- [8] Massobrio C. and Meyer M., Rigid-ion potential models for NiO and CoO : a comparison between experimental and calculated thermal expansion, *J. Phys. : Cond. Matter* 3, 279-284 (1991).
- [9] Karakasidis T. and Meyer M., Molecular dynamics simulation of the atomic structure of a NiO tilt grain boundary at high temperature, *Modelling and Simulation in Materials Science and Engineering* 8, 117-132 (2000).
- [10] Karakasidis T. and Evangelakis G., A molecular dynamics study of cationic vacancy diffusion on NiO(001) surface", *Surface Science* 436, 193-201 (1999).
- [11] Karakasidis T.E., Papageorgiou D.G. and Evangelakis G.A., Structure and dynamics of NiO(001) and Ni/NiO(001) surfaces by molecular dynamics simulation, *Applied Surface Science* 162-163, 233-238 (2000).
- [12] Ewald P.P., *Ann. der. Physik* 64, 253 (1921).
- [13] Karakasidis T. 1995 Ph.D. Thesis (University Paris 6, France), CEA Report CEA R5723 (1996).
- [14] Bennett C.H. in *Diffusion in Solids* A.S. Nowick and J.J. Burton (Ed) (New York : Academic press) (1975) 73.
- [15] Verlet L., Computer experiments on classical fluids. I. Thermodynamical properties of Lennard-Jones molecules, *Physical Review* 159, 98-103 (1967).
- [16] Papanicolaou N. E., Lagaris I.E., Evangelakis G.A., *Surf. Sci.* 337, L819 (1995).
- [17] Atkinson A. and Taylor R.I., *Philos. Mag.* A 43, 979 (1981).

ANALYTICAL SOLUTION OF THE NONLINEAR DAMPED DUFFING OSCILLATOR

D. Panayotounakos

Department of Applied Mathematics and Physics, National Technical University of Athens,
GR-157 73, Athens, Greece

G. Exadaktylos

Department of Mineral Resources Engineering - Laboratory of Mine Design and Mechanics,
Technical University of Crete, GR-73100, Chania, Greece

A. Vakakis

Department of Applied Mathematics and Physics, National Technical University of Athens,
GR-157 73, Athens, Greece

1. SUMMARY

In this paper a systematic study of the Duffing differential equation that describes nonlinear oscillations with damping is performed. First, the 2nd order non-linear differential equation is transformed into a simpler equivalent Abel equation of the 2nd kind by virtue of appropriate functional transformations. In a second step the Taylor series solution of Abel's equation and the error estimation are given. Finally, the comparison of the numerical solution with the proposed analytical solution for a given initial condition is presented.

2. INTRODUCTION

The solution of special forms of the Duffing differential equation that describes the nonlinear oscillator without damping is well known [1-4] in terms of elliptic integrals and functions. Further, for the general case of oscillating systems with damping numerical solutions by recourse to any of the various forms of finite difference schemes have been achieved by previous investigators [e.g. 2]. However, up-to-date there is no analytical solution of this equation and from what it seems there do not exist known functions that can form its solution in an analytic manner.

In this work a first attempt is performed for the construction of analytical solutions of the Duffing equation by virtue of appropriate Taylor series form. It is demonstrated that the proposed solutions can successfully converge to the true solution obtained by special finite difference scheme. A proposition is made for the efficient construction and convergence of the analytical solution in terms of Taylor series. Finally, the comparison of the numerical solution with the proposed analytical solution for a given initial condition is presented graphically.

3. THE NONLINEAR DUFFING OSCILLATOR WITH DAMPING

The ordinary differential equation (ode) that governs the problem of nonlinear damped oscillations with damping in dimensionless form is the following [5]:

$$x''_{tt} + \lambda_1 x'_t + \lambda_2 x^3 = 0 \quad (1)$$

where $x = x(t)$ denotes the space variable, $x'_t(t) = dx/dt$, t is the time and λ_1, λ_2 are constants pertaining to the damping and the resistance factor of the system, respectively. The solution of the above ode for $\lambda_1 = 0$ in terms of elliptic integrals and functions is well known [5]. Also, for $\lambda_1 \neq 0$ the numerical solution with any of the various forms of finite difference schemes have been achieved by many investigators [1,2]. However, there is no analytical solution of this ode for $\lambda_1, \lambda_2 \neq 0$ and there are no up-to-date known functions that can form the solution of the aforementioned equation (1).

The initial conditions of the problem are postulated as follows:

$$\text{For } t = 0, x(0) = x_0 \text{ and } x'_t(0) = x'_0 \quad (2)$$

or

$$\text{For } t = 0, x(0) = 0 \text{ and } x'_t(0) = 1 \quad (3)$$

Herein the following non-linear initial boundary value problem is studied and solved:

$$y''_{xx} + \lambda_1 y'_x + \lambda_2 y^3 = 0, \quad (4)$$

For $x = 0, y(0) = 0$ and $y'_x(0) = y_0$.

By virtue of the transformation

$$y'_x = p(y) \Rightarrow y''_{xx} = \frac{dp}{dy} \frac{dy}{dx} = p'_y p \quad (5)$$

the Duffing equation (4) obtains the form:

$$p p'_y + \lambda_1 p + \lambda_2 y^3 = 0 \quad (6)$$

The above ode may be transformed into a more convenient form if we apply the transformation:

$$p(y) = -\alpha \eta(\xi); \quad \xi = \beta y \Rightarrow p'_y = -\alpha \beta \eta'(\xi) \quad (7)$$

in which α, β are constants to be determined. By recourse to relationships (7) equation (6) takes the form:

$$\alpha^2 \beta \eta \eta'_\xi - \alpha \lambda_1 \eta + \frac{\lambda_2}{\beta^3} \xi^3 = 0 \quad (8)$$

Next, by taking:

$$\alpha^2\beta = \alpha\lambda_1, \quad \alpha\lambda_1 = \frac{\lambda_2}{\beta^3} \Leftrightarrow \alpha = \frac{\lambda_1^2}{\sqrt{\lambda_2}}, \quad \beta = \frac{\sqrt{\lambda_2}}{\lambda_1} \quad (9)$$

Therefore, the final transformation:

$$y'_x = p(y) = -\frac{\lambda_1^2}{\sqrt{\lambda_2}}\eta(\xi); \quad \xi = \frac{\sqrt{\lambda_2}}{\lambda_1}y \quad (10)$$

reduces the nonlinear equation (6) into the following *Abel* equation of the *second kind*

$$\eta\eta'_\xi - \eta = -\xi^3 \quad (11)$$

According to (10) and (11) at each value of ξ the above differential equation (11) prescribes the slope of the solution η'_ξ (if η is known). The numerical solution of (11) may be performed by the Fehlberg fourth-fifth order Runge-Kutta method [6,7]. Integration is performed starting from the closer of two points to the desired output point. These points are chosen from the initial point or the most recently generated mesh point. In the event of an error being returned, the next attempt at integration will start from the initial point. A graphical representation of the numerical solution of (11) is illustrated in Fig. 1.

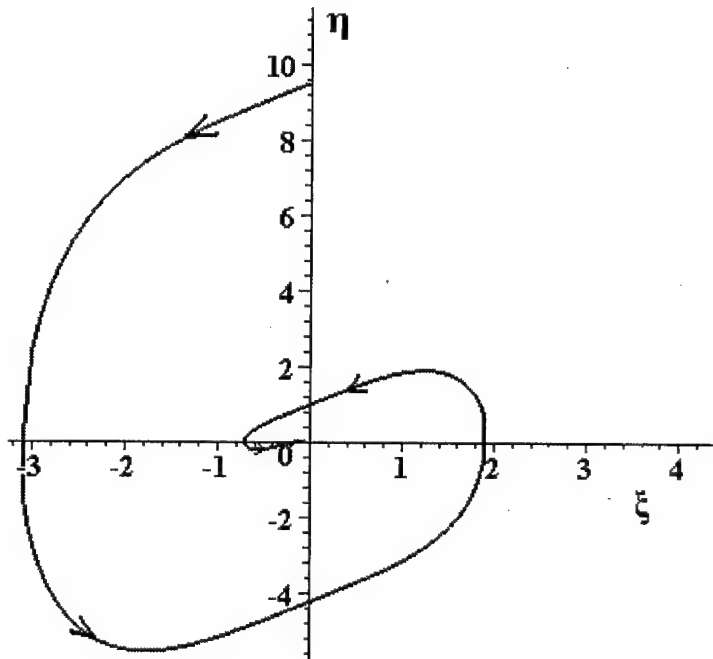


Fig. 1. Numerical solution of Abel's ode (11).

4. THE SOLUTION OF ABEL'S EQUATION AS TAYLOR SERIES

We proceed next to express the solution of the Abel equation (11) in Taylor series in the variable ξ . We assume that the solution η in the neighborhood of some point γ can be written as the following Taylor series:

$$\eta(\xi) \equiv \eta_T(\xi) = \sum_{v=0}^{\infty} \varepsilon_v (\xi - \gamma)^v \quad (12)$$

When this series is substituted in equation (11) and the coefficients of equal powers are equated, the following solution is obtained for the N-terms truncated series:

$$\eta_T(\xi) = A + \sum_{v=1}^N \sum_{k=1}^{3N+1} d_{v,k} \gamma^{k-1} (\xi - \gamma)^v + O([\xi - \gamma]^{N+1}) \quad (13)$$

in which $\eta_T(\gamma) = A$. The explicit values of the sequences of coefficients $d_{v,k}$ through $N=10$ that is $v=1, \dots, 10$ and $k=1, \dots, 31$ are given in the following manner:

[illegible]

$$d_{6,k} = \left[-\frac{1}{6} \frac{1}{A^3}, \frac{1}{2} \frac{1}{A^4}, -\frac{7}{8} \frac{1}{A^3}, -\frac{1}{2} \frac{1}{A^5}, \frac{469}{120} \frac{1}{A^4} + \frac{1}{6} \frac{1}{A^6}, -\frac{797}{120} \frac{1}{A^5}, \frac{607}{120} \frac{1}{A^6}, -\frac{105}{16} \frac{1}{A^5}, -\frac{29}{20} \frac{1}{A^7}, \frac{3983}{240} \frac{1}{A^6}, \right. \\ \left. -\frac{74}{5} \frac{1}{A^7}, \frac{413}{90} \frac{1}{A^8}, -\frac{175}{16} \frac{1}{A^7}, \frac{84}{5} \frac{1}{A^8}, -\frac{245}{36} \frac{1}{A^9}, 0, -\frac{105}{16} \frac{1}{A^9}, \frac{77}{16} \frac{1}{A^{10}}, 0, 0, -\frac{21}{16} \frac{1}{A^{11}}, 0, 0, 0, 0, \right. \\ \left. 0, 0, 0, 0, 0, 0, 0 \right]$$

$$d_{7,k} = \left[\frac{1}{7} \frac{1}{A^4}, -\frac{1}{4} \frac{1}{A^3}, -\frac{3}{7} \frac{1}{A^5}, \frac{41}{20} \frac{1}{A^4} + \frac{3}{7} \frac{1}{A^6}, -\frac{61}{10} \frac{1}{A^5}, -\frac{1}{7} \frac{1}{A^7}, \frac{121}{14} \frac{1}{A^6}, -\frac{6}{A^5}, -\frac{831}{140} \frac{1}{A^7}, \right. \\ \frac{1411}{60} \frac{1}{A^6} + \frac{223}{140} \frac{1}{A^8}, -\frac{2153}{60} \frac{1}{A^7}, \frac{701}{28} \frac{1}{A^8}, -\frac{325}{16} \frac{1}{A^7}, -\frac{241}{36} \frac{1}{A^9}, \frac{825}{16} \frac{1}{A^8}, -\frac{137}{3} \frac{1}{A^9}, \\ \frac{2519}{180} \frac{1}{A^{10}}, -\frac{385}{16} \frac{1}{A^9}, \frac{759}{20} \frac{1}{A^{10}}, -\frac{125}{8} \frac{1}{A^{11}}, 0, -\frac{189}{16} \frac{1}{A^{11}}, \frac{143}{16} \frac{1}{A^{12}}, 0, 0, -\frac{33}{16} \frac{1}{A^{13}}, \\ \left. 0, 0, 0, 0, 0, 0, 0, 0 \right]$$

$$d_{8,k} = \left[-\frac{1}{32} \frac{1}{A^3}, -\frac{1}{8} \frac{1}{A^5}, \frac{97}{160} \frac{1}{A^4} + \frac{3}{8} \frac{1}{A^6}, -\frac{53}{16} \frac{1}{A^5}, -\frac{3}{8} \frac{1}{A^7}, \frac{919}{112} \frac{1}{A^6} + \frac{1}{8} \frac{1}{A^8}, -\frac{123}{32} \frac{1}{A^5}, -\frac{2343}{224} \frac{1}{A^7}, \right. \\ \frac{1793}{80} \frac{1}{A^6} + \frac{1503}{224} \frac{1}{A^8}, -\frac{25367}{480} \frac{1}{A^7}, \frac{481}{280} \frac{1}{A^9}, \frac{211397}{3360} \frac{1}{A^8}, -\frac{3405}{128} \frac{1}{A^7}, -\frac{10573}{280} \frac{1}{A^9}, \\ \frac{63913}{640} \frac{1}{A^8} + \frac{10219}{1120} \frac{1}{A^{10}}, -\frac{69961}{480} \frac{1}{A^9}, \frac{40909}{420} \frac{1}{A^{10}}, -\frac{455}{8} \frac{1}{A^9}, -\frac{7207}{288} \frac{1}{A^{11}}, \frac{92829}{640} \frac{1}{A^{10}}, -\frac{8199}{64} \frac{1}{A^{11}}, \\ \frac{22451}{576} \frac{1}{A^{12}}, -\frac{3339}{64} \frac{1}{A^{11}}, \frac{10725}{128} \frac{1}{A^{12}}, -\frac{2233}{64} \frac{1}{A^{13}}, 0, -\frac{693}{32} \frac{1}{A^{13}}, \frac{2145}{128} \frac{1}{A^{14}}, 0, 0, -\frac{429}{128} \frac{1}{A^{15}}, 0, \\ \left. 0, 0, 0, 0, 0 \right]$$

$$d_{9,k} = \left[\frac{7}{90} \frac{1}{A^4} + \frac{1}{9} \frac{1}{A^6}, -\frac{181}{180} \frac{1}{A^5}, -\frac{1}{3} \frac{1}{A^7}, \frac{1153}{252} \frac{1}{A^6} + \frac{1}{3} \frac{1}{A^8}, -\frac{55}{32} \frac{1}{A^5}, -\frac{5135}{504} \frac{1}{A^7}, -\frac{1}{9} \frac{1}{A^9}, \frac{2377}{160} \frac{1}{A^6} + \frac{2035}{168} \frac{1}{A^8}, \right. \\ -\frac{3745}{72} \frac{1}{A^7}, -\frac{6217}{840} \frac{1}{A^9}, \frac{1444091}{15120} \frac{1}{A^8} + \frac{4609}{2520} \frac{1}{A^{10}}, -\frac{825}{32} \frac{1}{A^7}, -\frac{2952199}{30240} \frac{1}{A^9}, \frac{32519}{240} \frac{1}{A^8} + \frac{59191}{1120} \frac{1}{A^{10}}, \\ -\frac{46691}{160} \frac{1}{A^9}, -\frac{59753}{5040} \frac{1}{A^{11}}, \frac{9698711}{30240} \frac{1}{A^{10}}, -\frac{12355}{128} \frac{1}{A^9}, -\frac{169487}{945} \frac{1}{A^{11}}, \frac{2045681}{5760} \frac{1}{A^{10}} + \frac{738881}{18144} \frac{1}{A^{12}}, \\ -\frac{485947}{960} \frac{1}{A^{11}}, \frac{664807}{2016} \frac{1}{A^{12}}, -\frac{1197}{8} \frac{1}{A^{11}}, -\frac{213983}{2592} \frac{1}{A^{13}}, \frac{49049}{128} \frac{1}{A^{12}}, -\frac{21637}{64} \frac{1}{A^{13}}, \frac{176891}{1728} \frac{1}{A^{14}}, \\ \left. -\frac{7161}{64} \frac{1}{A^{13}}, \frac{23309}{128} \frac{1}{A^{14}}, -\frac{11011}{144} \frac{1}{A^{15}}, 0, -\frac{1287}{32} \frac{1}{A^{15}}, \frac{12155}{384} \frac{1}{A^{16}}, 0, 0, -\frac{715}{128} \frac{1}{A^{17}}, 0, 0, 0 \right]$$

$$d_{10,k} = \left[-\frac{79}{600} \frac{1}{A^5} - \frac{1}{10} \frac{1}{A^7} - \frac{397}{280} \frac{1}{A^6} + \frac{3}{10} \frac{1}{A^8} - \frac{33}{64} \frac{1}{A^5} - \frac{3249}{560} \frac{1}{A^7} - \frac{3}{10} \frac{1}{A^9} - \frac{19679}{2880} \frac{1}{A^6} + \frac{60701}{5040} \frac{1}{A^8} + \frac{1}{10} \frac{1}{A^{10}}, \right. \\
-\frac{255049}{7200} \frac{1}{A^7} - \frac{22889}{1680} \frac{1}{A^9} - \frac{607699}{6300} \frac{1}{A^8} + \frac{67411}{8400} \frac{1}{A^{10}} - \frac{605}{32} \frac{1}{A^7} - \frac{5103061}{33600} \frac{1}{A^9} - \frac{4861}{2520} \frac{1}{A^{11}}, \\
\frac{129943}{960} \frac{1}{A^8} + \frac{4698383}{33600} \frac{1}{A^{10}} - \frac{5867183}{14400} \frac{1}{A^9} - \frac{39301}{560} \frac{1}{A^{11}} - \frac{199513957}{302400} \frac{1}{A^{10}} + \frac{249821}{16800} \frac{1}{A^{12}}, \\
-\frac{31801}{256} \frac{1}{A^9} - \frac{7328653}{12096} \frac{1}{A^{11}} - \frac{2386373}{3840} \frac{1}{A^{10}} + \frac{15069769}{50400} \frac{1}{A^{12}} - \frac{918607}{720} \frac{1}{A^{11}} - \frac{1337237}{21600} \frac{1}{A^{13}}, \\
\frac{809954431}{604800} \frac{1}{A^{12}} - \frac{79695}{256} \frac{1}{A^{11}} - \frac{30967387}{43200} \frac{1}{A^{13}} - \frac{6525233}{5760} \frac{1}{A^{12}} + \frac{5667805}{36288} \frac{1}{A^{14}} - \frac{7638631}{4800} \frac{1}{A^{13}}, \\
\frac{4567277}{4480} \frac{1}{A^{14}} - \frac{48279}{128} \frac{1}{A^{13}} - \frac{649649}{2592} \frac{1}{A^{15}} - \frac{79695}{256} \frac{1}{A^{11}} - \frac{30967387}{43200} \frac{1}{A^{13}}, \\
\frac{6525233}{5760} \frac{1}{A^{12}} + \frac{5667805}{36288} \frac{1}{A^{14}} - \frac{7638631}{4800} \frac{1}{A^{13}} - \frac{4567277}{4480} \frac{1}{A^{14}} - \frac{48279}{128} \frac{1}{A^{13}} - \frac{649649}{2592} \frac{1}{A^{15}} - \frac{620477}{640} \frac{1}{A^{14}}, \\
-\frac{41041}{48} \frac{1}{A^{15}} - \frac{2229227}{8640} \frac{1}{A^{16}} - \frac{30459}{128} \frac{1}{A^{15}} - \frac{250393}{640} \frac{1}{A^{16}} - \frac{5291}{32} \frac{1}{A^{17}}, 0, -\frac{19305}{256} \frac{1}{A^{17}}, \\
\left. \frac{46189}{768} \frac{1}{A^{18}}, 0, 0, -\frac{2431}{256} \frac{1}{A^{19}} \right]$$

Next, the following proposition for the construction of the analytical solution is postulated:

Proposition: The sequence of successive Taylor series solutions of the Abel equation (11) is produced by the following convergence criterion

$$\forall \quad \xi_k = \frac{k\xi_0}{v}; \quad k=0, \dots, v, \quad \exists \varepsilon > 0 \left(\varepsilon = O\left(\|\xi_{k+1} - \xi_k\|^1\right) \right); \quad (14) \\
|\eta_T(\xi_{k+1}) - \eta_T(\xi_k)| < \varepsilon \quad \wedge \quad \xi_k \in [0, \xi_0]$$

wherein $\xi_0: \eta_T(\xi_0) = 0$ that is ξ_0 is the root of the Taylor series expansion around zero for the given initial condition.

As an example of the efficiency of the proposed analytical solution (13) and the above proposition for $\varepsilon=0.03$, we construct the following diagram - with the numerical solution superimposed in the same diagram - for the initial condition

$$\eta(0) = 10 \quad (15)$$

In the same figure some of the points around which the Taylor series solution was applied for the first and the second branch of the curve are also displayed. A total number of 31 successive Taylor series solutions were employed for the complete solution of Abel's equation (11) with the given initial condition and maximum absolute error.

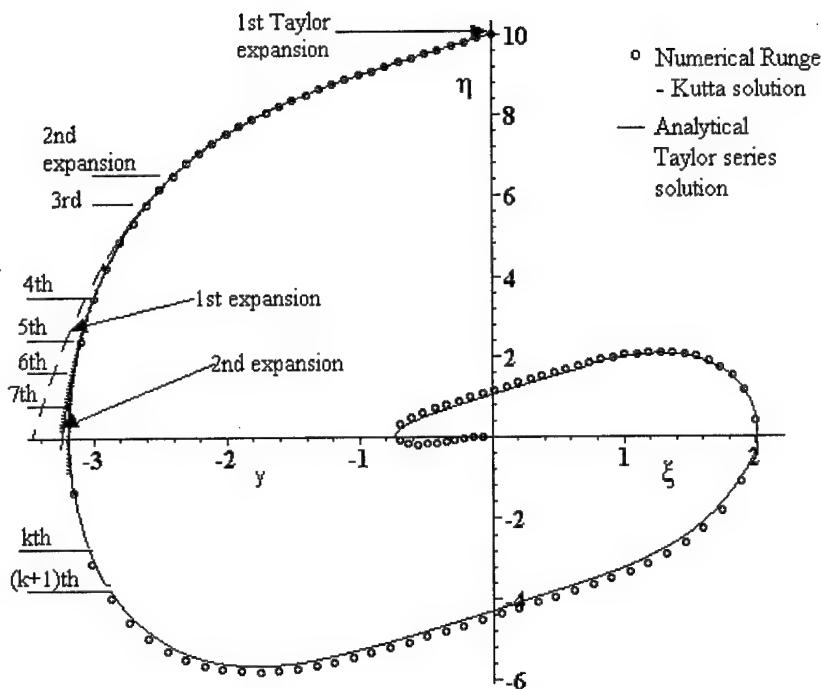


Fig. 2. Comparison of analytical with numerical solution of Abel's equation (11) with initial condition $\eta(0) = 10$.

5. REFERENCES

- [1] Nayfeh, T.A. and Mook, D., Nonlinear oscillations, Wiley Interscience, 1984.
- [2] Gendelman, O. and Vakakis A.F., Transitions from localization to nonlocalization in strongly nonlinear damped oscillators, Chaos, Solitons and Fractals (Special Issue on Localization problems in Engineering), Vol. 11, pp. 1535-1542, 2000.
- [3] Salenger, G., Vakakis, A.F., Gendelman, O., Manevich, L. and Andrianov, I., Transitions from strongly-to-weakly nonlinear motions of damped nonlinear oscillators, Nonlinear Dynamics, Vol. 20, No. 2, pp. 99-114, 1999.
- [4] Ludeke, C.A. and Wagner, W.S., The generalized Duffing equation with large damping, Int. J. Nonlinear Mechanics, 3, pp. 383-395, 1968.
- [5] Davis, H.T., Introduction to nonlinear differential and integral equations, Dover, 1962.
- [6] Gear, C.W., Numerical Initial Value Problems in Ordinary Differential Equations, Prentice-Hall, 1971.
- [7] Hindmarsh, A.C., Stepleman R.S. *et al.* (eds.), Odepack, a Systemized Collection of ODE Solvers, North-Holland, Amsterdam, 1983.

NONLINEAR EFFECTS ON THE ELASTIC STABILITY OF A COLUMN-FOOTING SYSTEM ON ELASTIC BASE

Christos J. Younis

Assist. Prof., Labor. of Struct. Mech., Depart. of Rural & Surv. Engineering,

Dimitrios E. Panayotounakos

Professor, Section of Mechanics, Depart. of Appl. Math. & Phys. Scien.
National Technical University of Athens

ABSTRACT

An orthogonal footing is considered resting on linearly elastic base and loaded axisymmetrically by a vertical load. The relation between the loading eccentricity and the rotation of the footing is derived, with emphasis on the case that the load acts outside the core of the footing area (uplift). Then a column/footing system is considered, with elastic supports and arbitrary loading at the column top, resting on elastic base, as above. The rotation of the footing versus the column load is studied, along with the stability of the system, and its buckling load is evaluated. The bifurcation of equilibrium of the system is also investigated.

1. INTRODUCTION

The study of stability of prismatic columns is very important in the analysis of structures. The basis of stability of impressive columns is the Euler buckling load, the value of which among others depends on the kind of the supports. Considering elastically fixed supports we obtain very good approximation of the real conditions [1-5]. Generally, in the case of elastic fixing, linear relation between rotation and moment holds. A rigid footing on elastic base does not fall into the case of linear elastic fixing, when the load acts out of the core of the resting area. In this case the appearance of working portion and neutral portion (uplift) renders the relation between rotation and moment nonlinear.

In this work the above nonlinear relation is established and used in the study of the deflection of a column/footing system, with elastic supports and a general loading at its top, which rests on elastic base. The buckling load of this system is evaluated and found to be smaller than the Euler critical load. A parametric study is carried out and the conditions of bifurcation of equilibrium of the column/footing system are investigated.

2. THE ROTATION OF THE FOOTING

Consider a rigid footing-plate of rectangular plan with dimensions $\ell \times b$ loaded by a vertical force P acting in the one plane of symmetry with eccentricity e . The footing is resting on a linearly elastic base with coefficient of subgrade reaction $C[KN/m^3]$ (Winkler model). It is valid that

$$\sigma = Cv, \quad (2.1)$$

where $v[m]$ is the vertical displacement of the footing-base interface at which compressive stresses $\sigma[KN/m^2]$ are developed. Fig. 1a shows the vertical displacement and the rotation of the rigid footing, as

well as the working and the neutral portion in the case that the load P acts out of the core of the area (uplift) ($\ell/6 \leq |e|$). Fig. 2a depicts the compressive stresses in the working area for the above mentioned case (uplift). The rotation φ of the footing is given by the relation

$$\varphi = v_{\max}/3(\ell/2 - |e|) = \sigma_{\max}/3C(\ell/2 - |e|). \quad (2.2)$$

An analogous relation is valid in the case that P acts inside the core ($|e| \leq \ell/6$). Expressing the stresses σ in terms of the parameters $P; e; b, \ell$, one obtains

$$\varphi = 12Pe/Cb\ell^3, \quad \text{if} \quad -\ell/6 \leq e \leq \ell/6, \quad (2.3)$$

and

$$\varphi = \text{sgn}(e)8P/9C(\ell - 2|e|)^2 b, \quad \text{if} \quad e \leq -\ell/6 \text{ or } \ell/6 \leq e. \quad (2.4)$$

Finally, we introduce the moment $M = P \cdot e$ of the load P with respect to the center of gravity of the area, as well as the length L and the flexural rigidity $EJ[KNm^2]$ of a column that will be used in the next section.

Introducing the following quantities for nondimensionalization

$$\begin{aligned} a &= (PL/EJ)^{1/2} = \text{vertical load;} \\ \mu &= ML/EJ = \text{moment with respect to the center of gravity of the footing plan;} \\ c &= Cb\ell^4/EJ = \text{coefficient of subgrade reaction;} \\ \varepsilon &= e/\ell = \text{eccentricity;} \\ q &= \ell/L = \text{length of the footing plan} \end{aligned} \quad (2.5)$$

and solving equations (2.3) and (2.4) for $\mu(\varphi)$, one obtains

$$\mu(\varphi) = cq^3/12\varphi, \quad \text{if} \quad -\varphi^* \leq \varphi \leq \varphi^* \quad (2.6)$$

and

$$\mu(\varphi) = \text{sgn}(\varphi) a^2 q \left[\frac{1}{2} - \frac{1}{3} \frac{a}{q} \left(\frac{2}{c|\varphi|} \right)^{1/2} \right], \text{ if } \varphi \leq -\varphi^* \text{ or } \varphi^* \leq \varphi, \quad (2.7)$$

respectively.

In these relations φ^* denotes the value of the angle φ developed when the load P acts on the limits of the core. Fig. 2a shows the graphics of equations (2.6) and (2.7) involving several specific characteristics, while Fig. 2b depicts the influence of the vertical load “a” (P) on the dimensionless bending moment “ μ ”.

3. ANALYSIS OF THE COLUMN-FOOTING SYSTEM

In Fig. 3 a column-footing system is shown consisting of a column of length L and flexural rigidity EJ , connected at its top with the rest structure which can be represented by an horizontal spring of stiffness $G[KN/m]$ and a rotational spring of stiffness $C_1[KNm/rad]$. Also, the column is loaded by a vertical load P , an horizontal force H_0 , and a moment M_0 . The bottom end of the column is fixed into the prescribed footing of eccentricity e_f . The deflection of the column is governed by the known linear ODE

$$EJy'''' + Py'' = 0, \quad (3.1)$$

The general solution of this equation is

$$y(x) = c_1 \cos(ax/L) + c_2 \sin(ax/L) + c_3(x/L) + c_4. \quad (3.2)$$

where c_i ($i=1, \dots, 4$) are constants and a is given in equations (2.5).

The boundary conditions accompanying the ODE (3.1) are:

(i) Horizontal force equilibrium at the top of the column

$$Gy(0) + Py'(0) + EJy'''(0) = H_0 \quad (3.3)$$

(ii) Moment equilibrium at the top of the column

$$C_1 y'(0) - EJy''(0) = M_0 \quad (3.4)$$

(iii) Horizontal displacement of the lower end of the column

$$y(L) + hy'(L) = 0 \quad (3.5)$$

(iv) Moment equilibrium of the footing

$$EJy''(L) + EJhy'''(L) + M(\varphi) = Pe_f. \quad (3.6)$$

Substituting Eqn. (3.2) into Eqns (3.3) +(3.6), nondimensionalizing by using

$h_0 = H_0 L^2 / EJ =$ top column applied horizontal force;

$\mu_0 = M_0 L / EJ =$ top column applied moment;

$g = GL^3 / EJ =$ top column horizontal spring;

$s = C_1 L / E =$ top column rotational spring;

$\varepsilon_f = e_f / \ell =$ eccentricity of the footing;

(3.7)

$r = \frac{h}{\ell}$ = height of the footing

$\kappa_i = c_i/L$ = coefficients of the general solution,

and employing the obvious relation

$$\varphi = y'(L) = -c_1 \frac{a}{L} \sin a + c_2 \frac{a}{L} \cos a + \frac{c_3}{L}, \quad (3.8)$$

one obtains the following system of transcendental equations

$$\begin{aligned} k_1 g + k_3 a^2 + k_4 g &= h_0; \\ k_1 a^2 + k_2 a s + k_3 s &= \mu_0; \\ k_1 \cos a + k_2 \sin a + k_3 + k_4 + r q \varphi &= 0; \\ -k_1 a \sin a + k_2 a \cos a - k_3 - \varphi &= 0; \\ k_3(1 + r q) + k_4 + \mu(\varphi)/a^2 &= q \varepsilon_f. \end{aligned} \quad (3.9)$$

In the last equation it holds that

$$\mu(\varphi)/a^2 = c q^3 \varphi / 12 a^2, \text{ if } \varphi_1^* \leq \varphi \leq \varphi_2^* \quad (3.10)$$

or

$$\mu(\varphi)/a^2 = \operatorname{sgn}(\varphi) q \left[\frac{1}{2} - \frac{1}{3} \frac{a}{q} \left(\frac{2}{c|\varphi|} \right)^{1/2} \right], \text{ if } \varphi \leq \varphi_1^* \text{ or } \varphi_2^* \leq \varphi \quad (3.11)$$

One observes that if the values for a or φ are given, then solving the system (3.9), one can evaluate the parameters $\varphi; \kappa_1; \kappa_2; \kappa_3; \kappa_4$, or, $a; \kappa_1; \kappa_2; \kappa_3; \kappa_4$, respectively. In any case the selection of the proper of the equations (3.10) or (3.11) which will be used, depends on which of the inequalities

$$\varphi \leq 2a^2/cq^2 \text{ or } \varphi \geq 2a^2/cq^2 \quad (3.12)$$

holds, as Fig. 2a shows.

The evaluation of the maximum value of the load, a_{\max} , for which the system loses its equilibrium, is obtained by the differentiation of the system (3.9) in combination with the condition

$$da/d\varphi = 0. \quad (3.13)$$

This procedure leads to a system of ten transcendental equations with equal unknowns a_{\max} ; φ_{\max} ; κ_i ; $d\kappa_i/d\varphi$ ($i=1, \dots, 4$), the solution of which furnishes the values a_{\max} and φ_{\max} .

4. RESULTS AND CONCLUSIONS

In the system (3.9) the parameters of geometry $(\varepsilon_f; q; r)$, the parameters of elasticity $(c; g; s)$, and the parameters of the applied actions $(\mu_0; h_0)$ are involved. For various values of the dimensionless vertical load a one deduces the values for the angle φ and vice versa. The results are shown in Figs 4 and 5. Fig. 4 holding for $\mu_0 = h_0 = 0$, shows the area which corresponds to action of the vertical load inside the core of the footing (area between the two symmetric parabolas $\varphi = 2a^2/cq^2$). Also, in Fig. 4 are shown the areas corresponding to action of the vertical force P out of the core (uplift) (the areas on the left and on the right of the above two symmetric parabolas). Finally, Fig. 4 depicts the curve (φ, a) corresponding to a central footing ($\varepsilon_f = 0$), as well as the curves (φ, a) corresponding to a footing with eccentricities $\varepsilon_f = 0.05, -0.10$ and 0.15 . One observes that, for a central footing, the curve (φ, a) surrounds the curves which correspond to any eccentric footing. Also, the buckling load for a central footing coincides with the well-known Euler buckling load a_{cr} . On the contrary, the buckling load for eccentric footings coincides with the maximum a_{max} of the associating curve (φ, a) , and is always located inside the uplift areas. It is valid that $a_{max} < a_{cr}$, as well as that a_{max} is an increasing function of the coefficient of subgrade reaction c , and a decreasing function of the eccentricity ε_f .

Fig. 5 depicts the curves (φ, a) corresponding to $\varepsilon_f = 0.10, \mu_0 = 1$ and 7 , and $h_0 = 0$. As in the case that $\mu_0 = 0$, similarly for $\mu_0 \neq 0$, the curve $(\varepsilon_f = 0, \mu_0 = 0)$ surrounds all the curves (φ, a) . For $\mu_0 = 1$, one observes that φ increases continuously from negative to large positive values, causing instability. In the contrary, for $\mu_0 = 7$, φ increases up to a specific value, and then decreases up to large negative values, thus causing instability. It is obvious that there exists an intermediate value $\mu_{0,bif}$ of the applied moment, for which bifurcation of equilibrium of the system takes place. For every value of the eccentricity ε_f there exists a value $\mu_{0,bif}$, which can be evaluated.

5. REFERENCES

- [1] Timoshenko, S.P. and Gere, J.N., *Theory of Elastic Stability*, 2nd edn. McGraw-Hill, New York (1961).
- [2] Dimitrov, N.S., *Nichtlineare Baustatik* (Forschungsberichte aus dem Institut für Tragkonstruktionen und Konstruktives Entwerfen), Heft No. 2, University of Stuttgart (1979).
- [3] Pflüger, A., *Stabilitätsprobleme der Elastostatik*, Berlin (1950).
- [4] Schmid, E., Kuhn, R. and Lurtz, A., Stabilitätsfälle im Skelettbau. *Bautechnik* 2, 42-48 (1978).
- [5] Younis, C.J. and Panayotounakos, D.E., *Linear Buckling Analysis of a Column-Footing System Resting on Elastic Soil*, Computers and Structures, Vol. 40, No 3, pp. 619-627, 1991.

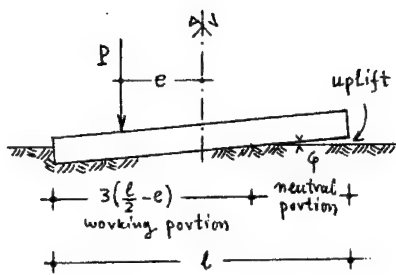


Fig. 1a. Rotation of the Footing

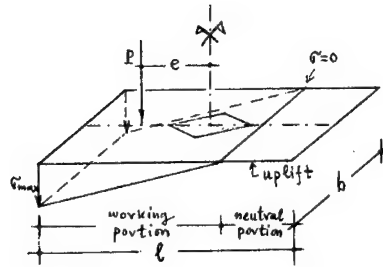


Fig. 1b. Stresses under the Footing

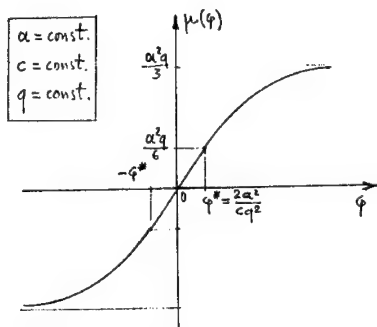


Fig. 2a. Moment versus Angle of Rotation

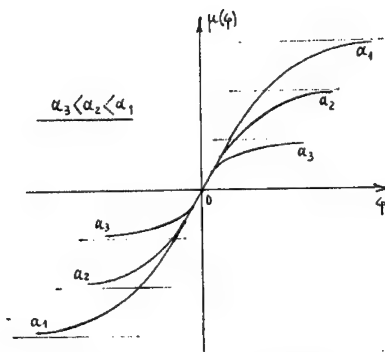


Fig. 2b. The effect of "α" on "μ(φ)/q"

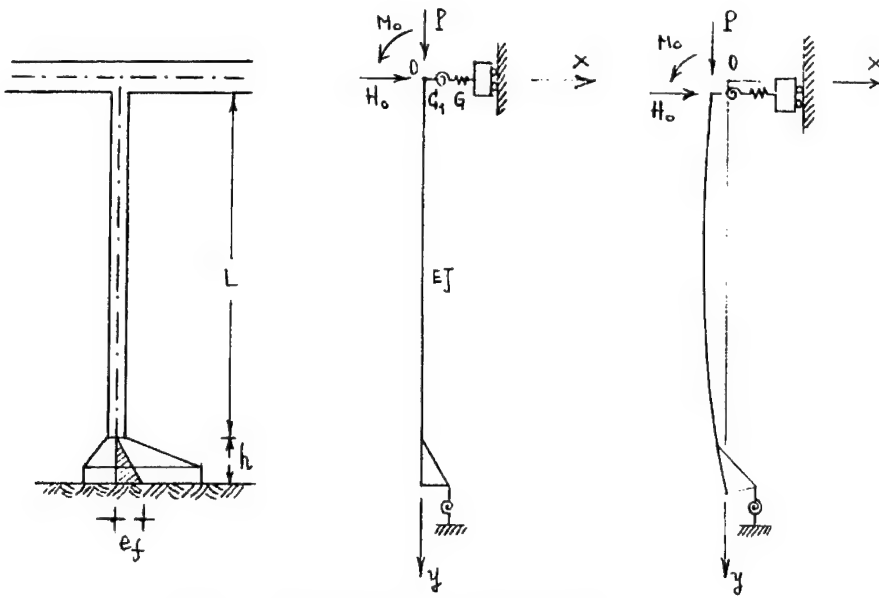


Fig. 3. The Column/Footing System

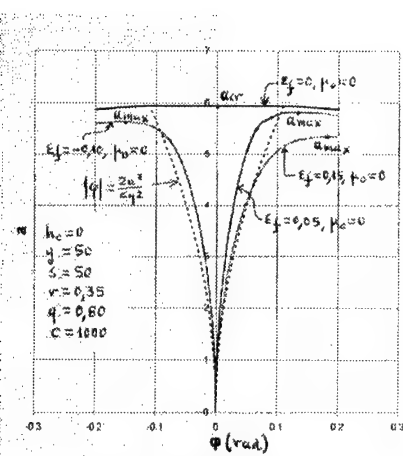


Fig. 4. Curves (ϕ, a) for $\mu_c = 0$

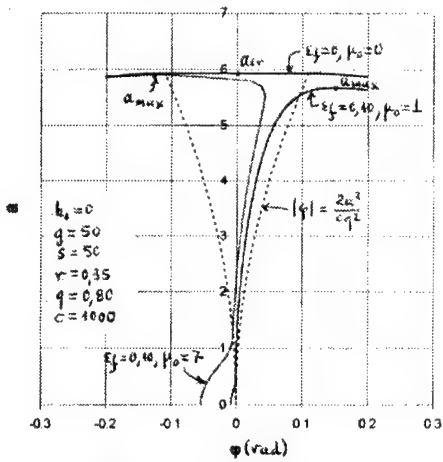


Fig. 5. Curves (ϕ, a) for $\mu_c \neq 0$.

NON-LINEAR DYNAMIC BEHAVIOUR OF BASE ISOLATORS

V. K. Koumousis

Institute of Structural Analysis & Aseismic Research
NTUA, Zografou Campus 157 73 Athens, Greece

1. SUMMARY

The non-linear dynamic behaviour of hysteretic and friction base-isolators is investigated following a state-space approach. The characteristics of these systems are analysed for free and forced vibrations. The response is determined and technical problems related to their behaviour are discussed.

2. INTRODUCTION

The dynamic non-linear behaviour of hysteretic Lead Rubber Bearing (LRB) and Friction Pendulum Systems (FPS) is investigated [1]. The restoring force of these isolators is modeled using a modified viscoplasticity model. A single mass-isolator system is considered with additional external damping. The free vibration of this system is governed by a second order ordinary differential equation (ODE) that depends on a dimensionless hysteretic parameter, which is governed by a first order ODE in time. The two equations are converted into a state space form, i.e. a system of three first order ODEs. This system is solved numerically using a integrator for stiff equations. For different sets of initial conditions the phase portraits are presented and their characteristics are discussed.

The restoring forces in the x and y direction of a mass-isolator system are not coupled, whereas the dimensionless hysteretic parameters in x and y direction are governed by a coupled system of ODEs. This often leads to a coupled behaviour in the x and y direction. Following a procedure similar to that of the one-dimensional isolator, a system of six first order differential equations is formulated that governs the response of the two-degree of freedom system. For different sets of initial conditions the phase portraits are presented and their characteristics are discussed.

3. HYSTERETIC ISOLATOR

The restoring force of a Lead Rubber Bearing (LRB) isolator is given as:

$$F(t) = a \frac{F_y}{u_y} u(t) + (1-a) F_y z(t) \quad (1)$$

where, F_y is the yield force of the isolator, u_y is the yield displacement, α is the ratio of post yielding to elastic stiffness and $z(t)$ a dimensionless hysteretic parameter obeying the differential equation:

$$\dot{z}(t) = \frac{1}{u_y} \left[A - |z(t)|^\eta (\gamma \text{sign}(\dot{u}(t)z(t)) + \beta) \right] \dot{u}(t) \quad (2)$$

where, A , γ , β and η are dimensionless quantities related to the shape of the hysteresis loop.

The equation of motion of a mass-isolator system with external damping c is given as:

$$m\ddot{u}(t) + c\dot{u}(t) + F(t) = f(t) \quad (3)$$

where, $f(t)$ is the excitation force.

Substituting relation (1) into equation (3) the following equation is obtained:

$$m\ddot{u}(t) + c\dot{u}(t) + a\frac{F_y}{u_y}u(t) + (1-a)F_y z(t) = f(t) \quad (4)$$

Equations (4) and (2) are transformed into a state-space form as follows:

$$x_1(t) = u(t), \quad x_2(t) = \dot{u}(t), \quad x_3(t) = z(t) \quad (5)$$

$$\begin{Bmatrix} \dot{x}_1(t) \\ \dot{x}_2(t) \\ \dot{x}_3(t) \end{Bmatrix} = \begin{Bmatrix} x_2(t) \\ -\frac{1}{m} \left[cx_2(t) + \alpha \frac{F_y}{u_y} x_1(t) + (1-\alpha)F_y x_3(t) - f(t) \right] \\ \frac{1}{u_y} \left[\left(A - |x_3(t)|^\eta (\gamma \text{sign}(x_2(t)x_3(t)) + b) \right) x_2(t) \right] \end{Bmatrix} \quad (6)$$

The above system of three first order non-linear ODEs is solved numerically following Livermore stiff ODE integrator which is based on a "predictor-corrector" method [2].

In fig.1 the phase portraits of an isolator with parameters: $F_y=2.86$ kN, $u_y=0.111$ cm $A=1$ $\beta=0.1$ and $\gamma=0.9$, while the mass $m = 2.86$ kNsec²/m and $c=0$, are presented for an initial velocity $v=\dot{u}(0)=2$ cm/sec for different values of the post yielding to elastic stiffness ratio α . For small values of α , as the system tends to approach the perfectly plastic behaviour, it loses its ability to return to its initial position and rests at a displaced position. In addition, as the ratio α increases the system damps its motion less rapidly. Similar results are produced for initial displacements or mixed initial conditions.

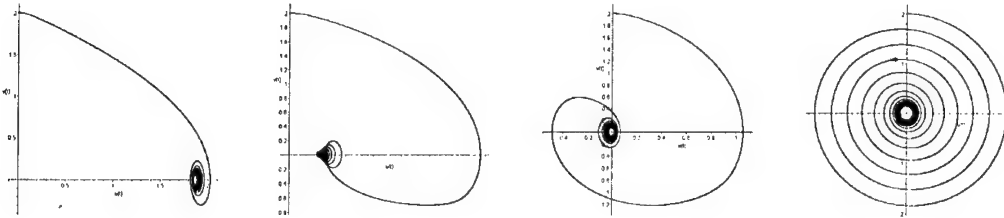


Fig. 1. Phase portraits for $\alpha=0.003, 0.1, 0.25$, and 0.75

In fig. 2. the hysteretic parameter $z(t)$ is plotted for different values of α . It is observed that it behaves like a unit step function followed by a cyclic function for elastic displacements.

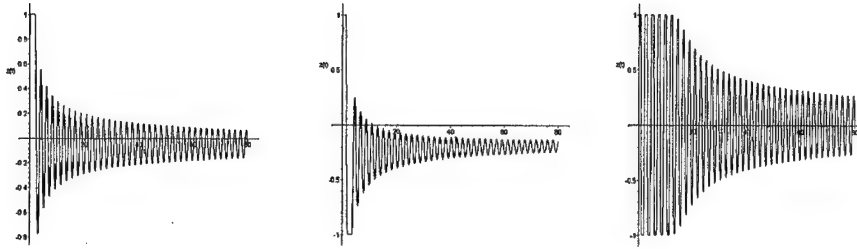


Fig. 2. Dimensionless hysteretic parameter for $\alpha=0.003, 0.1$ and 0.75

The system of ODEs and the hysteretic quantity $z(t)$ offers the ability to model a variety of systems, from elastoplastic to a general hysteretic one, with high computational efficiency, since there is no need to trace the hysteresis loops by keeping track of the entire history.

4. TWO-DEGREE OF FREEDOM HYSTERETIC ISOLATOR

The behaviour of a mass-isolator system in two directions x and y is governed by a system of two ODEs of second order in time (7). These equations are coupled through the dimensionless hysteretic variables $z_x(t)$ and $z_y(t)$ governed by the system of non-linear equations (8), developed by Park et al. [3].

$$\begin{aligned} \begin{bmatrix} m & 0 \\ 0 & m \end{bmatrix} \begin{Bmatrix} \ddot{u}_x(t) \\ \ddot{u}_y(t) \end{Bmatrix} + \begin{bmatrix} c_1 & 0 \\ 0 & c_2 \end{bmatrix} \begin{Bmatrix} \dot{u}_x(t) \\ \dot{u}_y(t) \end{Bmatrix} + \begin{bmatrix} a_x \frac{F_x^y}{u_x^y} & 0 \\ 0 & a_y \frac{F_y^y}{u_y^y} \end{bmatrix} \begin{Bmatrix} u_x(t) \\ u_y(t) \end{Bmatrix} + \\ + \begin{bmatrix} (1-a_x)F_x^y & 0 \\ 0 & (1-a_y)F_y^y \end{bmatrix} \begin{Bmatrix} z_x(t) \\ z_y(t) \end{Bmatrix} = \begin{Bmatrix} f_x(t) \\ f_y(t) \end{Bmatrix} \end{aligned} \quad (7)$$

$$\begin{Bmatrix} \dot{z}_x(t) u_x^y \\ \dot{z}_y(t) u_y^y \end{Bmatrix} = AI \begin{Bmatrix} \dot{u}_x(t) \\ \dot{u}_y(t) \end{Bmatrix} - \begin{bmatrix} z_x^2(\gamma \text{sign}(\dot{u}_x(t)z_x(t)) + \beta) & z_x z_y(\gamma \text{sign}(\dot{u}_y(t)z_y(t)) + \beta) \\ z_x z_y(\gamma \text{sign}(\dot{u}_x(t)z_x(t)) + \beta) & z_y^2(\gamma \text{sign}(\dot{u}_y(t)z_y(t)) + \beta) \end{bmatrix} \begin{Bmatrix} \dot{u}_x(t) \\ \dot{u}_y(t) \end{Bmatrix} \quad (8)$$

The above system of differential equations is converted into a system of six non-linear first order equations in state space form by introducing additional equations as follows:

$$\begin{aligned} x_1(t) &= u_x(t), & x_2(t) &= \dot{u}_x(t), & x_3(t) &= z_x(t) \\ x_4(t) &= u_y(t), & x_5(t) &= \dot{u}_y(t), & x_6(t) &= z_y(t) \end{aligned} \quad (9)$$

$$\begin{Bmatrix} \dot{x}_1(t) \\ \dot{x}_2(t) \\ \dot{x}_3(t) \\ \dot{x}_4(t) \\ \dot{x}_5(t) \\ \dot{x}_6(t) \end{Bmatrix} = \begin{Bmatrix} x_2(t) \\ -\frac{1}{m}[c_x x_2(t) + a_x \frac{F_x^y}{u_x^y} x_1(t) + (1-a_x)F_x^y x_3(t) - f_x(t)] \\ \frac{1}{u_x^y} \{ [A - x_3^2(t)(\gamma \text{sign}(x_2(t)x_3(t)) + \beta)] x_2(t) - x_3(t)x_6(t)(\gamma \text{sign}(x_5(t)x_6(t)) + \beta)x_5(t) \} \\ x_5(t) \\ -\frac{1}{m}[c_y x_5(t) + a_y \frac{F_y^y}{u_y^y} x_4(t) + (1-a_y)F_y^y x_6(t) - f_y(t)] \\ \frac{1}{u_y^y} \{ [A - x_6^2(t)(\gamma \text{sign}(x_5(t)x_6(t)) + \beta)] x_5(t) - x_6(t)x_3(t)(\gamma \text{sign}(x_2(t)x_3(t)) + \beta)x_2(t) \} \end{Bmatrix} \quad (10)$$

In fig. 3 the displacements along x and y directions are presented, together with the phase portraits in x and y directions, for free vibration with an initial displacement of 1 cm in the x and y direction and initial velocities 4 and -2 cm/sec in the x the y directions respectively. The parameters of the isolator are: $\alpha=0.1$, $F_y=2.86$ kN, $u_y=0.111$ cm $A=1$ $\beta=0.1$ and $\gamma=0.9$, while the mass $m = 2.86$ kNsec²/m and $c=0$ in both directions.

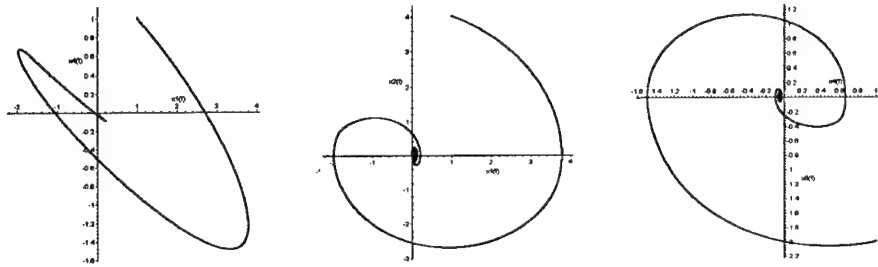


Fig. 3. x and y displacements and phase portraits in x and y directions

The behaviour of the isolator in two directions is similar to the unilateral case especially for the common in practice case, which has the same parameters in both directions. Coupling of the behaviour is established through the hysteretic variables.

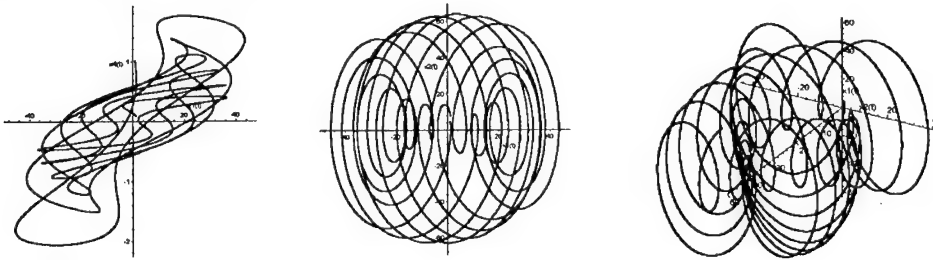


Fig. 4. x and y displacements, phase portrait and its evolution with time for a forced motion

In fig. 4. the displacements along x and y directions are presented, together with the phase portrait in the x direction and its evolution with time. This corresponds to a forcing function of $f(t) = -mg \cdot 0.10 \cdot \sin(3 \cdot t)$ acting in x direction, for an isolator having the same parameters and initial conditions as the one in fig.3.

5. FRICTION SYSTEMS

A Coulomb friction sliding system requires multiple stick-slip conditions that result into a complicated system of equations, whereas a modified viscoplasticity model leads to a convenient formulation. This describes accurately the behaviour of a sliding system [4] especially for Teflon-steel interfaces, where the coefficient of friction increases with velocity. According to this model the friction force is determined as:

$$F(t) = \mu_s(mg)z(t) \quad \text{with,} \quad \mu_s = f_{\max} - \Delta f \cdot \exp(-\alpha|\dot{u}(t)|) \quad (11)$$

where, f_{\max} is the coefficient of friction at a large velocity of sliding, Δf is the difference between the coefficient of friction at a large and a very low velocity and α is constant. The

dimensionless quantity $z(t)$ follows again equation (2) and controls the stick-slip conditions. For slip conditions, $z(t) = \pm 1$, while for stick conditions (elastic behaviour) $|z(t)| < 1$.

Substituting the friction force into relation (3) the equation of motion of a sliding system is determined. The response of the system for free vibrations with an initial velocity 4 cm/sec and in addition with a displacement 2 cm as initial conditions is presented in fig. 5 for $\alpha=0.6$, $f_{\max}=0.01193$, $\Delta f=0.00927$, $m=2.86$, $c=0$, and $u_y=0.005$ cm, and $z(t)$ of the second case.

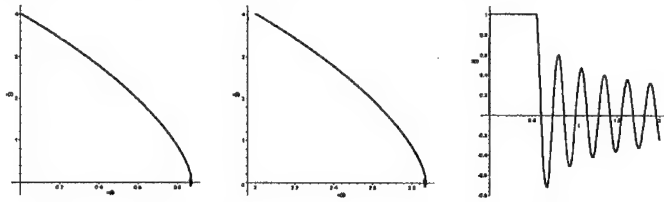


Fig. 5. Phase portraits of a sliding system and the dimensionless parameter

It is observed that the system slides in the second case for almost 2.87 cm within 0.55 sec and then slows down rapidly to stick to a displaced position, having no tendency to return to its initial position. Considering sliding on a cylindrical surface alters this behaviour by adding the pendulum effect expressed by the term, $-mgu(t)/R$, in the second equation of state space ODE system. This is illustrated in fig. 6 for the above system having various radii of curvature, although some of them rest at a displaced position close to the origin.

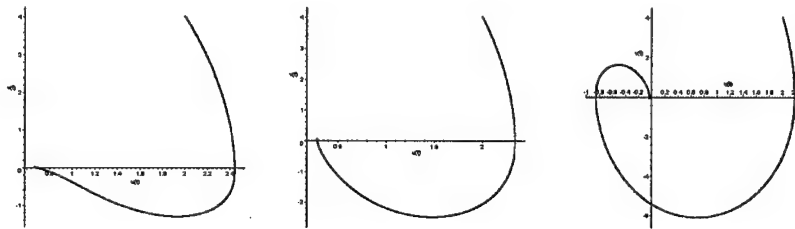


Fig. 6. Phase portraits of a Friction Pendulum System with $R=250, 150$ and 60 cm.

Using the restoring force equation in the x and y direction a two d.o.f. system is determined similar to that of equation (10). The system is used for the free and forced vibrations.

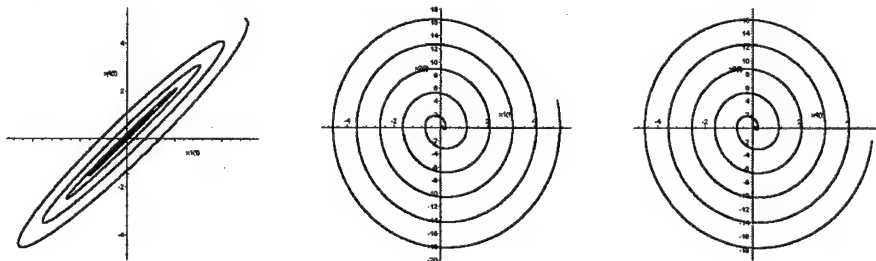


Fig. 7. x and y displacements and Phase Portraits in x and y direction

In fig. 7 the free vibration is presented for 5 cm initial displacements and 4 and -2 cm/sec initial velocities in x and y respectively. In fig. 8 the forced vibrations for $-0.04mg \sin(t)$ in x and $-0.08mg \sin(t)$ in the y direction with previous initial conditions are presented.

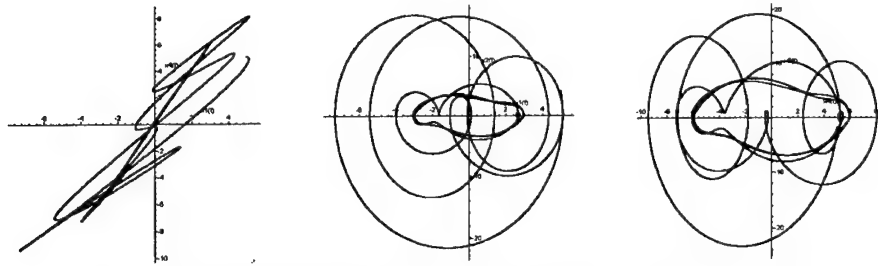


Fig. 8. x and y displacements and Phase Portraits in x and y direction

Comparing both systems it observed that although they have similarities there is no direct equivalence between them. The restoring force of LRB systems are characterized by three parameters namely α , F_y and u_y , that do not depend on the mass of the system. FPS systems depend on the weight they carry, the radius of curvature R of the spherical surface and the variable coefficient of friction that depends on three parameters (f_{\max} , Δf and α). The stiffness, $\alpha F_y / u_y$ of the LRB system is compared with mg / R of the FPS isolators whereas, the hysteretic terms differ considerably for variable coefficient of friction that depends on the velocity. For a constant coefficient of friction equivalence can be established for $\alpha = 0.5$, $u_y = R\mu_s$ and $F_y = 2\mu_s mg$ although is difficult to accomplish in practice. FPS isolators are characterized by more abrupt changes in their response as compared to LRB systems.

6. CONCLUDING REMARKS

From the above analyses it becomes evident that a viscoplasticity model developed by Bouc [5], Wen [6], Park et al. [3], and extended by Constantinou [4], [7] offers a unified base for the analyses of LRB and FPS isolators. These isolators exhibit similar behaviour but with substantial differences. For LRB isolators the ratio of post yielding to elastic stiffness α has to be greater than a certain amount to retract the isolator to zero displacement. For friction pendulum systems the radius R of a cylindrical or spherical surface has to be less than a certain value to succeed to return to zero displacement. If this is not the case isolators are left at displaced positions interacting with the superstructure above them.

7. REFERENCES

- [1] Buckle, I. G., and Mayes, R., L., "Seismic Isolation History: Application and Performance- a world review", *Earthquake Spectra*, 6, pp.161-201, 1990.
- [2] Alan C. Hindmarsh Scientific Computing, "Odepack, a Systemized Collection of ODE Solvers", R. S. Stepleman et al. (eds.) North-Holland, Amsterdam, 1983.
- [3] Park, Y., J., Wen, Y. K. and Ang, A.H.S., "Random Vibration of Hysteretic Systems Under Bidirectional Ground Motion", *Earthquake Engineering and Structural Dynamics*, 14, 4, pp. 543-557, 1986.
- [4] Constantinou, M. C. and Mokha, A. "A Model of Friction of Teflon Sliding Bearings", Report to NSF, Dept. of Civil Engineering, SUNY at Buffalo, April, 1989.
- [5] Bouc, R., "Modele Mathematique d'Hysteresis", *Acustica*, 24, 16-25, 1971.
- [6] Wen, Y. K. "Method of Random Vibration of Hysteretic Systems", *Journal of Engineering Mechanics Division, ASCE*, 102, EM2, 249-263, 1976.
- [7] Nagarajaiah, S., Reinhorn, A., M. and Constantinou, M., C., "Nonlinear Dynamic Analysis of 3D-Base-Isolated Structures, *Journal of Structural Engineering ASCE*, 117(7), pp. 2035-54, 1990.

THE CONTINUOUS TIME HOMOGENEOUS MARKOV SYSTEM WITH FIXED SIZE AS A LINEAR ELASTIC CONTINUUM

George Tsaklidis,

Mathematics Department, University of Thessaloniki, Thessaloniki 54006, Greece

Email address: tsaklidi@ccf.auth.gr

Kostas Soldatos

Pope Building, University of Nottingham, Nottingham NG7 2RD, UK

1. SUMMARY

Every attainable structure of a continuous time homogeneous Markov system (HMS) with n states and fixed size is considered as a point-particle of \mathbb{S}^n . Thus, the motion of an attainable structure corresponds to the motion of the respective point-particle in \mathbb{S}^n . Under the assumption that "the motion of every particle at every time point is due to its interaction with its surroundings", \mathbb{S}^n becomes a continuum (Tsaklidis (1998,1999)). The evolution of the set of the attainable structures corresponds to the motion of the continuum. Given the rate of transition probabilities matrix of an HMS with two or three states, it is examined to what extent the HMS could be considered as a linear elastic continuum.

2. INTRODUCTION

Basic results concerning continuous time Markov process models in manpower systems can be found in [1], [2], [3], [5], [9], [11] and [12]. The main problems examined in connection with these models are the asymptotic behaviour, stability, asymptotic stability, control, variability, attainability, maintainability, entropy ([6], [10] for the discrete time) etc.

In the present paper we describe first the continuous time Homogeneous Markov System (HMS) with fixed size (section 2). In the third section, we outline the concepts of stress and stress tensor in 2 or 3 dimensions. In the fourth section we consider the set of the attainable structures of a continuous time HMS as a homogeneous, isotropic linear elastic continuum. It is examined whether this model could explain the evolution of the HMS.

In an example application considered in section 5, we take a closer look into the case of a two-dimensional HMS. Using the field equations of a linear elastic continuum, we evaluate the explicit form of the stress tensor under the assumption that the density is position independent. Hence, we conclude that the evolution of this HMS may successfully be interpreted by the deformation of an elastic rod having variable elastic and material density properties.

3. THE CONTINUOUS TIME HOMOGENEOUS MARKOV SYSTEM WITH FIXED SIZE

Denote by $S=\{1,2,\dots,n\}$ the state space of the system, where $n=2$ or 3 . The states are exclusive and exhaustive, i.e. every member of the system may be in one and only one state at some time point t . Let $R=(r_{ij})_{i,j \in S}$ be the matrix of transition intensities, i.e. the element r_{ij} represents the transition intensity for a member in the i -th state to move to state j . Also let $T(t)$ denote the size of the system at time t , $p_o=(p_{oi})_{i \in S}$ the $n \times 1$ recruitment probability vector, the i -th component of which is the probability for a recruit to enter the system in state i , and $r_{n+1}=(r_{i,n+1})_{i \in S}$ the $n \times 1$ vector, the i -th component of which is the transition intensity for a member in the i -th state to leave the system. Assume that the size of the HMS is constant, i.e. $T(t)=T$, $T \in \mathbb{R}$, for every t (this means that every leaver (if anyone) will immediately be replaced by a new entrant) and define the matrix $Q=(q_{ij})_{i,j \in S}$, where

$$q_{ij} = r_{ij} + r_{i,n+1} \cdot p_{oj}, \quad i, j \in S.$$

The quantity q_{ij} represents a rate of "transition" from i to j , which corresponds either to a direct transition from i to j , or to an indirect "transition" from i to j through the "state" $n+1$ ($i \rightarrow (n+1) \rightarrow j$). This sense of transition defined by q_{ij} is the motive for introducing the idea of the "membership" ([12]): every member of the HMS possesses a membership; if a member leaves the system, then the membership will be transmitted to a recruit, who can be regarded as the replacement of the leaver. Using the concept of the membership, the HMS with fixed size can be considered as a closed HMS. The matrix Q will be called the matrix of transition intensities of the memberships.

Now, let $x(t)=(x_i(t))_{i \in S}$ be the $n \times 1$ probability vector, the i -th component of which is the probability for a membership to be in state i at time t . Then, under the assumption that the transitions between the states follow Poisson processes, we get that

$$x_j(t+\delta t) = \sum_{i=1,2,\dots,n} x_i(t)(\delta_{ij} + q_{ij}\delta t) + o(\delta t), \quad \text{for every } j \in S, t \geq 0, \quad (2.1)$$

where δ_{ij} is the Kronecker delta, having the value 1 when $i=j$ and 0 when $i \neq j$, and $o(\delta t)$ denotes a quantity that becomes negligible when compared to δt as $\delta t \rightarrow 0$; that is, $\lim_{\delta t \rightarrow 0} (o(\delta t)/\delta t) = 0$.

Relation (2.1) leads to

$$\dot{x}'(t) = x'(t) \cdot Q, \quad \text{for every } t \geq 0, \quad (2.2)$$

where $\dot{x}(t)$ means the derivative of the vector $x(t)$ with respect to t , and the prime means transposition of the respective vector (or -generally- of a matrix).

4. THE CONTINUUM VIEWPOINT

The system of linear differential equations (2.2) determines the motion of a stochastic structure in \mathbb{S}^n . Then, the trajectory of every initial structure $x(0)$ is given by

$$x'(t) = x'(0)e^{Qt}, \quad \text{for } t \geq 0.$$

If we consider every structure of the HMS as a 'particle' of the n -dimensional space \mathbb{R}^n , then we can assign material behaviour to \mathbb{R}^n . Note, from (2.2), that the velocity $\dot{\mathbf{x}}(t)$ depends on the position. Then, by adopting the viewpoint-assumption that

$$\begin{aligned} &\text{"the motion of the particle at every time point is} \\ &\text{due to the interaction of it with its surroundings"} \end{aligned} \quad (3.1)$$

\mathbb{R}^n can be regarded as a continuum. Now, as the initial state vectors $\mathbf{x}(0)$ run over all stochastic n -tuples, we get the respective set of solutions $\mathbf{x}(t)$ of (2.2), which is denoted by A_t and called 'the set of the attainable structures' of the HMS. Denote by $A_n(t)$ the region of \mathbb{R}^n defined by A_t . We are interested in the motion-evolution of the continuum possessing the region $A_n(0) \subset \mathbb{R}^n$ at time $t=0$ in the velocity field defined by (2.2). Every part of the "material continuum" $A_n(t)$, $t \geq 0$, is supposed to be subjected to surface forces. The $n \times 1$ stress vector $\mathbf{t}^{(n)}$ at some point P enclosed by the infinitesimal surface S , is defined by

$$\mathbf{t}^{(n)} = \lim_{\Delta S \rightarrow 0} (\Delta \mathbf{f} / \Delta S) = d\mathbf{f} / dS,$$

where \mathbf{n} is the $n \times 1$ outward unit normal of the surface element ΔS of S (i.e. ΔS lies on the hyperplane of \mathbb{R}^n which is perpendicular to \mathbf{n}) and $\Delta \mathbf{f}$ the resultant force exerted across ΔS upon the material within S by the material outside of S . The state of stress at the point P is given by the set of $\mathbf{t}^{(n)}$ generating from all the unit vectors \mathbf{n} , according to the formula

$$\mathbf{t}^{(n)} = \mathbf{T} \cdot \mathbf{n},$$

where \mathbf{T} is the (symmetric) $n \times n$ stress tensor.

5. THE CONTINUOUS TIME HMS WITH FIXED SIZE AS A LINEAR ELASTIC CONTINUUM

Equation (2.2) represents a system of n linear differential equations. Because of the stochasticity condition $x_1(t) + x_2(t) + \dots + x_n(t) = 1$, the variables $x_i(t)$, $i=1,2,\dots,n$, are dependent, and the motion takes place on the hyperplane (Π) : $x_1 + x_2 + \dots + x_n = 1$. Now, assume -without loss of generality- that \mathbf{Q} is irreducible. Then, it can be easily verified ([1],[4] or [7]) that (2.2) has a stochastic stability point, which will be denoted by π . Consider at π an orthogonal coordinate system $\{\mathbf{f}_1, \mathbf{f}_2, \dots, \mathbf{f}_n\}$, where $\mathbf{f}_1, \mathbf{f}_2, \dots, \mathbf{f}_{n-1}$, belong to (Π) and $\mathbf{f}_n \perp (\Pi)$, and let

$$\mathbf{F} = [\mathbf{f}_1, \mathbf{f}_2, \dots, \mathbf{f}_n] = [\mathbf{F}_1 \mid \mathbf{f}_n],$$

where $\mathbf{F}_1 = [\mathbf{f}_1 \mid \mathbf{f}_2 \mid \dots \mid \mathbf{f}_{n-1}]$. Denote by z_1, z_2, \dots, z_n the components of some point $\mathbf{z} \in E^n$ with respect to the coordinate system $\{\mathbf{f}_1, \mathbf{f}_2, \dots, \mathbf{f}_n\}$. Since we are interested in the case of stochastic vectors \mathbf{z} , then $\mathbf{z} \in (\Pi)$ and consequently $z_n = 0$. Hence, in dealing with the hyperplane (Π) only, equation (2.2) with respect to the coordinate system $\{\mathbf{f}_1, \mathbf{f}_2, \dots, \mathbf{f}_n\}$, is reduced into the form $\dot{\mathbf{z}}'(t) = \mathbf{z}'(t) \cdot \mathbf{G}$, or simply

$$\dot{\mathbf{z}}' = \mathbf{z}' \cdot \mathbf{G} \quad (4.1)$$

where $\mathbf{z} = (z_1, z_2, \dots, z_{n-1})'$ and $\mathbf{G} = \mathbf{F}_1' \mathbf{Q} \mathbf{F}_1$. Thus, equation (2.2) is reduced to (4.1); note that the number of the differential equations of the system (4.1) is $n-1$, while that of (2.2) is n . In what follows we will use (4.1) instead of the (equivalent) initial formula (2.2).

Under the assumptions of section 3, we will examine if equation (4.1) could be considered as expressing the velocity field of a homogeneous, isotropic, linear elastic

continuum. For this purpose it is necessary for the respective stress tensor $\mathbf{T}=(T_{ij})$, $i,j=1,2,\dots,n-1$, to satisfy Cauchy's equation of motion at every point P of the continuum, i.e.

$$\rho(t)\mathbf{a}(t)=\operatorname{div}\mathbf{T}, \quad (4.2)$$

where $\mathbf{a}(t)$ is the acceleration at the point P at time t with respect to the coordinate system $\{\mathbf{f}_1, \mathbf{f}_2, \dots, \mathbf{f}_{n-1}\}$, $\rho(t)$ the density of the region at P at time t , and $\operatorname{div}\mathbf{T}=(\sum_{j=1,2,\dots,n-1}(\partial T_{ij}/\partial z_j))$, $i=1,2,\dots,n-1$.

Denote by $m(t)$ the mass, and by $V(t)$ the volume of the continuum at time t . Since $m(t)=\rho(t)V(t)=\text{const}$ for every t , then $\rho(t)V(t)=\rho(0)V(0)$ for every t . Since, $V(t)=V(0)e^{-\operatorname{tr}\mathbf{G}t}$ (by [7]), then

$$\rho(t)V(0)e^{-\operatorname{tr}\mathbf{G}t}=\rho(0)V(0), \text{ for every } t,$$

so that

$$\rho(t)=\rho(0)e^{-\operatorname{tr}\mathbf{G}t}, \quad t \geq 0. \quad (4.3)$$

Note by (4.3), that since $\operatorname{tr}\mathbf{G}=\operatorname{tr}\mathbf{Q}<0$, then the field defined by (4.1) is compressible.

As regards the acceleration $\mathbf{a}(t)$ in (4.2), we have that $\mathbf{a}(t)=\partial\mathbf{v}/\partial t + \nabla\mathbf{v} \cdot \mathbf{v}$, where the (i,j) entry of the $(n-1) \times (n-1)$ matrix $\nabla\mathbf{v}$ is equal to $\partial v_i/\partial z_j$. Then, from (4.1) we get $\mathbf{a}(t)=\nabla\mathbf{v} \cdot \mathbf{v}=\mathbf{G}' \cdot \dot{\mathbf{z}}=(\mathbf{G}')^2 \cdot \mathbf{z}$. Hence,

$$\mathbf{a}(t)=\mathbf{a}=(\mathbf{G}^2)' \cdot \mathbf{z}, \text{ for every } t, \quad (4.4)$$

where \mathbf{z} is the position vector of P .

The example application that follows in section 5 may be considered as a particular case of a homogeneous isotropic elastic material, the constitutive equation of which is

$$\mathbf{T}=\lambda \cdot \operatorname{tr}\mathbf{E} \cdot \mathbf{I} + 2\mu\mathbf{E}. \quad (4.5)$$

In this equation, λ and μ are the Lamé coefficients, \mathbf{I} is the $(n-1) \times (n-1)$ identity matrix and $\mathbf{E}=(\varepsilon_{ij})$ is the $(n-1) \times (n-1)$ strain tensor. Relation (4.5) reflects the evolution of the HMS through a particular form of the generalized Hooke's law. The strain-displacement relations are

$$\varepsilon_{ij}=\frac{1}{2}\left(\frac{\partial u_i}{\partial x_j}+\frac{\partial u_j}{\partial x_i}\right),$$

or in matrix notation $\mathbf{E}=(\mathbf{u}\nabla+\nabla\mathbf{u})/2$, where $\mathbf{u}=(u_i)$ stands for the displacement vector.

6. AN EXAMPLE: THE TWO-DIMENSIONAL HMS AS A LINEAR ELASTIC ROD

($N=2$)

If the cardinality of the system's state space is two, then the 2×2 matrix of intensity rates has the form [1]

$$\mathbf{Q}=\begin{pmatrix} -a & a \\ b & -b \end{pmatrix}, \quad a, b \in \mathbb{R}^+.$$

The stability point of the HMS is the stochastic left eigenvector π of Q associated with the eigenvalue 0. It can be easily verified that $\pi = (\frac{b}{\sqrt{1+a^2}}, \frac{a}{\sqrt{1+a^2}})'$.

In order to determine an orthogonal coordinate system $\{f_1, f_2\}$ with origin at π , let

$$f_1 = (\frac{\sqrt{2}}{2}, -\frac{\sqrt{2}}{2})' \text{ and } f_2 = (\frac{\sqrt{2}}{2}, \frac{\sqrt{2}}{2})'.$$

Then,

$$G = f_1' Q f_1 = (\frac{\sqrt{2}}{2}, -\frac{\sqrt{2}}{2})' \begin{pmatrix} -a & a \\ b & -b \end{pmatrix} (\frac{\sqrt{2}}{2}, -\frac{\sqrt{2}}{2})' = -(a+b) = g_{11} < 0,$$

and $G^2 = g_{11}^{(2)} = (a+b)^2 > 0$.

The dimension of the hyperplane (II) is 1, thus the motion is one-dimensional. The equation of motion is $v = \dot{z} = g_{11} z$, from which we get

$$z = z(0)e^{Gt} = z(0)e^{g_{11}t} = z(0)e^{-(a+b)t}$$

and

$$a = \ddot{z} = g_{11} \dot{z} = g_{11}^{(2)} z = g_{11}^2 z.$$

The strain tensor E becomes an 1×1 tensor, namely a scalar, given by

$$E = \varepsilon_{11} = \frac{\partial u_1}{\partial z_1} = e^{-(a+b)t} - 1,$$

and is independent of the spatial coordinate z . This one-dimensional strain state is next considered to be the strain state of a certain homogeneous isotropic elastic finite rod. The corresponding stress state is then described by

$$T = t_{11} = \lambda \cdot \text{tr} E \cdot I + 2\mu E = (\lambda + 2\mu)(e^{-(a+b)t} - 1) = k(e^{-(a+b)t} - 1), \quad (5.1)$$

where $k = \lambda + 2\mu$ is now a single elasticity parameter that characterizes the one-dimensional elastic response of the rod. Note that, since $t_{11} = 0$ at $t = 0$, the rod is unstressed at the beginning of time. Under this considerations the equation (4.2) yields

$$\rho \ddot{z} = \frac{\partial t_{11}}{\partial z} = \frac{\partial k}{\partial z} (e^{-(a+b)t} - 1) = \frac{\partial k}{\partial z} (e^{g_{11}t} - 1),$$

or

$$\rho g_{11}^2 z = \frac{\partial k}{\partial z} (e^{-(a+b)t} - 1) = \frac{\partial k}{\partial z} (e^{g_{11}t} - 1),$$

where $\rho = \rho(z, t)$. It follows that

$$\frac{\partial k}{\partial z} = \rho g_{11}^2 z (e^{g_{11}t} - 1)^{-1} = \varphi(z, t), \quad (5.2)$$

and therefore

$$k = \int \varphi(z, t) dz = F(z, t) + h(t), \quad (5.3)$$

where $h(t)$ is an arbitrary function of t . In order to perform the integration denoted in (5.3) we have to determine the form of the material density ρ by solving the following continuity equation

$$\frac{\partial \rho}{\partial t} + v \frac{\partial \rho}{\partial z} + \rho \frac{\partial v}{\partial z} = 0.$$

If we assume, for simplicity, that $\rho = \rho(t)$, which means that ρ is position independent and therefore the mass is uniformly distributed, then (5.3) is reduced to

$$\frac{d\rho}{dt} + \rho g_{11} = 0,$$

and therefore

$$\rho(t) = \rho(0)e^{-g_{11}t}.$$

Hence, equation (5.3) yields

$$k(z, t) = \lambda(z, t) + 2\mu(z, t) = -\frac{\rho(0)g_{11}^2}{2e^{g_{11}t}(1 - e^{g_{11}t})}z^2 + h(t),$$

where the arbitrary function $h(t)$ will be determined by means of the zero stress boundary conditions applied at the ends of the rod.

7. CLOSURE

The example application given in section 5 suggests that the evolution of a HMS with $n=2$ states may successfully be interpreted by the deformation of a linearly elastic rod. The constitutive equation (4.5) of an isotropic material considered in this example application is however only a particular case of the most general constitutive equation of a generally anisotropic elastic material. It becomes then of particular interest to study whether more complicated forms of the constitutive equations of a linearly elastic body could further interpret successfully the evolution of HMS's with $n>2$ states.

8. REFERENCES

- [1] D. J. Bartholomew, *Stochastic models for social processes*, third edn., Wiley, New York, 1982.
- [2] G. S. Davies, 'Structural control in a graded manpower system', *Man.Sci.* **20**, 76-84 (1973a).
- [3] G. S. Davies, 'Attainable and maintainable regions in Markov chain control', *Recent Theoret. Developm. in Control*, 371-381. (1978).
- [4] D. L. Isaacson, and R. W. Madsen, *Markov chains theory and applications*, Wiley, New York, 1976.
- [5] S. I. McClean, 'Continuous time stochastic models for a multigrade population', *J. Appl. Prob.*, **15**, 26-37 (1978).
- [6] S.I. Mclean, 'Extending the entropy stability measure for manpower planning', *J. Operat. Res. Soc.*, **37**, 1133-1138 (1986a).
- [7] G. Tsaklidis, 'The evolution of the attainable structures of a continuous time homogeneous Markov system with fixed size', *J. Appl. Prob.*, **33**, 34-47 (1996).
- [8] G. Tsaklidis, 'The continuous time homogeneous Markov system with fixed size as a Newtonian fluid (?)' Presented in the 7th *Internat. Sympos. on Appl. Stochastic Models and Data Analysis*, Dublin 12-15 June, Ireland, (1995).
- [9] S. Vajda, *Mathematics of manpower planning*, Wiley, New York, 1978.
- [10] P.-C.G. Vassiliou, 'Entropy as a measure of the experience distribution in a manpower system', *J. Operat. Res. Soc.*, **35**, 1021-1025 (1984).

- [11] P.-C.G. Vassiliou, A. C. Georgiou and N.Tsantas, 'Control of asymptotic variability in non-homogeneous Markov systems', *J. Appl. Prob.*, **27**, 756-766 (1990).
- [12] P.-C.G. Vassiliou, and A. A. Papadopoulou, 'Non-homogeneous semi-Markov systems and maintainability of the state sizes', *J. Appl. Prob.*, **29**, 519-534 (1992).

STUDY OF THE DYNAMIC CHARACTERISTICS DURING CALLUS FORMATION

G. Foutsitzi

Dept. of Material Sciences, University of Ioannina, 45110 Ioannina, Greece

A. Charalambopoulos

Division of Mathematics, Polytechnic School
Aristotle University of Thessaloniki, 54006 Thessaloniki, Greece

D. I. Fotiadis

Dept. of Computer Science and Ioannina Biomedical Research Institute,
University of Ioannina, 45110 Ioannina, Greece

C. V. Massalas

Dept. of Material Sciences and Ioannina Biomedical Research Institute,
University of Ioannina, 45110 Ioannina, Greece

1. SUMMARY

We propose a theoretical approach to study the dynamic characteristics of a human long bone during callus formation. The shifting of the eigenfrequency spectrum proves to be a major indicator in the monitoring and diagnosis of the healing process. The bone diaphysis is assumed to be a finite length hollow piezoelectric cylinder of crystal class 6 while the callus area consists of isotropic, elastic material.

2. INTRODUCTION

The monitoring of the bone fracture healing using non-invasive techniques (e.g. wave propagation) has proven of great importance compared to widely used methods such as manual sensing or x-rays. Several researchers have studied wave propagation in long bones, considered it as an infinite piezoelectric cylinder of crystal class 6 with circular or arbitrary cross section [1-5]. A limited number of papers [6-7] address the vibration of bone of finite length. In Ref. [8] the evolution of the dynamic characteristics of isotropic elastic bone during the healing process is studied.

In a previous work [5] we considered wave propagation in a piezoelectric bone of arbitrary cross section. In this work we extend this approach to study the dynamic characteristics of bone during callus formation. The bone diaphysis is modeled as a finite length hollow piezoelectric cylinder of crystal class 6 while the callus area, which approximately follows the same geometry, is made of isotropic elastic material. The analysis can be proven very efficient for the understanding of the relation between the stage of fracture healing and the changes in the eigenfrequency spectrum of the system under consideration.

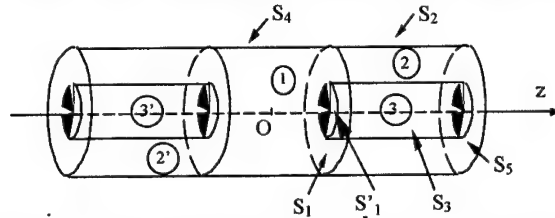
The description of the problem is based on the three-dimensional theory of elasticity and piezoelectricity (in quasi-static approximation). The solution of the wave equations for the piezoelectric cylinder is derived analytically as it is described in [2]. The solution of the

problem for the isotropic callus is presented in terms of the Navier vector eigenfunctions for cylindrical coordinates [7].

The boundary conditions on the plane ends of the cylinder are responsible for the selection of the specific solution (odd or even in z -coordinate) from the general representation. They correspond to those imposed by the external fixator used in the treatment of long bone fracture. The lateral surfaces of the isotropic and piezoelectric parts are assumed to be free of fields (stress and electric potential), while on the contact surfaces of the layers conditions of continuity of the fields are considered. The satisfaction of the boundary conditions on the lateral surfaces leads to discretization of the initially continuous range of the wave numbers for the isotropic and piezoelectric part. The remaining boundary conditions are satisfied by an orthogonalization procedure, which finally leads to the frequency equation.

3. GOVERNING EQUATIONS

The geometry of the system under consideration is shown in the figure below.



Region 1 corresponds to the callus and it is assumed to be filled with isotropic elastic material. Regions 2 and 2' correspond to the cortical bone and they are assumed to be filled with piezoelectric material having crystal class 6 properties, while regions 3 and 3' are assumed to be empty (bone marrow is not included in our model). The cylindrical coordinates are used in the sequel with the z -axis along the axis of the cylinder.

The equation of motion for the isotropic material after suppressing the time-harmonic dependence is

$$c_t^2 \nabla^2 \mathbf{u}^{(1)}(\mathbf{r}) + (c_l^2 - c_t^2) \nabla (\nabla \cdot \mathbf{u}^{(1)}(\mathbf{r})) + \Omega^2 \mathbf{u}^{(1)}(\mathbf{r}) = 0, \quad (1)$$

where $\mathbf{u}^{(1)} = (u_x, u_\theta, u_z)$ is the elastic displacement vector field, $\mathbf{r} = (x, \theta, z)$ is the dimensionless position vector, c_t, c_l are the dimensionless velocities of the transverse and the longitudinal waves, respectively, and Ω is the dimensionless frequency.

The elastic displacement vector field $\mathbf{u}^{(1)}$ can be represented using Navier eigenfunctions [7]. In order to separate the odd and the even eigenstates of the system under consideration (due to the specific geometric symmetry), we introduce the parameter s ($s = 1$, for odd solutions and $s = 2$, for even solutions). The components of the displacement field can be represented as

$$u_x^{(1)} = \sum_{i=\frac{1}{2}}^{\lfloor \frac{1}{2} \rfloor + s + 1} \sum_{\alpha=1}^2 \sum_{m=0}^{+\infty} \int_0^{+\infty} \left\{ a_{i,\alpha}^m(\lambda) j^{m,1}(x_i^i x) + m b_{i,\alpha}^m(\lambda) \frac{j^{m,1}(x_i^i x)}{x_i^i x} + c_{i,\alpha}^m(\lambda) (-1)^i \lambda^2 j^{m,1}(x_i^i x) \right\} \Theta_\alpha^m(\theta) Z_{1,i}(z, \lambda) d\lambda,$$

$$u_\theta^{(1)} = \sum_{i=\frac{1}{2}}^{\lfloor \frac{1}{2} \rfloor + s + 1} \sum_{\alpha=1}^2 \sum_{m=0}^{+\infty} \int_0^{+\infty} \left\{ m a_{i,\alpha}^m(\lambda) \frac{j^{m,1}(x_i^i x)}{x_i^i x} + b_{i,\alpha}^m(\lambda) j^{m,1}(x_i^i x) \right\}$$

$$\begin{aligned}
& + c_{i,\alpha}^m (\lambda) (-1)^i \lambda^2 m \frac{J^{m,1}(x_i^i x)}{x_i^i x} \left\{ \frac{1}{m} \frac{\partial \Theta_\alpha^m(\theta)}{\partial \theta} Z_{1,i}(z, \lambda) d\lambda, \right. \\
u_z^{(1)} = & \sum_{i=\lfloor \frac{s}{2} \rfloor + s}^{\lfloor \frac{s}{2} \rfloor + s + 1} \sum_{\alpha=1}^2 \sum_{m=0}^{+\infty} \int_0^{+\infty} \left\{ a_{i,\alpha}^m (\lambda) \frac{J^{m,1}(x_i^i x)}{x_i^i} + c_{i,\alpha}^m (\lambda) x_i^i J^{m,1}(x_i^i x) \right\} \Theta_\alpha^m(\theta) \frac{\partial Z_{1,i}(z, \lambda)}{\partial z} d\lambda, \quad (2)
\end{aligned}$$

where $x_\beta^i = \sqrt{k_\beta^2 + (-1)^i \lambda^2}$ for $i=1,2,3,4$, with $k_\beta = \frac{\Omega}{c_\beta}$ for $\beta=l,t$ and λ is the dimensionless wavenumber, $\Theta_\alpha^m(\theta) = \cos(m\theta)$ for $a=1$ and $\Theta_\alpha^m(\theta) = \sin(m\theta)$ for $a=2$,

$$Z_{j,i}(z, \lambda) = \begin{cases} \sin \left[\lambda \left(z - \left[\frac{j}{2} \right] L \right) \right] & \text{for } i=1, \\ \cos \left[\lambda \left(z - \left[\frac{j}{2} \right] L \right) \right] & \text{for } i=2, \\ \sinh \left[\lambda \left(z - \left[\frac{j}{2} \right] L \right) \right] & \text{for } i=3, \\ \cosh \left[\lambda \left(z - \left[\frac{j}{2} \right] L \right) \right] & \text{for } i=4, \end{cases} \quad j=1,2$$

where $2L$ is the length of the cylinder and $[x]$ is the integer part of x , and

$$J^{m,l}(ax) = \begin{cases} J^m(ax), & l=1 \quad (\text{Bessel function of 1st kind}) \\ Y^m(ax), & l=2 \quad (\text{Bessel function of 2nd kind}) \end{cases} \text{ for } a^2 > 0.$$

We note that for $a^2 < 0$ the Bessel functions are replaced by the modified ones. Also $j^{m,l}$ denotes the derivative of $J^{m,l}$ with respect to its argument.

The stress tensor for an isotropic elastic material is given by the constitutive relation:

$$\mathbf{T}^{(1)} = \mathbf{c}^{(1)} : \nabla_s \mathbf{u}^{(1)}, \quad (3)$$

where $\nabla_s \mathbf{u}$ denotes the symmetric gradient of \mathbf{u} and the components of the stiffness tensor

$$\mathbf{c}^{(1)} \text{ are given as } c_{ijkl} = \lambda \delta_{ji} \delta_{kl} + \mu (\delta_{jk} \delta_{il} + \delta_{jl} \delta_{ik}). \quad (4)$$

Using relations (2)-(4) we can calculate the components of the stress tensor $\mathbf{T}^{(1)}$.

The equations describing the behavior of a piezoelectric material are the equation of motion and the Gauss equation given as

$$\text{div} \mathbf{T}^{(2)} = \rho_2 \frac{\partial^2 \mathbf{u}^{(2)}}{\partial t^2}, \quad \nabla \cdot \mathbf{D} = 0, \quad (5)$$

where $\mathbf{u}^{(2)}$ is the displacement field for the piezoelectric material, ρ_2 is the mass density, $\mathbf{T}^{(2)}$ and \mathbf{D} are the stress tensor and the electric displacement field, respectively, given by the constitutive relations:

$$\mathbf{T}^{(2)} = \mathbf{c}^{(2)} : \nabla_s \mathbf{u}^{(2)} + \mathbf{e} \cdot \nabla V, \quad \mathbf{D} = \mathbf{e} : \nabla_s \mathbf{u}^{(2)} - \boldsymbol{\epsilon} \cdot \nabla V. \quad (6)$$

In the above relations, V denotes the electrostatic potential, \mathbf{c} the stiffness tensor, \mathbf{e} the piezoelectric stress tensor and $\boldsymbol{\epsilon}$ the dielectric tensor (for a piezoelectric material of crystal class 6 are given in Ref. [2]).

Using the methodology proposed in Ref.[2], we can find a wave-type solution in the form

$$\begin{aligned}
 u_x^{(2)} &= \sum_{i=\frac{s}{2}+s}^{\frac{s}{2}+s+1} \sum_{j=1}^4 \sum_{l=1}^2 \sum_{m=0}^{+\infty} \int_0^{+\infty} \left\{ \left[\alpha_{i,j}^{m,l}(\lambda) \delta_{i,j}^{p1} k_{i,j} J^{m,l}(k_{i,j}x) + \beta_{i,j}^{m,l}(\lambda) m \delta_{i,j}^{p2} \frac{J^{m,l}(k_{i,j}x)}{x} \right] \cos(m\theta) + \right. \\
 &\quad \left. + \left[-\alpha_{i,j}^{m,l}(\lambda) m \delta_{i,j}^{p2} \frac{J^{m,l}(k_{i,j}x)}{x} + \beta_{i,j}^{m,l}(\lambda) \delta_{i,j}^{p1} k_{i,j} J^{m,l}(k_{i,j}x) \right] \sin(m\theta) \right\} Z_{2,i}(z, \lambda) d\lambda e^{-i\Omega t} \\
 u_\theta^{(2)} &= \sum_{i=\frac{s}{2}+s}^{\frac{s}{2}+s+1} \sum_{j=1}^4 \sum_{l=1}^2 \sum_{m=0}^{+\infty} \int_0^{+\infty} \left\{ \left[-\alpha_{i,j}^{m,l}(\lambda) \delta_{i,j}^{p2} k_{i,j} J^{m,l}(k_{i,j}x) + \beta_{i,j}^{m,l}(\lambda) m \delta_{i,j}^{p1} \frac{J^{m,l}(k_{i,j}x)}{x} \right] \cos(m\theta) + \right. \\
 &\quad \left. - \left[\alpha_{i,j}^{m,l}(\lambda) m \delta_{i,j}^{p1} \frac{J^{m,l}(k_{i,j}x)}{x} + \beta_{i,j}^{m,l}(\lambda) \delta_{i,j}^{p2} k_{i,j} J^{m,l}(k_{i,j}x) \right] \sin(m\theta) \right\} Z_{2,i}(z, \lambda) d\lambda e^{-i\Omega t} \\
 u_z^{(2)} &= \sum_{i=\frac{s}{2}+s}^{\frac{s}{2}+s+1} \sum_{j=1}^4 \sum_{l=1}^2 \sum_{m=0}^{+\infty} \int_0^{+\infty} \left\{ \left[\alpha_{i,j}^{m,l}(\lambda) \delta_{i,j}^{p3} J^{m,l}(k_{i,j}x) \right] \cos(m\theta) + \right. \\
 &\quad \left. + \left[\beta_{i,j}^{m,l}(\lambda) \delta_{i,j}^{p3} J^{m,l}(k_{i,j}x) \right] \sin(m\theta) \right\} \frac{1}{\lambda} \frac{\partial Z_{2,i}(z, \lambda)}{\partial z} d\lambda e^{-i\Omega t} \\
 V &= \sum_{i=\frac{s}{2}+s}^{\frac{s}{2}+s+1} \sum_{j=1}^4 \sum_{l=1}^2 \sum_{m=0}^{+\infty} \int_0^{+\infty} \left\{ \left[\alpha_{i,j}^{m,l}(\lambda) \delta_{i,j}^{p4} J^{m,l}(k_{i,j}x) \right] \cos(m\theta) + \right. \\
 &\quad \left. + \left[\beta_{i,j}^{m,l}(\lambda) \delta_{i,j}^{p4} J^{m,l}(k_{i,j}x) \right] \sin(m\theta) \right\} \frac{1}{\lambda} \frac{\partial Z_{2,i}(z, \lambda)}{\partial z} d\lambda e^{-i\Omega t}, \quad (7)
 \end{aligned}$$

where the coefficients $\delta_{i,j}^{pq}, k_{i,j}$ ($i, j, p, q = 1, 2, 3, 4$) depend on λ, Ω and the material constants. Substituting Eqs. (7) into the constitutive relations (6) we can calculate the components of the stress tensor $\mathbf{T}^{(2)}$ and the electric displacement vector \mathbf{D} .

4. BOUNDARY CONDITIONS

The unknown coefficients entering the solution of the field equations are determined by the boundary conditions. We assume that the lateral surfaces S_2, S_3 and S_4 are stress-free and that S_2 and S_3 are coated with electrodes which are shorted. Also it is assumed that continuity conditions apply on S_1 , while the plane surface S_1' is stress free. Finally, for the surfaces S_5 and S_5' we can impose two sets of boundary conditions:

- (i) $u_x^{(2)} = u_\theta^{(2)} = T_{zz}^{(2)} = 0,$
- (ii) $T_{zx}^{(2)} = T_{z\theta}^{(2)} = u_z^{(2)} = 0.$

It can be proved that the (i) set of boundary conditions implies that the parameter $i = 1, 2$ in the expressions of the solution (7) (odd solution), while the set of boundary conditions (ii) implies $i = 3, 4$ (even solution).

On the surface S_4 the following conditions are hold:

$$T_{xx}^{(1)} = T_{zx}^{(1)} = T_{x\theta}^{(1)} = 0. \quad (8)$$

Introducing the solution (7) in the above conditions, we are leading for every pair m, i to a system of algebraic equations

$$\mathbf{D}_{1,i}^m(\Omega, \lambda) \mathbf{x}_{1,i}^m(\lambda) = \mathbf{0}, \quad (9)$$

where

$$\mathbf{x}_{1,i}^m(\lambda) = [a_{i,\alpha}^m, b_{i,\alpha}^m, c_{i,\alpha}^m], \quad m = 0, 1, 2, \dots, i = \left\lfloor \frac{s}{2} \right\rfloor + s, \left\lfloor \frac{s}{2} \right\rfloor + s + 1, \alpha = 1, 2$$

In order that the system (9) to have non-trivial solutions the following equation must be satisfied

$$\det \{ \mathbf{D}_{1,i}^m(\Omega, \lambda) \} = 0 \quad (10)$$

This equation discretizes the continuous range of λ in the expressions (2) to be transformed to sums over the possible values of λ 's which form the sequence

$$\lambda_{1,i}^{m,1}(\Omega), \lambda_{1,i}^{m,2}(\Omega), \dots, \lambda_{1,i}^{m,n}(\Omega), \dots$$

which depends explicitly on Ω .

On the lateral surfaces S_2, S_3 the following boundary conditions are hold:

$$T_{xx}^{(2)} = T_{zx}^{(2)} = T_{x\theta}^{(2)} = 0 = V \quad (11)$$

When the appropriate solution for the stresses and electrostatic potential are substituted into these boundary conditions we obtain for each pair m, i the system

$$\mathbf{D}_{2,i}^m(\Omega, \lambda) \mathbf{x}_{2,i}^m(\lambda) = \mathbf{0} \quad (12)$$

where

$$\mathbf{x}_{2,i}^m(\lambda) = [\alpha_{i,1}^{m,1}, \dots, \alpha_{i,4}^{m,1}, \alpha_{i,1}^{m,2}, \dots, \alpha_{i,4}^{m,2}, \beta_{i,1}^{m,1}, \dots, \beta_{i,4}^{m,1}, \beta_{i,1}^{m,2}, \dots, \beta_{i,4}^{m,2}],$$

$$\text{for } m = 0, 1, 2, \dots, i = \left\lfloor \frac{s}{2} \right\rfloor + s, \left\lfloor \frac{s}{2} \right\rfloor + s + 1,$$

In order that the system (12) to have non-trivial solutions the following equation must be satisfied

$$\det \{ \mathbf{D}_{2,i}^m(\Omega, \lambda) \} = 0. \quad (13)$$

This equation gives rise to a sequence

$$\lambda_{2,i}^{m,1}(\Omega), \lambda_{2,i}^{m,2}(\Omega), \dots, \lambda_{2,i}^{m,n}(\Omega), \dots$$

of the possible values of λ for every value of Ω .

Since the boundary conditions examined until now, have discretized the parameter λ , the corresponding coefficients in the expressions (2) and (7) depend on n giving

$$a_{i,\alpha}^m(\lambda) = a_{i,\alpha}^{m,n}, b_{i,\alpha}^m(\lambda) = b_{i,\alpha}^{m,n} \text{ etc.}$$

The remaining boundary conditions are the following:

$$u_x^{(1)} = u_x^{(2)}, \quad u_\theta^{(1)} = u_\theta^{(2)}, \quad u_z^{(1)} = u_z^{(2)}, \quad V = 0, \quad \text{on } S_1$$

$$\begin{aligned} T_{zx}^{(1)} &= T_{zx}^{(2)}, \quad T_{z\theta}^{(1)} = T_{z\theta}^{(2)}, \quad T_{zz}^{(1)} = T_{zz}^{(2)}, \quad D_z = 0, \quad \text{on } S_1 \\ T_{zz}^{(1)} &= T_{zx}^{(1)} = T_{z\theta}^{(1)} = 0 \quad \text{on } S_1'. \end{aligned} \quad (14)$$

These boundary conditions are satisfied by making the solution orthogonal to a complete set of functions $J_0(\xi_k x)$, where $\xi_k, k=1,2,\dots$ stand for the roots of equation $J_0(\xi_k R)=0$ [8, 9]. After projecting equations (14) onto the basis $J_0(\xi_k x)$ we obtain, for each m , an infinite system of algebraic equations

$$\mathbf{D}^m(\Omega) \mathbf{x}^m = \mathbf{0}, \quad (15)$$

where

$$\mathbf{x}^m = [\mathbf{x}_i^{m,1}, \mathbf{x}_i^{m,2}, \dots, \mathbf{x}_i^{m,n} \dots], \quad \mathbf{x}_i^{m,n} = [\alpha_{i,j}^{m,1,n}, \alpha_{i,j}^{m,2,n}, \beta_{i,j}^{m,1,n}, \beta_{i,j}^{m,2,n}, a_{i,\alpha}^{m,n}, b_{i,\alpha}^{m,n}, c_{i,\alpha}^{m,n}],$$

$$\text{and } m = 0, 1, 2, \dots, i = \left\lfloor \frac{s}{2} \right\rfloor + s, \left\lfloor \frac{s}{2} \right\rfloor + s + 1.$$

Truncating suitably the system (15) we obtain a sequence of linear algebraic homogeneous systems of increasing dimension N :

$$\mathbf{D}_N^m(\Omega) \mathbf{x}_N^m = \mathbf{0}, \quad (16)$$

which lead to the equations

$$\det \{\mathbf{D}_N^m(\Omega)\} = 0, \quad N = 1, 2, 3, \dots \quad (17)$$

The truncated system (17) is solved numerically to provide with the shown frequency Ω [8].

Acknowledgements: This work is partially supported by the European Commission (IST – 2000 – 26350: USBone A Remotely Monitored Wearable Ultrasound Device for the Monitoring and Acceleration of Bone Healing).

6. REFERENCES

- [1] Ambardar, A. and Ferris C. D. Wave Propagation in a Piezoelectric Two-Layered Cylindrical Shell with Hexagonal Symmetry: Some Implications for Long Bone, J. Acoust. Soc. Am. 63(3), 781-792 (1978).
- [2] Fotiadis, D. I., Foutsitzi, G. and Massalas, C. V. Wave Propagation Modelling in Human Long Bone, Acta Mechanica 137, 65-81 (1999).
- [3] Paul, H. S. and Venkatensan, M. Wave Propagation in a Piezoelectric Bone with a Cylindrical Cavity of Arbitrary Shape, Int. J. of Engng. Sci. 29, 1601-1607 (1991).
- [4] Paul, H. S. and Venkatensan, M. Wave Propagation in a Piezoelectric Human Bone of Arbitrary Cross Section with a Circular Cylindrical Cavity, J. Acoust. Soc. Am. 89, 196-199 (1991).
- [5] Fotiadis, D. I., Foutsitzi, G. and Massalas, C. V. Wave Propagation in a Piezoelectric Bone of Arbitrary Cross Section, Int. J. Engng. Sci. 38, 1553-1591 (2000).
- [6] Paul, H. S. and Natarajan, K. J. Axisymmetric Free Vibrations of Piezoelectric Finite Cylindrical Bone, J. Acoust. Soc. Am. 96(1), 213-220 (1994).
- [7] Charalambopoulos, A., Fotiadis, D. I. and Massalas, C.V. Wave Propagation in Human Long Bones, Acta Mechanica XXX, 1-17 (1999).
- [8] Charalambopoulos, A., Fotiadis, D. I. and Massalas, C.V. The Evolution of Dynamic Characteristics during the Bone Healing Process (submitted).
- [9] Hutchinson, J. R. Axisymmetric Vibrations of a Free Finite-Length Rod, J. Acoust. Soc. Am. 51, 233-240 (1972).

ON THE ELECTROENCEPHALOGRAPHY (EEG) PROBLEM FOR THE ELLIPSOIDAL BRAIN MODEL

Gregory Kamvyssas and Fotini Kariotou

Department of Chemical Engineering
University of Patras and ICEHT/FORTH
GR-265 00 Patras, Greece

1. SUMMARY

The present work deals with the development of mathematical techniques, which are directed towards a better understanding of the EEG problem for the human brain. In fact, we will attempt to generalize existing results from the simplified spherical brain model to the realistic ellipsoidal one. As it is well known, the surface of an ellipsoid is the simplest closed surface which takes under consideration the complete anisotropy of the three dimensional space. On the other hand, the ellipsoidal coordinate system is the most general second-degree system in which Laplace's operator enjoys a spectral decomposition. Therefore, every boundary value problem that involves Laplace's operator in ellipsoidal geometry can, at least partially, be analytically handled. The reported results are applied to the electric potential, in the interest of reproducing the field due to an electric dipole inside a homogeneous ellipsoidal conductor. This potential field is experimentally measurable and provides useful data to the understanding and to the interpretation of the electroencephalographic process.

2. INTRODUCTION

Among the noninvasive methods of investigating the human brain functioning, the electroencephalography one has the widest acceptance. This technique involves registration of electric brain potentials on the head surface. The goal of an EEG interpretation problem, is to localize primary bioelectric sources within the brain, which constitute the inverse EEG problem. To solve this problem we need to know the electric field due to a dipole situated inside a volume conductor. So far, exact analytical solutions for the electric forward problem are only known for special volume conductors, with the sphere being the one that approaches best the geometry of the human head [1-5].

On the other hand, solution for complex geometries can only be obtained by numerical methods, which carry inherently drawbacks as time consuming, requirement for large amount of disk space, the possibility to exhibit large errors on solutions and so on [6].

In the present work we consider the ellipsoidal brain model, being the most realistic geometrical model, as the human brain is considered to be an ellipsoid with average semiaxis 6, 6.5 and 9cm. [7], and we seek for analytical solution for the electric forward problem.

3. STATEMENT OF THE PROBLEM

Let S be the ellipsoidal surface

$$\frac{x_1^2}{\alpha_1^2} + \frac{x_2^2}{\alpha_2^2} + \frac{x_3^2}{\alpha_3^2} = 1 \quad (1)$$

where $0 < \alpha_3 < \alpha_2 < \alpha_1 < +\infty$ and let V^- be the space interior to S and V^+ the unbounded space exterior to S . In terms of the ellipsoidal coordinates (ρ, μ, v) [8], which are connected to the Cartesian coordinates (x_1, x_2, x_3) by

$$x_1 = \frac{\rho\mu v}{h_2 h_3} \quad (2)$$

$$x_2 = \frac{\sqrt{\rho^2 - h_3^2} \sqrt{\mu^2 - h_3^2} \sqrt{h_3^2 - v^2}}{h_1 h_3} \quad (3)$$

$$x_3 = \frac{\sqrt{\rho^2 - h_2^2} \sqrt{h_2^2 - \mu^2} \sqrt{h_2^2 - v^2}}{h_1 h_2} \quad (4)$$

where $0 \leq v^2 \leq h_3^2 \leq \mu^2 \leq h_2^2 \leq \rho^2 < +\infty$ and

$$h_1 = (\alpha_2^2 - \alpha_3^2)^{1/2} \quad (5)$$

$$h_2 = (\alpha_1^2 - \alpha_3^2)^{1/2} \quad (6)$$

$$h_3 = (\alpha_1^2 - \alpha_2^2)^{1/2} \quad (7)$$

denote the semifocal distances, the surface S is specified by $\rho = \alpha_1$, the exterior space V^+ by $\rho > \alpha_1$ and the interior space V^- by $\sqrt{\alpha_1^2 - \alpha_3^2} \leq \rho < \alpha_1$.

Both the exterior space V^+ and the space $V^- \cup S$ are considered to be filled with an isotropic and homogeneous conductive medium specified by the physical constants of conductivity σ and magnetic permeability μ , which take the values $\sigma = 0$, $\mu = \mu_0$ in V^+ and $\sigma > 0$, $\mu = \mu_0$ in $V^- \cup S$, respectively.

In the interior of the ellipsoid, at the point \mathbf{r}_0 , there exists an electric dipole with moment \mathbf{Q} which generates the electric potential

$$u_0(\mathbf{r}) = \frac{1}{4\pi\sigma} \mathbf{Q} \cdot \frac{\mathbf{r} - \mathbf{r}_0}{|\mathbf{r} - \mathbf{r}_0|^3} \quad (8)$$

the electric field

$$\mathbf{E}_0(\mathbf{r}) = -\nabla_{\mathbf{r}} u_0(\mathbf{r}) \quad (9)$$

and the magnetic field

$$\mathbf{B}_0(\mathbf{r}) = \frac{\mu_0}{4\pi} \mathbf{Q} \times \frac{\mathbf{r} - \mathbf{r}_0}{|\mathbf{r} - \mathbf{r}_0|^3}. \quad (10)$$

Consequently, in the region V^- we require a solution of the Poisson's equation for the electric potential

$$\Delta u^-(\mathbf{r}) = \frac{1}{\sigma} \nabla \cdot \mathbf{J}(\mathbf{r}), \quad \mathbf{r} \in V^- \quad (11)$$

where

$$\mathbf{J}(\mathbf{r}) = \mathbf{Q} \delta(\mathbf{r} - \mathbf{r}_0) \quad (12)$$

while in the region V^+ we require a solution of the Laplace's equation

$$\Delta u^+(\mathbf{r}) = 0, \quad \mathbf{r} \in V^+ \quad (13)$$

which vanishes at infinity and satisfies the following transmission conditions on S

$$u^-(\mathbf{r}) = u^+(\mathbf{r}), \quad \mathbf{r} \in S \quad (14)$$

$$\partial_n u^-(\mathbf{r}) = 0, \quad \mathbf{r} \in S \quad (15)$$

where

$$\partial_n = \hat{\mathbf{n}} \cdot \nabla = \frac{\alpha_2 \alpha_3}{[(\alpha_1^2 - \mu^2)(\alpha_1^2 - \nu^2)]^{1/2}} \frac{\partial}{\partial \rho} \quad (16)$$

stands for the outward normal derivative on S .

After long calculations we obtain the following expressions for the potential field u^- in the interior of the ellipsoid $\rho = \alpha_1$

$$\begin{aligned} u^-(\rho, \mu, \nu) = & c_0^0 + \frac{\mathbf{Q}}{4\pi\sigma} \cdot \frac{\mathbf{r} - \mathbf{r}_0}{|\mathbf{r} - \mathbf{r}_0|^3} - \frac{3}{4\pi\sigma} \sum_{m=1}^3 \left(\alpha_m I_1^m(\alpha_1) - \frac{\alpha_m}{\alpha_1 \alpha_2 \alpha_3} \right) Q_m \frac{x_m}{\alpha_m} \\ & + \frac{5}{4\pi\sigma(\Lambda - \Lambda')} \sum_{m=1}^3 Q_m x_{0m} \left[\left(I_2^1(\alpha_1) - \frac{1}{2\Lambda \alpha_1 \alpha_2 \alpha_3} \right) \frac{(\Lambda - \alpha_1^2)(\Lambda - \alpha_2^2)(\Lambda - \alpha_3^2)}{(\Lambda - \alpha_m^2)} \left(\sum_{\kappa=1}^3 \frac{x_\kappa^2}{(\Lambda - \alpha_\kappa^2)} + 1 \right) \right. \\ & \left. - \left(I_2^2(\alpha_1) - \frac{1}{2\Lambda' \alpha_1 \alpha_2 \alpha_3} \right) \frac{(\Lambda' - \alpha_1^2)(\Lambda' - \alpha_2^2)(\Lambda' - \alpha_3^2)}{(\Lambda' - \alpha_m^2)} \left(\sum_{\kappa=1}^3 \frac{x_\kappa^2}{(\Lambda' - \alpha_\kappa^2)} + 1 \right) \right] \end{aligned}$$

$$\begin{aligned}
& -\frac{15}{4\pi\sigma} \left[\alpha_1 \alpha_2 I_2^3(\alpha_1) - \frac{1}{(\alpha_1^2 + \alpha_2^2) \alpha_3} \right] (x_{01} Q_2 + x_{02} Q_1) \frac{x_1 x_2}{\alpha_1 \alpha_2} \\
& -\frac{15}{4\pi\sigma} \left[\alpha_1 \alpha_3 I_2^4(\alpha_1) - \frac{1}{(\alpha_1^2 + \alpha_3^2) \alpha_2} \right] (x_{01} Q_3 + x_{03} Q_1) \frac{x_1 x_3}{\alpha_1 \alpha_3} \\
& -\frac{15}{4\pi\sigma} \left[\alpha_2 \alpha_3 I_2^5(\alpha_1) - \frac{1}{(\alpha_2^2 + \alpha_3^2) \alpha_1} \right] (x_{02} Q_3 + x_{03} Q_2) \frac{x_2 x_3}{\alpha_2 \alpha_3} + O\left(\frac{x}{\alpha}\right)^3
\end{aligned} \quad (17)$$

where $\frac{x}{\alpha}$ denotes a measure of the ratio of the observation point to the geometrical characteristics of the ellipsoid. Similarly, for the exterior solution u^+ we obtain

$$\begin{aligned}
u^+(\rho, \mu, \nu) &= \frac{c_0^0}{I_0^1(\alpha_1)} + \frac{3}{4\pi\sigma\alpha_1\alpha_2\alpha_3} \sum_{m=1}^3 \frac{I_1^m(\rho)}{I_1^m(\alpha_1)} \alpha_m Q_m \left(\frac{x_m}{\alpha_m} \right) \\
&+ \frac{5}{8\pi\sigma\alpha_1\alpha_2\alpha_3(\Lambda - \Lambda')} \sum_{m=1}^3 Q_m x_{0m} \left[-\frac{I_2^1(\rho)}{I_2^1(\alpha_1)} \frac{(\Lambda - \alpha_1^2)(\Lambda - \alpha_2^2)(\Lambda - \alpha_3^2)}{\Lambda(\Lambda - \alpha_m^2)} \left(\sum_{\kappa=1}^3 \frac{x_\kappa^2}{(\Lambda - \alpha_\kappa^2)} + 1 \right) \right. \\
&+ \left. \frac{I_2^2(\rho)}{I_2^2(\alpha_1)} \frac{(\Lambda' - \alpha_1^2)(\Lambda' - \alpha_2^2)(\Lambda' - \alpha_3^2)}{\Lambda'(\Lambda' - \alpha_m^2)} \left(\sum_{\kappa=1}^3 \frac{x_\kappa^2}{(\Lambda' - \alpha_\kappa^2)} + 1 \right) \right] \\
&+ \frac{15}{4\pi\sigma\alpha_3(\alpha_1^2 + \alpha_2^2)} (Q_2 x_{01} + Q_1 x_{02}) \frac{I_2^3(\rho)}{I_2^3(\alpha_1)} \frac{x_1 x_2}{\alpha_1 \alpha_2} \\
&+ \frac{15}{4\pi\sigma\alpha_2(\alpha_1^2 + \alpha_3^2)} (Q_1 x_{03} + Q_3 x_{01}) \frac{I_2^4(\rho)}{I_2^4(\alpha_1)} \frac{x_1 x_3}{\alpha_1 \alpha_3} \\
&+ \frac{15}{4\pi\sigma\alpha_1(\alpha_2^2 + \alpha_3^2)} (Q_2 x_{03} + Q_3 x_{02}) \frac{I_2^5(\rho)}{I_2^5(\alpha_1)} \frac{x_2 x_3}{\alpha_2 \alpha_3} + O\left[\left(\frac{x}{\alpha}\right)^4\right]
\end{aligned} \quad (18)$$

where $\mathbf{r}_0 = (x_{01}, x_{02}, x_{03})$ is the point of singularity, $\mathbf{r} = (x_1, x_2, x_3)$ is the observation point, the parameters Λ, Λ' are given by

$$\left. \begin{matrix} \Lambda \\ \Lambda' \end{matrix} \right\} = \frac{1}{3} \left[\sum_{i=1}^3 \alpha_i^2 \pm \left(\sum_{i=1}^3 \left(\alpha_i^4 - \frac{\alpha_i^2 \alpha_2^2 \alpha_3^2}{\alpha_i^2} \right) \right)^{1/2} \right] \quad (19)$$

and

$$I_n^m(\rho) = \int_{\rho}^{+\infty} \frac{du}{[E_n^m(u)]^2 (u^2 - \alpha_1^2 + \alpha_2^2)^{1/2} (u^2 - \alpha_1^2 + \alpha_3^2)^{1/2}}, \quad n = 0, 1, 2, \dots, m = 1, 2, \dots, 2n + 1$$

(20)

are elliptic integrals. The functions $E_n^m(u)$ denote the Lamé functions of the first kind [9]. The above results can be reduced in such a way as to recover the solution of the corresponding problem for the sphere brain model, which is obtained by following similar process in the form

$$u^-(r, \theta, \phi) = c_0^0 + \frac{\mathbf{Q}}{4\pi\sigma} \cdot \frac{\mathbf{r} - \mathbf{r}_0}{|\mathbf{r} - \mathbf{r}_0|^3} + \frac{\mathbf{Q} \cdot \hat{\mathbf{r}}}{2\pi\sigma\alpha^2} \left(\frac{r}{\alpha} \right) + \frac{3(3\mathbf{r}_0\mathbf{Q} - \mathbf{r}_0\mathbf{Q}\tilde{\mathbf{I}}) : \hat{\mathbf{r}}\hat{\mathbf{r}}}{8\pi\sigma\alpha^3} \left(\frac{r}{\alpha} \right)^2 + O\left[\left(\frac{r}{\alpha}\right)^3\right] \quad (21)$$

for the interior solution, and in the form

$$u^+(r, \theta, \phi) = \alpha c_0^0 + \frac{3\mathbf{Q} \cdot \hat{\mathbf{r}}}{4\pi\sigma\alpha^2} \left(\frac{\alpha}{r} \right) + \frac{5(3\mathbf{r}_0\mathbf{Q} - \mathbf{r}_0\mathbf{Q}\tilde{\mathbf{I}}) : \hat{\mathbf{r}}\hat{\mathbf{r}}}{8\pi\sigma\alpha^3} \left(\frac{\alpha}{r} \right)^3 + O\left[\left(\frac{\alpha}{r}\right)^4\right] \quad (22)$$

for the exterior solution, where α is the radius of the sphere.

Acknowledgements: The first author acknowledges support of the present work from the Research Committee of the University of Patras under the "Karatheodory" program.

4. REFERENCES

- [1] Nolte, G., Fiesder, T., Curio, G., Perturbative analytical solutions of the magnetic forward problem for realistic volume conductors, *Journal of applied Physics*, Vol 89, 4 (2001).
- [2] Sarvas, J., Basic mathematical and electromagnetic concepts of the biomagnetic inverse problem, *Phys. Med. Biol.*, Vol 32, 1 (1987).
- [3] Munck, J. C. and Peters, M.J., *IEEE Trans. Biomed. Eng.*, Vol 40, 1166 (1993).
- [4] Berry, D. A., *Ann. N.Y. Acad. Sci.*, Vol 65, 1126 (1956).
- [5] Ferguson, A.S. and Stroink, G., *Journal of applied Physics*, Vol. 76, 7671 (1994).
- [6] Fuchs, M., Drenckhahn, R., Wischmann, H.-A., Wagner M., *IEEE Trans. Biomed. Eng.*, Vol 45, 980 (1988).
- [7] Snyder, W. S., Ford, M. R. and Warner, G. G., MIRD 5, Revised: Estimates of Absorbed Fractions for Mono-energetic Photon Sources Uniformly Distributed in Various Organs of a Heterogeneous Phantom, *The Society of Nuclear Medicine*, January (1978).
- [8] Hobson, E. W. "The Theory of Spherical and Ellipsoidal Harmonics", Chelsea, New York (1955).
- [9] Miloh, T., "Maneuvering Hydrodynamics of Ellipsoidal Forms", *J. Ship Res.*, 23, 66-75 (1979).
- [10] Dassios, G. and Miloh, T., "Rayleigh Scattering for the Kelvin-Inverted Ellipsoid", *Quarterly of Applied Mathematics*, 37, 4, 757-770 (1999).

MATHEMATICAL MODELS FOR BIOMAGNETIC FLUID FLOW AND APPLICATIONS

E. E. Tzirtzilakis and N. G. Kafoussias

Department of Mathematics, Section of Applied Analysis,
University of Patras, 26500 Patras, Greece

1. SUMMARY

In this work a mathematical model governing the biomagnetic fluid flow is presented. Expressions describing the variation of the saturation magnetization of the fluid with temperature or the magnetic field intensity are also given. After proper simplifications of the above-mentioned mathematical model the flow in a rectangular channel of a biomagnetic fluid (blood) under the action of an applied magnetic field is studied. The results obtained from the numerical solution of this problem, showed that the fluid flow is appreciably influenced by the applied magnetic field.

2. INTRODUCTION

During the last decades an extensive research work has been done on the fluid dynamics of biological fluids in the presence of magnetic field due to bioengineering and medical applications [1-3].

A biomagnetic fluid is a fluid that exists in a living creature and its flow is influenced by the presence of a magnetic field. The most characteristic biomagnetic fluid is the blood, which can be considered as a magnetic fluid because the red blood cells contain the hemoglobin molecule, a form of iron oxides, which is present at a uniquely high concentration in the mature red blood cells. It is found that the erythrocytes orient with their disk plane parallel to the magnetic field [4] and also that the blood possesses the property of diamagnetic material when oxygenated and paramagnetic when deoxygenated [5].

In order to examine the flow of a biomagnetic fluid under the action of an applied magnetic field, Haik et. al [6] developed a mathematical model for the Biomagnetic Fluid Dynamics (BFD) in which the saturation or static magnetization is given by the Langevin magnetization equation. BFD differs from MagnetoHydroDynamics (MHD) in that it deals with no electric current and the flow is affected by the magnetization of the fluid in the magnetic field. In MHD, which deals with conducting fluids, the mathematical model ignores the effect of polarization and magnetization.

The behavior of a biomagnetic fluid when it is exposed to magnetic field (magnetized) is described by the magnetization property M . Magnetization is the measure of how much the magnetic field is affecting the magnetic fluid and is a function of the magnetic field intensity H and the temperature T .

In the present work, the mathematical model, describing the biomagnetic fluid flow, is presented and relations are given, expressing the dependence of the saturation magnetization M_0 on the temperature and the magnetic field intensity. A simplification of this mathematical

model is used to obtain numerical solution of the differential equations describing the fluid flow (blood) in a rectangular channel under the action of a magnetic field. The obtained numerical results, presented graphically, showed that the flow is appreciably influenced by the magnetic field. These results indicate that application of a magnetic field, in the flow of a biomagnetic fluid, could be useful for medical and engineering applications.

3. MATHEMATICAL FORMULATION

The mathematical model for the Biomagnetic Fluid Dynamics is based on the modified Stokes principles and on the assumption that besides the three thermodynamic variables P , ρ and T the biomagnetic fluid behavior is also a function of magnetization M [6]. Under these assumptions, the governing equations for incompressible fluid flow are similar to those derived for FerroHydroDynamics (FHD) [7], and are given by :

Continuity Equation

$$\vec{\nabla} \cdot \vec{V} = 0 \quad (1)$$

Linear Momentum

$$\rho \frac{D\vec{V}}{Dt} = -\vec{\nabla}P + \rho\vec{F} + \eta\vec{\nabla}^2\vec{V} + \xi(\vec{\nabla}^2\vec{V} + 2\vec{\nabla} \times \vec{\omega}) + \mu_0(\vec{M} \cdot \vec{\nabla})\vec{H} + [\vec{\nabla} \times \vec{H}] \times \vec{B} \quad (2)$$

Angular Momentum

$$\rho I \frac{D\vec{\omega}}{Dt} = \mu_0 \vec{M} \times \vec{H} + \eta' \vec{\nabla}^2 \vec{\omega} + 2\xi(\vec{\nabla} \times \vec{V} - 2\vec{\omega}) \quad (3)$$

Magnetization

$$\frac{D\vec{M}}{Dt} = \vec{\omega} \times \vec{M} - \frac{1}{\tau} [\vec{M} - \vec{M}_0] \quad (4)$$

Maxwell Equations (Amperes law and Gauss second law)

$$\vec{\nabla} \times \vec{H} = \vec{J} = \sigma(\vec{\nabla} \times \vec{B}) \quad (5)$$

$$\vec{\nabla} \cdot \vec{B} = \vec{\nabla} \cdot (\vec{H} + \vec{M}) = 0$$

Magnetization Equations

These equations describe the dependence of saturation or static magnetization M_0 on the applied magnetic field intensity H and temperature T and the appropriate expressions are given below.

In the above equations \vec{V} is the velocity field, ρ is the fluid density, P is the pressure, \vec{F} is the body force per unit volume, η and ξ are the coefficients of dynamical and rotational viscosity, respectively, $\vec{\omega}$ is the angular velocity, μ_0 is the magnetic permeability, \vec{M} is the magnetization, \vec{H} is the magnetic field intensity, \vec{B} is the magnetic induction, I is the moment of inertia, per unit mass, η' is the shear spin viscosity, τ is the magnetic relaxation time, \vec{M}_0 is the saturation magnetization and σ is the electrical conductivity of the fluid.

3.1 Equilibrium Flow

The above set of equations is a very complicated system and simplifications must be made in order to solve it for a specific problem.

As a first approximation we can consider that biofluids are poor conductors and the induced current is negligibly small. Thus, unlike MHD, Lorentz forces (the last term in eq.(2)) are much smaller in comparison to the magnetization force (the last but one term in eq.(2)). Also,

for medium shear rates, like blood flow in artery, the diffusion of the spin term is much smaller than that of the magnetic torque or the exchange between internal and external momentum.

The major simplification however, can take place if we consider that the magnetic fluid has either achieved instantaneous magnetization or time has elapsed beyond the relaxation time, after the flow has exposed to the magnetic field. In this situation the flow can be considered as **equilibrium flow** and once the particle reaches saturation magnetization it will not have addition magnetization even if the magnetic field is further increased. Under the equilibrium assumption the fluid magnetization vector, \vec{M} , at any given instant is parallel to the vector of the magnetic field intensity, \vec{H} , and the property of magnetization is determined by the fluid temperature, density and magnetic field intensity $M=M(T, \rho, H)$. Although the equilibrium flow is an idealization for the physical behavior of the biomagnetic fluid, it provides a good insight to the biomagnetic fluid flow since the governing equations are much more simpler than the complete set of equations derived in the previous sections for non equilibrium case.

The equations of motion for the equilibrium flow can be written now as:

Continuity Equation

$$\vec{\nabla} \cdot \vec{V} = 0, \quad (6)$$

Linear Momentum

$$\rho \frac{D\vec{V}}{Dt} = -\vec{\nabla} p + \rho \vec{F} + \eta \vec{\nabla}^2 \vec{V} + \mu_0 M_0 \vec{\nabla} H, \quad (7)$$

where $H = [H_x^2 + H_y^2]^{1/2}$.

3.2 Saturation Magnetization Equations

In equilibrium situation the magnetization property is generally determined by the fluid temperature, density and magnetic field intensity and various equations, describing the dependence of M_0 on these quantities, are given in bibliography [6], [7]. The simplest relation is the linear equation of state, given in [8]:

$$M_0 = K(T_c - T), \quad (8)$$

where K is a constant called pyromagnetic coefficient and T_c is the Curie temperature.

Above the Curie temperature the biofluid does not subjected to magnetization.

Another equation for magnetization, below the Curie temperature T_c is given in [9]

$$M_0 = M_1 \left(\frac{T_c - T}{T_1} \right)^\beta, \quad (9)$$

where β is the critical exponent for the spontaneous or saturation magnetization. For iron $\beta=0.368$, $M_1=54$ Oe and $T_1=1.45$ K.

A linear equation involving the magnetic intensity H and temperature T is given in [10]

$$M_0 = KH(T_c - T). \quad (10)$$

Finally, Higashi et. al [4], found that the magnetization process of red blood cells behaves like the following function, known as Langevin function,

$$M_0 = mN \left[\coth \left(\frac{\mu_0 mH}{kT} \right) - \frac{kT}{\mu_0 mH} \right], \quad (11)$$

where m is the particle magnetization, N is the number of particles per unit volume and k the Boltzman's constant.

In all the above cases the magnetization M_0 is dependent on the temperature T of the fluid. In such a case (non-isothermal case), it is also necessary to consider in the mathematical model, describing the problem under consideration, the energy equation containing the temperature T of the fluid. This equation can be written as [8]

$$\rho C_p \frac{DT}{Dt} + \mu_0 T \frac{\partial M_0}{\partial T} [\vec{V} \cdot (\vec{\nabla} H)] = k \nabla^2 T + \eta \Phi \quad (12)$$

where k is the coefficient of thermal conductivity of the fluid, C_p the specific heat and Φ the dissipation function.

4. APPLICATIONS

Biomagnetic fluid flow in a Channel

As a simple, but representative, application of biomagnetic fluid flow we consider the steady two-dimensional laminar flow of an incompressible viscous biomagnetic fluid (blood) in a space between two parallel flat plates (channel). The length of the plates is L and the distance between them is h ($h \ll L$). We assume that the flow at the entrance is fully developed and that the upper plate is at temperature T_u , while the lower at T_L , such that $T_L < T_u < T_c$. The origin of the Cartesian coordinate system is located at the leading edge of the lower plate and the flow is subjected to a magnetic dipole, which is placed very close to the lower plate and below it. At the outlet of the channel we assume that all physical quantities are independent of x . The equations describing the flow field in this channel, under the action of the applied magnetic field, are the continuity equation (6), the momentum equation (7) and the energy equation (12). For the variation of saturation magnetization M_0 , with the magnetic field intensity H and temperature T , we consider equation (10). The numerical solution of the dimensionless equations and boundary conditions, describing the problem under consideration, is obtained by adopting the vorticity-stream function formulation and by using

an efficient upwind finite difference scheme [11] for the case $Re=12.5$ (Reynolds number), $Pr=0.141$ (Prandtl number), $Ec=0.00023$ (Eckert number), for the dimensionless "Curie temperature" $\epsilon=T_u/(T_u-T_L)=7.2$ and for different values of the magnetic number Mn . The obtained results are shown on Figures 1 to 12. In Figures 1-3 the dimensionless skin friction coefficient is shown at the lower and upper plate. In the region near the location ($x=4$)

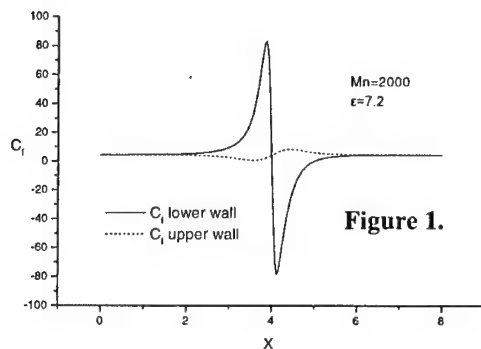


Figure 1.

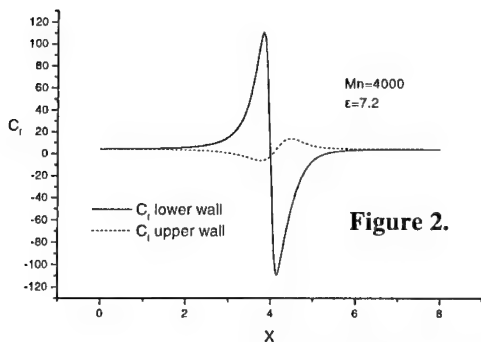


Figure 2.

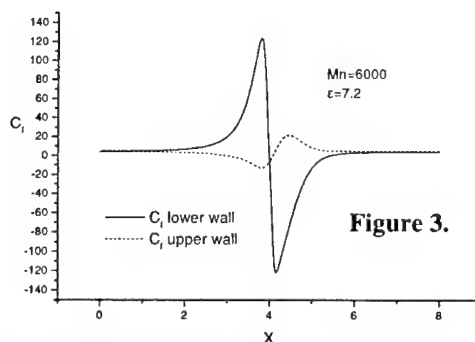


Figure 3.

Figures 1-3: Variation of skin friction coefficient C_f

of the magnetic source the friction coefficient is increased substantially due to the action of the magnetic field. The contours of the stream function, for various magnetic numbers, are shown in Figures 4-6. The magnet affects the fluid flow and two vortices are created near the magnetic pole, as the magnetic field strength is increased. The contours of vorticity function are shown in Figures 7-9 and of temperature function in Figures 10-12. Near the pole we observe a slight increase of the temperature as a result of additional energy from the magnetic field of the pole. It should be remarked that in the absence of the magnetic field straight lines represent temperature, stream as well as the vorticity function. Thus, the formation of these contours is the result of the action of the applied magnetic field on the flow field. These results show that in the presence of the magnetic field, the flow field is changing drastically, and especially the skin friction coefficient, which is affected near the area of the magnetic pole. These conclusions suggest that a careful choice of the imposed magnetic field will affect the flow characteristics and hence can be utilized for medical and engineering applications.

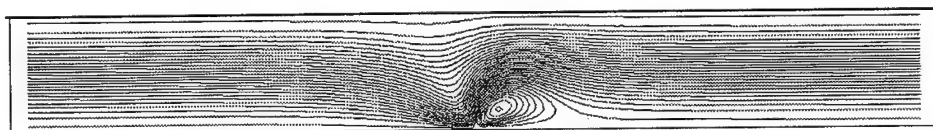


Figure 4. Contours for stream function for $Mn=2000$

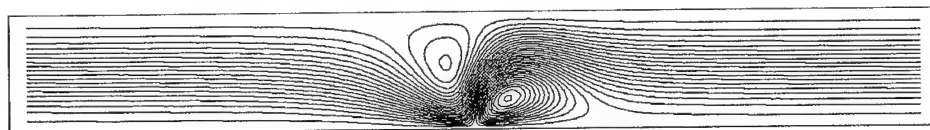


Figure 5. Contours for stream function for $Mn=4000$

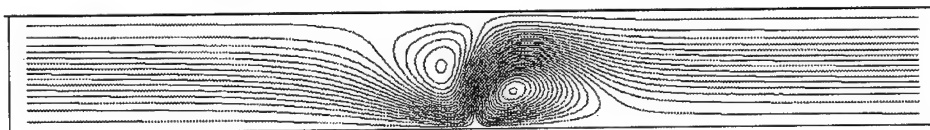


Figure 6. Contours for stream function for $Mn=6000$

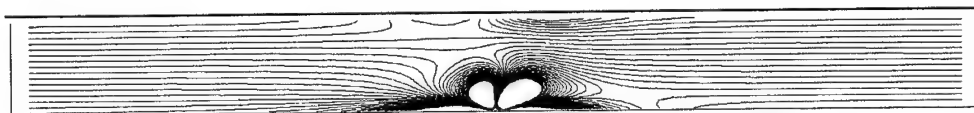


Figure 7. Contours for vorticity function for $Mn=2000$



Figure 8. Contours for vorticity function for $Mn=4000$



Figure 9. Contours for vorticity function for $Mn=6000$



Figure 10. Contours for temperature function for $Mn=2000$



Figure 11. Contours for temperature function for $Mn=4000$

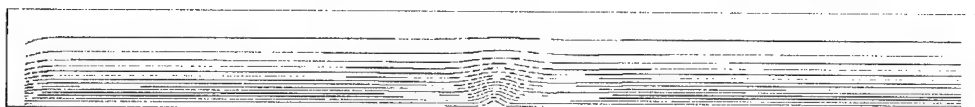


Figure 12. Contours for temperature function for $Mn=6000$

Acknowledgements: The program "K. Karatheodoris" No. 2439 - University of Patras-Research Committee, financially supported this work.

5. References

- [1] Haik, Y., Pai, V. and Chen C.J., *Development of magnetic device for cell separation*, Journal of Magnetism and Magnetic Materials, **194**, 254-261 (1999).
- [2] Ruuge, E. K. and Rusetski, A.N., *Magnetic fluid as Drug Carriers: Targeted Transport of Drugs by a Magnetic Field*, Journal of Magnetism and Magnetic Materials, **122**, 335-339 (1993).
- [3] Plavins, J. and Lauva, M., *Study of Colloidal Magnetite Binding Erythrocytes: Prospects for Cell Separation*, Journal of Magnetism and Magnetic Materials, **122**, 349-353 (1993).
- [4] Higashi, T., Yamagishi, A., Takeuchi, T., Kawaguchi, N., Sagawa, S., Onishi, S. and Date, M., *Orientation of Erythrocytes in a strong static magnetic field*, J. Blood, **82**(4), 1328-1334 (1993).
- [5] Pauling, L. and Coryell, C. D., *The magnetic Properties and Structure of Hemoglobin, Oxyhemoglobin and Carbonmonoxy Hemoglobin*, Proceedings of the National Academy of Science, USA, **22**, 210-216 (1936).
- [6] Haik, Y., Chen, J.C. and Pai V.M., In: Winoto, S.H., Chew Y.T., *Development of bio-magnetic fluid dynamics*, Proceedings of the IX International Symposium on Transport Properties in Thermal Fluids Engineering, Singapore, Pacific Center of Thermal Fluid Engineering, Wijesundera N.E. (eds.), Hawaii, U.S.A., 121-126 (June 25-28, 1996).
- [7] Rosensweig, R.E., *Ferrohydrodynamics*, Cambridge University Press (1985).
- [8] Andersson, H. I. and Valnes, O. A., *Flow of a heated ferrofluid over a stretching sheet in the presence of a magnetic dipole*, Acta Mechanica, **128**, 39-47 (1998).
- [9] Arrott, A.S., Heinrich, B. and Templeton, T.L., *Phenomenology of Ferromagnetism: I. Effects of Magnetostatics on Susceptibility*, IEEE Transactions on Magnetism, **25**, 4364-4373 (1989).
- [10] Matsuki, H., Yamasawa, K. and Murakami, K., *Experimental Considerations on a new Automatic Cooling Device Using Temperature Sensitive Magnetic Fluid*, IEEE Transactions on Magnetism, **13** (5), 1143-1145 (1977).
- [11] Mazumdar J.N., *Biofluid Mechanics*, World Scientific Publishing Co., Singapore (1992).

ON A NEW CRACK MODEL FOR PIEZOELECTRIC SOLIDS

C. Dascalu, D. Homentcovschi

Institute of Applied Mathematics, Romanian Academy,
P.O. Box 1-24, Bucharest, Romania.

V. K. Kalpakides, E. Hadjigeorgiou

University of Ioannina, GR-45110, Ioannina, Greece

1. SUMMARY

The aim of this paper is to study a boundary value problem arising in electro-elastic fracture theory. In recent years it became evident that the electrically impermeable or the perfect electric contact boundary conditions on the crack faces may over- or underestimate the electric field influence on the propagation process. The crack model here investigated is intermediate between these two limit cases. The plane problem of an infinite piezoelectric body with a central crack is converted into a system of integro-differential equations and is solved by combination of partial analytic and numeric solutions.

2. INTRODUCTION

The electrical boundary condition to be imposed on the crack faces is still an open subject of the fracture theory. A first proposition was made by Parton [6] who considered the condition of perfect electric contact, that is the potential and the normal component of the induction to be continuous across the crack line. This means that the medium inside the flaw (e.g. air), with a lower permittivity, has no influence on the fields in the piezoelectric body. A second boundary condition given by Pak [5] is based on the assumption that the electric induction inside the flaw may be neglected. In this case the normal components of the induction must vanish on the crack faces. This model was further employed in [8].

A critical evaluation of these approaches was done by Suo *et al.* [8], Tobin and Pak [9], McMeeking [4]. The general conclusion of these studies is that the permeable condition underestimates the electric field influence on the crack propagation, while the impermeable condition may overestimate this contribution. In such a case, an intermediate model would be appropriate. Such a model was proposed by Parton and Kudryavtsev [7] who derived new boundary conditions for cracks in piezoelectrics, by an approximate analysis of a thick dielectric layer embedded in the electro-elastic body. Our purpose is to study the solution of the boundary value problem constructed with this non-classical boundary conditions.

3. BASIC EQUATIONS AND ANALYTIC SOLUTIONS

Consider a Griffith crack of length $2a$ in an infinite piezoelectric solid. A system of Cartesian coordinates $x_i, i = 1, 2, 3$ is chosen so that the crack lies in the x_1, x_3 -plane, with the crack fronts parallel to the x_3 -axis, located at $x_1 = \pm a$. The equilibrium and electrostatics equations leads to:

$$C_{ijkl} \frac{\partial^2 u_k}{\partial x_i \partial x_j} + e_{kij} \frac{\partial^2 \varphi}{\partial x_k \partial x_j} = 0 \quad (1)$$

$$e_{ikl} \frac{\partial^2 u_k}{\partial x_l \partial x_i} - \epsilon_{ij} \frac{\partial^2 \varphi}{\partial x_i \partial x_j} = 0 \quad (2)$$

Here C_{ijkl} is the fourth-order tensor of elasticity coefficients, e_{ikl} is the third-order tensor of piezoelectricity coefficients and ϵ_{ij} is the tensor of dielectric constants. It is assumed that C_{ijkl} and ϵ_{ij} are positive-definite tensors. The electric field vector E_i is derived from the electric potential φ by $E_i = -\frac{\partial \varphi}{\partial x_i}$. We assume that the three components of displacement and the electric potential depend only on in-plane coordinates, i.e. $u_i = u_i(x_1, x_2), i = 1, 2, 3$ and $\varphi = \varphi(x_1, x_2)$. We also suppose that remote stresses $\sigma_{2j}^\infty, j = 1, 2, 3$ and electric displacement D_2^∞ are given.

Following Ref. [7, p.323-324], on the crack line we consider the boundary conditions

$$\sigma_{2j}^\pm = 0 \quad (3)$$

$$D_2^+ = D_2^-; D_2 + \alpha(\varphi^+ - \varphi^-) = 0 \quad (4)$$

where the \pm superscripts correspond to the upper and, respectively, lower faces of the crack. The parameter $\alpha = \frac{\epsilon_0}{2h}$, where ϵ_0 is the electric permittivity of the interior medium and $2h$ is the thickness of the flaw. We note that the electrically impermeable boundary condition used by Pak [5] can be obtained from (3-4) for $\alpha = 0$, while the perfect permeability condition of Parton [6] results for $\alpha \rightarrow \infty$.

In what follows we use the four-dimensional formalism of Refs. [8], [2] for linear piezoelectrics. The equations (1-2) can be written in matrix notation as

$$\mathbf{Q} \frac{\partial^2 \mathbf{v}}{\partial x_1^2} + (\mathbf{R} + \mathbf{R}^T) \frac{\partial^2 \mathbf{v}}{\partial x_1 \partial x_2} + \mathbf{T} \frac{\partial^2 \mathbf{v}}{\partial x_2^2} = \mathbf{0} \quad (5)$$

where $\mathbf{v}^T = (u_1, u_2, u_3, \varphi)$, with T meaning the transpose, and

$$Q_{ik} = \begin{cases} C_{i1k1} & i, k = 1, 2, 3 \\ e_{1i1} & i = 1, 2, 3; k = 4 \\ e_{1k1} & i = 4; k = 1, 2, 3 \\ -\epsilon_{11} & i = 4; k = 4 \end{cases} \quad R_{ik} = \begin{cases} C_{i1k2} & i, k = 1, 2, 3 \\ e_{2i1} & i = 1, 2, 3; k = 4 \\ e_{1k2} & i = 4; k = 1, 2, 3 \\ -\epsilon_{12} & i = 4; k = 4 \end{cases} \quad (6)$$

$$T_{ik} = \begin{cases} C_{i2k2} & i, k = 1, 2, 3 \\ e_{2i2} & i = 1, 2, 3; k = 4 \\ e_{2k2} & i = 4; k = 1, 2, 3 \\ -\epsilon_{22} & i = 4; k = 4 \end{cases}$$

Define $\mathbf{t}^T = (\sigma_{21}, \sigma_{22}, \sigma_{23}, D_2)$ which, from (6), can be expressed as

$$\mathbf{t} = \mathbf{R}^T \frac{\partial \mathbf{v}}{\partial x_1} + \mathbf{T} \frac{\partial \mathbf{v}}{\partial x_2} \quad (7)$$

and let $\mathbf{d}(x_1) = \mathbf{v}(x_1, +0) - \mathbf{v}(x_1, -0)$ be the jump of \mathbf{v} across the x_1 -axis. Then the boundary conditions (3-4) become

$$\mathbf{t}^+ = \mathbf{t}^- ; \quad \mathbf{t} + \mathbf{K}\mathbf{d} = \mathbf{0}, \quad |x_1| < a \quad (8)$$

where the only non-vanishing element of the four-dimensional matrix \mathbf{K} is $K_{44} = \alpha$. At infinity the vector \mathbf{t} is prescribed.

Let $\mathbf{k}^T = (K_{II}, K_I, K_{III}, K_{IV})$, where K_I, K_{II}, K_{III} are the stress intensity factors and K_{IV} is the electric displacement intensity factor (e.g. [8], [2]). Introducing

$$\mathbf{\Gamma}(x_1) = -\mathbf{H}^{-1}\mathbf{d}(x_1) \quad (9)$$

with a non-singular matrix \mathbf{H} defined in (16). It is proved that

$$\mathbf{k} = -\lim_{x_1 \rightarrow a} \left(\sqrt{\frac{\pi}{2(a-x_1)}} \mathbf{\Gamma}(x_1) \right) \quad (10)$$

The fracture parameter adopted in this paper is the energy release rate G (see [8], [1], [2]). Suo *et al.* [8] calculated G for electrically impermeable cracks and since it can be shown that the asymptotic structure of the solution of our problem is the same as for impermeable cracks, their result still holds:

$$G = \lim_{\lambda \rightarrow 0^+} \left(\frac{1}{2\lambda} \int_a^{a+\lambda} \mathbf{t}^T(x_1) \mathbf{d}(x_1 - \lambda) dx_1 \right) = \frac{1}{4} \mathbf{k}^T \mathbf{H} \mathbf{k} \quad (11)$$

Full-field solutions to the problem were given in Refs. [8] for impermeable cracks (i.e. $\alpha = 0$). In what follows we study the problem for arbitrary values of α . When the Fourier transform with respect to x_1 is applied to (5) one obtains

$$\xi^2 \mathbf{Q} \hat{\mathbf{v}} + i\xi (\mathbf{R} + \mathbf{R}^T) \frac{\partial \hat{\mathbf{v}}}{\partial x_2} - \mathbf{T} \frac{\partial^2 \hat{\mathbf{v}}}{\partial x_2^2} = \mathbf{0} \quad (12)$$

This equation has solutions of the form

$$\hat{\mathbf{v}} = \mathbf{a} e^{-i\eta x_2} \quad (13)$$

The complex number η and the column \mathbf{a} are determined from the eigenvalue equation

$$[\mathbf{Q} + p(\mathbf{R} + \mathbf{R}^T) + p^2 \mathbf{T}] \mathbf{a} = \mathbf{0} \quad (14)$$

where we have introduced $p = \frac{\eta}{\xi}$. The matrix in brackets must have a vanishing determinant and this leads to an equation for p . It has been shown in Ref. [8] that this equation has no real roots. Let $p_i, i = 1, 2, 3, 4$ be the roots with positive imaginary part and $\mathbf{a}_i, i = 1, 2, 3, 4$ the associated eigenvectors. For a given ξ one can define $\eta_i = p_i \xi$ for $\xi > 0$ and $\eta_i = \bar{p}_i \xi$ for $\xi < 0$, so that $\Im(\eta_i) > 0$. Note that $\bar{\mathbf{a}}_i$ are also eigenvectors, corresponding to \bar{p}_i (or, equivalently, to $\bar{\eta}_i$). When these eigenvalues are distinct, the general solution of (12) is a linear combination of the eight particular solutions of the form (13). Then, further calculations allow us to reduce the problem to a system of integro-differential eqs. on the crack line. If one introduces the matrices

$$\mathbf{P} = \text{diag} [p_1, p_2, p_3, p_4] ; \quad \mathbf{A} = [\mathbf{a}_1, \mathbf{a}_2, \mathbf{a}_3, \mathbf{a}_4] \quad (15)$$

$$\mathbf{B} = \mathbf{R}^T \mathbf{A} + \mathbf{T} \mathbf{A} \mathbf{P} ; \quad \mathbf{H} = 2 \Re(i \mathbf{A} \mathbf{B}^{-1}) \quad (16)$$

we can obtain the system

$$\mathbf{\Gamma}(x_1) = \mathbf{0}, \quad |x_1| > a \quad (17)$$

$$\frac{1}{\pi} \int_{-a}^a \frac{\mathbf{\Gamma}'(s)}{x_1 - s} ds - \mathbf{KH}\mathbf{\Gamma}(x_1) = \mathbf{t}^d, \quad |x_1| < a \quad (18)$$

where the integral is a principal value in the sense of Cauchy. The particular structure of the matrix \mathbf{K} allows us to write (18) as

$$\frac{1}{\pi} \int_{-a}^a \frac{\Gamma'_i(s)}{s - x_1} ds = \sigma_{2i}^\infty, \quad i = 1, 2, 3 \quad (19)$$

$$\frac{1}{\pi} \int_{-a}^a \frac{\Gamma'_4(s)}{s - x_1} ds + \alpha(h_{14}\Gamma_1 + h_{24}\Gamma_2 + h_{34}\Gamma_3 + h_{44}\Gamma_4) = D_2^\infty \quad (20)$$

where h_{ij} are the elements of the matrix \mathbf{H} . Note that the special choice of the unknown functions Γ_i led to the decoupled system (19-20). The equations (19) admit the analytic solutions

$$\mathbf{\Gamma}_i(x_1) = -\sqrt{a^2 - x_1^2} \sigma_{2i}^\infty, \quad i = 1, 2, 3 \quad (21)$$

providing the classical expressions for the stress intensity factors

$$K_{II} = \sqrt{\pi a} \sigma_{21}^\infty; \quad K_I = \sqrt{\pi a} \sigma_{22}^\infty; \quad K_{III} = \sqrt{\pi a} \sigma_{23}^\infty \quad (22)$$

as in the case of impermeable cracks (see [8]). However, for the determination of K_{IV} one needs to solve (20). Note that the integro-differential equation (20) is similar to the Prandtl's equation of aerodynamics (e.g. Ref. [3]). Since there are no closed-form solutions for an equation of this type, a numerical integration of (20) needs to be performed.

5. NUMERICAL SOLUTIONS

In this section we consider that the piezoelectric is a poled ceramic of the type PZT-5H. Such a material exhibits transverse symmetry around the poling axis.

Let the crack plane $x_1 - x_3$ be perpendicular to the poling axis x_2 , with the crack front along the x_3 -axis. Suppose that $\sigma_{21}^\infty = \sigma_{23}^\infty = 0$. In this case, we have $\mathbf{\Gamma}_1 = \mathbf{\Gamma}_3 = 0$ and using the expression of $\mathbf{\Gamma}_2$ we obtain from (20)

$$\frac{1}{\pi} \int_{-a}^a \frac{\Gamma'_4(s)}{s - x_1} ds + \alpha h_{44} \Gamma_4 = D_2^\infty + \alpha h_{24} \sqrt{a^2 - x_1^2} \sigma_{22}^\infty \quad (23)$$

A numerical procedure based on Gauss-type quadrature formulae, as given by Dragos [3], is employed to solve (23). The expression of the energy release rate reduces in this case to

$$G = \frac{1}{4} (h_{22} K_I^2 + 2h_{24} K_I K_{IV} + h_{44} K_{IV}^2) \quad (24)$$

in which K_I is given by (22) and K_{IV} is derived from the numerical solution.

The numerical values of G as a function of E_2^∞ are plotted in Fig. 1 for different values of h ($\alpha = \epsilon_0/2h$, $\epsilon_0 = 8.85 \times 10^{-12} \text{CV}^{-1}\text{m}^{-1}$). We took the length $a = 10^{-3}\text{m}$. Also represented are the energy release rate G_I for electrically impermeable boundary condition ($\alpha = 0$) and G_P for permeable condition ($\alpha = \infty$). G_I is given by (24) in which the intensity factor K_{IV} is replaced by

$$K'_{IV} = \sqrt{a\pi} D_2^\infty \quad (25)$$

The critical value of G is taken to be $G_{cr} = 10.0 N/m$ (see [5], [9]) and the fracture criterion is $G = G_{cr}$. We see that for $h > 5 \times 10^{-6} m$, G approaches G_I , while for $h < 10^{-8} m$, G is very close to G_P . For values of $10^{-8} m < h < 5 \times 10^{-6} m$ the energy release rate G takes intermediate values between these limit models and significantly different from them. It is observed that the electric field has an arresting influence on the crack propagation which is smaller than in the impermeable case, but which is not vanishing, as for the permeable model.

To decide between these three fracture parameters we consider the "exact" problem of an elliptic cavity, with the electric permeability ϵ_0 , the major semi-axis a and the minor semi-axis h , embedded in an infinite piezoelectric body. In the plane case, the energy release rate is denoted by G_E for such a problem. In Fig. 2 we plotted $G - G_E$, as a function of E_2^∞ . Its behavior shows that for a particular range of values of h , about $2 \times 10^{-7} m$, we have $G = G_E$. In this case, the model leads to the same fracture predictions as the exact problem. For $h > 2 \times 10^{-7}$, $G - G_E$ grows up. Since for such values we recover the impermeable model, as it results from Fig. 1., this clearly shows that the impermeable conditions do not provide an accurate description. For $h < 2 \times 10^{-7}$, $G - G_E$ remains close to 0. However, as we see from Fig. 1., for very small values of h we recover the perfect contact conditions, which are inconsistent with the experimental results (see for instance Ref. [9]). We remark that for the values of h for which $G = G_E$, G is different from both G_I and G_P , as it results from Fig. 1.

References

- [1] C. Dascalu *Electroelasticity equations and energy approaches to fracture*, Int. J. Engng. Sci. **35** (1997), p. 1185-1194.
- [2] C. Dascalu and G.A. Maugin, *On the dynamic fracture of piezoelectric materials*, Quart. J. Mech. Appl. Math., **48** (1995), 237-255.
- [3] L. Dragos, *Integration of Prandtl's equation with the aid of quadrature formulae of Gauss type*. Quart. Appl. Math. **LII** (1994), 23-29.
- [4] R.M. McMeeking, *Electrostrictive stresses near crack-like flaws*, J. Appl. Math. Phys. **640** (1989), 615-627.
- [5] Y.E. Pak, *Crack extension force in a piezoelectric material*. J. Appl. Mech. **57** (1990), 647-653.
- [6] V.Z. Parton, *Fracture mechanics of piezoelectric materials*. Acta Astronaut. **3** (1976), 671-683.
- [7] V.Z. Parton and B.A. Kudryavtsev, *Electromagnetoelasticity*, Gordon and Breach, New York, 1988.
- [8] Z. Suo, C-M. Kuo, D.M. Barnett and J.R. Willis, *Fracture mechanics for piezoelectric ceramics*. J. Mech. Phys. Solids **40** (1992), 739-765.
- [9] A. Tobin and Y.E. Pak, *Effect of electric fields on fracture behavior of PZT ceramics*, SPIE North American Conference on Smart Structures and Materials, Albuquerque, New Mexico, Feb. 1-4, 1993.

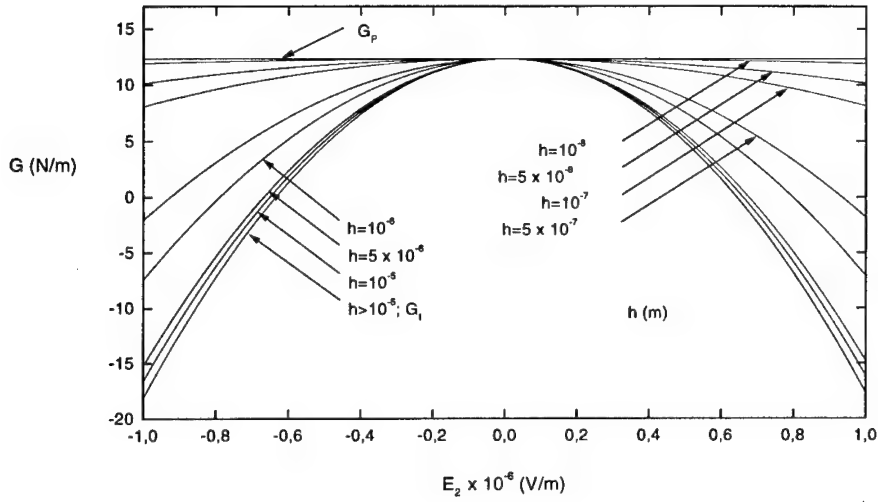


Figure 1: Energy release rates G , G_I and G_P vs. electric field E_2^∞ in the plane case, for $\sigma_{22}^\infty = 2 \times 10^7 \text{ Nm}^{-2}$.

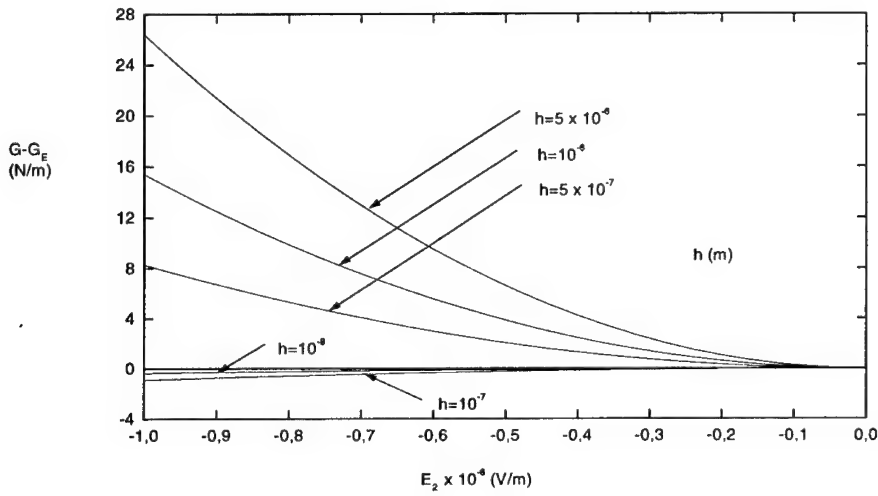


Figure 2: The difference between the fracture parameters of the crack and, respectively, the ellipse problem in the plane case.

LAMELLAR INHOMOGENEITIES IN PIEZOELECTRIC SOLIDS

C. Dascalu, D. Homentcovschi

Institute of Applied Mathematics, Romanian Academy,
P.O. Box 1-24, RO-70700 Bucharest, Romania.

1. SUMMARY

We study the problem of a lamellar inhomogeneity of arbitrary shape embedded in a piezoelectric matrix of infinite extent. Uniform asymptotic solutions for the equations of elastostatics and electrostatics on this configuration are obtained. The first order terms, in the inhomogeneity thickness, are explicitly determined for piezoelectric inclusions. Cracks and rigid inclusions can be similarly analyzed. Detailed first order solutions are obtained for elliptic and lemon-shaped inhomogeneities. It is found that, while for elliptic piezoelectric inclusions the perturbation stresses and electric displacements at the inclusion ends have the same order as those given at infinity, for a lemon-shaped inclusion they are an order-of-magnitude smaller.

2. INTRODUCTION

In recent years, a lot of effort has been expended for the study of inhomogeneities, like inclusions or cracks, in piezoelectric materials. However, most of the obtained results concern the cases of elliptic inclusions or line cracks. The objective of this paper is to give solutions for arbitrary-shaped lamellar inhomogeneities. We consider inclusions embedded in an infinite matrix subject to a uniform stress at infinity. Both the matrix and the inclusion consist of general piezoelectric materials.

In approaching the problem we shall employ the extended Stroh formalism for piezoelectrics (see Barnett and Lothe 1975, Suo *et al.* 1992, Dascalu and Maugin 1995, Ting 1996). Each complex function involved in the general solution for the external domain will be represented as a superposition of complex logarithmic singularities spread along a line segment located inside the lamellar region. A general form of the complex functions entering in the representation of the solution inside the thin region will be deduced as asymptotic expansions around their values on the body axis. By imposing the continuity of the displacements and tractions across the interface curve we obtain a system of integral equations for determining the fields in the lamellar region and the density of the singularities for the external solution. The use of sum rules and identities for the matrices involved in these equations allow us to convert the complex-form system into a real one. The resulting system of integral equations is solved asymptotically, for a small thickness

ratio ε of the lamellar region, by using the similar technique to that developed by Geer and Keller (1968), Homentcovschi (1984), Homentcovschi and Dasalu (2000) and, for anisotropic elastic materials, by Dasalu and Homentcovschi (1999).

3. BASIC EQUATIONS

Consider an infinitely extended piezoelectric body \mathcal{D}^e that contains an inhomogeneity \mathcal{D}^* . We assume that the interface boundary C is described by the equations

$$z_{\pm} = x_1 + i\varepsilon Y_{\pm}(x_1) \quad ; \quad Y_{\pm}(x_1) = S(x_1) \pm \sqrt{D(x_1)} \quad (1)$$

where $S(x_1)$ and $D(x_1)$ are twice differentiable functions on the interval $[-1, 1]$, satisfying $\max |S(x_1) \pm \sqrt{D(x_1)}| = 1$ and vanishing at the endpoints ± 1 .

Let $C_{ijkl}^e, e_{lij}^e, \varepsilon_{il}^e$ be, respectively, the elastic, piezoelectric and dielectric constants of the exterior medium \mathcal{D}^e and $C_{ijkl}^*, e_{lij}^*, \varepsilon_{il}^*$ the corresponding coefficients for the inside body \mathcal{D}^* . The elastic and dielectric tensors for both media are assumed to be fully symmetric and positive definite. The equilibrium equations can be written as (see Maugin (1988))

$$C_{ijkl}^e \frac{\partial^2 u_k^e}{\partial x_i \partial x_j} + e_{lij}^e \frac{\partial^2 \varphi^e}{\partial x_i \partial x_j} = 0 \quad (2)$$

$$e_{ikl}^e \frac{\partial^2 u_k^e}{\partial x_l \partial x_i} - \varepsilon_{il}^e \frac{\partial^2 \varphi^e}{\partial x_l \partial x_i} = 0 \quad (3)$$

where repeated indices imply summation. Here $u_k^e, k = 1, 2, 3$ and φ^e are, respectively, the elastic displacements and the electric potential in the matrix \mathcal{D}^e and they are supposed to depend on x_1 and x_2 only. Let $\varepsilon_{ij}^e = \frac{1}{2}(\frac{\partial u_i^e}{\partial x_j} + \frac{\partial u_j^e}{\partial x_i})$ be the strain tensor, $E_i^e = -\frac{\partial \varphi^e}{\partial x_i}$ the electric field, σ_{ij}^e is the elastic stress and D_i^e is the electric displacement.

We assume that the two bodies have a perfect bonding along their common interface which means that the elastic displacements, the surface tractions, the electric potential and the normal electric displacements are continuous:

$$u_k^* = u_k^e ; \quad \sigma^* \mathbf{n} = \sigma^e \mathbf{n} ; \quad \varphi^* = \varphi^e ; \quad \mathbf{D}^* \mathbf{n} = \mathbf{D}^e \mathbf{n} \quad (4)$$

where \mathbf{n} is the unit normal vector on C directed toward \mathcal{D}^e from \mathcal{D}^* .

It can be shown (Barnett and Lothe 1975, Ting 1996) that the stresses and the electric displacements can be expressed in terms of a four-dimensional generalized stress function vector ϕ^e by

$$\sigma_{i1}^e = -\frac{\partial \phi_i^e}{\partial x_2} ; \quad \sigma_{i2}^e = \frac{\partial \phi_i^e}{\partial x_1} ; \quad D_1^e = -\frac{\partial \phi_4^e}{\partial x_2} ; \quad D_2^e = \frac{\partial \phi_4^e}{\partial x_1} \quad (5)$$

If we also define a generalized displacement vector $\mathbf{u}^e = (u_1^e, u_2^e, u_3^e, \varphi^e)$ then the perfect bonding conditions in (4) become

$$\mathbf{u}^* = \mathbf{u}^e ; \quad \phi^* = \phi^e \quad \text{on } C \quad (6)$$

We suppose that a uniform stress $\sigma^e = \sigma^\infty$ and electric displacements $\mathbf{D}^e = \mathbf{D}^\infty$ are applied at infinity. The corresponding solution for the homogeneous plane is:

$$\mathbf{u}^\infty = x_1 \gamma_1^\infty + x_2 \gamma_2^\infty ; \quad \phi^\infty = x_1 \mathbf{t}_2^\infty - x_2 \mathbf{t}_1^\infty \quad (7)$$

where $\gamma_1^\infty = (\epsilon_{11}^\infty, 0, 2\epsilon_{13}^\infty, -E_1^\infty)$, $\gamma_2^\infty = (2\epsilon_{21}^\infty, \epsilon_{22}^\infty, 2\epsilon_{23}^\infty, -E_2^\infty)$, $\mathbf{t}_1^\infty = (\sigma_{11}^\infty, \sigma_{12}^\infty, \sigma_{13}^\infty, D_1^\infty)$ and $\mathbf{t}_2^\infty = (\sigma_{21}^\infty, \sigma_{22}^\infty, \sigma_{23}^\infty, D_2^\infty)$. Then the general expression for the perturbations $\mathbf{u} = \mathbf{u}^e - \mathbf{u}^\infty$ and $\phi = \phi^e - \phi^\infty$ is:

$$\mathbf{u}(z) = 2\Re(\mathbf{A}\mathbf{F}(\mathbf{Z})) \quad ; \quad \phi(z) = 2\Re(\mathbf{B}\mathbf{F}(\mathbf{Z})) \quad (8)$$

$$\mathbf{u}^*(z) = 2\Re(\mathbf{A}^*\mathbf{F}^*(\mathbf{Z}^*)) \quad ; \quad \phi^*(z) = 2\Re(\mathbf{B}^*\mathbf{F}^*(\mathbf{Z}^*)) \quad (9)$$

with $\mathbf{F}(\mathbf{Z}) = (F_1(z_1), F_2(z_2), F_3(z_3), F_4(z_4))$, $\mathbf{Z} = (z_1, z_2, z_3, z_4)$ and where $z = x_1 + ix_2$, $z_\alpha = x_1 + p_\alpha x_2$, $\alpha = 1, 2, 3, 4$. The complex numbers p_α are the eigenvalues with positive imaginary parts and $A_{k\alpha}$ are the eigenvectors of the problem:

$$(Q_{lk} + p_\alpha(R_{lk} + R_{kl}) + p_\alpha^2 T_{lk})A_{k\alpha} = 0 \quad (10)$$

without summation on α and where the matrices \mathbf{Q} , \mathbf{R} and \mathbf{T} are constructed with the material constants (e.g. Suo *et al.* 1992, Dascalu and Maugin 1995). We assume that the eigenvalues p_α are all distinct. The matrix \mathbf{B} is given by $B_{i\alpha} = R_{ki}A_{k\alpha} + p_\alpha T_{ik}A_{k\alpha}$. The corresponding quantities $\mathbf{F}^*(\mathbf{Z}^*)$, \mathbf{Z}^* , z_α^* , p_α^* , $A_{i\alpha}^*$, $B_{i\alpha}^*$ are defined in a similar way.

We also introduce the stress-like vectors

$$\mathbf{t}_1 = (\sigma_{11}, \sigma_{12}, \sigma_{13}, D_1) \quad ; \quad \mathbf{t}_2 = (\sigma_{21}, \sigma_{22}, \sigma_{23}, D_2) \quad (11)$$

and the diagonal matrix $\mathbf{P} = \text{diag} [p_1, p_2, p_3, p_4]$. By substituting \mathbf{u} , \mathbf{u}^* , ϕ and ϕ^* from (8-9) in the interface relations (6), we obtain

$$\mathbf{u}^\infty(z) + 2\Re(\mathbf{A}\mathbf{F}(\mathbf{Z})) = 2\Re(\mathbf{A}^*\mathbf{F}^*(\mathbf{Z}^*)) \quad (12)$$

$$\phi^\infty(z) + 2\Re(\mathbf{B}\mathbf{F}(\mathbf{Z})) = 2\Re(\mathbf{B}^*\mathbf{F}^*(\mathbf{Z}^*)) \quad (13)$$

for $z \in C$. These equations will be studied in the following section.

4. PIEZOELECTRIC INCLUSIONS

In order to solve the equations (12-13) we look for $F_\alpha(z_\alpha)$ in the form

$$\begin{aligned} F_\alpha(z_\alpha) &= -\frac{1}{\pi i} \int_{c_\alpha}^{d_\alpha} \frac{\widetilde{f}_\alpha(\xi)}{\sqrt{(d_\alpha - \xi)(\xi - c_\alpha)}} \ln(z_\alpha - \xi) d\xi \\ &= -\frac{1}{\pi i} \int_{-1}^1 \frac{f_\alpha(t)}{\sqrt{1-t^2}} \ln\left(z_\alpha - \frac{c_\alpha + d_\alpha}{2} - \frac{d_\alpha - c_\alpha}{2}t\right) dt \end{aligned} \quad (14)$$

with $c_\alpha, d_\alpha \in C$ belonging to \mathcal{D}^* . Note that each potential function F_α will be given by a different distribution of line sources. From the asymptotic development of $F_\alpha(z_\alpha)$ one can deduce the formulae

$$\frac{1}{2}(F_\alpha(z_{\alpha+}) + F_\alpha(z_{\alpha-})) = \mathcal{K}_0 f_\alpha(x_1) + \varepsilon p_\alpha \mathcal{K}_1 f_\alpha(x_1) + O(\varepsilon^2) \quad (15)$$

$$\frac{1}{2}(F_\alpha(z_{\alpha+}) - F_\alpha(z_{\alpha-})) = \mathcal{L}_0 f_\alpha(x_1) + \varepsilon p_\alpha \mathcal{L}_1 f_\alpha(x_1) + O(\varepsilon^2) \quad (16)$$

for $z_{\alpha\pm} = x_1 + p_\alpha \varepsilon Y_\pm(x_1)$ and $x_1 \in (-1, 1)$. Here \mathcal{K} and \mathcal{L} are integral operators. In these relations we have $f_\alpha = f_\alpha(x_1, \varepsilon)$ and we develop the density functions f_α as

$$f_\alpha(x_1, \varepsilon) = f_\alpha^0(x_1) + \varepsilon f_\alpha^1(x_1) + O(\varepsilon^2) \quad (17)$$

In what concerns the solution in the interior domain \mathcal{D}^* we use a Taylor expansion about $\varepsilon = 0$:

$$F_\alpha^*(z_{\alpha\pm}) = f_\alpha^*(x_1) + p_\alpha^* \varepsilon Y_\pm(x_1) f_\alpha^{*(1)}(x_1) + O(\varepsilon^2) \quad (18)$$

where $f_\alpha^{*(1)} \equiv \frac{df_\alpha^*}{dx_1}$. Similarly, we set

$$f_\alpha^*(x_1, \varepsilon) = f_\alpha^{0*}(x_1) + \varepsilon f_\alpha^{1*}(x_1) + O(\varepsilon^2) \quad (19)$$

These asymptotic expansions will be used in the equations (12-13). Before that, we introduce the following real densities, written in vectorial form:

$$\mathbf{u}^n(x_1) = 2\Re(\mathbf{A}\mathbf{f}^n(x_1)) \quad ; \quad \phi^n(x_1) = 2\Re(\mathbf{B}\mathbf{f}^n(x_1)) \quad (20)$$

$$\mathbf{u}^{n*}(x_1) = 2\Re(\mathbf{A}^*\mathbf{f}^{n*}(x_1)) \quad ; \quad \phi^{n*}(x_1) = 2\Re(\mathbf{B}^*\mathbf{f}^{n*}(x_1)) \quad (21)$$

for $n = 0, 1$. By addition and subtraction of the equations (12-13) and by use of the expansions (15-19), after identification of the coefficients of each power of ε , we obtain equations for the real densities \mathbf{u}^n , ϕ^n , \mathbf{u}^{n*} and ϕ^{n*} . The solution involves the matrices $\mathbf{S} = i(2\mathbf{A}\mathbf{B}^T - \mathbf{I})$, $\mathbf{H} = 2i\mathbf{A}\mathbf{A}^T$ and $\mathbf{L} = -2i\mathbf{B}\mathbf{B}^T$, introduced by Barnett and Lothe (1975). They are real and nonsingular, \mathbf{H} and \mathbf{L} being symmetric. Consider also

$$\mathbf{N}_1 = -\mathbf{T}^{-1}\mathbf{R}^T; \mathbf{N}_2 = \mathbf{T}^{-1}; \mathbf{N}_3 = \mathbf{R}\mathbf{T}^{-1}\mathbf{R}^T - \mathbf{Q} \quad (22)$$

The matrices \mathbf{N}_2 and \mathbf{N}_3 are symmetric.

As an example, we give below the solution of $O(\varepsilon)$:

$$\mathbf{u}^1(x_1) = -\frac{D'(x_1)\sqrt{1-x_1^2}}{2\sqrt{D(x_1)}} \mathbf{d}^{1,\infty}, \quad \phi^1(x_1) = -\frac{D'(x_1)\sqrt{1-x_1^2}}{2\sqrt{D(x_1)}} \mathbf{d}^{2,\infty} \quad (23)$$

$$\mathbf{u}^{*1}(x_1) = S(x_1) \mathbf{d}^{1,\infty} + (\mathbf{S}\mathbf{d}^{1,\infty} + \mathbf{H}\mathbf{d}^{2,\infty}) \frac{1}{\pi} \int_{-1}^1 \frac{\sqrt{D(t)}}{t-x_1} dt \quad (24)$$

$$\phi^{*1}(x_1) = S(x_1) \mathbf{d}^{2,\infty} - (\mathbf{L}\mathbf{d}^{1,\infty} - \mathbf{S}^T \mathbf{d}^{2,\infty}) \frac{1}{\pi} \int_{-1}^1 \frac{\sqrt{D(t)}}{t-x_1} dt \quad (25)$$

where we have introduced $\mathbf{d}^{1,\infty} = \gamma_2^\infty - \mathbf{N}_1^* \gamma_1^\infty - \mathbf{N}_2^* \mathbf{t}_2^\infty$ and $\mathbf{d}^{2,\infty} = -(\mathbf{t}_1^\infty + \mathbf{N}_3^* \gamma_1^\infty + \mathbf{N}_1^{*T} \mathbf{t}_2^\infty)$

Let us explicitly calculate this solution for some specific geometries of the interface boundary C . For an inclusion of elliptic geometry we have

$$S(x_1) = 0 \quad ; \quad D(x_1) = 1 - x_1^2 \quad (26)$$

When (26) are used in the general solutions (23-25) we find

$$\mathbf{u}^1(x_1) = x_1 \mathbf{d}^{1,\infty} \quad ; \quad \phi^1(x_1) = x_1 \mathbf{d}^{2,\infty} \quad (27)$$

These solutions provide the expressions of generalized stresses at the interface:

$$\mathbf{t}_1 = -\varepsilon x_1 [(\mathbf{N}_3 \mathbf{d}^{1,\infty} + \mathbf{N}_1^T \mathbf{d}^{2,\infty}) \hat{h}^\pm(x_1) + ((\mathbf{N}_3 \mathbf{S} - \mathbf{N}_1^T \mathbf{L}) \mathbf{d}^{1,\infty} + (\mathbf{N}_1^T \mathbf{S}^T + \mathbf{N}_3 \mathbf{H}) \mathbf{d}^{2,\infty}) \tilde{h}^\pm(x_1)] \quad (28)$$

$$\mathbf{t}_2 = -\varepsilon x_1 [\hat{h}^\pm(x_1) - (\mathbf{L} \mathbf{d}^{1,\infty} - \mathbf{S}^T \mathbf{d}^{2,\infty}) \tilde{h}^\pm(x_1)] \quad (29)$$

where \hat{h}^\pm and \tilde{h}^\pm are the real and the imaginary parts of h^\pm . By introducing

$$\mu(x_1) = \arg(1 + x_1(1 - \frac{\varepsilon^2 p_\alpha^2}{2}) + \varepsilon p_\alpha Y_\pm), \quad \nu(x_1) = \arg(1 - x_1(1 - \frac{p_\alpha^2 \varepsilon^2}{2}) - \varepsilon p_\alpha Y_\pm) \quad (30)$$

with $\mu = 0$ and $\nu = 0$ for $\varepsilon = 0$, we can completely explicitate (28-29). We shall do this for $x_1 = \pm 1$ (when $Y_{\pm} = 0$). We have

$$h^{\pm}(\pm 1) = \frac{\cos(\frac{\mu+\nu}{2}(\pm 1)) - i \sin(\frac{\mu+\nu}{2}(\pm 1))}{\varepsilon \sqrt{\{[2 \mp \frac{\varepsilon^2}{2}(\bar{p}_{\alpha}^2 - \tilde{p}_{\alpha}^2)]^2 + \varepsilon^4 \bar{p}_{\alpha}^2 \tilde{p}_{\alpha}^2\} [\bar{p}_{\alpha}^2 \tilde{p}_{\alpha}^2 + \frac{1}{4}(\bar{p}_{\alpha}^2 - \tilde{p}_{\alpha}^2)^2]}} \quad (31)$$

where \bar{p}_{α} and \tilde{p}_{α} stand for the real and, respectively, imaginary parts of p_{α} . Substitution into (28-29) shows that, at the endpoints, the stresses and the electric displacements have the same order (in ε) as those given at the infinity. In the purely elastic case, this result was obtained in Homentcovschi and Dascalu (2000) for isotropic materials.

Consider now a lemon-shaped piezoelectric inclusion. In this case, the boundary C is described by

$$S(x_1) = 0; \quad D(x_1) = (1 - x_1^2)^3 \quad (32)$$

With these solutions, we obtain the displacement-like vectors at the interface as

$$\mathbf{u}(x_1) = \varepsilon \left[\frac{2x_1^3 - 3x_1}{2} (\mathbf{S}\mathbf{d}^{1,\infty} + \mathbf{H}\mathbf{d}^{2,\infty}) \mp \sqrt{(1 - x_1^2)^3} \mathbf{d}^{1,\infty} \right] \quad (33)$$

and the interface generalized stresses

$$\mathbf{t}_1 = -\varepsilon \left[\frac{3}{2}(2x_1^2 - 1)((\mathbf{N}_3\mathbf{S} - \mathbf{N}_1^T\mathbf{L}))\mathbf{d}^{1,\infty} + (\mathbf{N}_1^T\mathbf{S}^T + \mathbf{N}_3\mathbf{H})\mathbf{d}^{2,\infty} \right. \\ \left. \pm 3x_1\sqrt{1 - x_1^2}(\mathbf{N}_3\mathbf{d}^{1,\infty} + \mathbf{N}_1^T\mathbf{d}^{2,\infty}) \right] \quad (34)$$

$$\mathbf{t}_2 = \varepsilon \left[\frac{3}{2}(2x_1^2 - 1)(-\mathbf{L}\mathbf{d}^{1,\infty} + \mathbf{S}^T\mathbf{d}^{2,\infty}) \pm 3x_1\sqrt{1 - x_1^2}\mathbf{d}^{2,\infty} \right] \quad (35)$$

for $|x_1| < 1$.

Since the vectors \mathbf{t}_1 and \mathbf{t}_2 have physical relevance, it is important to compare the formulae (34-35), with the corresponding ones (28-29), for elliptic inclusions. While in the elliptic case the endpoints mechanical stresses and electric displacements have the same order as the remote fields, for a lemon-shaped inclusion they are an order-of-magnitude smaller. That is, the lemon-shaped inclusion is more convenient than the elliptic one, from the point of view of the mechanical resistance of the composite structure.

Finally, for a lemon shaped inclusion we give the generalized displacements and stresses on the axis Ox_1 with $|x_1| > 1$. We have

$$\mathbf{u}(x_1) = \varepsilon \left\{ \left[\frac{3}{4}(\operatorname{sgn}(x_1)\sqrt{x_1^2 - 1} - x_1) \right. \right. \\ \left. \left. - \frac{1}{4}(\operatorname{sgn}(x_1)\sqrt{x_1^2 - 1} - x_1)^3 \right] (\mathbf{S}\mathbf{d}^{1,\infty} + \mathbf{H}\mathbf{d}^{2,\infty}) \right\} \quad (36)$$

where $\operatorname{sgn}(x_1) = 1$ for $x_1 > 1$ and $\operatorname{sgn}(x_1) = -1$ for $x_1 < -1$. The stress-like vector functions up to $O(\varepsilon)$ are given by

$$\mathbf{t}_1 = \varepsilon \left[\frac{3}{2}(1 - 2x_1^2 + 2|x_1|\sqrt{x_1^2 - 1}) \right. \\ \left. \times ((\mathbf{N}_3\mathbf{S} - \mathbf{N}_1^T\mathbf{L}))\mathbf{d}^{1,\infty} + (\mathbf{N}_1^T\mathbf{S}^T + \mathbf{N}_3\mathbf{H})\mathbf{d}^{2,\infty} \right] \quad (37)$$

$$\mathbf{t}_2 = -\varepsilon \left[\frac{3}{2}(1 - 2x_1^2 + 2|x_1|\sqrt{x_1^2 - 1})(-\mathbf{L}\mathbf{d}^{1,\infty} + \mathbf{S}^T\mathbf{d}^{2,\infty}) \right] \quad (38)$$

Note that at the endpoints, the formulae (33-35) and, respectively, (36-38) provide the same fields values.

5. CONCLUSIONS

Uniform valid asymptotic solutions for arbitrary-shaped lamellar inhomogeneities embedded in infinite piezoelectric materials were obtained. Real-form expressions of the elastic and electric fields at the common boundary of the two bodies and on the Ox_1 -axis, outside the lamellar domain, have been obtained.

As concrete examples, we considered the case of an elliptic lamellar piezoelectric inclusion, corresponding to finite curvature radius at the ends, and also the case of a lemon-shaped inclusion, when we have a zero radius of curvature at the ends of the body. It was found that, while for elliptic piezoelectric inclusions the perturbation stresses and electric displacements at the inclusion ends have the same order as the fields given at infinity, for a lemon-shaped inclusion they are an order-of-magnitude smaller. The result is important since the stress and the electric displacement concentrations may strongly affect the mechanical resistance of composite structures.

Similar solutions have been obtained for rigid inclusions of electric conductor and also for cracks with/without inside electric field.

References

- [1] Barnett, D.M., Lothe, J., 1975, Dislocations and line charges in anisotropic piezoelectric insulators. *Phys. Status Solidi B* 67, 105-111.
- [2] Dascalu, C., Maugin, G.A., 1995, On the dynamic fracture of piezoelectric materials, *Q.J. Mech. appl. Mat.* 48, p. 237-251.
- [3] Dascalu, C., Homentcovschi, D., 1999, Uniform asymptotic solutions for lamellar inhomogeneities in anisotropic elastic solids, *SIAM J. Appl. Math.* 60, pp.18-42.
- [4] Geer, J.F., Keller, J.B., 1968, Uniform asymptotic solutions for potential flow around a thin airfoil and the electrostatic potential about a thin conductor, *SIAM J. Appl. Math.* 16, pp. 75-101.
- [5] Homentcovschi, D., 1984, Uniform asymptotic solutions of two-dimensional problems of elasticity for the domain exterior to a thin region, *SIAM J. Appl. Math.* 44 , pp. 1-10.
- [6] Homentcovschi, D., Dascalu, C., 2000, Uniform asymptotic solutions for lamellar inhomogeneities in plane elasticity, *J. Mech. Phys. Solids* 48, 153-173.
- [7] Maugin, G.A., 1988, *Continuum mechanics of electromagnetic solids*, North-Holland, Amsterdam.
- [8] Suo, Z., Kuo, C-M., Barnett, D.M., Willis, J.R., 1992, Fracture mechanics for piezoelectric ceramics, *J. Mech. Phys. Solids* 40, pp. 739-765.
- [9] Ting, T.C.T., 1996, *Anisotropic elasticity: theory and applications*, Oxford University Press, New York.

6th National Congress on Mechanics

Session C

Volume II

ON THE STOCHASTIC MICROMECHANICAL THEORY OF DISCRETE MATERIAL SYSTEMS

Y. M. Haddad

Department of Mechanical Engineering
University of Ottawa, Ottawa, Ontario K1N 6N5, Canada

1. SUMMARY

This paper first introduces the basic concepts and postulates pertaining to the stochastic micromechanical theory of discrete material systems. Here, continuum mechanics concepts are generally replaced by considerations of microstructural response variables in the form of discrete statistical functions. Second, the deformation kinematics are presented in the light of the geometry of the underlying random microstructure. The latter is established within well-defined measuring scales defining the levels of observation into the material system. In this context, the establishment of the connection between the response behaviour of the individual elements of the microstructure, their interactional effects, and the observable macroscopic behaviour would be an essential requirement. The fulfilment of such requirement seems possible by the introduction of the principles of set theory, together with the concepts of measure theory. The formulation of the micromechanical behaviour of the discrete material system is then attempted via material operators within the scope of a deformation process of a Markov-type which leads to Chapman-Kolmogorov functional presentation.

2. INTRODUCTION

The micromechanical approach has been recognized as a promising tool for the description of the response behaviour of engineering materials with the inclusion of the so-called "*local*" or "*microstructural*" effects. The microstructure of a large class of such materials, however, is discrete in the sense of being heterogeneous and/or discontinuous. In view of this fact, the so-called "*deterministic micromechanics*", that are based on the concepts of continuum mechanics, could no longer be accepted for the interpretation of the experimental results concerning the behaviour of discrete materials. It has been, therefore, increasingly appreciated that a more appropriate representation of the response behaviour of real materials would only be achieved by including the random characteristics of the inherent microstructure. Further, the response behaviour of such microstructure is often time- and/or loading-history dependent. Thus, the

inherent deformation process and its space- and time-evolutions are expected to be stochastic. In this context, the establishment of the connections between the response behaviour of the individual elements of the microstructure, their interactional effects, and the observable macroscopic behaviour would be an essential objective. Thus, in the stochastic micromechanical formulations, continuum mechanics concepts are generally replaced by considerations of microstructural response variables in the form of discrete statistical functions. The latter are established within well-defined "*measuring scales*" defining the levels of observation into the material system. Thus, in order to describe the mechanical response of the material from a microstructural point of view, it is necessary to consider the response of the individual structural elements which on a local scale could differ considerably from an average response if the phenomenological continuum approach was taken. Such local deviations in the response, which are usually neglected if one ignores the microstructure, are directly related to basic properties of the nonhomogeneous material system. Accordingly, the present analysis begins with a definition of the "*structural element*" of the particular material system under consideration and deals with the formulation of its response behaviour in a probabilistic sense. In order to extend the analysis to the practical case of a macroscopic material system, it is necessary to make use of "*intermediate quantities*" arising from the consideration of the existence of a statistical ensemble of structural elements within an intermediate domain of the material specimen. Further, it is equally important to find a connection between the microscopic and the macroscopic response formulations. Thus, the analysis aims at the formulation of a set of "*governing response equations*" for the structured material system that, in contrast to the classical continuum mechanics formulations, are based on the concepts of statistical theory and probabilistic micromechanics; see Axelrad [1,2], Haddad [3,4], and Axelrad and Haddad [5]. In this context, it has been found useful to employ operational representation of the various relations. Hence, the notion of a "*Material Operator*" characteristic of the response behaviour of an intermediate domain of the material is introduced. This material operator provides the connection between the stress field and the occurring deformations within the material domain under consideration; it contains in its argument those stochastic variables or functions of such variables distinctive of the response behaviour of the microstructure.

3. THE STOCHASTIC MICROMECHANICAL APPROACH

The following four basic concepts constitute the basis of the stochastic micromechanical approach introduced in this paper:

- 1) The microstructure of the material being dealt with is random in nature. This would translate into both geometrical and physical randomness, which by virtue would lead to randomness in response behaviour on the microscopic level.
- 2) In view of the randomness of the microstructure, as stipulated under (i) above, the micromechanical approach, presented here, adopts the concepts of the mathematical theory of probability and statistical micromechanics. As the inherent deformation process of the material microstructure is often time-dependent, the pertaining evolution process will be generally stochastic.
- 3) Three measuring scales.
Structural element. Such an element, be it physical as for example one crystal in a polycrystalline solid or numerical as in the identification of a statistical trial, may be indexed and countable. A structural element ' κ ' is defined as the smallest part of the medium that represents the mechanical and physical characteristics of the microstructure at the '*micro*' level. In case of a polycrystal, for instance, this

element may be chosen to represent an individual grain (*microelement*) of the microstructure as well as the binding interaction between two matching grains.

Mesodomain. It is associated with a countable set (finite) of structural elements ' κ '; ($\kappa = 1, \dots, n$) where n is large enough to comply with the law of large numbers of statistical theory. The '*meso*' scale is of utmost significance, in the stochastic micromechanical approach, since it defines a statistical set of structural elements where all the statistics of the physical, geometrical and field quantities governing the behaviour of the elements of the microstructure are considered.

Macrodomain. It is defined as the union of disjoint mesodomains. It is the mathematical manifold representing the macroscopic body of the medium.

- 4) Material operator. It provides the connection between the stress field and the occurring deformations within the particular mesodomain under consideration. Such material operator contains in its argument those stochastic variables or functions of such variables distinctive of the response behaviour of the real microstructure.

3.1 Deformation Kinematics

Following the concepts of the micromechanical theory of structured media [1-6], all microscopic field quantities within the intermediate domain are considered to be stochastic functions of primitive random variables. Thus, the components of the microstress, for instance, are seen as stochastic functions ${}^{\kappa}\xi_i(\mathbf{r}, t)$ that can be regarded as a family of random variables ${}^{\kappa}\xi_i(\mathbf{r})$ within the intermediate domain depending on the time parameter t , or a family of curves ${}^{\kappa}\xi_i(t)$ depending on the structural element position vector ${}^{\kappa}\mathbf{r}$. The basic kinematic quantities pertaining to the deformation of the material microstructure considered here are the microelement deformation vector:

$${}^{\alpha}\mathbf{d}: {}^{\alpha}d_i; i = 1, 2, 3$$

and the interfacial bonding deformation within the inter-elemental boundary ' $\alpha\beta$ ' between two adjoining microstructural elements α and β , i.e.

$${}^{\alpha\beta}\mathbf{d}: {}^{\alpha\beta}d_j; j = 1, 2, 3$$

Within a mesodomain of the medium, the above kinematic quantities are considered to be stochastic functions of primitive random variables.

The basic kinematic parameters, at any particular time, which describe the changes that have taken place in the structural element, may be seen as the outcome (κ) due to the deformation process and is designated by

$${}^{\kappa}\eta: {}^{\kappa}\eta_{\zeta} \quad \zeta = 1, 2, \dots, m$$

where $\eta = 6$ represents the number of basic kinematic parameters above. The entire set of possible outcomes define the sample space \sum , i. e. ${}^{\kappa}\eta \in \sum$. It is understood, however, that due to experimental limitations, ${}^{\kappa}\eta$ cannot be determined in an exact fashion. This, then, calls for a "*parameter cell*" type of formulation which is common in statistical mechanics. Thus, the event Ξ is taken to be the experimentally specified parameter cell in \sum , such that

$$\Xi : (\eta, \eta + \Delta \eta) ; \Xi \in \Sigma$$

where $\Delta \eta$ is the experimental range of the measurement of the kinematic parameter. Thus, during the deformation process, the probability of the kinematic parameter being a value of the event Ξ is a probability measure that changes with time and may be designated by $\{\Xi\}$. Thus, one could identify this probability measure by arbitrarily setting

$$\{^a \eta \in \Xi\} \equiv \{\eta = \Omega\}$$

where Ω indicates a particular value of the event Ξ .

Now, consider the basic kinematic random deformation variable (vector) $\mathbf{d}_t(s)$ for some fixed time (s); the most convenient definition of such variable may be provided by the choice of the image set

$$\mathbf{d}_t(\eta, s) = \eta$$

i.e., the value of the random variable at this particular time (s) is the outcome η . Furthermore, the probabilistic distribution for the random variable is established by the condition that the set

$$\{\mathbf{d}_t(s) \leq \Omega\} = \{\eta \in \Sigma : \mathbf{d}_t(\eta, s) \leq \Omega\}$$

is an event for all values of $\Omega \in \Sigma$. The basic kinematic stochastic process \mathbf{d}_t can be considered, thus, as an extension of the foregoing, as a family of random variables $\{\mathbf{d}_t(s); s, t > 0\}$, where its probability distribution function can be read as

$$P \{\mathbf{d}_t(\Omega, t)\} = P \{\mathbf{d}_t \leq \Omega\}$$

3.2 Time-evolution of the Distributions of Local Strains (Markovian Models)

The theory of Markov processes provides a good approximation to the time-evolution of the distributions of local strains in a random microstructure [1,2]. In discussing such Markovian models, it may be instructive to consider first the response of the material during the “steady-state”, whereby the stochastic microstrain ε_t is a measurable function in the “time-continuous” case satisfying first order smoothness conditions in that space. In this context, One can consider a one-parameter family of transformations or mappings $\{L_t\}$ such that:

$$L_t : \varepsilon \rightarrow \sum(\varepsilon) \text{ for all } t \in T : [0, \infty] ; \varepsilon_t \in \sum(\varepsilon) \quad (1)$$

where T indicates the entire range of the experiment. If this space is identified with the space of all P^e -regular measurable function of ε , and correspondingly of $\dot{\varepsilon} \in \Sigma(\varepsilon)$, leads, by recognizing the duality with the stress-space or stress-rate space, respectively, as subspaces of the probability space X , to the establishment of constitutive relations in operational form (see Axelrad [1,2]). Hence, considering at any particular time $t \in T$, the whole process ε_t is representable by a set of function spaces where ε_t is a measurable function in the “time-continuous” case satisfying first

order smoothness conditions in that space [5]. Thus considering the time-sequence $t_1 < t_2 < \dots < t_n$, one may define an operator $L_{\Delta t}$ such that:

$$L_{\Delta t} E_r(\epsilon) = E_{r+1}(\epsilon); r = 1, 2, \dots, N-1, \Delta t = t_{r+1} - t_r \quad (2)$$

Hence for a purely reversible response by using the probabilistic distribution of microstrains P^ϵ , one has:

$$P^\epsilon \{ E_{r+1}(\epsilon) \} = P^\epsilon \{ E_r(\epsilon) \}; r = 1, 2, \dots, N-1 \quad (3)$$

In the theory of Markov processes, this operator is called "*transition probability*". It plays an important role in the description of the transient responses. Considering a closed time interval $[t, s] \in T$ and a point $\tau \in [t, s]$, $\tau > t$, this transition probability satisfies the Chapman-Kolmogorov relation (e.g., Bharucha-Reid [7]), i. e.,

$$P \{ t, s \} = \int P \{ t, \tau \} P \{ \tau, s \} d\tau \quad (4)$$

Writing a Borel set related to the strain space at time t_r corresponding to the state i and a Borel set at time t_s to another state j , one obtains for fixed i, j , as a replacement of the relation (4), the matrix relation:

$$P_{ij}(t_r + t_s) = \sum_k P_{ik}(t_r) P_{kj}(t_s) \quad (5)$$

for all possible states i, j . One can also write for the relationship (5):

$$\mathbf{P}(t_r + t_s) = \mathbf{P}(t_r) \mathbf{P}(t_s) \quad (6)$$

If the process is time-homogeneous, it has been shown in [1,2] that the transition probabilities $P_{ij}(t) \in \mathbf{P}$ satisfy certain limiting conditions. Hence, it may be concluded that, in general with reference to (6), the strain-time behaviour will be determined by the initial distribution at time t and the above transition probabilities. Consequently, introducing an intensity matrix \mathbf{Q} , one can rewrite the expression (6) in form of a matrix differential equation, viz:

$$\frac{d\mathbf{P}(t, s)}{dt} = \mathbf{Q}(t) \mathbf{P}(t, s); [t, s] \in T; \mathbf{P}(0) = \mathbf{I} \quad (7)$$

in which the elements of $\mathbf{Q}(t)$ can be denoted by an intensity factor λ , i. e.,

$$q_{ii} = -\lambda, \text{ for } i = 0, 1, 2, \dots \text{ and } q_{ij} = \begin{cases} \lambda & \text{for } j = i + 1 \\ 0 & \text{otherwise} \end{cases} \quad (8)$$

4. CASE-STUDIES

The presented stochastic micromechanical approach will be further demonstrated by giving reference to two classes of heterogenous materials; namely, a loading-history dependent polycrystalline solid and a time-history dependent fibrous structure.

5. CONCLUSIONS

In this paper, the material system is considered as a heterogenous medium of actual microstructural elements. These elements are seen to exhibit random geometrical and physical characteristics. Due to the discrete nature of the microstructure, the inherent deformation process and its space- and time- evolutions are seen to be stochastic. Thus, the overall response behaviour of the material is formulated by the use of probabilistic concepts and statistical theory. The formulation of the micromechanical behaviour of the discrete material system is then attempted via material operators within the scope of a deformation process of a Markov-type which leads to Chapman-Kolmogorov functional presentation.

6. ACKNOWLEDGEMENTS

The author wishes to acknowledge the financial grants provided to him by NSERC- Natural Sciences and Engineering Council of Canada.

7. REFERENCES

- [1] Axelrad, D. R., *Foundations of the Probabilistic Mechanics of Discrete Media*, Pergamon Press, Oxford (1984).
- [2] Axelrad, D. R., *Stochastic Mechanics of Discrete Media*, Springer-Verlag, Berlin (1993).
- [3] Haddad, Y. M., A Microstructural Approach to the Mechanical Response of a Class of Polycrystalline Systems, *Res Mechanica* (1990) 28, 177-196.
- [4] Haddad, Y.M., *Viscoelasticity of Engineering Materials*, Kluwer, Dordrecht (1995).
- [5] Axelrad, D. R. and Haddad, Y. M., On the Behavior of Materials with Binary Microstructures, in Proceedings NATO ARW, Kiev, Ukraine, *Advanced Multilayered and Fibre-Reinforced Composites*, Y. M. Haddad (Ed.), Kluwer, Dordrecht (1997).
- [6] Haddad, Y. M., *Mechanical Behaviour of Engineering Materials, Vol. 2: Dynamic Loading and Intelligent Material Systems*, Kluwer, Dordrecht (2000).
- [7] Bharucha Reid, A. T., *Elements of the Theory of Markov Processes and their Applications*, McGraw-Hill, NewYork (1960).

A CONSTITUTIVE LAW FOR POWDER COMPACTION

S. J. Subramanian and P. Sofronis

Department of Theoretical and Applied Mechanics and

Materials Research Laboratory

University of Illinois at Urbana-Champaign, Urbana, IL 61801, U.S.A.

1. ABSTRACT

A general methodology to obtain the overall strain-rate of powder compacts is presented. The strain-rate is derived from a potential function that depends on material properties, relative density of the compact, and external loads. The model developed and implemented in this study accounts for multiple deformation mechanisms and surface energy effects. Numerical results are presented for the case of diffusion-dominated densification.

2. INTRODUCTION

In powder densification, the closing of porosity typically occurs by various deformation mechanisms such as linear elasticity, rate-independent plasticity, power-law creep, diffusion along the interparticle contacts and pore surfaces, and interparticle slip (Ashby, 1974). Most of the models to date have dealt with these mechanisms in isolation, and hence effects of their interaction have not been studied. An overview of the analytical investigations into powder compaction can be found in the work of Cocks (1994).

A micromechanical model that captures the coupled action of power-law creep deformation in the bulk of the consolidating particles, stress-driven driven diffusion on the interparticle contact areas, and surface diffusion on the void surface in the presence of surface energy effects is employed in this paper (Subramanian and Sofronis, 2001a, 2001b). Following Hill (1967) and Sofronis and McMeeking (1992), a constitutive law is proposed in the form of a strain-rate potential which is quantitatively evaluated and validated through numerical computations.

3. MATERIAL CONSTITUTIVE LAWS

The bulk of the particles is incompressible and obeys the creep law

$$\dot{\epsilon}_{ij} = \frac{\partial \phi^c}{\partial \sigma_{ij}}, \quad (1)$$

where $\dot{\epsilon}_{ij} = (v_{i,j} + v_{j,i})/2$ is the creep strain rate, v_i is the velocity, ϕ^c is the creep potential such that

$$\phi^c = \frac{1}{1+n} \dot{\epsilon}_0 \sigma_0 \left(\frac{\sigma_e}{\sigma_0} \right)^{1+n}, \quad (2)$$

$\sigma_e = \sqrt{3s_{ij}s_{ij}/2}$ is the effective stress, $s_{ij} = \sigma_{ij} - (\sigma_{kk}/3)\delta_{ij}$ is the deviatoric stress, n is the creep exponent, $\dot{\epsilon}_0$ and σ_0 are material parameters in the uniaxial tension relation $\dot{\epsilon}/\dot{\epsilon}_0 = (\sigma/\sigma_0)^n$, δ_{ij} is the Kronecker delta, $(\cdot)_{,j} = \partial(\cdot)/\partial x_j$, and the superposed dot denotes differentiation with respect to time. From Eqs. (1) and (2), one obtains $\dot{\epsilon}_{ij} = 3C\sigma_e^{n-1}s_{ij}/2$, where $C = \dot{\epsilon}_0/\sigma_0^n$ is the creep modulus.

Diffusion along the interparticle contact areas or the pore surface is driven by chemical potential gradients such that

$$j_b = \mathcal{D}_b d\sigma_n/ds \quad (3)$$

along the interparticle area, and

$$j_p = \mathcal{D}_p d(\gamma_p k)/ds \quad (4)$$

along the pore surface. Here, j_b and j_p are the volumetric fluxes per unit length along a

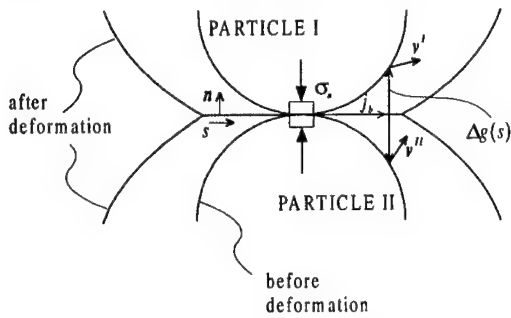


Figure 1. The interparticle contact area: s is the arclength, \mathbf{n} is the unit normal vector, σ_n is the normal stress, j_b is the flux and $\Delta g(s)$ is the non-negative gap function.

direction s tangential to the interparticle and the pore surface areas respectively, $\mathcal{D}_b = D_b \delta_b \Omega / KT$ and $\mathcal{D}_p = D_p \delta_p \Omega / KT$ are correspondingly interparticle and pore surface diffusivities having dimensions of volume divided by stress per unit time, D_b and D_p are the corresponding diffusion coefficients, δ_b and δ_p are the corresponding effective thicknesses through which matter diffuses, σ_n is the stress normal to the contact area between the particles, k and γ_p are respectively the curvature and the energy of the pore surface, Ω is the atomic volume of the diffusing species, K is Boltzmann's constant, and T is the

absolute temperature. Further, the tangential stresses vanish everywhere on the interparticle contact areas since these are assumed to be freely slipping.

Matter conservation along the interparticle contact area requires (Subramanian and Sofronis, 2001a)

$$\frac{dj_b(s)}{ds} + \dot{h}(s) = 0, \quad (5)$$

where $\dot{h}(s)$ is the normal overlapping rate that would have resulted had the particles been free to plough into one another. Along the pore surface, matter conservation dictates that

$$\frac{dj_p}{ds} + \dot{\alpha}(s) = 0, \quad (6)$$

where $\dot{\alpha}(s)$ is the local particle expansion rate (Subramanian and Sofronis, 2001a), measured normal to the particle surface, and is positive when matter is deposited on the pore surface and negative when the pore surface is eroded. Equilibrium at any arbitrary point on the pore surface is described by the standard Laplace equation (Rice and Chuang, 1981) that relates the normal stress σ_n in the adjoining bulk material to the local curvature k

$$\sigma_n(s) = \gamma_p k(s). \quad (7)$$

In the present model, surface tension γ_p is assumed to be constant and therefore, the tangential stress on the pore surface is zero (Rice and Chuang, 1981). At the junction of the contact area and the pore surfaces (tip), both volumetric flux and chemical potential are continuous.

4. THE UNIT CELL MODEL AND DIMENSIONLESS GROUPS

The problem of densification of a periodic square array of cylinders under hydrostatic loading is considered. Due to the symmetry of the square particle arrangement, the densification is studied by considering the deformation of just one quadrant of the cylinder. This particular choice of unit cell has been made in view of the fact that the normals to the contact areas are known *a priori*. This offers a significant simplification with respect to the numerical evaluation of the contact areas and reduces the number of iterations and computation time considerably. Starting with the variational statement of Needleman and Rice (1980), a variational scheme has been developed to solve the initial boundary value problem for the unit cell under small-strain conditions. Details of this small-strain scheme can be found in Subramanian and Sofronis (2001a, 2001b). A set of non-linear finite element equations is obtained and solved for the displacement increments and pore surface expansion increments. Since the size of the contact areas is not known beforehand and the particle bulk deforms nonlinearly, the numerical scheme is iterative.

The overall densification of the aggregate occurs under the simultaneous action of multiple mechanisms characterized by a large number of parameters. Therefore, in order to interpret the results of numerical computations meaningfully, it is necessary to obtain quantitative measures of the relative strengths of these mechanisms. To this end, a dimensional analysis has been performed over the geometric, material, and loading parameters, leading to the following dimensionless groups (Subramanian and Sofronis, 2001a, 2001b):

$$\psi_b = \frac{\gamma_b}{\sigma_a R}, \quad \psi_p = \frac{\gamma_p}{\sigma_a R}, \quad \chi_b = \frac{D_b}{C \sigma_a^{n-1} a^2 R}, \quad \chi_p = \frac{D_p \gamma_p}{C \sigma_a^n R^4}, \quad (8)$$

where R is the particle radius, a is a characteristic size of the area over which interparticle diffusion occurs, and σ_a is the applied macroscopic stress. The parameters χ_b and χ_p measure respectively the strength of the interparticle and surface diffusion processes relative to the power-law creep process in the bulk; ψ_b and ψ_p represent the strengths of the interface and pore surface tension in relation to the applied stress. With regard to the interparticle diffusion length scale a , since the present study pertains to the earlier stages of densification when the size of the contacts is quite small compared to the radius of the particles, a contact size of $R/20$ has been used for a .

5. STRAIN-RATE POTENTIAL

For the problem at hand, an *admissible* stress state $[\sigma_{ij}^*, T_i^*]$ is defined to be one that (i) obeys the equilibrium equations in the bulk of the particles A , (ii) satisfies traction boundary conditions such that $T_i^* = \sigma_{ij}^* n_j$ is equal to the traction specified on the surface S_T (n being the unit outward normal) where tractions are prescribed, and (iii) satisfies the Laplace relation $\sigma_n^* = \gamma_p k$ relating the normal stress to the curvature on S_p . On the other hand, by definition, a *kinematically admissible* state $[v_i^*, \dot{\epsilon}_{ij}^*, j_b^*]$ is such that the velocity field v_i^* (i) possesses

continuous first partial derivatives in A so that $\dot{\epsilon}_{ij}^* = (\dot{v}_{i,j}^* + \dot{v}_{j,i}^*)/2$, and (ii) relates to the flux field j_b^* through the mass conservation equation (5) on S_b . By writing out the principle of virtual power for any admissible stress state and admissible kinematic state, and making appropriate choices for each of these (Subramanian and Sofronis, 2001b), one arrives at the following expression for the macroscopic strain rate \dot{E}_{ij} :

$$\dot{E}_{ij} = \frac{\partial \Phi}{\partial \Sigma_{ij}}, \quad (9)$$

where

$$\Phi = \frac{1}{A} \left[\int_A \frac{1}{n+1} C \sigma_e^{n+1} dA + \int_{S_b} \frac{1}{2} \mathcal{D}_b \sigma_{n,s}^2 ds \right] \quad (10)$$

is the macroscopic potential for the deformation of the aggregate. The complete solution to the initial boundary value problem for the unit cell yields all the information necessary to numerically compute Φ .

Computations were carried out to simulate the hydrostatic compaction of TiAl wires with a radius of 5 microns at 625°C. Applied stresses $\Sigma_{11} = \Sigma_{22} = -\Sigma_m$ ranged from 200 to 600 MPa and the creep exponent n used was 2. Under these conditions, the computations indicated that the contribution to Φ from the first integral of Eqn. (10) was negligible, i.e., the densification was diffusion-dominated. Further, the computations also showed that the dimensionless potential $\Phi/C\Sigma_m^3$ was proportional to $1/\Sigma_m$. Since the dimensionless groups of Eqn. (8) depend on material and particle geometry parameters and the applied stress Σ_m , Φ is sought in the following form:

$$\Phi/C\Sigma_m^3 = \frac{c}{h(D)} \chi_b^{k_1} \chi_p^{k_2} \psi_p^{k_3} \psi_b^{k_4}, \quad \text{with} \quad h(D) = \left(\frac{D - \sqrt{D/D_0 - 1}}{D_0 - \sqrt{1 - D_0/D}} (1 - D_0/D) \right)^b, \quad (11)$$

where $D_0 = \pi/4$ is the initial relative density for the square array, i.e., when the cylinders are in point contact, and b, c, k_1, k_2, k_3 , and k_4 are constants to be determined. The expression above for $h(D)$ was arrived at by using simple qualitative arguments involving the power dissipated through interparticle diffusion and the geometry of the particle arrangement, as detailed in Subramanian and Sofronis, 2001b. Through a systematic program of computations, the undetermined parameters of Eqn. (11) are evaluated and the final result for Φ for the case of diffusion-dominated densification is

$$\frac{\Phi}{C\Sigma_m^3} = \frac{0.00469}{\left(\frac{D - \sqrt{D/D_0 - 1}}{D_0 - \sqrt{1 - D_0/D}} (1 - D_0/D) \right)^{1.65}} \frac{\chi_b^{0.9338} \chi_p^{0.0366}}{\psi_p^{0.0120}}. \quad (12)$$

Then, the in-plane macroscopic strain rate $\dot{E}_m = (\dot{E}_{11} + \dot{E}_{22})/2$ can be calculated straightforwardly from Eqn. (9) using the above expression, and the result is

$$\frac{\dot{E}_m}{C\Sigma_m^2} = \frac{0.00469}{\left(\frac{D - \sqrt{D/D_0 - 1}}{D_0 - \sqrt{1 - D_0/D}} (1 - D_0/D) \right)^{1.65}} \frac{\chi_b^{0.9338} \chi_p^{0.0366}}{\psi_p^{0.0120}} \quad (13)$$

6. DISCUSSION

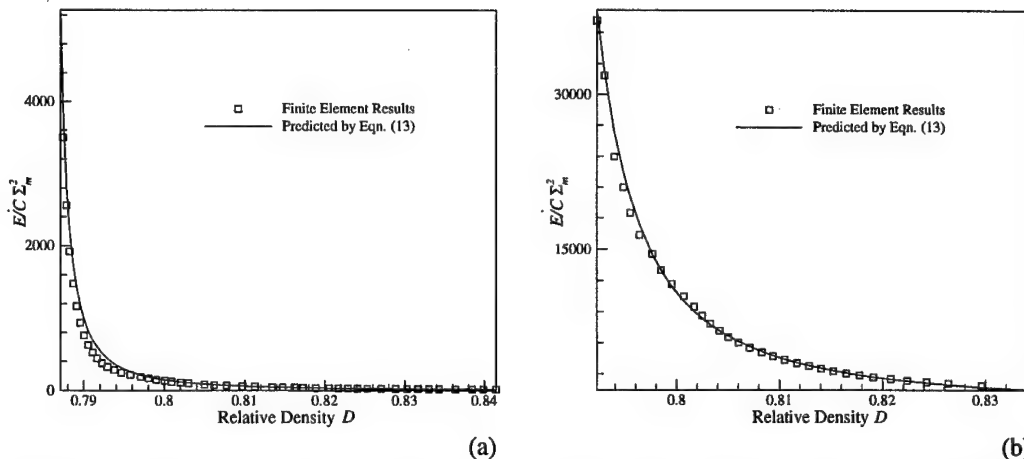


Figure 2. Strain rates predicted by Eqn. (13) and those obtained directly from FEM calculations with $\chi_p = 1000$, $\psi_p = 0.001$, and $\psi_b = 0.00033$; $\chi_b = 40$ in (a) and $\chi_b = 4000$ in (b).

The predictive capabilities of Eqn. (12) were evaluated using comparisons of Eqn. (13) with strain rates obtained directly from finite-element computations. Shown in Fig. 3a is the comparison for a case of pore surface diffusion that is fast relative to interparticle diffusion, which itself is faster than the power-law creep process, whereas in the Fig. 3b the diffusion processes are of comparable strengths, both being much faster than the creep process. The figures show that in both cases, the present model predicts the macroscopic strain rates very accurately. Indeed, more such comparisons were made for the cases of extremely fast surface diffusion and very slow surface diffusion, and even in these cases the present model is very effective in predicting the strain rates (Subramanian and Sofronis, 2001b). Thus, the predicted strain rates are accurate over a wide range of material and loading parameters, and therefore one can deem the present model to be a fairly robust one for diffusion-dominated densification.

Although the present model is similar to existing models (McMeeking and Kuhn, 1992; Riedel, 1990) in that it pertains to diffusion-dominated densification, it differs markedly in that it accounts for pore surface diffusion of arbitrary strength, as well as surface energy. Numerical results indicate that the neglect of these features leads to significantly different macroscopic strain rates (Subramanian and Sofronis, 2001b).

7. CLOSURE

A general framework for the derivation of macroscopic constitutive laws for powder compaction has been presented. This framework has been applied to the case of diffusion-dominated isostatic compaction of cylinders. The procedure used is based on numerical

computations starting from point contact between particles and studying the evolution of deformation with time. The derived constitutive law has been shown to be very sensitive to relative density; and is almost linearly dependent on the interparticle diffusion strength. Further, it exhibits significant dependence on the pore surface energy and the rate of the pore surface diffusion process.

Acknowledgement: This work was supported by the Department of Energy under grant DEFGO2-91ER45439.

8. REFERENCES

- [1] Ashby, M. F., 1974. A first report on sintering diagrams. *Acta Metal.* 22 (3), 275-289.
- [2] Cocks, A. C. F., 1994. The structure of constitutive laws for the sintering of fine-grained materials. *Acta Metal. Mater.* 42 (7), 2191-2210.
- [3] Hill, R., 1967. The essential structure of constitutive laws for metal composites and polycrystals. *J. Mech. Phys. Solids.* 15 (1), 79-95.
- [4] McMeeking, R. M. and Kuhn, L. T., 1992. A diffusional creep law for powder compacts. *Acta Metal. Mater.* 40 (5), 961-969.
- [5] Needleman, A. and Rice, J. R., 1980. Plastic creep flow effects in the diffusive cavitation of grain boundaries. *Acta Metal.* 28 (10), 1315-1332.
- [6] Rice, J. R. and Chuang, T.-J., 1981. Energy variations in diffusive cavity growth. *J. Am. Cer. Soc.* 64 (1), 46-53.
- [7] Riedel, H. 1990. A constitutive model for the finite-element simulation of sintering - distortions and stresses. In: *Ceramic Transactions, Ceramic Powder Science III* (eds. G. L. Messing, S.-I. Hirano and H. Hausner), Vol. 12, pp. 619-630, Westerville, Ohio.
- [8] Sofronis, P. and McMeeking, R. M., 1992. Creep of power-law material containing spherical voids. *J. Appl. Mech.* 59 (2), 88-95.
- [9] Subramanian, S. J. and Sofronis, P., 2001a. Modeling the interaction between densification mechanisms in powder compaction. To appear in *Int. J. of Sol. Struct.*
- [10] Subramanian, S. J. and Sofronis, P., 2001b. On the calculation of a constitutive potential for isostatic compaction. In preparation.

CONTINUUM MICROPOLAR MODELLING OF DISCONTINUOUS MASONRY-LIKE SYSTEMS

P. Trovalusci

Dipartimento di Ingegneria Strutturale e Geotecnica
University of Rome "La Sapienza", 00197 Rome, Italy

R. Masiani

Dipartimento di Ingegneria Strutturale e Geotecnica
University of Rome "La Sapienza", 00197 Rome, Italy

1. SUMMARY

A constitutive micropolar model to describe the mechanical behaviour of masonry-like systems (i.e. brick-block masonry, jointed rocks, matrix/particle composite) is proposed. The model is derived by requiring the equivalence in terms of virtual work with a lagrangian system of rigid interacting particles. Assuming linear elastic or no-tension and frictional interactions for the discrete assembly, linear elastic and non-linear response functions for the stress measures of the Cosserat continuum are derived respectively. This model proves effective in modelling problems in which the work of the skew-symmetrical part of the stress or the work of the microcouples is important.

2. INTRODUCTION

A micropolar continuum equivalent to discrete systems of rigid particles interacting two by two is proposed. It can represent the behaviour of brick/block masonry as well as jointed rocks or matrix/particle composites. The behaviour of these media depends on the mechanical properties of the constituents and is strongly influenced by the shape, the size, the orientation and the arrangement of the units. Although a detailed modelling, based on the description of these media as discrete systems, is the most obvious way of taking into account the above features [1], it is often advisable to opt for a macroscopic modelling in terms of continuum. In earlier works [2, 3], an integral procedure of equivalence has been adopted to identify the effective moduli of a linear elastic Cosserat continuum. According to the molecular theory of elasticity [4], this procedure requires the equivalence of the virtual power expended by a lagrangian system of interacting blocks and the micropolar continuum in "corresponding" motions. Even in the elastic frame, such Cosserat continuum shows various important possibilities: the possibility of taking into account the geometry and the texture of the units, besides the mechanical properties of the components; the possibility to discern the behaviour of systems made of different size; the possibility to describe the effect of the geometrical and mechanical unsymmetries along different planes. These last two features cannot be described

using a Cauchy continuum. Moreover, with regard to the first feature, the response of a Cauchy material is even less marked, compared to a Cosserat continuum, to the variation in the masonry texture, that is the variation of the symmetry class of the material. This because the symmetry group of the Cosserat material, which proves to correspond to the one of the lagrangian system, is in general included in the symmetry group of the classical material [3].

In this work, in order to take into account the low capability to carry tensions and the friction at the interfaces between elements, a non-linear constitutive micropolar model is derived using the same equivalence procedure and defining non-linear response functions for the interactions in the lagrangian system. The non-linear problem is solved through a finite element procedure based on the iterative adjustment of the constitutive tensor due to the occurrence of some limit situation for the contact actions in the discrete model. Various numerical analyses carried out on masonry walls, made of blocks of different size, point out the above essential features and the differences between the classical and the micropolar model, which are amplified in the non-linear frame.

2. LINEAR ELASTIC EQUIVALENT CONTINUUM

To describe the mechanical behaviour of masonry-like materials we resort to two distinct models: a lagrangian system of rigid bodies interacting two by two through longitudinal, transversal and rotational springs (micromodel) and a micropolar continuum (macromodel). To evaluate the constitutive functions we employ a procedure of equivalence in terms of virtual work between the micro and the macromodel [2]. Selected a small representative periodical neighbourhood of particles named "module", the rigid particles of the module are considered corresponding to the material points of a neighbourhood of the Cosserat continuum. By assuming, in a linearised frame, a correspondence with the strain measures of the micropolar continuum: $\mathbf{U} = \text{grad} \mathbf{w} - \mathbf{W}$ and $\mathbf{R} = \text{grad} \mathbf{W}$ - where $\mathbf{w}(X)$ and $\mathbf{W}(X)$ are respectively the vector of the displacement and the skew-symmetric tensor of the rotation (microrotation) of a point X of the continuum - the strain measures of the module result expressed in terms of smooth homogeneous fields. By asking the equivalence between the virtual mean work of the micromodel, over the volume of the module V , and the virtual work density of the macro-model, the stress measures of the micropolar continuum - represented by the second order stress tensor, \mathbf{S} , and the third order couple-stress tensor, \mathbf{C} - are obtained as functions of the contact actions of the module - the vector of the contact forces, \mathbf{t}_c , and the skew-symmetric tensor of the contact couples, \mathbf{C}_c - and as functions of the fabric vectors $(\mathbf{B}-\mathbf{A})$, $(\mathbf{C}-\mathbf{A})$, $(\mathbf{C}-\mathbf{B})$, $(\mathbf{A}-\mathbf{X})$ and $(\mathbf{B}-\mathbf{X})$ which represent the geometry of the module

$$\mathbf{S}(X) = \frac{1}{V} \sum_c \mathbf{t}_c \otimes (\mathbf{B} - \mathbf{A}), \quad (1)$$

$$\begin{aligned} \mathbf{C}(X) = \frac{1}{V} \sum_c \{ & 2\mathbf{t}_c \otimes [(\mathbf{C} - \mathbf{B}) \otimes (\mathbf{B} - \mathbf{X}) - (\mathbf{C} - \mathbf{A}) \otimes (\mathbf{A} - \mathbf{X})] \\ & + \mathbf{C}_c \otimes (\mathbf{B} - \mathbf{A}) \}, \end{aligned}$$

Assuming linear elastic response functions for the contact actions of the module, and resorting to the above mentioned correspondence between the kinematical descriptors of the two models, we obtain these actions terms of continuum strain measures

$$\begin{aligned} \mathbf{t}_c &= \mathbf{K}_c \{ \mathbf{U}(\mathbf{B} - \mathbf{A}) + [\mathbf{R}(\mathbf{B} - \mathbf{X})](\mathbf{C} - \mathbf{B}) - [\mathbf{R}(\mathbf{A} - \mathbf{X})](\mathbf{C} - \mathbf{A}) \} \\ \mathbf{C}_c &= \mathbf{K}'_c \mathbf{R}(\mathbf{B} - \mathbf{A}), \end{aligned} \quad (2)$$

where the second and fourth order tensors \mathbf{K}_c e \mathbf{K}_c^r , the stiffness tensor and the drilling stiffness tensor respectively, have for components the stiffness of the springs interposed among the particles. Then the linear elastic constitutive relations of the micropolar equivalent model write

$$\begin{aligned} \mathbf{S} &= \mathbf{A}(\mathbf{U}) + \mathbf{B}(\mathbf{R}) \\ \mathbf{C} &= \mathbf{C}(\mathbf{U}) + \mathbf{D}(\mathbf{R}), \end{aligned} \quad (3)$$

where the constitutive tensors \mathbf{A} , \mathbf{B} , \mathbf{C} , \mathbf{D} , of the fourth, fifth, fifth and sixth order respectively, have components which depend on the elastic constants of the matrix, the shape, the size, the arrangement and the orientation of the elements. In addition, for hyperelastic materials it has $\mathbf{A} = \mathbf{A}^T$, $\mathbf{B}^t = \mathbf{C}$ and $\mathbf{D} = \mathbf{D}^T$, where "T" and "t" are the major and the minor transposition index respectively. The internal length parameter typical of the microstructure does not appear in the tensor \mathbf{A} . For materials with periodical internal structure (materials with the central symmetry) the tensors \mathbf{B} and \mathbf{C} are zero and the contact actions on the module as functions of the continuum stress measures are

$$\begin{aligned} \mathbf{t}_c &= \mathbf{K}_c \{ (\mathbf{A}^{-1} \mathbf{S})(\mathbf{B} - \mathbf{A}) + [(\mathbf{D}^{-1} \mathbf{C})(\mathbf{B} - \mathbf{X})](\mathbf{C} - \mathbf{B}) - [(\mathbf{D}^{-1} \mathbf{C})(\mathbf{A} - \mathbf{X})](\mathbf{C} - \mathbf{A}) \} \\ \mathbf{C}_c &= \mathbf{K}_c^r (\mathbf{D}^{-1} \mathbf{C})(\mathbf{B} - \mathbf{A}), \end{aligned} \quad (4)$$

Since the constitutive functions of a Cosserat continuum accounts for the dimensions of the bricks, it proves effective to take properly into account the scale effects. On the contrary, a simple (grade 1) Cauchy model cannot include any internal length scale and is inadequate to describe the variation of the response when the dimensions of the bricks change.

Therefore, due to the presence of an internal length scale the micropolar model, differently from the classical model, can adequately treat problems in which the dimension of the macroscale is bigger or of the same order of magnitude of the microscale, as for example in presence of load or geometrical singularities. In this case the work of the couple-stress can be important and the micropolar solution can greatly differ from the classical solution.

As an example a two-dimensional wall, made of an orthotropic texture, subjected to a couple of forces with vanishing resulting torque acting along the diagonal between its left top edge and its right bottom edge was analysed as a discrete, as a Cosserat and as a Cauchy model. The Cauchy equivalent model was obtained by properly constraining the Cosserat model (Appendix in [2]). The discrete solution was obtained by means of a standard general purpose F. E. program using rigid constraint equations for the bricks and two nodes elastic springs for the joints. The results from the Cosserat continuum were evaluated by means of a F.E. discretization using a three nodes triangular element having three degrees of freedom per node: two in-plane translations and one in-plane rotation. The same plane element without the drilling degree of freedom was employed to obtain the Cauchy solution. In Figure 1 the contour lines of the vertical component of the displacement for the three models are shown. The results obtained with the discrete model are in a good agreement with the ones obtained with the Cosserat equivalent model while they substantially differ with the results of the Cauchy model.

The differences between the response of a micropolar and a classical continuum, both equivalent to the same discrete assembly, has been widely investigated with reference to masonry walls made of bricks of various dimensions and dispositions [2, 3]. As in the case here analysed, the results of the Cauchy model, which are independent on the size of the

bricks and weakly depend on the change in their disposition, generally differs from those of the discrete and the micropolar model, which are very sensitive to the variation of the size and the texture of the units. Moreover, we showed that the Cosserat continuum does not behave as a Cauchy continuum even when the size of the bricks is small with respect to the dimension of the wall, unless the masonry has at least the orthotetragonal symmetry, that is unless the masonry is made of square bricks assembled together without interlocking.

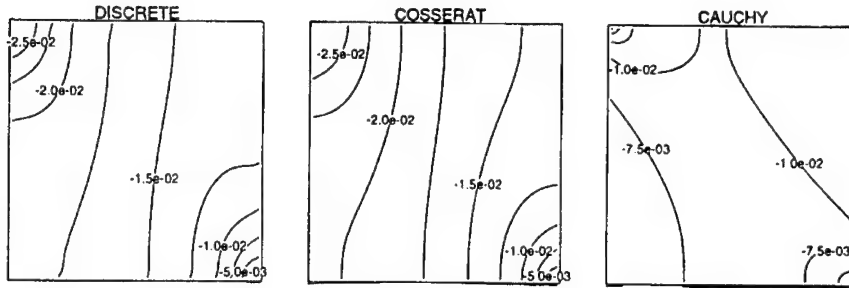


Figure 1: Wall with concentrated diagonal load. Contour lines for the vertical component of displacement in the micromodel and in the macromodels

3. NON-LINEAR CONTINUOUS MATERIAL

Just think to the low tensile strength of masonry-like systems the constitutive behaviour cannot often be linear elastic. The non-linear constitutive model is derived by checking the admissibility of the stress on the lagrangian system and by constructing, using the above mentioned equivalence procedure, the macroscopic constitutive tensor step-by-step.

Since we consider materials with elements dry-assembled or with joints filled by poor and scattered mortar, the lack of coherence is supposed concentrated along the joints. The contact surfaces between elements are modelled using non-linear longitudinal, transversal and rotational springs, while the elements are supposed to have infinite strength and are still modelled as rigid. Friction along the joints is also considered.

The assumption that bricks cannot break is not restrictive in a continuum smeared conception and, on the other end, we wish focus the attention on investigation of the influence of the geometry of the assembly on the ultimate behaviour of the masonry rather than of the strength of the units.

Restricting, for simplicity, the analysis to the two-dimensional frame, we assume that the contact forces on each joint of the micromodel are subject to the inequalities

$$\begin{aligned} \mathbf{t}_c \cdot \mathbf{n}_c &\leq a \\ |\mathbf{t}_c \cdot \mathbf{m}_c| &\leq \tan \phi (a - \mathbf{t}_c \cdot \mathbf{n}_c) \\ |\mathbf{C}_c \cdot \mathbf{n}_c \otimes \mathbf{m}_c| &\leq \frac{d}{2} (a - \mathbf{t}_c \cdot \mathbf{n}_c) \end{aligned} \quad (5)$$

where \mathbf{n}_c and \mathbf{m}_c are the unit vectors outward normal and tangent to the c -th joint, ϕ is the friction angle, d the width of the joint, $a = tg\phi$ is the cohesion force.

Until the inequalities (5) are verified the contact forces and couples are linear elastic. When one of the limits (5b, 5c) is exceeded, the contact force tangential to the joint and the contact couple are maintained equal to their limit value and the joint is considered partially fractured. If the limit (5a) is reached the contact force normal to the joint is relaxed and the joint is considered completely fractured.

Such an approach is generally implemented by writing yield relations in the stress space of the equivalent continuum model, starting from the analysis of yield situations in the micromodel according to various standards [5]. However, just looking to Equations (4), when the macromodel is provided with a microstructure, the relations between the stresses in the continuum and the internal actions in the discrete are much complex. Therefore, to obtain explicitly the yield criteria on \mathbf{S} and \mathbf{C} can be a difficult task.

We thought more useful to adopt a different approach: we test the compatibility of the action directly in the micromodel, working in one or two-dimensional stress spaces, avoiding the problematical definition of yield surfaces in the macromodel. We set up an algorithm working for small load steps as follows:

- (i) Given a load step, the continuum problem with a finite elements technique is solved.
- (ii) Through the expressions (4) the contact actions for each joint of the module are defined.
- (iii) The compatibility of the contact actions is checked in the micromodel through inequalities (5). If the compatibility is not fulfilled the constitutive tensors, \mathbf{K}_C e \mathbf{K}_C^r , are modified by cancelling the relevant terms and the corresponding increments of the components of the contact actions.
- (iv) By the explicit expressions obtained using the equivalence procedure, the components of the new tensor of the continuum equivalent to the "fractured" discrete are estimated and, with the usual techniques, the new stiffness matrix is evaluated.
- (v) The load is increased and the algorithm goes back to point (i).

The cycle stops at the end of the load path or when it is no longer possible to find a balanced solution to the field problem.

In order to make comparisons the same algorithm, using plane stress triangular finite elements and checking the static admissibility with the first two inequalities of (5), gives the classical solution.

As sample problem an orthotropic masonry wall – size 400x400 - subjected to a raked body force, in the 1:6 ratio between the horizontal and the vertical component, was analysed. This is the classical problem of the simplified modelling of the seismic actions as static forces. By modifying the value of the cohesion linear and non-linear solutions for the Cosserat and the Cauchy model were obtained. Moreover, the micropolar solution was obtained by varying the size of the bricks. In the linear elastic field, the differences observed between the Cosserat and the Cauchy models are slight; in addition the size of the blocks is not crucial. These effects are due to the substantial regularity of the load and to a not significant work of the skew-symmetrical stress and of the couple-stress.

Figure 2 shows the contour lines of the vertical component of the displacement fields with respect to the micropolar model with large bricks - heightxlength: 10x20 - (a); to the micropolar model with small bricks - 1x2 - (b) and to the Cauchy model (c). The classical continuum model provides results that do not depend from the size of the blocks.

Unlike the linear solution, the work of the couple-stress varies with the size of the bricks which greatly affects the results. This different behaviour is a direct result, proved both by experimental tests and by the computation of the collapse multiplier through non-linear

programming techniques [1]. In the cases (b) and (c) a band, on the right of the panel, stands out where there is a concentration of all the strains, and in a sense, of the "break" in the wall. In the case (a), instead, the bigger size of the block prevents their relative rotation among and their crumbling.

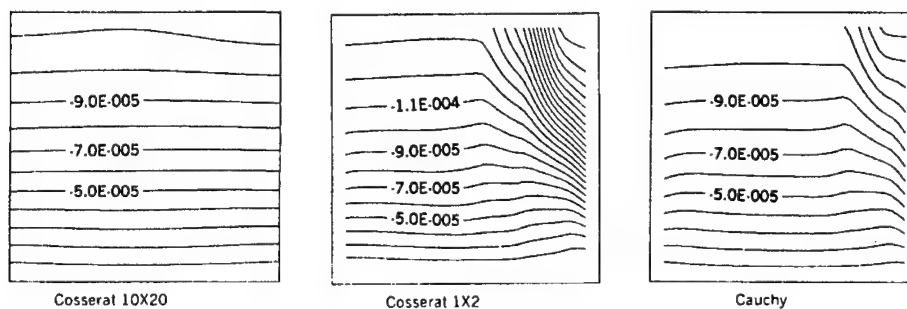


Figure 2: Wall with inclined body action.
Contour lines for the vertical component of displacement in the Cosserat model with large bricks (a), small bricks (b) and in the Cauchy model (c).

4. CONCLUDING REMARKS

The response of masonry-like materials with internal structure strongly depends on the shape, the size and the disposition of their elements. To describe the mechanical behaviour of these media a continuum model which retains memory of the geometry of the assembly and particularly of the dimensions of the bricks, like a Cosserat equivalent continuum should be preferred to a simple (grade 1) classical continuum. In particular, the micropolar model proves effective whenever the work of the non-standard components of stress is prominent.

5. REFERENCES

- [1] Baggio, C. and Trovalusci, P., Collapse behaviour of three-dimensional brick-block systems using non linear programming, *Structural Engineering and Mechanics*, 10 (2), 181-195 (2000).
- [2] Masiani, R. and Trovalusci, P., Cauchy and Cosserat materials as continuum models of brick masonry, *Meccanica*, 31, 421-432 (1996).
- [3] Trovalusci, P. and Masiani, R., "Material symmetries of micropolar continua equivalent to lattices", *International Journal of Solids and Structures*, 14, 2091-2108 (1999).
- [4] Ericksen, J. L., Special topics in elastostatics, in *Advances in Applied Mechanics*, Academic Press, New York (1977) 189-244.
- [5] Dai, C., Mühlhaus, H. -B., Meek J. and Duncan Fama, M., Modelling of blocky rock masses using the Cosserat method, *International Journal of Rock Mechanics and Mining sciences*, 33, 425-432 (1996).

SOME ASPECTS OF A MICROPOLAR PLASTICITY THEORY

P. Grammenoudis

Department of Mechanics

Darmstadt University of Technology, D-64289 Darmstadt, Germany

Ch. Tsakmakis

Department of Mechanics

Darmstadt University of Technology, D-64289 Darmstadt, Germany

1. INTRODUCTION

Internal length scales may be elaborated in the constitutive theory in a natural way by assuming the hypothesis of "substructure" assigned to every material point. If this substructure behaves like a rigid body which may be rotate then the continuum is called micropolar. The aim of the paper is to present a micropolar plasticity theory, which satisfies the second law of thermodynamics in every admissible process. For the sake of simplicity only kinematic hardening is considered.

2. PRELIMINARIES – DECOMPOSITION OF DEFORMATION

2.1 NOTATION

In the following we consider isothermal deformations and write $\dot{\phi}(t)$ for the material time derivative of a function $\phi(t)$, where t is the time. We use bold face letters for second-order tensors. In particular **1** represents the identity second-order tensor and \mathbf{A}^T denotes the transpose of a second-order tensor **A**. We write $\text{tr} \mathbf{A}$ for the trace of **A**, $\mathbf{A}^D = \mathbf{A} - 1/3 (\text{tr} \mathbf{A}) \mathbf{1}$ for the deviator of **A** and $\mathbf{A} \cdot \mathbf{B} = \text{tr}(\mathbf{A} \mathbf{B}^T) = \text{tr}(\mathbf{A}^T \mathbf{B})$ for the inner product of **A** and **B**. Also we use the notation $\mathbf{A}^{T-1} = (\mathbf{A}^{-1})^T$, provided that \mathbf{A}^{-1} exists.

2.2 DECOMPOSITION OF DEFORMATION

Consider a material body **B**, which occupies a region \mathbf{R}_R in the three dimensional Euclidean point space E in the reference configuration ($t = 0$). Each particle of the material body **B** can be identified by a position vector **X** to the place **X** in \mathbf{R}_R after having chosen a fixed point (origin) in E . The configuration at time t is called actual configuration \mathbf{R}_t . The position of a particle with place **x** in this configuration is identified by the position vector **x**.

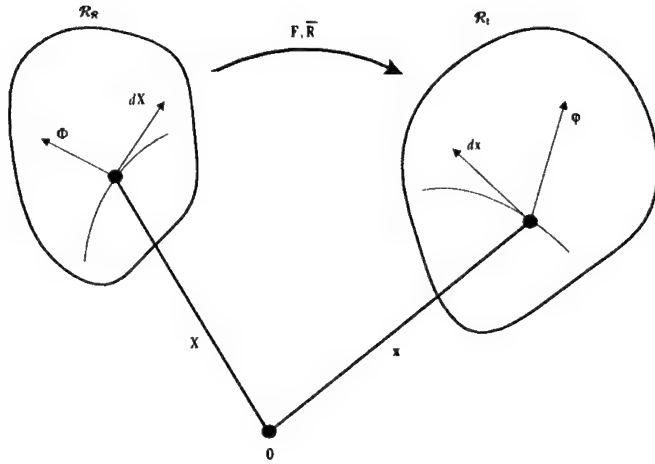


Fig. 1: Motion, reference and actual configuration.

A motion of \mathbf{B} in \mathbf{E} is described by the relation

$$\mathbf{x} = \hat{\mathbf{x}}(\mathbf{X}, t). \quad (2.1)$$

The deformation gradient tensor corresponding to (2.1) is denoted by

$$\mathbf{F} = \mathbf{F}(\mathbf{X}, t) = \frac{\partial \hat{\mathbf{x}}}{\partial \mathbf{X}} = \text{GRAD } \hat{\mathbf{x}}. \quad (2.2)$$

For \mathbf{F} ($\det \mathbf{F} > 0$) the polar decomposition

$$\mathbf{F} = \mathbf{R}\mathbf{U} = \mathbf{V}\mathbf{R} \quad (2.3)$$

applies, where \mathbf{R} represents a proper orthogonal second-order tensor.

Following Eringen et al. [2, 3, 4], (cf. also Mindlin [5]), we define a micropolar continuum to have attached to every material point a substructure. The substructure itself behaves like a rigid body, which may be rotate, the rotation tensor being $\bar{\mathbf{R}}$. Using $\bar{\mathbf{R}}$, tensors $\bar{\mathbf{U}}$ and $\bar{\mathbf{V}}$ may be defined by

$$\mathbf{F} = \bar{\mathbf{R}}\bar{\mathbf{U}} = \bar{\mathbf{V}}\bar{\mathbf{R}}. \quad (2.4)$$

In order to introduce some strain measures, we first concentrate on pure elasticity. In this case the specific free energy function ψ is supposed to depend on \mathbf{F} , $\bar{\mathbf{R}}$ and $\text{GRAD } \bar{\mathbf{R}}$:

$$\psi = \bar{\psi}(\mathbf{F}, \bar{\mathbf{R}}, \text{GRAD } \bar{\mathbf{R}}). \quad (2.5)$$

$GRAD \bar{\mathbf{R}}$ introduces an internal length scale in the constitutive theory. With respect to convective coordinates, it is given by

$$GRAD \bar{\mathbf{R}} = \frac{\partial \bar{\mathbf{R}}}{\partial \theta^k} \otimes \mathbf{G}_k, \quad (2.6)$$

so that $GRAD \bar{\mathbf{R}}$ represents a third-order tensor. By using the principle of material objectivity, it is a routine matter to obtain the reduced form

$$\psi = \bar{\psi}(\tilde{\boldsymbol{\varepsilon}}, \tilde{\mathbf{K}}) \quad (2.7)$$

where

$$\tilde{\boldsymbol{\varepsilon}} = \bar{\mathbf{U}} - \mathbf{1}, \quad (2.8)$$

$$\tilde{\mathbf{K}} = \bar{\mathbf{R}}^T GRAD \bar{\mathbf{R}}. \quad (2.9)$$

In these equations, $\tilde{\boldsymbol{\varepsilon}}$ is the micropolar Lagrangean strain tensor and $\tilde{\mathbf{K}}$ the Lagrangean curvature tensor. Rate-dependent or rate-independent elastic-plastic material properties may be described by assuming the multiplicative decompositions

$$\mathbf{F} = \mathbf{F}_e \mathbf{F}_p, \quad \bar{\mathbf{R}} = \bar{\mathbf{R}}_e \bar{\mathbf{R}}_p, \quad (2.11)$$

which introduce a so-called plastic intermediate configuration (see Fig. 2).

Moreover, $\det \mathbf{F}_p > 0$ and $\det \bar{\mathbf{R}}_p > 0$ are assumed to apply so that the polar decompositions

$$\mathbf{F}_p = \mathbf{R}_p \mathbf{U}_p, \quad (2.12)$$

$$\bar{\mathbf{F}}_p = \bar{\mathbf{R}}_p \bar{\mathbf{U}}_p \quad (2.13)$$

apply as well.

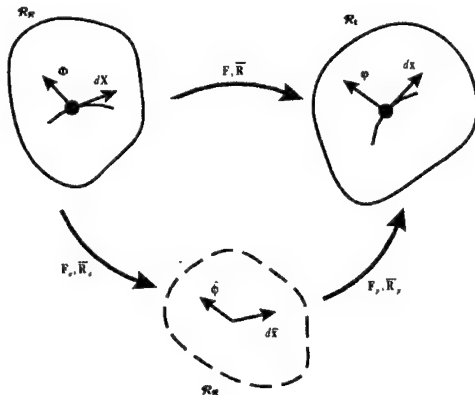


Fig. 2: A sketch of the decomposition of deformation.

It can be shown (see Grammenoudis et al. [6]) that the multiplicative decompositions of \mathbf{F} and $\bar{\mathbf{R}}$ imply additive decompositions for $\tilde{\boldsymbol{\varepsilon}}$ and $\tilde{\mathbf{K}}$ in the form

$$\tilde{\boldsymbol{\varepsilon}} = \tilde{\boldsymbol{\varepsilon}}_e + \tilde{\boldsymbol{\varepsilon}}_p, \quad (2.14)$$

$$\tilde{\mathbf{K}} = \tilde{\mathbf{K}}_e + \tilde{\mathbf{K}}_p. \quad (2.16)$$

Also, these decompositions of strains may be transformed to the actual and the plastic intermediate configurations, the counterparts of $\tilde{\boldsymbol{\varepsilon}}$, $\tilde{\mathbf{K}}$ being $\boldsymbol{\varepsilon}$, \mathbf{K} and $\hat{\boldsymbol{\varepsilon}}$, $\hat{\mathbf{K}}$, respectively.

3. SECOND LAW OF THERMODYNAMICS

We assume isothermal deformations with uniform distribution of temperature. Then, the generalized Clausius-Duhem inequality for micropolar materials (cf. Eringen et al. [2, 3, 4]) reads as follows:

$$\mathbf{S} \cdot \overset{\Delta}{\boldsymbol{\varepsilon}} + \mathbf{S}_c \cdot \overset{\Delta}{\mathbf{K}} - \rho_R \dot{\psi} \geq 0. \quad (3.1)$$

Here, ρ_R is the mass density in the reference configuration, \mathbf{S} the weighted Cauchy stress tensor and \mathbf{S}_c the so-called weighted couple stress tensor, respectively; $\overset{\Delta}{\boldsymbol{\varepsilon}}$, $\overset{\Delta}{\mathbf{K}}$ denote specific objective derivatives as defined in Grammenoudis et al. [6]. Note in passing that \mathbf{S} , $\boldsymbol{\varepsilon}$ are non-symmetric second-order tensors. As above, ψ is the specific free energy function, which now is supposed to obey the decomposition

$$\psi(t) = \psi_e(t) + \psi_p(t). \quad (3.2)$$

3.1 ELASTICITY LAWS

The free energy function ψ is supposed to exhibit, with respect to the reference and plastic intermediate configuration, the following representations:

$$\psi_e = \hat{\psi}_e(\hat{\boldsymbol{\varepsilon}}_e, \hat{\mathbf{K}}_e) = \tilde{\psi}_e(\tilde{\boldsymbol{\varepsilon}}, \tilde{\boldsymbol{\varepsilon}}_p, \tilde{\mathbf{K}}, \hat{\mathbf{K}}_p). \quad (3.3)$$

By inserting (3.2), (3.3) into (3.1), and by using standard arguments, the potential relations

$$\begin{aligned} \hat{\mathbf{T}} &= \rho_R \frac{\partial \hat{\psi}_e}{\partial \hat{\boldsymbol{\varepsilon}}_e}, \\ \hat{\mathbf{T}}_c &= \rho_R \frac{\partial \hat{\psi}_e}{\partial \hat{\mathbf{K}}_e} \end{aligned} \quad (3.4)$$

may be established, where $\hat{\mathbf{T}}$ and $\hat{\mathbf{T}}_c$ represent counterparts of \mathbf{S} and \mathbf{S}_c , respectively in the plastic intermediate configuration. This way, after some algebraic calculations, the second law (3.1) reduces to the dissipation inequality

$$D = \hat{\mathbf{P}} \cdot \overset{\Delta}{\hat{\boldsymbol{\varepsilon}}}_p + \hat{\mathbf{P}}_c \cdot \overset{\Delta}{\hat{\mathbf{K}}}_p - \rho_R \dot{\psi}_p \geq 0, \quad (3.5)$$

where use has been made of the definitions

$$\hat{\mathbf{P}} := (\mathbf{1} + \hat{\boldsymbol{\varepsilon}}_e^T) \hat{\mathbf{T}}, \quad (3.6)$$

$$\hat{\mathbf{P}}_c := \hat{\mathbf{T}}_c. \quad (3.7)$$

3.2 KINEMATIC HARDENING

We focus attention on pure kinematic hardening and define ψ_p to obey the representation

$$\psi_p = \hat{\psi}_p(\hat{\mathbf{Y}}, \hat{\mathbf{Y}}_c), \quad (3.9)$$

where $\hat{\mathbf{Y}}$ and $\hat{\mathbf{Y}}_c$ are strain and curvature measures responsible for kinematic hardening with geometrical meaning similar to that of $\hat{\boldsymbol{\varepsilon}}_p$ and $\hat{\mathbf{K}}_p$, respectively. The counterparts of $\hat{\mathbf{Y}}$ and $\hat{\mathbf{Y}}_c$ with respect to the reference configuration are $\tilde{\mathbf{Y}}$ and $\tilde{\mathbf{Y}}_c$.

Next, we introduce the thermodynamic conjugated forces

$$\hat{\mathbf{Z}} = \rho_R \frac{\partial \hat{\psi}_p}{\partial \hat{\mathbf{Y}}}, \quad (3.10)$$

$$\hat{\mathbf{Z}}_c = \rho_R \frac{\partial \hat{\psi}_p}{\partial \hat{\mathbf{Y}}_c}$$

and define back-stress tensors by

$$\hat{\boldsymbol{\xi}} := (\mathbf{1} - \hat{\mathbf{Y}}^T) \hat{\mathbf{Z}}, \quad (3.11)$$

$$\hat{\boldsymbol{\xi}}_c := \hat{\mathbf{Z}}_c, \quad (3.12)$$

respectively. It follows that the dissipation inequality (3.5) may be recasted in the form

$$D = (\hat{\mathbf{P}} - \hat{\boldsymbol{\xi}}) \cdot \hat{\boldsymbol{\varepsilon}}_p + (\hat{\mathbf{P}}_c - \hat{\boldsymbol{\xi}}_c) \cdot \hat{\mathbf{K}}_p + \hat{\mathbf{Z}} \cdot \hat{\boldsymbol{\beta}} + \hat{\boldsymbol{\xi}}_c \cdot \hat{\boldsymbol{\beta}}_c \geq 0. \quad (3.13)$$

In order to exploit this inequality, we postulate the existence of a yield function

$$f = f(\hat{\mathbf{P}}, \hat{\mathbf{P}}_c, \hat{\boldsymbol{\xi}}, \hat{\boldsymbol{\xi}}_c). \quad (3.14)$$

Plastic flow occurs for $f = 0$ and plastic loading. Also, the associated normality rules ($\dot{s} \geq 0$)

$$\begin{pmatrix} \hat{\boldsymbol{\varepsilon}}_p \\ \hat{\mathbf{K}}_p \end{pmatrix} = \dot{s} \begin{pmatrix} \frac{\partial f}{\partial \hat{\mathbf{P}}} \\ \frac{\partial f}{\partial \hat{\mathbf{P}}_c} \end{pmatrix} \quad (3.15)$$

are assumed to apply. Then, it can be shown (see Grammenoudis et al. [6]), that

$$D = \hat{\mathbf{Z}} \cdot \hat{\mathbf{\beta}} + \hat{\xi}_c \cdot \hat{\mathbf{\beta}}_c \geq 0 \quad (3.16)$$

is a sufficient condition for (3.13). Finally, evolution equations governing the response of kinematic hardening may be derived as sufficient conditions for the validity of (3.16):

$$\begin{aligned} \hat{\mathbf{\beta}} &= \mathbf{M}[\hat{\mathbf{Z}}], \\ \hat{\mathbf{\beta}}_c &= \hat{\mathbf{M}}_c[\hat{\xi}_c] \end{aligned} \quad (3.17)$$

4. CONCLUDING REMARKS

The micropolar plasticity model proposed has to be extended in order to take into account isotropic hardening effects. However, it is convenient, above all, to implement the theory in a finite element code. This will enable to check the capabilities of the developed theory as well as to compare the predicted responses with those according to other models involving nonlocalities, like that of Aifantis [1].

5. REFERENCES

- [1] Aifantis, E. C., *The Physics of Plastic Deformation*, International Journal of Plasticity, 3, 211-247, 1987.
- [2] Eringen, A. C., *Microcontinuum Field Theories, I. Foundations and Solids*, Springer, New York, 1999.
- [3] Eringen, A. C., *Nonlinear Theory of Simple Micro-elastic Solids - I*, Int. J. Engng. Sci. Vol. 2, 189-203, 1964.
- [4] Suhubi, E. S., Eringen, A. C., *Nonlinear Theory of Simple Micro-elastic Solids - II*, Int. J. Engng. Sci. Vol. 2, 389-404, 1964.
- [5] Mindlin, R., *Influence of Couple-stresses on Stress Concentrations*, Experimental Mechanics Vol. 3, 1-7, 1963.
- [6] Grammenoudis, P., Tsakmakis, Ch., *Hardening rules for finite deformation micropolar plasticity: Restrictions imposed by the second law of thermodynamics and the postulate of Il'iusin*, submitted for publication, 2001.

DESCRIPTION OF PLASTIC ANISOTROPY EFFECTS AT LARGE DEFORMATIONS

D. Schick

Department of Mechanics
Darmstadt University of Technology, 64289 Darmstadt, Germany

Ch. Tsakmakis

Department of Mechanics
Darmstadt University of Technology, 64289 Darmstadt, Germany

1. INTRODUCTION

Plastic anisotropy effects may be described by employing in the constitutive theory a set of suitable defined internal variables. These variables have to model the hardening response of the material under consideration as e.g. to describe the rotation of some symmetry axes. Such axes are imagined to be related with the development of the material substructure assumed, or, correspondingly, with the state variables characterizing this development.

2. PRELIMINARIES - NOTATION

We consider isothermal deformations and write $\dot{\phi}(t)$ for the material time derivative of a function $\phi(t)$, where t is the time. Second-order tensors, like vectors, are denoted by bold-face letters, whereas fourth-order tensors are denoted by calligraphic letters. In particular, $\mathbf{1}$ represents the identity second-order tensor and \mathbf{A}^T denotes the transpose of a second-order tensor \mathbf{A} . We write $\text{tr}\mathbf{A}$ for the trace of \mathbf{A} , $\mathbf{A}^D = \mathbf{A} - 1/3 (\text{tr}\mathbf{A})\mathbf{1}$ for the deviator of \mathbf{A} , $\mathbf{A} \cdot \mathbf{B} = \text{tr}(\mathbf{A}\mathbf{B}^T) = \text{tr}(\mathbf{A}^T\mathbf{B})$ for the inner product and $\mathbf{A} \otimes \mathbf{B}$ for the tensor product of \mathbf{A} and \mathbf{B} . We also use the notation $\mathbf{A}^{T-1} = (\mathbf{A}^{-1})^T$, provided that \mathbf{A}^{-1} exists. Finally, \mathcal{E} is a fourth-order tensor with the property $\mathcal{E}[\mathbf{A}] = \mathbf{A}_s = 1/2(\mathbf{A} + \mathbf{A}^T)$ for every symmetric second-order tensor \mathbf{A} .

2.1 MULTIPLICATIVE DECOMPOSITION OF DEFORMATION

Let \mathbf{F} ($\det \mathbf{F} > 0$) be the deformation gradient tensor and suppose the multiplicative decomposition of \mathbf{F} , $\mathbf{F} = \mathbf{F}_e \mathbf{F}_p$, to apply, where \mathbf{F}_e ($\det \mathbf{F}_e > 0$) and \mathbf{F}_p denote the elastic and plastic part of \mathbf{F} , respectively. Assuming plastic incompressibility, $\det \mathbf{F}_p = 1$. The multiplicative decomposition of \mathbf{F} introduces a so-called plastic intermediate configuration, which in general is not compatible and therefore not an Euclidean one. By designating quantities referred to the plastic intermediate configuration by a superposed symbol \wedge , the plastic velocity gradient tensor $\hat{\mathbf{L}}_p$ is given through

$$\hat{\mathbf{L}}_p = \dot{\mathbf{F}}_p \mathbf{F}_p^{-1} = \hat{\mathbf{D}}_p + \hat{\mathbf{W}}_p, \quad (2.1)$$

where

$$\hat{\mathbf{D}}_p = 1/2(\hat{\mathbf{L}}_p + \hat{\mathbf{L}}_p^T), \quad \hat{\mathbf{W}}_p = 1/2(\hat{\mathbf{L}}_p - \hat{\mathbf{L}}_p^T) \quad (2.2)$$

denote the symmetric and skew-symmetric parts, respectively. Because of plastic incompressibility,

$$\text{tr} \hat{\mathbf{L}}_p = \text{tr} \hat{\mathbf{D}}_p = 0. \quad (2.3)$$

We may use $\mathbf{F}_e, \mathbf{F}_p$ to obtain the following kinematical relations:

$$\mathbf{F}_e = \mathbf{R}_e \hat{\mathbf{U}}_e = \mathbf{V}_e \mathbf{R}_e, \quad \mathbf{F}_p = \mathbf{R}_p \mathbf{U}_p = \hat{\mathbf{V}}_p \mathbf{R}_p, \quad (2.4)$$

$$\hat{\mathbf{C}}_e = \frac{1}{2}(\hat{\mathbf{C}}_e - \mathbf{1}), \quad \hat{\mathbf{C}}_e = \mathbf{F}_e^T \mathbf{F}_e = \hat{\mathbf{U}}_e^2, \quad (2.5)$$

$$\hat{\mathbf{F}}_p = \frac{1}{2}(\mathbf{1} - \hat{\mathbf{B}}_p^{-1}), \quad \hat{\mathbf{B}}_p = \mathbf{F}_p \mathbf{F}_p^T = \hat{\mathbf{V}}_p^2, \quad (2.6)$$

$$\hat{\mathbf{F}} = \hat{\mathbf{F}}_e + \hat{\mathbf{F}}_p, \quad (2.7)$$

$$\mathbf{E} = \frac{1}{2}(\mathbf{C} - \mathbf{1}) = \mathbf{F}_p^T \hat{\mathbf{F}} \mathbf{F}_p, \quad \mathbf{C} = \mathbf{F}^T \mathbf{F}, \quad (2.8)$$

$$\mathbf{E}_e = \mathbf{F}_p^T \hat{\mathbf{F}}_e \mathbf{F}_p, \quad (2.9)$$

$$\mathbf{E}_p = \frac{1}{2}(\mathbf{C}_p - \mathbf{1}) = \mathbf{F}_p^T \hat{\mathbf{F}}_p \mathbf{F}_p, \quad \mathbf{C}_p = \mathbf{F}_p^T \mathbf{F}_p, \quad (2.10)$$

$$\mathbf{E} = \mathbf{E}_e + \mathbf{E}_p. \quad (2.11)$$

Here, Eqs.(2.4) represent the polar decomposition of \mathbf{F}_e and \mathbf{F}_p , respectively, with $\mathbf{R}_e, \mathbf{R}_p$ being the corresponding rotations, while $\hat{\mathbf{U}}_e, \mathbf{V}_e, \mathbf{U}_p, \hat{\mathbf{V}}_p$ are the corresponding symmetric, positive definite stretch tensors. $\hat{\mathbf{C}}_e$ and $\hat{\mathbf{B}}_e$ are the elastic right Cauchy-Green and the plastic left Cauchy-Green tensors, respectively. Also, the tensors $\hat{\mathbf{F}}_e$ and $\hat{\mathbf{F}}_p$ are called the elastic Green- and the plastic Almansi strain tensors with respect to the plastic intermediate configuration, respectively. On the basis of these relations, we can see that

$$\hat{\mathbf{D}}_p = \hat{\mathbf{F}}_p^{\Delta} \hat{\mathbf{F}}_p = \mathbf{F}_p^{T-1} \dot{\mathbf{E}} \mathbf{F}_p^{-1}, \quad \hat{\mathbf{F}} = \mathbf{F}_p^{T-1} \dot{\mathbf{E}} \mathbf{F}_p^{-1} = \mathbf{F}_e^T \mathbf{D} \mathbf{F}_e, \quad (2.12)$$

where

$$\mathbf{D} = \frac{1}{2}(\mathbf{L} + \mathbf{L}^T), \quad \mathbf{L} = \dot{\mathbf{F}} \mathbf{F}^{-1}, \quad (2.13)$$

and

$$\hat{\mathbf{X}}^{\Delta} = \dot{\hat{\mathbf{X}}} + \hat{\mathbf{L}}_p^T \hat{\mathbf{X}} + \hat{\mathbf{X}} \hat{\mathbf{L}}_p \quad (2.14)$$

for a second-order tensor $\hat{\mathbf{X}}$ relative to the plastic intermediate configuration. Eq.(2.12)₁ indicates that $\hat{\mathbf{D}}_p$ may be interpreted as a particular Oldroyd derivative of $\hat{\mathbf{F}}_p$. We denote by \mathbf{T} the Cauchy stress tensor, by \mathbf{S} the weighted Cauchy stress tensor, $\mathbf{S} = (\det \mathbf{F}) \mathbf{T}$, and by $\hat{\mathbf{T}} = \mathbf{F}_e^{-1} \mathbf{S} \mathbf{F}_e^{T-1}$, $\tilde{\mathbf{T}} = \mathbf{F}_p^{-1} \hat{\mathbf{T}} \mathbf{F}_p^{T-1} = \mathbf{F}^{-1} \mathbf{S} \mathbf{F}^{T-1}$, the second Piola-Kirchhoff stress tensors relative to the plastic intermediate and the reference configuration, respectively. Another stress tensor, which, as we shall see, is related to the plastic dissipation is the stress tensor $\hat{\mathbf{P}} := \mathbf{F}_e^T \mathbf{S} \mathbf{F}_e^{T-1} = (\mathbf{1} + 2\hat{\mathbf{F}}_e) \hat{\mathbf{T}} = \hat{\mathbf{C}}_e \hat{\mathbf{T}}$. Following Lubliner (1986), we call $\hat{\mathbf{P}}$ the Mandel stress tensor. It is well-known (see e.g. Green and Naghdi (1971), (1980), Casey and Naghdi (1981) that the decomposition of \mathbf{F} is uniquely determined except for a rigid body rotation $\bar{\mathbf{Q}}$ superposed on the plastic intermediate configuration.

3. SECOND LAW OF THERMODYNAMICS

We assume isothermal deformations with uniform distribution of temperature. Then, the generalized Clausius-Duhem inequality reads (cf. Truesdell and Noll, 1965, Sect. 79, 82) as follows:

$$\mathbf{S} \cdot \mathbf{D} - \rho_R \dot{\psi} \geq 0. \quad (3.1)$$

Here ρ_R is the mass density in the reference configuration and ψ the specific free energy. For our purpose, it is useful to rewrite (3.1) as follows:

$$\hat{\mathbf{T}} \cdot \hat{\mathbf{\Gamma}} - \rho_R \dot{\psi} \geq 0. \quad (3.2)$$

Next, we assume the specific free energy ψ to be additively decomposed in elastic and plastic parts, $\psi(t) = \psi_e(t) + \psi_p(t)$.

3.1 ELASTICITY LAWS

We concentrate on elasticity responses exhibiting anisotropy of orientational type. In accordance with Dafalias (1987, 1998), the anisotropy effects are elaborated by assuming ψ_e to be a function, besides of \mathbf{F}_e , of $\Phi(t)$, where Φ is a proper orthogonal second-order tensor:

$$\psi_e(t) = \bar{\psi}_e(\mathbf{F}_e(t), \Phi(t)), \quad \Phi^T = \Phi^{-1}. \quad (3.3)$$

Now, inequality (3.2) may be recasted in the form

$$\begin{aligned} & \left(\hat{\mathbf{T}} - \rho_R \Phi \frac{\partial \bar{\psi}_e}{\partial \hat{\mathbf{\Gamma}}_e} \Phi^T \right) \cdot \hat{\mathbf{\Gamma}} + (1 + 2\hat{\mathbf{\Gamma}}_e) \left(\rho_R \Phi \frac{\partial \bar{\psi}_e}{\partial \hat{\mathbf{\Gamma}}_e} \Phi^T \right) \cdot \hat{\mathbf{D}}_p \\ & + 2\hat{\mathbf{\Gamma}}_e \left(\rho_R \Phi \frac{\partial \bar{\psi}_e}{\partial \hat{\mathbf{\Gamma}}_e} \Phi^T \right) \cdot (\hat{\mathbf{W}}_p - \dot{\Phi} \Phi^T) - \rho_R \dot{\psi}_p \geq 0. \end{aligned} \quad (3.4)$$

By inserting (3.3) into (3.2) and using similar arguments as in Coleman and Gurtin (1967), we may prove that in the case of viscoplasticity the relations

$$\hat{\mathbf{T}} = \rho_R \Phi \frac{\partial \bar{\psi}_e}{\partial \hat{\mathbf{\Gamma}}_e} \Phi^T, \quad (3.5)$$

$$\begin{aligned} \Delta_{\text{int}} := & (1 + 2\hat{\mathbf{\Gamma}}_e) \left(\rho_R \Phi \frac{\partial \bar{\psi}_e}{\partial \hat{\mathbf{\Gamma}}_e} \Phi^T \right) \cdot \hat{\mathbf{D}}_p \\ & + 2\hat{\mathbf{\Gamma}}_e \left(\rho_R \Phi \frac{\partial \bar{\psi}_e}{\partial \hat{\mathbf{\Gamma}}_e} \Phi^T \right) \cdot (\hat{\mathbf{W}}_p - \dot{\Phi} \Phi^T) - \rho_R \dot{\psi}_p \geq 0 \end{aligned} \quad (3.6)$$

are necessary and sufficient conditions in order for inequality (3.4) to be valid in every admissible process. That means, our viscoplasticity theory falls in the general framework of Coleman and Gurtin's (1967) thermodynamics with internal state variables (cf. also Kratochil and Dillon (1969). For plasticity, (3.5) and (3.6) are generally only sufficient conditions for (3.4). Eq. (3.5) represents a general elasticity law, characterizing materials with anisotropy of orientational type.

3.2 FLOW RULE FOR PLASTICITY

From (3.5) and (3.6) the internal dissipation is given by

$$\Delta_{\text{int}}(\hat{\mathbf{P}}, \hat{\mathbf{L}}_p - \dot{\Phi} \Phi^T, \dot{\psi}_p) = \hat{\mathbf{P}} \cdot (\hat{\mathbf{L}}_p - \dot{\Phi} \Phi^T) - \dot{\psi}_p \geq 0. \quad (3.7)$$

Let us assume the existence of a yield function $f = \hat{f}(\hat{\mathbf{P}}, \dots)$, (cf. also Aravas, (1992)). Moreover, we assume the postulate of maximal dissipation, as explained in Tsakmakis (2001). Then, it can be shown, that convexity of the yield surface $\hat{f} = 0$ and a normality rule for $\hat{\mathbf{L}}_p - \dot{\Phi}\Phi^T$ are sufficient conditions for (3.7). The term normality rule means that $\hat{\mathbf{L}}_p - \dot{\Phi}\Phi^T$ has to be directed along the outward normal on the yield surface, which is assumed to be smooth,

$$\hat{\mathbf{L}}_p - \dot{\Phi}\Phi^T = \sqrt{2/3} \dot{s} \hat{\mathbf{N}}, \quad \hat{\mathbf{N}} := \frac{\partial \hat{f}}{\partial \hat{\mathbf{P}}} \cdot \left\| \frac{\partial \hat{f}}{\partial \hat{\mathbf{P}}} \right\|^{-1}. \quad (3.8)$$

In (3.8), \dot{s} is a positive scalar for plastic loading. Of course (3.8) can be decomposed into symmetric and skew-symmetric parts, respectively:

$$\hat{\mathbf{D}}_p = \sqrt{2/3} \dot{s} \hat{\mathbf{N}}_S, \quad \hat{\mathbf{\Omega}}^{(e)} := \hat{\mathbf{W}}_p - \dot{\Phi}\Phi^T = \sqrt{2/3} \dot{s} \hat{\mathbf{N}}_A. \quad (3.9)$$

In the terminology of Dafalias (1998), $\dot{\Phi}\Phi^T$ represents the constitutive spin associated with the elasticity law and $\hat{\mathbf{\Omega}}^{(e)}$ the corresponding plastic spin, while $\hat{\mathbf{W}}_p$ is the plastic material spin. Also, (3.8) represents our flow rule for rate independent plasticity, where \dot{s} has to be determined from the so-called consistency condition $d/dt \hat{f} = 0$. In the case of viscoplasticity, \dot{s} has to be given by a constitutive law, defined appropriately.

3.3 KINEMATIC HARDENING

We focus attention on pure kinematic hardening and suppose ψ_p to consist only of contributions arising from kinematic hardening:

$$\psi_p = \bar{\bar{\psi}}_p(\hat{\mathbf{Y}}, \Delta) = \tilde{\psi}_p(\hat{\mathbf{Y}}), \quad \mathbf{Y} := \Delta^T \hat{\mathbf{Y}} \Delta, \quad \Delta^T = \Delta^{-1}. \quad (3.10)$$

Here, $\hat{\mathbf{Y}}$ is an internal, symmetric second-order strain tensor, which operates in the plastic intermediate configuration, while the proper orthogonal tensor Δ (two-point tensor field) is defined to rotate some symmetry axes, related to the kinematic hardening response, from the reference to the plastic intermediate configuration. We denote by $\hat{\mathbf{Z}}$ the internal stress tensor which is thermodynamically conjugate to $\hat{\mathbf{Y}}$ and set

$$\hat{\mathbf{Z}} := \rho_R \frac{\partial \bar{\bar{\psi}}_p}{\partial \hat{\mathbf{Y}}} = \rho_R \Delta \frac{\partial \tilde{\psi}_p}{\partial \hat{\mathbf{Y}}} \Delta^T. \quad (3.11)$$

Evidently, the tensor $\hat{\mathbf{Z}}$ is symmetric and operates in the plastic intermediate configuration. Kinematic hardening is described by the back-stress tensors $\hat{\xi}$, which is postulated to possess the structure of a Mandel stress tensor. Formally, $\hat{\xi}$ can be defined, in analogy to $\hat{\mathbf{P}}$, through

$$\hat{\xi} = (\mathbf{1} + 2\hat{\mathbf{Y}})\hat{\mathbf{Z}} = \hat{\xi}_A + \hat{\xi}_S, \quad (3.12)$$

where

$$\hat{\xi}_S = \hat{\mathbf{Z}} + \hat{\mathbf{Y}}\hat{\mathbf{Z}} + \hat{\mathbf{Z}}\hat{\mathbf{Y}}, \quad \hat{\xi}_A = \hat{\mathbf{Y}}\hat{\mathbf{Z}} - \hat{\mathbf{Z}}\hat{\mathbf{Y}}. \quad (3.13)$$

We suppose the yield function to exhibit, besides kinematic, also orientational hardening:

$$f = \bar{\bar{f}}(\hat{\mathbf{P}}, \hat{\xi}, \Pi), \quad \Pi^T = \Pi^{-1}, \quad (3.14)$$

where Π , like Φ and Δ , is an orthogonal tensor, which rotates some symmetry axes related to the yield condition. Next, we turn to inequality (3.6), which now takes the form

$$\begin{aligned} \Delta_{\text{irr}} &= (\hat{\mathbf{P}} - \hat{\xi}) \cdot (\hat{\mathbf{L}}_p - \dot{\Phi}\Phi^T) + \hat{\xi} \cdot (\hat{\mathbf{L}}_p - \dot{\Phi}\Phi^T) - \rho_R \dot{\psi}_p \\ &= \sqrt{2/3} \dot{s} (\hat{\mathbf{P}} - \hat{\xi}) \cdot \hat{\mathbf{N}} + \hat{\mathbf{Z}} \cdot \hat{\mathbf{D}}_p + 2\hat{\mathbf{Y}}\hat{\mathbf{Z}} \cdot \hat{\mathbf{D}}_p + \hat{\xi}_A \cdot \hat{\mathbf{\Omega}}^{(e)} - \rho_R \dot{\psi}_p \geq 0. \end{aligned} \quad (3.15)$$

We assume $\tilde{\psi}_p(\tilde{\mathbf{Y}})$ to be given by

$$\psi_p = \tilde{\psi}_p(\tilde{\mathbf{Y}}) = \frac{1}{2\rho_R} \tilde{\mathbf{Y}} \cdot \tilde{\mathbf{X}}^{(k)} [\tilde{\mathbf{Y}}], \quad (3.16)$$

where $\tilde{\mathbf{X}}^{(k)} := \frac{\partial^2 \tilde{\psi}_p}{\partial \tilde{\mathbf{Y}} \partial \tilde{\mathbf{Y}}}$ denotes a time independent, symmetric, positive definite fourth-order tensor. From (3.10), (3.11) and (3.16),

$$\psi_p = \tilde{\psi}_p(\hat{\mathbf{Y}}, \Delta) = \frac{1}{2\rho_R} \hat{\mathbf{Y}} \cdot \hat{\mathbf{X}}^{(k)}(\Delta) [\hat{\mathbf{Y}}], \quad \hat{\mathbf{Z}} = \hat{\mathbf{X}}^{(k)} [\hat{\mathbf{Y}}], \quad (3.17)$$

with $\hat{\mathbf{X}}^{(k)}$ being given by $\hat{\mathbf{X}}^{(k)} := \frac{\partial^2 \tilde{\psi}_p}{\partial \hat{\mathbf{Y}} \partial \hat{\mathbf{Y}}}$. Let $\tilde{\mathbf{M}}^{(k)}$, $\hat{\mathbf{M}}^{(k)}$ be a fourth-order tensors with $\tilde{\mathbf{M}}^{(k)} \tilde{\mathbf{X}}^{(k)} = \tilde{\mathbf{X}}^{(k)} \tilde{\mathbf{M}}^{(k)} = \mathbf{E}$, $\hat{\mathbf{M}}^{(k)} \hat{\mathbf{X}}^{(k)} = \hat{\mathbf{X}}^{(k)} \hat{\mathbf{M}}^{(k)} = \mathbf{E}$. Then, from (3.16) and (3.11), it follows that

$$\rho_R \frac{\partial \tilde{\psi}_p}{\partial \tilde{\mathbf{Y}}} = \tilde{\mathbf{X}}^{(k)} [\tilde{\mathbf{Y}}], \quad \tilde{\mathbf{Y}} = \tilde{\mathbf{M}}^{(k)} \left[\rho_R \frac{\partial \tilde{\psi}_p}{\partial \tilde{\mathbf{Y}}} \right] = \tilde{\mathbf{M}}^{(k)} [\Delta^T \hat{\mathbf{Z}} \Delta]. \quad (3.18)$$

Using the above relations, it can be seen, after some algebraic manipulations, that

$$\hat{\mathbf{Z}} \cdot \dot{\hat{\mathbf{Y}}} = \dot{\hat{\mathbf{Y}}} \cdot \hat{\mathbf{Z}} - 2\hat{\xi}_A \cdot (\Delta \Delta^T), \quad (3.19)$$

$$\dot{\hat{\mathbf{Y}}} \cdot \hat{\mathbf{Z}} = \tilde{\mathbf{M}}^{(k)} [\Delta^T \hat{\mathbf{Z}} \Delta] \cdot \Delta^T \hat{\mathbf{Z}} \Delta + 2\hat{\mathbf{Y}} \hat{\mathbf{Z}} \cdot \hat{\mathbf{D}}_p + \hat{\xi}_A \cdot \hat{\mathbf{W}}_p. \quad (3.20)$$

On inserting (3.19), (3.20) in (3.15), after some rearrangement of terms,

$$\Delta^T \hat{\mathbf{Z}} \Delta \cdot \left\{ \Delta^T \hat{\mathbf{D}}_p \Delta - \tilde{\mathbf{M}}^{(k)} \left[\Delta^T \hat{\mathbf{Z}} \Delta \right] \right\} + \hat{\xi}_A \cdot (\hat{\Omega}^{(e)} - \hat{\Omega}^{(k)}) \geq 0, \quad (3.21)$$

where the skew-symmetric tensor $\hat{\Omega}^{(k)}$ is given by

$$\hat{\Omega}^{(k)} := \hat{\mathbf{W}}_p - \dot{\Delta} \Delta. \quad (3.22)$$

$\dot{\Delta} \Delta$ is the constitutive spin related to the kinematic hardening and $\hat{\Omega}^{(k)}$ is the corresponding plastic spin. Clearly

$$\left\{ \Delta^T \hat{\mathbf{D}}_p \Delta - \tilde{\mathbf{M}}^{(k)} \left[\Delta^T \hat{\mathbf{Z}} \Delta \right] \right\} \geq 0, \quad \hat{\xi}_A \cdot (\hat{\Omega}^{(e)} - \hat{\Omega}^{(k)}) \geq 0 \quad (3.23)$$

are sufficient conditions for (3.21). In order to fulfill (3.23)₁, we assume

$\left\{ \Delta^T \hat{\mathbf{D}}_p \Delta - \tilde{\mathbf{M}}^{(k)} \left[\Delta^T \hat{\mathbf{Z}} \Delta \right] \right\}$ to be given by

$$\Delta^T \hat{\mathbf{Z}} \Delta \cdot \left\{ \Delta^T \hat{\mathbf{D}}_p \Delta - \tilde{\mathbf{M}}^{(k)} \left[\Delta^T \hat{\mathbf{Z}} \Delta \right] \right\} = \dot{s} \left(\tilde{\mathbf{M}}^{(k)} \tilde{\mathbf{B}}^{(k)} \right) [\Delta^T \hat{\mathbf{Z}} \Delta], \quad (3.24)$$

where $\tilde{\mathbf{B}}^{(k)}$ represents a symmetric, positive semi definite fourth-order tensor. From (3.24)

$$\hat{\mathbf{Z}} = \Delta \left(\tilde{\mathbf{X}}^{(k)} [\Delta^T \hat{\mathbf{D}}_p \Delta] \right) \Delta^T - \dot{s} \Delta \left(\tilde{\mathbf{B}}^{(k)} [\Delta^T \hat{\mathbf{Z}} \Delta] \right) \Delta^T, \quad (3.25)$$

or

$$\hat{\mathbf{Z}} = \tilde{\mathbf{X}}^{(k)} [\hat{\mathbf{D}}_p] - \dot{s} \tilde{\mathbf{B}}^{(k)} [\hat{\mathbf{Z}}]. \quad (3.26)$$

A simple sufficient condition for (3.23)₂ may be constructed by assuming the existence of a function

$$\chi = \hat{\chi}(\hat{\xi}_A, \dots) \geq 0, \quad (3.27)$$

which is convex with respect to $\hat{\xi}_A$, remains unaltered if rigid body rotations $\bar{\mathbf{Q}}$ are superposed on the plastic intermediate configuration and satisfies the property $\hat{\chi}(\mathbf{0}, \dots) = 0$. Then the condition

$$\hat{\mathbf{\Omega}}^{(e)} - \hat{\mathbf{\Omega}}^{(k)} = \dot{s} \frac{\partial \hat{\chi}}{\partial \hat{\xi}_A} \quad (3.28)$$

is sufficient for (3.23)₂. Furthermore,

$$\hat{\mathbf{\Omega}}^{(k)} = \sqrt{2/3} \dot{s} \hat{\mathbf{N}}_A - \dot{s} \frac{\partial \hat{\chi}}{\partial \hat{\xi}_A}. \quad (3.29)$$

Eqs. (3.26) and (3.29) represent the evolution equations governing the response of kinematic hardening. Eq. (3.28) indicates, that the plastic spin related to the elasticity law is always equal to the plastic spin related to the kinematic hardening rule, provided, the tensor $\partial \hat{\chi} / \partial \hat{\xi}_A$ vanishes identically.

4. CONCLUDING REMARKS

Summarizing, we have presented a theory for anisotropic plastic yielding, which relies upon an anisotropic free energy function and an anisotropic yield function. The various directions of symmetry in the substructure of the model-material are elaborated by appropriate rotation tensors. For the evolution of the substructure itself only the plastic spins associated to these rotations are needed. The constitutive equations governing the response of the plastic spin tensors are derived as sufficient conditions for the second law of thermodynamics. An example for the so obtained constitutive theory is given in Häusler and Tsakmakis (2001), where in particular transversely isotropic constitutive properties, modeled with structural tensors, are discussed.

5. REFERENCES

- [1] Aravas, N., 1992, *Finite elastoplastic transformations of transversally isotropic metals*, International Journal of Solids and Structure 29, 2137-2157. 7.
- [2] Casey, J., Naghdi, P., 1981, *A correct definition of elastic and plastic deformation and its computational significance*, Journal of Applied Mechanics 48, 983-985.
- [3] Coleman, B. D., Gurtin, M. E., 1967, *Thermodynamics with internal state variables*, J. Chem. Phys. 47, 597-613.
- [4] Dafalias, Y. F., 1987, *Issues on the constitutive formulation at large elastoplastic deformations, Part I: Kinematics*, Arch. Mech. 69, 119-138.
- [5] Green, A. E., Naghdi, P., 1971, *Some remarks on elastic-plastic deformations at finite strains*, International Journal of Engineering Science 9, 1219-1229.
- [6] Häusler, O., Tsakmakis, C., 2001, *Description of plastic anisotropy effects at large deformations, Part II: The case of transversal isotropy*, submitted for publication.
- [7] Kratochvil, J., Dillon, Jr., O. W., 1969, *Thermodynamics of elastic-plastic materials as a theory with internal state variables*, Journal of Applied Physics 40, 3207-3218. 12.

- [8] Lubliner, J., 1986, *Normality rules in large-deformation plasticity*, Mechanics of Materials 5, 29-34. 5.
- [9] Lubliner, J., 1990, *Large-deformation plasticity*, in "Plasticity Theory", chapter 8, pp. 438-470. Macmillan Publishing Company, New York. 5.
- [10] Truesdell, C., Noll, W., 1965, *The nolinear field theories of mechanics*, in Flügge, S., "Handbuch der Physik", volume III/3, Berlin-Heidelberg-New York: Springer-Verlag.
- [11] Tsakmakis, Ch.; 2001, *Description of plastic anisotropy effects at large deformations. Part I: Restrictions imposed by the second law and the postulate of Il'iushin*, submitted for publication.

“COLD” WORK AND STABILITY IN SOFTENED MATERIALS

N.C. Charalambakis

Department of Civil Engineering
Aristotle University of Thessaloniki, GR-54006 Thessaloniki, Greece

1. SUMMARY

The fraction ζ of plastic work, stored as energy for the creation and rearrangements of crystal defects and often called “cold” work, is usually taken equal to a constant. In this paper, which presents some results of [5] and [6], we show that ζ , assumed to be a function of strain, strain-rate and temperature, can complete the shear stability and instability criteria of softened materials.

2. INTRODUCTION

During plastic deformation of metals, a small portion of plastic work, ζ , is held into the material. This portion is called latent energy of cold work or cold work and is related to the new situation of crystal defects. The remainder quantity of plastic work is transformed into heating. In softened materials, the material resistance is decreasing with respect to temperature. Then, if the later is highly non-uniform, there exist zones of weakened material, especially under intense straining or high strain-rate. Initial strain non-uniformities, due to geometrical defects, may cause additional weakness. The localized shear deformation may lead to the formation of adiabatic shear bands and, eventually, to catastrophic fracture. The adiabatic process is approached if the shearing is applied very rapidly and the heat cannot be conducted far from the shear bands.

In this paper, we study the specific role of cold work in the shear stability and instability regime of softened materials. To this end, we suppose that the cold work ζ is a function of strain γ , strain-rate $\dot{\gamma}$, and temperature θ . The dependence of ζ on strain and strain-rate is supposed to comply with the very interesting experimental findings of Hodowany, Ravichandran, A. Rosakis and P. Rosakis [1], while the dependence (ζ, θ) is unknown, but necessary [2]. In [1], it is shown that the materials used, an aluminium 2024-T3 alloy and an a-titanium, exhibit a strain-sensitive ζ in the following manner: for small strain, ζ is

increasing until a critical value of strain, after which ζ is decreasing, becoming constant after a second critical value of strain. On the other hand, the experimental behavior of ζ with respect to strain-rate differs from material to material used, being always non-increasing with respect to strain-rate.

An interesting question is how the above assumption on ζ modifies the thermoviscoplastic instability mechanism, based on the leading role of softening. In other words, how the existing stability and instability criteria, based on the assumption that ζ is a material constant, are influenced by the experimentally observed history of ζ .

The classical thermoviscoplastic instability mechanism is related to the outcome of the competition between the thermomechanical parameters, which measure the strain hardening, strain-rate sensitivity and thermal softening. According to the relationship between these parameters, we may have the following types of large time behavior: (i) strong stability, with a time-independent asymptotic strain, (ii) weak stability, with an uniform time-increasing straining and (iii) shear banding, leading to additional shear bands and/or shear fracture. The last behavior is characterized by highly non-uniform straining. Generally speaking, there exist additional parameters, such as the thermal diffusivity, the strength of material inhomogeneities and the pressure sensitivity (for polymers), but it seems that, in adiabatic shearing of metals, the thermal softening is the leading factor of instability.

The efficient mathematical way to detect shear banding, is to identify it with the "blow-up" of strain or strain-gradient. Then, the elegant application of non-linear analysis techniques [3] permitted to Tzavaras to establish stability and instability criteria between the thermomechanical parameters. Tzavaras proved that a sufficient and necessary condition for stability of power law materials, is that the thermal softening must be inferior than the combined effect of strain hardening and strain-rate sensitivity, confirming previous works of Clifton and Molinari (see, for instance, [4]). In this paper, we present some results of a recent work [5,6], according to which the above condition is always valid, provided that an additional sufficient condition, between the maximum and minimum values of ζ , the thermal softening, a , and the strain hardening, m , is valid. Moreover, in the case of instability and for big initial temperature and/or small initial strain, the critical time at which the stability regime ceases, depends crucially on the maximum value of ζ . It seems that the stability regime exhibits a "long life", if the amount of energy stored by rearrangements of crystal defects, is large.

A second, less accurate, way to obtain stability conditions, is the linearized stability analysis. We apply this method to the shearing of a mild steel exhibiting the Costin et al [7] and Litonski [8] flow stress. The results indicate that the stable response of the uniform shearing is ensured only by the increasing branch of the curve (ζ, γ) , combined with moderate values of the slopes of (ζ, γ_t) (we note that ζ is decreasing with respect to γ_t [1]) and (ζ, θ) . During this stage, the leading factors of stability are the hardening capacity, m , and the stored energy of the metal. We note that the strain-rate sensitivity, which always plays a stabilizing role in the competition with thermal softening, exhibits now a parallel, opposite effect by reducing the cold work portion and finally favoring the emergence of instability.

3. STABILITY AND INSTABILITY CONDITIONS

In this section we summarize the results obtained in [5,6]. We first consider a material characterized by the power law

$$\sigma = \theta^a \gamma^m \gamma_t^n, \quad a > m.$$

The shearing process is caused by prescribed steady boundary velocities or stresses. Then, it turns out [5] that the shear banding is excluded provided that

$$(a/m) \zeta_{\max} - \zeta_{\min} < (a/m) - 1$$

and

$$m+n-a > 0.$$

This result is a generalization of the stability condition of Tzavaras [3] and Molinari and Clifton [4], valid for constant ζ . The second inequality is a necessary and sufficient condition, while the first one imposes a bound on the variations of the cold work and seems to be valid for many materials used in experiments.

Concerning the instability condition, it turns out [5] that if

$$-p = m+n-a < 0,$$

then the shearing process, caused by a prescribed shear force σ^* at the boundaries, exhibits shear banding at the critical time

$$t_{cr} = n/\sigma^* \{ p [\min((1-\zeta_{\max}), \theta_0/\gamma_0)]^{a/n} \gamma_0^p \},$$

where θ_0 , γ_0 the initial temperature and strain at the boundary, in which shear banding is manifested. We easily verify that, in the case of small initial boundary temperature and/or strain, the experimentally observed function of ζ , exhibiting a regime with large values of cold work, followed by a regime with small values, may prolong the stable material response, in the sense that we obtain values of t_{cr} which are larger than the corresponding to a "mean" value of ζ .

Similar results can be obtained for a material characterized by the constitutive law

$$\sigma = (1-\theta)(1+\gamma)^n \varphi(\gamma), \quad \varphi_\gamma > 0.$$

It turns out [5] that the uniform shearing process, caused by a steady strain-rate η , is stable, as long as ζ is increasing with respect to strain and, at the same time, its slope of decrease with respect to strain-rate is moderate enough. However, the above conditions may be valid only at the early stages of deformation, during a regime of increasing cold work with respect to strain. After this regime, the work converted into heating becomes increasing with respect to strain, and, as it is also increasing with respect to strain-rate from the beginning of the process [1], a destabilizing mechanism appears, causing the loss of stability. It seems that, together with the strain hardening capacity, the second crucial factor of stability is the slope ω of the curve (β, γ) , where

$$\beta = 1 - \zeta$$

is the work converted into heating. It turns out [6] that a sufficient stability condition is the following

$$\omega < (1/(1+\eta)^n) \varphi^2 \varphi_\gamma - (1+n\eta/(1+\eta))\beta,$$

which is satisfied if the maximum value of β (which corresponds to the minimum value of cold work), is sufficiently small and, at the same time, if the hardening capacity of the material ϕ_y is sufficiently large, in order to keep the right member of the above inequality positive.

4. REFERENCES

- [1] Hodowany J., Ravichandran G., Rosakis A.J. and Rosakis P., Partition of plastic work into heat and stored energy in metals, *Journal of Experimental Mechanics* 40, 113-123 (2000).
- [2] Rosakis P., Rosakis A.J., Ravichandran A.J. and Hodowany J., A thermodynamic internal variable model for the partition of plastic work into heat and stored energy in metals, *Journal of the Mechanics and Physics of Solids* 48, 582-607 (2000).
- [3] Tzavaras A., Nonlinear analysis techniques for shear band formation at high strain rates, *Applied Mechanics Reviews* 45, 82-94 (1992).
- [4] Molinari A. and Clifton R.J., Analytical characterization of shear localization in thermo-viscoplastic materials, *Journal of Applied Mechanics* 54, 806-812 (1987).
- [5] Charalambakis N., Shear stability and strain, strain-rate and temperature dependent "cold" work, *International Journal of Engineering Science* (in press).
- [6] Charalambakis N., On the role of strain, strain-rate and temperature dependent fraction of work converted into heating during adiabatic shearing, *Proceedings of the Fourth International Congress on Thermal Stresses*, Osaka, June 2001.
- [7] Burns T.J., Approximate linear stability analysis of a model of adiabatic shear band formation, *Quarterly of Applied Mathematics* 43, 65-83 (1985).
- [8] Litonski J., Plastic flow of a tube under adiabatic torsion, *Bulletin de l' Academie Polonaise des Sciences* (1) 25, 7-14 (1977).

SOME BASIC SOLUTIONS TO DYNAMIC PROBLEMS IN RANDOM MEDIA

C.Z. Karakostas¹ and G.D. Manolis²

¹ITSAK, Finikas, Thessaloniki, GR-55102, Greece

²Department of Civil Engineering, AUTH, Thessaloniki, GR-54006, Greece

1. SUMMARY

In this work, we develop Green's functions for elastic waves in unbounded random media, which in turn can be used within the context of BEM solutions to wave scattering problems. We distinguish two basic cases: First, continua exhibiting small amounts of randomness, in which case the methodology used is a perturbation of all dependent variables about their mean value. Next, we focus on continua with large randomness, whereby we employ a polynomial series expansion. Finally, some examples are presented to contrast the effect of large versus small randomness.

2. INTRODUCTION

Problems involving random media are governed by stochastic differential equations. The key assumption made is decomposition of the differential operator into deterministic plus random parts. Subsequently, the stochastic differential equation and its boundary conditions can be recast as a random integral equation. Solutions can then be found iteratively through use of the resolvent kernel. Alternatively, the dependent variable can be expanded as a Neumann series. Approximate solutions can also be generated, i.e., by applying the expectation operator to the random integral equation and then using various closure approximations, by perturbations with the usual restriction of small fluctuations about a mean value, or by other techniques [1].

In the case of wave motions, two basic representations of material stochasticity are possible, i.e., a random collection of pre-defined scatterers [2] or a random continuum [3]. Propagation of elastic waves in a random medium that differs only slightly from the homogeneous case was first considered by Karal and Keller [4] using the random integral equation formulation. This technique was subsequently extended to multi-layered systems through use of transfer matrices [5]. From a numerical viewpoint, two broad classes for evaluating the dynamic response of random media can be distinguished, namely simulation techniques [6] and perturbation methods [7]. When using the latter technique, numerical implementation is through a Taylor series expansion of key system parameters, in both FEM [8] and BEM [9] environments. Finally, in an effort to overcome the limitation of small parameter uncertainty, series expansions of the random response of a system in terms of polynomials that are orthogonal with respect to the expectation operator have appeared [10]. In this work, we examine some basic fundamental solutions to the equations of elastodynamics, by employing both perturbations and the polynomial chaos technique.

3. ELASTODYNAMIC THEORY

The fundamental laws of elastodynamics are combined to give the Navier-Cauchy equations as

$$(\lambda + \mu) u_{i,jj} + \mu u_{j,ii} + \rho b_j = \rho \ddot{u}_j \quad (1)$$

where λ and μ are the Lamé coefficients, u the displacement, b the body force per unit volume and ρ the material density. The above equations can be re-written in terms of the wave propagation velocities $c_1^2 = (\lambda + 2\mu) / \rho$ (for P-waves) and $c_2^2 = \mu / \rho$ (for S-waves). Also, the summation convention holds for repeated indices. Furthermore, we prescribe

$$u_i(\mathbf{x}, t) = U_i \quad \text{for } \mathbf{x} \in S_1 \quad \text{and} \quad t_i(\mathbf{x}, t) = \sigma_{ij} n_j = T_i \quad \text{for } \mathbf{x} \in S_2 \quad (2)$$

as boundary conditions on the surface $S = S_1 \cup S_2$, where t_i are the tractions and n_j is the outward normal vector to the surface. In the case of time-harmonic motions, all dependent variables are decomposed into an amplitude term (bar superscript) times the $\exp(i\omega t)$ factor.

4. PERTURBATION METHOD

An extension to the case of a random medium is achieved through use of the method of perturbations. The basic assumption is that the wave propagation velocities are functions of random parameter γ , and can be expanded as

$$c_1(\gamma) = c_1^m + c_1^f(\gamma) \quad c_2(\gamma) = c_2^m + c_2^f(\gamma) \quad (3)$$

where c_i^m is a mean (or reference) value and $c_i^f(\gamma)$ is the fluctuation about this mean. If we have a zero-mean fluctuation, a simple representation for the wave propagation velocities is

$$c_1(\gamma) = c_{01}(1 + \gamma) \quad c_2(\gamma) = c_{02}(1 + \gamma) \quad (4)$$

where c_{01} , c_{02} are mean velocities. For γ , we have that $\langle \gamma \rangle = 0$ and $\langle \gamma^2 \rangle = \sigma_\gamma^2$, with the expectation operator $\langle \rangle$ denoting statistical averaging.

The next step is to expand all problem variables in Taylor series. We focus on the fundamental displacement solution \bar{G}_{ij} of eqn (1) for a point impulse in the unbounded continuum and under radiation-type boundary conditions. Specifically,

$$\bar{G}_{ij}(r, s, \gamma) = \bar{G}_{ij}^m + \gamma \bar{G}_{ij}^f = \bar{G}_{ij}(r, s, 0) + \gamma \left. \frac{\partial \bar{G}_{ij}(r, s, \gamma)}{\partial \gamma} \right|_{\gamma=0} \quad (5)$$

where superscripts m and f denote mean and fluctuation parts, respectively, while r is the relative distance between source and receiver. Application of the expectation operator yields a mean value for the first fundamental solution, which coincides with the deterministic one

$$\langle \bar{G}_{ij}(r, s, \gamma) \rangle = \bar{G}_{ij}^m = \bar{G}_{ij}(r, s, 0) \quad (6)$$

If higher order terms are included here, then the mean and deterministic solutions no longer coincide. Furthermore, the covariance between two receivers at r_k and r_l is

$$\langle [\bar{G}_{ij}(r_k, s, \gamma) - \bar{G}_{ij}^m(r_k, s)] [\bar{G}_{ij}(r_l, s, \gamma) - \bar{G}_{ij}^m(r_l, s)] \rangle = \sigma_\gamma^2 [\bar{G}_{ij}^f(r_k, s)] [\bar{G}_{ij}^f(r_l, s)] \quad (7)$$

where σ_γ^2 is the variance of random variable γ . The variance can finally be obtained from the covariance by setting $r_k = r_l = r$.

The fundamental solutions for 2D wave propagation in the Laplace transformed domain have been derived in Ref. [11], where details can be found. The displacement solution is given here, after noting that for $s = i\omega$, the Fourier transform is recovered as

$$\bar{G}_{ij}(r, s, \gamma) = \frac{1}{2\pi\rho c_2(\gamma)^2} \{ \psi(r, s, \gamma) \delta_{ij} - \varphi(r, s, \gamma) r_i r_j \} = \frac{1}{2\pi\rho c_2(\gamma)^2} V(r, s, \gamma) \quad (8a)$$

$$\psi(r, s, \gamma) = K_0\left(\frac{sr}{c_2(\gamma)}\right) + \frac{c_2(\gamma)}{sr} \left\{ K_1\left(\frac{sr}{c_2(\gamma)}\right) - \frac{c_2(\gamma)}{c_1(\gamma)} K_1\left(\frac{sr}{c_1(\gamma)}\right) \right\} \quad (8b)$$

$$\varphi(r, s, \gamma) = K_2\left(\frac{sr}{c_2(\gamma)}\right) - \frac{c_2(\gamma)^2}{c_1(\gamma)^2} K_2\left(\frac{sr}{c_1(\gamma)}\right) \quad (8c)$$

In the above expressions, K_n are modified Bessel functions of order n . The mean value is

$$\langle \bar{G}_{ij}(r, s, \gamma) \rangle = \bar{G}_{ij}^m = \bar{G}_{ij}(r, s, 0) = \frac{1}{2\pi\rho c_{02}^2} \{ \psi(r, s, 0) \delta_{ij} - \varphi(r, s, 0) r_i r_j \} \quad (9)$$

while the covariance is given by eqn (7). The fluctuation term required there is computed as

$$\begin{aligned} \bar{G}_{ij}^f(r, s, 0) &= \frac{\partial \bar{G}_{ij}(r, s, \gamma)}{\partial \gamma} \Big|_{\gamma=0} = \frac{1}{2\pi\rho} \left\{ \left[\frac{\partial}{\partial \gamma} \left(\frac{1}{c_2^2} \right) \right] V(r, s, \gamma) + \frac{1}{c_2^2} \frac{\partial V(r, s, \gamma)}{\partial \gamma} \right\} \Big|_{\gamma=0} \\ &= \frac{1}{2\pi\rho} \left\{ D(\gamma) V(r, s, \gamma) + \frac{1}{c_2^2} E(r, s, \gamma) \right\} \Big|_{\gamma=0} \end{aligned} \quad (10)$$

where the various terms appearing above are all given in Ref. [11]. These solutions have been tested against results given by Monte-Carlo simulations and have been found to be quite accurate, when randomness is kept within the limits of perturbation theory (i.e., fluctuations of no more than 10% of the mean).

5. POLYNOMIAL CHAOS METHOD

This method will be applied for the case of time-harmonic elastic waves in a 3D continuum under anti-plane strain conditions, which is governed by Helmholtz's equation

$$\nabla^2 u(\mathbf{x}, \gamma) + k^2(\gamma) u(\mathbf{x}, \gamma) = f(\mathbf{x}, \gamma) \quad (11)$$

We have that u is the displacement component in the z -direction and k is the wave number equal to $\omega/c(\gamma)$, where ω is the frequency and c the wave speed. The solution to eqn (11)

when the forcing function is Dirac's delta function with magnitude f_0 is Green's function. For the deterministic case, the above equation in cylindrical coordinates becomes

$$\frac{d^2 u(r)}{dr^2} + \frac{1}{r} \frac{du(r)}{dr} + k_0^2 u(r) = \delta(r) \quad (12)$$

with k_0 the mean wave number. The solution for outgoing waves is well known, i.e.,

$$u(r) = (i/4) H_0^{(1)}(k_0 r) \quad (13)$$

where $H_0^{(1)}$ is the Hankel function of first kind, zero order.

Stochasticity results due to randomness in the wave number, which is defined in terms of a mean plus a fluctuating component as

$$k(\gamma) = k_0 + k_1 \gamma \quad (14)$$

In the above, k_1 is a coefficient and γ is zero mean with unit variance σ_γ^2 . Thus, a second moment representation of the wave number is

$$\left. \begin{aligned} \langle k(\gamma) \rangle &= \langle k_0 \rangle = k_0 \\ \langle k^2(\gamma) \rangle &= \langle (k_0 + k_1 \gamma)^2 \rangle = k_0^2 + k_1^2 \sigma_\gamma^2 = k_1^2 \end{aligned} \right\} \quad (15)$$

The next step is to expand both fundamental solution $u(r, \gamma)$ and forcing function $f(r, \gamma)$ as a series in terms of an orthogonal set of polynomials in γ . This implies separation of variables, since polynomials P_n are weighted by spatially dependent coefficients U_n and F_n in the form

$$\left. \begin{aligned} u(r, \gamma) &= \sum_{n=0}^N P_n(\gamma) U_n(r) \\ f(r, \gamma) &= \sum_{n=0}^N P_n(\gamma) F_n(r) \end{aligned} \right\} \quad (16)$$

where N is the order of approximation in the random space. The choice of the polynomial basis is dictated by the fact that the expectation is essentially an orthogonality condition, i.e.,

$$\langle P_n(\gamma) P_m(\gamma) \rangle = \int_{\Gamma} pdf(\gamma) P_n(\gamma) P_m(\gamma) d\gamma = \delta_{nm} \quad (17)$$

with $pdf(\gamma)$ the probability density function of the random variable γ . Therefore, the selection of the polynomials basis depends on the pdf assumed for the wave number, with Hermite polynomials corresponding to a Gaussian distribution.

The above expansions are substituted into the governing equation of motion, followed by pre-multiplication by $H_m(\gamma)$ and application of the expectation operator. This yields the following coupled set of equations:

$$\begin{aligned} & \langle H_m H_n \rangle \nabla_r^2 U_n + \\ & \left[k_0^2 \langle H_m H_n \rangle + 2k_0 k_1 \langle \gamma H_m H_n \rangle + k_1^2 \langle \gamma^2 H_m H_n \rangle \right] U_n = \langle H_m H_n \rangle F_n \end{aligned} \quad (18)$$

Use of the recurrence relations for Hermite polynomials in conjunction with the orthogonality property yields a coupled system of Helmholtz differential equations, which govern the spatially dependent coefficients $U_n(r)$ of the random fundamental solution. We thus have

$$\begin{aligned} & h_{m,n} \nabla_r^2 U_n + \\ & \left[(k_1^2/4) h_{m,n+2} + k_0 k_1 h_{m,n+1} + (k_0^2 + k_1^2(n+1/2)) h_{m,n} + 2n k_0 k_1 h_{m,n-1} + n(n-1) k_1^2 h_{m,n-2} \right] U_n = \\ & = h_{m,n} F_n \end{aligned} \quad (19)$$

with the “weights” $h_{m,n}$ given as $h_{m,n} = \langle H_m(\gamma) H_n(\gamma) \rangle = \sqrt{\pi} 2^n (n!) \delta_{nm}$. By expanding the above equations we recover the following matrix differential equation of the Helmholtz type:

$$\frac{d^2}{dr^2} \{U\} + \frac{1}{r} \frac{d}{dr} \{U\} + [K] \{U\} = \{F\} \quad (20)$$

In order to uncouple eqn (20), system matrix $[K]$ must be diagonalized. This can be achieved by using its eigenvalues $[\lambda_1, \lambda_2, \dots, \lambda_n]$ and the corresponding eigenvector matrix $[\Phi] = [\{\phi\}_1, \{\phi\}_2, \dots, \{\phi\}_n]$. Although $[K]$ is non-symmetric, its coefficients are all positive, real numbers and thus it will possess a complete set of complex eigenvalues and eigenvectors. Details are given in Ref. [12], and we finally get a system of uncoupled Helmholtz equations as

$$\frac{d^2}{dr^2} V_n(r) + \frac{1}{r} \frac{d}{dr} V_n(r) + \lambda_n V_n = b_n \delta(r) \quad (21)$$

with $n=0,1,2,\dots$. The solution for outgoing SH-waves is simply

$$V_n(r) = (i/4) H_0^{(1)}(\lambda_n r) \quad (22)$$

where λ_n is the appropriate wave number corresponding to the n -th expansion term.

Next, the mean value of the original fundamental solution is

$$\begin{aligned} m_u(r) &= \langle u(r, \gamma) \rangle = \langle H_n(\gamma) \rangle U_n(r) = \langle H_n H_0 \rangle U_n = \\ &= h_{0,0} U_0 + h_{0,1} U_1 + \dots = \sqrt{\pi} U_0(r) + 0 + \dots = \sqrt{\pi} U_0(r) \end{aligned} \quad (23)$$

which no longer equals the deterministic one. In fact, the former solution exceeds the latter in absolute value, and the physical explanation for this is the interference effect caused by continuous scattering of the propagating signal as it travels through the random medium [4]. Finally, we determine the covariance of $u(r, \gamma)$ as

$$\begin{aligned} \text{cov}_u(r_1 r_2) &= \langle [u(r_1, \gamma) - m_u(r_1)] [u(r_2, \gamma) - m_u(r_2)] \rangle = \\ &= \left\langle \left[H_0^* U_0(r_1) + H_1 U_1(r_1) + \dots \right] \left[H_0^* U_0(r_2) + H_1 U_1(r_2) + \dots \right] \right\rangle = \end{aligned}$$

$$\begin{aligned}
&= \langle H_0^* H_0^* \rangle U_0(r_1) U_0(r_2) + \langle H_1 H_1 \rangle U_1(r_1) U_1(r_2) + \dots = \\
&= h_{0,0}^* U_0(r_1) U_0(r_2) + h_{1,1} U_1(r_1) U_1(r_2) + \dots
\end{aligned}
\quad (24)$$

where $H_0^* = H_0 - \sqrt{\pi}$. The above result can be written as

$$\text{cov}_u(r_i, r_j) = (1 - \sqrt{\pi})^2 h_{0,0} + \sum_{n=1}^{\infty} h_{n,n} U_n(r_i) U_n(r_j) \quad (25)$$

with $h_{0,0} = \sqrt{\pi}$, $h_{1,1} = 2\sqrt{\pi}$, $h_{2,2} = 8\sqrt{\pi}$, $h_{3,3} = 48\sqrt{\pi}$, $h_{4,4} = 384\sqrt{\pi}$, etc.

6. NUMERICAL EXAMPLES

6.1. Unlined circular tunnel enveloped by a P-wave

In this example, the fundamental solutions developed in section 4 are incorporated in a 2D, time-harmonic BEM program with inverse transformation capabilities [11]. The boundary-value problem that is solved is a circular unlined tunnel of radius $R=5$ m placed at some depth in the ground and enveloped by a P-wave propagating along the negative X-direction, as shown in Fig. 1. This wave produces stresses along the propagation path ($\sigma_{xx} = -10$ MPa) as well as in the lateral direction ($\sigma_{yy} = \nu \sigma_{xx} / (1 - \nu)$). The mean material properties of the surrounding soil are $\lambda = \mu = 8000$ MPa and $\rho = 2550$ kg/m³, which give mean wave velocities of $c_{01} = 3068$ m/sec and $c_{02} = 1770$ m/sec. Finally, $t=0$ is the instant the P-wave arrives at station 1.

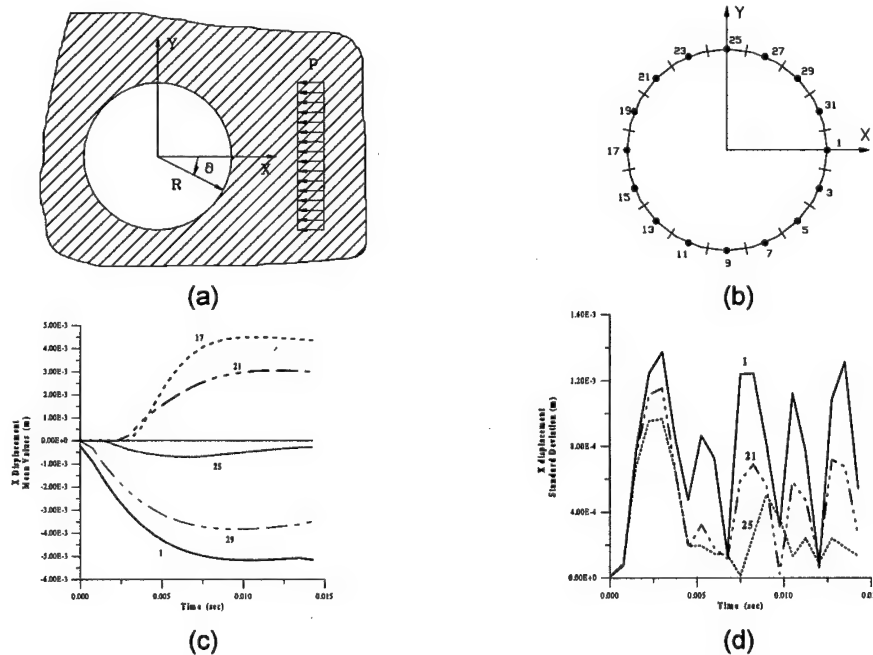


Figure 1: Circular tunnel under a P-wave: (a) geometry, (b) discretization, (c) mean values and (d) standard deviations of horizontal displacements u_x versus time.

The statistical measures of the tunnel response are evaluated for a given variance of the wave velocity. Starting with the value of $\sigma_\gamma^2=0.10$ for the variance of random parameter γ , the standard deviations of the two wave velocities c_1 and c_2 are 970 m/sec and 560 m/sec, respectively. The total time span examined is 0.015 sec (i.e., triple the time necessary for the wave to fully envelope the tunnel), discretized into 20 equal steps, while 16 three-noded boundary elements are used for modeling the cavity surface. In Fig. 1, the central node of each element is numbered and denoted by a full circle; the computed mean values for the displacements at various nodes are also depicted. The accuracy of the numerical results for the mean values was gauged against the deterministic ones obtained by Baron and Matthews [13] and found to be entirely satisfactory. Finally, we plot the standard deviation (SD) of the displacements at nodes 1, 21 and 25. We note that for a SD of the random parameter γ equal to $\sigma_\gamma=32\%$, the SD of the displacements is of the order of 15%.

6.2. SH-wave moving along a ray

As a second example, consider SH-waves moving through a continuous geological medium with a shear wave velocity $c_s = 6.28$ km/sec and at a frequency $\omega = 1$ Hz = 2π rad/sec. For this case, the reference deterministic wave number is $k_0 = 1.0$ km⁻¹. Also, the amount of randomness in the wave number $k(\gamma)$ is 50 % of k_0 , where we can expect significant departure from the usual results obtained for mild randomness. Starting with a unit impulse at the source, we place 40 receivers along a straight-line path from the source and for a distance of $r = 10$ km. For comparison, the reference wavelength of the SH-wave at this frequency is $l_0=2\pi/k_0=6.28$ km. Figure 2 plots the mean amplitude, mean phase angle, variance amplitude and variance phase angle of $u(r,\gamma)$ for both perturbation method with $\sigma_\gamma = 1$ and the polynomial chaos method with the five-term (N=5) and three-term (N=3) expansions.

Generally speaking, we see that the perturbation method yields a mean solution equal to the deterministic one, plus a variance that at high randomness is essentially a scaled version of what is obtained at low randomness. By contrast, the polynomial chaos method gives a markedly different picture. Specifically, the mean value amplitude is no longer a smoothly decreasing function of distance, but significantly overshoots the deterministic amplitude at small distances from the source and subsequently exhibits an oscillatory behavior. Furthermore, past a distance of $r = 2$ km, the N=3 and the N=5 term expansion results start to differ. As far as the variance is concerned, the polynomial chaos method no longer predicts a nearly linear increase in amplitude, which is an indication of the cumulative effect that small randomness has on the propagating signal. In fact, the variance attains large values close to the source of the disturbance, then decreases and at the same time exhibits an oscillatory behavior.

7. CONCLUSIONS

This work presents two basic techniques for handling randomness in continuous media, both of which yield the mean response plus the covariance matrix solution of problems in elastodynamics. Specifically, the perturbation method is used for 2D problems with small amounts of randomness. For large randomness, the polynomial chaos has been presented for anti-plane strain wave propagation problems. In either case, these fundamental solutions can be incorporated within the framework of BEM solutions to problems of engineering interest.

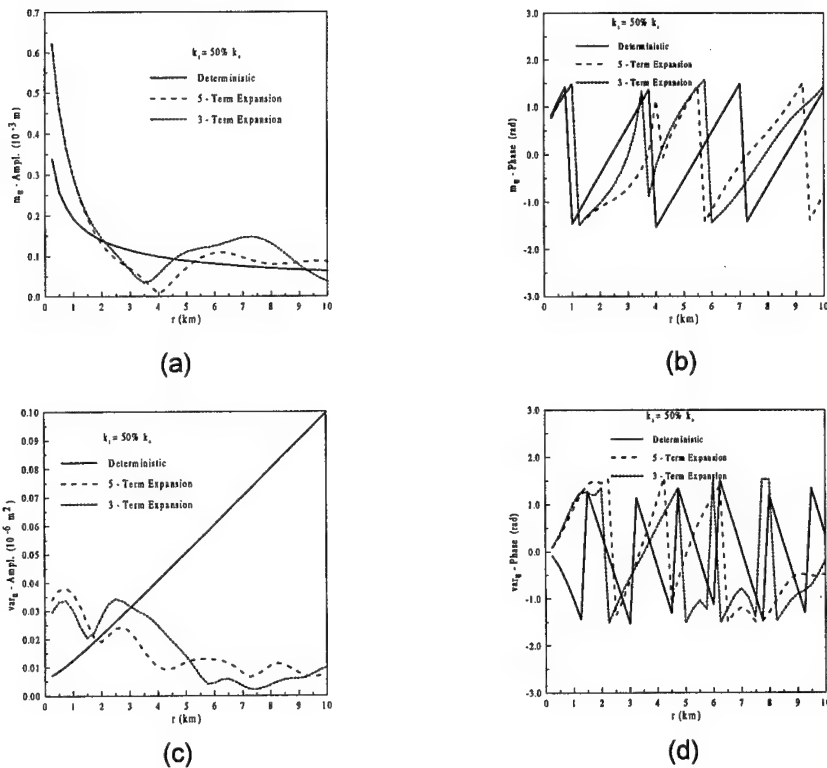


Figure 2: Fundamental solution $u(r, \gamma)$: (a) mean amplitude, (b) mean phase angle, (c) variance amplitude, and (d) variance phase angle versus distance from source for $k_l = 0.50k_0$

8. REFERENCES

- [1] Adomian G., *Stochastic Systems*, Academic Press, New York (1983).
- [2] Sobczyk K., Elastic wave propagation in a discrete random medium, *Acta Mechanica* **25**, 13-28 (1976).
- [3] Chernov L.A., *Wave Propagation in a Random Medium*, Dover, New York (1962).
- [4] Karal F.C. and Keller J.B., Elastic, electromagnetic and other waves in a random medium, *Journal of Mathematical Physics* **5**(4), 537-549 (1964).
- [5] Hryniewicz Z., Mean response to distributed dynamic loads across the random layer for anti-plane shear motion, *Acta Mechanica* **90**, 81-89 (1991).
- [6] Shinozuka M., Digital simulation of random processes and its application, *Journal of Sound and Vibration* **25**, 111-128 (1972).
- [7] Sobczyk K., *Stochastic Wave Propagation*, Elsevier, Amsterdam, 1985.
- [8] Vanmarke E., Shinozuka M., Nakagiri S., Schueller G.I. and Grigoriu M., Random fields and stochastic finite elements, *Structural Safety* **3**, 143-166 (1986).

-
- [9] Burczynski T., Stochastic boundary element methods : Computational methodology and applications, Chapter 12 in P. Spanos and W.Wu (eds.), *Probabilistic Structural Mechanics, an IUTAM Symposium*, Springer-Verlag, Berlin (1993).
 - [10] Spanos P.D. and Ghanem R., Stochastic finite element expansion for random media, *Journal of Engineering Mechanics of ASCE* **115**(5), 1035-1053 (1989).
 - [11] Karakostas C.Z. and Manolis G.D., Dynamic response of unlined tunnels in soil with random properties, *Engineering Structures*, **22**(8), 1013-1027 (2000).
 - [12] Manolis G.D. and Pavlou S., Fundamental solutions for SH waves in a continuum with large randomness, *Engineering Analysis with Boundary Elements* **23**, 721-736 (1999).
 - [13] Baron M.L. and Matthews A.T., Diffraction of a pressure wave by a cylindrical cavity in an elastic medium, *Journal Applied Mechanics* **28**, 347-354 (1961).

ANALYSIS OF RAYLEIGH WAVES IN MICROSTRUCTURED SOLIDS BY DIPOLAR GRADIENT ELASTICITY

H.G. Georgiadis , I. Vardoulakis and E.G. Velgaki

Mechanics Division, National Technical University of Athens,
5 Heroes of Polytechnion Ave., Zographou GR-15773, Greece

1. SUMMARY

The linear theory of dipolar gradient elasticity is employed to analyze surface waves of the Rayleigh type propagating along the surface of a half-space. It is shown that these waves are dispersive at high frequencies. Their dispersion curves have the same form as that provided by the atomic theory of lattices (discrete particle theory).

2. INTRODUCTION

The present work is concerned with Rayleigh-type surface wave propagation in a material with microstructure. To explain *dispersion phenomena* at high frequencies (small wavelengths) occurring in practical situations (see e.g. Gazis et al. [1]; Farnell [2]; Vardoulakis and Vrettos [3]), the problem is attacked with a generalized-continuum elasticity theory. This is an effective version of the dipolar gradient theory of Mindlin [4], and Green and Rivlin [5]. No such a theory was proposed up to now to deal with Rayleigh-wave motions. Similar theories, however, were recently proposed by the authors (see e.g. Vardoulakis and co-workers [6]-[9]; Georgiadis and Vardoulakis [10]; Georgiadis et al. [11]) and other investigators (see e.g. Fleck et al. [12]; Wei and Hutchinson [13]; Manolis [14]) to deal with different wave-propagation and stress-concentration problems.

It is of notice that the classical theory of isotropic elasticity predicts no dispersive Rayleigh-wave motions at any frequency, a result that contradicts experimental data. To remedy this shortcoming, dipolar internal forces of collinear type (no couple-stress effects) and higher-order displacement gradients, in both strain and kinetic energies, are considered here in a simple but yet rigorous version of the general Mindlin – Green/Rivlin theory. Both isotropic and anisotropic material response is considered in an effort to model the phenomena controlling the dispersion of high-frequency surface waves as adequately as possible and to provide means for *estimating* the *micro-mechanical* material parameters involved in gradient theories. Displacement potentials and two-sided Laplace transforms are employed in our study to derive dispersion curves for the high-frequency Rayleigh waves. Further analysis, details and results are given by the present authors elsewhere [15].

3. BASIC CONCEPTS AND EQUATIONS

In this Section we briefly present the basic ideas and equations which describe the dynamics of *gradient-elastic* (*dipolar* or *grade two* elastic) homogeneous materials without couple-stress effects. The point of departure is the following expressions for the strain-energy density W and kinetic-energy density T in a 3D continuum, with respect to a Cartesian coordinate

system $Ox_1x_2x_3$. The gradient-type continuum is viewed as a collection of material cells (see Fig. 1) and is taken to be composed wholly of unit cells. Then, one may write [4],[7],[15]

$$W = \frac{1}{2} c_{pqsj} \epsilon_{pq} \epsilon_{sj} + \frac{1}{2} d_{pqsjlm} \kappa_{pq} \kappa_{lm} + f_{pqsjl} \kappa_{pq} \epsilon_{jl}, \quad (1)$$

$$T = \frac{1}{2} \rho \dot{u}_p \dot{u}_p + \frac{1}{6} \rho h^2 \left(\partial_p \dot{u}_q \right) \left(\partial_p \dot{u}_q \right), \quad (2)$$

where $(c_{pqsj}, d_{pqsjlm}, f_{pqsjl})$ are tensors of material constants, ρ is the mass density, $2h$ is the internal characteristic length of the structured continuum, u_p is the displacement vector, $\epsilon_{pq} = (1/2)(\partial_p u_q + \partial_q u_p)$ is the usual linear strain tensor with $\partial_p \equiv \partial/\partial x_p$, $\kappa_{pq} = \partial_p \epsilon_{qs} = \partial_p \epsilon_{sq}$, $(\dot{})$ denotes time differentiation, and the Latin indices span the range (1,2,3).

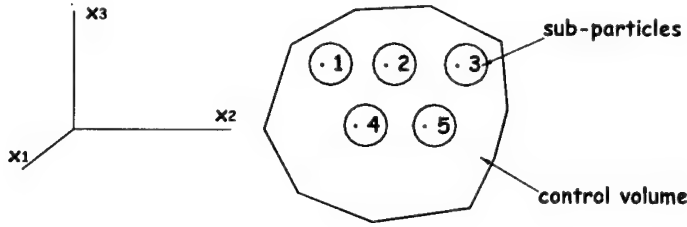


Figure 1: A continuum with microstructure

Further, appropriate definitions for the stresses follow from the variation of W

$$\tau_{pq} = \frac{\partial W}{\partial \epsilon_{pq}}, \quad m_{pqs} = \frac{\partial W}{\partial \kappa_{pqs}} \equiv \frac{\partial W}{\partial (\partial_p \epsilon_{qs})}, \quad (3a,b)$$

where τ_{pq} is the (symmetric) Cauchy stress tensor and $m_{pqs} = m_{psq}$ is the double (or dipolar) stress tensor. The latter tensor follows from the notion of *multipolar* forces, which naturally arise from the following expansion of the mechanical power $M = F_p \dot{u}_p + F_{pq} \left(\partial_p \dot{u}_q \right) + F_{pqs} \left(\partial_p \partial_q \dot{u}_s \right) + \dots$, where F_p are the usual forces (monopolar forces) within the classical continuum mechanics (monopolar continuum mechanics), and (F_{pq}, F_{pqs}, \dots) are referred to as multipolar forces (double forces, triple forces and so on). Thus, the resultant force on an ensemble of particles (material cells) can be viewed as being decomposed into *external* and *internal* forces with the latter ones being self-equilibrating. However, these self-equilibrating forces (which are multipolar forces) produce *non-vanishing* stresses (double stresses, triple stresses and so on).

Next, from Hamilton's principle and variational considerations on (1) and (2), where the only independent variation is δu_p , one obtains the following equations of motion (in the absence of body forces) and pertinent traction boundary conditions [4],[7],[15]

$$\partial_p(\tau_{pq} - \partial_s m_{spq}) = \rho \ddot{u}_q - \frac{\rho h^2}{3} (\partial_{pp} \ddot{u}_q) \quad (4)$$

The traction boundary conditions involve both a surface force per unit area, and a surface double force (without moment) per unit area [4]. Finally, it is convenient to introduce the tensor σ_{pq} (which, however, in the general *inertial* case is not an objective quantity) defined as $\sigma_{pq} \equiv \tau_{pq} + \alpha_{pq}$, where $\alpha_{qs} = I \left(\partial_q \ddot{u}_s \right) - \partial_p m_{pqs}$ with $I = \rho h^2/3$, so that Eq. (4) can take the more familiar form $\partial_p \sigma_{pq} = \rho \ddot{u}_q$.

Now, the simplest possible form of the strain-energy density function in (1) is considered (Vardoulakis and co-workers [7],[8]): $W = \frac{1}{2} \lambda \varepsilon_{pp} \varepsilon_{qq} + \mu \varepsilon_{pq} \varepsilon_{qp} + \frac{1}{2} \lambda c (\partial_s \varepsilon_{pp}) (\partial_s \varepsilon_{qq}) + \mu c (\partial_s \varepsilon_{pq}) (\partial_s \varepsilon_{pq}) + \frac{1}{2} \lambda b_s \partial_s (\varepsilon_{pp} \varepsilon_{qq}) + \mu b_s \partial_s (\varepsilon_{pq} \varepsilon_{qp})$, which along with the definitions (3) leads to the following *constitutive relations*

$$\tau_{pq} = (\lambda \delta_{pq} \varepsilon_{ss} + 2\mu \varepsilon_{pq}) + b_s \partial_s (\lambda \delta_{pq} \varepsilon_{ss} + 2\mu \varepsilon_{pq}), \quad (5)$$

$$m_{spq} = (b_s + c \partial_s) (\lambda \delta_{pq} \varepsilon_{jj} + 2\mu \varepsilon_{pq}), \quad (6)$$

where λ and μ are the standard Lamé's constants, c is the gradient coefficient (positive constant with dimensions of square length), $b_s \equiv b v_s$ is a material director, with $v_s v_s = 1$ and b being another material parameter with dimensions of length. In the present study, we consider the particular case $v_s \equiv -n_s$, where n_s is the outward unit normal to the boundary. This seems natural for a body in the form of a half-space and corresponds physically to a weakening or strengthening (this depends upon the choice of a positive or a negative b , respectively) of the body along the direction normal to the surface. In this way, *surface effects* (e.g. material decohesion or surface tension) can *directly* be taken into account in the material constitutive behavior by introducing a kind of *anisotropic* material response.

In summary, Eqs. (4)-(6) are the governing equations for the gradient elasticity theory with no couple stresses. Combining these equations leads to the field equations of the problem. Pertinent *uniqueness* theorems can be proved on the basis of the constraint of a positive definite strain-energy density. As the work in [15] shows, the latter restriction requires the following inequalities for the material constants appearing in the theory: $(3\lambda + 2\mu) > 0$, $\mu > 0$, $c > 0$, $-1 < (b/c^{1/2}) < 1$. Finally, *stability* of the field equation was proved in [15] and to accomplish this the condition $c > 0$ is a necessary one.

4. TIME-HARMONIC RESPONSE IN A HALF-SPACE UNDER CONDITIONS OF PLANE-STRAIN

In order to analyze Rayleigh-wave motions, we consider the following two-dimensional time-harmonic response in the half-space $y \geq 0$ having as a boundary the plane (x,z)

$$u_x(x,y,t) = u_x(x,y) \cdot \exp(i\omega t) \quad , \quad u_y(x,y,t) = u_y(x,y) \cdot \exp(i\omega t) \quad , \quad (7a,b)$$

where u_x and u_y are the displacement components, t is the time, and ω is the frequency. We also take $b_x = 0$ and $b_y = b$ in Eqs. (5) and (6). Below, we first derive the field equations of the problem and then we find general solutions via the Lamé potentials ϕ and ψ (these are utilized to decouple the equations of motion) and by utilizing the two-sided Laplace transform.

From Eqs. (4)-(7), one obtains

$$\sigma_{xx} = (1 - c\nabla^2)(\lambda(\partial_x u_x + \partial_y u_y) + 2\mu\partial_x u_x) - I\omega^2 \partial_x u_x \quad , \quad (8)$$

$$\sigma_{xy} = (1 - c\nabla^2)(\mu(\partial_y u_x + \partial_x u_y)) - I\omega^2 \partial_x u_y \quad , \quad (9)$$

$$\sigma_{yx} = (1 - c\nabla^2)(\mu(\partial_y u_x + \partial_x u_y)) - I\omega^2 \partial_y u_x \quad , \quad (10)$$

$$\sigma_{yy} = (1 - c\nabla^2)(\lambda(\partial_x u_x + \partial_y u_y) + 2\mu\partial_y u_y) - I\omega^2 \partial_y u_y \quad , \quad (11)$$

$$\partial_x \sigma_{xx} + \partial_y \sigma_{yx} = -\rho\omega^2 u_x \quad , \quad \partial_x \sigma_{xy} + \partial_y \sigma_{yy} = -\rho\omega^2 u_y \quad . \quad (12),(13)$$

Combining now Eqs. (8)-(11) with (12) and (13) leads to a system of *coupled* PDEs for the displacement components u_x and u_y . Further, by using the new functions - Lamé-type potentials - (ϕ, ψ) defined by $u_x = (\partial\phi/\partial x) + (\partial\psi/\partial y)$ and $u_y = (\partial\phi/\partial y) - (\partial\psi/\partial x)$, and after some tedious algebra, we obtain the following *uncoupled* PDEs as the field equations of the problem

$$c\nabla^4 \phi - g_L \nabla^2 \phi - k_L^2 \phi = 0 \quad , \quad c\nabla^4 \psi - g_T \nabla^2 \psi - k_T^2 \psi = 0 \quad . \quad (14),(15)$$

In the above equations, we have employed the following definitions

$$g_L = 1 - \frac{I\omega^2}{\lambda + 2\mu} \quad , \quad g_T = 1 - \frac{I\omega^2}{\mu} \quad , \quad k_L^2 = \frac{\rho\omega^2}{\lambda + 2\mu} \quad , \quad k_T^2 = \frac{\rho\omega^2}{\mu} \quad , \quad (16)-(19)$$

$$\nabla^2 = \frac{\partial^2}{\partial x^2} + \frac{\partial^2}{\partial y^2} \quad , \quad \nabla^4 = \frac{\partial^4}{\partial x^4} + 2\frac{\partial^4}{\partial x^2 \partial y^2} + \frac{\partial^4}{\partial y^4} \quad , \quad (20),(21)$$

and we also notice that $k_L = \omega/V_L$ and $k_T = \omega/V_T$, where V_L and V_T are, respectively, the velocities of the longitudinal and transverse waves in the *classical* (i.e. non-gradient) elasticity theory.

5. GENERAL SOLUTION AND DISPERSION CURVES

The two-sided Laplace transform $f^*(p, y) = \int_{-\infty}^{\infty} f(x, y) \cdot e^{-px} dx$ is utilized to suppress the x -dependence in the field equations and the boundary conditions, and this gives (through Eqs. (14) and (15)) two ODEs, which possess the following general *transformed* solution for $y \geq 0$: $\phi^*(p, y) = B(p) \cdot e^{-\beta_L y} + C(p) \cdot e^{-\gamma_L y}$ and $\psi^*(p, y) = D(p) \cdot e^{-\beta_T y} + E(p) \cdot e^{-\gamma_T y}$, where $(\beta_L, \beta_T, \gamma_L, \gamma_T)$ are functions of the complex variable p , and also depend upon the material constants and the frequency. The functions (B, C, D, E) are yet unknown functions (*amplitude functions*), which can be determined in each specific problem through the enforcement of boundary conditions. Finally, since we seek here solutions of the surface-wave type, pertinent branch cuts should be introduced in the complex p -plane in order to secure exponentially decaying solutions with the distance y from the half-space surface (see in Vardoulakis and Georgiadis [9], and in Georgiadis et al. [11] for a related analysis concerning SH and torsional surface waves).

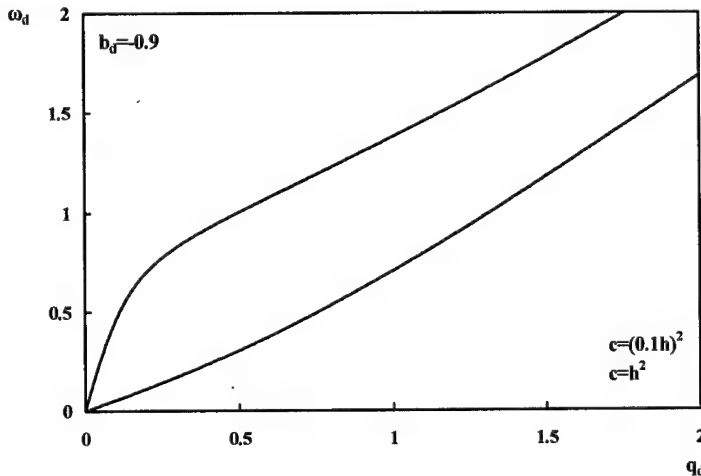


Figure 2: Dispersion curves for different relations between c and h
 $(b_d = b/c^{1/2}, \omega_d$ is a normalized frequency, q_d is a normalized wavenumber)

Next, the appropriate *traction-free* boundary conditions are considered for unforced Rayleigh-wave propagation: $\sigma_{yy} - (\partial m_{yx} / \partial x) = 0$, $\sigma_{yx} - (\partial m_{yy} / \partial x) = 0$, $m_{yy} = 0$ and $m_{yx} = 0$. Combining now the general solution with the transformed boundary conditions provides a system of four equations for the unknown functions (B, C, D, E) . The vanishing of the determinant of the coefficients of the unknowns (eigenvalue problem) gives the *dispersion* equation for the propagation of Rayleigh waves in a microstructured material characterized by gradient elasticity. Numerical results were derived from this equation through some elaborate FORTRAN programming [15]. Only some representative results are given here in the diagrams of Fig. 2. From such results, one can estimate the relation between the various microstructural parameters involved in the present modeling of microstructured media. For example, in Fig. 2 above, the relation $c = (0.1h)^2$ between the gradient coefficient

c and the grain size $2h$ seems to be more appropriate than the relation $c = h^2$, because the former case corresponds to a dispersion curve that is closer to the one derived from atomic lattice calculations (the latter are given in Gazis et al. [1]).

Acknowledgements: The authors acknowledge with thanks support of this research by the Greek General Secretariat for Research and Technology under the program PENED 99 ED 642. Also, the authors are thankful to Profs. L.M. Brock (Univ. Kentucky), N. Aravas (Univ. Thessaly) and G. Exadaktylos (TU Crete) for discussions on subjects related to the present work.

6. REFERENCES

- [1] Gazis, D.C., Herman, R. and Wallis, R.F., 'Surface elastic waves in cubic crystals', *Physical Review* 119, 533-544 (1960).
- [2] Farnell, G.W., 'Types and properties of surface waves', in *Acoustic Surface Waves*, A.A. Oliner (Ed.), Springer-Verlag, Berlin (1978) 13-60.
- [3] Vardoulakis, I. and Vrettos, Ch., 'Dispersion law of Rayleigh-type waves in a compressible Gibson half-space', *International Journal for Numerical and Analytical Methods in Geomechanics* 12, 639-655 (1988).
- [4] Mindlin, R.D., 'Micro-structure in linear elasticity', *Archive for Rational Mechanics and Analysis* 16, 51-78 (1964).
- [5] Green, A.E. and Rivlin, R.S., 'Multipolar continuum mechanics', *Archive for Rational Mechanics and Analysis* 17, 113-147 (1964).
- [6] Vardoulakis, I. and Frantziskonis, G., 'Micro-structure in kinematic-hardening plasticity', *European Journal of Mechanics A/Solids* 11, 467-486 (1992).
- [7] Vardoulakis, I. and Sulem, J., *Bifurcation Analysis in Geomechanics*, Blackie Academic and Professional (Chapman and Hall), London (1995).
- [8] Vardoulakis, I., Exadaktylos, G. and Aifantis, E., 'Gradient elasticity with surface energy: Mode-III crack problem', *International Journal of Solids and Structures* 33, 4531-4559 (1996).
- [9] Vardoulakis, I. and Georgiadis, H.G., 'SH surface waves in a homogeneous gradient-elastic half-space with surface energy', *Journal of Elasticity* 47, 147-165 (1997).
- [10] Georgiadis, H.G. and Vardoulakis, I., 'Anti-plane shear Lamb's problem treated by gradient elasticity with surface energy', *Wave Motion* 28, 353-366 (1998).
- [11] Georgiadis, H.G., Vardoulakis, I. and Lykotrafitis, G., 'Torsional surface waves in a gradient-elastic half-space', *Wave Motion* 31, 333-348 (2000).
- [12] Fleck, N.A., Muller, G.M., Ashby, M.F. and Hutchinson, J.W., 'Strain gradient plasticity: Theory and experiment', *Acta metallurgica et materialia* 42, 475-487 (1994).
- [13] Wei, Y. and Hutchinson, J.W., 'Steady-state crack growth and work of fracture for solids characterized by strain gradient plasticity', *Journal of the Mechanics and Physics of Solids* 45, 1253-1273 (1997).
- [14] Manolis, G.D., 'Some issues on wave motion through non-uniform media', *Proceedings of the International Symposium on 'Recent Advances in Mechanics'*, held in Athens in honor of Professor and Academician A.N. Kounadis (Eds.: J.T. Katsikadelis, D.E. Beskos and E.E. Gdoutos) (2000) 114-121.
- [15] Georgiadis, H.G., Vardoulakis, I. and Velgaki, E.G., 'Dispersive Rayleigh-wave propagation in solids characterized by dipolar gradient elasticity', submitted (2001).

THE 3D THERMO-ELASTODYNAMIC PROBLEM OF MOVING LOADS IN A HALF-SPACE

G. Lykotrafitis and H.G. Georgiadis*

Mechanics Division, National Technical University of Athens,
5 Heroes of Polytechnion Avenue, Zographou GR-15773, Greece
(*E-mail: georgiad@central.ntua.gr)

1. SUMMARY

An integral transform procedure is developed to obtain fundamental thermoelastic 3D solutions for thermal and/or mechanical concentrated loads moving steadily over the surface of a half-space. These solutions are exact within the bounds of the coupled thermo-elastodynamic theory, and results for surface displacements are obtained over the entire speed range (i.e. for subsonic, transonic and supersonic source speeds). Our solution technique is based on the use of the Radon transform and certain results from distribution theory.

2. INTRODUCTION

The *rapid* motion of a point thermal and/or mechanical load over the surface of a half-space is a problem that mainly concerns the fields of Contact Mechanics, Tribology and Dynamic Fracture Mechanics. Typical cases are: (i) Motion of an asperity developed on the mating surface. Such an asperity may be a material inclusion or some thermo-mechanical deformation of the mating surface (see e.g. Barber and Ciavarella [1]). (ii) Brake systems (see e.g. Huang and Ju [2], Georgiadis and Barber [3]). (iii) Crack face contact in intersonic interfacial rapid fracture of bimaterial plates (see e.g. Rosakis et al. [4]). (iv) Ground deformation due to the motion of high-speed modern trains or supersonic aircraft.

In many cases, the problem described above can be modeled as a *steady-state* situation involving a half-space under a concentrated mechanical / thermal load, which moves over the half-space surface at a constant velocity. This is the problem examined here and its solution is obtained by considering a material response governed by the coupled thermo-elastodynamic theory of Biot [5]. Additional aspects of this theory and solutions to specific problems were presented by, among others, Chadwick [6], Dassios and Grillakis [7], Massalas et al. [8], Brock and Georgiadis [9], and Georgiadis et al. [10,11]. In particular, the situation considered here is the 3D analogue of the plane strain problem considered by Brock and Georgiadis [12]. We also mention that in the absence of thermal effects, the above situation degenerates into the problem considered by Barber [13]. Due to space limitations, we give here only results concerning the surface vertical displacement due to a vertical force P . Additional results, more details and further analysis are provided by the authors elsewhere [14].

3. PROBLEM STATEMENT

Consider a thermally conducting linearly elastic body in the form of a half-space $z' \geq 0$. This otherwise unloaded body is at rest at a uniform temperature T_0 , but is then disturbed by the motion of a mechanical / thermal source over the half-space surface (see Fig. 1). The concentrated point load has components P and S , whereas the point heat source has intensity KQ , with K denoting the thermal conductivity and Q being a multiplier expressed in (length) (degrees of temperature). Further, under the assumption that the load has been applied for a long time and is moving at a constant speed V , a *steady-state* is created around this source (see e.g. Brock and Georgiadis [9,12]).

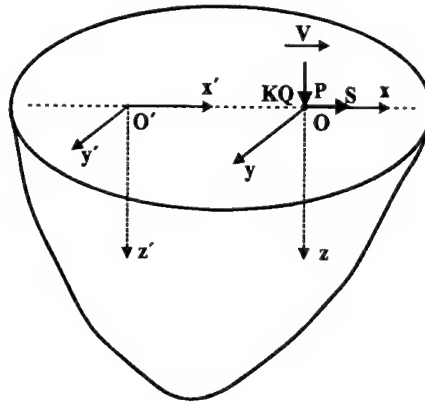


Figure 1: A point mechanical / thermal load moving at constant velocity over the surface of a half-space.

Using the steady-state assumption, considerable simplification is gained in analyzing the problem at hand. Indeed, the Galilean transformation $x = x' - Vt$, $y = y'$, $z = z'$ can be introduced, so that the time derivative in the fixed Cartesian system becomes $-V \partial / \partial x$, and both the field equations and the boundary conditions are independent of t . Consequently the field equations of coupled thermoelasticity in the moving reference system are written as

$$\mathbf{s} = \mu(\nabla \mathbf{u} + \mathbf{u} \nabla) + \mu(m^2 - 2)(\nabla \cdot \mathbf{u}) + \mu \kappa \theta \mathbf{1}, \quad (1)$$

$$\nabla^2 \mathbf{u} + (m^2 - 1)\nabla(\nabla \cdot \mathbf{u}) + \kappa \nabla \theta - m^2 c^2 \frac{\partial^2 \mathbf{u}}{\partial x^2} = 0, \quad (2)$$

$$\frac{K}{\mu} \nabla^2 \theta + C_v \frac{mc}{V_T} \frac{\partial \theta}{\partial x} - \kappa T_0 c V_L \frac{\partial(\nabla \cdot \mathbf{u})}{\partial x} = 0, \quad (3)$$

where \mathbf{s} is the stress tensor with components $(\sigma_{xx}, \sigma_{xy}, \sigma_{xz}, \dots, \sigma_{zz})$, \mathbf{u} is the displacement vector with components (u_x, u_y, u_z) , $\mathbf{1}$ is the identity tensor, T is the temperature,

$\theta = T - T_0$ is the change in temperature, ∇ is the 3D gradient operator, $\nabla \cdot \mathbf{u}$ is the 3D dilatation, ∇^2 is the 3D Laplace operator, $m = V_L/V_T > 1$ with $V_L = [(\lambda + 2\mu)/\rho]^{1/2}$ being the longitudinal (L) wave speed in the absence of thermal effects and $V_T = (\mu/\rho)^{1/2}$ being the transverse (T) wave speed, (λ, μ) are the Lamé constants, and ρ is the mass density. Also, $\kappa = \kappa_0(4 - 3m^2) < 0$ with κ_0 being the coefficient of thermal expansion, C_v is the specific heat at constant deformation, while $c \equiv M_L = V/V_L$ and $mc \equiv M_T = V/V_T$ are the Mach numbers. The boundary conditions for σ_{zz} , σ_{zx} and $\partial\theta/\partial z$ involve the product $\delta(x) \cdot \delta(y)$, with $\delta(\cdot)$ being the Dirac delta distribution, whereas $\sigma_{xy}(x, y, z=0) = 0$.

4. RADON TRANSFORM ANALYSIS

The solution of the previous problem will be effected through a novel technique based on the Radon transform (see e.g. Deans [15]) and pertinent coordinate transformations. This general procedure reduces the original 3D problem to a pair of auxiliary problems, i.e. a corresponding 2D plane-strain problem and a 2D anti-plane shear problem. In particular, it should be noticed that the 2D plane-strain problem is *completely* analogous to the original 3D problem, not only regarding the field equations but also regarding the boundary conditions. This makes the present technique more advantageous than other techniques (see e.g. Barber [13]), which require first the determination of a fictitious auxiliary 2D plane-strain problem through the solution of an integral equation. As will become apparent below, after establishing the correspondence principle (equivalence) between the 3D problem and the two auxiliary problems, the solution to the original problem follows by performing first a coordinate transformation and then taking the inverse Radon transform of the known plane-strain and anti-plane shear solutions.

The 2D Radon transform a function $f(\mathbf{r})$, with $|\mathbf{r}| = (x^2 + y^2)^{1/2}$, is defined as [15]

$$R(f(\mathbf{r})) \equiv \tilde{f}(q, \omega) = \iint f(\mathbf{r}) \cdot \delta(q - \mathbf{n} \cdot \mathbf{r}) d\mathbf{r} = \int_L f(x, y) ds, \quad (4)$$

where L denotes all straight lines in the plane Oxy and ds is the infinitesimal length along such a line. The lines L are defined by $\mathbf{n} \cdot \mathbf{r} = q$, with $\mathbf{n} \equiv (n_x, n_y) = (\cos \omega, \sin \omega)$, and the Radon transform is in fact the integral of $f(\mathbf{r})$ over all these straight lines in the plane. The inverse 2D Radon transform is given by

$$f(x, y) = f(r, \varphi) = -\frac{1}{4\pi^2} \int_0^{2\pi} \left(\int_{-\infty}^{+\infty} \frac{\partial \tilde{f}(q, \omega)}{\partial q} \cdot \mathbf{PF} \left(\frac{1}{q - r \cdot \cos(\omega - \varphi)} \right) dq \right) d\omega, \quad (5)$$

where the symbol $\mathbf{PF}(\cdot)$ stands for the *principal-value* pseudo-function (or distribution) [16].

Next, the two auxiliary problems will be obtained as transformed problems of the original problem. Operating with the Radon transform (4) on the governing equations, using standard

properties of the Radon transform (like linearity, derivative and distribution transforms) and performing a rotation of the original (x, y, z) coordinate system through the angle ω about the z -axis, gives the following equations in the new coordinate system (q, s, z)

$$\frac{\partial^2 \tilde{u}_q}{\partial q^2} + \frac{\partial^2 \tilde{u}_q}{\partial z^2} + (m^2 - 1) \frac{\partial}{\partial q} \left(\frac{\partial \tilde{u}_q}{\partial q} + \frac{\partial \tilde{u}_z}{\partial z} \right) + \kappa \frac{\partial \tilde{\theta}}{\partial q} - m^2 c_x^2 \frac{\partial^2 \tilde{u}_q}{\partial q^2} = 0, \quad (6a)$$

$$\frac{\partial^2 \tilde{u}_z}{\partial q^2} + \frac{\partial^2 \tilde{u}_z}{\partial z^2} + (m^2 - 1) \frac{\partial}{\partial z} \left(\frac{\partial \tilde{u}_q}{\partial q} + \frac{\partial \tilde{u}_z}{\partial z} \right) + \kappa \frac{\partial \tilde{\theta}}{\partial z} - m^2 c_x^2 \frac{\partial^2 \tilde{u}_z}{\partial q^2} = 0, \quad (6b)$$

$$\frac{K}{\mu} \left(\frac{\partial^2 \tilde{\theta}}{\partial q^2} + \frac{\partial^2 \tilde{\theta}}{\partial z^2} \right) + C_v \frac{mc_x}{V_T} \frac{\partial \tilde{\theta}}{\partial q} - \kappa T_0 c_x V_L \frac{\partial}{\partial q} \left(\frac{\partial \tilde{u}_q}{\partial q} + \frac{\partial \tilde{u}_z}{\partial z} \right) = 0, \quad (6c)$$

$$(1 - m^2 c_x^2) \frac{\partial^2 \tilde{u}_s}{\partial q^2} + \frac{\partial^2 \tilde{u}_s}{\partial z^2} = 0, \quad (7)$$

$$\tilde{\sigma}_{zz}(q, \omega, z=0) = -P \cdot \delta(q), \quad \tilde{\sigma}_{zq}(q, \omega, z=0) = -S \cdot \cos \omega \cdot \delta(q), \quad (8a, b)$$

$$\frac{\partial \tilde{\theta}(q, \omega, z=0)}{\partial z} = -Q \cdot \delta(q), \quad \tilde{\sigma}_{zs}(q, \omega, z=0) = S \cdot \sin \omega \cdot \delta(q), \quad (8c), (9)$$

where $c_x \equiv cn_x$, and

$$\begin{pmatrix} \tilde{u}_q \\ \tilde{u}_s \end{pmatrix} = \begin{pmatrix} \cos \omega & \sin \omega \\ -\sin \omega & \cos \omega \end{pmatrix} \begin{pmatrix} \tilde{u}_x \\ \tilde{u}_y \end{pmatrix}, \quad \begin{pmatrix} \tilde{\sigma}_{zq} \\ \tilde{\sigma}_{zs} \end{pmatrix} = \begin{pmatrix} \cos \omega & \sin \omega \\ -\sin \omega & \cos \omega \end{pmatrix} \begin{pmatrix} \tilde{\sigma}_{zx} \\ \tilde{\sigma}_{zy} \end{pmatrix}. \quad (10a, b)$$

Now, one may observe that (6) and (8) form a 2D *plane-strain* problem in the (q, z) coordinate system. This problem (*first* auxiliary problem) involves a thermoelastic body in the form of the half-plane $z \geq 0$ that is disturbed by the steady-state motion of a concentrated line load. The mechanical / thermal load has components P , $S \cdot \cos \omega$ and KQ , and is moving along the q -axis with velocity $V_q \equiv V \cdot \cos \omega$. On the other hand, (7) and (9) form a 2D *anti-plane shear* problem in the (q, z) coordinate system. This problem (*second* auxiliary problem) involves a linearly elastic body in the form of the half-plane $z \geq 0$ that is disturbed by the steady-state motion of a concentrated anti-plane shear load. In this case, the load $S \cdot \sin \omega$ is moving along the q -axis with velocity $V_q \equiv V \cdot \cos \omega$. The solutions to the first and second auxiliary problems have been obtained in [12] and [17], respectively.

5. INVERSION PROCEDURE AND RESULTS

The 3D solution follows from the transformed solution in two steps. First, the inversion of the coordinate transformation in (10) is performed providing the set $(\tilde{u}_z, \tilde{u}_x, \tilde{u}_y)$ in terms of the rotated Radon-transformed displacements $(\tilde{u}_z, \tilde{u}_q, \tilde{u}_s)$. Then, the Radon-transform inversion according to (5) gives the set (u_z, u_x, u_y) in the physical plane. Representative final results for the vertical surface displacement due to the vertical load P in the entire speed range are

given below. Operating with (5) on the solution of the first auxiliary problem and using results from distribution theory along with results concerning the Hilbert transform of generalized functions (Lauwerier [16]), provides the surface vertical displacement as

$$u_z^{(P)}(r, \varphi, z=0) = -\frac{P}{\mu r} \left\{ \frac{1}{2} F_1^{(P)}(M_T \sin \varphi, \varepsilon) + \frac{\cos \varphi}{\pi^2} \left[\int_0^1 F_2^{(P)}(M_T (1-\zeta^2)^{1/2}, \varepsilon) \cdot \text{PF} \left(\frac{1}{\cos^2 \varphi - \zeta^2} \right) d\zeta \right] \right\}, \quad (11)$$

where the functions $F_1^{(P)}(\cdot)$ and $F_2^{(P)}(\cdot)$ are given in [14], and $\varepsilon = (T_0/C_v)(\kappa V_T/m)^2$ is the dimensionless coupling coefficient. From the result in (11) and considering appropriate radiation conditions, one may derive particular results in the entire speed range [14], i.e. for $0 < V < V_R$, $V_R < V < V_T$, $V_T < V < V_{Le}$ and $V_{Le} < V$, where V_R is the steady-state thermoelastic Rayleigh wave velocity [12] and $V_{Le} = V_L(1+\varepsilon)^{1/2}$ is the steady-state thermoelastic longitudinal wave velocity.

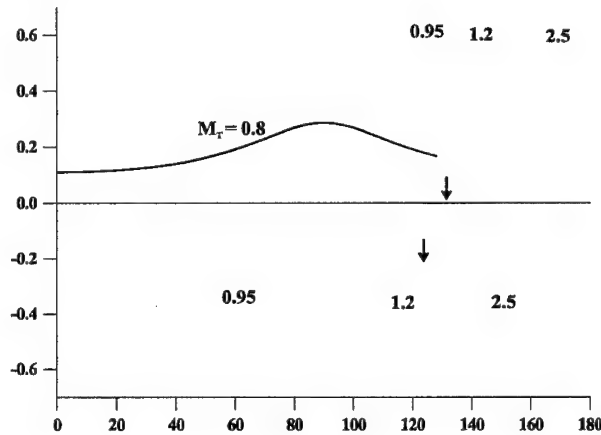


Figure 2: Displacement $U_z^{(P)}$ vs. polar angle φ for various source speeds.

The Rayleigh wave fronts occur at $\varphi = 102.39^\circ, 129.35^\circ, 158.21^\circ$

for $M_T = 0.95, 1.2, 2.5$, respectively.

These results are given in the form of graphs (Fig. 2) showing the variation of the normalized surface vertical displacement $U_z^{(P)} = u_z^{(P)} \mu r / P$ with the polar angle $\varphi = \tan^{-1}(y/x)$. The distance from the moving load is $r = (x^2 + y^2)^{1/2}$. The numerical results were derived for a steel-like material with Poisson's ratio $\nu = 0.3$, shear modulus $\mu = 7.92 \times 10^{10} \text{ Nm}^{-2}$, mass density $\rho = 7.85 \times 10^{-3} \text{ kg cm}^{-3}$, and coefficient of thermal expansion $\kappa_0 = 12 \times 10^{-6} (\text{°K})^{-1}$. The reference temperature was taken $T_0 = 290 \text{ °K}$ and the coupling coefficient $\varepsilon = 0.011$.

Acknowledgement: HGG acknowledges with thanks support of this research by the Greek General Secretariat for Research and Technology under the program PENED 99 ED 642.

6. REFERENCES

- [1] Barber, J.R. and Ciavarella, M., Contact Mechanics, *International Journal of Solids and Structures* 37, 29-43 (2000).
- [2] Huang, J.H. and Ju, F.D., Thermomechanical cracking due to moving frictional loads, *Wear* 102, 81-104 (1985).
- [3] Georgiadis, H.G. and Barber, J.R., On the super-Rayleigh/subseismic elastodynamic indentation problem, *Journal of Elasticity* 31, 141-161 (1993).
- [4] Rosakis, A.J., Samudrala, O., Singh, R.P. and Shukla, A., Intersonic crack propagation in bimaterial systems, *Journal of the Mechanics and Physics of Solids* 46, 1789-1813 (1998).
- [5] Biot, M.A., Thermoelasticity and irreversible thermodynamics, *Journal of Applied Physics* 27, 240-253 (1956).
- [6] Chadwick, P., Thermoelasticity: the dynamical theory, In: *Progress in Solid Mechanics*, Vol. 1, I.N. Sneddon and R. Hill (Eds.), North-Holland, Amsterdam (1960) 263-328.
- [7] Dassios, G. and Grillakis, M., Dissipation rates and partition of energy in thermoelasticity, *Archive for Rational Mechanics and Analysis* 87, 49-91 (1984).
- [8] Massalas, C.V., Anagnostaki, E. and Kalpakidis, V.K., Some considerations on the coupled thermoelastic problems, *Letters in Applied and Engineering Science* 23 (6), 677-683 (1985).
- [9] Brock, L.M. and Georgiadis, H.G., Convection effects for rapidly moving mechanical sources on a half-space governed by fully coupled thermoelasticity, *ASME Journal of Applied Mechanics* 66, 347-351 (1999); see also Brock, L.M. and Georgiadis, H.G., Sliding contact with friction of a thermoelastic solid at subsonic, transonic and supersonic speeds, *Journal of Thermal Stresses* 23, 629-656 (2000).
- [10] Georgiadis, H.G., Brock, L.M. and Rigatos, A.P., Transient concentrated thermal/mechanical loading of the faces of a crack in a coupled-thermoelastic solid, *International Journal of Solids and Structures* 35, 1075-1097 (1998).
- [11] Georgiadis, H.G., Rigatos, A.P. and Brock, L.M., Thermoelastodynamic disturbances in a half-space under the action of a buried thermal/mechanical line source, *International Journal of Solids and Structures* 36, 3639-3660 (1999).
- [12] Brock, L.M. and Georgiadis, H.G., Steady-state motion of a line mechanical / heat source over a half-space: a thermoelastodynamic solution, *ASME Journal of Applied Mechanics* 64, 562-567 (1997).
- [13] Barber, J.R., Surface displacements due to a steadily moving point force, *ASME Journal of Applied Mechanics* 63, 245-251 (1996).
- [14] Lykotrafitis, G. and Georgiadis, H.G., The three-dimensional steady-state thermoelastodynamic problem of moving sources over a half-space, submitted (2001).
- [15] Deans, S.R., *The Radon Transform and Some of Its Applications*, John Wiley & Sons, New York (1983).
- [16] Lauwerier, H.A., The Hilbert problem for generalized functions, *Archive for Rational Mechanics and Analysis* 13, 157-166 (1963).
- [17] Georgiadis, H.G. and Lykotrafitis, G., A method based on the Radon transform for three-dimensional elastodynamic problems of moving loads, submitted (2001).

THE ATTITUDE MOTION OF A CARRIER-ROTOR SYSTEM WITH ALMOST SYMMETRIC INERTIA ELLIPSOID, UNDER BODY-FIXED TORQUES

K. Dimitrakopoulou, A.G. Mavraganis

National Technical University of Athens, Faculty of Applied Sciences
Department of Mechanics, Zographou Campus, Theocaris Bld.
GR-157 73, Athens, Greece

1. ABSTRACT

Although the carrier-rotor systems are deeply involved in many technical problems, especially in spacecraft dynamics, closed form solutions are not available. So, a comprehensive theory does not exist in the literature, able to cover completely the aspects of the attitude behaviour of any such system. In the present paper approximate solutions are derived for a system, with almost axisymmetric inertia ellipsoid, in response to constant external torques. The very accurate results of the numerical applications render them quite reliable and therefore convenient for the study of typical spinning spacecraft problems.

2. INTRODUCTION

The last two decades numerous of works on the carrier-rotor systems have been published, giving useful informations for the spacecraft attitude dynamics, when the spacecraft is simulated by a gyrostat. An extensive list of references is given by Hughes (1986) able to place in contact with the literature those who want to work on this subject. Although the questions discussed so far cover widely the gyrostat dynamics, the problem remains quite open to investigation, because of its nonlinear character. The equations of motion can not be integrated, unless one simplifies their form by special assumptions. Such is the case which is examined in this paper with a gyrostat in response to a constant external torque. The assumptions concern the structure of the gyrostat and the transverse portion of its attitude behaviour. Precisely speaking we assume that the rotor is mounted to the carrier with the symmetry axis in coincidence with the major principal axis of the system and yet that two of the principal moments of inertia are almost equal. Further, we assume that the magnitude of the vector $\omega_r = (\omega_x, \omega_y)$ remains small during the motion compared to the component ω_z . With these we derive the solutions in terms of the known Fresnel integrals, based on the procedure followed in the analogous problem for rigid bodies (Tsiotras P. and Longuski J.M. 1991). These solutions are proved by means of numerical examples, quite convenient for the study of the actual attitude behaviour of the spinning gyrostats.

3. EQUATIONS OF MOTION

As known (Hughes, P., 1986) the motion of a carrier-rotor system (such as a gyrostat and a dual-spin satellite), when it is acted upon by a torque $M = (M_x, M_y, M_z)$, is governed by the equations

$$\begin{aligned} \frac{Ad\omega_x}{M_x + (B-C)\omega_y\omega_z - h(a_z\omega_y - a_y\omega_z)} &= \frac{Bd\omega_y}{M_y + (C-A)\omega_x\omega_z - h(a_x\omega_z - a_z\omega_x)} = \\ &= \frac{Cd\omega_z}{M_z + (A-B)\omega_y\omega_x - h(a_y\omega_x - a_x\omega_y)} = dt \end{aligned} \quad (1)$$

where A, B, C ($A > B > C$) are the principal moments of inertia of the system, $\omega = (\omega_x, \omega_y, \omega_z)$ is the angular velocity of the carrier expressed in the triad $O\hat{x}\hat{y}\hat{z}$ of the central principal axes, $a = (a_x, a_y, a_z)$ is the symmetry axis of the rotor and h is the angular momentum of the rotor relative to the carrier. In general the internal angular momentum h is a function of the time, determined by an appropriate actuator (e.g. an electric motor). This controls the spin of the rotor in a way that the time rate of change of the function h absorb the angular impulse of the external torques. So the motion of the carrier maintains a desired attitude. In many cases the so resulting function $h(t)$ varies so slowly that be considered for long almost constant i.e. $h(t) = h_s \approx \text{constant}$. But even so, eqs. (1) are not susceptible of direct integration, unless one reduces their form by convenient simplifications. To do so, we assume first that the rotor is mounted to the carrier with its axis of symmetry in coincidence with the major or the minor principal axis of the system (here the z -axis). A second assumption concerns the inertial character of the system. Precisely we assume that two of the inertia tensor components are almost equal, namely $B = A - \varepsilon$, with $\varepsilon \ll A$ (Figure 1). This occurs very often in technical applications because of the small differences between the materialization and the original design of the structures. Mostly, these differences come from unavoidable human mistakes, as for example, are the unsuccessful thruster alignment, the mismatch of the several parts of the structure, the failure to establish precisely the desired symmetry, etc.

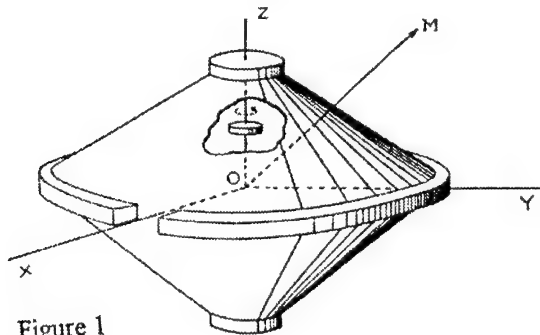


Figure 1

Under these circumstances eqs. (1) are reduced to the form

$$\frac{Ad\omega_x}{M_x + (A - C - A\delta)\omega_z\omega_y - h_s\omega_y} = \frac{A(1-\delta)d\omega_y}{M_y + (C - A)\omega_x\omega_z + h_s\omega_x} = \frac{Cd\omega_z}{M_z + \delta\omega_x\omega_y} = dt \quad (2)$$

where $\delta = \varepsilon/A$, but even so they remain still non-integrable. However, it is possible to derive analytic solutions if, going further the previous simplification, we neglect the product $\delta\omega_x\omega_y$, presuming small values for both ω_x and ω_y . This seems as an extremely special case but actually is not. The experience shows that, spin-stabilized vehicles with rigid-body structure (such as rockets and spacecraft), being acted upon by constant torques, tend during the motion, to keep small the magnitude of the vector $\omega_T = (\omega_x, \omega_y)$ compared to ω_z . This is valid not only when the distribution of mass implies the equality $A = B$ but even when $A \neq B$, provided that $M_x^2 + M_y^2 < C^2\omega_{z0}^4$, where M_x and M_y are the transverse components of the exerted torque (Kia-Longuski, 1984). The same happens in gyrostats with axisymmetric or almost axisymmetric inertia ellipsoid when the quantity h is small compared to the angular momentum H of the carrier (we notice that the attitude motion of a gyrostat degenerates to the motion of a single rigid body when $h \ll H$ (Hughes, P. 1986)).

4. THE INTEGRATION OF EQS. (2)

Solving the last of eqs. (2) in view of the latter assumption, we yield the approximate solution

$$\omega_z(t) \cong \frac{M_z}{C}t + \omega_{z0} \quad (3)$$

Substitution of this form into the first two of eqs (2) provides

$$\frac{Ad\omega_x}{M_x + \left[(A - C - A\delta) \left(\frac{M_z}{C}t + \omega_{z0} \right) - h_s \right] \omega_y} = \frac{A(1-\delta)d\omega_y}{M_y - \left[(A - C) \left(\frac{M_z}{C}t + \omega_{z0} \right) - h_s \right] \omega_x} = dt \quad (4)$$

If we use now the variables

$$\Omega_x = \sqrt{k_y}\omega_x, \quad \Omega_y = \sqrt{k_x}\omega_y$$

where

$$k_x = \frac{A - C - A\delta}{A}, \quad k_y = \frac{A - C}{A(1-\delta)}, \quad k^2 = k_x k_y$$

and make the replacement $(1-\delta)^{-1} \cong 1+\delta$, we obtain

$$\frac{d\Omega_x}{\frac{M_x}{A}\sqrt{k_y} + \left[k\left(\frac{M_z}{C}t + \omega_{zo}\right) - \frac{h_s k_y}{Ak} \right] \Omega_y} = \frac{d\Omega_y}{\frac{M_y(1+\delta)}{A}\sqrt{k_x} - \left[k\left(\frac{M_z}{C}t + \omega_{zo}\right) - \frac{h_s(1+\delta)k_x}{Ak} \right] \Omega_x} = dt \quad (5)$$

The relative error of the above replacement is equal to $-\delta^2$, hence the error which is introduced in the form of the second equation is insignificant. The reason for this change will become obvious later.

Next we make the substitution of the quantities k_y and $(1+\delta)k_x$ inside the brackets by their average μ and introduce the complex variable $w = \Omega_x + i\Omega_y$. After some arrangement we yield the complex equation

$$\dot{w} + i \left[k\left(\frac{M_z}{C}t + \omega_{zo}\right) - \frac{h_s \mu}{Ak} \right] w = \frac{1}{A} \left[M_x \sqrt{k_y} + i M_y (1+\delta) \sqrt{k_x} \right] \quad (6)$$

The use of μ implies an evaluation error which, relative to the exact values of the replaced quantities, is equal to $-\varepsilon/2(A-C-\varepsilon)$ and $\varepsilon/2(A-C)$ respectively. We notice the dependence of these errors, upon the difference $A-C$. It is easy to show that, for relative errors less than a desired value b , the difference $A-C$ fulfils the inequality

$$A-C \geq \varepsilon \frac{1+2b}{2b}.$$

Thus for example, for $b=0.01$, the least value of this difference is equal to 51ε .

Eq. (6) has the typical form of the first order linear differential equations with a time-varying coefficient. Hence, its general solution will have the form

$$w(t) = e^{-\int P dt} \int Q e^{\int P dt} dt + \lambda e^{-\int P dt} \quad (7)$$

where P and Q are the coefficients of the second and third term respectively. Carrying out the integration of the exponential terms we obtain

$$\int P dt = i \left[\frac{k M_z}{C} \frac{t^2}{2} + \left(k \omega_{zo} - \frac{h_s \mu}{Ak} \right) t + \gamma \right]$$

The term γ is a constant which for convenience is chosen equal to:

$$\gamma = \frac{C}{2kM_z} \left(k \omega_{zo} - \frac{h_s \mu}{Ak} \right)^2$$

so that the above integral to be written

$$\int P dt = i \frac{C}{2kM_z} (at + \beta)^2$$

with the abbreviations

$$a = \frac{kM_z}{C}$$

$$\beta = k\omega_{z0} - \frac{h_s \mu}{kA}$$

Through this eq. (7) becomes

$$w(t) = \left[Q \sqrt{\frac{2C}{kM_z}} \int \cos \tau^2 dt + i Q \sqrt{\frac{2C}{kM_z}} \int \sin \tau^2 d\tau + \lambda \right] (\cos \tau^2 - i \sin \tau^2) \quad (8)$$

where $\lambda = \lambda_1 + i\lambda_2 = \text{const}$, and

$$\tau^2 = \frac{C}{2kM_z} (\alpha t + \beta)^2.$$

The integrals inside the brackets have one of the alternative forms of Fresnel integrals

$$C_1(x) = \sqrt{\frac{2}{\pi}} \int_0^x \cos \xi^2 d\xi, \quad S_1(x) = \sqrt{\frac{2}{\pi}} \int_0^x \sin \xi^2 d\xi$$

whose properties and tabulated values are exhibited in most mathematical handbooks (e.g. Abramowitz and Stegun, 1972). Thus, the solution $w(t)$ is written

$$w(t) = \frac{1}{A} \sqrt{\frac{C\pi}{kM_z}} \left[M_x \sqrt{k_y} + iM_y(1+\delta)\sqrt{k_x} \right] \left[C_1(\tau) + iS_1(\tau) \right] \exp(-i\tau^2) + (\lambda_1 + i\lambda_2) \exp(-i\tau^2) \quad (9)$$

where

$$\lambda_1 + i\lambda_2 = w(t=0)e^{i\tau_0^2} - \frac{1}{A} \sqrt{\frac{C\pi}{kM_z}} \left[M_x \sqrt{k_y} + iM_y(1+\delta)\sqrt{k_x} \right] \left[C_1(\tau_0) + iS_1(\tau_0) \right]$$

$$\tau_0^2 = \frac{C}{2kM_z} \beta^2$$

Turning back to the variables ω_x and ω_y , we yield after making the separation of the real and imaginary parts of w

$$\begin{aligned}
\omega_x(t) = & \frac{1}{A} \sqrt{\frac{C\pi}{kM_z}} \left\{ \left[M_x C_1(\tau) - M_y(1+\delta) \sqrt{\frac{k_x}{k_y}} S_1(\tau) \right] \cos \tau^2 + \left[M_x S_1(\tau) + M_y(1+\delta) \sqrt{\frac{k_x}{k_y}} C_1(\tau) \right] \sin \tau^2 - \right. \\
& - \left[M_x C_1(\tau_0) - M_y(1+\delta) \sqrt{\frac{k_x}{k_y}} S_1(\tau_0) \right] \cos \tau^2 - \left[M_x S_1(\tau_0) + M_y(1+\delta) \sqrt{\frac{k_x}{k_y}} C_1(\tau_0) \right] \sin \tau^2 \Big\} + \\
& \left(\omega_{xo} \cos \tau_0^2 - \omega_{yo} \sqrt{\frac{k_x}{k_y}} \sin \tau_0^2 \right) \cos \tau^2 + \left(\omega_{xo} \sin \tau_0^2 + \omega_{yo} \sqrt{\frac{k_x}{k_y}} \cos \tau_0^2 \right) \sin \tau^2 \quad (10a)
\end{aligned}$$

$$\begin{aligned}
\omega_y(t) = & \frac{1}{A} \sqrt{\frac{C\pi}{kM_z}} \left\{ \left[M_x \sqrt{\frac{k_y}{k_x}} S_1(\tau) + M_y(1+\delta) C_1(\tau) \right] \cos \tau^2 - \left[M_x \sqrt{\frac{k_y}{k_x}} C_1(\tau) - M_y(1+\delta) S_1(\tau) \right] \sin \tau^2 - \right. \\
& - \left[M_x \sqrt{\frac{k_y}{k_x}} S_1(\tau_0) + M_y(1+\delta) C_1(\tau_0) \right] \cos \tau^2 + \left[M_x \sqrt{\frac{k_y}{k_x}} C_1(\tau_0) - M_y(1+\delta) S_1(\tau_0) \right] \sin \tau^2 \Big\} + \\
& \left(\omega_{xo} \sqrt{\frac{k_y}{k_x}} \sin \tau_0^2 + \omega_{yo} \cos \tau_0^2 \right) \cos \tau^2 - \left(\omega_{xo} \sqrt{\frac{k_y}{k_x}} \cos \tau_0^2 - \omega_{yo} \sin \tau_0^2 \right) \sin \tau^2 \quad (10b)
\end{aligned}$$

where

$$\omega_{xo} = \frac{\sqrt{k_x}}{k} \Re[w(t=0)] \text{ and } \omega_{yo} = \frac{\sqrt{k_y}}{k} \Im[w(t=0)]$$

From these we find easily, by recalling the property $\lim_{x \rightarrow \infty} C_1(x) = \lim_{x \rightarrow \infty} S_1(x) = \frac{1}{2}$ that

$$\begin{aligned}
\omega_x^* = \lim_{t \rightarrow \infty} \omega_x(t) = & \frac{1}{2A} \sqrt{\frac{C\pi}{kM_z}} \left[M_x - M_y(1+\delta) \sqrt{\frac{k_x}{k_y}} \cos 2\tau^2 \right] - \\
& \left\{ \frac{1}{A} \sqrt{\frac{C\pi}{kM_z}} \left[M_x C_1(\tau_0) - M_y(1+\delta) \sqrt{\frac{k_x}{k_y}} S_1(\tau_0) \right] - \left(\omega_{xo} \cos \tau_0^2 - \omega_{yo} \sqrt{\frac{k_x}{k_y}} \sin \tau_0^2 \right) \right\} \cos \tau^2 - \\
& - \left\{ \frac{1}{A} \sqrt{\frac{C\pi}{kM_z}} \left[M_x S_1(\tau_0) + M_y(1+\delta) \sqrt{\frac{k_x}{k_y}} C_1(\tau_0) \right] - \left(\omega_{xo} \sin \tau_0^2 + \omega_{yo} \sqrt{\frac{k_x}{k_y}} \cos \tau_0^2 \right) \right\} \sin \tau^2 \\
\omega_y^* = \lim_{t \rightarrow \infty} \omega_y(t) = & \frac{1}{2A} \sqrt{\frac{C\pi}{kM_z}} \left[M_x \sqrt{\frac{k_y}{k_x}} \cos 2\tau^2 + M_y(1+\delta) \right] - \\
& \left\{ \frac{1}{A} \sqrt{\frac{C\pi}{kM_z}} \left[M_x \sqrt{\frac{k_y}{k_x}} S_1(\tau_0) + M_y(1+\delta) C_1(\tau_0) \right] - \left(\omega_{xo} \sqrt{\frac{k_y}{k_x}} \sin \tau_0^2 + \omega_{yo} \cos \tau_0^2 \right) \right\} \cos \tau^2 + \\
& + \left\{ \frac{1}{A} \sqrt{\frac{C\pi}{kM_z}} \left[M_x \sqrt{\frac{k_y}{k_x}} C_1(\tau_0) - M_y(1+\delta) S_1(\tau_0) \right] - \left(\omega_{xo} \sqrt{\frac{k_y}{k_x}} \cos \tau_0^2 - \omega_{yo} \sin \tau_0^2 \right) \right\} \sin \tau^2
\end{aligned}$$

We remark that the magnitude of the vector ω_T tends with the time to become periodic, while the component ω_z increases infinitely, with consequence after long the gyrostat's behaviour to seem as resulting exclusively from ω_z . Thus at the limit the contribution of ω_T is absorbed from ω_z , but this does not mean at all that the motion is reduced to a single rotation, since the components ω_x and ω_y are neither equal to zero nor so small to be neglected.

Finally it is not difficult to verify that, when δ is extremely small, i.e. when $\delta \rightarrow 0$, the forms (10) are reduced to the solutions for a gyrostat with perfect axisymmetric inertia ellipsoid, namely with $A = B$.

5. NUMERICAL APPLICATIONS

The previously derived solutions are illustrated by application to the spin-up maneuvers of a gyrostat, with $A = 5000 \text{ kg} \cdot \text{m}^2$, $C = 2500 \text{ kgm}^2$, $\varepsilon = 50 \text{ kg} \cdot \text{m}^2$ and $h_s = \pm 400 \text{ kg} \cdot \text{m}^2 \cdot \text{sec}^{-1}$, in response to the constant torque $M = (1.5, 2.0, 12.0) \text{ N} \cdot \text{m}$. For simplicity we assume that the motion starts with $\omega_{x0} = \omega_{y0} = 0$ and $\omega_{z0} = 0.5 (\text{in rad/s})$. The results are drawn in the same diagram with the "exact" solution, which is obtained by numerical integration of eqs. (2), but as they are indistinguishable, we give also the differences $\Delta\omega_x, \Delta\omega_y$ and $\Delta\omega_z$. Note that the method used for the numerical integration is that developed by Tsitouras team (1996) on the basis of the classical Runge-Kutta method. Inspecting the diagrams of the errors $\Delta\omega_x, \Delta\omega_y$ and $\Delta\omega_z$ we deduce that the forms (3) and (10) furnish a very satisfactory approximation of the actual motion, at least in the interval $[0, 300]$. Analogous results we obtain for the spin-down maneuvers of the system.

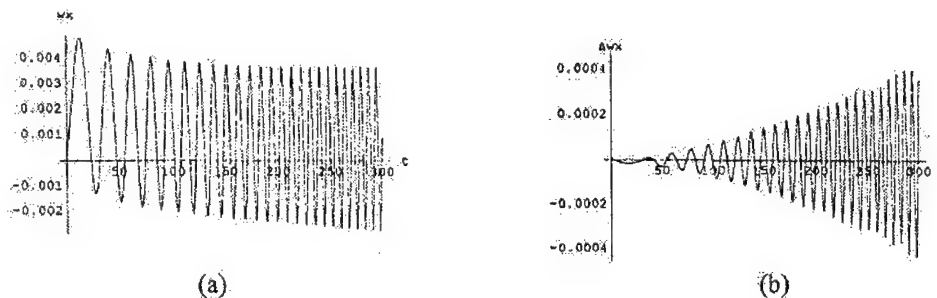


Figure 2

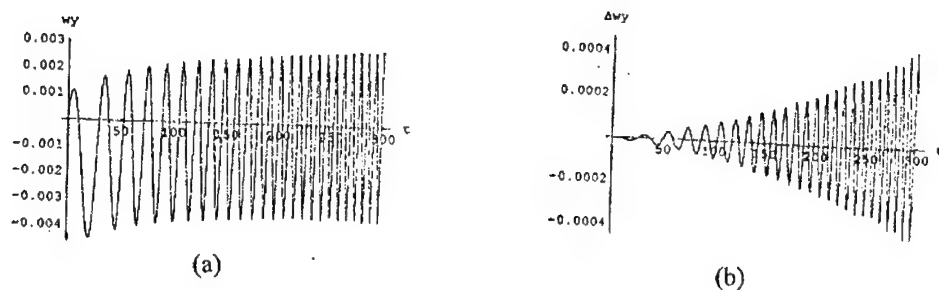


Figure 3

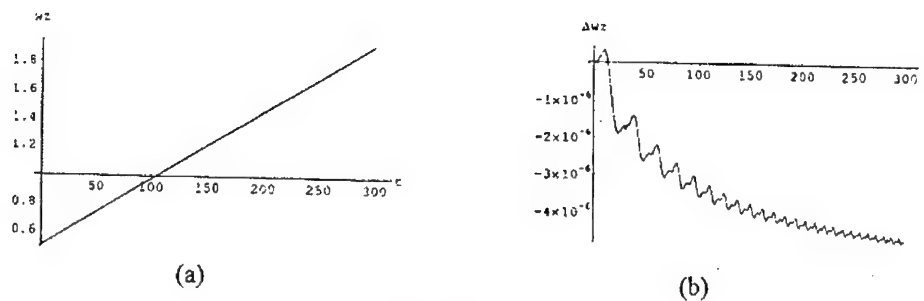


Figure 4

6. REFERENCES

- [1] Abramowitz, M. and Stegun, I.A.: A handbook of mathematical functions. Dover Publications Inc., New York, 1972.
- [2] Hughes, P., Space Attitude Dynamics, John Wiley and Sons, Inc. New York, 1986.
- [3] Kia, T. and Longuski, J.M.: Error analysis of analytic solutions for self-excited near symmetric rigid bodies. A numerical study. AIAA/AAS, Astrodyn. Conf. Paper 84-2018, Seattle, Washington, 1984.
- [4] Papakostas, S.N.; Tsitouras, CH.; Papageorgiou G.: Siam J. Numer. Anal. **33** (1996) 3, 917-936.
- [5] Tsiotras, P. and Longuski, J.M.: A complex analytic solution for the attitude motion of a near-symmetric rigid body under body-fixed torques, Cel. Mech. 51/3 (1991).

GRADIENT ANISOTROPIC DAMAGE IN MMCS FOR BRIDGING LENGTH SCALES BETWEEN MACROSCOPIC RESPONSE AND MICROSTRUCTURE

George Z. Voyiadjis and Robert J. Dorgan
Department of Civil and Environmental Engineering
Louisiana State University
Baton Rouge, Louisiana 70803 USA

1. SUMMARY

A thermodynamically consistent framework for the gradient approach in coupled damage-plasticity is proposed. The idea of multiple scale effects is made more general and complete by introducing damage and plasticity internal state variables and the corresponding gradients at both the macro and mesoscale levels. The mesoscale gradient approach allows one to obtain more precise characterization of the nonlinearity in the damage distribution; to address issues such as lack of statistical homogeneous state variables at the macroscale level such as debonding of fibers in composite materials, crack, voids, etc; and to address nonlocal influences associated with crack interaction. The macroscale gradients allow one to address non-local behavior of materials and interpret the collective behavior of defects such as dislocations and cracks.

2. INTRODUCTION

Engineering materials contain defects that lead in some cases to specific pattern formation due to a coupling of inelastic mechanisms of microcrack and microvoid growth with plastic flow and fracture. Initially, loading of heterogeneous materials causes non-interacting microcracks and microvoids; however, further loading will cause failure mechanisms to occur at localized zones of damage and plasticity where interaction and coalescence of microcracks and microvoids take place. These interactions lead to a degradation of the global stiffness and to a subsequent decrease of the load carrying capacity of the material. As damage localizes over a narrow region of the continuum (Figure 1), the characteristic length scale governing the variations of damage falls far below the scale of the state variables of strain and damage normally used to describe the response of the continuum. This leads to the case where the wavelength of the damage distribution is predicted to be much smaller than the size of the material heterogeneities 0.



Figure 1: Localized zone of damage occurring as fiber breakage and debonding

Localization problems due to plasticity and damage can be handled by using the gradient approach at the macroscale 0. However, it is observed that for a given value of macroscopic damage variable variation, the macroscale response function associated with the representative volume elements (RVE) consisting of different distributions of defects are attributable to the differences in the size, orientation, and spatial distribution of defects within the RVEs. These are important factors that make the evolution function statistically inhomogeneous below the RVE scale. Macroscale strain and damage gradient approaches cannot capture this sub-representative volume element (SRVE) length scale effect. Lacy et. al. 0 proposed a mesoscale gradient approach in order to obtain more precise characterization of the nonlinearity in the damage distribution, nonlocal influences associated with crack interaction, and statistical inhomogeneity of evolution related damage variables.

This work addresses non-local effects by incorporating the gradient of both plasticity and damage internal state variables. The combined coupled concept of introducing gradients at the mesoscale and macroscale enables one to address two issues simultaneously. The mesoscale gradients allow one to address issues such as lack of statistical homogeneous state variables at the macroscale level such as debonding of fibers in composite materials, crack, voids, etc. The macroscale gradients allow one to address non-local behavior of materials and interpret the collective behavior of defects such as dislocations and cracks. This coupled proposed gradients formulation allows one to model size dependent behavior of the materials together with localization.

3. GRADIENT MODEL USING NON-LOCAL INTERNAL STATE VARIABLES

The use of nonlocal continua theory is made to represent the stress response at a material point, which is assumed to depend on the state of its neighborhood in addition to the state of the point itself. Kuhl et al 0 derived the gradient continuum enhancement as a special case of the general concept of nonlocal continua. The nonlocal tensor $\bar{\mathbf{A}}$ can be expressed as the weighted average of its local counterpart \mathbf{A} over a surrounding volume V such that

$$\bar{\mathbf{A}} = \frac{1}{V} \int_V \mathbf{h}(\zeta) \mathbf{A}(\mathbf{x} + \zeta) dV \quad (1)$$

where $\mathbf{h}(\zeta)$ is a weight function that decays smoothly with distance and in this work is given by $\mathbf{h}(\zeta) = \mathbf{I} h(\zeta)$ where \mathbf{I} is an identity tensor.

Eq. (1) can be approximated by a partial differential equation through the Taylor expansion at $\zeta=0$. Assuming only an isotropic influence of the averaging equation, integrals of odd terms in the Taylor expansion will vanish. Thus, the Taylor expansion up to the quadratic term leads to the following partial differential equation 0:

$$\bar{\mathbf{A}} = \frac{1}{V} \int_V \mathbf{h}(\zeta) \mathbf{A}(\mathbf{x}) dV + \frac{1}{2!V} \int_V \mathbf{h}(\zeta) \nabla^2 \mathbf{A}(\mathbf{x}) \zeta^2 dV = \mathbf{A} + a \nabla^2 \mathbf{A} \quad (2)$$

where ∇^2 denotes the 2nd order gradient operator and $\frac{1}{V} \int_V [h(\zeta)] dV = 1$. In Eq. (2), "a" is a constant proportional to a length squared and weights each component of the gradient term identically.

A similar expression to the non-local internal variable $\bar{\mathbf{A}}$ may be obtained at the mesoscale to characterize interface damage such as debonding of the fiber from the matrix such that $\bar{\mathbf{A}} = \hat{\mathbf{A}} + a \hat{\nabla}^2 \hat{\mathbf{A}}$. This allows one to describe $\bar{\mathbf{A}}$ at a SRVE where the internal variable can only be statistically homogeneous at a subvolume of the RVE and $\hat{\nabla}^2 \hat{\mathbf{A}}$ is its corresponding gradient.

4. REPRESENTATIVE VOLUME AND SUB- REPRESENTATIVE VOLUME ELEMENTS

The internal state variables are categorized into two categories. The first category is statistically homogeneous at the RVE, while the second is statistically homogeneous at the SRVE. The definition of the RVE and SRVE is detailed in the work of Nemat-Nasser and Hori 0.

In the literature the RVE is the necessary minimum observation window that is used for the determination of the statistically homogenous elastic stiffness. The RVE implied in this work is the matrix with a single fiber in the middle of the RVE (Figure 2).

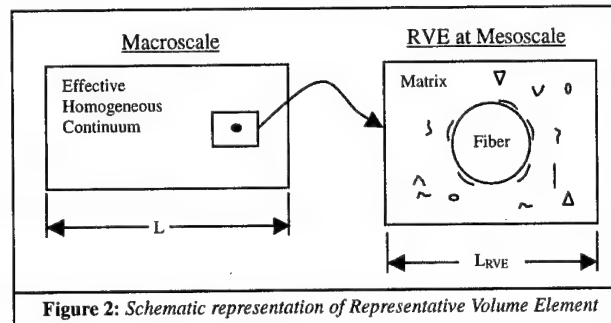


Figure 2: Schematic representation of Representative Volume Element

For an RVE made of two phase materials the defects in each constituent and in the interphase (debonding) cannot be categorized as statistically homogenous for the RVE unless a very low order of measure of these defects is used to characterize damage or plasticity. The subvolume characterization of damage and plasticity at a level below the RVE allows one to adequately characterize the details of these defects. This SRVE definition for the composite material in the case of multiscale analysis is introduced by defining an equivalent minimum observation window for each constituent of the composite where the response function of each constituent is statistically homogenous within the equivalent RVEs (Figure 3). Then the SRVE damage distribution of each constituent can be characterized at a point within the corresponding RVEs.

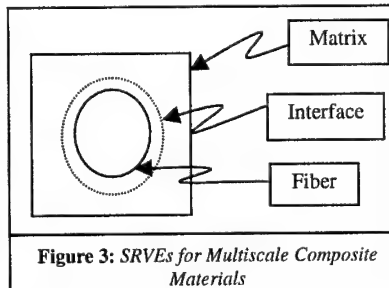


Figure 3: SRVEs for Multiscale Composite Materials

5. MACROSCALE - MESOSCALE COUPLED PLASTICITY AND DAMAGE GRADIENT THEORY

5.1 NONLOCAL INTERNAL STATE VARIABLES

The thermoelastic Helmholtz free energy may be expressed in terms of the nonlocal internal state variables as

$$\Psi = \Psi(\epsilon_{ij}^{(e)}, T, {}^{(p)}\bar{\alpha}_{ij}, {}^{(p)}\bar{p}, {}^{(d)}\bar{\phi}_{ij}^{(u)}, {}^{(d)}\bar{\gamma}_{ij}^{(u)}, {}^{(d)}\bar{\kappa}^{(u)}) \quad \text{where } u = m, f, i \quad (3)$$

where the subscripted letters after the variables indicate the tensorial nature of the variables. The bracketed superscripts 'e', 'p', and 'd' imply elasticity, plasticity, and damage related internal state variables, respectively. The superscripted letter 'u' indicates that the internal state variable is used to characterize damage associated with different material constituents. The composite material is separated into matrix (m), fiber (f), and interface (i).

In the above equation, the nonlocal internal state variables $\bar{\kappa}^{(u)}$ and $\bar{\gamma}_{ij}^{(u)}$ (\bar{p} and $\bar{\alpha}_{ij}$) variables characterize the isotropic and kinematic hardening flux variables in damage (plasticity). $\bar{\phi}_{ij}$ is the nonlocal damage second order tensor. Additive decomposition of the strain is assumed with ϵ'_{ij} being the elastic component and ϵ''_{ij} being the corresponding plastic component. Stresses and strains are macro-variables that maybe computed using the macro-, meso-, and micro-structure internal state variables of the material. Thus in this work, gradient effects for the strains and stresses are introduced only through the internal state variables associated with plasticity and damage.

In lieu of section 1, with regard to using gradients to describe the non-local behavior of the material, the following relations are given here in a similar form to that given by Eq. (2) such that:

$$\begin{aligned} \bar{\alpha}_{ij} &= \alpha_{ij} + {}^{(p)}A \nabla^2 \alpha_{ij} + {}^{(p)}A \nabla^2 \bar{\alpha}_{ij} & \bar{p} &= p + {}^{(p)}B \nabla^2 p + {}^{(p)}B \nabla^2 \bar{p} \\ \bar{\phi}_{ij}^{(u)} &= \phi_{ij}^{(u)} + {}^{(d)}C^{(u)} \nabla^2 \phi_{ij}^{(u)} + {}^{(d)}C^{(u)} \nabla^2 \bar{\phi}_{ij}^{(u)} & (\text{where } u = m, f, i) & \\ \bar{\gamma}_{ij}^{(u)} &= \gamma_{ij}^{(u)} + {}^{(d)}A^{(u)} \nabla^2 \gamma_{ij}^{(u)} + {}^{(d)}A^{(u)} \nabla^2 \bar{\gamma}_{ij}^{(u)} & \bar{\kappa}^{(u)} &= \kappa^{(u)} + {}^{(d)}B^{(u)} \nabla^2 \kappa^{(u)} + {}^{(d)}B^{(u)} \nabla^2 \bar{\kappa}^{(u)} \end{aligned} \quad \text{Eqs. (4)}$$

The constants in Eqs. (4) are constants similar to the constant "a" given by Eq. (2). If one chooses the same weight function $h(\zeta)$ for both plasticity and damage macro-related internal state variables, then ${}^{(p)}A = {}^{(p)}B = {}^{(d)}A^{(u)} = {}^{(d)}B^{(u)} = {}^{(d)}C^{(u)} = a$. However, this will not be the case for the micro-related internal variables since the region of the sub-volume will change for different internal variables.

The isotropic hardening variable of plasticity, p, is a scalar quantity and is expressed in terms of the plastic strain rate. The gradient terms of p characterize measures of the dislocation density $\dot{\rho}$. The gradient terms referring to the backstress characterizes the internal embedded stress variations introduced by dislocation pile-ups, etc. The average mesoscale gradients of kinematic and isotropic hardening in plasticity may be used to characterize discrete dislocations in the formulation if that is paramount to the analysis.

The second order tensor, ϕ_{ij} , characterizes a kinematic measure of damage due to volume or surface reduction associated with the evolution of voids or cracks 0 - 0, and is characterized through the individual damages of the matrix, fiber, and interface. For the case of matrix damage, $\nabla^2 \phi_{ij}^{(m)}$ is used, while for fiber damage, $\nabla^2 \phi_{ij}^{(f)}$ is used. However, for interface damage, the averaged mesoscale gradient $\bar{\nabla}^2 \hat{\phi}_{ij}^{(i)}$ is used which is averaged at the sub-volume of the RVE. The overall damage is obtained directly from Voyiadjis and Park 0.

To simplify the formulation, we introduce the notation ${}^{(r)}\mathbf{f} = \nabla^2 {}^{(r)}\mathbf{f}$ and ${}^{(r)}\mathbf{f} = \bar{\nabla}^2 {}^{(r)}\hat{\mathbf{f}}$ where ${}^{(r)}\mathbf{f}$ represents a macroscale internal state variable and ${}^{(r)}\hat{\mathbf{f}}$ represents a mesoscale internal state variable. Thus, after incorporating the constant 'a', Eqs. (4) can be written in the following form:

$$\begin{aligned} \bar{\alpha}_{ij} &= {}^{(p)}\alpha_{ij} + a {}^{(p)}\alpha_{ij} + {}^{(p)}A {}^{(p)}\alpha_{ij} & \bar{p} &= {}^{(p)}p + a {}^{(p)}p + {}^{(p)}B {}^{(p)}p \\ \bar{\phi}_{ij}^{(u)} &= {}^{(d)}\phi_{ij}^{(u)} + a {}^{(d)}\phi_{ij}^{(u)} + {}^{(d)}C {}^{(u)}\phi_{ij}^{(u)} & (\text{where } u = m, f, i) & \\ \bar{\gamma}_{ij}^{(u)} &= {}^{(d)}\gamma_{ij}^{(u)} + a {}^{(d)}\gamma_{ij}^{(u)} + {}^{(d)}A {}^{(u)}\gamma_{ij}^{(u)} & \bar{\kappa}^{(u)} &= {}^{(d)}\kappa^{(u)} + a {}^{(d)}\kappa^{(u)} + {}^{(d)}B {}^{(u)}\kappa^{(u)} \end{aligned} \quad \text{Eqs. (5)}$$

5.2 LOCAL INTERNAL STATE VARIABLES

In this proposed work, the terms A and $\nabla^2 A$ given in Eq. (2) are identified as two independent internal state variables with different physical interpretations and initial conditions. Certain internal state variables such as the dislocation density expressed through $\nabla^2 p$ and the accumulated plastic strain, p , each have a different physical interpretation that guides one to use different evolution equations for $\nabla^2 p$ and p . Using the non-local internal variable \bar{p} will enforce both internal state variables to have a single evolution expression. Similar arguments may be used for the flux related back-stress plasticity tensor $\bar{\alpha}_{ij}$.

Eq. (3) may now be expressed in terms of the macroscale internal variables and averaged mesoscale gradients as

$$\Psi = \Psi({}^{(e)}\epsilon_{ij}, T, {}^{(p)}\alpha_{ij}, {}^{(p)}p, {}^{(d)}\phi_{ij}^{(u)}, {}^{(d)}\gamma_{ij}^{(u)}, {}^{(d)}\kappa_{ij}^{(u)}) \quad k = 1, 2, 3 \quad (6)$$

We use Eq. (6) because Eq. (3) will lead to coupling terms of the nature $\alpha_{ij} \nabla^2 (\alpha_{ij})$, etc, which may not have a physical interpretation in material behavior.

Since the internal state variables are selected independently of one another, one can express the analytical form of the Helmholtz free energy given by Eq. (3) as the quadratic form in terms of its internal state variables as:

$$\begin{aligned} \rho\Psi &= \frac{1}{2} \epsilon'_{ij} E_{ijkl} \epsilon'_{kl} + \sum_{k=1}^3 \left(\frac{1}{2} {}^{(p)}a {}^{(p)}\alpha_{ij} {}^{(p)}\alpha_{ij} + \frac{1}{2} {}^{(p)}b {}^{(p)}p {}^{(p)}p \right) + \\ &\sum_{u=m, f, i} \sum_{k=1}^3 \left(\frac{1}{2} {}^{(d)}a {}^{(d)}\phi_{ij}^{(u)} {}^{(d)}\phi_{ij}^{(u)} + \frac{1}{2} {}^{(d)}b {}^{(d)}\gamma_{ij}^{(u)} {}^{(d)}\gamma_{ij}^{(u)} + \frac{1}{2} {}^{(d)}c {}^{(d)}\kappa_{ij}^{(u)} {}^{(d)}\kappa_{ij}^{(u)} \right) \end{aligned} \quad (7)$$

In Eq. (7), the coefficients are dependent on material and geometrical properties of the composite. In the case of composites the geometrical properties may include size, shape, and spacing of the fibers as well as the gradient of the fiber size and fiber spacing variation. The functional dependency of these coefficients can be obtained by studying the interaction problem of an inclusion embedded in an infinite homogeneous matrix subjected to a macroscopic stress rate and corresponding strain rate at infinity 0.

Substituting the time derivative of Eq. (6) into the Clausius-Duhem inequality provides the thermodynamic state laws given in Table 1, where X_{ij} , R , $Y_{ij}^{(u)}$, $\Gamma_{ij}^{(u)}$, and $K^{(u)}$ are defined as the thermodynamic conjugate forces corresponding to the internal state flux variables α_{ij} , p , $\phi_{ij}^{(u)}$, $\gamma_{ij}^{(u)}$, and $\kappa^{(u)}$. The total dissipation can now be expressed as the sum of the plastic and damage dissipations where the dissipation processes are given as follows:

$$\Pi^p = \sigma_{ij} \dot{\epsilon}_{ij}'' - \sum_{k=1}^3 \left(\binom{p}{(k)} X_{ij} \binom{p}{(k)} \dot{\alpha}_{ij} + \binom{p}{(k)} R \binom{p}{(k)} \dot{p} \right) \quad (8)$$

$$\Pi^d = - \sum_{u=m,f,i} \sum_{k=1}^3 \left(\binom{d}{(k)} \Gamma_{ij}^{(u)} \binom{d}{(k)} \dot{\gamma}_{ij}^{(u)} + \binom{d}{(k)} K^{(u)} \binom{d}{(k)} \dot{\kappa}^{(u)} + \binom{d}{(k)} Y_{ij}^{(u)} \binom{d}{(k)} \dot{\phi}_{ij}^{(u)} \right) \quad (9)$$

Using the state laws in Table 1 along with Eq. (7), the definitions for the thermodynamic conjugate forces in Table 1 can be obtained.

The thermodynamic conjugate forces can be obtained through the evolution relations of the internal state variables which are obtained by assuming the physical existence of the dissipation potential at the macroscale. Evolution equations for the averaged mesoscale based gradients maybe obtained through the use of discrete elements or micromechanical - based models. In this

		State Laws	Conjugate Forces
Thermo-elastic Laws	<i>Elastic deformation</i>	$\sigma_{ij} = \rho \left(\partial \Psi / \partial \epsilon'_{ij} \right)$	
	<i>Thermal entropy</i>	$s = -\partial \Psi / \partial T$	
Plasticity	<i>Kinematic hardening</i>	$\binom{p}{(k)} X_{ij} = \rho \left(\partial \Psi / \partial \binom{p}{(k)} \alpha_{ij} \right)$	$\binom{p}{(k)} X_{ij} = \binom{p}{(k)} a \binom{p}{(k)} \alpha_{ij}$
	<i>Isotropic hardening</i>	$\binom{p}{(k)} R = \rho \left(\partial \Psi / \partial \binom{p}{(k)} p \right)$	$\binom{p}{(k)} R = \binom{p}{(k)} b \binom{p}{(k)} p$
Damage	<i>Damage tensor</i>	$\binom{d}{(k)} Y_{ij}^{(u)} = \rho \left(\partial \Psi / \partial \binom{d}{(k)} \phi_{ij}^{(u)} \right)$	$\binom{d}{(k)} Y_{ij}^{(u)} = \binom{d}{(k)} c \binom{d}{(k)} \phi_{ij}^{(u)}$
	<i>Kinematic hardening</i>	$\binom{d}{(k)} \Gamma_{ij}^{(u)} = \rho \left(\partial \Psi / \partial \binom{d}{(k)} \gamma_{ij}^{(u)} \right)$	$\binom{d}{(k)} \Gamma_{ij}^{(u)} = \binom{d}{(k)} a \binom{d}{(k)} \gamma_{ij}^{(u)}$
	<i>Isotropic hardening</i>	$\binom{d}{(k)} K^{(u)} = \rho \left(\partial \Psi / \partial \binom{d}{(k)} \kappa^{(u)} \right)$	$\binom{d}{(k)} K^{(u)} = \binom{d}{(k)} b \binom{d}{(k)} \kappa^{(u)}$
Table 2: Thermodynamic state laws and definitions of conjugate forces			

work the evolution equations of the macroscale internal state variables are obtained through the use of the generalized normality rule of thermodynamics.

6. EVOLUTION EQUATIONS FOR THE INTERNAL STATE VARIABLES IN DAMAGE

In order to be consistent and satisfy the generalized normality rule of thermodynamics, the following form of the damage potentials, $G^{(u)}$, for a composite and the damage criterion, $g^{(u)}$ are defined here 0:

$$G^{(u)} = g^{(u)} + \frac{{}^d k}{2} \bar{\Gamma}_{ij}^{(u)} \bar{\Gamma}_{ij}^{(u)} \quad (10)$$

$$g^{(u)} = (\bar{\gamma}_{ij}^{(u)} - \bar{\Gamma}_{ij}^{(u)}) \bar{\Gamma}_{ijkl}^{(u)} (\bar{\gamma}_{kl}^{(u)} - \bar{\Gamma}_{kl}^{(u)}) - 1 \leq 0 \quad (11)$$

where ${}^{(d)}k$ is a constant used to adjust the units of the equation. The fourth order tensor $\bar{\Gamma}_{ijkl}^{(u)} = \bar{\Gamma}_{ijkl}^{(u)}(\bar{\phi}_{ij}^{(u)})$ describes the anisotropic nature of the damage growth and the initiation of damage 0.

Using a similar definition for the nonlocal term $\bar{\Gamma}_{ij}^{(u)}$ as given in Table 1, the following relation is obtained:

$$\bar{\Gamma}_{ij}^{(u)} = {}^{(d)}\bar{a}^{(u)} \bar{\gamma}_{ij}^{(u)} = {}^{(d)}\bar{A}^{(u)} {}^{(d)}\bar{\Gamma}_{ij}^{(u)} + {}^{(d)}\bar{A}^{(u)} {}^{(d)}\bar{\Gamma}_{ij}^{(u)} + {}^{(d)}\bar{A}^{(u)} {}^{(d)}\bar{\Gamma}_{ij}^{(u)} \quad (12)$$

where

$${}^{(d)}\bar{A}^{(u)} = {}^{(d)}\bar{a}^{(u)} \frac{{}^{(d)}A^{(u)}}{{}^{(d)}\bar{a}^{(u)}} \quad \left({}^{(d)}A^{(u)} = 1, {}^{(d)}A^{(u)} = a \right) \quad (13)$$

Similar relations are developed for $\bar{\gamma}_{ij}^{(u)}$ and $\bar{K}^{(u)}$. Damage evolution equations can now be obtained by using the generalized normality rule of thermodynamics:

$${}^{(d)}\bar{\phi}_{ij}^{(u)} = -\lambda^d \frac{\partial G^{(u)}}{\partial {}^{(d)}\bar{\gamma}_{ij}^{(u)}} \quad (14)$$

$${}^{(d)}\bar{K}^{(u)} = -\lambda^d \frac{\partial G^{(u)}}{\partial {}^{(d)}\bar{K}^{(u)}} = -\lambda^d {}^{(d)}\bar{B}^{(u)} \frac{\partial g^{(u)}}{\partial \bar{K}^{(u)}} \quad (k=1,2,3) \quad (15)$$

$${}^{(d)}\bar{\gamma}_{ij}^{(u)} = -\lambda^d \frac{\partial G^{(u)}}{\partial {}^{(d)}\bar{\Gamma}_{ij}^{(u)}} = -\lambda^d {}^{(d)}\bar{A}^{(u)} \left\{ \frac{\partial g^{(u)}}{\partial \bar{\Gamma}_{ij}^{(u)}} + {}^d k \bar{\Gamma}_{ij}^{(u)} \right\} \quad (k=1,2,3) \quad (16)$$

Alternatively, one may obtain an evolution equation for γ_{ij} only using the potential, G , and then the evolution equation for the corresponding gradient term, $\nabla^2 \gamma_{ij}$, is to be obtained directly by operating on γ_{ij} with the Laplacian. An evolution equation for the averaged mesoscale gradient term, $\hat{\nabla}^2 \hat{\gamma}_{ij}$, can be derived at the mesoscale level using $\hat{\gamma}_{ij}$ and averaged over the RVE. The same arguments apply for the subsequent evolution equations.

The damage multiplier λ^d can be obtained using the consistency condition for damage given as follows:

$$\dot{g}^{(u)} = \frac{\partial g}{\partial \sigma^{(u)}} : \dot{\sigma}^{(u)} + \frac{\partial g}{\partial \phi^{(u)}} : \dot{\phi}^{(u)} + \frac{\partial g}{\partial \bar{K}^{(u)}} \dot{\bar{K}}^{(u)} + \frac{\partial g}{\partial \bar{\Gamma}^{(u)}} : \dot{\bar{\Gamma}}^{(u)} = 0 \quad (17)$$

7. CONCLUSIONS

A thermodynamically consistent multiscale gradient approach for plasticity and damage is formulated in this paper. Thermodynamically consistent constitutive equations are derived here in order to investigate size effect on the strength of the composite, the strain and damage localization effects on the macroscopic response of the composite, and statistical inhomogeneity of the evolution related damage variables associated with the RVE. The interaction of the length scales is a paramount factor in understanding and controlling the material defects such as dislocation, voids, and cracks at the mesoscale and interpret them at the macroscale.

The calibration for the different material properties in the proposed approach may be difficult, or even impossible for certain cases. While the proposed framework is that of a general plasticity coupled with damage, one needs more studies to be performed in order to effectively assess the potential applications for this framework. The computational issue of this theoretical formulation with proper explanation of the boundary conditions associated with these gradients and of the model parameter and constants will be discussed in detail in a forth-coming paper. A detailed explanation for some of the non-standard boundary conditions of plasticity is given by de Borst et. al 0.

8. REFERENCES

- [1] Pijaudier-Cabot, G., 1995, Non Local Damage, *Continuum Models for Materials with Microstructure*, Jhon Wiley & Sons Ltd., 105-143.
- [2] Aifantis, E.C., 1984, On the microstructural origin of certain inelastic models, *Journal of Engineering Materials and Technology*, **106**:326-330.
- [3] Lacey, T.E., McDowell, D.L., and Talreja, R., 2000, Nonlocal Concepts for Evolution of Damage, *Mechanics of Materials*, **31**(12):831-860.
- [4] Kuhl, E., Ramm, E., and de Borst, R., 2000, An anisotropic gradient damage model for quassi-birttle materials, *Journal of Computer Methods in Applied Mechanics and Engineering*, **183**:87-103.
- [5] Muhlhaus, H.B. and Aifantis, E.C., 1991, A variational principle for gradient plasticity, *International Journal of Solid and Structures*, **28**:845-857.
- [6] Nemat-Nasser, S. and Hori, M., 1993, *Micromechanics: Overall Properties of Heterogeneous Materials*, North-Holland, Amsterdam, The Netherlands.
- [7] Kroner, E., 1967, Elasticity theory of materials with long range cohesive forces, *International Journal of Solid and Structures*, **3**:731-742.
- [8] Fleck, N.A. and Hutchinson, J.W., 1997, Strain Gradient Plasticity, *Advances in Applied, Mech.*, **33**:295-361.
- [9] Voyiadjis, G.Z. and Park, T., 1999, Kinematics description of damage for finite strain plasticity, *Journal of Engineering Science*, **37** #7:803-830.
- [10] Voyiadjis, G. Z. and Venson, A.R., 1995, Experimental Damage Investigation of SiC-Ti Aluminide Metal Matrix Composite, *International Journal of Damage Mechanics*, **4**:338-361.
- [11] Voyiadjis, G. Z. and Deliktas, B., 2000, A Coupled Anisotropic Damage Model for the Inelastic Response of Composite Materials, *Journal of Computer Methods in Applied Mechanics and Engineering*, **183**:159-199.

-
- [12] Voyiadjis, G. Z. and Park, T., 1995, Local and Interfacial Damage Analysis of Metal Matrix Composites, *International Journal of Engineering Science*, **33** No. 11:1595-1621.
 - [13] Voyiadjis, G. Z., Deliktas, B., and Aifantis, E.C., July 2001, Multi-scale Analysis of Multiple Damage Mechanisms Coupled with Inelastic Behavior of Composite Materials, *Journal of Engineering Mechanics, ASCE*.
 - [14] de Borst, R., Benellal, A., and Heeres, O., 1996, A gradient enhanced damage approach to fracture, *Journal de Physique*, **6**:491-502.

TWO SCALE DAMAGE MODEL FOR FATIGUE REPRESENTATION OF GRADIENT EFFECTS

Rodrigue Desmorat

Université Paris 6

Laboratoire de Modélisation et Mécanique des Structures (LM²S)

8, rue du Capitaine Scott, F-75015 PARIS, FRANCE

1 SUMMARY

We present a two scale damage model built for monotonic loading, low cycle (LCF) as well as high cycle fatigue (HCF). We only describe here the HCF applications.

The inputs of the model are the stress and strain history at the most loaded points of the structure. They are determined by an elastic finite element calculation. The time integration of the constitutive equations over the whole process up to a critical value of damage gives then the number of cycles to crack initiation.

A key point of the model is the description of the scale transition (from the RVE scale to the microdefects scale). The original model uses Eshelby-Kröner localization law, which is a "local" relationship between the meso-fields and the micro-fields. We propose a more realistic relationship, using a non-local law: we consider that the micro-fields also depend on the meso-stress and meso-strain gradients in the structure. Some comments are then given on the representation of the gradient effect in fatigue.

2 INTRODUCTION

Fatigue is usually modeled by considering the maximum stress versus number of cycles to failure curve, known as the Wöhler curve. This practical approach is uniaxial and may not be relevant when 3D states of stress arise in the structure (Crossland, 1956, Sines, 1959, Dang Van and Papadopoulos, 1987): How to represent then the mean stress effect? what is the fatigue limit for a complex loading (random and/or non-proportional)?

A two scale damage model has been developed to give answers to those questions (Sermage et al., 1999, Desmorat and Lemaitre, 2001). It is based on the representation of the micro-defects by a weak inclusion with an elasto-plastic behavior coupled to damage. The main feature of the model is that, even in fatigue, the constitutive law still is a relationship between stresses σ_{ij} and strains ϵ_{ij} (and eventually internal variables such as damage D), not between the amplitudes. The cyclic behavior (stress amplitude $\Delta\sigma$ as a function of number of cycles

to failure N_R) results of the time integration over the whole process of the state and evolution (rate) laws.

Two scales are considered (in addition to the macroscopic scale of structures):

- the meso-scale or scale of the Representative Volume Element (RVE) of Continuum Mechanics. For High Cycle Fatigue (HCF), the RVE remains elastic.
- the micro-scale or scale of a micro-defect (micro-voids, micro-cracks) embedded in the RVE. At this scale, micro-plasticity and micro-damage occur. Lemaitre's damage constitutive equations may be applied.

An initial elastic structure calculation (analytical or by Finite Element analysis) is needed to define the stress and strain fields at the meso-scale. The time history of the stresses and strains at the most loaded point(s) of the structure are then the inputs of the model. The main output is the evolution of the damage as a function of loading, time or number of cycles.

The present analysis may also model failure with (visco-)plasticity at meso-scale. In that case the meso-stresses and meso-strains may be the result of a mechanical analysis of the structure by means of a FE analysis or of any analytical or semi-analytical procedure like Neuber method following an elastic calculation (Desmorat, 2000).

3 DESCRIPTION OF THE TWO SCALE MODEL

Brittle and High Cycle Fatigue (HCF) damages are always very localized at a scale much smaller than the plastic strain. This is the reason to consider a two scale model in which the damage occurs in a weak micro-inclusion embedded in a meso Representative Volume Element elastic (or elasto-(visco-)plastic) and free of damage. This hypothesis allows to obtain the meso-stress and strain by a classical structure calculation elastic (or elasto-(visco-)plastic) with no damage at meso-scale and to solve the constitutive equations of elasto-(visco-)plasticity coupled with damage as a post-processor at micro-scale.

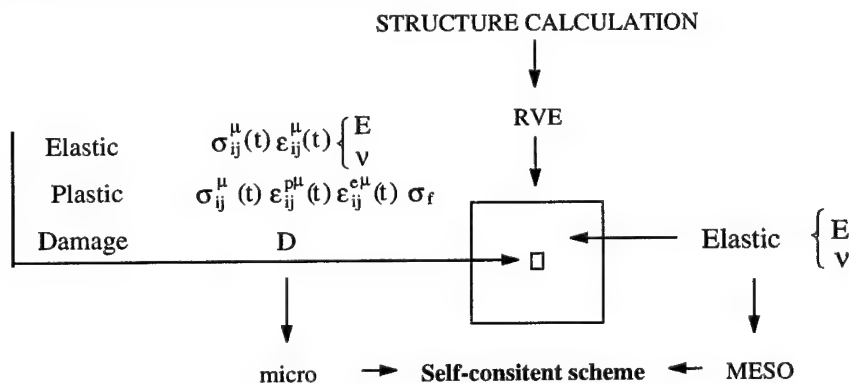


FIG. 1: Micro-element embedded in an elastic RVE

The mechanical behavior of the material is modelled from two different manners related to the two different scales.

- At the meso-scale the material is considered as elastic because HCF failure occurs at states of stresses below or close to the yield stress.

- At the micro-scale the behavior is modelled by elasto-plasticity coupled with damage. The weakness of the inclusion is related to its yield stress σ_y^μ taken equal to the true fatigue limit σ_f of the material below which we consider that no damage occurs. The elasto-plastic properties of the inclusion are those of the material at meso-scale below and above the yield stress. To simplify, only linear kinematic hardening is assumed at micro-scale, but with the same plastic modulus C than at meso-scale.

As damage is considered at micro-scale, the isotropic damage evolution law (Lemaitre, 1992) will in fact be written in terms of micro-stress, of micro-energy density release Y^μ rate and of micro-accumulated plastic strain p^μ , i.e.

$$\dot{D} = \left(\frac{Y^\mu}{S} \right)^s \dot{p}^\mu \quad \text{if } p^\mu > p_D \quad (1)$$

where S is the damage strength of the material, s the damage exponent and p_D is the loading dependent damage threshold.

Scale transition

The fields in the inclusion (stress tensor σ_{ij}^μ , total strain and plastic strain tensors ϵ_{ij}^μ , $\epsilon_{ij}^{\mu p}$, damage $D^\mu \dots$) have a μ -superscript meaning micro-scale when the fields at the meso-scale of the RVE are simply denoted σ_{ij} , ϵ_{ij} , ϵ_{ij}^p . Please note that we consider damage at micro-scale only and we will omit the μ -superscript in that case by setting $D^\mu = D$.

The scale transition is made by use of the Eshelby-Kröner localization law: the total and plastic strains at micro-scale are related to the strains at the mesolevel as (Eshelby, 1957, Kröner, 1961)

$$\epsilon_{ij}^\mu = \epsilon_{ij} + \beta(\epsilon_{ij}^{\mu p} - \epsilon_{ij}^p) \quad (2)$$

where β is given by Eshelby's analysis of a spherical inclusion,

$$\beta = \frac{2}{15} \frac{4 - 5\nu}{1 - \nu} \quad (3)$$

The law (2) may also be written in term of stresses or effective stresses taking into account the coupling between damage and elasticity and plasticity,

$$\bar{\sigma}_{ij}^\mu = \frac{\sigma_{ij}^\mu}{1 - D} = \sigma_{ij} - 2G(1 - \beta)(\epsilon_{ij}^{\mu p} - \epsilon_{ij}^p) \quad (4)$$

ν is the Poisson ratio, G the shear modulus and E the Young modulus.

3D model for any kind of loading

The history of the plastic strains $\epsilon_{ij}^p(t)$ and of the stresses $\sigma_{ij}(t)$ at the mesolevel being inputs, the fields at micro level are obtained from the time integration of the constitutive equations at micro-scale coupled together with the law of localization (2) even for fatigue cyclic loading. The equations to be solved are those of elasto-plasticity coupled with damage with linear kinematic hardening (yield function $f^\mu = (\bar{\sigma}^\mu - X^\mu)_{eq} - \sigma_f$ in which X_{ij}^μ is the back

stress and σ_f the fatigue limit):

$$\begin{aligned}
 \epsilon_{ij}^\mu &= \epsilon_{ij}^{\mu e} + \epsilon_{ij}^{\mu p} \\
 \epsilon_{ij}^\mu &= \epsilon_{ij} + \beta(\epsilon_{ij}^{\mu p} - \epsilon_{ij}^p) \\
 \epsilon_{ij}^{\mu e} &= \frac{1+\nu}{E} \bar{\sigma}_{ij}^\mu - \frac{\nu}{E} \bar{\sigma}_{kk}^\mu \delta_{ij}, \quad \bar{\sigma}_{ij}^\mu = \frac{\sigma_{ij}^\mu}{1-D} \\
 \dot{\epsilon}_{ij}^{\mu p} &= \frac{3}{2} \frac{\bar{\sigma}_{ij}^{\mu D} - X_{ij}^\mu}{(\bar{\sigma}^\mu - X^\mu)_{eq}} \frac{\dot{\lambda}}{1-D} \\
 \dot{X}_{ij}^\mu &= \frac{2}{3} C \dot{\epsilon}_{ij}^{\mu p} (1-D) \\
 \dot{D} &= \left(\frac{Y^\mu}{S} \right)^s \dot{p}^\mu \text{ if } p^\mu > p_D
 \end{aligned} \tag{5}$$

The strain energy release rate Y^μ taking into account the different behaviors in tension and in compression is defined as

$$\begin{aligned}
 Y^\mu &= \frac{1+\nu}{2E} \left[\frac{\langle \underline{\sigma}^\mu \rangle_+ : \langle \underline{\sigma}^\mu \rangle_+}{(1-D)^2} + h \frac{\langle \underline{\sigma}^\mu \rangle_- : \langle \underline{\sigma}^\mu \rangle_-}{(1-hD)^2} \right] \\
 &\quad - \frac{\nu}{2E} \left[\frac{\langle Tr \underline{\sigma}^\mu \rangle^2}{(1-D)^2} + h \frac{\langle -Tr \underline{\sigma}^\mu \rangle^2}{(1-hD)^2} \right]
 \end{aligned} \tag{6}$$

where $\langle . \rangle_+$ (resp. $\langle . \rangle_-$) denotes the positive part (resp. negative) of a tensor in terms of principal components and where $\langle . \rangle$ is the positive part of a scalar. By the introduction of the crack closure parameter h (for most of metals $h \approx 0.2$), the consideration of the damage law $\dot{D} = (Y^\mu/S)^s \dot{p}^\mu$ takes into account the partial closure of the micro-crack or micro-voids in the evolution of the damage. The case $h = 1$ corresponds to a damage law identical in tension and in compression.

The damage threshold is considered here as related to the energy stored in the RVE during plastic loading (Desmorat, 2000, Lemaitre et al., 2000). This allows to represent the very different values experimentally obtained for monotonic and for cyclic loading: the damage threshold for pure tension, noted ϵ_{pD} , is of the order of magnitude of few percents (steels) when p_D in fatigue may reach few hundreds of percents. Based on the calculation of the energy stored in the RVE, the following relationship has been derived for fatigue:

$$p_D = \epsilon_{pD} \left[\frac{\sigma_u - \sigma_y}{\frac{\sigma_{eq}^{\mu Max} + \sigma_{eq}^{\mu min}}{2} - \sigma_f} \right]^m \tag{7}$$

where the yield stress σ_y , the ultimate stress σ_u , the threshold in pure tension ϵ_{pD} and the exponent m are material parameters; $\sigma_{eq}^{\mu Max}$ (resp. $\sigma_{eq}^{\mu min}$) is the maximum (resp. minimum) von Mises stress at microscale reached over the cyclic loading.

Finally, $\dot{\lambda} = \dot{p}^\mu (1-D)$ is the plastic multiplier calculated from

- the consistency condition $\dot{f}^\mu = 0$ and $\dot{f}^\mu = 0$ in plasticity
- Norton's law $\dot{\lambda} = \left(\frac{f^\mu}{K} \right)^N$ in visco-plasticity.

C is the kinematic hardening parameter and K, N are Norton's parameters.

When the damage D reaches the critical value D_c there is initiation of a mesocrack.

It has been checked that this model contains the following properties: effect of stress or strain amplitude, effect of mean stress in tension, no effect in shear, effect of compression, non linear accumulation (due to the existence of a damage threshold), effect of an initial hardening or initial damage, fatigue limite in two or three dimensions, bi- or three-axial fatigue, effect of non proportional loading, fatigue under any history or random loading.

4 FORMULAE FOR PROPORTIONAL FATIGUE LOADING

Closed form expressions for the number of cycles to failure under uniaxial loading such as tension-compression or torsion may be derived (Desmorat, 2000). More generally we consider here proportional loading at meso-scale which correspond to a stress field $\sigma_{ij}(M, t)$ of constant principal directions proportional at the considered point M to a given tensor $T_{ij}(M)$,

$$\sigma_{ij} = \sigma(t) T_{ij}, \quad T_{eq} = \sqrt{\frac{3}{2} T_{ij}^D T_{ij}^D} = 1 \quad (8)$$

Tension-compression in the direction \vec{e}_1 is of course a proportional loading with $\underline{T} = \vec{e}_1 \otimes \vec{e}_1$, torsion also with $\underline{T} = (\vec{e}_1 \otimes \vec{e}_2 + \vec{e}_2 \otimes \vec{e}_1)/\sqrt{2}$.

For proportional cyclic loading at meso-scale $\sigma_{ij} = \sigma(t)T_{ij}$, $T_{eq} = 1$, of constant stress amplitude $\Delta\sigma_{ij} = \Delta\sigma T_{ij}$ between σ_{min} and $\sigma_{Max} = \sigma_{min} + \Delta\sigma$, it is possible to obtain accurate formulae for the number of cycles to crack initiation. For simplicity we assume here that $h = 1$ and we limit the analysis to the case of elastic fatigue ($\Delta\sigma \leq 2\sigma_f$).

The model will predict failure only if the stress amplitude at meso-scale is larger than twice the fatigue limit (i.e. if $\Delta\sigma > 2\sigma_f$). The plastic strain increment over one cycle $\int_{cycle} \dot{p}^\mu dt$ is then:

$$\frac{\delta p^\mu}{\delta N} = \frac{2(\Delta\sigma - 2\sigma_f)}{3G(1 - \beta)} \quad (9)$$

Damage will initiate after a number of cycles N_0 when the damage threshold p_D is reached

$$N_0 = \frac{p_D}{\frac{\delta p}{\delta N}}, \quad p_D = \epsilon_{pD} \left[\frac{6G(1 - \beta)}{C} \frac{\sigma_u - \sigma_y}{\Delta\sigma - 2\sigma_f} \right]^m \quad (10)$$

The damage increment over one cycle will then be

$$\frac{\delta D}{\delta N} = \left[\frac{\sigma_f^2(1 + \nu)}{3ES} \right]^s \frac{2(\Delta\sigma - 2\sigma_f)}{3G(1 - \beta)} \quad \text{if } T_{kk} = Tr \underline{T} = 0 \quad (11)$$

$$\frac{\delta D}{\delta N} = \frac{\sigma_f^{2s+1} \varphi_* \left(\frac{\sigma_{min}}{\sigma_f} T_{kk}, \frac{\sigma_{Max}}{\sigma_f} T_{kk} \right)}{T_{kk} 3G(1 - \beta)(2ES)^s} \quad \text{if } T_{kk} = Tr \underline{T} \neq 0 \quad (12)$$

where the adimensional function φ_* is introduced,

$$\varphi_*(x, y) = \int_{x+2}^y R_{\nu_*}^s(\xi) d\xi + \int_x^{y-2} R_{\nu_*}^s(\xi) d\xi \quad (13)$$

with the triaxiality function $R_{\nu*}$ defined by

$$R_{\nu*}(\xi) = \frac{2}{3}(1 + \nu) + \frac{1}{3}(1 - 2\nu)\xi^2 \quad (14)$$

The function $\varphi_*(x, y)$ can be easily calculated by using mathematics softwares. A simple conservative approximate formula may be derived only for small values of s ,

$$\varphi_*(x, y) \approx (y - x - 2) [R_{\nu*}^s(x) + R_{\nu*}^s(y)] \quad (15)$$

The formulae for the number of cycles at crack initiation are finally

$$N_R = N_0 + \left[\frac{3ES}{\sigma_f^2(1 + \nu)} \right]^s \frac{3G(1 - \beta)D_c}{2(\Delta\sigma - 2\sigma_f)} \quad \text{if } T_{kk} = 0 \quad (16)$$

$$N_R = N_0 + \frac{T_{kk}3G(1 - \beta)(2ES)^s D_c}{\sigma_f^{2s+1} \varphi_* \left(\frac{\sigma_{\min}}{\sigma_f} T_{kk}, \frac{\sigma_{\max}}{\sigma_f} T_{kk} \right)} \quad \text{if } T_{kk} \neq 0 \quad (17)$$

They exhibit

- a mean stress effect different in tension and in compression (obtained with $h < 1$). Usually for metals $h \approx 0.2$.
- no mean stress effect in shear as experimentally observed (Sines, 1959).

5 MODELING GRADIENT EFFECT IN FATIGUE

An important feature in fatigue of structure is the gradient effect (different from the size effect, see for instance the work of Papadopoulos and Panoskaltsis, 1996) which can be exhibited for example from bending tests: for a given local (meso) elastic loading, an inhomogeneous state of stress affects the fatigue limit.

The question is: how to model the gradient effect within the two scale damage model? The model by itself is local, as are the FE structure computation, the localization law and the plastic damageable behavior of the inclusion. The basic idea is to make each and/or all indredient nonlocal, the purpose being of course to keep the model as simple as possible.

1. Consider nonlocal behavior at microscale

To introduce the gradient effect within the plasticity coupled to damage framework is difficult to do. This is still today a research topic by itself and it cannot be done without considering gradient effects at meso-scale and/or within the localization law. In order to keep the model simple, we do not consider here this possibility.

2. Consider non local elasticity

For example, Hooke's law (at mesoscale) may be replaced by (Aifantis, 1992),

$$\underline{\sigma} = 2\mu \underline{\epsilon} + \lambda \text{tr } \underline{\epsilon} \underline{1} - c \nabla^2 [2\mu \underline{\epsilon} + \lambda \text{tr } \underline{\epsilon} \underline{1}] \quad (18)$$

where λ and μ are Lamé coefficients, ∇ is the gradient operator (∇^2 the Laplacian) and c is the scalar gradient coefficient.

In the same spirit one can also propose to write

$$\underline{\sigma} + c\nabla^2 \underline{\sigma} = 2\mu \underline{\epsilon} + \lambda \text{tr } \underline{\epsilon} \underline{1} \quad (19)$$

An internal length is introduced through c ($\sqrt{c/E}$ is a length). As a result of a non local FE computation, the meso-stress to consider as the input of the localization law (4) is then indirectly changed compared to the initial model,

$$\tilde{\underline{\sigma}}^\mu = \underline{\sigma} + c\nabla^2 \underline{\sigma} - 2G(1 - \beta)\underline{\epsilon}^{\mu p} \quad (20)$$

In practice the difficulty would be of course to perform the nonlocal elasticity FE computation.

3. Built a non local localization

Eshelby-Kröner localization law has been established for constant far field ($\underline{\sigma}$, $\underline{\epsilon}$) also called here meso-field. Following Aifantis (1995), let us consider here that the meso-field is not uniform and has average values ($\bar{\underline{\sigma}}$, $\bar{\underline{\epsilon}}$). As a first approximation Eshelby-Kröner law applies,

$$\tilde{\underline{\sigma}}^\mu = \bar{\underline{\sigma}} - 2G(1 - \beta)\underline{\epsilon}^{\mu p} \quad (21)$$

The definition of the average stress over the RVE V_0 is

$$\bar{\underline{\sigma}} = \bar{\underline{\sigma}}(\mathbf{x}) = \frac{1}{V_0} \int_{V_0} \underline{\sigma}(\mathbf{x} + \mathbf{r}) dV \quad (22)$$

with the formal Taylor expansion

$$\underline{\sigma}(\mathbf{x} + \mathbf{r}) = \underline{\sigma}(\mathbf{x}) + \nabla \underline{\sigma} \cdot \mathbf{r} + \frac{1}{2!} \nabla^{(2)} \underline{\sigma} \cdot (\mathbf{r} \otimes \mathbf{r}) + \dots \quad (23)$$

and where \cdot and \otimes denote the inner and dyadic products and $\nabla^{(n)} g$ is the n th gradient of g . Assuming that the representative volume element V_0 is a sphere of radius R_0 and noting that

$$\int_{V_0} \nabla^{(2n+1)} \mathbf{r}^{(2n+1)} dV = 0 \quad (24)$$

we get (Aifantis, 1995):

$$\bar{\sigma}_{ij} \approx \sigma_{ij} + \frac{R_0^2}{10} \nabla^2 \sigma_{ij} \quad (25)$$

We finally end up with the formulation of the following nonlocal localization law

$$\tilde{\underline{\sigma}}^\mu = \underline{\sigma} + \frac{R_0^2}{10} \nabla^2 \underline{\sigma} - 2G(1 - \beta)\underline{\epsilon}^{\mu p} \quad (26)$$

similar to eq. (20) but where the physical meaning of the gradient parameter is clear: R_0 is related to the size of the RVE as $R_0 = (3V_0/4\pi)^{1/3}$.

The gradient effect obtained is in fact a second order effect. This is due to the mathematical property (24) of vanishing odd integrals over the RVE. Such a result is consistent with torsion

experiments for which the stress gradient has no influence (as shown by Papadopoulos and Panoskaltsis, 1996, result also related to the no mean stress effect in shear).

Bending experiments exhibit an influence of the first order gradient term which cannot be neglected, in contradiction with eq. (26). In order to remain consistent with the experimental data in torsion and as isotropy is assumed, we propose a formulation introducing the first stress invariant (the hydrostatic stress $\sigma_H = \sigma_{kk}/3$). We now calculate

$$\bar{\sigma}_H = \frac{1}{V_0} \int_{V_0} \sigma_H + \nabla \sigma_H \cdot \mathbf{r} + \frac{1}{2!} \nabla^{(2)} \cdot \sigma_H (\mathbf{r} \otimes \mathbf{r}) + \dots dV \quad (27)$$

The third term in the integrand is already taken into account within the term $\frac{R_0^2}{10} \nabla^2 \underline{\sigma}$ of the law (26). If we assume that the second term does not vanish due to a strong inhomogeneity of the hydrostatic stress field, this term defines then a norm for $\nabla \sigma_H$. We can propose then a general localization law able to model the gradient effect in bending, as well as the lack of such an effect in torsion:

$$\bar{\sigma}^\mu = \underline{\sigma} + c_0 \|\nabla \sigma_H\| \underline{1} + \frac{R_0^2}{10} \nabla^2 \underline{\sigma} - 2G(1 - \beta) \underline{\epsilon}^{\mu p} \quad (28)$$

In order to use (28) within the two scale damage model for HCF applications, values for the material parameters c_0 and R_0 are needed. The radius $R_0 = (3V_0/4\pi)^{1/3}$ can be calculated from the RVE size (see for instance Lemaitre, 1992). The parameter c_0 needs to be identified from experimental results (bending tests).

6 FATIGUE LIMIT IN TORSION vs FATIGUE LIMIT IN BENDING

As an application consider first the fully reverse tension-compression loading between σ_{Max} and $\sigma_{min} = -\sigma_{Max}$. The meso stress field is homogeneous with vanishing gradient terms in eq. (28). Then, eq. (10) and (16) apply to give the numbers of cycles to damage initiation N_0 and to crack initiations N_R (in which $Tr \underline{T} = 1$).

Consider then a fully reverse 4 point bending test for which the stress field is locally uniaxial with the same maximum and minimum applied stresses than for the tensile test:

$$\sigma = \sigma_{xx} = \frac{M}{I} y, \quad \sigma_{Max} = -\sigma_{min} = \frac{M D}{I} \frac{1}{2} \quad (29)$$

D is the diameter of the specimen, I the quadratic momentum (as always for such a test, the bending momentum M is constant in the middle part of the beam).

The stress gradient has a non zero value and

$$\|\nabla \sigma\| = \frac{2\sigma_{Max}}{D} \quad (30)$$

The localization law with gradient effect (28) is now considered (note that the second order terms vanish) and writes at the most loaded point (on the lateral side $y = D/2$):

$$\bar{\underline{\sigma}} = \sigma \underline{T}, \quad \underline{T} = \begin{bmatrix} 1 + \frac{2c_0}{D} & 0 & 0 \\ 0 & \frac{2c_0}{D} & 0 \\ 0 & 0 & \frac{2c_0}{D} \end{bmatrix} \quad (31)$$

The number of cycles to damage initiation is unchanged compared to the tensile test. The number of cycles to failure N_R^∇ taking into account the gradient effect is still given by eq. (16), in which the input is now the meso-stress $\bar{\sigma}$ ($\sigma_{eq}^{Max} = \sigma_{eq}^{min} = \sigma_{Max}$ and $Tr \underline{T} = 1 + 6c_0/D$ have to be considered).

Using the approximation (15) we finally end up to

$$\frac{N_R^\nabla - N_0}{N_R - N_0} = \left(1 - \frac{6c_0}{D} \frac{\sigma_f}{(1 + \frac{6c_0}{D})\sigma_{Max} - \sigma_f} \right) \left[\frac{\frac{2}{3}(1 + \nu)\sigma_f^2 + \frac{1}{3}(1 - 2\nu)\sigma_{Max}^2}{\frac{2}{3}(1 + \nu)\sigma_f^2 + \frac{1}{3}(1 - 2\nu)(1 + \frac{6c_0}{D})\sigma_{Max}^2} \right]^s \quad (32)$$

and then for the same maximum applied stress σ_{Max} in tension-compression and in bending to

$$\begin{aligned} N_R^\nabla &< N_R & \text{if } c_0 > 0 \\ N_R^\nabla &> N_R & \text{if } c_0 < 0 \end{aligned} \quad (33)$$

If the fatigue limits are defined for a given number of cycles for which no failure is observed, the case $c_0 < 0$ corresponds to a fatigue limit in bending larger than the fatigue limit in tension-compression as observed experimentally (Findley et al., 1956).

7 CONCLUSION

As a conclusion, let us recall that the two scale damage model described applies to complex fatigue applications. It needs an accurate FE elastic computation as the input of the model is the history of the stress tensor at the most loaded point. The model works as a post-processor, called DAMAGE2000, programmed in FORTRAN.

For practical applications, the closed form expressions of the numbers of cycles to failure for tension-compression, torsion, and for any proportional loading are given. The mean stress effect is exhibited in tension-compression and, as observed, the model gives no mean stress in shear.

Finally the model is completed by the proposition and the use of a new localization law. This allows to take into account the well known gradient effects in fatigue.

8 ACKNOWLEDGEMENT

The author would like to thank professor E. Aifantis for the discussions and the help provided in order to introduce the gradient effect within the model.

9 REFERENCES

- Aifantis, E. C. On the role of gradients in the localization of deformation and fracture, *Int. J. Engng Sci.*, **30**(10), pp. 1279-1299, 1992.
- Aifantis, E. C., Pattern formation in plasticity, *Int. J. Engng Sci.*, **33**(15), pp. 2161-2178, 1995.
- Crossland, B., Effect of large hydrostatic pressures on the torsional fatigue strength of an alloy steel. *Proc. Int. Conf. on Fatigue of Metals*, I. Mech. E., London, U.K., pp. 138-149, 1956.

Dang Van, K., Papadopoulos, I. V., Multiaxial fatigue failure criterion: a new approach. Proc. Third Int. Conf. on Fatigue and Fatigue Thresholds - Fatigue'87. Ed. R. O. Ritchie and E. A. Starke, Jr. EMAS Warley, U. K., pp. 997-1008, 1987.

Desmorat, R., Modélisation et estimation rapide de la plasticité et de l'endommagement, Thèse d'Habilitation à Diriger des Recherches, Université Paris 6, 2000.

Desmorat, R., Fast determination of localized plasticity and damage by energetic methods, Int. J. of Solids and Structures, submitted for publication.

Desmorat, R., Lemaitre, J., Two scale damage model for quasi-brittle and fatigue damage, Handbook of Materials Behavior Models, Ed. J. Lemaitre, Academic Press, Chapter Continuous Damage, pp. 539-549 (2001).

Eshelby, J. D., The determination of the elastic field of an ellipsoidal inclusion and related problems, Proc. Roy. Soc., London, A241, 376, 1957.

Findley, W. N., Coleman, J. J., Hanley, B. C., Theory for combined bending and torsion fatigue with data for SAE 4340 steel. Proc. Int. Conf. on Fatigue of Metals, I. Mech. E., London, U.K., pp. 150-157, 1956.

Kröner, E., On the Plastic deformation of polycrystals, Acta Metall., vol. 9, pp. 155-161, 1961.

Lemaitre, J., A course on damage mechanics, Springer Verlag, 1992.

Lemaitre, J., Desmorat, R., Sauzay, M., Anisotropic damage law of evolution, Eur. J. Mech. A/Solids, vol. 19, pp. 187-208, 2000.

Papadopoulos, I. V., Panoskaltsis, V. P., Invariant formulation of a gradient dependent multiaxial high cycle fatigue criterion, Engng Fract. Mech., vol. 55(4), pp. 513-528, 1996.

Sermage, J. P., Lemaitre, J., Desmorat, R., A two scale damage concept applied to fatigue, Int. J. Fract., 97, pp. 67-81, 1999.

Sines, G., Behavior of metals under complex static and alternating stresses. Metal Fatigue, ed. G. Sines and J. L. Waisman. McGraw Hill, New York, pp. 145-169, 1959.

GRADIENT ELASTIC BARS UNDER UNIAXIAL STATIC OR DYNAMIC LOAD

K. G. Tsepoura

Department of Mechanical and Aeronautical Engineering
University of Patras, GR-26500 Patras, Greece

S. Papargyri-Beskou

General Department, School of Technology
Aristotle University of Thessaloniki, Gr-54006 Thessaloniki, Greece

D. Polyzos

Department of Mechanical and Aeronautical Engineering
University of Patras, GR-26500 Patras, Greece

D. E. Beskos

Department of Civil Engineering
University of Patras, GR-26500 Patras, Greece

1. SUMMARY

The problem of a bar under a static or dynamic uniaxial tension is studied analytically on the basis of the simple linear theory of gradient elasticity due to Aifantis. The governing equations of equilibrium and motion are obtained by a combination of the basic equations of the problem, while all possible boundary conditions (classical and non-classical) are obtained with the aid of the method of weighted residuals for both static and dynamic cases. Various boundary value problems are solved analytically and the gradient elasticity effect on the solutions is assessed.

2. INTRODUCTION

The effect of microstructure on the macroscopic description of the mechanical behavior of a linear elastic material can be adequately taken into account with the aid of higher-order gradient theories (e. g., [1]-[5]). The simple gradient elasticity theory of Aifantis and co-workers (e. g., [2]-[5]) has been used to eliminate singularities or discontinuities of classical elasticity theory and to demonstrate its ability to capture size effects and wave dispersion in cases where this was not possible in the classical elasticity framework.

In this paper the problem of a bar under static or dynamic uniaxial tension is studied analytically on the basis of the simple linear theory of gradient elasticity due to Aifantis and co-workers ([2]-[5]). The dynamic case deals with forced longitudinal vibrations. The same

problem has been also discussed in Altan et al [5] without determination of all possible boundary conditions (classical and non-classical) and consideration of forced vibrations. Here all possible boundary conditions are determined with the aid of the method of weighted residuals for both the static and dynamic cases. Thus the present work can also be viewed as a generalization and extension of the work of Altan et al [5]. Two boundary value problems, one under static and one under dynamic conditions, are solved analytically and the gradient elasticity effect on the solution is assessed.

3. STATIC GOVERNING EQUATION AND BOUNDARY CONDITIONS

Consider a straight prismatic bar under a static uniaxial tensile stress $\sigma(x)$ resulting in a displacement $u(x)$ along its longitudinal axis x . The basic equations of this bar are the equation of equilibrium, the strain-displacement relation and the stress-strain equation of the gradient elasticity [4,5], which read in the absence of body forces

$$\frac{d\sigma}{dx}=0, \quad \varepsilon = \frac{du}{dx}, \quad \sigma = E \left(\varepsilon - g^2 \frac{d^2\varepsilon}{dx^2} \right) \quad (1)$$

where $\varepsilon = \varepsilon(x)$ is the strain, E the modulus of elasticity and g the gradient coefficient with units of length. Substitution of Eqs (1)₂ and (1)₃ into Eq.(1)₁ results in the static governing equation of the bar

$$u'' - g^2 u'''' = 0 \quad (2)$$

where primes indicate differentiation with respect to x . Eq. (2) has a solution of the form

$$u = c_1 e^{\frac{x}{g}} + c_2 e^{-\frac{x}{g}} + c_3 x + c_4 \quad (3)$$

where c_i ($i=1,2,3,4$) are constants of integration to be determined with the aid of the boundary conditions (classical and non-classical) pertaining to the particular boundary value problem. All possible boundary conditions can be determined with the aid of the method of weighted residuals, which here reads

$$\int_0^L (u'' - g^2 u''') w dx = 0 \quad (4)$$

where $w = w(x)$ is a weighting function and L is the length of the bar. Integrating Eq. (4) by parts once and twice for u'' and u''' , respectively, one has

$$\begin{aligned} \int_0^L u'' w dx &= [u' w]_0^L - \int_0^L u' w' dx \\ \int_0^L u''' w dx &= [u'' w - u'' w']_0^L + \int_0^L u'' w'' dx \end{aligned} \quad (5)$$

Assuming that $w = \delta u$, where δ indicates variation, one obtains from Eq. (4) and Eq. (5)

$$\begin{aligned} \int_0^L (u'' - g^2 u''') \delta u dx &= [u' \delta u]_0^L - g^2 [u'' \delta u - u'' \delta u']_0^L \\ &\quad - \int_0^L u' \delta u' dx - g^2 \int_0^L u'' \delta u'' dx = 0 \end{aligned} \quad (6)$$

or the variational statement

$$\delta \left[\frac{1}{2} \int_0^L \left[(u')^2 + g^2 (u'')^2 \right] dx \right] = - \int_0^L (u'' - g^2 u^{IV}) \delta u \, dx + \left[(u' - g^2 u'') \delta u \right]_0^L + g^2 [u'' \delta u']_0^L = 0 \quad (7)$$

Eq. (7), which essentially represents the variation of the strain energy of the bar, is augmented by the variation of the work done by external classical and double stresses [1], i. e.,

$$\delta V = [\sigma \delta u]_0^L + [R \delta u']_0^L \quad (8)$$

In view of Eqs. (7), (8) the boundary conditions satisfy the equations

$$\begin{aligned} [\sigma(L) - E[u'(L) - g^2 u''(L)]] \delta u(L) - [\sigma(0) - E[u'(0) - g^2 u''(0)]] \delta u(0) &= 0 \\ [R(L) - g^2 E u''(L)] \delta u'(L) - [R(0) - g^2 E u''(0)] \delta u'(0) &= 0 \end{aligned} \quad (9)$$

For example, if one assumes the two classical boundary conditions to be $u(0)$ and $u(L)$ prescribed and the corresponding non-classical ones to be $u'(0)$ and $u'(L)$ prescribed, then $\delta u(0) = \delta u(L) = 0$ and $\delta u'(0) = \delta u'(L) = 0$ and Eqs (8) are all satisfied.

4. DYNAMIC GOVERNING EQUATION AND BOUNDARY CONDITIONS

Consider a straight prismatic bar under a dynamic uniaxial tensile stress $\sigma(x, t)$ resulting in a displacement $u(x, t)$ along its longitudinal axis x . The basic equations of this bar in the absence of body forces are the equation of motion

$$\frac{d\sigma}{dx} = \rho \ddot{u} \quad (10)$$

and the strain-displacement and stress-strain equations given by (1)₂ and (1)₃, respectively, where overdots denote time differentiation and ρ is the mass density of the bar. Substitution of Eqs (1)₂ and (1)₃ into Eq.(10) results in the dynamic governing equation of the bar

$$E(u'' - g^2 u^{IV}) = \rho \ddot{u} \quad (11)$$

All possible boundary and initial conditions can be determined with the method of weighted residuals, which here reads

$$E \int_{t_0}^{t_1} \int_0^L (u'' - g^2 u^{IV}) w \, dx \, dt - \rho \int_{t_0}^{t_1} \int_0^L \ddot{u} w \, dx \, dt = 0 \quad (12)$$

where $w = w(x, t)$ is a weighting function and t_0 and t_1 are the initial and final time values. Integrating by parts with respect to time once and assuming that $w = \delta u$, one can rewrite the second integral of Eq. (12) in the form

$$\rho \int_{t_0}^{t_1} \int_0^L \ddot{u} \delta u \, dx \, dt = \int_0^L \rho [\dot{u} \delta u]_{t_0}^{t_1} \, dx - \delta \int_{t_0}^{t_1} \int_0^L \frac{1}{2} \rho (\dot{u})^2 \, dx \, dt \quad (13)$$

Using Eq. (7) of the static case, one can rewrite the first integral of Eq. (12) in the form

$$E \int_{t_0}^{t_1} \int_0^L (u'' - g^2 u^{IV}) \delta u dx dt = E \int_{t_0}^{t_1} [u' \delta u]_0^L dt - E g^2 \int_{t_0}^{t_1} [u'' \delta u - u'' \delta u']_0^L dt -$$

$$\delta \int_{t_0}^{t_1} \int_0^L \frac{E}{2} (u')^2 dx dt - \delta \int_{t_0}^{t_1} \int_0^L \frac{E g^2}{2} (u'')^2 dx dt$$
(14)

Eq. (12), on the basis of Eqs (13) and (14), results in the variational statement

$$\delta \left[\int_{t_0}^{t_1} \int_0^L E \left[\frac{1}{2} (u')^2 + \frac{g^2}{2} (u'')^2 \right] dx dt - \int_{t_0}^{t_1} \int_0^L \frac{1}{2} \rho (\dot{u})^2 dx dt \right] =$$

$$= - \int_{t_0}^{t_1} \int_0^L [E(u'' - g^2 u^{IV}) - \rho \ddot{u}] \delta u dx dt - \int_0^L \rho [\dot{u} \delta u]_{t_0}^{t_1} dx +$$

$$+ E \int_{t_0}^{t_1} [(u' - g^2 u'') \delta u]_0^L dt + E g^2 \int_{t_0}^{t_1} [u'' \delta u']_0^L dt = 0$$
(15)

Eq. (15), which is the variation of the strain and kinetic energies of the bar, is augmented by the variation of the work done by external stresses σ and double stresses R in the time interval $[t_0, t_1]$

$$\delta V = - \int_{t_0}^{t_1} [R - E g^2 u''] \delta u' \Big|_0^L dt$$
(16)

Thus, the initial as well as the boundary conditions satisfy the equations

$$\dot{u}(x, t_1) \delta u(x, t_1) - \dot{u}(x, t_0) \delta u(x, t_0) = 0$$
(17)

and

$$[\sigma(L, t) - E[u'(L, t) - g^2 u''(L, t)]] \delta u(L, t) - [\sigma(0, t) - E[u'(0, t) - g^2 u''(0, t)]] \delta u(0, t) = 0$$

$$[R(L, t) - g^2 E u''(L, t)] \delta u'(L, t) - [R(0, t) - g^2 E u''(0, t)] \delta u'(0, t) = 0$$
(18)

respectively. For example, if one assumes the boundary conditions to be $u(0, t)$ and $u(L, t)$ (classical) and $u'(0, t)$ and $u'(L, t)$ (non-classical) prescribed, then $\delta u(0, t) = \delta u(L, t) = \delta u'(0, t) = \delta u'(L, t) = 0$ and Eqs (18) are satisfied. On the other hand Eq. (17) is satisfied if one assumes the initial conditions, e. g., $u(x, t_0)$ and $u(x, t_1)$ prescribed implying that $\delta u(x, t_0) = \delta u(x, t_1) = 0$.

5. SOLUTION OF BOUNDARY VALUE PROBLEMS

This section deals with the solution of two boundary value problems, one static and one dynamic. Consider a bar built in at one end ($x = 0$) and subjected to a given static axial traction T at the other end ($x = L$). Thus, the classical boundary conditions are $u(0) = 0$ and $\sigma(L) = T$ implying $u(L)$ is prescribed. The non-classical boundary conditions are assumed to

be $R \equiv g^2 E u''(0) = 0$ and $u'(L) = \varepsilon_0$, with ε_0 being a constant. All these conditions satisfy Eqs (8) and serve to determine the constants $c_1 - c_4$ in Eq. (3), which now takes the form

$$u(\xi) = g \frac{\sinh\left(\frac{L}{g}\xi\right)}{\cosh\left(\frac{L}{g}\right)} \left(\varepsilon_0 - \frac{T}{E}\right) + \frac{T}{E} L\xi \quad (19)$$

where $\xi = x/L$. The axial strain then reads

$$\varepsilon(\xi) = \frac{\cosh\left(\frac{L}{g}\xi\right)}{\cosh\left(\frac{L}{g}\right)} \left(\varepsilon_0 - \frac{T}{E}\right) + \frac{T}{E} \quad (20)$$

The classical solution ($g = 0$) reads

$$u_0(\xi) = (TL/E)\xi, \quad \varepsilon_0(\xi) = T/E \quad (21)$$

Figure 1 (a, b) shows the variation of $\bar{u} = u/(TL/E)$ and $\bar{\varepsilon} = \varepsilon/(T/E)$ versus ξ for various values of L/g and $\varepsilon_0 E/T = 0.5$. It is observed that \bar{u} increases with ξ and L/g and that the gradient solution decreases for decreasing values of L/g or increasing values of g . The classical solution is an upper bound. It is also observed that $\bar{\varepsilon}$ decreases very fast for $0.5 \leq \xi \leq 1$ as L/g increases with the classical solution been a constant upper bound value in that range of ξ .

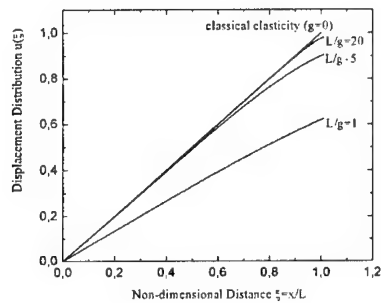


Figure 1a: Displacement Distribution

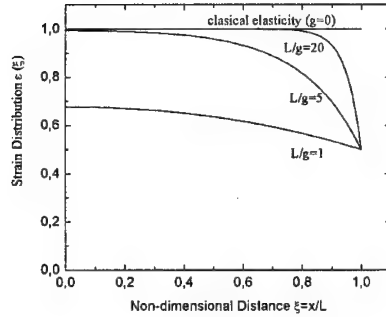


Figure 1b: Strain Distribution

Consider again the bar of the static case with the same boundary conditions but with T being a harmonic force of the form $T(t) = T_0 \sin \Omega t$, where Ω is the frequency of the harmonic excitation. In this case the problem becomes dynamic and Eq. (11) takes the form:

$$-g^2 \bar{u}^{IV} + \bar{u}'' + k^2 \bar{u} = 0 \quad (22)$$

where overbars denote amplitudes (e. g., $u = \bar{u} \sin \Omega t$) and

$$k^2 = \Omega^2 / c^2, \quad c^2 = E / \rho \quad (23)$$

The solution of (22) has the form

$$u(x, t) = (A_1 e^{\lambda_1 x} + A_2 e^{\lambda_2 x} + A_3 e^{\lambda_3 x} + A_4 e^{\lambda_4 x}) \sin \Omega t \quad (24)$$

where $A_1 - A_4$ are constants of integration to be determined from the boundary conditions and $\lambda_1 - \lambda_4$ are given by

$$\lambda_{1, \dots, 4} = \pm \left(\frac{1}{g\sqrt{2}} \right) \sqrt{1 \pm \sqrt{1 - 4g^2 k^2}} \quad (25)$$

The boundary conditions read

$$\begin{aligned} u(0, t) = 0, \quad u'(L, t) = \varepsilon_0, \quad u''(0, t) = 0 \\ \sigma(L, t) = T(t) \text{ or } E[u'(L, t) - g^2 u'''(L, t)] = T(t) \end{aligned} \quad (26)$$

Use of these boundary conditions in Eq. (24) serves to determine the constants of integration $A_1 - A_4$. The response $u(L, t)$ is obtained for various values of the gradient parameter g and shown in Figure 3.

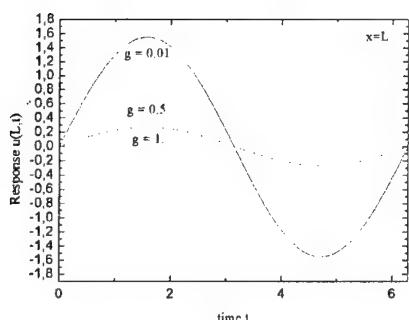


Figure 3: Dynamic response $u(L, t)$ versus time of a uniaxial bar subjected to a harmonic excitation, for various values of the gradient coefficient g

6. CONCLUSIONS

On the basis of the preceding developments one can draw the following conclusions:

- 1) Using the simple theory of gradient elasticity due to Aifantis, the governing equations of equilibrium and motion and the corresponding classical and non-classical boundary conditions of an axial bar have been determined.
- 2) The boundary conditions have been determined from a variational statement constructed with the aid of the method of weighted residuals without knowledge of the strain energy, which may not always be easy to establish, especially in gradient elasticity. This strain energy is obtained here as a byproduct of the present methodology.
- 3) Two characteristic boundary value problems (one static and one dynamic) have been solved and the gradient effect on the response has been found to be important in some cases.

Acknowledgements: The authors are grateful to Professor E. C. Aifantis for introducing them into the subject of gradient elasticity theory.

7. REFERENCES

- [1] Mindlin, R. D., Micro-structure in linear elasticity, *Archive for Rational Mechanics and Analysis* 16, 51-78 (1964).
- [2] Aifantis, E. C., On the role of gradients in the localization of deformation and fracture, *Int. J. Engng. Sci.* 30, 1279-1299 (1992).
- [3] Altan, B. S. and Aifantis, E. C., On the structure of mode-III crack tip in gradient elasticity, *Scripta Metall. Mater.* 26, 319-324 (1992).
- [4] Ru, C. Q. and Aifantis, E. C., A simple approach to solve boundary-value problems in gradient elasticity, *Acta Mechanica* 101, 56-68 (1993).
- [5] Altan, B. S., Evensen, H. and Aifantis, E. C., Longitudinal vibrations of a beam : a gradient elasticity approach, *Mech. Res. Comm.* 23, 35-40 (1996).
- [6] Vardoulakis, I. and Sulem, J., *Bifurcation Analysis in Geomechanics*, Blackie/Chapman and Hall, London (1995).
- [7] Graff, K. F., *Wave Motion in Elastic Solids*, Ohio State University Press, Columbus, 1975.

EVOLUTION OF PERSISTENT SLIP BANDS IN FATIGUED METALS

E. Douka, B. Polyzos and A. Trochidis

Department of Physics and Applied Mathematics
Aristotle University of Thessaloniki, GR-54006 Thessaloniki, Greece

1. SUMMARY

The mechanisms governing the evolution of persistent slip bands (PSB) in metals under fatigue are investigated. The metal is considered as an active medium whose properties depend on two dislocations species with different spatial dispersion namely, the mobile dislocations (inhibitor) and the immobile dislocations (activator). This allows analytical expressions for the characteristics of the dislocation pattern far from the bifurcation point. It is shown that the initial dislocation pattern is metastable and evolves towards a stable one, whose wavelength is selected between two extreme values through two mechanisms. The two mechanisms are investigated analytically and numerically. The obtained results are shown to be consistent with available experimental observations.

2. INTRODUCTION

Cyclic deformation of many materials results in the formation of localized bands of intense deformation with well-defined periodicity and amplitude known as persistent slip bands (PSBs). The fact that this regular structure appears above a certain value of the driving force (stress) leads to the treatment of PSBs formation as a bifurcation phenomenon and consequently to a modeling by nonlinear equations of reaction-diffusion type. In that vein a specific kinematic model for cyclic deformation, in analogy to the Brusselator model of chemical reaction was proposed by Walgreaf and Aifantis [1] and further elaborated by Glazov et al. [3].

In spite the substantial progress which has been achieved with respect to the modeling of PSBs formation and evolution, limited analytical insight on wavelength estimates and evolution mechanisms has been obtained and only in the regime close to the instability threshold. For situations far from the bifurcation point numerical simulations have been employed to get a better understanding of the kinetics of PSBs formation and evolution [2,3]. In the present work PSBs formation and evolution are considered within the framework of active media [4]. In this approach self-organization is regarded as a result of spontaneous formation and evolution of localized dissipative structures in the form of solitary static regions. This approach allows analytical estimates on the wavelength of pattern and the dislocations densities far from the instability region. The main result of this work is that the initially formed dislocation pattern close to the instability threshold is metastable and evolves

towards a stable one with a wavelength between two extreme values imposed by stability criteria.

3. DESCRIPTION OF THE MODEL

The Walgraef-Aifantis model for the PSBs occurring during cyclic deformation of single crystals distinguishes between mobile and immobile dislocations of densities ρ_m and ρ_i , which are assumed to evolve according to the following reaction-diffusion equations [1],

$$\frac{\partial \rho_i}{\partial t} = \varepsilon^2 \frac{\partial^2 \rho_i}{\partial x^2} - q(\rho_i, \rho_m, \beta) \quad (1)$$

$$\frac{\partial \rho_m}{\partial t} = \frac{\partial^2 \rho_m}{\partial x^2} - Q(\rho_i, \rho_m, \beta) \quad (2)$$

where x is measured in units of $\sqrt{D_m}$, $\varepsilon = \sqrt{D_i/D_m}$, with D_i, D_m denoting the diffusion-like

coefficients for the immobile and mobile dislocations respectively. The “sources” q and Q , are non-linear functions modeling the mechanisms of creation and annihilation of the two species and their coupling. The description of these mechanisms is analyzed in [2] and the proposed forms for q and Q read

$$q = \alpha - \alpha \rho_i + \beta \rho_i - \gamma \rho_m \rho_i^2 \quad (3)$$

$$Q = \gamma \rho_m \rho_i^2 - \beta \rho_i \quad (4)$$

where β , an increasing function of the stress amplitude, plays the role of the bifurcation parameter and the remaining parameters are constants.

The properties of many physical, chemical and biological systems are described by a system of nonlinear reaction-diffusion equations such as Eqs.(1) and (2). Equations of this type provide the basis for studying self-organization processes and autowaves in active media [5]. The presence of the parameter ε , which relates the characteristic length scales of the dislocation species, allows the analysis of pattern formation at arbitrary levels of non-equilibrium. A crystal under fatigue can be considered as an active medium of the activator-inhibitor type. The dislocation movement due to the applied stress tends to spread out the dislocation distributions, whereas the interaction of the dislocations tends to cluster them. The difference in the diffusion coefficients implies that the inhibitor ρ_m and the activator ρ_i exhibit different space dispersion. Since $D_m \gg D_i$ the mobile dislocations are incapable of damping locally the growth of fluctuations of immobile dislocations density $\delta \rho_i$ within a small region because of diffusion spreading. Above a certain threshold β_c the development of instability produces a stable pattern, the persistent slip band, with well-defined periodicity and amplitude.

4. CHARACTERISTICS OF THE BANDS

4.1 Dislocation densities

In the theory of active systems [5] an important characteristic determining the form of the structure, which may arise, is the null-cline of Eq.(1) given by the relation $q(\rho_i, \rho_m, \beta) = 0$, for $\beta = \text{const}$. This curve determines the dependence $\rho_m(\rho_i)$ in the region of

the band where $\rho_i(x)$ varies smoothly and is called local coupling (LC). It can be seen that the homogeneous state (ρ_{ih}, ρ_{mh}) , corresponding to the intersection point of the nullclines of Eqs. (1) and (2), depends on the bifurcation parameter β . The system of Eqs. (1) and (2) has been analyzed in Ref.[4]. The analysis was based on the small parameter ε , instead of using the supercriticality $(\beta - \beta_c)/\beta_c$. This allows the application of the concept of smooth and sharp distributions of the two dislocation densities. The smooth distributions describe the smooth variation of mobile and immobile dislocation densities within the band and between them. From the LC-curve the maximum dislocation density of immobile dislocations for the smooth distributions is calculated as $\rho_{io} = 2\alpha/(\alpha + \beta)$ and the corresponding value of the mobile dislocation density as $\rho_{mo} = (\alpha + \beta)^2/4\alpha\gamma$. The sharp distributions describe the wall of the bands where the immobile dislocation density changes rapidly from ρ_{il} to ρ_{imax} . The sharp distributions are realized in a region s , much smaller than the characteristic length of the variation of the mobile dislocation density, which is associated with the coefficient D_m . Thus, in this region of the rapidly varying distribution $\rho_i(x)$, the mobile dislocation density remains actually constant. Under this condition, Eqs. (1) and (2) determine the sharp distribution $\rho_i(x)$, which varies from $\rho_{il} = \rho_{io}/2$ to $\rho_{imax} = \rho_{il} + \beta/2\sqrt{D_i}$ (see Ref.[4]).

4.2 Periodicity of the bands

To investigate the periodicity of the PSB pattern the smooth distributions of the mobile and immobile dislocation densities are considered. As already mentioned, the length of these distributions is associated with the diffusion coefficient D_m of mobile dislocations. Thus, the smooth distributions correspond to the solution of Eqs. (1) and (2), with $\varepsilon = 0$. It follows from Eq.(2) that, for $\varepsilon = 0$, the distribution $\rho_m(x)$ is given by

$$\frac{d^2 \rho_m}{dx^2} = Q(\rho_i(\rho_m), \rho_m, \beta). \quad (5)$$

The wavelength λ of the pattern can be calculated by integrating Eq.(5) under the conditions $d\rho_m(\lambda/2)/dx = d\rho_m(0)/dx = 0$. The maximum wavelength λ_{max} is determined by the condition of instability called local breakdown. A local breakdown occurs because, as the band evolves with increasing excitation level, the value of the mobile dislocation density between the bands increases and reaches the maximum allowable value ρ_{mo} . A further increase of β results in a sharp increase of the mobile dislocation density and consequently a new band arises between the existing bands. Thus, the wavelength of the pattern becomes twice smaller.

Therefore, the maximum wavelength of a stable pattern is the value of λ , for which ρ_m between the bands reaches ρ_{mo} , given by

$$\lambda_{max} = \frac{\sqrt{2}}{2\alpha} \sqrt{\frac{D_m}{\gamma}} \frac{(\alpha + \beta)^{3/2}}{(\beta - \alpha)^{1/2}}. \quad (6)$$

From the stability analysis of the PSBs follows (see Ref.[4]) that at a certain value of the parameter β , the structure in the form of N bands of wavelength λ becomes unstable with respect to the growth of the fluctuations $\delta\rho_i$ of the immobile dislocation density of doubled period. This growth leads to an increase of the amplitude of one band at the expense of the amplitude of the neighboring band. As a result the number of bands may decrease by a factor of two. This process, known as pumping, leads to the limiting of the possible wavelength of

the stable PSB pattern. This process has been observed in numerical simulation performed by Glazov et al [3] and recently in Ref.[6] where PSBs formation has been treated as a strain localization phenomenon, a cyclic analogue of the shear banding.

The minimum allowable wavelength λ_{\min} has been calculated in Ref.[4] from the condition, which determines the threshold of the growth of the critical fluctuations $\delta\rho_i$. The result is

$$\lambda_{\min} = \left(\frac{15\pi^2}{2} \right)^{1/3} \frac{(\alpha + \beta)^{5/6} \sqrt{D_m}}{(\alpha\gamma)^{1/3} \beta^{2/3}} \varepsilon^{1/3}. \quad (7)$$

5. NUMERICAL SIMULATIONS

To investigate the mechanisms described in the previous section, the system of Eqs. (1) and (2) was treated numerically. To enable the comparison with existing numerical results [2,3] the integration was performed using the set of parameters proposed by Schiller and Walgraef [2]: $\alpha = 6\text{cy}^{-1}$; $\beta = 30\text{cy}^{-1}$; $\gamma = 200\text{cy}^{-1}$; $D_i = 3 \times 10^{-15} \text{m}^2\text{cy}^{-1}$; $D_m = 4 \times 10^{-11} \text{m}^2\text{cy}^{-1}$, with time measured in cycles. The initial density of immobile dislocations ρ_{ih} has been chosen to be 10^{14}m^{-2} . The simulation run was started with the initial densities of mobile and immobile dislocations on the steady branch. The value of the bifurcation parameter β was taken equal to $3.5\beta_c$ i.e. three times higher than the critical value necessary for the onset of spatial patterning in the system. In our simulations the initial state was disturbed using different conditions. After establishing the initial condition, the numerical integrator was turn on and the system started evolving in time. The value of the integration step was taken equal to 0.001 to avoid numerical instabilities.

The results of the numerical simulations are given in Figs.(1) to (3). The sequences display how a disturbance of an initially unstable homogeneous state develops into a periodic pattern. The concentration of mobile dislocations is so small that it is almost invisible in the pictures.

Fig.(1) shows how the PSB structure can appear starting from a single disturbance of the gaussian type at a certain position. It can be seen that the initial disturbance evolves and a single band is formed which exhibits an oscillatory behavior at its "tail". This can be interpreted as a reaction to the local decrease of the immobile dislocation density. The two nearest maxima in the distribution, which are located at a distance λ from the center of the band, act as nuclei for the formation of the new bands. As a result of this breakdown, new bands arise and the entire system is filled up with interacting bands.

Fig.(2) shows an analogous situation where the initial perturbation has the form of two small disturbances of the gaussian type located far apart each other. It can be seen that local breakdown and consequently formation of new bands occurs within bands separated by a distance greater than λ_{\max} .

Fig.(3) presents a different case. Here, the initial homogeneous state was disturbed by normally distributed random fluctuations with dispersion equal to 1% of the dislocation densities. It can be seen that initial small fluctuations become amplified. Some fluctuations grow rapidly and others are suppressed. The pumping process, i.e. the increase of the amplitude of some bands at the expense of the amplitude of the neighboring bands is obvious during the stages of the process. A pattern with wavelengths less than λ_{\min} is unstable and progressively due to pumping a stable configuration of a modulated ladder structure of the PBS that persists in time is formed.

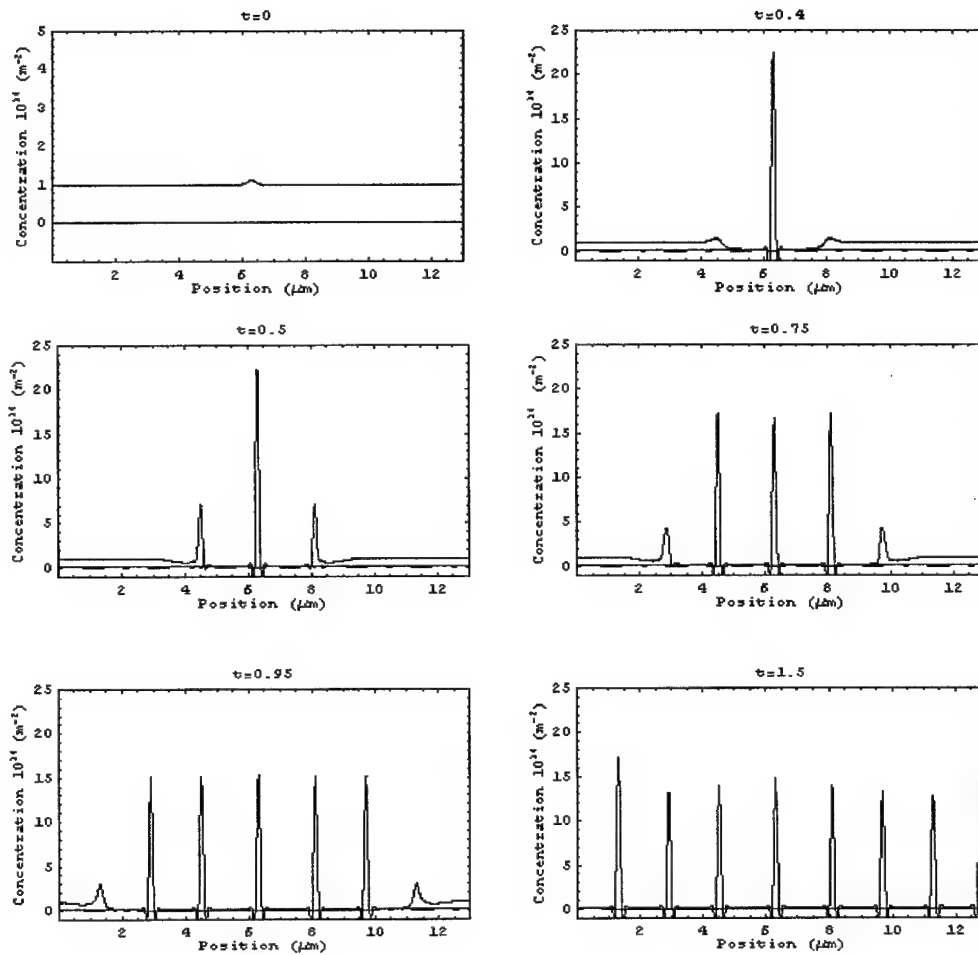


Figure1: Temporal evolution of the system in the case of a single perturbation of gaussian type

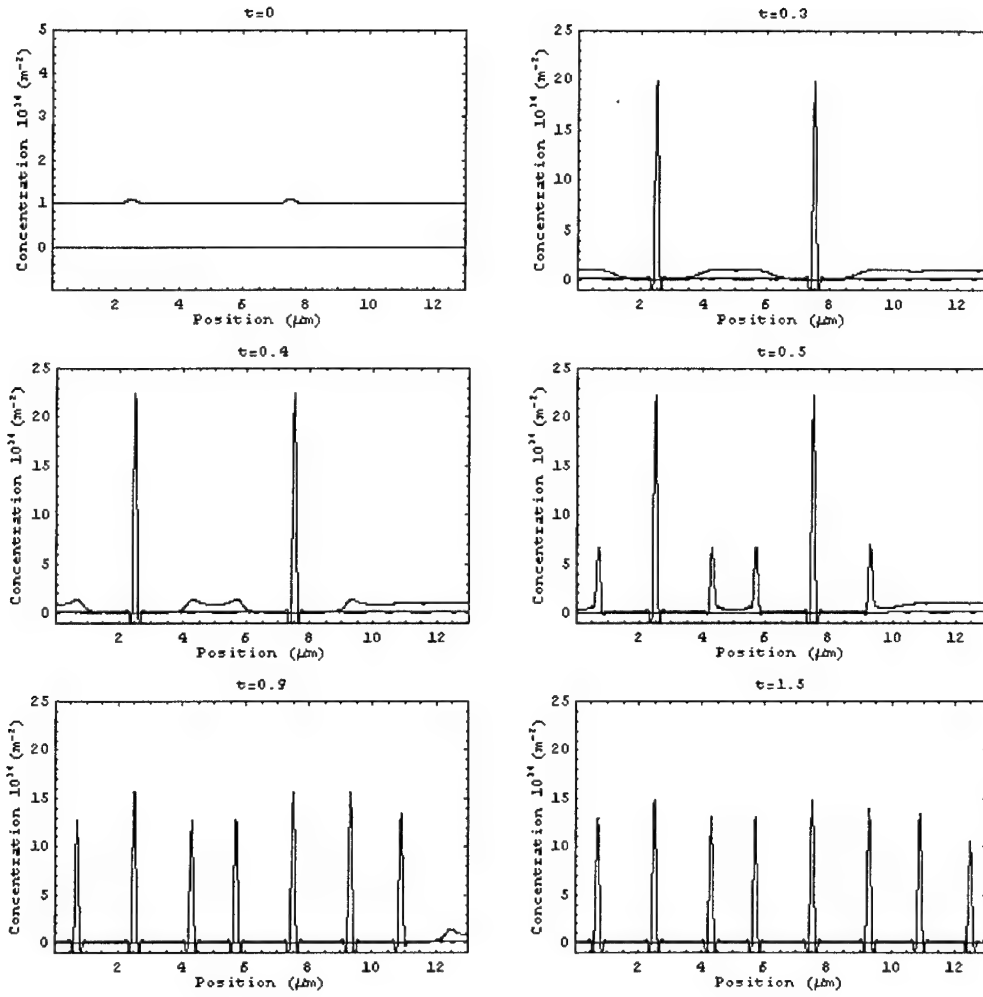


Figure 2: Temporal evolution of the system in the case of double perturbation of gaussian type

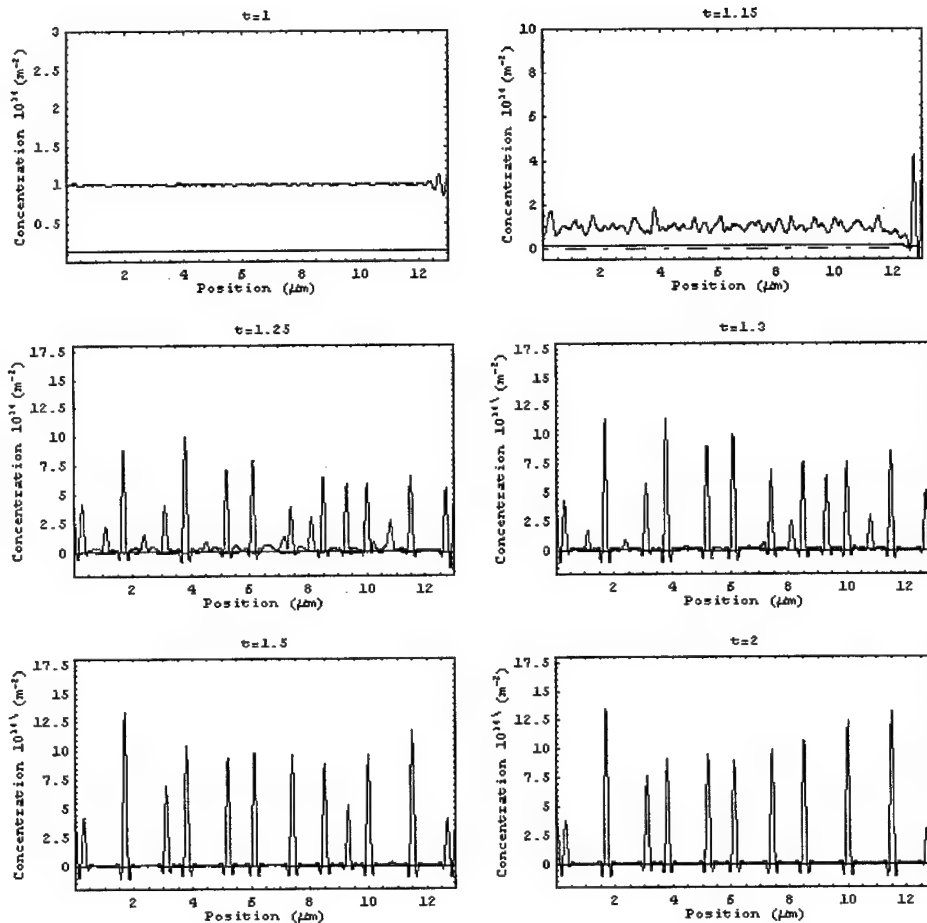


Figure 3: Temporal evolution of the system in the case of double perturbation of quasi type

6. REFERENCES

- [1] D. Walgraef and E.C. Aifantis, *Dislocation patterning in fatigued metals*, I, II, Int. J. Engng. Sci. 23, 1351-58, 24, 1789-93 (1985).
- [2] C. Shiller and D. Walgraef, *Numerical simulation of persistent slip band formation*, Acta Metall. 36, 563-574 (1988).
- [3] M. Glazov, L.M. Lanes and C. Laird, *Self-organized dislocations-structures (SODS) in fatigued metals*, Phys. Status Solidi (b), 149, 295 (1995).
- [4] A. Trochidis, E. Douka, and B. Polyzos, *Formation and evolution of persistent slip bands in metals*, J. Mech. Phys. Solids 48, 1761-1775 (2000).
- [5] B.S. Kerner and V.V. Osipov, in: *Autosolitons, A New Approach to Problem of Self-Organization and Turbulence*, Kluwer Academic Publishers, The Netherlands (1994).
- [6] M. Zaiser, M. Avlonitis and E.C. Aifantis, in: *Proc. NATO-PROBAMAT 21th Century Workshop*, Ed. G. Frantzisconis, Kluwer Academic Publishers, Amsterdam (1998).

CRACK IDENTIFICATION IN BEAM STRUCTURES

Y. Bamnios

T.E.I. of Thessaloniki, Faculty of Technological Applications, Dept. of Electronics,
P.O. Box 14561, GR-541 01 Thessaloniki, Greece

E. Douka

Aristotle Univ. of Thessaloniki, School of Technology
Mechanics Division
GR-54006Thessaloniki, Greece

A. Trochidis

Aristotle Univ. of Thessaloniki, School of Technology
Physics Division
GR-54006Thessaloniki, Greece

1. ABSTRACT

The influence of a transverse surface crack on the mechanical impedance of a cracked cantilever beam is studied. Analytical and experimental investigations provide a link between the changes in mechanical impedance to the location of the crack. The results are used to propose a new method of non-destructive testing for beam structures.

2. INTRODUCTION

The most common structural defect is the existence of a crack. If a structure is defective, there is a reduction on the stiffness of the structure in the region of the defect. A reduction in stiffness implies a reduction in natural frequencies of vibration and changes in modal shapes. Hence it is possible to use natural frequency measurements to detect cracks. The natural frequency method has been extensively studied and applied by Dimarogonas [1], Paipetis and Dimarogonas [2], Chondros and Dimarogonas [3], Adams and Cawley [4], Gudmunson [5], Anifantis et al [6]. In searching of an additional defect information carrier for crack appearance, the use of the mechanical impedance was introduced by Bamnios and Trochidis [7] in case of a cracked cantilever beam. Prabhakar et al [8] further investigated the changes in mechanical impedance in case of cracked rotor – bearing systems and they suggested that it could be used for crack detection.

In the present work the influence of a transverse surface crack on the mechanical impedance of a cantilever beam is investigated both analytically and experimentally. It is shown that the

mechanical impedance changes substantially due to the presence of the crack in case of flexural vibrations. The changes follow definite trends depending upon the location of the crack and consequently can provide the information required for accurate crack localization.

3. ANALYSIS

The physical system under consideration, shown in Fig. 1, is a beam of uniform rectangular cross-section with a crack located at a position x_c . For general loading, a local flexibility matrix relates displacements and forces. In our analysis, since only bending vibrations are considered, the rotational crack compliance is assumed to be dominant in the local flexibility matrix [3].



Figure 1: Model of a cracked cantilever beam

The bending spring constant K_T in the vicinity of the cracked section when a transverse crack of uniform depth a exists, is given by [2]

$$K_T = \frac{1}{c}, \quad c = \left(5.346 \frac{w}{EI} \right) J\left(\frac{a}{w}\right) \quad (1)$$

where c is the compliance, E is the modulus of elasticity of the beam material, I is the moment of inertia of the beam cross-section and the dimensionless local compliance function $J\left(\frac{a}{w}\right)$ has the form [2]

$$J\left(\frac{a}{w}\right) = 1.8624\left(\frac{a}{w}\right)^2 - 3.95\left(\frac{a}{w}\right)^3 + 16.37\left(\frac{a}{w}\right)^4 - 37.226\left(\frac{a}{w}\right)^5 + 76.81\left(\frac{a}{w}\right)^6 \\ - 126.9\left(\frac{a}{w}\right)^7 + 172\left(\frac{a}{w}\right)^8 - 43.97\left(\frac{a}{w}\right)^9 + 66.56\left(\frac{a}{w}\right)^{10} \quad (2)$$

Due to localized crack effect, the cracked beam can be simulated as two uniform beams joint together by a torsional spring at the crack location (Fig. 1).

A driving force $F = F_0 e^{j\omega t}$ is considered acting along the beam. Thus, the location of the driving force and the location of the crack divide the beam in three parts. Depending on the location of the driving force, one has to solve two problems with different boundary conditions to calculate the displacements $n(x)$ of the beam.

(a) Driving force between free end and crack.

The geometry of this case is shown in Fig. 2.

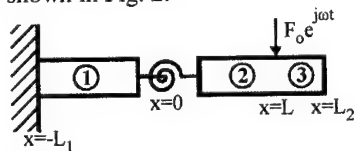


Figure 2: Cracked cantilever beam with driving force between free end and crack

The displacement on each part of the beam is

$$\begin{aligned}
 \text{part 1 : } n_1(x) &= c_1 \cosh K_B x + c_2 \sinh K_B x + c_3 \cos K_B x + c_4 \sin K_B x \\
 \text{part 2 : } n_2(x) &= c_5 \cosh K_B x + c_6 \sinh K_B x + c_7 \cos K_B x + c_8 \sin K_B x \\
 \text{part 3 : } n_3(x) &= c_9 \cosh K_B x + c_{10} \sinh K_B x + c_{11} \cos K_B x + c_{12} \sin K_B x
 \end{aligned} \tag{3}$$

The boundary conditions corresponding to the problem shown in Fig. 2 are

$$\begin{aligned}
 \text{at } x = -L_1 : n_1(-L_1) &= 0, n_1'(-L_1) = 0 \\
 \text{at } x = L_2 : M_3(L_2) &= 0, F_3(L_2) = 0 \\
 \text{at } x = 0 : n_1(0) &= n_2(0), M_1(0) = M_2(0), F_1(0) = F_2(0), \\
 & -EI \frac{\partial^2}{\partial x^2} n_1(0) = K_T \left[\frac{\partial}{\partial x} n_1(0) - \frac{\partial}{\partial x} n_2(0) \right] \\
 \text{at } x = L : n_2(L) &= n_3(L), n_2'(L) = n_3'(L), M_2(L) = M_3(L), F_2(L) - F_3(L) = F_o,
 \end{aligned} \tag{4}$$

where n' denotes derivative with respect to x .

(b) Driving force between crack and clamped end.

The geometry of this case is shown in Fig. 3.

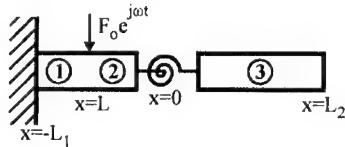


Figure 3: Cracked cantilever beam with driving force between crack and clamped end

Here, only the boundary conditions are different, i.e.

$$\begin{aligned}
 \text{at } x = -L_1 : n_1(-L_1) &= 0, n_1'(-L_1) = 0 \\
 \text{at } x = L_2 : M_3(L_2) &= 0, F_3(L_2) = 0 \\
 \text{at } x = 0 : n_2(0) &= n_3(0), M_2(0) = M_3(0), F_2(0) = F_3(0), \\
 & -EI \frac{\partial^2}{\partial x^2} n_2(0) = K_T \left[\frac{\partial}{\partial x} n_2(0) - \frac{\partial}{\partial x} n_3(0) \right] \\
 \text{at } x = L : n_1(L) &= n_2(L), n_1'(L) = n_2'(L), M_1(L) = M_2(L), F_1(L) - F_2(L) = F_o.
 \end{aligned} \tag{5}$$

The resulting characteristic equations, for the above mentioned two cases, are rather involved but can be solved numerically and both the eigenfrequencies and the mechanical impedances of the beam at different positions can be obtained. The mechanical impedance of the beam at an

arbitrary location x can be derived according to the relation $Z(x) = \frac{F_0}{j2\pi f n(x)}$, where $n(x)$ is the corresponding displacement and f is the frequency.

4. EFFECT OF MEASURING POINT

Using the analytical results obtained in the previous section, the mechanical mobility of a cracked cantilever beam was calculated. Instead of the impedance, the mobility was calculated for convenience, since mobility can be easier measured. In order to investigate the influence of the measuring point on the mobility, the location of the crack and its depth were kept constant and the driving force was systematically shifted along the beam. The calculations were made for a 35cm long plexiglas beam of rectangular cross-section $2 \times 2 \text{ cm}^2$. The crack was located 20cm from the free end and its depth was varied.

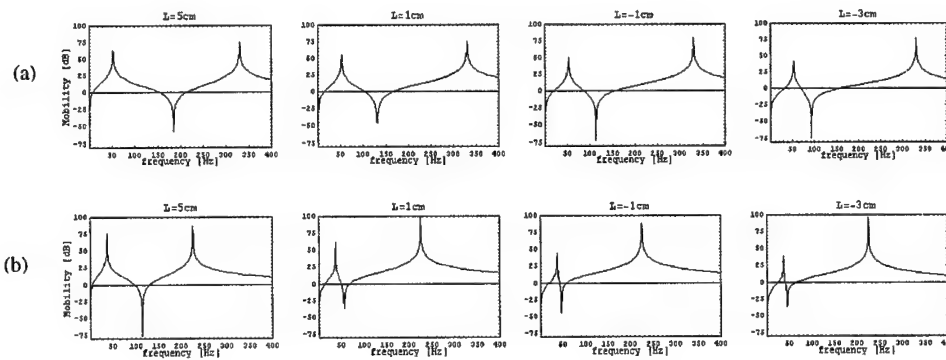


Figure 4: Predicted mechanical mobility at different positions along a 35cm long plexiglas beam of rectangular cross-section $2 \times 2 \text{ cm}^2$ (a) uncracked, (b) cracked (crack depth: 80%, crack location: 20cm from free end)

Figure 4 shows the predicted mechanical mobility at different positions along the beam for a crack depth of 80%. The expected reduction in natural frequencies of vibration compared to the uncracked beam is evident. The main result, however, is that the first antiresonance moves towards the first resonance as the driving point approaches the crack. In the vicinity of the crack tends to coincide with the first resonance. After crossing the crack, the position of the antiresonance remains unchanged. On the contrary, in case of an uncracked beam, the first antiresonance moves smoothly towards the first resonance.

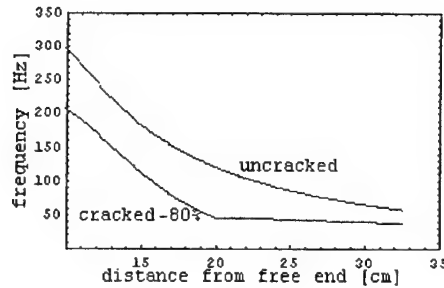


Figure 5: Predicted changes in the first antiresonance of a cracked beam versus location (crack depth: 80%, crack location: 20cm from free end)

Figure 5 shows the change in the first antiresonance as a function of the location along the beam. It can be seen that the influence of a crack on the mechanical impedance of the beam strongly depends on the crack's location. In the vicinity of the crack there is a jump in the slope of the curve depending on crack's depth.

5. EXPERIMENTAL INVESTIGATION

In order to validate the approximate model used in our analysis, a series of measurements were undertaken on plexiglas beams. The beams used in the experiments had square cross-section $2 \times 2 \text{ cm}^2$ and were cut from bars of commercial plexiglas. The crack was modeled by sawing cuts with a width of 0.3mm. Clamping of the beams was secured through the use of two heavy steel jaws. The cantilever beam was forced into oscillations by a 15mm diameter voice coil weighting 5gr. attached to the beam. The coil was placed in the field of a permanent magnet and was excited by a waveform oscillator (B&K 2010). The driving force was kept constant and the velocity at different locations along the beam was measured. The signals were transferred to an analyzer to give plots of the mobility versus frequency. The whole experimental set-up allowed the reproducibility of the results.

Five beams with the same geometry and material, cracked at different positions from the free end were tested. The mechanical mobility was measured in steps of 10mm. Using the mobility plots, the position of the first antiresonance at each location was estimated.

A typical plot of the antiresonance position as a function of the measuring position is shown in Fig. 6. This figure shows that in case of the cracked beam the change in the first antiresonance is not smooth. It exhibits a jump in the slope of the curve in the vicinity of the crack. The magnitude of the jump depends on the crack depth. The agreement between the results of predictions and measurements is very good. Moreover, the consistency of the experimental results in all cases tested was adequate.

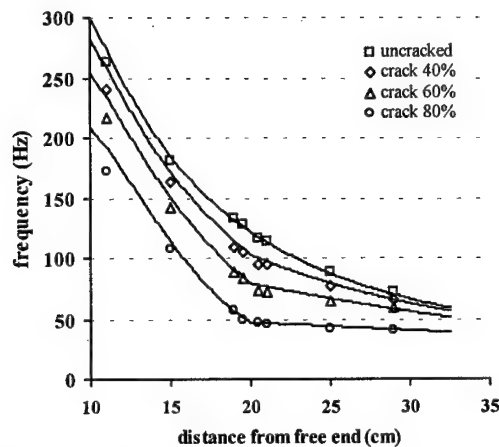


Figure 6: Change of the first antiresonance of a cracked beam versus measuring point along the beam for different crack depths. Comparison between prediction and measurements (crack location: 20cm from free end)

6. CONCLUSIONS

The effect of a transverse surface crack on the mechanical impedance of a cantilever beam was investigated both analytically and experimentally. It was shown that, far from the expected changes in natural frequencies, the mechanical impedance changes substantially. The changes depend on the location and the size of the crack. Thus, the mechanical impedance can be used as an additional defect information carrier, which complementary with natural frequencies changes can be used for crack identification.

Based on impedance measurements an efficient prediction scheme for crack location can be proposed. Starting from one end and moving towards the other the impedance will be measured and the shift of the first antiresonance will be estimated. In the vicinity of the crack the antiresonance coincides with the first resonance. After crossing the crack location, the antiresonance remains fairly constant. Thus, the crack exists in the neighborhood of the location where there is a jump in the slope of the curve of the antiresonance shift versus position.

The method can be used to locate the crack roughly and then other methods can be employed to determine the crack characteristics more precisely.

The method lacks accuracy for small cracks $\frac{a}{w} < 0.20$. This confines the range of application of the method to moderate cracks only. In most practical cases, however, a 20% crack is not usually an indication of immediate failure. The results of this work can be easily extended to include more complex structures and boundary conditions.

7. REFERENCES

- [1] Dimarogonas, A., *Vibration Engineering*, West Publishers, St. Paul, Minesota (1976).
- [2] Paipetis, S. A., and Dimarogonas, A. D., *Analytical Methods in Rotor Dynamics*, Elsevier Applied Science, London (1986).
- [3] Chondros, T. G. and Dimarogonas, A. D., *Identification of cracks in welded joints of complex structures*, Journal of Sound and Vibration, 69(4), 531-538 (1980).
- [4] Adams, R. D., and Cawley, P., *The location of defects in structures from measurements of natural frequencies*, Journal of Strain Analysis, 14, 49-57 (1979).
- [5] Gudmundson, P., *Eigenfrequency changes of structures due to cracks, notches or other geometrical changes*, Journal of Mechanics and Physics of Solids, 30 (5), 339-353 (1982).
- [6] Anifantis, N., Rizos, P., and Dimarogonas, A., *Identification of cracks by vibration analysis*, American Society of Mechanical Engineers, Design Division Publication, DE 7, 189-197.
- [7] Bamnios, G., and Trochidis, A., *Mechanical impedance of a cracked cantilever beam*, Journal of Acoustical Society of America 97, 3625-3635 (1995).
- [8] Prabhakar, S., Sekhar, A. S., and Mohanty, A. R., 2001, *Detection and monitoring of cracks using mechanical impedance of rotor-bearing system*, Journal of Acoustical Society of America (to appear).

FRACTALS AND FRACTIONAL CALCULUS IN SOLID MECHANICS

A. Carpinteri, B. Chiaia and P. Cornetti

Department of Structural Engineering
Politecnico di Torino, I-10129 Torino, Italy

1. SUMMARY

In this paper, the framework for the mechanics of solids, deformable over fractal subsets, is outlined. Anomalous mechanical quantities with fractal dimensions are introduced, i.e., the fractal stress $[\sigma^*]$, the fractal strain $[\epsilon^*]$ and the fractal work of deformation W^* . By means of the local fractional operators, the static and kinematic equations are obtained, and the Principle of Virtual Work for fractal media is demonstrated. Afterwards, from the definition of the fractal elastic potential ϕ^* , the linear elastic constitutive relation is derived. The direct formulation of the elastic problem is obtained in terms of the fractional Lamé operators and of the equivalence equations at the boundary. The variational form of the elastic problem is also obtained, through minimization of the total potential energy. Finally, discretization of the fractal medium is proposed, in the spirit of the Ritz-Galerkin approach, and a finite element formulation is obtained by means of devil's staircase interpolating splines.

2. LOCAL FRACTIONAL OPERATORS AND THE EQUATIONS OF STATICS AND KINEMATICS

Analysis of the response of a deformable body to a system of applied forces requires the definition of its constitutive law. The compatibility and equilibrium equations of continuum mechanics, which are intimately linked by the Principle of Virtual Work, need to be completed by the description of the specific material behaviour. In the presence of heterogeneous media, the classical constitutive laws (e.g. elasticity, plasticity or damage laws) need to be integrated by an appropriate modelization of the microstructure, which can considerably alter the basic formulations. This is the case, for instance, for micropolar elasticity models, higher-order gradient theories and for the large number of micromechanical models which developed in the last few years [1].

A particular class of solid materials is represented by those which are *deformable over a fractal subset* [2]. It is worth to notice that we are considering a generic body whose stress flux and deformation patterns have fractal characteristics, whereas the material itself does not need to have a fractal microstructure. This is the case of natural rocks and cementitious composites, which usually develop strain localization in some bands, mostly concentrated at the weak aggregate/matrix interfaces.

The singular stress flux through fractal media can be modelled by means of lacunar fractal sets of dimension Δ_σ , with $\Delta_\sigma = 2 - d_\sigma \leq 2$. An original definition of the fractal stress σ^*

acting upon lacunar domains was put forward by Carpinteri [3] by applying the renormalization group procedure to the nominal stress tensor $[\sigma]$. The fractal stress σ^* , whose dimensions are $[F][L]^{-(2-d_\sigma)}$, is a scale-invariant quantity. For simplicity, a uniaxial tensile field is considered in fig. 1, where an effective fractal stress is found by means of the renormalization group.

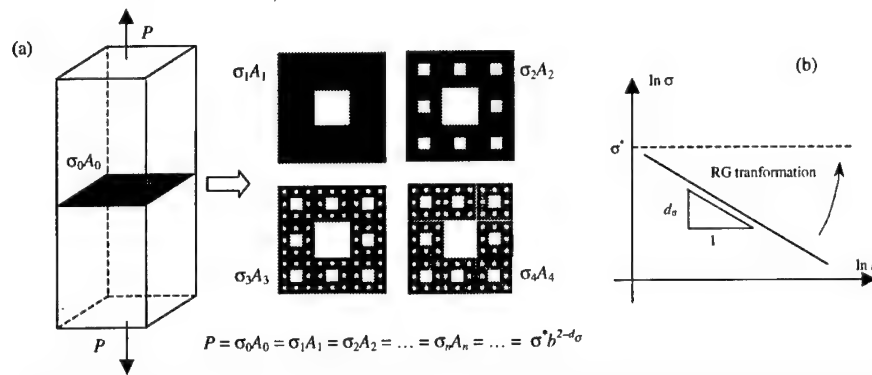


Figure 1. Renormalization of the stress over a Sierpinski carpet (a) and scaling of the nominal stress (b).

For the local definition of σ^* , exactly as in the case of the classical Cauchy stress, the limit:

$$\lim_{\Delta A^* \rightarrow 0} \left(\frac{\Delta P}{\Delta A^*} \right) \quad (1)$$

is supposed to exist and to attain finite values at any singular point of the support. This is mathematically possible for lacunar sets like that in fig. 1 which, although not compact, are dense in the surrounding of any singular point.

The kinematical conjugate of the fractal stress is the fractal strain ϵ^* [2, 4]. The basic assumption is that displacement discontinuities can be localized on an infinite number of cross-sections, spreading throughout the body. Experimental investigations have confirmed the fractal character of deformation, for instance in metals and in highly stressed rock masses [5, 6]. Considering the simplest uniaxial model, a slender bar subjected to tension, it can be argued that the horizontal projection of the cross-sections where deformation localizes is a lacunar fractal set, with dimension between zero and one. If the Cantor set ($\Delta_\epsilon = 0.631$) is assumed as the archetype of damage distribution, we may speak of the *fractal Cantor bar* (fig. 2a). The dilation strain tends to concentrate into singular stretched regions, while the rest of the body is practically undeformed. The displacement function can be represented by a *devil's staircase* graph, that is, by a singular function which is constant everywhere except at the points corresponding to a lacunar fractal set of zero Lebesgue measure (fig. 2b).

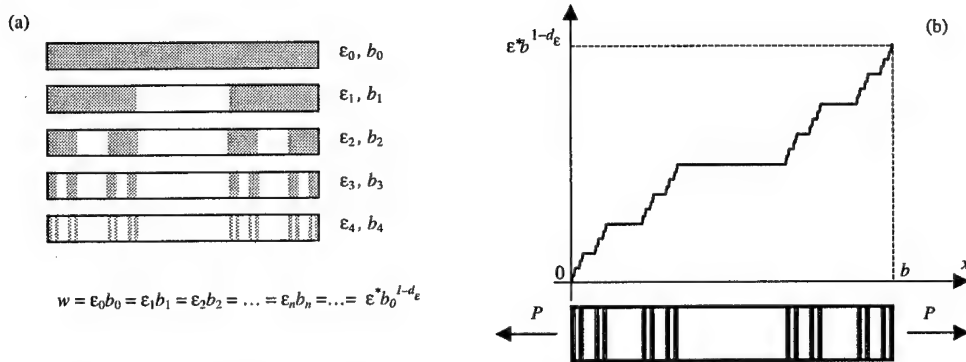


Figure 2. Renormalization of the strain over a Cantor bar (a) and singular displacement function (b).

Let $\Delta_\epsilon = 1 - d_\epsilon$ be the fractal dimension of the lacunar projection of the deformed sections. Since $\Delta_\epsilon \leq 1$, the fractional decrement d_ϵ is always between 0.0 (corresponding to strain smeared along the bar) and 1.0 (corresponding to the maximum localization of strain, i.e., to localized fracture surfaces). By applying the renormalization group procedure (see fig. 2a), the micro-scale description of displacement provides the product of an *effective* fractal strain ϵ^* times the fractal measure $b_0^{(1-d_\epsilon)}$ of the support. The fractal strain ϵ^* is the scale-independent parameter describing the kinematics of the fractal bar. Its physical dimension $[L]^{d_\epsilon}$ is intermediate between that of a pure strain $[L]^0$ and that of a displacement $[L]$, and synthesizes the conceptual transition between classical continuum mechanics ($d_\epsilon = 0$) and fracture mechanics ($d_\epsilon = 1$). Correspondingly, the kinematical controlling parameter changes, from the nominal strain ϵ , to the crack opening displacement w . By varying the value of d_ϵ (e.g. for different loading levels), the evolution of strain localization can be captured. The two limit situations are shown in fig. 3, the devil's staircase being an intermediate situation with $d_\epsilon = 0.369$. While the first case represents the classical homogeneous elastic strain field, the latter diagram shows a single displacement discontinuity, e.g., the formation of a sharp fracture.

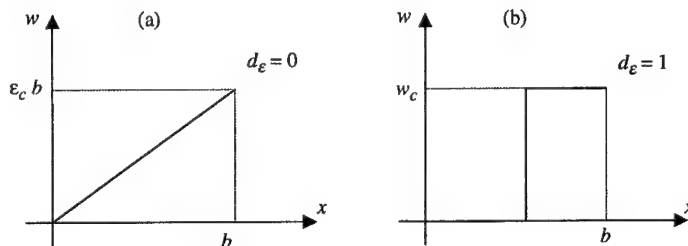


Figure 3. Homogeneous strain (a) and extremely localized deformation (b) over the bar (critical point).

During a generic loading process, the mechanical work W^* can be stored in the body as elastic strain energy (conservative process) or dissipated on the infinite lacunar cross-sections where strain is localized (dissipative process). In any case, the fractal domain W^* , with dimension $\Delta_w = 3 - d_w$, where the mechanical work is produced, must be equal to the cartesian product of the lacunar cross-section with dimension $2 - d_\sigma$, times the cantorian projection set with dimension $1 - d_\epsilon$. Since the dimension of the cartesian product of two

fractal sets is equal to the sum of their dimensions, one obtains the fundamental relation among the exponents as:

$$d_{\omega} = d_{\sigma} + d_{\epsilon} \quad (2)$$

In order to find mathematical tools suitable to work with functions and variables defined upon fractal domains, researchers started to examine the possibility of applying fractional operators, i.e. derivatives and integrals of noninteger order. Classical fractional calculus is based on nonlocal operators. On the other hand, Kolwankar & Gangal [7] have recently introduced a new operator called *local fractional integral or fractal integral*. The fractal integral is a mathematical tool suitable for the computation of fractal measures. In fact, it yields finite values if and only if the order of integration is equal to the dimension of the fractal support of the function $f(x)$. Otherwise, its value is zero or infinite, thus showing a behaviour analogous to that of the Hausdorff measure of a fractal set. Kolwankar & Gangal [7] introduced also the *local fractional derivative (LFD)* of order α ($0 < \alpha < 1$) of $f(x)$:

$$\left[D^{\alpha} f(x) \right]_{x=y} = D^{\alpha} f(y) = \lim_{x \rightarrow y} \frac{d^{\alpha}[f(x) - f(y)]}{[d(x - y)]^{\alpha}} \quad (3)$$

where $d^{\alpha}[f(x)]/[d(x-a)]^{\alpha}$ denotes the (classical) Riemann-Liouville fractional derivative of order α of the function $f(x)$ choosing a as lower limit [8]. Differently from the classical fractional derivative, the LFD is a function only of the $f(x)$ values in the neighborhood of the point y where it is calculated. The classical fractional derivative of a singular function exists as long as its order is lower than the Hölder exponent characterizing the singularities. Instead, in the singular points, the LFD is generally zero or infinite. It assumes a finite value if and only if the order α of derivation is exactly equal to the Hölder exponent of the graph. For instance, in the case of the devil's staircase graph (fig. 2b) the LFD of order $\alpha = \ln 2 / \ln 3$ (i.e. equal to the dimension of the underlying middle-third Cantor set) is zero everywhere except in the singular points where it is finite.

By means of the LFD, the fractal differential equations of kinematics and statics have been obtained [2]. The displacement field maintains the dimension of length. The noninteger dimensions of the fractal strain are: $[L]^{d_{\epsilon}}$. Therefore, it can be obtained by fractional differentiation of the displacement vector $\{\eta\}$, according to the definition of LFD outlined above. The fractional differential operator $[\partial^{\alpha}]$ can thus be introduced, where the order of differentiation is $\alpha = 1 - d_{\epsilon}$. Thereby, the kinematic equations for the fractal medium can be written, in the usual vector notation, as:

$$\{\epsilon^*\} = [\partial^{\alpha}] \{\eta\} \quad (4)$$

The above relation represents also a local definition of the fractal strain, as compared to the mean-field one provided by renormalization group (see fig. 2). Classical nondimensional strain is obtained when $\alpha = 1$ ($d_{\epsilon} = 0$). Instead, when $\alpha = 0$, strain is no longer homogeneously diffused and reduces to localized displacement discontinuities. The intermediate situations are described by generic values of α .

The static equations link the fractal stress vector $\{\sigma^*\}$ to the body forces vector $\{F^*\}$, which assumes noninteger dimensions according to the fractal dimension of the deformable subset

Ω^* , $[F][L]^{-(3-d_\omega)}$. On the other hand, the dimensions of the fractal stress are $[F][L]^{-(2-d_\sigma)}$. Therefore, the fractal equilibrium equations can be written, in the vector notation, as:

$$[\partial^\alpha]^T \{\sigma^*\} = -\{F^*\} \quad (5)$$

where the static fractional differential operator $[\partial^\alpha]^T$ is the transposed of the kinematic fractional differential operator $[\partial^\alpha]$. It is worth to observe that the fractional order of differentiation of the static operator in the fractal medium is $\alpha = 1 - d_\epsilon$, the same as that of the kinematic operator. This remarkable result is due to the fundamental relation among the exponents (eq. (2)), and represents the Duality Principle for Fractal Media [2]. Finally, equivalence at the boundary of the body requires that the stress vector coincides with the applied fractal boundary tractions $\{p^*\}$ (with physical dimensions $[F][L]^{-(2-d_\sigma)}$):

$$[\mathcal{N}]^T \{\sigma^*\} = \{p^*\} \quad (6)$$

In the case of fractal bodies, $[\mathcal{N}]^T$ can be defined, at any dense point of the boundary, as the cosine matrix of the outward normal to the boundary of the initiator of the fractal body.

3. PRINCIPLE OF VIRTUAL WORK AND LINEAR ELASTIC CONSTITUTIVE LAW FOR FRACTAL MEDIA

The Principle of Virtual Work is the fundamental identity of solid mechanics. It affirms the equality between the virtual external work (done by body forces and boundary tractions) and the virtual internal work (done by internal stresses). As is well known, the proof of the principle requires the application of the Gauss-Green Theorem. Some attempts of extending the Gauss-Green Theorem to fractal domains have been discussed in [2]. Considering two arbitrary functions $f(x, y, z)$ and $g(x, y, z)$, defined upon a fractal domain Ω^* , with the same Hölder exponent α , the general formula of *local fractional integration by parts* was obtained by the authors [2] as:

$$\int_{\Gamma^*} \Gamma^{(\beta-\alpha)} [gf] = \int_{\Omega^*} \Gamma^\beta [g D^\alpha f] + \int_{\Omega^*} \Gamma^\beta [D^\alpha g f] \quad (7)$$

where Γ^* is the boundary of the domain Ω^* . This result extends the Gauss-Green Theorem to 3D fractal domains. Based on eq. (7), the Principle of Virtual Work for fractal media was demonstrated [2]. It reads:

$$\int_{\Omega^* (3-d_\omega)} \{F_A^*\}^T \{\eta_B\} d\Omega^* + \int_{\Gamma^* (2-d_\sigma)} \{p_A^*\}^T \{\eta_B\} d\Gamma^* = \int_{\Omega^* (3-d_\omega)} \{\sigma_A^*\}^T \{\epsilon_B^*\} d\Omega^* \quad (8)$$

Both sides of eq. (8) possess the dimensions of work ($[F][L]$), since the operators are *fractal integrals* defined upon fractal domains. The external work may be done by fractal body forces $\{F^*\}$ and/or by fractal tractions $\{p^*\}$ acting upon the boundary Γ^* of the body. The internal work of deformation is defined as: $dW^* = \{\sigma^*\}^T \{d\epsilon^*\}$, with dimensions $[F][L]^{-(2-d_\omega)}$. If the (initial) loading process is conservative (no dissipation occurs in the material), and stress is a univocal function of strain, a *fractal elastic potential* ϕ^* (function of the fractal strain $\{\epsilon^*\}$)

can be introduced as an exact differential: $d\phi^* = \{\sigma^*\}^T \{d\epsilon^*\}$. The components of the fractal stress vector $\{\sigma^*\}$ can therefore be obtained by derivation: $\sigma_i^* = \partial\phi^*/\partial\epsilon_i^*$. Note that these are canonical first-order partial derivatives in the space of the fractal strains $\{\epsilon^*\}$. Therefore, the same arguments of classical mathematical elasticity can be followed. Performing the Taylor expansion around the undeformed state, and neglecting higher order derivatives, the following quadratic form can be easily obtained:

$$\phi^* = \frac{1}{2} \{\epsilon^*\} [H^*] \{\epsilon^*\} \quad (9)$$

where $[H^*]$ is the Hessian matrix of the fractal elastic potential. Dimensional arguments show that the anomalous dimensions of $[H^*]$ are: $[F][L]^{-(2+d_\epsilon-d_\sigma)}$. Thus, $[H^*]$ depends on both the dimensions of stress and strain. Thereby, depending on the difference $(d_\sigma - d_\epsilon)$, the nominal elastic constants (e.g., the shear and the Young's moduli) can be subjected to positive or negative size-effects. Each term in $[H^*]$ is obtained as the second-order partial derivative of the elastic potential by the corresponding fractal strain. From eq. (9), the *linear elastic constitutive law for fractal media* is provided as:

$$\{\sigma^*\} = [H^*] \{\epsilon^*\} \quad (10)$$

4. DIRECT LAMÉ' FORMULATION OF THE FRACTAL ELASTIC PROBLEM

If the fractal constitutive law (10) is inserted into the fractal static equations (5), and using the fractal cinematic equations (4), the so-called Lamé equation is provided in the operatorial form:

$$[L^*] \{\eta\} = -\{F^*\}, \quad \forall P \in \Omega^* \quad (11)$$

where the fractional Lamé operator $[L^*]_{3 \times 3}$ is defined as: $[L^*] = [\partial^\alpha]^T [H^*] [\partial^\alpha]$. The conditions of equivalence on the boundary of the medium (eq. (6)) where the tractions are imposed (Γ_1^*) can be expressed, as a function of the displacement vector, in the following manner:

$$[L_0^*] \{\eta\} = \{p^*\}, \quad \forall P \in \Gamma_1^* \quad (12)$$

where the fractional operator $[L_0^*]_{3 \times 3}$ is thus defined as: $[L_0^*] = [\mathcal{N}]^T [H^*] [\partial^\alpha]$. $[\mathcal{N}]^T$ is the cosine matrix of the outward normal to the boundary, exactly corresponding to the fractional derivatives in $[\partial^\alpha]^T$, in the spirit of the fractal Gauss-Green Theorem. Finally, the boundary condition on the part of the boundary (Γ_2^*) with imposed displacement is the following :

$$\{\eta\} = \{\eta_0\}, \quad \forall P \in \Gamma_2^* \quad (13)$$

5. VARIATIONAL FORMULATION AND DISCRETIZATION OF THE FRACTAL ELASTIC PROBLEM BY MEANS OF DEVIL'S STAIRCASE SPLINES

The total potential energy of a fractally deformable elastic body can be defined as the difference between the strain energy stored in the body minus the external work of the body forces $\{F^*\}$ and of the boundary tractions $\{p^*\}$:

$$W(\eta) = \int_{\Omega^*(3-d_\omega)} \phi^* d\Omega^* - \left(\int_{\Omega^*(3-d_\omega)} \{F^*\}^T \{\eta\} d\Omega^* + \int_{\Gamma^*(2-d_\sigma)} \{p^*\}^T \{\eta\} d\Gamma^* \right) \quad (14)$$

This functional, defined in the space of the admissible displacement and strain fields, attains its minimum value in correspondence of the (unique) solution of the fractal elastic problem [9]. This can be demonstrated by following the same arguments established for the canonical quantities, i.e., by considering an arbitrary kinematically admissible field $\{\tilde{\eta}\}$, $\{\tilde{\epsilon}^*\}$, obtained by adding, to the fields $\{\eta\}$, $\{\epsilon^*\}$, which are solution of the elastic problem (eqs (11-13)), a generic increment $\{\Delta\eta\}$, $\{\Delta\epsilon^*\}$ and evaluating the functional $W(\tilde{\eta})$. If the Principle of Virtual Work (eq. (8)) is applied to the statically admissible stress-force field (defined by eq. (5)) working by the incremental kinematic fields ($\{\Delta\eta\}$, $\{\Delta\epsilon^*\}$), using the Betti's Reciprocity Theorem one easily obtains:

$$W(\tilde{\eta}) - W(\eta) = \int_{\Omega^*(3-d_\omega)} \phi^* (\Delta\epsilon^*) d\Omega^* \quad (15)$$

Recalling that the fractal elastic potential is a quadratic positive form, the above relation implies that the total potential energy related to the displacement field $\{\eta\}$, solution of the elastic problem, is the minimum with respect to any other admissible field $\{\eta + \Delta\eta\}$:

$$W(\eta) = \text{minimum} \quad (16)$$

The above variational formulation is thus equivalent to the direct formulation of the elastic problem (eqs (11-13)) and represents the starting point of the Finite Element formulation. In the classical Ritz-Galerkin approach, the stationarity of the energy functional $W(\eta)$ is sought within a subspace of finite dimensions subtended by a series of linearly independent assigned functions. The problem is thus discretized, since the unknown displacement field $\{\eta\}$ is expressed as the sum of assigned independent functions $\{\eta_i\}$, $i = 1, 2, \dots, (g \times n)$:

$$\{\eta\} = \sum_{i=1}^{(g \times n)} \beta_i \{\eta_i\} \quad (17)$$

where n represents the number of nodes where the displacement has to be determined, each with g degrees of freedom. Note, incidentally, that the physical dimension of the functions $\{\eta_i\}$ is that of length. By inserting the above relation in the definition of the total potential energy, the following functional is obtained:

$$W(\beta) = \frac{1}{2} \{\beta\}^T [L] \{\beta\} - \{\beta\}^T [F] \quad (18)$$

where $\{\beta\}$ is the vector of the $(gx n)$ unknown coefficients of the linear combination (17). The $(gx n) \times (gx n)$ elements of the matrix $[L]$ are given by the following fractal integrals:

$$L_{ij} = - \int_{\Omega^* (3-d_\omega)} \{\eta_i\}^T [L^*] \{\eta_j\} d\Omega^* + \int_{\Gamma^* (2-d_\sigma)} \{\eta_i\}^T [L_0^*] \{\eta_j\} d\Gamma^* \quad (19)$$

Note that the matrix $[L]$ is symmetrical due to Betti's Theorem. The $(gx n)$ elements of the vector $[F]$ are given by the following fractal integrals:

$$F_{ij} = - \int_{\Omega^* (3-d_\omega)} \{\eta_i\}^T \{F^*\} d\Omega^* + \int_{\Gamma^* (2-d_\sigma)} \{\eta_i\}^T \{p^*\} d\Gamma^* \quad (20)$$

Minimization of the above energy functional requires the canonical first-order derivatives of eq. (18), with respect to each coefficient β_i , to be equal to zero. The result is the classical system of $(gx n)$ linear algebraic equations in terms of $(gx n)$ unknown coefficients β_i :

$$[L]\{\beta\} = [F] \quad (21)$$

We can choose as independent functions $\{\eta_i\}$ in the linear combination (eq. (17)) a family of functions that, henceforth, we will call *fractal splines*. These are defined only over subsets (finite elements) of the whole fractal domain Ω^* , and their value is equal to one in correspondence of the pertinent node i and to zero in all the other nodes within their subdomain of definition (see fig. 4). Since their linear combination gives the singular displacement field, the physical dimension of the fractal splines must be that of a length and, at the same time, they must be Cantor staircase kind functions, i.e. continuous functions everywhere constant except on a subset with null Lebesgue measure. For our purposes, the most important aspect related to the fractal splines is their ability to model the singular displacement field and to provide, by local fractional derivation, the associated strain field. Since the fractal splines in the 1D case for finite elements with two nodes (fig. 4) can be built connecting two devil's staircase, it is worthwhile considering more in detail this function, archetype of the Cantor staircase kind functions, already presented in section 2 and plotted in

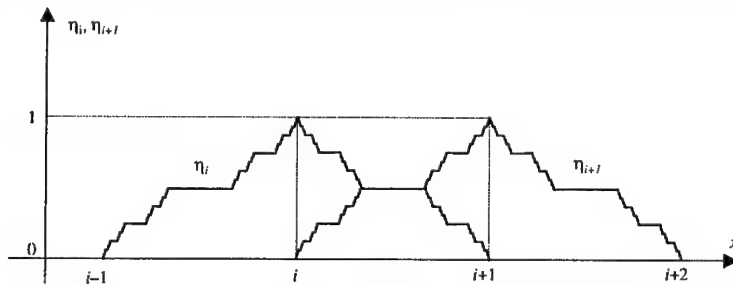


Figure 4. Fractal splines in the 1D case for two nodes finite elements.

fig. 2. The devil's staircase function $S(x)$ is a self-affine, monotone, nondifferentiable functions. The singularities of this function can be characterized by the Hölder exponent α

lower than 1. It can be easily demonstrated that the Hölder exponent of the function $S(x)$, in all the points belonging to the Cantor set, is exactly equal to the dimension $\Delta = \ln 2 / \ln 3$ of the fractal support where it grows. In other words, the devil's staircase is a function which is almost everywhere constant, except on a subset of points with dimension Δ , where it is singular of order $\alpha = \Delta$.

The classical fractional derivative (the lower extreme of integration being the origin) of the devil's staircase was studied by Schellnhuber & Seyler [10]. For these calculations, the devil's staircase can be conveniently approximated with a polygonal family of functions $S_n(x)$:

$$S_n(x) = \sum_{i=0}^{2^{n+1}-2} (-1)^i \left(\frac{3}{2}\right)^n H_{x_n(i)}(x) [x - x_n(i)] \quad (22)$$

where $H_{x_0}(x)$ is the unit step function with discontinuity in x_0 and $x_n(i)$ are the x -coordinates of the extremes of the segments of the n -th step in the iterative procedure leading to the construction of the Cantor set. It can be proved that the sequence $S_n(x)$ converges uniformly to $S(x)$ for n tending to infinity. The Riemann-Liouville fractional derivatives of the n -th approximation $S_n(x)$ can be calculated to give:

$$\frac{d^\alpha}{[dx]^\alpha} [S_n(x)] = \sum_{i=0}^{2^{n+1}-2} (-1)^i \left(\frac{3}{2}\right)^n \frac{H_{x_n(i)}(x)}{\Gamma(2-\alpha)} [x - x_n(i)]^{1-\alpha} \quad (23)$$

Schellnhuber & Seyler [10] demonstrated the uniform convergence of the series of fractional derivatives (23) for $\alpha < \ln 2 / \ln 3$, thus obtaining the fractional derivative of order α of $S(x)$. For $\alpha \geq \ln 2 / \ln 3$, the sequence (23) diverges. Thereby, the devil's staircase, although nondifferentiable in the classical sense, admits continuous fractional derivatives, provided that its order α is lower than Δ .

For our model, we are mainly interested in the local fractional derivative of the devil's staircase. Based on the classical fractional derivative (23), we can compute the local fractional derivative (LFD), for instance in the origin ([4], [8]):

$$D^\alpha S(0) = \lim_{n \rightarrow \infty} \left\{ \frac{d^\alpha}{[dx]^\alpha} [S_n(x)] \right\}_{x=1/3^n} = \frac{1}{\Gamma(2-\alpha)} \lim_{n \rightarrow \infty} \left(\frac{3^\alpha}{2} \right)^n \quad (24)$$

Therefore, the LFD (27) in the origin is zero if $\alpha < \Delta$, does not exist if $\alpha > \Delta$, and attains a finite value if and only if $\alpha = \Delta$. The same happens in all the singular points of the devil's staircase graph, while, where the graph is flat, the LFD is zero. In other words, we have shown that the devil's staircase can be characterized by the LFD of order equal to the dimension of the fractal support where it grows.

What have been done for the function $S(x)$ can be generalized to the fractal splines (fig. 4) and their linear combination eq. (17). Therefore, these functions can be seen as a suitable family of functions to interpolate the singular displacement field which arises in bodies deformable on fractal subsets. Moreover, choosing as order of fractional derivation the fractal

dimension of the subset where the body can get deformed, the LFD of the linear combination (17) can characterize the discontinuous strain fields of a fractally deformable medium.

Acknowledgements: Supports by the Italian Ministry of University and Scientific Research and by the EC-TMR Contract N° ERBFMRXCT 960062, are gratefully acknowledged.

6. REFERENCES

- [1] Aifantis, E.C., On the role of gradients in the localisation of deformation and fracture, *International Journal of Engineering Science* 30, 1279-1299 (1992).
- [2] Carpinteri, A., Chiaia, B. and Cornetti, P., Static-kinematic duality and the principle of virtual work in the mechanics of fractal media, *Computer Methods in Applied Mechanics and Engineering*, in print (2001).
- [3] Carpinteri, A., Fractal nature of materials microstructure and size effects on apparent mechanical properties, *Mechanics of Materials* 18, 89-101 (1994).
- [4] Cornetti, P., *Fractals and Fractional Calculus in the Mechanics of Damaged Solids*, Ph.D. Thesis (in Italian). Politecnico di Torino, Torino (1999).
- [5] Kleiser, T., and Bocek, M., The fractal nature of slip in crystals. *Zeitschrift für Metallkunde* 77, 582-587 (1986).
- [6] Poliakov, A.B., Herrmann, H.J., Podladchikov, Y.Y. and Roux, S., Fractal plastic shear bands, *Fractals* 2, 567-581 (1995).
- [7] Kolwankar, K.M., and Gangal, A.D., Local fractional calculus: a calculus for fractal space-time. *Proceedings of "Fractals: theory and Applications in Engineering"* Delft: Springer, 171-181, (1999).
- [8] Oldham, K.B. and Spanier, J., *The Fractional Calculus*. New York: Academic Press, (1974).
- [9] Carpinteri, A., Chiaia, B. and Cornetti, P. The fractal elastic problem: basic theory and finite element formulation, *Computer Methods in Applied Mechanics and Engineering*, submitted (2001).
- [10] Schellnhuber, H.J. and Seyler, A., Fractional differentiation on devil's staircase, *Physica A* 191, 491-500 (1992).

CHARACTERIZATION OF MATERIALS WITH PORES AND INCLUSIONS AT DIVERSE SCALES

G. Frantziskonis

Department of Civil Engineering and Engineering Mechanics
University of Arizona, Tucson, AZ 85721, USA

1. SUMMARY

The recently developed wavelet-based multiscale process is applied to characterize materials with microstructures in the form of pores and inclusions distributed over a wide range of spatial scales. The variance of the strain field for an approximated one-dimensional deformation problem is examined in detail. It is shown that with respect to crack initiation, there is a strong interplay between the distribution of pores and inclusions. Application to a cast aluminum alloy, where pores are, in general, about two orders of magnitude larger than the silicon particles (inclusions), explain recent experimental reports on crack initiation where the interplay of pores, inclusions, and boundaries is observed, yet not explained on a fundamental basis. The present work extends recent efforts on porous materials [1] and includes the interaction of pores at certain scales with inclusions at other scales presented extensively in [2].

2. INTRODUCTION

In materials processing and design, it is critical to understand the effect of microstructures, which appear at a hierarchy of spatial scales. The paper recognizes the fact that microstructures of (most) engineering materials appear at a wide hierarchy of spatial scales. For several materials, important microstructures are in the form of inclusions as well as pores appearing at a hierarchy of scales. Of particular interest to this contribution are cast aluminum alloys, which have great potential as replacements for ferrous castings and fabrications in the automobile and rail industries where energy efficiency and low cost component production are crucial; also, the application of aluminum castings in aerospace structures can result in significant cost reductions in aircraft manufacturing.

We examine two particular microstructures, i.e., pores and inclusions, known to be related to mechanical properties in aluminum castings such as A356, and attempt to characterize them using a wavelet-based multiscale approach. We concentrate on crack initiation under imposed external mechanical load, and for illustrating the wavelet-based multiscale process we study a 1-D problem, which, of course, involves certain simplifying assumptions. The 1-D results set

the foundation for 2-D as well as 3-D studies, which are presently undergoing.

3. PROPERTIES OF A MEDIUM WITH PORES AND INCLUSIONS

Consider a material containing both pores and inclusions embedded in a matrix. Each phase, i.e., matrix, inclusions and pores, are assumed homogeneous. Let F be a specific local property, e.g., Young's modulus, yield stress, failure stress, etc. Within the material, $F = F(x)$ is a function of the position vector x (x is a scalar in 1-D) and has a value equal to m, i, p , denoting the value of F for spatial positions within the matrix, inclusions, pores, respectively. For random spatial distribution of the pores and of the inclusions, F is a random function of space. Relevant works [13,14] for porous media setup an elegant framework for describing the geometry. For convenience, we shall refer to the former as medium-P and the latter as medium-I. Each component of the composite medium is built by placing a set of given arbitrary pores, inclusions, respectively, at random in space, while keeping the porosity, inclusion density, constant. Let φ_p denote the porosity and φ_i the volume density of inclusions. The following relations hold, where subscript P, I refer to medium-P, medium-I, respectively. Equations (1-4) can be directly derived from works on porous media [13,14] some of which can also be found in [1,2]. For the expected values, we have

$$\begin{aligned}\langle F_p(x) \rangle &= p\varphi_p + m(1-\varphi_p) \\ \langle F_i(x) \rangle &= i\varphi_i + m(1-\varphi_i)\end{aligned}\quad (1)$$

while the variances are given by

$$\begin{aligned}\text{Var}[F_p(x)] &= (m-p)^2 \varphi_p (1-\varphi_p) \\ \text{Var}[F_i(x)] &= (i-m)^2 \varphi_i (1-\varphi_i)\end{aligned}\quad (2)$$

Each of the components is considered stationary (and isotropic, even though this is irrelevant for the 1-D case), thus the autocorrelation $\rho(r)$ is a function of the distance r between two points in space. Each component of the composite medium is two-phase with exponential autocorrelation [13,1,2], thus for the autocorrelations ρ_{F_p}, ρ_{F_i} , of the matrix phase in both components, P, I, we have

$$\begin{aligned}\rho_{F_p}(r) &= \exp(-r/\ell_p) \\ \rho_{F_i}(r) &= \exp(-r/\ell_i)\end{aligned}\quad (3)$$

where ℓ_p, ℓ_i denote the autocorrelation distances of the matrix material for the medium-P and medium-I, respectively. The autocorrelation distance of the matrix phase for each component is expressed as

$$\begin{aligned}\ell_p &= \frac{4\varphi_p(1-\varphi_p)}{s_p} \\ \ell_i &= \frac{4\varphi_i(1-\varphi_i)}{s_i}\end{aligned}\quad (4)$$

where s_p, s_i denote the specific area of pores and inclusions, respectively, i.e., it is the ensemble average of the density of matrix-pores and matrix-inclusions interface elements, respectively. An illustrative example for, say, medium-I, can be created by placing at random disjoint spherical particles of radii R of probability density distribution $f(R)$. We have, from the definition of s_i , through straightforward geometrical calculations, for $i > m$

$$s_i = \frac{3\varphi_i \int_0^{\infty} R^2 f(R) dR}{\int_0^{\infty} R^3 f(R) dR} \quad (5)$$

Equation (5), for the special case of spheres of constant radius R , thus $f(R) = \delta(R)$, $\delta(\cdot)$ denoting the delta function, yields

$$s_i = \frac{3\varphi_i}{R} \quad (6)$$

and thus, from (4a), it follows that

$$\ell_i = \frac{4}{3}(1-\varphi_i)R \quad (7)$$

For lognormal distribution of the inclusions we have

$$s_i = \frac{3\varphi_i}{\langle R \rangle} \left(\frac{\langle R^2 \rangle}{\langle R \rangle^2} \right)^2 \quad (8)$$

$$\ell_i = \frac{4}{3}(1-\varphi_i) \langle R \rangle \left(\frac{\langle R^2 \rangle}{\langle R \rangle^2} \right)^2$$

for the specific area and correlation distance, respectively. In the case $i < m$ φ_i has to be replaced by $1-\varphi_i$ in (5) and in the ensuing relations.

For the composite medium, i.e., medium-P plus medium-I, we have

$$\langle F \rangle = \langle F_p \rangle + \langle F_i \rangle \quad (9)$$

for the expected value of F and

$$\text{Var}[F] = \text{Var}[F_p] + \text{Var}[F_i] \quad (10)$$

for its variance. The composite medium's autocorrelation reads

$$\rho(r) = \lambda_p \rho_p(r) + \lambda_i \rho_i(r) \quad (11)$$

and its correlation distance ℓ is expressed as

$$\ell = \lambda_p \ell_p + \lambda_i \ell_i \quad (12)$$

where

$$\lambda_p = \frac{\text{Var}[F_p]}{\text{Var}[F_p] + \text{Var}[F_i]} \quad (13)$$

$$\lambda_i = \frac{\text{Var}[F_i]}{\text{Var}[F_p] + \text{Var}[F_i]}$$

Given the above relations, we next investigate the statistical properties of an actual material with embedded pores and inclusions, i.e., a cast aluminum alloy, A356.2, as also presented in [2].

4. APPLICATION TO AN ALUMINUM ALLOY

Based on [2], the relations shown in the previous paragraph can be used in conjunction with wavelet analysis [1,2] in order to study the role of microstructures (pores and inclusions) on fracture initiation. The mechanical properties of aluminum castings such as A356.2 have been experimentally related to microstructural details such as pores and inclusions, cf., e.g., the extensive literature reviewed in [15]. Important microstructures of A356 at length scales

in the range of 1 micrometer to a few millimeters are the silicon particles, the pores, and oxides. These microstructures have been found to correlate far better with mechanical properties than microstructures appearing at smaller length scales such as precipitates, intermetallic particles, etc. We concentrate at those scales, yet the process can be extended to smaller (and larger if appropriate) scales. As mentioned in [15] the role of oxides on crack initiation is similar to that of pores in this material, thus oxides may be included in the description of porosity. The size and distribution of the pores/oxides and of the silicon particles (inclusions) depend strongly on the processing; the cooling rate is one of the major processing parameters in this regard. Thus, the pores as well as the inclusions in the material can vary in size and spatial distribution.

Micrographs of a A356.2 microstructure at various magnifications are available, and some are reported in [2]. Based on those, spatial correlations (up to second order) can be studied through the variance of increments of function F , defined as

$$V_F = \left\langle \left(F(x_2) - F(x_1) \right)^2 \right\rangle \quad (14)$$

where subscripts 1,2 imply two different positions in the x domain. Using (14) instead of the correlation function, which is related to V_F , is advantageous when the variance of the process is unknown. For stationary F , the following holds

$$\frac{V_F(r)}{\text{Var}[F]} = 1 - \rho_F(r) \quad (15)$$

Figure 1 shows the variance of increments $V_F(r)/\text{Var}[F]$ as a function of distance r between two points in space, obtained from various images [2].

As expected, the images at higher magnifications may not be large enough for convergence of (15) (assuming ergodicity). The variance of increments reaches a plateau for small magnifications, implying stationarity, but shows an erratic behavior for large ones. This may be due to: (a) the images at large magnifications are not large enough for convergence; (b) the structure is not statistically stationary. The latter case is not pursued further at this point, yet if the structure shows a self-affine character with an upper and a lower cutoff, the convergence at low magnifications could be explained [9]. We leave this issue for future study and in the following consider that the structure of the inclusions is statistically stationary.

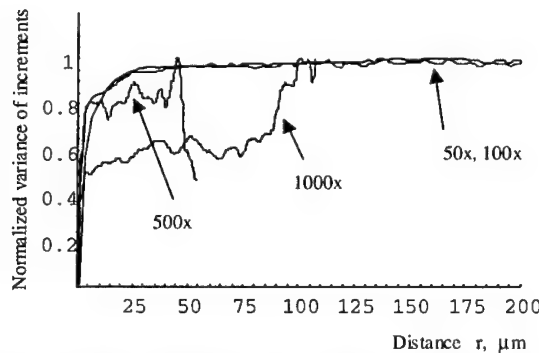


Figure 1. Variance of increments obtained from images of A356.2 at several agnifications.

The curves in Fig. 1 obtained from the 50x and 100x images fit an exponential curve of the type $1 - \text{Exp}[-r/\ell_i]$ well; a best fit process has yielded $\ell_i = 8.5 \mu\text{m}$. From the images at large

magnifications reported in [2], it is noticeable that the spatial statistics of the medium are mostly due to small clusters of inclusions rather than from individual ones. In a sense, the medium can be considered as built by placing clusters of inclusions at random. The same seems to hold for the pores, yet at the scale where they appear, it would be necessary to obtain very large images in order to see the distribution of pores. This is practically inconvenient and rather difficult with typical equipment used for obtaining images. Given the geometrical description of the pores and the inclusions in 2 or 3-D one can in principle study deformation problems and the effect of the pores as well as the inclusions. For example, simulations through FE (finite element) techniques can yield the statistics of the strain field, which is important for crack initiation studies. Yet, even with modern computers capable of handling a large number of FE, because of the multiscale nature of the problem it becomes practically impossible to simulate a reasonable size of the material. For A356.2, the pores are of size often up to 500 μm and the inclusions 3-6 μm in diameter. These two orders of magnitude range of scales make difficult the simulation of problems containing an appropriate number of inclusions and pores. Here, using the ability of wavelets to represent a medium at several scales concurrently, the process treats features at diverse scales naturally. For special cases such as isotropic porous media it has been demonstrated analytically in 1, 2 and 3-D in [1]. In [1], knowledge of the strain field near critical pores allowed analytical and in multiple dimensions investigation of the problem of failure of a porous brittle material (for isotropic media only). For inclusions, however, a similar treatment is very difficult to achieve. Thus, we make some simplifying assumptions (discussed in detail in [2]) leading to a 1-D approximation of a deformation problem, and thus analytically study crack initiation criteria. The 1-D treatment of the problem appears in [2], and comparison of theoretical results to actual experiments are also presented.

Acknowledgements: Support from the National Science Foundation under grant No CMS-9812834 is gratefully acknowledged. I am grateful to Drs. Pil Sung and David Poirier, postdoctoral fellow and professor, respectively, of the MSE Department of the University of Arizona for insightful conversations and for providing the images of A356 samples used in this study.

5. REFERENCES

- [1] G. Frantziskonis, "Wavelet-based Multiscaling - Application to Material Porosity and Identification of Dominant Scales," under review.
- [2] G. Frantziskonis, "Multiscale characterization of materials with distributed pores and inclusions and application to crack formation in an aluminum alloy," *Prob. Engr. Mechanics*, under review.
- [3] M. Mullins and M.A. Dokainish, "Simulation of the (001) Plane Crack in α -iron Employing a New Boundary Scheme," *Phil. Mag. A* 46, 771 (1982).
- [4] H. Kitagawa, A. Nakatani, and Y. Sibutani, "Molecular Dynamics Study of Crack Process Associated with Dislocation Nucleated at the Tip," *Mat. Sci. & Engr. A* 176, 263 (1994).
- [5] E.B. Tadmor, R. Phillips and M. Ortiz, "Mixed Atomistic and Continuum Models of Deformation in Solids," *Langmuir*, 12, 4529 (1996).
- [6] J.H. Simmons, "Structural and Dynamic Modeling of Mechanical Behavior of Solids," *J. Computer-Aided Mater. Design*, 4, 207-213 (1998).

-
- [7] Jackson A.G. and M.D. Benedict, "Discrete Modeling via Function Approximation Methods: Bridging Atomic and Microscales," JOM-e, 51 (8), (1999).
 - [8] G. Frantziskonis, P.A. Deymier, "Wavelet Methods for Analyzing and Bridging Simulations at Complementary Scales – the Compound Wavelet Matrix and Application to Microstructure Evolution," *Modelling Simul. Mater. Sci. Eng.*, 8, 649-664, 2000.
 - [9] G. Frantziskonis & A. Hansen, "Wavelet-based Multiscaling in Self-affine Random Media," *Fractals*, 8, 403-411, 2000.
 - [10] C. Haymie & G. Frantziskonis, "Multiscale Material Characterization and Application to Artificially Created Microstructures," Proc. 10th IACMAG, Tucson, Arizona, 7-12 January 2001, C.S. Desai et al., Eds., Balkema, Rotterdam, pp. 529-532.
 - [11] "Computational Materials Science Network Workshop on Scale-Parity Multi-Scale Simulation of Chemo-Mechanical Processes," Organized by the MSSMM Group, University of Florida, St. Augustine, Florida Feb. 25-26, 2000.
 - [12] Trickey S.B. and Deymier P.A., "Challenges and State of the Art in Simulation of Chemo-mechanical Processes," 198th meeting of the Electrochemical Society, G1-4th International Symposium on Chemical- mechanical Polishing, Pheonix AZ, Oct. 22-27, 2000.
 - [13] Debye, P., Anderson, H.R., & Brumberger, H., "Scattering by an Inhomogeneous solid. II. The Correlation Function and Its Application, J. Appl. Phys., 28, 679-683 (1957).
 - [14] Matheron, G., *Elements pour Une Theorie des Milieux Poreux*, Masso et Cie, Paris (1967).
 - [15] Zhang B., Poirier D.R. & Chen W., Microstructural Effects on High-Cycle Fatigue-Crack Initiation in A356.2 Casting Alloy, *Mettal. Matl. Trans. A*, 30A, 2659-2666 (1999).
 - [16] Gall K., Horstemeyer M., McDowell D.L. and Fan J.H., "Finite element analysis of the stress distributions near damaged Si particle clusters in cast Al-Si alloys," *Mechs. of Materials*, 32, 277-301 (2000).

SEMI-ANALYTICAL SOLUTION FOR A 1-D SIMPLIFIED THMPC MODELLING OF A NON-SATURATED SOIL

M-A. Abellan and J-M. Bergheau

Laboratoire de Tribologie et Dynamique des Systèmes (LTDS), UMR CNRS 5513
Ecole Nationale d'Ingénieurs de Saint-Etienne, FR-42023 Saint-Etienne, France

J.M Huyghe

Department of Mechanical Engineering
Eindhoven University of Technology, Eindhoven, The Netherlands

R. de Borst

Faculty of Aerospace Engineering
Delft University of Technology, 2600 GB Delft, The Netherlands

1. SUMMARY

Couplings between physical phenomena are major difficulties when modelling environmental evolutions. They give rise to delicate numerical problems for the control of which a semi-analytical simplified solution can be helpful. This paper presents such a semi-analytical solution for a 1-D simplified case study in a non-saturated soil, cast within a general conceptual approach for heterogeneous media.

2. INTRODUCTION

Environmental previsions are of great interest for managing natural hazards such as consequences of underground heat storage or contaminations of soils and/or aquifers by pollutants. However these types of complex problems are not so easy to model due to the strong couplings existing between the various physical phenomena. Many efforts have been made to understand them and to propose theoretical [1], computational [2] and experimental tools able to tackle the difficulties of such modelling. They are linked to the large number of variables, the complexity of the coupled constitutive relations, the variety of thermodynamic evolutions depending on numerous boundary conditions and physically admissible initial conditions [3]. Up to now these difficulties have been tackled by complex numerical modelling based on a general thermo-hydro-mechanical and physico-chemical (THMPC) approach of heterogeneous media [4]. A successful implementation was achieved using a finite difference approach [5]. However, this implementation was restricted to one-dimension (1D), and delicate numerical problems arise when implementing the theory in a 3-D finite element context. To validate such an implementation, a semi-analytical simplified solution can be useful.

This paper proposes such a semi-analytical solution for a 1-D simplified case study in a non-saturated soil.

3. THEORETICAL BACKGROUND

Within the above framework it is possible to analyse all the coupled phenomena existing between mass, momentum and energy transfer within and between constituents [6]. In order to control the large number of relations and variables an automatic programming set-up [7] is used at the different stages of the modelling: defining the whole set of variables, setting the constitutive relations and the possible assumptions, defining the initial state and the boundary conditions, computing the different variables and exploiting the results.

4. PROCEDURES

The simplified 1-D case study chosen here is an L-meter thick non-saturated clayey-silt column. Four constituents are present: dry air ($\pi = a$), water vapour ($\pi = v$), liquid water ($\pi = w$) and clayey-silt ($\pi = s$). Assumptions are taken in order to focus the study and the discussion on settlements of the column and phase changes between liquid water and water vapour. On this basis, the constitutive relations include for each constituent: the mass and momentum balance relations plus the material equilibrium and non-equilibrium relations. These relations are summarized below assuming small deformations and concentration variations with variables that are functions of the vertical Eulerian component z of the reference frame chosen equal to the configuration of the solid.

Generalized balance equations for $\pi = a, v, w, s$

Proceeding from [4] [5] the generalized mass balance equation for π is given by

$$\frac{\partial}{\partial t} \rho_{\pi} + \frac{\partial}{\partial z} (\rho_{\pi} v_z) = - \frac{\partial}{\partial z} (\rho_{\pi} w_{\pi z}) + \hat{c}_{\pi} \quad (1)$$

with the following notations: ρ_{π} apparent mass density of π , v_z vertical component of the velocity of the solid, $w_{\pi z}$ vertical component of the relative velocity of π with respect to the solid and \hat{c}_{π} mass supply to π due to other constituents per volume and time unit.

For constituent π the generalized momentum balance equation equals:

$$\begin{aligned} \frac{\partial}{\partial t} [\rho_{\pi} (w_{\pi z} + v_z)] + \frac{\partial}{\partial z} [\rho_{\pi} (w_{\pi z} + v_z) v_z] = & - \frac{\partial}{\partial z} [\rho_{\pi} (w_{\pi z} + v_z) w_{\pi z} + \sigma_{\pi zz}] \\ & - \rho_{\pi} g + (w_{\pi z} + v_z) \hat{c}_{\pi} + \hat{p}_{\pi z} \end{aligned} \quad (2)$$

with $\sigma_{\pi zz}$ the stress tensor of constituent π , g the gravity acceleration, $\hat{p}_{\pi z}$ vertical component of the momentum supply vector to π due to other constituents.

Material equilibrium relations for $\pi = a, v, w, s$

The chemical potentials μ_{π} of water vapour and liquid water are given by

$$\mu_{\pi} = \mu_{\pi 0} + \frac{1}{M_{\pi}} R T \ln \frac{S(\sigma_{\pi}^{rev})}{n_{\pi}} \quad (3)$$

with $\mu_{\pi 0}$ the standard chemical potential of π , M_{π} the molar mass of π , R the universal gas constant, T the temperature, n_{π} the volume ratio of π and $S(\sigma_{\pi}^{rev})$ a function of σ_{π}^{rev} .

The fluids are assumed to be ideal. As a consequence the reversible stress σ_{π}^{rev} of constituents $\pi=a,v$ are respectively given by the idealized gas law:

$$\sigma_{\pi}^{rev} = \frac{1}{M_{\pi}} \rho_{\pi} R T \quad (4)$$

Under isothermal conditions, an incremental linear relation (5) is assumed to express the reversible stress σ_w^{rev} of liquid water under the form:

$$-d \left\{ \left[\frac{\sigma_a^{rev} + \sigma_v^{rev}}{n_v} - \frac{\sigma_w^{rev}}{n_w} \right] \frac{n_w}{\rho_w g} \right\} = F_w dp_w \quad (5)$$

where F_w is an experimentally determined function of the mass density ρ_w .

Assuming linear isotropic elasticity for the total medium, the reversible strains of the solid are deduced from the reversible strains of the total medium. Hence the relation between stresses σ_{szz} and reversible strains of the solid ϵ_{szz} reads as follows

$$\sigma_{szz} = (\lambda + 2\mu) \epsilon_{szz} - \sum_{\pi=a,v,w} [\sigma_{\pi zz} + \rho_{\pi} w_{\pi z} v_z] \quad (6)$$

with λ and μ the elastic coefficients.

Material non-equilibrium relations for $\pi = a, v, w, s$

The rates of condensation and evaporation are expressed by

$$\hat{c}_v = L_{\pi} \frac{1}{T} [\mu_w - \mu_v] \text{ and } \hat{c}_w = -\hat{c}_v \quad (7)$$

where L_{π} is an experimentally determined coefficient.

Neglecting couplings between velocity and heat flux the generalized Darcy's law expresses gas flow through a porous medium by means of a permeability coefficient k_g . This law leads to the expression (8) for the relative velocity of dry air:

$$w_{az} = \left(1 + \frac{\rho_v}{\rho_a} \right) \left\{ -\frac{k_g}{n_v} \frac{\partial}{\partial z} \left[\frac{\sigma_a^{rev} + \sigma_v^{rev}}{(\rho_a + \rho_v)g} - z \right] \right\} - \frac{\rho_v}{\rho_a} w_{vz} \quad (8)$$

With the same assumption diffusion of water vapour through a gas phase of a porous medium is expressed by Fick's law with k_c the diffusion coefficient in a porous medium. This relation has the form :

$$w_{vz} = -\frac{k_g}{n_v} \frac{\partial}{\partial z} \left[\frac{\sigma_a^{rev} + \sigma_v^{rev}}{(\rho_a + \rho_v)g} - z \right] - k_c \left(1 + \frac{\rho_a}{\rho_v} \right) \frac{\partial}{\partial z} \left[\frac{\rho_v}{\rho_a + \rho_v} \right] \quad (9)$$

Again under the same assumption, flow of liquid water through a porous medium is given by the generalized Darcy's law (10) where k_w is the permeability of liquid water.

$$w_{wz} = - \frac{k_w}{n_w} \frac{\partial}{\partial z} \left[\frac{\sigma_w^{rev}}{\rho_w g} - z \right] \quad (10)$$

The rate of momentum exchanges of the solid is deduced from the constraint:

$$\hat{p}_{sz} = - \sum_{\pi=s,v,w} \hat{p}_{\pi z} \quad (11)$$

For ideal viscous fluids the irreversible stress σ_{π}^{irr} is given by relation (12) equivalent to the classical viscous stress tensor of a Newtonian fluid where $\tilde{\mu}_{\pi}$ is its dynamic viscosity.

$$\sigma_{\pi z}^{irr} = n_{\pi} \frac{4}{3} \tilde{\mu}_{\pi} \left(\frac{\partial w_{\pi z}}{\partial z} + \frac{\partial v_z}{\partial z} \right) \quad (12)$$

5. SEMI-ANALYTICAL RESOLUTION

For each constituent a bijective relation is defined between variables and equations. Then, as in a numerical process, an incremented time process uses this bijection as well as appropriate initial and boundary conditions [5] to obtain the semi-analytical solution of the coupled non-linear system written in section 4. The strategy consists in solving, constituent after constituent, each equation for its associated variable considering that values of all other necessary variables have been at the previous time step. This strategy is applied assuming all variables to be known at stage "n" for all constituents. The aim is to make a loop on the constituents to determine the update at a new, yet unknown stage "n+1". This is performed assuming constant material parameters with respect to time during the time step. Notice that for simplicity the equations (1) to (12) are handled in their order of appearance and the way to update a given variable is explained only briefly.

Relation (1) and apparent mass density of π

Applying a Laplace transform to relation (1) leads to a first order differential equation of the unknown $\bar{\rho}_{\pi n+1}(p, z)$: the Laplace transform of $\rho_{\pi n+1}(z, t)$ where p is the Laplace variable. The solution of this equation has the form

$$\bar{\rho}_{\pi n+1}(p, z) = e^{\left(- \int_0^z P_{\pi n}(p, y) dy \right)} \left[\int_0^z e^{\int_0^y P_{\pi n}(p, s) ds} G_{\pi n}(p, s) ds + Q_{\pi n}(z) \right] \quad (13)$$

where $P_{\pi n}(p, z)$, $G_{\pi n}(p, z)$ are the coefficients of the first order differential equation and $Q_{\pi n}(z)$ is a constant with respect to variable p .

The unknown inverse of the Laplace transform (13) incorporating initial and boundary conditions can be found using the Bromwich infinite integral and applying the residuals theorem. For this purpose the integrand is rewritten as a fraction of two polynomials $R_1(p)$ and $R_2(p)$ using adequate Taylor series expansions with the degree of $R_2(p)$ greater than that of $R_1(p)$. Therefore the apparent mass density of constituent π is simply given by:

$$\rho_{\pi n+1}(z, t) = \sum_r \frac{1}{(m_r - 1)!} \lim_{p \rightarrow p_r} \frac{d^{m_r-1}}{dp^{m_r-1}} \left[(p - p_r)^{m_r} \frac{R_1(p)}{R_2(p)} \right] \quad (14)$$

with r number of poles of the integrand and p_r pole of order m_r .

Relation (2) and rate of momentum exchanges for a fluid or displacement for a solid

For a fluid ($\pi = a, v, w$) and taking into account the initial and boundary conditions relation (2) gives directly an expression for the update of the vertical component of its rate of momentum exchanges:

$$\hat{p}_{\pi z, n+1} = \frac{\partial}{\partial t} [\rho_{\pi, n+1} (w_{\pi z, n} + v_{z, n})] + \frac{\partial}{\partial z} [\rho_{\pi, n+1} (w_{\pi z, n} + v_{z, n})^2] - \sigma_{\pi z z, n} + \rho_{\pi, n+1} g - (w_{\pi z, n} + v_{z, n}) \hat{c}_{\pi, n} \quad (15)$$

For the solid ($\pi = s$) the treatment of relation (2) is slightly different. Proceeding from relations (2) written for $\pi = a, v, w, s$ and from relation (14), neglecting inertia, substituting for the stresses of the solid from relation (6) and assuming constant elastic parameters leads to a second order partial differential equation of the displacement $u_z(z, t)$ of the solid.

$$(\lambda + 2\mu) \frac{\partial^2}{\partial z^2} u_{z, n+1} + \sum_{\pi=a, v, w, s} [\rho_{\pi, n+1} g] = 0 \quad (16)$$

Integrating with respect to z and incorporation of boundary conditions of the form $u_z(0, t) = u_0$ and $u_z(L, t) = u_L$ gives for the displacement:

$$u_{z, n+1} = -\frac{g}{+2\mu} \int_0^z \left(\int_0^l \sum_{\pi=a, v, w, s} \rho_{\pi, n+1} ds \right) dl + \left[\frac{u_L - u_0}{L} + \frac{g}{L(+2\mu)} \int_0^L \left(\int_0^l \sum_{\pi=a, v, w, s} \rho_{\pi, n+1} ds \right) dl \right] z + u_0 \quad (17)$$

Relation (3) and chemical potentials of $\pi = v, w$

The increment $\Delta\mu_{\pi, n+1}$ of the chemical potential of constituent π is determined by the incremental form of relation (3) and leads to: $\mu_{\pi, n+1} = \mu_{\pi, n} + \Delta\mu_{\pi, n+1}$.

Relation (4) and reversible stress for $\pi = a, v$

Substitution of expression (14) in the incremental form of relation (4) gives the contribution to the reversible stress increment of constituent π . Hence the associated update takes the form: $\sigma_{\pi}^{rev, n+1} = \sigma_{\pi}^{rev, n} + \Delta\sigma_{\pi}^{rev, n+1}$.

Relation (5) and reversible stress for $\pi = w$

The reversible stress increment $\Delta\sigma_w^{rev, n+1}$ is computed by means of relation (5) leading to: $\sigma_w^{rev, n+1} = \sigma_w^{rev, n} + \Delta\sigma_w^{rev, n+1}$.

Relation (6) and stresses of $\pi = s$

Assuming infinitesimal deformations, taking into account the update of the displacement of the solid (17) and incorporating expressions (14) for all constituents in relation (6) gives the increment $\Delta\sigma_{szz, n+1}$. Therefore the stress update of $\pi = s$ is given by $\sigma_{szz, n+1} = \sigma_{szz, n} + \Delta\sigma_{szz, n+1}$.

Relation (7) and rate of phase changes for $\pi = v, w$

Rates of condensation or evaporation are estimated under the form $\hat{c}_{\pi, n+1} = \hat{c}_{\pi, n} + \Delta\hat{c}_{\pi, n+1}$ with increments obtained by relations (7).

Relations (8) to (10) and associated relative velocities

The relative velocities of $\pi=a,v,w$ are determined by $w_{\pi z, n+1} = w_{\pi z, n} + \Delta w_{\pi z, n+1}$, respectively, with the increments deduced from relations (8), (9) and (10).

Relation (11) and rate of momentum exchanges for $\pi=s$

Relation (11) gives directly the vertical component of the rate of momentum exchanges of the solid as soon as those of the other constituents have been updated.

Relation (12) and irreversible part of stresses for $\pi=a,v,w$

The irreversible part of the stress tensor of π is updated with $\sigma_{\pi}^{irr, n+1} = \sigma_{\pi}^{irr, n} + \Delta \sigma_{\pi}^{irr, n+1}$ with the increment $\Delta \sigma_{\pi}^{irr, n+1}$ deduced from relation (12).

6. CONCLUSION

A 1-D semi-analytical solution has been obtained for a simplified THMPC case study to help controlling and validating more complex numerical THMPC modelling.

Acknowledgements: The research of dr. J.M. Huyghe was made possible through a fellowship of the Royal Netherlands Academy of Arts and Sciences.

7. REFERENCES

- [1] Van Meerveld, J., Molenaar, M.M., Huyghe, J.M., Baaijens, F.P.T., Analytical solution of compression, free swelling and electrical loading of saturated charged porous media, *Transport in Porous Media* (2000).
- [2] Groen, A.E., de Borst, R., Van Eekelen, S.J.M., An elastoplastic model for clay: Formulation and algorithmic aspects, in G.N. Pande, S. Pietruszczak (Ed), *Numerical Methods in Geomechanics*, Balkema, Rotterdam (1995) 27-33.
- [3] Abellan, M-A., Jouanna, P., Brocas, S., Assessing an initial state in a thermo-plastic and physico-chemical complex situation by a perturbation method, *PLASTICITY'2000*, Whistler, Canada, 17-21 July (2000).
- [4] Jouanna, P., Abellan, M-A., A generalized approach to heterogeneous media, *Transport in Porous Media* 25, 351-374 (1996).
- [5] Abellan, M-A., Approche phénoménologique généralisée et modélisation systématique de milieux hétérogènes. Illustration sur un sol non-saturé en évolution thermo-hydro-mécanique et physico-chimique. Tome 1 (Concepts) et Tome 2 (Illustration), Ph. D. thesis, University Montpellier II, France (1994).
- [6] Abellan, M-A., Jouanna, P., Ability of computational methods to predict coupled phenomena not accessible to direct experimentations. A typical example in an unsaturated soil. *Proceedings of NAFEMS'97*, Stuttgart, Germany, 9-11 April 1997, 1, 311-322, ISBN 1 874376 20 4 (1997).
- [7] Jouanna, P., Abellan, M-A., General and automatic programming set-up for thermo-hydro-mechanical and physico-chemical evolutions in heterogeneous media, in J-X Yuan (Ed), *Computer Methods and Advances in Geomechanics*, *Proceedings of 9th ICCMAG'97*, Wuhan, China, 2-7 November 1997, A.A. Balkema, Rotterdam, Brookfield, ISBN 90 5410 904 1 (1997) 1165-1170.

COMPACT, HIGH-POWER, SYNTHETIC JET ACTUATORS FOR FLOW SEPARATION CONTROL

J. L. Gilarranz and O. K. Rediniotis

Department of Aerospace Engineering, Texas A&M University
College Station, Texas, 77843-3141, USA

1. SUMMARY

Although strong potential of synthetic jets as flow separation control actuators has been demonstrated in the existing literature, there is a large gap between the synthetic jet actuators (SJA) used in laboratory demonstrations and the SJAs needed in realistic full-scale applications, in terms of compactness, weight, efficiency, control authority and power density. In most cases, the SJAs used in demonstrations are either too large or too weak for realistic applications. In this work, we present the development of compact, high-power synthetic jet actuators for realistic flow separation control applications and demonstrate the developed SJA technology in representative, flow separation control problems, including control of steady separation/stall. The developed actuators are compact enough to fit in the interior of a 14.75" chord, NACA0015 wing, have maximum power of 2.0 HP and can produce (for the tested conditions) exit velocities as high as 70 m/sec. Flow visualization and pressure results for flow separation control were obtained over a 14.75" chord, NACA 0015 wing at angles of attack and free stream velocities as high as 25 degrees and 45 m/s, respectively. In addition to flow separation control data, we also present results corresponding to hot wire measurements performed at the exit of the slot for the characterization of the flowfield generated by these synthetic jet actuators.

2. INTRODUCTION

The separation of the boundary layer is associated with large energy losses, and in most applications adversely affects the aerodynamic loads in the form of lift loss and drag increase. Therefore, there is a strong incentive to delay or manipulate the occurrence of flow separation. For example, if the separation of the boundary layer formed over a bluff body is delayed, the pressure drag is greatly reduced; also separation delay will permit the operation of an airfoil/wing at higher angles of attack. Mc Cormick (2000) showed that delay or elimination of separation can increase the pressure recovery in a diffuser. Hence, separation control is of great importance to most of the systems involving fluid flow, such as air, land or underwater vehicles, turbomachines, diffusers, etc.

Many researchers have developed and tested methods of separation control in a variety of applications. Gad-el-Hak and Bushnell (1991) provide a comprehensive review on the research in the area of separation control previous to the year 1991. Typically the separation

control techniques may be grouped in two categories: passive and active techniques. Some of the parameters affecting the selection of a separation control technique include, but are not limited to: weight of system, power consumption (active type), power density, parasitic drag of device, size, reliability, cost and efficiency.

In the recent years the development of the so-called "synthetic jet" or "zero mass flux" devices and their potential for flow control has received a great amount of attention from the fluid dynamics community. This type of systems mostly involves small-scale, typically high-frequency actuators, whose operation is based on the concentrated input of energy at high receptivity regions of the flowfield. They take advantage of the physical flow evolution processes to amplify the applied disturbance, which stands apart from the traditional brute force macro-scale control. Moreover, in terms of practical implementation, they offer significant benefits over oscillatory blowing techniques from an existing air supply. The latter technique requires supply lines that deliver the air from the supply source to the location of flow control. Even in fixed wing configurations, this increases the complexity, cost and weight of the overall system. In rotary wing flow control applications, for example rotating blade stall in helicopters (Greenblatt et al., 1998), the situation is further complicated by the need to transfer, via pneumatic connections, the air from a supply source that resides in the fixed fuselage frame to the rotating frame of the blade; a practical impossibility. In contrast, a synthetic jet actuator (SJA) can be a stand-alone unit installed at the location where the flow control is needed, requiring very little communication with hardware away from that site. In this case, the communication is mostly in the form of electrical power and signals. Furthermore, the SJA could be integrated with flow sensors, control circuitry and control algorithms that can all reside in the vicinity of the flow control site, further reducing the system's need to communicate with remote hardware.

Current research of synthetic jet actuation includes investigation of the performance of this technology for modifying the lift, drag and flight control characteristics of unconventional airfoils as well as flow separation over bluff bodies (Amitay et al., 1998; Smith et al., 1998; Seifert et al., 1993; Seifert and Pack, 1999). This technology could lead to elimination, reduction or manipulation of steady and unsteady flow separation over a wing/blade, via active flow control and in a "hingeless" manner (no conventional moving control surfaces). A result of this technology can be the active modification of the pressure distribution over an aerodynamic surface, leading to "dynamic virtual shaping". Flow separation manipulation (not just separation delay) could open new horizons in vehicle control and presents an exciting alternative over conventional control surfaces, since: (a) it can alter the aerodynamic loading over a larger wing/blade area, providing higher control authority and (b) could eliminate leading-edge or trailing-edge moving surfaces.

The existing literature presents very promising applications of the synthetic jet technology to flow separation (Greenblatt and Wagnaski, 1998; Greenblatt et al., 1998; Seifert and Pack, 1999). In most efforts in the existing literature, the synthetic jet actuators (SJA) are either powered piezoelectrically (Rathnasingham and Breuer, 1997; Seifert et al., 1998) or are powered from external hardware. For example, in Greenblatt and Wagnaski (1998), as well as in Seifert and Pack (1999), the mechanism used to generate the pressure oscillations necessary for the zero-mass-flux flow control was a hardware-intensive pneumatic mechanism, with most of the hardware residing outside the test section. For most air and water vehicle applications, the SJAs will need to be compact in order to be housed inside the control surface of the body whose aerodynamic/hydrodynamic characteristics they are trying to modify. On the other hand, piezoceramic-based synthetic jet actuators, which can be small enough to be housed inside the control surface, exhibit performance deterioration when operating at frequencies away from the actuator resonance frequencies, have limited

maximum amplitudes and generally quickly deteriorate at off-design conditions. There is an explicit need for the development of compact, high-power synthetic jet actuators that can meet the size, weight, efficiency and power density requirements of full-scale flow control applications. The present work addresses these needs, via development and characterization of compact, high power synthetic jet actuators, and demonstration of the developed SJA technology in representative flow control problems.

3. ACTUATOR DESIGN PRINCIPLES

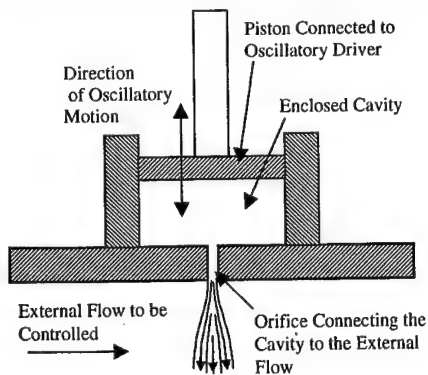


Figure 1. Principle of Operation of a Synthetic Jet Actuator.

This work addresses the need for compact, zero-mass-flux actuators that can be entirely housed inside a wing/blade. We are presenting the development and characterization of such compact, high-power actuators. These actuators do not share the limitations of often used piezoceramic-based SJAs, which exhibit performance deterioration when operating at frequencies away from the actuator resonance frequencies, have limited maximum amplitudes and generally quickly deteriorate at off-design conditions.

The principle of operation of a synthetic jet actuator is illustrated in figure 1, which presents a cross-sectional view of a sample axisymmetric actuator. The actuator consists of a closed cavity

in which one of the ends is covered by an oscillating piston. A rigid wall with a small orifice covers the other end. This orifice is the only communication of the cavity with the external flow to be controlled by the actuator. The oscillation of the piston produces a fluctuation of the pressure field in the cavity and at the orifice, causing it to periodically act as a source or a sink. The result of this is a net jet emanating from the orifice. So, although there is no net mass addition, a jet is formed (hence the term "synthetic").

Simple calculations for real-life flight applications (Gilarranz and Rediniotis, 2001), based on optimal reduced frequency values and minimum required jet-momentum coefficient values, indicate that the expected peak-to-peak strokes of the SJA membrane/piston would be on the order of 5mm at a frequency around 300Hz. The numbers are far from optimal for piezoelectric actuation. The required amplitudes are significantly larger than what piezoceramics are typically capable of, and the required frequencies are quite lower than those at which piezoceramics have competitive power densities. In contrast, these numbers are ideal for rotary motor actuation. Compact electric motors exist, off-the-shelf, with optimal performance at around 18,000 rpm (or 300 Hz), measuring 25mm in diameter and 37mm in length, weighing 2.5 ounces (70 grams) and with very competitive power densities (400 Watts per 70 grams, or 5.7KW/kg).

The proposed principle of the SJA driving mechanism is well-developed and has been extensively utilized in a variety of engines. Details of the driving mechanism for these actuators may be found in the work of Gilarranz and Rediniotis (2001). It consists of a DC motor with its shaft connected eccentrically to a piston, which is in turn connected to the membrane/piston of the SJA. Due to the eccentricity, the rotary motion of the motor is translated to linear motion of the SJA membrane/piston. This design offers significant benefits over, for examples, piezoceramic driving mechanisms:

- it can achieve membrane/piston oscillation amplitudes at least an order of magnitude higher
- it eliminates the dependence of oscillation amplitude on the oscillation frequency, which plagues piezoceramic mechanisms
- with available state-of-the-art, high power-density electric motors it can match and exceed the power densities of piezoceramic mechanisms
- it requires significantly smaller driving voltages

In the developed DC motor driven SJAs, electric motors drive a series of “off the shelf” small gasoline engines which are used as reciprocating compressors. The cylinder head of each of these engines is perforated and attached to a common plenum, which is closed on all sides except for a slot machined on one of the walls (figure 2). The engines are synchronized, therefore all of the pistons operate at the same frequency. The change in the cavity volume of the plenum of the actuator is equal to the displacement of the pistons multiplied by the area of the pistons. The use of the available engine technology reduces the effort to manufacture pistons with no leakage, thus simplifying the design and construction of the SJA.

4. DESIGN FABRICATION AND TESTING OF A 2-HP COMPACT SJA ARRAY

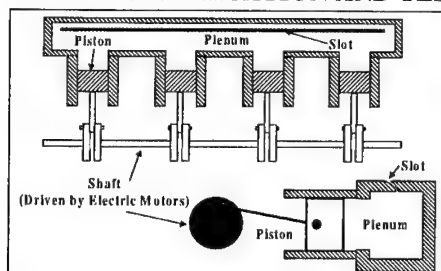


Figure 2. Schematic of DC motor driven SJA array.

The knowledge gained from previous experience with DC motor driven SJA's (Rao et al., 2000; Gilarranz and Rediniotis, 2001) and a first-generation SJA array, was used to develop a second generation, significantly more powerful array that could fit within a NACA 0015 wing. The wing had a chord length of 14.75 inches, and a maximum thickness of 2.25 inches. The wing was made out of Freeman Industries Repro 95 aluminum filled epoxy. It was molded in two halves (top and bottom) with an internal chamber to house the actuator. The exit slot was placed at

a distance of 1.7" from the leading edge on the upper half of the wing. The exit slot was machined so that it exits tangentially to the surface of the wing, it has a variable width (from 1mm to 4mm) and a length (spanwise) of 10 inches. It is important to mention that this actuator fits inside the cavity of the wing, making this SJA completely self-contained. To the authors' knowledge, besides the piezoelectrically driven actuators mentioned previously, this is one of the first non-piezoelectrically driven self-contained SJA. The second generation array is composed of 6 reciprocating compressors (engines) which are driven by two DC motors. Each engine had a displacement volume of 0.809 cubic inches, with a peak-to-peak piston stroke of 0.866". Each motor measured 2.66" in length and 1.47" in diameter, had a maximum power of 800 W and weighed 12 oz. The motors were arranged in parallel to the camshaft in order to keep the span of the device smaller than the span of the wing internal cavity. Compared to the first generation array, this was a significantly more powerful, high maximum exit velocity array.

Figure 3 shows pictures of the second generation SJA array illustrating details on cylinder arrangement, motor mounting, slot geometry and cylinder phasing. It should be noted that the cylinders had to be properly phased in order to reduce array vibration. By referring to the rightmost picture of figure 3 and numbering the cylinders from 1 to 6, starting from the left, the phasing was as follows: cylinders 1 and 6 at 240 degrees, cylinders 2 and 5 at 120 degrees and cylinders 3 and 4 at 0 degrees. It was found that the reduction in vibration severity from the unphased to the phased SJA operation was dramatic. This phasing in turn required the

compartmentalization of the plenum, as it is obvious that if the plenum was not divided into six individual compartments, each one corresponding to each of the six cylinders, the engine phasing would result in zero net volume change during an operation cycle and thus no synthetic jet effect.

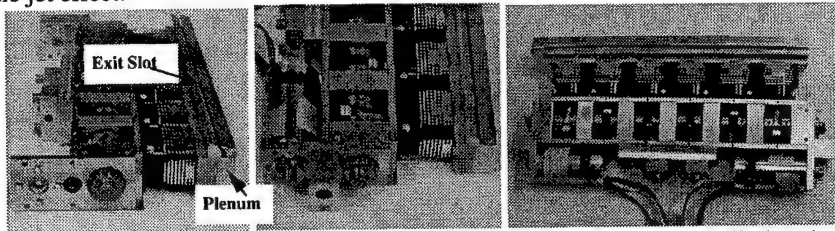


Figure 3. Pictures of second generation array, showing motor mounting, cylinder phasing, exit slot geometry.

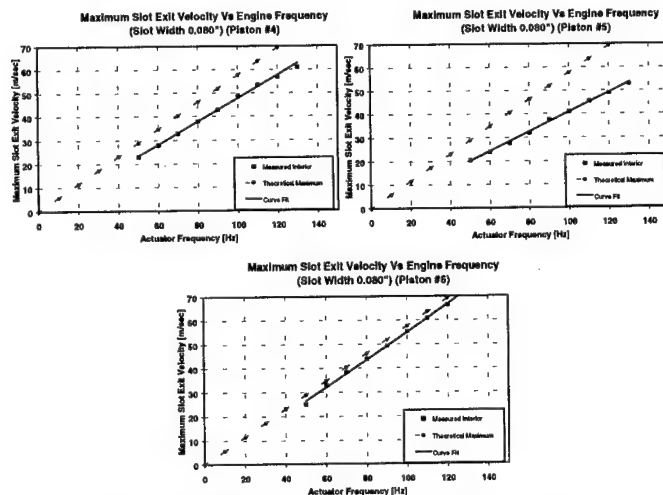


Figure 4. Maximum exit velocity as a function of frequency at the center of the slot for each piston location.

The array was first tested outside the wing in order to document, via hot wire anemometry, the maximum exit velocity as a function of frequency, as well as investigate the effects of cylinder phasing and plenum compartmentalization to the flow. The results are shown in figure 4. Velocity magnitudes as high as 70 m/sec were achieved for frequencies up to 130 Hz. The deviations between the theoretical and measured curves are due to the interaction between adjacent out-of-phase pistons. As it may be seen in the figures for any given operating frequency, for piston 5 (and 2; not shown), the exit velocity is the lowest. This is due to the fact that for these pistons (2 and 5), both of the neighboring pistons are out-of-phase. On the other hand, for piston 6 (and 1), the exit velocity is the highest due to the fact that they (1 and 6) only have one neighboring out-of-phase piston. Finally, for the case of pistons 4 (and 3), they have one out-of-phase piston on one side and one in-phase piston on the other side, for this case the exit velocity reaches an intermediate value.

Figure 5 shows the distribution of the maximum exit slot velocity as a function of spanwise position for all of the pistons. This plot was generated by traversing a hot wire along the jet exit slot. Note that this figure presents the same trend discussed for figure 4, i.e. the maximum velocity is obtained for pistons number 1 and 6 and the minimum velocity for pistons 2 and 5. Figure 5 also shows that there is a very strong interaction between the pistons which are out-of-phase. The authors believe that this interaction will be greatly reduced by extending the walls that separate the individual plenum chambers into the exit slot in order to have separate slots for each piston.

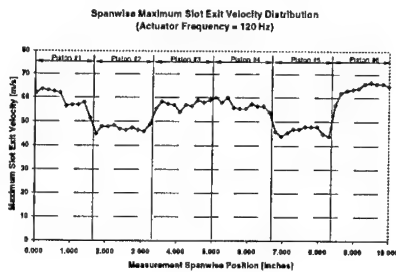


Figure 5. Maximum exit velocity as a function of spanwise location

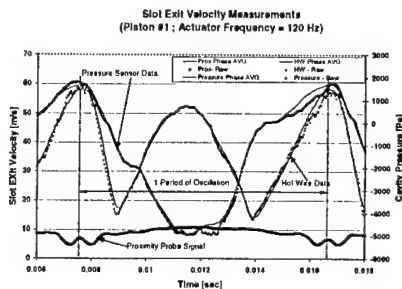


Figure 6. Sample pressure and slot exit velocity measurements.

In addition to the effect of the piston phasing over the spanwise velocity distribution of the actuator, the performance of the actuator may be affected by other phenomena such as: compressibility effects at high frequencies of actuation and pressure losses in the cavity/slot due to geometric factors. More tests are currently being conducted to identify the dominant phenomena that affect the performance of the actuator in order to manipulate them, if possible, to obtain the best possible actuator performance.

In order to aid us in the modeling and characterization of the performance of the synthetic jet actuator, we are currently performing tests in which we measure the slot exit velocity, the

pressure inside the chamber and the position of the pistons simultaneously. This data will be of great use in the determination of the presence of compressibility effects in the actuator, as well as provide invaluable data to be used in the dynamic modeling of the actuator. Figure 6 shows a sample plot with the data from one of these experiments. These results have been phased averaged and the figure is only showing one period of actuation. Note that the pressure inside the chamber is practically in phase with the measured exit velocity of the actuator, with the velocity lagging slightly. This is expected as it is the pressure that drives the flow in the actuator. The signal from a proximity probe is used to determine the position of the pistons in order to provide us with phase information. The measurements shown in the figure were performed at the center of the slot corresponding to piston 1 operating at a frequency of 120Hz. It is important to mention that the ensemble-averaged data agrees very well with the raw data shown in the figures. This is an indication that there is virtually no variation in the behavior of the actuator from one period of operation to the next. Finally, note that for the case of the velocity measurements performed with the hot wire the data presented in figure 6 shows a positive value for the slot exit velocity during the suction part of the period in which the velocity reverses its direction, this is due to the fact that the hotwire sensor rectifies the velocity signal. Hence, during the suction part of the period, when the pressure in the chamber is negative, the sign of the velocity shown in the figure should be inverted to account for the reversed direction of the flow.

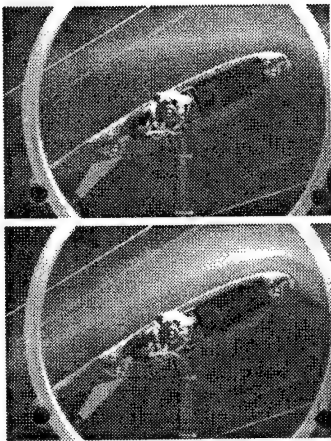


Figure 7. Flow visualization over the wing, without (top) and with (bottom) SJA actuation.

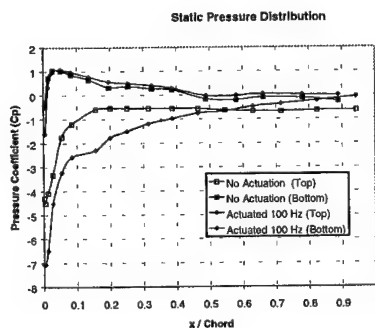


Figure 8. Pressure distribution over the wing (with and without actuation). $\alpha = 25^\circ$, freestream velocity = 30 m/s.

chord, NACA 0015 wing, have maximum power of 2.0 HP and could produce exit velocities as high as 70 m/sec, for the conditions tested (up to frequencies of 120 Hz). With the use of a higher-power power supply, we expect to be able to operate at frequencies as high as 250Hz, with a resulting slot exit velocity as high as 120m/sec. Hot-wire measurements at the exit of the SJA plenum showed the existence of a strong interaction between the jets produced by the pistons due to the fact that they are out of phase. Previous research showed that the compressibility effects are also important for this type of actuators. These effects are higher as the actuator frequency increases, the exit slot width decreases and the combined plenum-cylinder internal volume increases. Tests will be performed in order to detect and minimize these effects. Flow separation control was demonstrated over a 14.75" chord, NACA 0015 wing at angles of attack and free stream velocities as high as 25° and 45 m/s, respectively. Flow visualization was performed and showed that for the case of the wing at an angle of attack of 25° , the flow over the wing was separated when no actuation was applied. On the

Upon completion of the preliminary testing of the actuator, the array was installed inside the test wing. The wing was equipped with 32 pressure ports distributed on its upper and lower surfaces. The pressure ports were connected, via Tygon tubing, to a 32-channel ESP pressure scanner with a nominal pressure range of ± 10 inches of water. The pressure scanner was also installed inside the wing. The wing-SJA-ESP assembly was then tested in the 3'x4' Aerospace Engineering Wind Tunnel. Flow visualization and pressure measurement tests were performed over a range of test conditions. Figure 7 presents the visualized flow over the wing, at an angle of attack of 25° with a freestream velocity of 30 m/s, without (top) and with (bottom) SJA actuation. Without SJA actuation, the flow separates very close to the leading edge and the wing is in the post-stall region. With SJA actuation, the flow remains attached over the entire the wing chord. These results were also confirmed by the pressure data, as shown in figure 8.

5. CONCLUSIONS

In this paper, we presented our work on the development of compact, high-power synthetic jet actuators for realistic flow separation control applications and showed that the developed SJA technology is capable of controlling steady separation/stall. The new actuators have piston oscillation amplitudes at least two orders of magnitude higher than those achieved by piezoelectric actuators and eliminate the dependence of oscillation amplitude on the oscillation frequency, which plagues piezoceramic mechanisms. The developed actuators are compact enough to fit in the interior of a 14.75"

other hand, when the actuator was operated, it was capable of completely reattaching the flow. Pressure data was also recorded during these tests and confirmed the separation control capabilities of our actuator. Also of interest was the fact that for high angles of attack the vortex shedding off the wing (for the case of no actuation), caused the wing support structure to vibrate, on the other hand, this vibration was eliminated when the actuator was operated due to flow reattachment.

More work is being conducted to optimize the actuator operation and more importantly model its operation and its effects on the flow. Further investigations on the effects of the compartmentalization of the plenum over the flowfield generated by these actuators are also being conducted.

Acknowledgements: This work was sponsored by the United States Air Force Office of Scientific Research, under the contract number F49620-01-1-0012. Dr. Thomas Beutner is the technical monitor.

6. REFERENCES

- [1] Amitay M., Smith B.L. and Glezer A., "Aerodynamic Flow Control Using Synthetic Jet Technology," AIAA Paper No. 98-0208, 36th Aerospace Sciences Meeting & Exhibit, Reno, NV, Jan. 1998.
- [2] Gad-el-Hak, M. and Bushnell, D., "Separation Control: Review", ASME Journal of Fluids Engineering, Vol. 113, 1991, pp. 5-30. (1991)
- [3] Gilarranz, J. L., and Rediniotis, O. K., "Compact, High-Power Synthetic Jet Actuators for Flow Separation Control", AIAA Paper No. AIAA-2001-0737, 39th Aerospace Sciences Meeting and Exhibit, Reno, Nevada, January 2001.
- [4] Greenblatt, D., Darabi, A., Nishri, B., and Wygnanski, I., "Separation Control By Periodic Addition of Momentum with Particular Emphasis on Dynamic Stall," Proceedings Heli Japan 98, Paper T3-4, American Helicopter Society, April 1998.
- [5] Greenblatt, D. and Wygnanski, I., "Dynamic Stall Control by Oscillatory Forcing", AIAA Paper No. 98-0676, January 1998
- [6] McCormick, D., "Boundary Layer Separation Control with Directed Synthetic Jets", AIAA Paper 2000-0519, 38th Aerospace Sciences Meeting and Exhibit, Reno, Nevada, January 2000.
- [7] Rao, P. Gilarranz, J.L., Ko, J. Strgnac, T. and Rediniotis, O.K., "Flow Separation Control Via Synthetic Jet Actuation", AIAA Paper 2000-0407, 38th Aerospace Sciences Meeting and Exhibit, Reno, Nevada, January 2000.
- [8] Rathnasingham, R. and Breuer, K. "Coupled Fluid-Structural Characteristics of Actuators for Flow Control," *AIAA Journal*, Vol. 35, May 1997, pp. 832-837.
- [9] Seifert A., Bachat T., Koss D., Shepshelovich M., Wygnanski I., "Oscillatory Blowing: A Tool to Delay Boundary-Layer Separation", *AIAA Journal*, Vol. 31, No. 11, Nov. 1993, pp. 2052-2060.
- [10] Seifert A., Eliahu S, Greenblatt D, Wygnanski I, "On the use of Piezoelectric Actuators for Airfoil Separation Control", submitted to AIAA Journal on 1/20/98, obtained by private communication with the authors.
- [11] Seifert, A., and Pack, L., "Oscillatory Excitation of Unsteady Compressible Flows Over Airfoils at Flight Reynolds Number", AIAA Paper No. 99-0925, January 1999.
- [12] Seifert, A. and Pack, L., "Oscillatory Control of Separation at High Reynolds Numbers", *AIAA Journal*, Vol. 37, No. 9, 1999, pp. 1062-1071.
- [13] Smith D., Amitay M., Kibens V., Parekh D. and Glezer A. "Modifications of Lifting Body Aerodynamics Using Synthetic Jet Actuators," AIAA Paper No. 98-0209, 36th Aerospace Sciences Meeting & Exhibit, Reno, NV, Jan. 1998.

LOCALIZED PERIODIC MOTIONS IN SYSTEMS OF COUPLED OSCILLATORS

V. Koukouloyannis, S. Ichtiaroglou

Department of Physics, Aristotle University of Thessaloniki, 54006 Thessaloniki, Greece
vkouk@skiathos.physics.auth.gr

1. SUMMARY

We study a one-dimensional chain of discrete nonlinear maps with a weak coupling. We consider solutions of the integrable anticontinuous limit, where one or more "central" oscillators move in resonant non-isolated periodic orbits while the other oscillators are at rest. We prove the continuation of these motions for weak non-zero coupling and determine their initial conditions and stability. We apply the above results and perform numerical investigation in the case where the uncoupled motion of each oscillator is described by the integrable Suris map.

2. CONTINUATION OF PERIODIC ORBITS AND STABILITY

We consider a two-dimensional map of the following form

$$\begin{aligned} x' &= x + 4\pi^2 y' \mod 2\pi \\ y' &= y + V'(x) \end{aligned} \quad (1)$$

where $V'(x)$ is a suitable function, such that the map (1) is integrable, i.e. it possesses an integral of motion Φ such that $\Phi(x', y') = \Phi(x, y) = c$. We assume that (1) has a stable fixed point, which can be assumed, without loss of generality, to be in $(x, y) = (0, 0)$.

Equations (1) define a canonical transformation, which can be constructed by a generating function of the second type,

$$S_0(y', x) = y'x + 2\pi^2 y'^2 - V(x)$$

by the relations

$$x' = \frac{\partial S_0}{\partial y'}, \quad y' = \frac{\partial S_0}{\partial x}.$$

We consider an infinite chain of oscillators, such that the motion of each one of them is described by the map (1) with a weak nearest-neighbor coupling that is controlled by a sufficiently small parameter ε .

$$\begin{aligned} x'_k &= x_k + 4\pi^2 y'_k \\ y'_k &= y_k + V'(x_k) + \varepsilon f(x_{k+1}, x_k, x_{k-1}) \end{aligned} \quad \forall k \in \mathbb{Z}. \quad (2)$$

We assume that the perturbed map is also symplectic and can be produced, from the generating function of the second type

$$S(y', x) = S_0(x, y') + \varepsilon S_1(x, y') = \sum_{k=-\infty}^{\infty} y'_k x_k + 2\pi^2 y_k'^2 - V(x_k) + \varepsilon \sum_{k=-\infty}^{\infty} F_k$$

by the equations
$$x'_k = \frac{\partial S}{\partial y'_k}, \quad y_k = \frac{\partial S}{\partial x_k}$$

with $F_k = F(x_k, x_{k-1})$ such that $f(x_{k+1}, x_k, x_{k-1}) = \frac{\partial F_{k+1}}{\partial x_k} + \frac{\partial F_k}{\partial x_k}$.

In the anticontinuous limit $\varepsilon = 0$, we consider the central oscillator ($k=0$) to be on a q -periodic point of a q/p resonant circle of (1), while the other oscillators lie on the stable fixed point $(0,0)$. We assume that this periodic motion of the integrable case is continued to a q -periodic motion of the system for sufficiently small but nonzero ε .

Since the periodic motion of the central oscillator for $\varepsilon = 0$ is non-isolated, the existence of unit eigenvalues of the tangent map L of (1) precludes the application of the usual continuation methods. In order to overcome this difficulty, we shall apply a method originally proposed by Poincaré ([4] §42) for Hamiltonian flows, which has recently been applied to symplectic maps by Wodnar et al. [6].

We perform the action-angle canonical transformation $(x, y) \rightarrow (w, J)$ to the central oscillator in the integrable case $\varepsilon = 0$. This transformation is defined as

$$J = \frac{1}{2\pi} \oint y(x, c) dx \quad \text{and} \quad w = \frac{\partial W}{\partial J} \quad \text{where} \quad W(x, c(J)) = \int y(x, c) dx.$$

Then (2) become

$$\begin{aligned} x'_k &= x_k + 4\pi^2 y'_k \\ y'_k &= y_k + V'(x_k) + \varepsilon f(x_{k+1}, x_k, x_{k-1}), \quad k \in \mathbb{Z}, \quad k \neq 0 \\ w'_0 &= w_0 + 2\pi\alpha(J_0) \\ J'_0 &= J_0 + \varepsilon f(x_1, x_0(w_0, J_0), x_{-1}). \end{aligned}$$

where $\alpha(J)$ is the rotation number and we assume that it holds $d\alpha/dJ \neq 0$. The periodicity conditions for q -periodic motion are

$$\begin{aligned} x_k^{(q)} - x_k^{(0)} &= g_{k_+}(x_k^{(0)}, y_k^{(0)}; \varepsilon) = 0 \\ y_k^{(q)} - y_k^{(0)} &= g_{k_-}(x_k^{(0)}, y_k^{(0)}; \varepsilon) = 0, \quad k \neq 0 \\ w_0^{(q)} - w_0^{(0)} &= 2\pi \sum_{n=0}^{q-1} \alpha(J_0^{(n)}) - 2\pi p + O(\varepsilon) = 0 \\ \frac{J_0^{(q)} - J_0^{(0)}}{\varepsilon} &= \frac{\partial \Sigma^{(q)}}{\partial w_0^{(0)}} + O(\varepsilon) = 0. \end{aligned}$$

By taking the limit $\varepsilon \rightarrow 0$ we obtain the conditions $a(J_0) = \frac{p}{q}$, $\frac{\partial \Sigma^{(q)}}{\partial w_0^{(0)}} = 0$, which must hold for the continuation.

The first of the above equations is the condition that the rotation number of the invariant circle $J_0 = \text{const.}$ must be rational for periodic motion. The second equation defines the points w_0 on the resonant circle, which may be continued as q -periodic points for $\varepsilon \neq 0$.

By using the results of the Krein theory we find that the continued motion is stable if the condition $\lambda^q \neq \pm 1$ is satisfied, where λ are the eigenvalues of the oscillators which lie

initially on the fixed point and they coincide for $\varepsilon = 0$ and q is the period of the motion. The localization of the periodic motion is proven by using Theorem 2 of [1].

3. APPLICATION TO THE COUPLED SURIS MAP

We consider that, for $\varepsilon = 0$, the motion of each oscillator is described by a simple case of the integrable symplectic Suris map [5] which is of the form (1) with

$$V'(x, \delta) = \frac{dV}{dx} = -\frac{1}{\pi^2} \arctan \left(\frac{\delta \sin x}{1 + \delta \cos x} \right)$$

where $0 < \delta < 1$ is a constant, which we select to be $\delta = 1/3$. This map is interesting because it is the only known symplectic, integrable map with a homoclinic loop, with integral

$$\Phi(x, y) = \cos(2\pi^2 y) + \delta \cos(x - 2\pi^2 y).$$

We put the nearest-neighbor coupling to be of the form

$$f(x_{k+1}, x_k, x_{k-1}) = \sin(x_{k+1} - x_k) + \sin(x_{k-1} - x_k).$$

By performing a stability analysis we discover that we cannot have stable solutions of period- q if

$$q = \frac{k\pi}{\cos^{-1} \left(\frac{1-\delta}{1+\delta} \right)}, \quad k \in \mathbb{Z}.$$

In our case, where $\delta = 1/3$ we cannot have stable solutions with $q = 3k$, $k \in \mathbb{Z}$.

For the numerical investigation we use a finite chain of $2N+1$ oscillators with fixed endpoints, i.e.

$$x'_N = x_N, \quad y'_N = y_N, \quad x'_{-N} = x_{-N}, \quad y'_{-N} = y_{-N}.$$

In order to calculate the initial conditions for a q -periodic breather solution, we need to know the point of the resonant torus of the Suris map which will be continued under small perturbation. We fix a q -periodic torus and we calculate the corresponding value $c = \Phi(x_0, y_0)$ of the integral on it. The generating function of the perturbation terms is

$$S_1 = \sum_{i=-(N+1)}^N \cos(x_{i+1} - x_i).$$

In order to apply the continuation method, we evaluate $\Sigma^{(q)} = \Sigma^{(q)}(x_0^{(0)}, y_0^{(0)})$, by using the map to the form (2) with the specific coupling. The continued periodic points are $O(\varepsilon)$ close to the points $(x_0^{(0)}, y_0^{(0)})$ where

$$\frac{\partial \Sigma^{(q)}}{\partial w_0}(x_0^{(0)}, y_0^{(0)}) = 0.$$

This derivative is

$$\frac{\partial \Sigma^{(q)}}{\partial w_0^{(0)}} = \frac{\partial \Sigma^{(q)}}{\partial x_0^{(0)}} \frac{\partial x_0^{(0)}}{\partial w_0^{(0)}} + \frac{\partial \Sigma^{(q)}}{\partial y_0^{(0)}} \frac{\partial y_0^{(0)}}{\partial w_0^{(0)}}. \quad (3)$$

We do not know the explicit expression of the derivatives of $x_0^{(0)}, y_0^{(0)}$ with respect to $w_0^{(0)}$ since the transformation to action-angle variables is not computable in this case. We know however the expression $y = y(x, c)$ (4) for the specified torus. Let W be the generating function of the transformation to action-angle variables. Then it holds that

$$w = \frac{\partial W}{\partial J} \quad \text{and} \quad y = \frac{\partial W}{\partial x}.$$

From the above relations we obtain

$$\frac{\partial w}{\partial x} = \frac{\partial y}{\partial J} = \frac{\partial y}{\partial c} \cdot \frac{dc}{dJ} \Leftrightarrow \frac{\partial x}{\partial w} = \left(\frac{\partial y(x, c)}{\partial c} \right)^{-1} \cdot \frac{dJ}{dc}$$

and

$$\frac{\partial y(x, c)}{\partial w} = \frac{\partial y}{\partial x} \frac{\partial x}{\partial w} \Leftrightarrow \frac{\partial y}{\partial w} = \frac{\partial y}{\partial x} \left(\frac{\partial y}{\partial c} \right)^{-1} \cdot \frac{dJ}{dc}.$$

Under the assumption that on the resonant circle the integral Φ does not attain a stationary value, (3) becomes

$$\frac{\partial \Sigma^{(q)}}{\partial x_0} + \frac{\partial \Sigma^{(q)}}{\partial y_0} \cdot \frac{\partial y_0(x_0, c)}{\partial x_0} = 0, \quad (5)$$

so we obtain the initial conditions (x_0, y_0) by solving the system of equations (4) and (5).

Since the point $(x_0^{(0)}, y_0^{(0)})$ is $O(\varepsilon)$ near the periodic orbit, we use a bisection method to approximate the initial conditions of the q -periodic orbit of the system for $\varepsilon \neq 0$.

With this method we evaluated several breather solutions for the system. In fig.1a period-8 breather is shown. The system consists of 31 ($N = 15$) oscillators. In order to visualize it, we take samples of $\Phi(x_i, y_i)$ which is used as a measure of the amplitude of the oscillations. The system is evolved for 1 million iterations of the map and the breather remains intact.

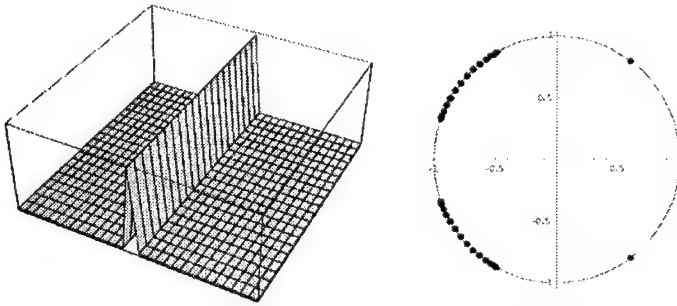


Fig1: The period-8 breather and the eigenvalues of L for $\varepsilon = 0.002$

If we increase the coupling parameter ε , the eigenvalues of L are moving and for a particular value of ε the eigenvalues of the central oscillator collide with the eigenvalues of another oscillator. This collision causes the eigenvalues to leave the unit circle and to generate complex instability. This fact forces the breather to, eventually, collapse (fig.2).

We want to obtain an estimation of the number of iterations which are needed for the breather to collapse. As a measure for this we use the number of iterations n needed in order for the central oscillator to change the value of Φ by an amount $\Delta\Phi \geq 1.5\%$ and plot n vs ε . Let d be the distance from the unit circle of the eigenvalue with the greatest modulus. We also plot b/d versus ε , where b is a constant scale factor. Since d is a measure of the instability, these two plots should look alike. As can be seen in fig.3, for $b = 80$ the two diagrams almost coincide.

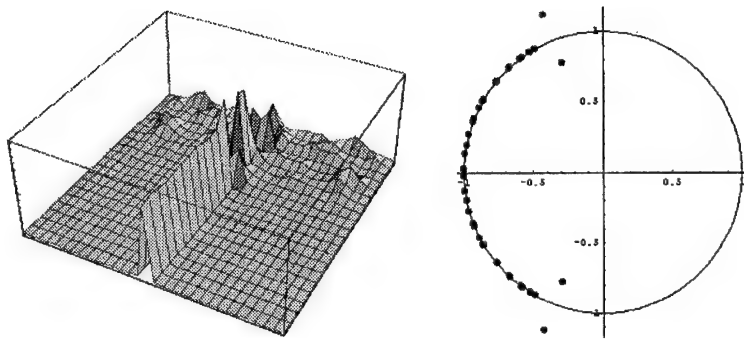


Fig. 2: The destruction of the period-8 breather caused by the complex instability

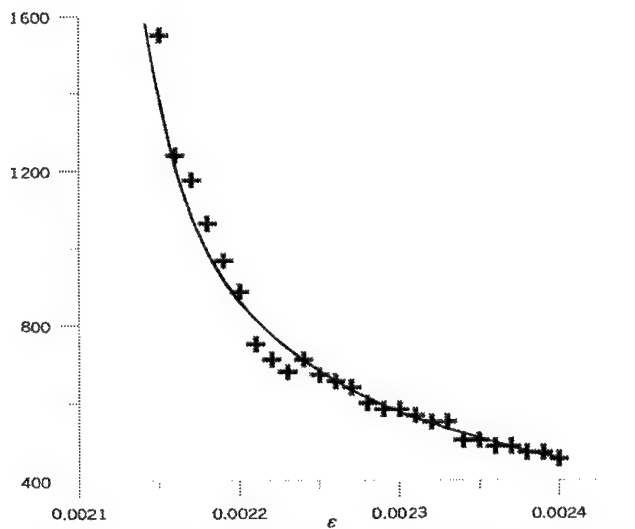


Fig. 3: Stability diagram of the period-8 breather vs. ϵ . The continuous line corresponds to b/d and the crosses to n .

4. REFERENCES

- [1] C. Baesens and R. S. MacKay, "Nonlinear localized periodic solutions in a coupled map lattice", *Nonlinearity* **10** 1997, pp. 931-940.
- [2] R. S. MacKay and S. Aubry, "Proof of existence of breathers for time-reversible or Hamiltonian networks of weakly coupled oscillators", *Nonlinearity* **7** (1994), pp. 1623-1643.

-
- [3] H. Poincaré, "Sur le Problème des Trois Corps et les Equations de la Dynamique", *Acta Math.* **13** (1890), pp.1-270.
 - [4] H. Poincaré, *Les Méthodes Nouvelles de la Méchanique Céleste*, Vol I, Gauthier-Villars, Paris, 1892. English translation: Goroff D.L. (ed.), *New Methods in Celestial Mechanics*, American Institute of Physics, 1993.
 - [5] Yu. B. Suris, "Integrable Mappings of the Standard Type", *Func. Anal. Appl.* **23** (1989), pp. 74-76.
 - [6] K. Wodnar, E. Meletlidou and S. Ichtiaroglou, "Non--integrability and Continuation of Fixed Points of $2n$ -dimensional Perturbed Twist Maps", *Physica D* **128** (1999), pp. 70-86.
 - [7] V. A. Yakubovich and V. M. Starzhinskii, *Linear Differential Equations with Periodic Coefficients*, Wiley, New York, 1975.

EFFECT OF THE PARAMETERS ON THE DYNAMIC BEHAVIOR OF A SMALL PARTICLE IN AN ANNULAR DISTRIBUTION OF N BODIES

T.J. Kalvouridis and F. Psarros

National Technical University of Athens, Department of Applied Mathematics and Physics,
Section of Mechanics, Athens, Greece

1. SUMMARY

The influence of the mass parameter on the dynamic behavior of a small body which subjects to the combined gravitational attraction of N bodies in an annular arrangement, is mainly investigated in this paper. Special attention is paid on the variation of the simple periodic orbits and their distribution in the phase space. The results obtained so far show that this parameter is a significant and fundamental factor which plays a decisive role on the dynamics of such systems.

2. INTRODUCTION

The N -body problem is still under investigation and the study of various proposed models is in the front-line of the scientific research. In this contribution we present some of the results obtained by investigating a symmetric $(N+1)$ -body system, called the "ring problem" after its geometric configuration (Kalvouridis, 1999). The small body S of negligible mass compared to the total mass of the system, moves under the combined gravitational attraction of N primaries, of which the $\nu=N-1$ have equal masses and are located at the vertices of a regular polygon, while the N th primary has a different mass and is located at the center of mass of the system (fig.1). Two parameters characterize the above system, the number of the peripheral primaries $\nu=N-1$ and the ratio β of the central mass to a peripheral one. The above general configuration reduces to many known problems of Celestial Dynamics as for example the Copenhagen case of the restricted three-body problem, the restricted five-body problem of Ollongren (1988), the restricted four-body problem proposed by Maranhao and Llibre (1995), the Caledonian problem (Roy and Steves, 1998,1999) and so on.

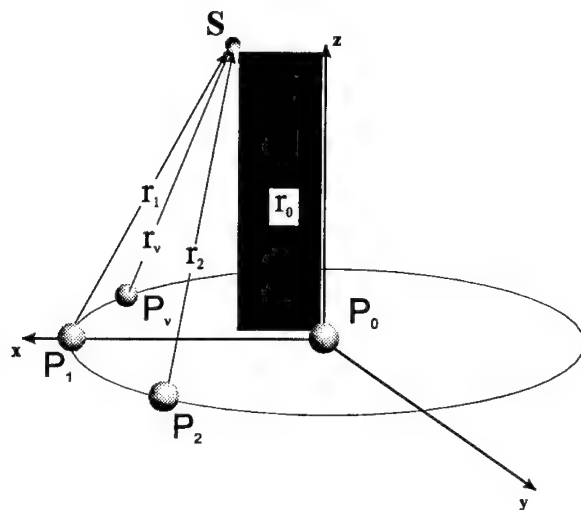


Figure 1. The general configuration of the ring problem.

We assume that the peripheral primaries are rotating with constant angular velocity. Then the motion of the small body S is described in a synodic reference coordinate system P_0xyz by means of the following differential equations

$$\begin{aligned}\ddot{x} - 2\dot{y} &= \frac{\partial U}{\partial x} \\ \ddot{y} + 2\dot{x} &= \frac{\partial U}{\partial y}, \\ \ddot{z} &= \frac{\partial U}{\partial z}\end{aligned}$$

whereas

$$U(x, y, z) = \frac{1}{2}(x^2 + y^2 + z^2) + \frac{1}{\Delta} \left[\frac{\beta}{r_0} + \sum_{i=1}^v \frac{1}{r_i} \right]$$

is the potential function, r_0 and r_i , $i = 1, \dots, v$ are the distances of the particle from each individual primary and $\Delta = M(\Lambda + \beta M^2)$, where Λ and M are given by the expressions

$$\Lambda = \sum_{i=2}^v \frac{\sin^2 \theta \cos(\frac{v}{2} + 1 - i)\theta}{\sin^2(v + 1 - i)\theta}, \quad M = [2(1 - \cos \psi)]^{\frac{1}{2}},$$

θ and ψ are the angles formed between the primaries.

The problem is autonomous and the equations of motion admit a Jacobian type integral of motion,

$$C = 2U - (\dot{x}^2 + \dot{y}^2 + \dot{z}^2)$$

where C is a constant.

3. THE CHARACTERISTIC CURVES OF THE PERIODIC ORBITS AND THEIR VARIATION WITH THE MASS PARAMETER

Periodic motions and the information we get from their study help us to understand better how the particular dynamic system behaves. Symmetric orbits, being a subset of the periodic orbits, have all their general qualitative characteristics and are easier to be found.

For each value of the parameter v we have a distinct configuration. As v increases, the number of the families of periodic orbits of any kind (simple or multiple) increases too.

In our case, we have considered a model consisting of $v=16$ co-orbital peripheral primaries and we have limited our research to the symmetric simple periodic orbits and their initial conditions lying in a rectangular area of the $C-x_0$ space which is determined by the values $-2.5 < x_0 < 0$ and $-2.2 < C < 2.5$. Although this area covers only part of the half plane of the phase space, the results obtained so far give us valuable information on the influence of the mass parameter on the particle motion when this parameter varies from $\beta=0.5$ to $\beta=100$. Due to the very extended range of the β values, any method based on the perturbation theory is not applicable. For this reason, we have studied numerically and separately for each value of β the equations of motion. Figures 2 and 3 show the distribution of the characteristic curves of nine families of simple periodic orbits found in the aforementioned area for the cases $\beta=0.5$ and $\beta=50$. Each family is assigned two letters. The first letter indicates the multiplicity of the orbits (S stands for simple periodic orbits), while the second denotes the name of the particular family.

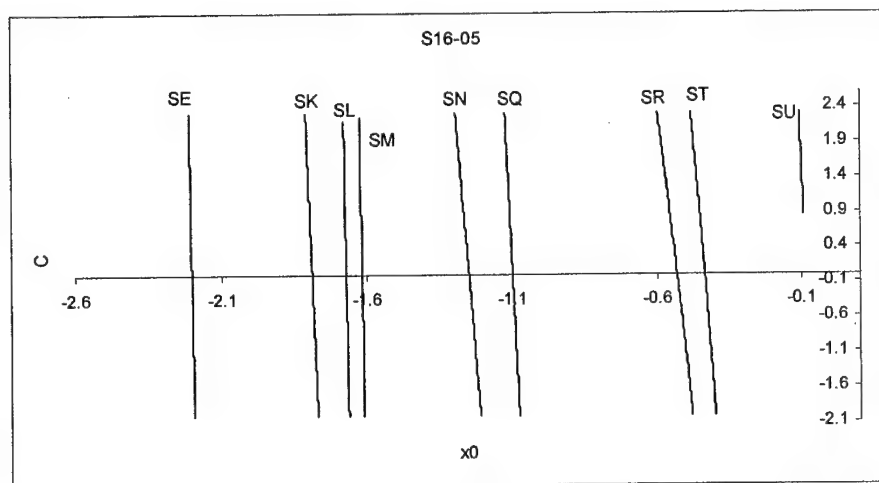


Figure 2. Distribution of the characteristics in the $C-x_0$ space for the case $\beta=0.5$.

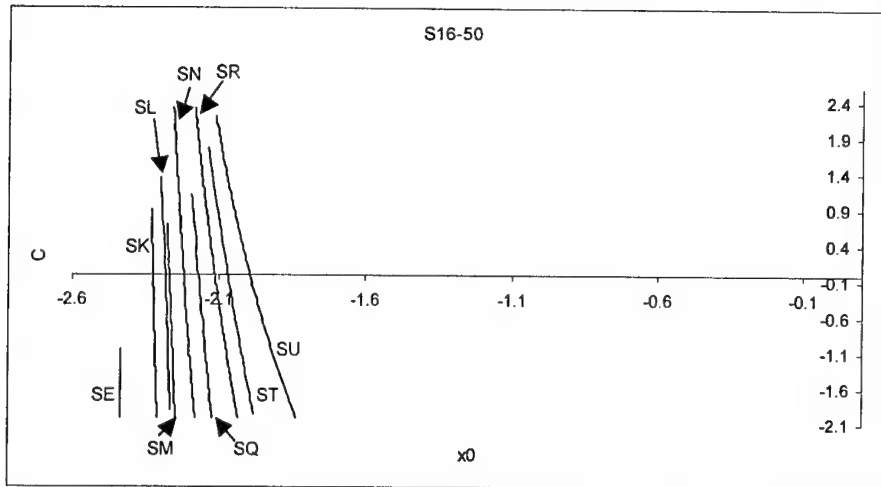


Figure 3. Distribution of the characteristics in the C - x_0 space for the case $\beta=50$.

Comparing figures 2 and 3, one can easily notice, that the curves of the families are shifted to the left and at the same time they approach each other, as the mass parameter increases. For very large values of β ($\beta > 1000$) the families are so crowded in a very narrow region near the limiting circle of the peripheral primaries that it is extremely difficult to distinguish them. We also observe that for large β these curves start to bend, especially those which "face" the central primary. The curves usually end following the Birkhoff's termination principle (Szebehely, 1967).

The particle is moving around and between the primaries, it winds and twists and it forms peculiar shapes. It encircles two or more peripheral and maybe the central primary. The orbits are simple or double symmetric. In figures 4 and 5 we have plotted some members of two concrete families, namely SL and ST for various values of β . We observe that the orbits grow and they are gradually approaching the peripheral primaries as the mass parameter increases. For very large values of β these orbits become more or less circular tending to the periphery of the circle where the primaries are arranged. From this point onwards, serious problems arouse from the fact that the particle comes very near to the primaries. Then the numerical integration fails and a regularization process must be applied. It also may be noted that for a given C , the period of the orbits of a family increases with β . On the contrary the velocity at the half period decreases when β increases.

The stability of the orbits has been determined in the sense of Liapunov. We denote by U the unstable orbits and by S the stable ones. We have noticed that there is not a change on the stability status for the considered interval of the β values. Tables I and II contain some measures of the orbits exposed in the figures.

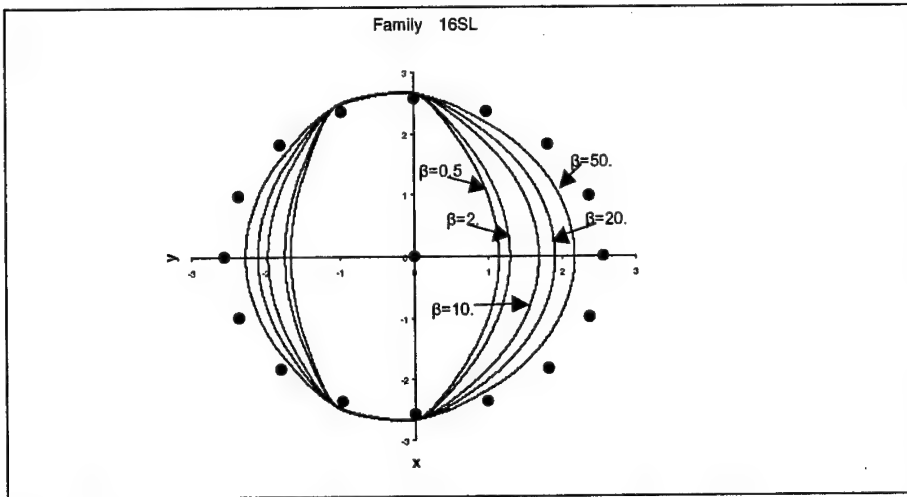


Figure 4. Evolution of the simple periodic orbits of the family SL for various values of the mass parameter β and for $C = -1.0$. The dots show the positions of the primaries.

TABLE I. Family SL ($C = -1.0$).

β	x_0	\dot{y}_0	$x_{T/2}$	$\dot{y}_{T/2}$	$T/2$	S
0.5	-1.66959891	5.96324123	1.14049500	-5.68717020	1.03428813	U
2.0	-1.74729982	5.85010338	1.29069626	-5.68402666	1.08344362	U
10.	-1.97511911	5.45456988	1.68219277	-5.40441478	1.25727849	U
20.	-2.10834741	5.22110100	1.89954502	-5.18267738	1.37379810	U
50.	-2.27502530	4.96275089	2.16349487	-4.92497666	1.52725479	U

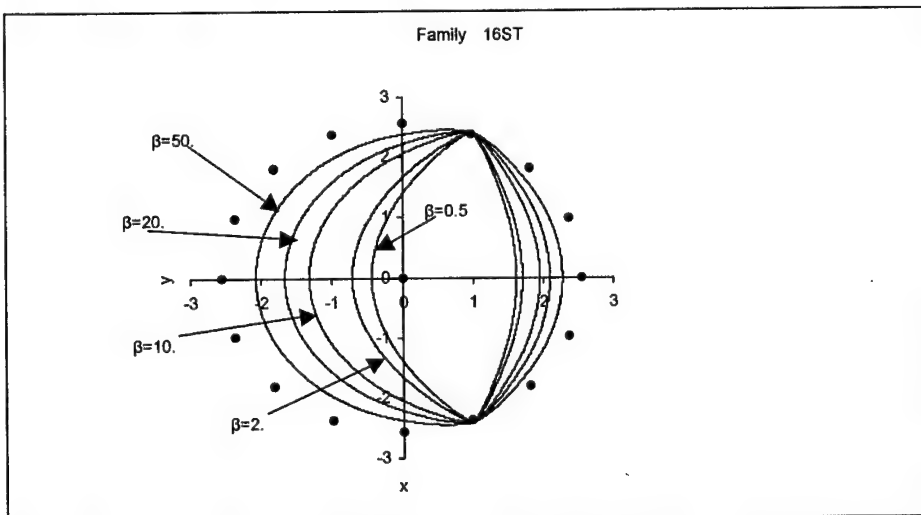


Figure 5. Evolution of the simple periodic orbits of the family ST for various values of the mass parameter β and for $C = 0.1$. The dots show the positions of the primaries.

TABLE II. Family ST (C=0.1).

β	x_0	\dot{y}_0	$x_{T/2}$	$\dot{y}_{T/2}$	$T/2$	S
0.5	-0.43779297	5.64340962	1.61936971	-5.83333769	0.88126701	U
2.	-0.71258398	5.77476132	1.70503663	-5.72973039	0.93714088	U
10.	-1.32046680	5.41853808	1.95133098	-5.34309962	1.14335588	U
20.	-1.66639844	5.11912683	2.09444587	-5.10896339	1.29412835	U
50.	-2.07611279	4.80648786	2.27230469	-4.84909250	1.49934665	U

4. CONCLUSIONS AND REMARKS

As it is expected, the mass parameter plays an important role not only on the distribution of the characteristic curves in the phase space, but also on the evolution and the particular features of the orbits themselves. In any case, as the mass parameter increases, all the simple periodic orbits tend to become circular approaching the circle of the primaries. We hope that a further study of this effect in more complicated models, that is with more peripheral primaries, will provide additional information on the dynamics of such systems.

5. REFERENCES

- [1] Kalvouridis, T., J.:1999, "A planar case of the $n+1$ body problem: The ring problem", *Astrop.Sp.Sci.*, **260** (3), 309-325.
- [2] Kalvouridis, T.J.: 1999, "Periodic solutions in the ring problem", *Astroph. Sp. Sci.*, **266**, No 4, 467-494.
- [3] Maranhao, D., Llibre, J.: 1999, "Ejection- collision orbits and invariant punctured tori in a restricted four-body problem", *Cel.Mech. and Dynam. Astron.*, **71**, 1-14.
- [4] Ollongren, A. : 1988, "On a particular restricted five- body problem. An analysis with Computer Algebra", *J. Symbolic Computation*, **6**,117-126.
- [5] Roy, A.E., Steves, B.A. : 1998, "Some special restricted four-body problems-II From Caledonian to Copenhagen", *Planet.Space Sci.*, **46**, No 11/12, 1475-1486.
- [6] Steves, B. A., Roy, A.E. : 1998, *Some special restricted four-body problems- I. Modeling the Caledonian problem*", *Planet.Space Sci.*, **46**, No 11/12, 1465-1474.
- [7] Szebehely, V.: 1967, "Theory of orbits", Academic Press.

6th National Congress on Mechanics

Special Session

Volume II

RESEARCH AND CHALLENGES OF ENGINEERING MECHANICS AND MATERIALS IN THE TWENTY FIRST CENTURY

Ken P. Chong

Director of Mechanics and Materials Program, Directorate for Engineering
National Science Foundation, Arlington, VA 22230, USA

Daniel C. Davis

Dean, School of Science and Technology, Texas Southern Univ., Houston,
TX 77004, USA [Formerly at the National Science Foundation]

1. SUMMARY

Mechanics and materials are essential elements in all of the transcendent technologies in the twenty first century and in the new economy. The transcendent technologies include nanotechnology, microelectronics, information technology and biotechnology. Research opportunities and challenges of the theoretical and applied mechanics as well as engineering materials in the exciting information age are presented and discussed.

2. INTRODUCTION

The National Science Foundation (NSF) has supported basic research in engineering and the sciences in the United States for a half century and it is expected to continue this mandate through the next century. As a consequence the United States is likely to continue to dominate vital markets because diligent funding of basic research does confer a preferential economic advantage [1]. Concurrently over this past half century, technologies have been the major drivers of the U. S. economy, and as well, NSF has been a major supporter of these technological developments. According to the former NSF Director for Engineering, Eugene Wong, there are three *transcendental* technologies [2]:

- Microelectronics – Moore's Law: doubling the capabilities every two years for the last 30 years; unlimited scalability; nanotechnology is essential to continue the miniaturization process.
- Information Technology [IT] – NSF and DARPA started the Internet revolution about three decades ago; confluence of computing and communications.
- Biotechnology – molecular secrets of life with advanced computational tools as well as advances in biological engineering, biology, chemistry, physics, engineering including mechanics and materials.

By promoting research and development at critical points where these technological areas intersect, NSF can foster major developments in engineering. The solid mechanics and materials engineering (M&M) communities will be well served if some specific linkages or alignments are made toward these technologies. Some thoughtful examples for the M&M communities are:

- | | |
|---------------------------------|---|
| • Bio-mechanics/materials | • Simulations/modeling |
| • Thin-film mechanics/materials | • Micro-electro-mechanical systems (MEMS) |
| • Wave Propagation | • Smart materials/structures |
| • Nano-mechanics/materials | • Designer materials |

Considerable NSF resources and funding will be available to support basic research related to these technologies. These opportunities will be available for the individual investigator, teams, small groups and larger interdisciplinary groups of investigators. Nevertheless, most of the funding at NSF will continue to support unsolicited individual investigator proposals on innovative "blue sky" ideas.

3. IT AND NANOTECHNOLOGY

In addition to NSF, there is also a sense that U. S. Federal agency research support is increasingly being driven by broad systemic initiatives. One of these initiative is *Information Technology* (IT), listed above as one of the *transcendental* technologies. The former President's Information Technology Advisory Committee (PITAC) advised that an "immediate and vigorous information technology research and development (R&D) effort in Information Technology be initiated. IT is essential for the United States to have economic growth and prosperity in the 21st Century." PITAC (www.ccic.gov) concluded that current U. S. Federal support for research in IT is inadequate and these current efforts also take "a short-term focus for immediate returns." PITAC recommends IT R&D with long term priorities focusing on "software development that is far more usable, reliable, and powerful, scalable information infrastructures that satisfy the demands of large numbers of users, high-end computing systems with both rapid calculation and rapid data movement, and IT education and training for the citizenry." Achieving these ends requires diversified modes of research support to foster projects of broader scope, longer duration and emphasis on projects involving multiple investigators over several years. Of most importance is using these new information technologies to advance critical application domains for the benefit our nation and the world.

Initiated by the senior author [KPC], with the organization and help of researchers from Brown [K. S. Kim, et al], Stanford, Princeton and other universities, a NSF Workshop on Nano- and Micro-Mechanics of Solids for Emerging Science and Technology was held at Stanford in October 1999. The following is extracted from the Workshop Executive Summary. Recent developments in science have advanced capabilities to fabricate and control material systems on the scale of nanometers, bringing problems of material behavior on the nanometer scale into the domain of engineering. Immediate applications of nanostructures and nano-devices include quantum electronic devices, bio-surgical instruments, micro-electrical sensors, functionally graded materials, and many others with great promise for commercialization. The branch of mechanics research in this emerging field can be termed nano- and micro-mechanics of materials. A particularly challenging aspect of fostering research in the nano- and micro-mechanics of materials is its highly cross-disciplinary

character. Important studies of relevance to the area have been initiated in many different branches of science and engineering. A subset of these, which is both scientifically rich and technologically significant, has mechanics of solids as a distinct and unifying theme. The presentations at the workshop, and the open discussion precipitated by them, revealed the emergence of a range of interesting lines of investigation built around mechanics concepts which have potential relevance to microelectronics, information technology, bio-technology and other branches of nanotechnology. It was also revealed, however, that the study of complex behavior of materials on the nanometer scale is in its infancy. More basic research, which is well coordinated and which capitalizes on progress being made in other disciplines, is needed if this potential for impact is to be realized. In addition to the expected benefit to the target areas, such research invariably advances other technologies, conventional or emerging, through a spill-over effect; this serendipitous benefit can also be anticipated from focused mechanics research in nano technology.

Recognizing that this area of nanotechnology is in its infancy, substantial basic research must be done to establish an engineering science base; this link between the discoveries of basic science and the design of commercial devices must be completed to realize the potential of this area. Such a commitment to nano-and micro-mechanics will lead to a strong foundation of understanding and confidence underlying this technology based on capabilities in modeling and experiment embodying a high degree of rigor. The potential of various concepts in nanotechnology will be enhanced, in particular, by exploring the nano- and micro-mechanics of coupled phenomena and of multi-scale phenomena. Examples of coupled phenomena discussed in this workshop include modification of quantum states of materials caused by mechanical strains, ferroelectric transformations induced by electric field and mechanical stresses, chemical reaction processes biased by mechanical stresses, and change of bio-molecular conformality of proteins caused by environmental mechanical strain rates. Multi-scale phenomena arise in situations where properties of materials to be exploited in applications at a certain size scale are controlled by physical processes occurring on a size scale which are orders of magnitude smaller. Important problems of this kind arise, for example, in thermo-mechanical behavior of thin-film nano-structures, evolution of surface as well as bulk nano-structures caused by various material defects, nano-indentation, nano-tribological response of solids, and failure processes of MEMS structures. Details of this workshop report can be found in: [<http://en732c.engin.brown.edu/nsfreport.html>].

Coordinated by M. Roco, NSF recently announced a program [NSF 00-119; see: www.nsf.gov] on collaborative research in the area of nanoscale science and engineering. The goal of this program is to catalyze synergistic science and engineering research in emerging areas of nanoscale science and technology, including: biosystems at nanoscale; nanoscale structures, novel phenomena, and quantum control; device and system architecture; design tools and nanosystems specific software; nanoscale processes in the environment; multi-scale, multi-phenomena modeling and simulation at the nanoscale; and studies on societal implications of nanoscale science and engineering. This program or initiative provides support for: Nanoscale Interdisciplinary Research Teams (NIRT), Nanoscale Science and Engineering Centers (NSEC), and Nanoscale Exploratory Research (NER). Key research areas have been identified in advanced materials, nanobiotechnology (e.g. nano-photosynthesis), nanoelectronics, advanced healthcare, environmental improvement, efficient energy conversion and storage, space exploration, economical transportation, and bionanosensors. The National Nanotechnology Initiative (NNI - published on February 7, 2000 and is available on www.nano.gov) will ensure that investments in this area are made in

a coordinated and timely manner (including participating federal agencies – NSF, DOD, DOE, EPA and others), and will accelerate the pace of revolutionary discoveries now occurring. In addition, individual investigator research in nanoscale science and engineering will continue to be supported in the relevant Programs and Divisions outside of this initiative.

4. DISCUSSION

Consistent with this theme, the National Science Foundation Directorate for Engineering in collaboration with other NSF Directorates and Federal agencies recently announced several IT-related initiatives. The NSF Directorate for Computer and Information Science and Engineering (CISE) and the Directorate for Engineering in cooperation with Division of International Programs jointly announced the *Wireless Information Technology and Networks* initiative (Program Announcement NSF 99-68) in early 1999. “The great demand for Internet services, wireless cable television distribution, and information technology, makes the development of broadband wireless mobile communication systems a national imperative in the 21st Century.” Researchers face many technical challenges, but “data rates of tens of megabits per second (enabling broadband Internet access, for example) are apparently realizable in the near future.”

The Engineering Directorate research initiative on *Engineering Microsystems: “XYZ on a Chip”* (Program Announcement NSF 99-31) focuses on non-electronic applications of microelectronic technologies and exploration of non-electrical processes at the micro-scale. Here XYZ refers to any non-electrical phenomena such as “biology, genomics, chemistry, optics, mechanics, materials, sensors, actuators, and software.” Examples of solid mechanics and materials engineering XYZ related phenomena could include MEMS, nanomechanics, microactuation, etc.

The initiative *Engineering Sciences for Modeling and Simulation-Based Life-Cycle Engineering* (Program Announcement NSF 99-56) is a three-year collaborative research program by NSF and the Sandia National Laboratories (Sandia) focusing on advancing the fundamental knowledge needed to support advanced computer simulations. This collaborative initiative capitalizes on the missions of both organizations. NSF’s mission is to advance the fundamental science and engineering base of the United States. Sandia has the responsibility to provide solutions to a wide range of engineering problems pertinent to national security and other national issues. It is moving toward engineering processes in which decisions are based heavily on computational simulations [see e.g. Ref. 3]; thus, capitalizing on the available high performance computing platforms. This initiative has sought modeling and simulation advances in key engineering focus areas such as thermal sciences, mechanics and design. About 24 awards were made totaling \$7m.

The NSF-wide research initiative, *Biocomplexity: Research on the Functional Interrelationships between Microorganisms and Biological, Chemical, Geological, Physical and Social Systems* [NSF 00-22], is a long-term effort to support “integrated research on the functional interrelationships between microorganisms and the biological, chemical, geological, physical, and/or social systems that jointly comprise complex systems.” Understanding biological complexity requires sophisticated approaches of integrating scientists from a range of disciplines. These include: “biology, physics, chemistry, geology, hydrology, social sciences, statistics, mathematics, computer science and engineering

(including mechanics and materials)." These collaborations cannot be constrained by institutional, departmental or disciplinary boundaries.

The NSF Civil and Mechanical Systems (CMS) Division developed an initiative on *Model-based Simulation* (MBS), see (NSF 00-26). Model-based simulation is a process that integrates physical test equipment with system simulation software in a virtual test environment aimed at dramatically reducing product development time and cost. This initiative will impact many civil/mechanical areas: "structural, geotechnical, materials, mechanics, surface science, and natural hazards (e.g., earthquake, wind, tsunami, flooding and land-slides)." MBS would involve "combining numerical methods such as finite element and finite difference methods, together with statistical methods and reliability, heuristics, stochastic processes, etc., all combined using super-computer systems to enable simulations, visualizations, and virtual testing." Expected results could be fewer physical testing, or at best, better strategically planned physical testing in the conduct of R&D. Examples of the use of MBS in research, design and development exist in the atmospheric sciences, biological sciences, and the aerospace, automotive and defense industries. The manufacturing of the prototype Boeing 777 aircraft, for example, was based on computer-aided design and simulation.

In the future one should expect the continued introduction of bold innovative research initiatives related to important national agenda such as the environment, civil and mechanical infrastructure, the service industry and the business enterprises.

5. CHALLENGES

The challenge to the mechanics and materials research communities is: How can we contribute to these broad-base and diverse research agenda? Although the mainstay of research funding will support the traditional programs for the foreseeable future, considerable research funding will be directed toward addressing these research initiatives of national focuses. At the request of the senior author [KPC] a NSF research workshop has been organized by F. Moon of Cornell University to look into the research needs and challenges facing the mechanics communities.

Mechanics and materials engineering are really two sides of a coin, closely integrated and related. For the last decade this cooperative effort of the M&M Program has resulted in better understanding and designed of materials and structures across all physical scales, even though the seamless and realistic modeling of different scales from nano-level to system integration-level (Fig. 1) is not yet attainable. In the past, engineers and material scientists have been involved extensively with the characterization of given materials.

MATERIALS		STRUCTURES		INFRASTRUCTURE
nano-level (10^{-9})	micro-level (10^{-6})	meso-level (10^{-3})	macro-level (10^{+0})	systems-level (10^{+3}) m
<i>Molecular Scale</i>	<i>Microns</i>	<i>Meters</i>	<i>Up to Km Scale</i>	
*nano-mechanics	*micro-mechanics	*meso-mechanics	*beams	* bridge systems
*self-assembly	*micro-structures	*interfacial-structures	*columns	* lifelines
*nanofabrication	* smart materials	*composites	*plates	*airplanes

Fig. 1. Physical scales in materials and structural systems [6]

With the availability of advanced computing, and new developments in material sciences, researchers can now characterize processes, design and manufacture materials with desirable performance and properties. One of the challenges is to model short-term micro-scale material behavior, through meso-scale and macro-scale behavior into long term structural systems performance. Accelerated tests to simulate various environmental forces and impacts are needed [NSF 98-42]. Supercomputers and/or workstations used in parallel are useful tools to solve this scaling problem by taking into account the large number of variables and unknowns to project micro-behavior into infrastructure systems performance, and to model or extrapolate short term test results into long term life-cycle behavior [4, 5].

6. ACKNOWLEDGMENTS AND FEEDBACK

The authors would like to thank their colleagues and many members of the research communities for their comments and inputs during the writing of this opinion paper. We would appreciate further feedback from the research communities at large. We can be reached by e-mail at: [kchong@nsf.gov] and [Davis_DC@TSU.EDU]. Information on NSF initiatives, announcements and awards can be found in the NSF website:[www.nsf.gov].

7. DISCLOSURE AND COPYRIGHT POLICY

The opinions expressed in this article are the authors only, not necessarily those of the National Science Foundation nor representative of their positions at NSF. This paper was written by U.S. Government employees. It may not be copyrighted and is intended for wide dissemination. An earlier version of this paper has been published in *AAM Mechanics* and elsewhere.

8. REFERENCES

- [1] Wong, E. "An Economic Case for Basic Research", *Nature*, Vol. 381, pp.187-188, May. (1996)
- [2] Wong, E. "Engineering the Service Industry," www.eng.nsf.gov/engnews/1999, 5 pp. (1999).
- [3] Boresi, A. P., Chong, K. P. and Saigal, S., *Approximate Solution Methods in Engineering Mechanics*, John Wiley, New York (2001).
- [4] NSF "Long Term Durability of Materials and Structures: Modeling and Accelerated Techniques", NSF 98-42, National Science Foundation, Arlington, VA. (1998)
- [5] Chong, K. P. "Smart Structures Research in the U.S.", *Keynote paper, Proc. NATO Adv. Res. Workshop on Smart Structures*, held in Pultusk, Poland, 6/98, *Smart Structures*, Kluwer Publ. (1999) pp. 37-44.
- [6] Boresi, A. P. and Chong, K. P. *Elasticity in Engineering Mechanics*, John Wiley, New York (2000).

DAMAGE MECHANICS APPLICATION ON REPAIR OF DESTROYED STRUCTURES

D. Sumarac

Department of Civil Engineering
University of Belgrade, YU-11000 Belgrade, Yugoslavia

1. SUMMARY

In the present paper the way of determination of elastic parameters of the body weakened by elliptical voids is presented. Starting from arbitrary placed single elliptical void in plane sheet, decrease of Young's modulus and Poisson's ratio is obtained. After that, using statistical distribution of voids, the decrease of overall elastic constants is found. In this procedure there are two ways, Taylor and Self-consistent model. In the first method interaction of defects is ignored, while in the second, so-called weak interaction is incorporated. Both methods are applied for small concentration of defects. In the case of large concentration of voids Aifantis' gradient approach can be applied. In the paper it is shown that cracks and circles are special cases of the model derived in this study. Such obtained model is applied for determination of stiffness of steel members of the truss of bridge destroyed during last war by shrapnel of bombshells. Such calculated stiffness is input for static and dynamic analysis of bridges using FEM. This approach is applied for analysis of The Pivnica Bridge, across The Ibar River, on the railway track Belgrade-Thessaloniki, destroyed during last war. It is shown that with increasing a damage of members of the bridge the time period of free vibrations is increasing to, while natural frequency is decreasing. For such destroyed and repaired structures special attention should be paid to the problem of fatigue.

2. PLANE SHEET WEAKEND BY ELIPTICAL VOID

Consider the problem of the elliptic cylinder ($a_3 \rightarrow \infty$) (Fig.1.) embedded in the elastic isotropic material with the same elastic parameters E (Young's modulus) and ν (Poisson's ratio). Eshelby in his 1957 [1] paper referred to "eigenstrains" as stress-free transformation strains. He proved that the uniform "eigenstrain" ϵ_{ij}^* within the elliptical inclusion, cause the uniform "eigenstresses" σ_{ij}^* in the same region (see also Mura, [4]):

$$\sigma_{11}^* = \frac{\mu}{1-\nu} \left\{ -2 + \frac{a_2^2 + 2a_1a_2}{(a_1 + a_2)^2} + \frac{a_2}{a_1 + a_2} \right\} \epsilon_{11}^*$$

$$\begin{aligned}
& + \frac{\mu}{1-\nu} \left\{ \frac{a_2^2}{(a_1+a_2)^2} - \frac{a_2}{a_1+a_2} \right\} \varepsilon_{22}^* - \frac{2\mu\nu}{1-\nu} \frac{a_1}{a_1+a_2} \varepsilon_{33}^* \\
\sigma_{22}^* &= \frac{\mu}{1-\nu} \left\{ -2 + \frac{a_1^2 + 2a_1a_2}{(a_1+a_2)^2} + \frac{a_1}{a_1+a_2} \right\} \varepsilon_{22}^* \\
& + \frac{\mu}{1-\nu} \left\{ \frac{a_1^2}{(a_1+a_2)^2} - \frac{a_1}{a_1+a_2} \right\} \varepsilon_{11}^* - \frac{2\mu\nu}{1-\nu} \frac{a_2}{a_1+a_2} \varepsilon_{33}^* \\
\sigma_{33}^* &= -\frac{2\mu\nu}{1-\nu} \frac{a_1}{a_1+a_2} \varepsilon_{11}^* - \frac{2\mu\nu}{1-\nu} \frac{a_2}{a_1+a_2} \varepsilon_{22}^* - \frac{2\mu}{1-\nu} \varepsilon_{33}^* \\
\sigma_{12}^* &= -\frac{2\mu}{1-\nu} \frac{a_1a_2}{(a_1+a_2)^2} \varepsilon_{12}^* \\
\sigma_{23}^* &= -2\mu \frac{a_2}{a_1+a_2} \varepsilon_{23}^* \\
\sigma_{31}^* &= -2\mu \frac{a_2}{a_1+a_2} \varepsilon_{31}^*
\end{aligned} \tag{2.1}$$

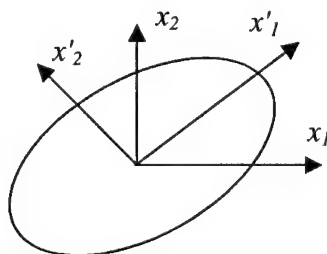


Fig.1. Elliptical void (inclusion) in the global and local (primed) coordinate system

In the above expressions $a_1=a$ and $a_2=\alpha a$ are half axes of the elliptical region, while μ and ν are the shear modulus and Poisson's ratio respectively. According to equivalent inclusion method, Mura 1987 [4], the total stress within the elliptical region under far field stresses σ_{ij}^* , and one that is caused by the "eigenstrain" given by the expressions (2.1) should be zero everywhere in the elliptical region if the region should represent the void:

$$\sigma_{11}^* + \sigma_{11}^* = 0, \quad \sigma_{22}^* + \sigma_{22}^* = 0, \quad \sigma_{12}^* + \sigma_{12}^* = 0. \tag{2.2}$$

Expression (2.2) is written for plane stress condition. Substituting governing values from the expression (2.1) into (2.2) leads to the system of equations with respect to unknown "eigenstrains" ε_{11}^* , ε_{22}^* and ε_{12}^* . The solution of the system of equations is:

$$\left. \begin{aligned}
\varepsilon_{11}^* &= \frac{1-\nu}{2\mu} \left[(1+2\alpha)\sigma_{11}^* - \sigma_{22}^* \right] \\
\varepsilon_{22}^* &= \frac{1-\nu}{2\mu} \left[\frac{2+\alpha}{\alpha}\sigma_{22}^* - \sigma_{11}^* \right] \\
\varepsilon_{12}^* &= \frac{1-\nu}{2\mu} \frac{(1+\alpha)^2}{\alpha} \sigma_{12}^*
\end{aligned} \right\} \tag{2.3}$$

Once the ε_{ij}^* are known, the increase of the strain energy of the body due to presence of elliptical void is obtained as:

$$\Delta W = -\frac{1}{2} V \sigma'_{ij} \varepsilon_{ij}^* = -\frac{1}{2} \pi a_1 a_2 \sigma'_{ij} \varepsilon_{ij}^*, \quad (2.4)$$

Substituting (2.3) into (2.4) yields to:

$$\Delta W = \frac{\pi \alpha a^2}{2E} \left[(1+2\alpha)(\sigma'_{11})^2 - 2\sigma'_{11}\sigma'_{22} + \frac{(2+\alpha)}{\alpha}(\sigma'_{22})^2 + \frac{2(1+\alpha)^2}{\alpha}(\sigma'_{12})^2 \right] \quad (2.5)$$

Differentiating expressions (2.5) twice with respect to stresses yields to the compliances:

$$S_{ij}^{(k)*} = \frac{\partial^2 W}{\partial \sigma'_i \partial \sigma'_j} \quad (2.6)$$

where Voigt notation, $\sigma'_1 = \sigma'_{11}$, $\sigma'_2 = \sigma'_{22}$ and $\sigma'_6 = \sigma'_{12}$ is used. Also in the expression (2.6) (k) refers to a single elliptical void and (*) stands for the increase of the governing value of the compliance due to presence of the void. Once the compliances $S_{ij}^{(k)*}$, in the local coordinate system are determined, using the transformation rule, Horii and Nemat-Nasser [2] the compliances in the global coordinate system $S_{ij}^{(k)*}$ can be determined.

Mean field theory (uniform distribution of voids)

In the case of many voids the total compliance would be, Horii and Nemat-Nasser [2], Sumarac and Krajcinovic [5]:

$$\bar{S}_{ij} = S_{ij} + \bar{S}_{ij}^* \quad (2.7)$$

In the above expression (*) refers to the increase of the value due to presence of voids, and S_{ij} is the compliance matrix of the undamaged (virgin) material.

In the case of Taylor model system of equation (2.7) leads to:

$$\frac{\bar{E}^{tm}}{E} = \frac{1}{1 + \omega(\alpha^2 + \alpha + 1)}, \quad (2.8)$$

$$\frac{\bar{v}^{tm}}{v} = \frac{1 + \frac{\omega\alpha}{v}}{1 + \omega(\alpha^2 + \alpha + 1)}. \quad (2.9)$$

In the case of Self-consistent model equations (2.7) are:

$$\frac{1}{\bar{E}} = \frac{1}{E} + \frac{\omega}{\bar{E}}(\alpha^2 + \alpha + 1), \quad -\frac{\bar{v}}{\bar{E}} = -\frac{v}{E} - \frac{\omega}{\bar{E}}\alpha. \quad (2.10)$$

Solution of them is:

$$\frac{\bar{E}^{sc}}{E} = 1 - \omega(\alpha^2 + \alpha + 1), \quad (2.11)$$

$$\frac{\bar{v}^{sc}}{v} = 1 - \omega(\alpha^2 + \alpha + 1) + \frac{\omega\alpha}{v}. \quad (2.12)$$

The total overall compliance for matrix in the case of Self-consistent approximation for uniform distribution of elliptical voids is:

$$\frac{\bar{S}_{ij}^{sc}}{S_{ij}} = \begin{bmatrix} \frac{1}{1-\omega A} & -1 - \frac{\omega \alpha}{v(1-\omega A)} & 0 \\ -1 - \frac{\omega \alpha}{v(1-\omega A)} & \frac{1}{1-\omega A} & 0 \\ 0 & 0 & \frac{1+v-\omega v A + \omega \alpha}{(1+v)(1-\omega A)} \end{bmatrix} \quad (2.13)$$

3. DAMAGE AND REPAIR OF BRIDGE PIVNICA

In the present paper the damage of the bridge Pivnica across The Ibar River on the railway Belgrade-Thessaloniki is presented. The bridge was destroyed during the bombardment of our country. Rebuilding of the bridge was performed using one temporary support at the place of most severe damage. The two new spans were built in factory, but other damage was repaired on site. The static and dynamic characteristics of rebuild structure are analyzed in the present paper according to damage mechanics and theory of structures. It is shown that for more amount of damage structure of the bridge becomes more compliant or in another words period of free vibration is slightly increased. In the paper the problem of fatigue of material, especially of parts which undergone the low cycle fatigue is shortly outlined.

Bridge Pivnica was hit during bombardment two times. First bombshell hit the middle part of bridge, but it didn't fell down. Second projectile hit diagonal above support, and then bridge felt into river (Fig.2). Due to impact, the bottom members suffered plastic deformation. Besides that there was a lot of damages due to bomb shrapnel. Holes in the members can be approximated as ellipses. In the first section it is explained in details how the decrease of Young's modulus can be expressed in terms of damage, see eq.(2.8) and (2.11). It should be noted that for reconstruction of bridge it is spent 75t of steel. Total weight of the bridge is 440t (Fig.4). In Fig.3. statical scheme is shown for finite element method.

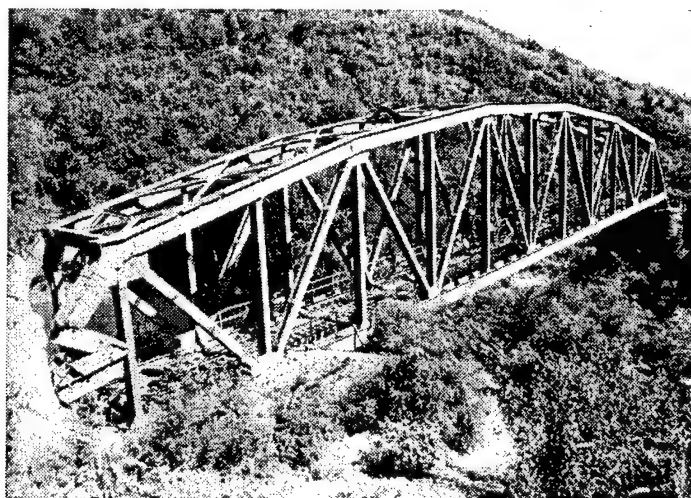


Figure 2: Destroyed bridge Pivnica

Dynamical characteristics of reconstructed bridge

All static and dynamic characteristics are analyzed using FEM procedure. First step was to find free vibrations for first three modes. They are: $T_1=0.731s$, $T_2=0.2491s$, $T_3=0.1212s$. For the damaged bridge it is calculated $\omega=0.1$, $\omega=0.2$ and $\omega=0.3$ for the two spans of bottom members and four spans of top members. For instance in case of $\omega=0.3$ $T_2(\omega=30\%)=0.2551$. This result was expected. If structure is more damaged, period of vibration is larger.

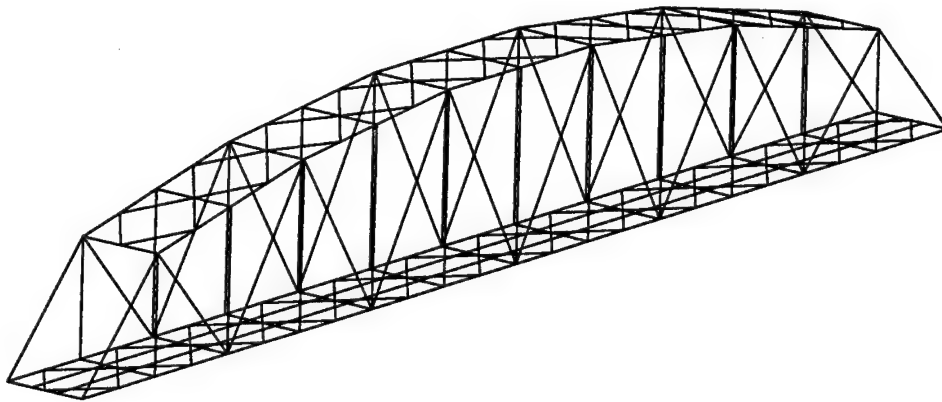


Figure 3: Reconstructed bridge Pivnica-static scheme

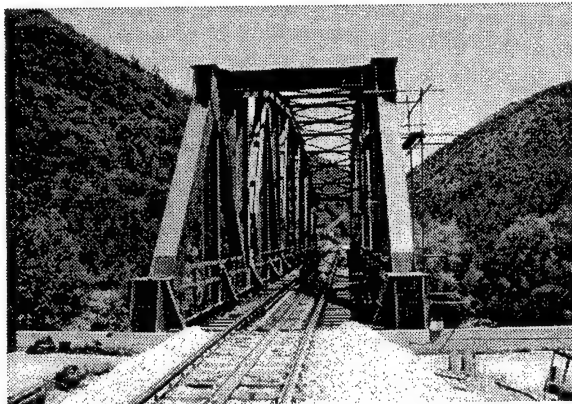


Figure 4: Reconstructed bridge Pivnica

Problem of Fatigue

It is well known that railway bridges are designed against high cycle fatigue. However during the bombardment some elements are destroyed. Neighboring parts suffered low cycle fatigue. It was impossible to change all elements. It is important to check behavior of elements, which suffered low cycle fatigue, and they are still in construction. Especially this is important during the winter when temperatures are well below zero.

4. REFERENCES

- [1] Eshelby, J.D., The determination of the elastic field of an ellipsoidal inclusion and related problems, Proc. Roy. Soc., A241, 376-396, 1957.
- [2] Horii, H. and Nemat-Nasser, S., Overall moduli of solids with microcracks: load induced anisotropy, J. Mech. Phys. Solids, 31, 155-171, 1983.
- [3] Krajcinovic, D., *Damage Mechanics*, Elsevier, Amsterdam, 1996.
- [4] Mura, T., *Micromechanics of defects in solids*, Martinus Nijhoff Publishers, 1987.
- [5] Sumarac, D. and Krajcinovic, D., A mesomechanical model for brittle deformation processes: Part II, J. Appl. Mech., 56, 57-62, 1989.

AUTHOR INDEX

Volume I

- Z. Agioutantis, 191
P. Anagnostopoulos, 39, 66
G. Anastassopoulos, 381
G. Arampatzis, 416
K. Arvanitis, 240
V. Assouti, 72
A. Avdelas, 228
B. Badalouka, 388
G. Badaloukas, 388
R. Barber, 52
A. Bekos, 381
D. Beskos, 210
V. Bontozoglou, 33
A. Boudouvis, 21
I. Chatjigeorgiou, 408
B. Coric, 282
H. Cramer, 298
I. Daniel, 320
J. Demetriou, 102, 108, 121
Y. Dimakopoulos, 84
D. Dimitriou, 102
C. Dimou, 275
A. Elenas, 254
R. Findei, 298
D. Fotiadis, 327
K. Gagas, 72
C. Galiotis, 401
C. Gantes, 261
E. Gdoutos, 320, 394
K. Giannakoglou, 72
P. Giokas, 333
T. Goudoulas, 27
S. Goutianos, 401
M. Hadjinicolaou, 59
N. Hajdin, 178, 282
D. Hatzichristou, 381
G. Hatzigeorgiou, 210
P. Kakavas, 375
N. Kalinderis, 381
A. Kaounis, 72
D. Karalekas, 394
E. Kastrinakis, 27, 96
J. Katsikadelis, 172, 204, 222
I. Kevrekidis, 21
S. Kobayashi, 290
C. Koimtzoglou, 401
P. Koliopoulos, 254
E. Koronaki, 21
V. Kostopoulos, 365
V. Koumousis, 275
C. Kouris, 45
S. Kourkoulis, 339, 348
S. Kourtakis, 184
A. Koutras, 66
D. Krajcinovic, 155
J. Kratochvil, 14
V. Kytopoulos, 339
P. Ladeveze, 140
N. Lagaros, 246
J. Lemaitre, 163
A. Likas, 327
A. Liolios, 254
V. Loukopoulos, 90
D. Lucic, 282
J. Lytras, 381
I. Mademlis, 228
N. Malamataris, 33
R. Mandic, 178
D. Margaris, 114
Lj. Markovic, 146
N. Markovic, 282
S. Marnoutsidis, 228
G. Maugin, 1
S. Mavrakos, 408
G. Michaltsos, 234
V. Moulianitis, 381
H. Mpimpas, 39
K. Nanou-Giannarou, 121
N. Ninis, 348
S. Nychas, 27, 96

- Th. Panidis, 127
 S. Panteliou, 381
 A. Papachristidis, 388
 M. Papadrakakis, 246
 Y. Pappas, 365
 G. Paschalis, 191
 N. Pelekasis, 78
 N. Pnevmatikos, 261
 C. Pourliotis, 108
 I. Prassianakis, 333
 C. Providakis, 184
 D. Ruzic, 146
 M. Sakellari, 254
 T. Salonikios, 267
 E. Sapountzakis, 222
 P. Sarantos, 108
 D. Saravanos, 357
 R. Schapery, 134
 C. Sciammarella, 314
 F. Sciammarella, 314
 S. Seitanis, 66
 M. Sfakianakis, 210
 W. Sharpe Jr., 306
 G. Sideridis, 96
 D. Smyrniaios, 78
 K. Soldatos, 216
 A. Soldatos, 240
 D. Sophianopoulos, 234
 C. Sophocleous, 216
 K. Spiliopoulos, 198
 G. Stavroulakis, 240
 R. de Stefano, 365
 C. Stiakakis, 191
 M. Sunaric, 381
 D. Theodorakopoulos, 210
 C. Theodoropoulos, 21
 M. Titsias, 327
 J. Tsamopoulos, 45, 78, 84
 G. Tsiatas, 172
 Ch. Tzimopoulos, 416
 P. Vafeas, 59
 K. Valanis, 9
 D. Varelis, 357
 L. Vasiliadis, 254
 M. Vlachogiannis, 33
 D. Vlachos, 365
 N. Volakos, 52
 K.-A. Wang, 320
 W. Wunderlich, 298
 J. Yiotis, 204
 E. Zacharenakis, 240
 D. Zacharopoulos, 394
 T. Zervogiannis, 72

Volume II

- M. Abellan, 365
 E. Amanatidou, 149
 I. Andreadis, 177
 N. Anifantis, 52
 H. Antes, 28
 N. Aravas, 149
 Y. Bamnios, 342
 C. Baniotopoulos, 70, 78
 A. Bardzokas, 13
 D. Bardzokas, 22
 J. Bergheau, 365
 D. Beskos, 163, 328
 M. Betti, 78
 D. Bollas, 63
 C. Borri, 78
 D. Briassoulis, 57
 A. Carpinteri, 349
 N. Charalambakis, 276
 A. Charalambopoulos, 216
 C. Charitidis, 40
 B. Chiaia, 349
 K. Chong, 391
 P. Cornetti, 349
 C. Dascalu, 233, 239
 G. Dassios, 109
 D. Davis, 391
 R. de Borst, 365
 B. Demakos, 102
 R. Desmorat, 318
 A. Diamantopoulou, 46

- K. Dimitrakopoulou, 301
 R. Dorgan, 309
 E. Douka, 335
 E. Douka, 342
 P. Entchev, 120
 G. Exadaktylos, 140, 155, 189
 M. Filshtinsky, 22
 D. Fotiadis, 216
 G. Foutsitzi, 216
 G. Frantziskonis, 359
 C. Galiotis, 63
 H. Georgiadis, 289, 295
 D. Georgiou, 90
 E. Gerde, 1
 J. Gilarranz, 371
 P. Grammenoudis, 263
 P. Gupta, 33
 Y. Haddad, 245
 E. Hadjigeorgiou, 239
 D. Homentcovschi, 233, 239
 J. Huyghe, 365
 S. Ichtiaroglou, 379
 J. Jaric, 115
 X. Jiang, 170
 N. Kafoussias, 227
 V. Kalpakides, 126, 239
 T. Kalvouridis, 385
 G. Kamvyssas, 222
 T. Karakasidis, 177, 183
 C. Karakostas, 280
 F. Kariotou, 222
 D. Katsareas, 52
 A. Kekatou, 52
 K. Kishimoto, 115
 M. Kontoleon, 70, 78
 V. Koukoulouyannis, 379
 S. Kourkoulis, 140
 D. Lagoudas, 120
 S. Logothetidis, 40
 G. Lykotrafitis, 295
 G. Manolis, 280
 M. Marder, 1
 R. Masiani, 257
 C. Massalas, 216
 A. Massih, 7
 G. Maugin, 126
 A. Mavraganis, 301
 E. Meletis, 33
 E. Mistakidis, 84, 90, 96
 X. Nie, 33
 M. Omiya, 115
 M. Pagitsas, 46
 O. Panagouli, 84
 D. Panayotounakos, 189, 196
 S. Papargyri-Beskou, 163, 328
 J. Parthenios, 63
 N. Politis, 90
 D. Polyzos, 163, 328
 B. Polyzos, 335
 G. Psarras, 63
 F. Psarros, 385
 O. Rediniotis, 371
 D. Sazou, 46
 E. Schettini, 57
 D. Schick, 269
 V. Sfakiotakis, 52
 V. Singh, 33
 P. Sofronis, 251
 K. Soldatos, 209
 J. Stabouloulou, 133
 G. Stavroulakis, 28
 S. Subramanian, 251
 D. Sumarac, 397
 E. Theotokoglou, 133
 A. Trochidis, 335, 342
 P. Trovalusci, 257
 G. Tsaklidis, 209
 Ch. Tsakmakis, 263, 269
 K. Tsepoura, 163, 328
 E. Tzirtzilakis, 227
 A. Vakakis, 170, 189
 I. Vardoulakis, 140, 289
 A. Varias, 7
 E. Velgaki, 289
 G. Voyiadjis, 309
 T. Wang, 115
 C. Younis, 196
 A. Zobnin, 13
 M. Zygomalas, 70

Volume III

- | | | | |
|------------------|---------------------|---------------|------------|
| E. Aifantis | 29, 35, 67, 73, 102 | M. Latzel | 53 |
| H. Ait-Amokhtar | 22 | S. Lisina | 90 |
| H. Askes | 1 | S. Luding | 53 |
| K. Chihab | 22 | G. Maugin | 67 |
| F. Chmelik | 16 | E. Meletlidou | 67 |
| R. de Borst | 1 | H. Neuhauser | 9, 16 |
| B. Devincre | 47 | A. Nortmann | 9 |
| H. Dierke | 9 | A. Potapov | 85, 90, 96 |
| A. Fernandes | 61 | J. Pouget | 61, 67, 73 |
| I. Groma | 35 | V. Rodyushkin | 85 |
| S. Gromov | 96 | G. Stagika | 35 |
| M. Gutierrez | 1 | P. Sutcliffe | 79 |
| S. Ichtiaroglou | 35 | A. Tokiy | 40 |
| T. Ioannidou | 73 | N. Tokiy | 40 |
| V. Kazhaev | 96 | G. Utkin | 90 |
| F. Klose | 9 | V. Varyukhin | 40 |
| T. Konstantinova | 40 | G. Wells | 1 |
| L. Kubin | 47 | M. Zaiser | 102 |
| D. Kugiumtzis | 29 | A. Ziegenbein | 9, 16 |